SECOND

EUROPEAN CONFERENCE

on

SMART STRUCTURES

and

MATERIALS

Edited

by

A McDonach · P T Gardiner · R S McEwen · B Culshaw

Smart Structures Research Institute

SPIE VOLUME 2361

19941230 021

SMART STRUCTURES AND MATERIALS

McDonach · Gardiner · McEwen · Culshaw

SSRI

SPIE VOLUME 2361

DRAFT SF 298

1. Report Date (dd-mm-yy) 18 Nov 94	2. Report Type conference proceedings	3. Dates covered (from... to) 11-14 Oct 1994
4. Title & subtitle Second European Conference on Smart Structures & Materials		5a. Contract or Grant # N00014--94-J-9030
		5b. Program Element #
6. Author(s) Alaster McDonach, Peter T. Gardiner, Ron S. McEwen, Brian Culshaw, editors		5c. Project # 5202
		5d. Task # EUR
		5e. Work Unit #
7. Performing Organization Name & Address Smart Structures Research Institute, Royal College building, 204 George Street, Glasgow G1 1XW Scotland		8. Performing Organization Report #
9. Sponsoring/Monitoring Agency Name & Address Office of Naval Research Europe PSC 802 BOX 39 FPO AE 09499-0700		10. Monitor Acronym ONREUR
		11. Monitor Report #
12. Distribution/Availability Statement A		
13. Supplementary Notes		

14. Abstract

The future of molecularly based Smart Mateials hinges on the development of integrated technologies addressing synthesis, assembly, shaping etc and some of these are now becoming clear. Even in the bolt on era new technologies will allow issues of commensurate engineering to be addressed.

15. Subject Terms

Smart Structures, Materials Applications

Security Classification of			19. Limitation of Abstract	20. # of Pages	21. Responsible Person (Name and Telephone #)
16. Report Unclassified	17. Abstract Unclassified	18. This Page Unclassified	Unlimited	382	Mike Shear, 011-44-0171-514-4921

Second European Conference on

Smart Structures and Materials

Alaster McDonach
Peter T. Gardiner
Ron S. McEwen
Brian Culshaw
Editors

Held at the Glasgow Hilton
Glasgow, Scotland
12-14 October 1994

DTIC QUALITY INSPECTED 2

Sponsored by
Glasgow Development Agency (UK)
University of Strathclyde (UK)
U.S. Army European Research Office
U.S. European Office of Aerospace Research and Development
Commission of the European Communities, BRITE/EURAM Programme
Smart Structures Research Institute (UK)
U.S. Office of Naval Research

Cosponsored by
Institute of Mechanical Engineering (IMechE)
The Royal Aeronautical Society (UK)
Institute of Materials (UK)
European Association of Composite Materials (EACM)
The Institution of Electrical Engineers (IEE)
SPIE—The International Society for Optical Engineering
The Institute of Physics (IOP)
IEEE (UKRI Section)

A-1

Volume 2361

SPIE (The Society of Photo-Optical Instrumentation Engineers) is a nonprofit society dedicated to the advancement of optical and optoelectronic applied science and technology.

The papers appearing in this book comprise the proceedings of the meeting mentioned on the cover and title page. They reflect the authors' opinions and are published as presented and without change, in the interests of timely dissemination. Their inclusion in this publication does not necessarily constitute endorsement by the editors or by SPIE.

Please use the following format to cite material from this book:
Author(s), "Title of paper," in *Second European Conference on Smart Structures and Materials*, Alaster McDonach, Peter T. Gardiner, Ron S. McEwen, Brian Culshaw, Editors, Proc. SPIE 2361, page numbers (1994).

Library of Congress Catalog Card No. 94-67683
ISBN 0-8194-1700-9

Published by
SPIE—The International Society for Optical Engineering
P.O. Box 10, Bellingham, Washington 98227-0010 USA
Telephone 206/676-3290 (Pacific Time) • Fax 206/647-1445

Copyright ©1994, The Society of Photo-Optical Instrumentation Engineers.

Copying of material in this book for internal or personal use, or for the internal or personal use of specific clients, beyond the fair use provisions granted by the U.S. Copyright Law is authorized by SPIE subject to payment of copying fees. The Transactional Reporting Service base fee for this volume is $6.00 per article (or portion thereof), which should be paid directly to the Copyright Clearance Center (CCC), 222 Rosewood Drive, Danvers, MA 01923. Other copying for republication, resale, advertising or promotion, or any form of systematic or multiple reproduction of any material in this book is prohibited except with permission in writing from the publisher. The CCC fee code is 0-8194-1700-9/94/$6.00.

The content of the information presented in these proceedings and at the conference does not necessarily reflect the position or the policy of the U.S. Government or any other sponsor and no official endorsement should be inferred.

Printed in the United States of America.

Contents

xi *Technical Committee and Chairman*
xiii *Local Organising Committee*
xv *Welcome Address*

PLENARY SESSION

2 **Smart materials, surfaces transforms, and interfaces: the commensurate engineering dimension (Invited Paper)**
D. T. Clark, EPSRC RUSTI and Surfaces Transforms Ltd. (UK)

11 **Smart structures research in aerospace engineering (Invited Paper)**
E. J. Breitbach, R. Lammering, J. Melcher, F. Nitzsche, German Aerospace Research Establishment (FRG)

19 **Polymer electromechanics: mechanical sensing and actuation properties of organic macromolecular systems (Invited Paper)**
D. De Rossi, Univ. of Pisa (Italy)

27 **Intelligent materials for civil engineering: proposal of ken materials (Invited Paper)**
H. Yanagida, Univ. of Tokyo (Japan); M. Sugita, Shimizu Corp. (Japan); N. Muto, Sogo Security Services Co., Ltd. (Japan)

31 **Smart hydrogels in devices (Invited Paper)**
N. B. Graham, Univ. of Strathclyde (UK)

SESSION 1

36 **Fault detection employing transducer optimisation procedures (Invited Paper)**
K. Worden, G. R. Tomlinson, A. P. Burrows, Univ. of Manchester (UK)

47 **Cellular automaton generating topological structures**
N. Inou, N. Shimotai, T. Uesugi, Tokyo Institute of Technology (Japan)

51 **Recursive architecture for large-scale adaptive system**
K. Hanahara, Y. Sugiyama, Univ. of Osaka Prefecture (Japan)

55 **Fault detection in a mechanical system by neural networks**
M. D. Thomas, S. J. Flockton, Univ. of London (UK)

59 **Intelligent aircraft structures: a technique to verify sensor integrity**
P. D. Dean, Lockheed Missiles & Space Co., Inc. (USA)

63 **Fuzzy neural network for in-process error compensation**
E. Zhou, Bolton Institute of Higher Education (UK); D. K. Harrison, D. Link, Staffordshire Univ. (UK); R. Healey, Bolton Institute of Higher Education (UK)

67 **Energy evaluation on bounded nonlinear control laws for civil engineering applications**
V. Gattulli, Univ. di Roma "La Sapienza" (Italy)

71 **Stress distribution in a simple adaptive structure actuated in bending mode**
R. Barboni, P. Gaudenzi, G. Strambi, Univ. di Roma "La Sapienza" (Italy)

75 **Asymptotic analysis of thin space structures**
D. Cioranescu, Lab. Analyse Numerique/CNRS (France); J. Saint Jean Paulin, Univ. de Metz-Mathematiques (France)

SESSION 2

80 **Research need for piezoactuators in adaptive structures (Invited Paper)**
P. Jänker, W. Martin, Daimler Benz AG (FRG)

86 **Results on a dynamic model of phase transitions in shape memory alloys with nonconvex Landau-Ginzburg free energy**
R. D. Spies, Conicet—Univ. Nacional del Litoral (Argentina)

90 **Smart structures with shape memory alloy actuators**
R. Lammering, German Aerospace Research Establishment (FRG)

94 **Cyclic response of shape memory alloy smart composite beams**
C. M. Friend, N. B. Morgan, Cranfield Univ. (UK)

98 **Effect of prestrain on the actuation performance of embedded shape memory alloy wires**
C. J. Doran, Defence Research Agency (UK)

102 **Control surface mirror with local heaters**
V. V. Reznichenko, V. Kulagina, M. Lutinskaya, Yu. Leonov, S.I. Vavilov State Optical Institute (Russia)

109 **Characterisation of static actuation behaviour of encapsulated PZT**
C. J. Doran, Defence Research Agency (UK); R. J. Butler, ADC Ltd.—Newport Pagnell (UK)

113 **Characterization of actuator-based materials using optical fiber sensors**
D. Sun, M. K. Burford, K. A. Murphy, R. O. Claus, Virginia Polytechnic Institute and State Univ. (USA); J. A. Greene, T. A. Tran, Fiber and Sensor Technologies, Inc. (USA); G. P. Carman, Univ. of California/Los Angeles (USA)

117 **Progress towards a robust user-friendly system for active structural damping**
S. S. J. Roberts, AEA Technology (UK); R. J. Butler, ADC Ltd. (UK); R. Davidson, AEA Technology (UK)

121 **Shape control of adaptive composite reflector panels**
R. Paradies, W. J. Elspass, K. Schindler, Swiss Federal Institute of Technology (Switzerland)

SESSION 3

128 **Electrical potential techniques for damage sensing in composite structures**
C. Thiagarajan, Cranfield Univ. (UK); I. M. Sturland, D. Tunnicliffe, BAE Sowerby Research Ctr. (UK); P. E. Irving, Cranfield Univ. (UK)

132 **Applications of a new solid state structural health monitoring technology**
L. D. Thompson, B. D. Westermo, Strain Monitor Systems, Inc. (USA)

136 **Self-sensing composites for smart damage detection using electrical properties**
M. Kemp, Defence Research Agency (UK)

140 **Monitoring vibration of sandwich plates and delamination detection with fibre optic sensors**
A. E. Jensen, Norwegian Defence Research Establishment; H. Støroy, F. Irgens, O. J. Løkberg, Univ. of Trondheim (Norway); G. Wang, Norwegian Defence Research Establishment

144 **Fiber sensors for monitoring structural strain and cracks**
K. F. Voss, K. H. Wanser, California State Univ./Fullerton (USA)

148 **Remote monitoring of instrumented structures using the Internet information superhighway**
P. L. Fuhr, D. R. Huston, T. P. Ambrose, Univ. of Vermont (USA)

152 **Smart aircraft by continuous condition monitoring of aircraft structures and components**
D. Allaei, QRDC, Inc. (USA)

154 **Monitoring of bridges subject to transversal cracks**
C. Abdunur, Lab. Central des Ponts et Chaussées (France)

SESSION 4

162 **Bragg grating fiber optic sensing for bridges and other structures (Invited Paper)**
R. M. Measures, A. T. Alavie, R. Maaskant, S. H. Huang, M. LeBlanc, Univ. of Toronto (Canada)

168 **Influence of concrete and alkaline solutions on different surfaces of optical fibres for sensors**
W. R. Habel, M. Höpcke, F. Basedau, H. Polster, Institute for Maintenance and Modernization of Structures (FRG)

172 **Design and operation of a galvanic sensor for in-service monitoring of the corrosion of steel in concrete**
N. R. Short, C. L. Page, G. K. Glass, Aston Univ. (UK)

176 **Determination of structural parameters concerning load capacity based on fibre Fabry-Perot interferometers**
W. R. Habel, D. Hofmann, Institute for Maintenance and Modernization of Structures (FRG)

180 **Strain measurements in reinforced concrete walls during the hydration reaction by means of embedded fibre interferometers**
W. R. Habel, D. Hofmann, Institute for Maintenance and Modernization of Structures (FRG)

SESSION 5

186 **Optical fibre grout-flow monitor for post-tensioned reinforced tendon ducts**
W. C. Michie, I. McKenzie, B. Culshaw, P. T. Gardiner, A. McGown, Univ. of Strathclyde (UK)

190 **Active response control using a rotor fin for wind-induced structural vibrations**
Y. Mukai, E. Tachibana, Y. Inoue, Osaka Univ. (Japan)

194 **Global and local health monitoring of civil structures using smart ferroelectric sensors and electronically steerable antennas**
V. K. Varadan, V. V. Varadan, The Pennsylvania State Univ. (USA)

198 **Vibration and noise control in civil structures by smart design**
D. Allaei, QRDC, Inc. (USA)

202 **Monitoring techniques facilitating the long-term assessment of structures**
I. L. Curtis, M. J. Dill, Laing Technology Group: Structural Monitoring and Testing Service (UK)

206 **Application of fuzzy logic to active structural control**
F. Casciati, L. Faravelli, T. Yao, Univ. of Pavia (Italy)

210 **Fiber optic smart structure system for natural structures**
E. Udd, Blue Road Research, Inc. (USA)

SESSION 6

216 **Low-coherence interferometry for the monitoring of civil engineering structures**
D. Inaudi, Swiss Federal Institute of Technology; A. Elamari, Geneva Univ. (Switzerland); S. Vurpillot, Swiss Federal Institute of Technology

220 **Thermal expansion measurements of a concrete structure by embedded fiber optic: an effective example of simultaneous strain-temperature detection**
V. Gusmeroli, M. Martinelli, A. Barberis, CISE Tecnologie Innovative (Italy); P. Escobar, ENEL/Ctr. Ricerca Idraulica e Strutturale (Italy); P. Morabito, CISE Tecnologie Innovative (Italy)

224 **Embedded optical fibre strain gauges for civil engineering: application to concrete monitoring**
J. J. Guerin, M. Lequime, Bertin & Cie (France); E. Toppani, M. Leygonie, EDF/Direction de l'Equipement/TEGG (France); D. Chauvel, EDF/Direction de l'Equipement/SEPTEN (France)

228 **Demonstration of twisted polarimetric optical fiber sensor embedded in carbon-epoxy composite**
H. D. Simonsen, Per Udsen Co. Aircraft Industry A/S (Denmark)

232 **Average strain measurement in a structure by beat-length determination in homogeneous zones**
S. Téral, Alcatel Cable (France); J.-M. Caussignac, Public Works Research Lab./LCPC (France); A. Tardy, M. Jurczyszyn, Alcatel Alsthom Recherche (France)

236 **Microwave subcarrier optical fiber strain sensor**
B. Noharet, M. Turpin, Thomson-CSF LCR (France); J. Chazelas, P. Bonniau, Thomson-CSF RCM (France); D. Walsh, W. C. Michie, B. Culshaw, Univ. of Strathclyde (UK)

SESSION 7

242 **Overview of smart structure concepts for helicopter rotor control**
J. P. Narkiewicz, G. T. S. Done, City Univ. (UK)

246 **Modal parameter identification of controlled flexible space structures**
T. Kasai, K. Komatsu, M. Sano, National Aerospace Lab. (Japan)

250 **Feedback controllers for broadband active noise reduction**
B. Petitjean, I. Legrain, ONERA (France)

254 **Active damping control systems for satellites**
C. R. Pietsch, H. Baier, Dornier GmbH (FRG)

258 **Machine tool chatter reduction via active structural control**
S. O'Regan, J. Miesner, R. Aiken, AT&T Advanced Technology Systems (USA); A. Packman, United Technologies Pratt & Whitney (USA); E. A. Unver, AT&T Advanced Technology Systems (USA); S. Akerley, United Technologies Pratt & Whitney (USA)

SESSION 8

264 **Potentials and problems in space applications of smart structures technology**
D. C. G. Eaton, ESA/ESTEC (Netherlands); D. P. Bashford, ERA Technology Ltd. (Netherlands)

269 **Dynamic analysis on smart materials**
W. B. Wu, Chang Gung College of Medicine and Technology (Taiwan)

273 **Efficient use of induced-strain actuators in aeroelastic active control**
V. Giurgiutiu, Z. A. Chaudhry, C. A. Rogers, Virginia Polytechnic Institute and State Univ. (USA)

277 **Smart structure application for the Challenger aircraft**
L. Grenier, National Defence Headquarters (Canada); F. A. Blaha, Canadian Marconi Co.

282 **Remotely interrogated sensor electronics (RISE) for smart structures applications**
W. B. Spillman, Jr., S. Durkee, W. W. Kuhns, BFGoodrich Aerospace/Simmonds Precision Aircraft Systems (USA)

286 **Dynamic load monitoring of composite structures using fiber optic interferometric strain gauges**
N. Fürstenau, W. Schmidt, D. D. Janzen, R. Schütze, H. C. Goetting, German Aerospace Research Establishment (FRG)

290 **Fibre Bragg grating strain sensors for aerospace smart structures**
P. D. Foote, British Aerospace Operations Ltd. (UK)

SESSION 9

296 **Enabling architecture**
C. Price, Cedric Price Architects (UK)

297 **Designing adaptive systems for buildings**
A. Adekola, M. Rastogi, Innovative Design Systems (UK)

301 **New approach to inexpensive printed electrochromic displays**
J. P. Coleman, Monsanto Chemical Group (USA)

305 **Potential of incorporated accelerometers for the in-vivo assessment of hip-stem loosening**
G. Lowet, G. Van der Perre, Katholieke Univ. Leuven (Belgium)

307 **Smart consumer products with a pathfinder product development strategy**
A. Robertson, De Montfort Univ. (UK)

312 **Single-crystal indicators of fatigue and plastic deformation damage**
Yu. G. Gordienko, E. E. Zasimchuk, Institute of Physics for Metals (Ukraine)

316 **Stress-fail indicator for agricultural packaging materials**
A. McDonach, Univ. of Strathclyde (UK); J. Nichols, Agripac Ltd. (UK)

320 **Designing building skins as energy-efficient modulators**
A. Adekola, M. Rastogi, Innovative Design Systems (UK)

324 **Current research in timed release of repair chemicals from fibers into matrices**
C. M. Dry, Univ. of Illinois/Urbana-Champaign (USA)

SESSION 10

330 **Electro-optomechanical design of fiber optic smart structures (Invited Paper)**
J. S. Sirkis, Univ. of Maryland/College Park (USA)

338 **Distributed strain sensing with fiber Bragg grating arrays embedded in Continuous Resin Transfer Molding (CRTM)™ composites**
E. J. Friebele, C. G. Askins, M. A. Putnam, Naval Research Lab. (USA); J. Florio, Jr., A. A. Fosha, Jr., R. P. Donti, C. D. Mosley, BP Chemicals, Inc. (USA)

342 **Structural strain mapping using a wavelength/time-division-addressed fiber Bragg grating array**
M. A. Davis, D. G. Bellemore, A. D. Kersey, Naval Research Lab. (USA)

346 **Finite element modeling of three-dimensional integral sensors for the control of aeroelastic structures**
M. N. Abdul-Wahed, Aleppo Univ. (Syria); T. A. Weisshaar, Purdue Univ. (USA)

350 **Eight-element time-division multiplexed fiber grating sensor array with integrated-optic wavelength discriminator**
T. A. Berkoff, SFA, Inc.; A. D. Kersey, Naval Research Lab. (USA)

354 **Novel fibre optic stress/strain sensor using the near-infrared SPATE effect (FONI-SPATE)**
J. P. Dakin, J. L. Cruz, P. A. S. Reed, I. Sinclair, Univ. of Southampton (UK)

358 **Ferroelectric ceramic and epoxy composite films as pyroelectric detectors**
M. P. Wenger, Univ. of Wales (UK); P. Blanas, R. J. Shuford, U.S. Army Research Lab. (USA); D. K. Das-Gupta, Univ. of Wales (UK)

362 **Fibre optic sensor of electrostatic field with mechanical resonator**
A. V. Churenkov, M. A. Skorobogatyi, A. D. Loiko, Moscow Institute of Physics and Technology (Russia)

366 **Multiplexed fibre optic system for both local and spatially averaged strain monitoring**
H. Geiger, M.-G. Xu, M. A. Longstaff-Tyrell, J. P. Dakin, Univ. of Southampton (UK); N. C. Eaton, Consultant to Westland Aerospace (UK); P. J. Chivers, Westland Aerospace (UK)

371 **Finite element analysis of embedded optical fiber sensors**
N. C. Eaton, Consultant to Westland Aerospace (UK); R. C. Drew, Duetto Ltd. (UK); H. Geiger, Univ. of Southampton (UK); P. J. Chivers, Westland Aerospace (UK); J. P. Dakin, Univ. of Southampton (UK)

375 **Smart integrated transducer for an optoelectronic (bio-) chemical sensor**
A. A. Beloglazov, P. I. Nikitin, General Physics Institute (Russia)

379 **Analysis of the local stress field in a composite material with an embedded extrinsic Fabry-Perot interferometer (EFPI) sensor**
K. Levin, S. Nilsson, FFA/Aeronautical Research Institute of Sweden

383 *Author Index*

Second European Conference on Smart Structures & Materials
12-14 October 1994, Glasgow Hilton

TECHNICAL COMMITTEE & CHAIRMAN

Conference Chairman:
Prof. R.S. McEwen
Sowerby Research Centre
British Aerospace plc, UK

Dr. Gary Anderson
US Army Research Office
USA

Dr. Christian Boller
Daimler Benz TEA
GERMANY

Prof. F. Casciati
Dept of Structural Mechanics
University of Pavia, ITALY

Mr. Jean-Marie Caussignac
Laboratoire Central des Ponts et Chaussées (LCPC), FRANCE

Dr. Richard O. Claus
Fibre & Electro-Optic Research Centre, Virginia Poly., USA

Prof. L. Eric Cross
Materials Research Laboratory
Pennsylvania State Univ., USA

Dr. Roger Davidson
AEA Technology
UK

Prof. Danilo de Rossi
Centro 'E. Piaggio'
ITALY

Mr. Alan Dodgson
M^2 Technology Limited
UK

Mr. David C.G. Eaton
European Space Agency
The NETHERLANDS

Dr. Clifford M. Friend
Smart Materials Group
Cranfield University, UK

Mr. R.W. Griffiths
G2 Systems Corporation
USA

Mr. James Innes
Scottish Office Roads Directorate, UK

Dr. A. Iqbal
Ciba-Geigy Limited
SWITZERLAND

Dr. G. Jeronimidis
Department of Engineering
University of Reading, UK

Prof. Per Kartvedt
Department of Architecture
University of Strathclyde, UK

Prof. A. Kelly
University of Surrey
UK

Dr. Gareth J. Knowles
Active Systems Inc.
USA

Dr. Alain Le Mehauté
Institut Supérieur des Materiaux da Nans
FRANCE

Mr. Michel Lequime
Société Bertin
FRANCE

Prof. Mario Martinelli
Electronics & Informations Dept
Politecnico di Milano, ITALY

Prof. Sami F. Masri
Dept. Civil & Mechanical Eng.
University of Southern California, USA

Prof. Yuji Matsuzaki Ph.D
Dept. of Aerospace Engineering
Nagoya University, JAPAN

Prof. Alan McGown
Department of Civil Engineering
University of Strathclyde, UK

Dr. Ray M. Measures
Institute for Aerospace Studies
Univ. of Toronto, CANADA

Prof. Roger Ohayon
Chair of Mechanics
CNAM/ONERA, FRANCE

Mr. Richard T. Potter
Defence Research Agency - Structural Materials Centre, UK

Dr. Steven J. Prosser
Lucas Advanced Engineering Centre, UK

Dr. Craig A. Rogers
C I M S S
Virginia Polytechnic, USA

Prof. Annamaria Scheggi
IROE CNR
ITALY

Dr. W.B. Spillman Jr.
BF Goodrich Aerospace
USA

Prof. Kiyoshi Takahashi
Dept of Physical Electronics
Tokyo Institute of Technology, JAPAN

Mr. Marc Turpin
Thomson-CSF
FRANCE

Mr. Eric Udd
Blue Road Research
USA

Prof. Sadayuki Ujihashi
Faculty of Engineering
Tokyo Institute of Technology
JAPAN

Prof. Vijay Varadan
Dept. of Engineering Science & Mechanics, Pennsylvania State University, USA

Mr. Nabil Zahlan
ICI Materials Research Centre
UK

Second European Conference on Smart Structures & Materials
12-14 October 1994, Glasgow Hilton

LOCAL ORGANISING COMMITTEE

Prof. Brian Culshaw
Optoelectronics Division, EEE
University of Strathclyde
UK

Mr. Peter Gardiner
Director, Smart Structures Research Institute
University of Strathclyde
UK

Dr. Alaster McDonach
Smart Structures Research Institute
University of Strathclyde
UK

Mrs. Linda Paterson
(Conference Secretary)
Smart Structures Research Institute
University of Strathclyde
UK

Welcome Address.....

Scotland has long been a country associated with engineering. If popular literature and films are to be believed, the chief engineer of every ship, in the English-speaking world at least, from the humblest Clyde steamer to the star-ship Enterprise, is a Scotsman. Stephenson and Watt testify to the inventive as well as the operational prowess of our indigenous engineerings, while Kelvin's fundamental sciences underlying engineering have also received some attention among these hills and valleys.

Contemporary science and technology have made it increasingly apparent that engineering need not exclusively associate different functions with different classes of material or with different elements of structure. Radomes, transparent conductors and Goretex breathable waterproof material have long been examples of multifunctionality. New methods of integrating different materials and sub-structural units are creating a new and often more holistic approach to engineering. We now perceive the ultimate fulfilment of this process to lie in structures and machines with sensing, actuation and control functions integrated totally with the fabric of the artefact. The term Smart Structures and Materials encapsulates this concept.

The taxonomy of Science and Engineering is infinitely varied, but the canny folks of Strathclyde undoubtedly took a trick when they coined this term for their Institute a little over three years ago. Scientists and Engineers of the rest of the world, you are welcome to this meeting of minds on one of the most interesting and perhaps one of the most significant developments of contemporary technology. While continuing as in our first conference to examine the underlying science, in this second conference, we increase our exploration of the practical benefits which can be obtained by the application of the Smart Structures and Materials concept.

In the two and a half years since we first met here, the world has moved along and with it the emphasis of smart structures and material applications. Many in the aerospace industry still continue to worry at the prospect of still more layers of sophistication and about how smart systems will agree with their existing technology. Now that the performance dominated, high-tech military game is subjugated as never before to Adam Smith's "dismal science", aerospace activity in this field seems less reported. Doubtless activity continues on topics which companies do not like to discuss at conferences.

Space scientists and engineers are used to waiting half their lives for the fulfilment of their plans. Their enthusiastic vibrations remain undamped.

But the Smart Structures and Materials concept has many strings to its bow. Cunningly implemented, it can enhance safety and prolong performance and thereby save money! It is not surprising therefore that smart concepts are invading the more down-to-earth world of buildings and bags, medicine and manufacturing. Examples of these applications will be found in this conference, affirmation that the subject is moving along with a life of its own.

We are here to enjoy all of that. Listen, read the posters, discuss, argue - contribute actively to the festival of invention. Ample time and opportunity has been set aside for this. Also an ample supply of that smartest of Scottish spirits, which will untie the tongue of the dourest Scotsman, the most silent Scandinavian or the most reserved Russian is to hand. But there is more to Scotland than whisky, bagpipes and golf. Enjoy too the treasures afforded by this city and the glory that is the Scottish countryside. Get out and walk in the hills.

Conferences take organisation and hard work and thanks is due to all who gave of their efforts ungrudgingly - the Technical Programme Committee and the dedicated team at the Institute, especially Peter Gardiner, Brian Culshaw, Alaster McDonach, Aileen Mitchell and Linda Paterson. But ultimately, the success of a conference is determined by the enthusiasm of its attendees and the quality of their contributions. I thank you all for coming and venture to hope that you will always associate your professional enjoyment with this small north European country and will keep supporting our meetings in the years ahead.

Prof. R.S. McEwen, Conference Chairman

PLENARY SESSION

Paper presented at the Second European Conf. on Smart Structures and Materials, Glasgow 1994, Plenary Session

SMART Materials; Surfaces Transforms and Interfaces; the Commensurate Engineering Dimension.

Professor D T Clark[+]

Scientific Director, EPSRC RUSTI, DRAL
+ Chairman of Surfaces Transforms Ltd

ABSTRACT

The future of molecularly based Smart Materials hinges on the development of integrated technologies addressing synthesis, assembly, shaping etc and some of these are now becoming clear. Even in the bolt on era new technologies will allow issues of commensurate engineering to be addressed.

0-8194-1700-9/94/$6.00

1. INTRODUCTION

In any paper dealing with signposts for the future particularly from a "Technology Push" perspective it is perhaps appropriate to start with the strategic vision.

The five ages of SMART materials have been described elsewhere [1] but it is nonetheless useful to look at the stepping stones to the eventual goal of having a molecularly based capability of synthesis, assembly, shaping to a self repairing environmentally adaptive structure and this is indicated in figure 1

1st generation
- Hybrid approach
- "Bolt on" actuators, sensors etc
- Use what is available
- External processing of data to generate knowledge
- Incommensurate engineering as an issue (the CRAY driven microstructure syndrome)

2nd generation
- Hybrid approach
- "Bolt on" actuators, sensors etc
- External data reductions to knowledge
- Elements of incommensurate engineering

3rd generation
- Hybrid microsensors, actuators, key enablers, LIGA etc.
- Some "in structure" knowledge generation
- Issues of commensurate engineering addressed.

4th generation
- Optical preprocessing of spatially resolved data AMACRONICS writ large.
- Hybrid approach
- Analogues of Nature's communications/intelligence start to emerge

5th generation
- Molecular level design and integration
- Spatially and temporally resolved chemistry direct to functional shapes
- Issues of spatial and temporal modification to activate response and repair addressed.
- Tranform concept (interface engineering)

Figure 1 - The Five ages of Smart Materials Development

Three things follow from this. Firstly, since there is no intermediate stage "products" we will need to move towards a "parallel" integration of synthesis, assembly, characterisation, modelling, market, application (cf figure2) rather than the piecemeal development we see now, in which the engineered solution is decoupled from the materials system development. This gives rise to the issues of incommensurate engineering so evident in today's rudimentary structures where a "bolt-on use what's available" philosophy inevitably prevails.

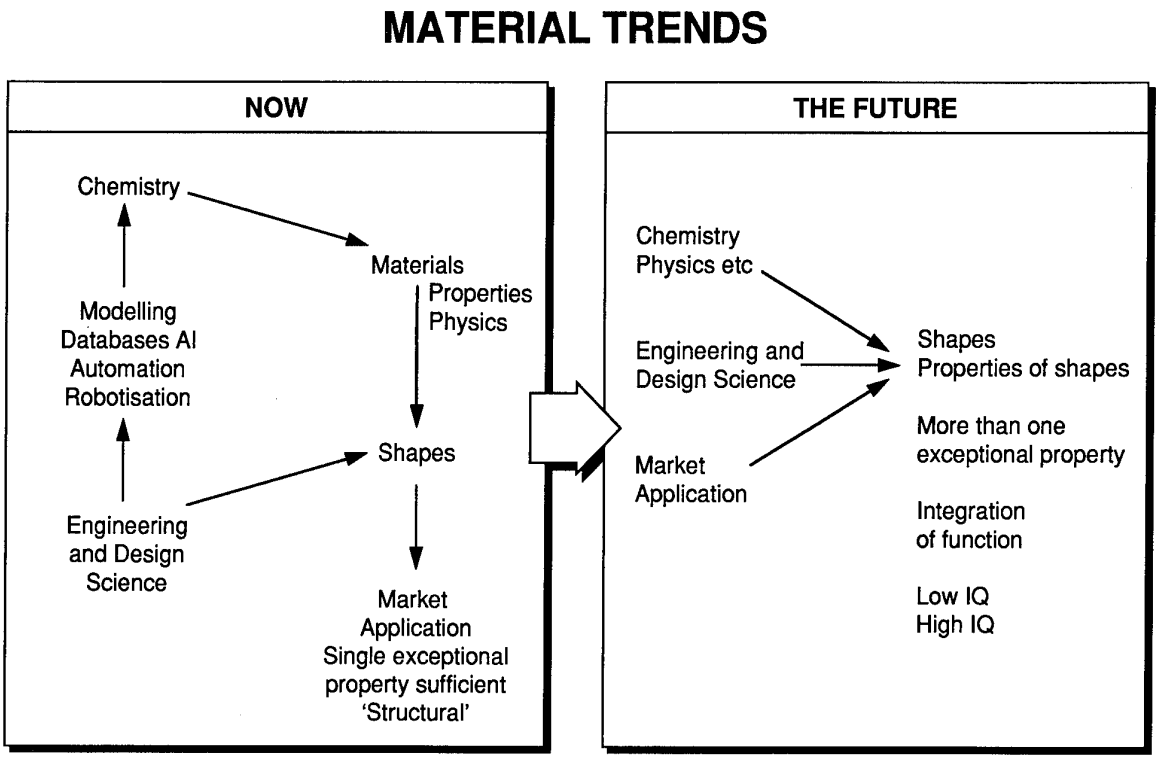

Figure 2: Comparison of the future "parallel" engineering of approaches to materials research compared with the current sequential approaches.

Secondly, new unit operations need to be developed to address issues of spatially and temporally resolved synthesis direct to shapes the issues perhaps being somewhat clearer by reference to figure 3.

Thirdly, when issues of materials system design are considered, methodologies need to be developed to address the linkage between the chemistry and physics size scales dominating as they do the intrinsic properties of materials with the engineering size scales linking as they do intrinsic properties with extrinsic and intrinsic properties of shapes and significant developments are occurring in this direction in the meoscopic modelling area.

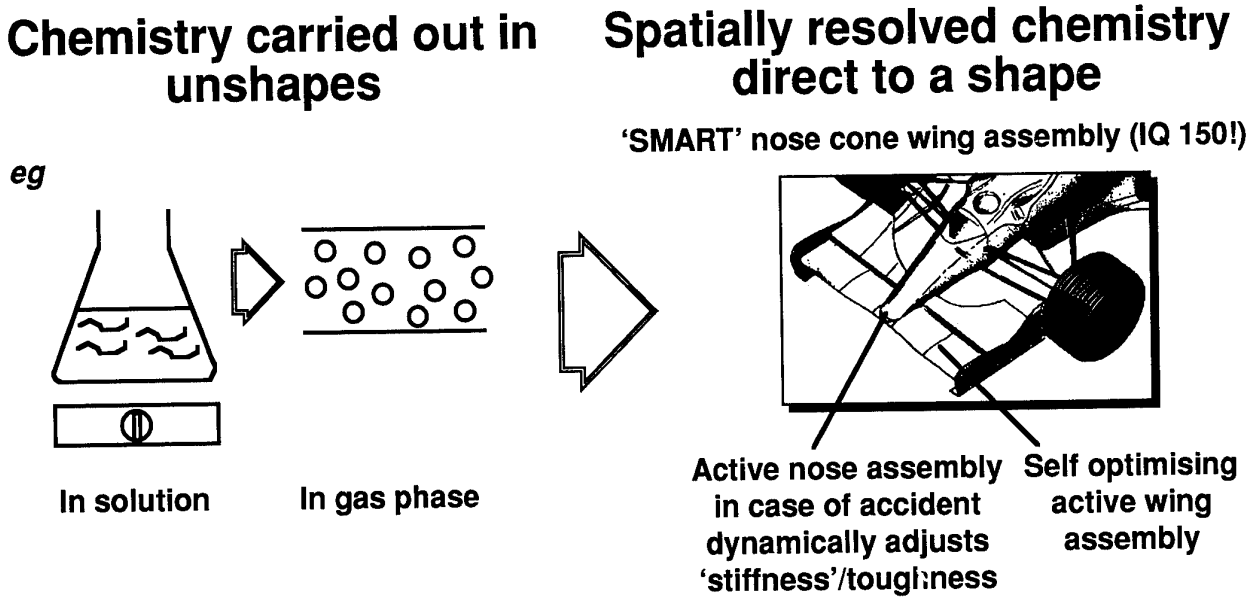

Figure 3: From the era of chemistry in unshapes to spatially resolved chemistry to shapes.

With this background we now consider in outline some of the key enabling scientific and technological developments that are required. We should however also briefly reflect on the "Market Pull". In many senses we are in the "pre walkman era" in that the level of understanding of the opportunities provided by integrating function in materials systems design is at a low level of appreciation. Before Walkmans appeared from the technology push of electronics miniaturisation, the "market" had not appreciated the possibilities for recorded media "on the move" and a catalytic induction period was therefore necessary to create the market. Until there is a similar reconceptionalisation of how an engineered solution to a market need is enormously empowered by thinking in terms of an integrated SMART structure, progress will still be in the hands of a limited community of enthusiasts. In recognising this it is already clear (and will be a major issue in Technology development for the future) that "materials supply" will not be a viable business position since synthesis and assembly will utlimately address the design, shaping and functional issues of the SMART Materials systems at the outset. The long term winners will need to be vertically integrated since the materials design ultimately at the molecular level will be directly tied to production of the active materials system/shape. This will either be done solely in house or more likely via strategic partnerships which at the basic science end will almost certainly provide exciting new opportunities for entrepreneurial academics.

Although we may anticipate that aspects of "smart technology" will be all pervuasive by the year 2020, its introduction will almost certainly be via a two pronged attack. Firstly,

in low volume high added value specialist applications and secondly in volume demonstrators in the sports/consumer arena eg the Smart Golf Club. This route will win the technology, public acceptance, with materials systems being viewed as "more natural", (employing as they will many of natures design paradigms), and will also provide a cash flywheel for the niche applications that genuinely provide new opportunities for the designer engineer.

2. THE ENABLING SCIENCE AND TECHNOLOGIES

In a short article such as this we merely highlight some of the key developments and their relationship to the interests of the current symposium.

As a starting point figure 4 outlines some of the enabling technologies to which must be added the important spatially resolved characterisation capability particularly of the important surface interface structures which in an anistropically designed smart materials system of the future constitutes a significant fraction of the total structure.

Synthesis Assembly	**Spatial and temporal data generation**	**Data to knowledge**	**Activation**	**Self Repair**
○ Self Assembly ○ Re-entrant structures ○ Reactive Hot Isostatic Processing ○ High Rate Laser Processing ○ 4th state techniques ○ Conducting polymers	○ Electronic ○ Ionic ○ Photonic interrogation	○ Optical pre and post processing AMACRONICS ○ Neural techniques ○ Ionic carrier recognition	○ Micromecahnics LIGA ○ Negative Poisson ○ Piezo volume pressure activation	○ *In situ* laser processing ○ Nanotube delivery systems
Computational Modelling : the meososcopic dimension				

Figure 4 : Some enabling technologies

If we start with synthesis coupled with assembly then the scope and scale of the problem can perhaps be illustrated by means of the hypothetical Smart Materials structure illustrated in Figure 5.

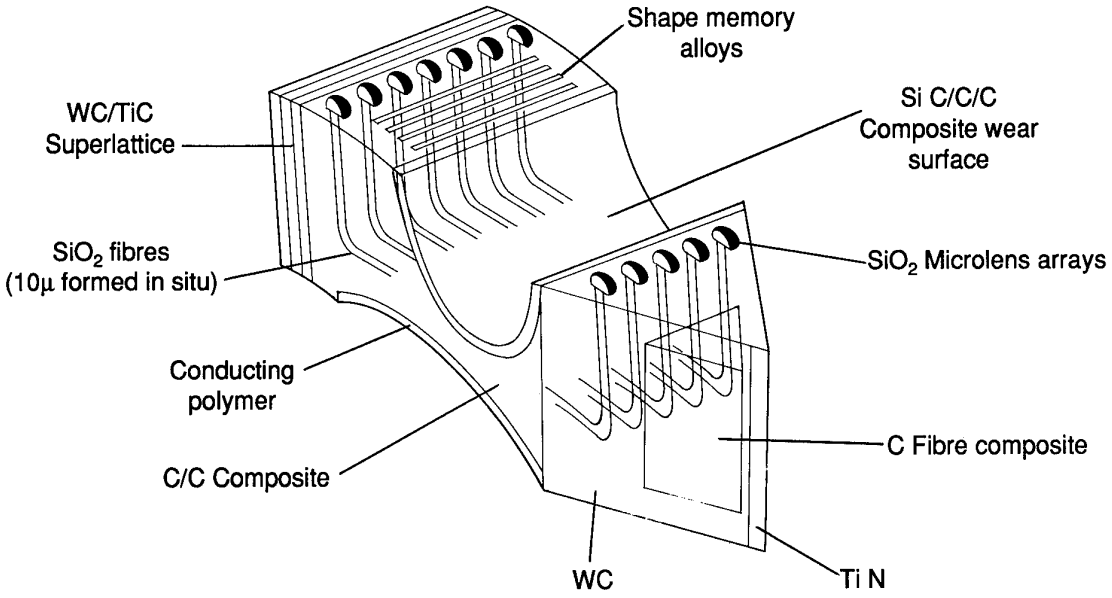

Figure 5 Idealised Spatially Resolved Materials Systems

In essence one would like to be able to synthesize/assemble this structure in a limited number of unit operations and in addition to the importance in small scale structures of self assembly, we highlight briefly the exciting opportunities for novel spatially resolved synthesis at a variety of scales provided by four new technologies.

- Reactive Hot Isostatic Processing RHIP
- High Rate Laser Synthesis HRLS
- High Rate Plasma (4th state) Deposition via cascaded Arcs and Itensified ICPs HRPD
- Unbalanced magnetron sputtering UBMS

Further details of the various techniques can be found elsewhere [2,3,4] and we merely note here the potential of each technique for novel synthesis/assembly either in their own right or as a precursor to a genuine ability to shape whilst reactively processing as for example the RHIP technology.

The emphasis therefore is less on small molecule assembly to polymers but on the broader issue of new strategies for creating "shaped" interfaces with other materials.

This is indicated schematically in figure 6.

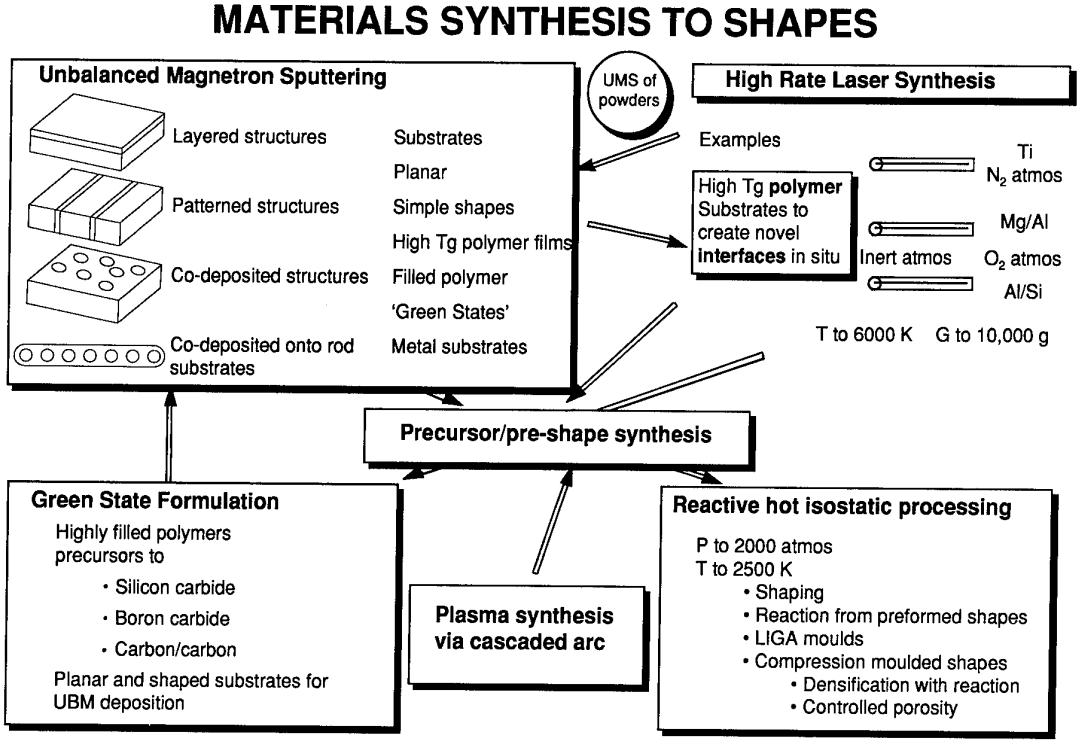

Figure 6 Spatially Resolved Materials Synthesis- Some New Techniques

Unbalanced Magnetron Sputtering

Important developments in magnetron sputtering now allows the high rate (>2 $\mu n\ min^{-1}$) deposition of a variety of metals and ceramics onto a wide variety of substrates. The close control of interface stoichiometry which can now be achieved and the ability to make kinetically stable metallic alloys provides an exciting launching pad for the creation of new interfaces not previously available via conventional techniques. Two examples [3] illustrating this are the preparation of polymer/TiB coated ignition delay lines for explosive and automative airbag applications and the synthesis of novel Al/Mg alloys for "bright" corrosion resistant fasteners for aerospace applications. With the use of patterns and multiple targets, layered and co deposited patterns may now be produced onto a variety of substrates including polymers.

Plasma Deposition

Whilst plasma polymerisation and the use of plasma for deposition of high temperature (eg inorganic) materials on low temperature substrates (eg polymers) have been demonstrated at small scales (eg postage stamp) and low rates (AS sec^{-1}), the development of novel plasma technology particularly cascaded arcs and intensified ICP's potentially offer the hope of cost effective plasma deposition as a basis for technological exploitations with deposition rates .20 μn^{-1} being achievable. The creation of new intrinsic properties as well as important extrinsic properties such as barrier to permeation become feasible with these developments [4].

High Rate Laser Synthesis

Although high rate annealing and texturing of eg metal surfaces by high powered lasers has reached industrial scale exploitation the more interesting possibility of coupling a CO_2 laser, as a directed heat source, with a methodology for preshape fabrication (eg by centrifugal processing) has only recently been demonstrated and potentially offers new routes to polymer to metal, ceramic and semiconductor interface fabrication, and again potentially as a precursor to RHIP shaping [2]. Since lasers can rapidly be moved spatially controlled deposition also becomes a possibility with the in principle ability to again make patterned depositions without a mask. The rapidly developing field of Free Electron Lasers provides great scope for cost effective materials synthesis via such routes longer term.

2.1. Spatially Resolved Data to Knowledge Transduction

The existing generation of smart materials make extensive use of optical fibre technology however the issue of spatially resolved data to knowledge transduction requires massively parallel processing/pattern recognition and recent developments in binary optics/AMACRONICS look to provide a solution to this problem in somewhat of an analogy with optical preprocessing associated with eye structures found in nature [5]. Polymeric materials with the ability to rapidly emboss etc offer some novel design opportunities in this area and the related problem of storage and retrieval is also being addressed eg with spectral hole burning and ultimately molecular electronics levels of integration with a terrabyte stored in 10^{-5} cm^3 .

2.2. Micromachinery

One of the significant inhibitors to progress during the "bolt on" era of rudimentary smart structures is the availability of commensurately engineered actuators, sensors, accelerometers, gyros, motors etc.

The development of integrated technologies based on fine line lithography deep x-ray lithography employing the intense ~4A synchrotron radiation from the DRAL facility followed by electrodeposition and moulding which constitutes the LIGA process [6] affords the opportunity of fabricating a new generation of micromachinery which while still adopting a bolt on approach would allow significant new developments to be made.

The exciting possibility of coupling the UMS and RHIP technologies would allow the fabrication of optimised systems from the materials perspective. It is already clear for example that considerable thought will be needed for efficient tribological design of micromachinery, and for rotating structures it would be advantageous to already have in place strategies for controlling the inertia as well as having

wear resistant surfaces. An example might be a 100μ gear train with the bearing surfaces being Titanium Nitride the body being carbon/carbon and the teeth being silicon carbide. In principle the methodologies in 2.1 will be key enablers in facilitating these developments.

References

1. D T Clark Materials World 144-146 (1994)

2. D T Clark Makromol Chem Macromol Symp 75 1-34 (1993)

3. R D Arnell Surface and Coatings Technology 60 597-602 (1993)

4. D C Schram Europhys New 18 28 (1987)

5. W B Vedlkamp Scientific American 266 50-55 (1992)

6. LIGA Lithographic Galvanoformung Abformung IMM Mainz Microparts Karlsruhe FRG.

SMART STRUCTURES RESEARCH IN AEROSPACE ENGINEERING

Elmar J. Breitbach, Rolf Lammering, Jörg Melcher and Fred Nitzsche

Institute of Structural Mechanics, German Aerospace Research Establishment (DLR)
Lilienthalplatz 7, D-38108 Braunschweig, Germany

ABSTRACT

This paper summerizes the experience of the DLR in various subdisciplines of smart structures technology and shows how this joint experience is gathered in the development of smart structures. Some smart structural systems which are currenty under investigation are presented.

1 INTRODUCTION

The increasing demands on the performance of structural systems for aeronautical and astronautical applications as well as the necessity of lightwight constructions require a new class of structural systems, so called smart, adaptive or intelligent structures.

Adaptive structures are characterized by integrated actuators and sensors that are interconnected by adaptive real-time controllers. Among others, the most promising canditate materials for sensor/actuator applications in adaptive structures are piezoelectric and magnetostrictive materials as well as shape memory alloys. The high degree of integration of these materials into the structure results in multifunctional components with sensor, actuator and load bearing capabilities.

Adaptive structures overcome the shortcomings of conventional passive structures because they independently react against both environmental influences as well as changes in the structure itself. Therefore, they allow for

- vibration suppression,
- shape control,
- alignment precision control, and
- damage detection.

Current work and technology assessment studies give the highly interdisciplinary and system-oriented adaptive structures technology a promising forecast for future applications in a wide range of industrial areas. Exemplary, the following space applications which have been identified by the European Space Agency ESA (Ref. 1), are listed:

- reduction of vibrational disturbance at the interface of sensitive equipments (e.g. optical payloads),
- attenuation of equipment support panel vibrations due to acoustic noise,
- high accuracy antenna reflectors and optical benches,
- high precision robot arms,
- micro vibration monitoring systems, which are used to verify the health conditions of mechanism, such as momentum wheels, and to assist in the characterization of potential wear or other problems, and
- monitoring and controlling of processing parameters during the curing process of composite structures in order to get higher quality composite products with less scatter on the mechanical characteristics.

This paper focusses on individual aspects of smart structures as well as on integrated systems, which are currently being developed at DLR.

2 DESIGN OF SMART COMPOSITE TRUSS MEMBERS

Lightweight Carbon Fiber Reinforced Plastic (CFRP) sandwich struts build the basic components in the development of smart truss structures. These struts have been described by Schütze (Refs. 2,3). The walls of the

0-8194-1700-9/94/$6.00

strut consist of load-bearing fiber reinforced layers. Lightweight foam used as core material supports the surrounding CFRP layers. Two different types of struts are depicted in Fig. 1.

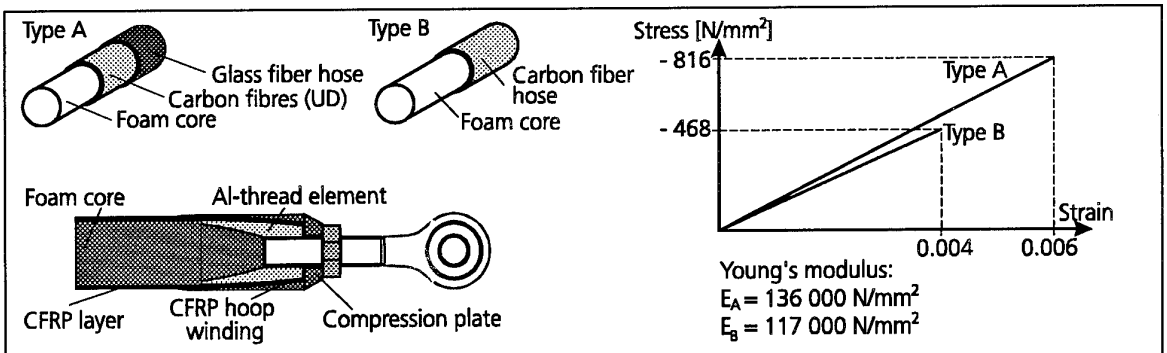

Fig. 1: CFRP struts, corresponding stress-strain curves in the compressive range, and load transfer element

Optical fibers have been identified as excellent sensor candidates because of their light weight, small size (making point sensing possible), extremely high frequency, immunity to electromagnetic interference, lack of Joule heating, high bandwith and data rates, and, finally, because their filamentary geometry offers the possibility of embedding them into fiber composite hosts. They consist of a thin wave-guiding core with ca. 4µm diameter surrounded by a cladding layer of lower index of refraction. The fibers are protected against damage and fracture by means of a thermoplastic coating. The total diameter of the fiber is ca. 100µm (standard communication fiber).

Two methods for the integration of the optical fibers into the struts are currently under investigation: Adhesion to the foam core and integration into the unidirectional layer of the sandwich strut. For optimal fiber to structure adhesion, in any case it is necessary to remove the protective thermoplastic coating of the fiber before integration into the structure.

When the foam core is used for the adhesion of the optical fiber, the fiber is carefully adjusted in the longitudinal direction and fixed at the ends. Then the fiber is bonded by a narrow trace of epoxy resin in the region, where the strain is to be measured and where the thermoplastic coating is removed. In the manufacturing process of struts, foam core cylinders that are equipped in this way can be used like normal foam cores. Furthermore, the characteristics of the load bearing carbon fibers are not altered, which must be considered another great advantage.

The second method of embedding the optical fiber into the UD layer of the sandwich strut is the simultaneous introduction of the glass fiber and the carbon fiber roving into the fabrication facility. One possible limitation of this integration method is the size of the sensor. Although the optical fiber is only 100µm in diameter, this is ten times the diameter of a typical reinforcing fiber. It must be assumed that this integration method may perturb the local strain field, even in the case when the reinforcing fibers and the sensor are aligned in parallel. In the literature, the influence of the coating material on the local stress behavior has been analysed, and optical coating material properties as well as optimal dimensions of the coating have been investigated.

In both cases of integration the optical fiber is subjected to strains which may be caused by the process of composite fabrication and could affect the sensor performance. On the other hand, the sensor material is well protected and cannot be easily damaged.

Further investigations are concerned with the integration of piezoelectric materials and shape memory alloy wires into CFRP structures. In contrast to optical fibers, these materials allow for sensing as well as for actuating. So far, experiments on a CFRP truss structure have been performed with commercially available piezoelectric actuators consisting of stacked piezoelectric ceramics in metal cases. Since this actuator does not meet the demands of a lightweight construction, it is necessary to develop lightweight active composite struts (e.g. for space applications) which are based on piezoelectric ceramics. A promising step forward is the recent development of piezoelectric fibers. Further improvement of these fibers enable the direct integration of this active material into fiber reinforced plastics and allow for the construction of lightweigt and active structures.

3 ANALYSIS AND OPTIMIZATION OF SMART STRUCTURES

In order to be able to effectively design, evaluate and select adaptive structures before their construction, in any particular application it is necessary to precisely understand their static and dynamic behavior. For this purpose methods for the analysis and optimization of smart structures are currently being developed. The main emphasis is put on

- the development of constitutive equations of smart materials and their implementation into finite element codes,
- the formulation of mathematical models for multifunctional components, and
- the development of optimization algorithms in order to compute most efficient sensor and actuator positions.

Since piezoelectric materials can be used for actuator as well as for sensor applications, they are very attractive in smart structures technology. Piezoelectric materials are able to exert large forces when an electric field is applied. This feature is used in the design of actuators. On the other hand, mechanical stresses cause an electric field and make piezoelectric materials well-suited for sensor applications. Moreover, these materials offer the following advantages: wide frequency range, high resolution in positioning applications, extremely short reaction times, low energy loss factor, and vacuum ability. Piezoelectric devices for sensing/actuating purposes are commercially available as stacked piezoelectric ceramics, thin plates of piezoelectric ceramics, and thin foils of piezoelectric polymers.

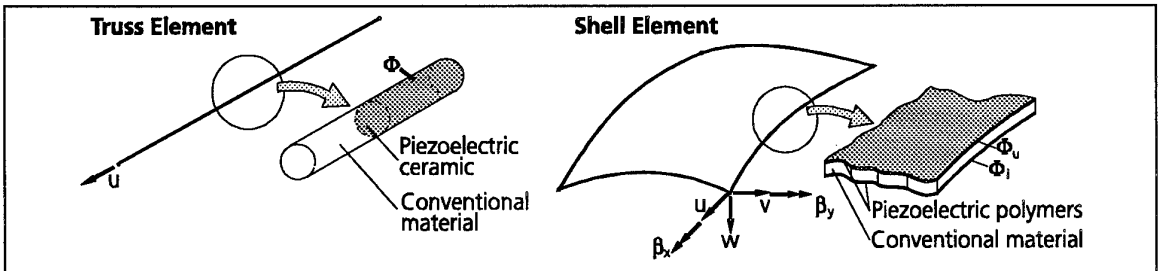

Fig. 2: Piezoelectric finite truss and shell element

A linear finite element formulation which allows for the analysis of shell structures with piezoelectric layers bonded to the surfaces and of truss structures with piezoelectric members replacing conventional ones has been developed. It takes into account the coupling between the elastic field and the electric field (Refs. 4,5). The shell element as well as the truss element are depicted in Fig. 2. It can be seen that the electric potential is introduced as an additional degree of freedom besides the nodal displacements and rotations. Several test cases illustrating the potential of these finite elements are presented in Refs. 4,5,6.

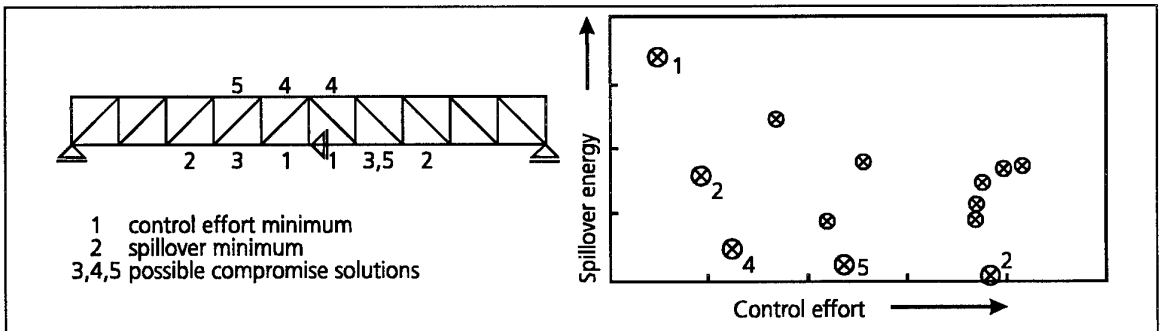

Fig. 3: Optimal actuator placement with spillover consideration. Control of the 1st and 2nd mode. Consideration of the spillover into the the 3rd and the 4th bending mode.

In the design of actively controlled structures, the determination of the actuator locations is a very important issue. In order to find the optimal placements of piezoelectric actuators in adaptive truss structures, optimal placement strategies have been developed in conjunction with the independent modal space control method (Ref. 5). For this purpose, the finite truss element presented in section 3.1 is utilized and allow for the calculation of nodal displacements as well as electric potentials. The optimization algorithm makes use of the electric potentials in order to minimize the control effort by an optimal actuator placement. The

minimization of the spillover energy into uncontrolled modes is an additional objective which can be taken into account by the optimization procedure.

Fig. 3 shows a truss structure of which the optimal actuator positions are calculated in order to minimize the control effort of the first two bending modes and the spillover into the 3rd and 4th bending modes. It can be seen that the minimization of the control effort is obtained when the actuators are located at the truss elements 1, whereas the minimization of the spillover energy is achieved at the truss elements 2. Furthermore, it can be seen that there are compromise solutions, such as 3, 4 and 5.

4 CONTROL CONCEPTS

Recent developments of high speed processors have made it possible to run controllers under real-time conditions resulting in a decisive step toward the breakthrough of adaptive structures. The main goals for the controller in adaptive structures applications are to

- process the signals from the multifunctional sensors and
- generate the optimal driving signals for the multifunctional actuators.

Adaptive structures are systems that may vary with time in face of changing nonstationary environments or system requirements. In situations where structural system parameters are variable or not accurately known (e.g. in space applications), adaptive or self-optimizing controllers must be used. These controllers are able to adapt their behavior and performance to their environment according to the desired criterion. They consist of two components: a digital filter system and a corresponding adaptation algorithm.

The digital filter system is used to generate the actuator driving signals from the sensor signals. Various types of digital filter systems (e.g. transversal and recursive digital filters) have been developed and are available for the solution of a wide range of control problems. In any case it is advantageous to design the controller of a structural system in a way that its structure is conform to the underlying problem and that the property of structural conformity is achieved. The optimal adjustment of the filter itself is guaranteed by the second controller component, the adaptation algorithm.

MX Filters for Performance Tests of Adaptive Structural Systems

As the rapidly growing field of adaptive structures develops, issues of material and material system selection, design, characterization and manufaction become increasingly important. The number of new designed actuator/sensor constructions embedded in adaptive structures is expanding and therewith the problems of optimal design and accurate performance checks arise. The resulting demand for a measuring technique tool that allows for an online or real-time system identification (even when the structural properties vary with time) can be met by use of the recently developed MX-filter.

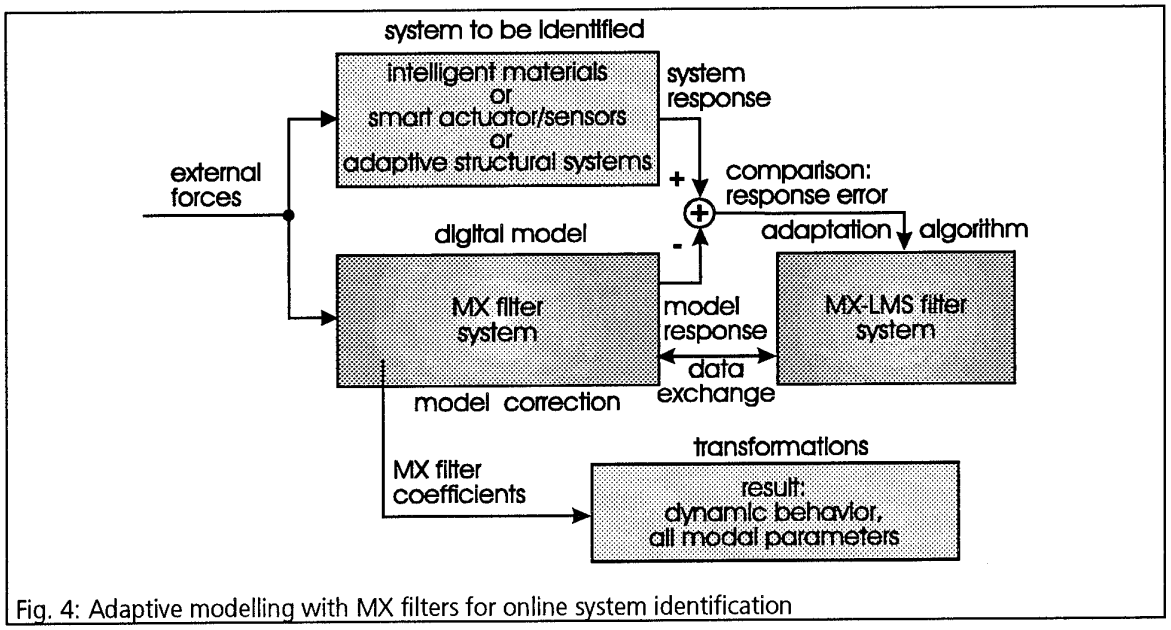

Fig. 4: Adaptive modelling with MX filters for online system identification

The concept of the proposed online system identification tool is based on the procedure of adaptive modelling, as shown in Fig. 4. Both the system to be identified and the model realized by a digital MX filter system are fed identically by external forces. A corresponding adaptation algorithm, the MX-LMS filter system, calculates the optimal model parameters (in this case the filter coefficients) to minimize the error signals. A block of transformations contains few mathematical operations that compute the modal parameters from the adapted coefficients.

The two filter systems, the MX and the MX-LMS are the main ideas of the new identification method. The MX filter system is based on digital lattice-type filterings. It represents a linear dynamic system with any modal density. At each time step it is iteratively corrected by the MX-LMS filter system. The latter needs data from the model in order to copy new or better coefficients to the MX filter. The adaptation algorithm yields the information as to whether or not the model is already operating perfectly from the error signal.

The signal flow and the form of the MX filter system are shown in Fig. 5 and was proposed by Melcher, Refs. 7 and 8. Similar filter forms have been suggested in Refs 9,10, and 11. In the discrete form presented here, the filter is non-canonical (the number of delays z^{-1} is higher than the the order of the represented transfer function). In cases of m modes it has (1+4m) real coefficients: the transversal coefficients c, a_i', a_i'' and the recursive coefficients b_i', b_i'', with $i \in [1, m]$. The functional relationship between the input samples f(n) (n is the discrete integer time step) and the resulting output samples y(n) is described in Ref. 8. The transfer function of the MX filter system is

$$H(z) = \left[c(n) + \sum_{i=1}^{m} \left(\frac{a_i(n)}{1 - b_i(n) z^{-1}} + \frac{a_i^*(n)}{1 - b_i^*(n) z^{-1}} \right) \right] z^{-1}$$

with the substitutions $a_i(n) := a_i' + j a_i''$ and $b_i(n) := b_i' + j b_i''$ for all $i \in [1, m]$, where the sign * denotes complex conjugation. This equation clearly demonstrates three essential properties:

- the MX filter system represents only systems that can be formulated mathematically with conjugate complex pairs of residues a_i and poles b_i,
- the stability of this filter system can be proved easily by taking the conditions $b_i'^2(n) + b_i''^2(n) < 1, \ \forall i \in [1, m]$ at each time step n, and
- H(z) is modelling a structural transfer function multiplied by z^{-1}.

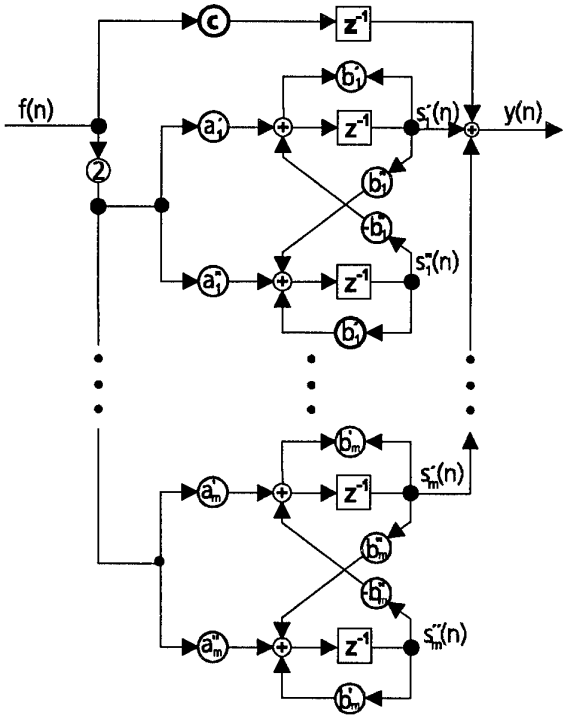

Fig. 5: Signal flow of the MX filter system representing m modes

The adaptation algorithm that optimizes the MX filter system respective to its response by varying the filter coefficients is based on the minimization of the mean square error function and is called MX-LMS filter system. It has been shown in Ref. 8 that although the MX filter system is linear, activation of the MX-LMS filter leads to a non-linear adaptive model.

A comparison between the modal description of the dynamic system to be identified and the model description leads to the time-dependent relation between the system parameters as eigenfrequencies f and damping factors respectively, and the recursive MX filter coefficients. The formulas can be found in Ref. 8 and are not repeated here for brevity's sake.

Experiments on a smart test structure, a graphite epoxy composite beam with embedded shape memory alloy wires, clearly demonstrates the performance and facilities of this new tool: structural parameters can be identified althought they are varying due to internally induced stress. The following experimental observations have been made:

- The adaptation algorithm is stable for many variations of the convergence matrix.
- The filter system works also for MDOF applications.
- A pre-knowledge of the number of modes to be identified is not necessary. Experience: assume more modes than exist.
- Useful broadband input/exitation signals are noise, step sine, chirp or transients.

5 ADAPTIVE WIND TUNNEL STING

Wind tunnel stings that are used for aerodynamic investigations and that carry aircrafts or other structures like spacecrafts, propulsions and automobiles are heavily affected by vibrations. Small vibration amplitudes reduce the quality of the measurements, larger ones can damage the model as well as the sting itself. The sting vibrations are caused on the one hand side by the airstream that starts the model oscillating. The model on its part passes the vibrations to the sting. On the other hand, vibrations arise when the angle of attack of the model is changed stepwise in order to investigate starts and landings of an aircraft. The demands for high precision measurements and safety require for vibration suppression.

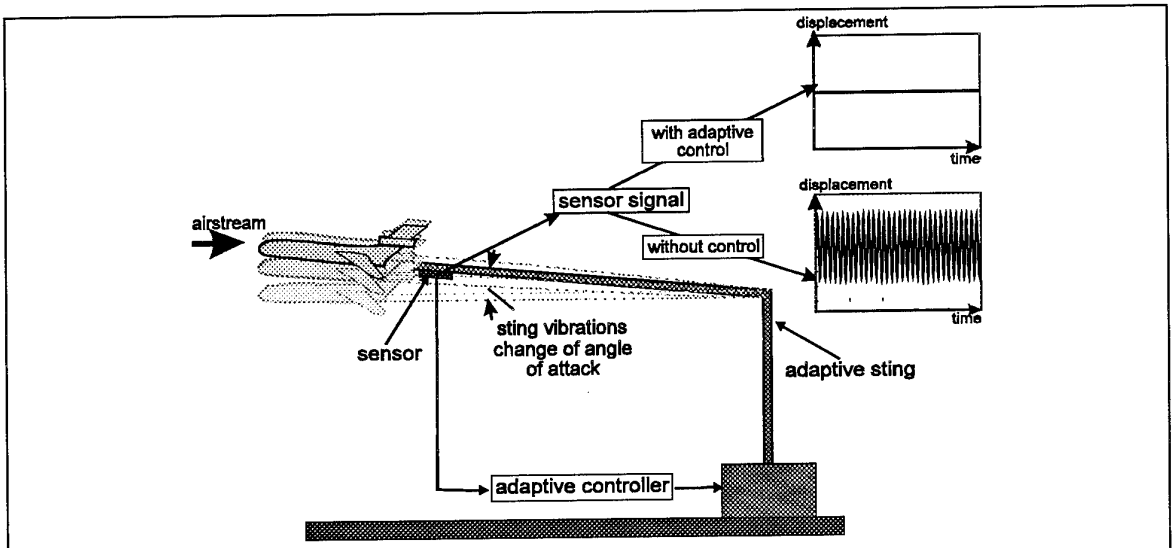

Fig. 6: Schematic of an adaptive wind tunnel sting

This goal cannot be met by an improved (e.g. stiffer) sting construction or by use of materials with a higher damping capacity since these measures are ineffective in the case of the critical low-frequency vibrations. Therefore, an active vibration suppression has been developed by the DLR and successfully tested in the German Dutch Wind Tunnel (DNW) (Ref. 12). Fig. 10 shows the sting which is used to carry and to move the model. In the DNW it is 10m long and 8m high. Its weight is ca. 30t, the model has a mass of 2.5 t. The movement of the sting is carried out by a powerful hydraulic system. Sensors measure unwanted vibrations and forward their signals to an adaptive controller. This high-speed controller is able to calculate the signals that are necessary to cancel the vibrations in a time period of some micro seconds. The controller has to

guarantee high security and stability requirements. Since it cannot make use of a reference signal for the calculation of the vibration excitation forces and since the eigenfrequencies vary extremely due to the changing sting geometry and the sting non-linearities, a novel concept was realized: adaptive signal processing and signal generation with a predictive character. The software is implemented on high-speed digital signal processors that allow for real-time conditions. The goals met by the adaptive vibration suppression are

- high-precision measurements,
- increased security for the model and the sting,
- delay of fatigue,
- reduced measurement time, and
- innovative measurement technique.

6 HELICOPTER APPLICATIONS

The active control of the vibration characteristics of helicopter blades has been a matter of considerable research effort in the last decade. The different approaches that have been suggested for the active control of rotary wings may be classified in two groups, according to their general philosophy. In the first, the time-dependent pitch control of the rotor is introduced in the non-rotating frame attached to the aircraft. This method is called higher harmonic control or shortly HHC. It is characterized by actuation in all blades simultaneously by injection of a single higher harmonic frequency in the rotor through the swashplate. The second group calls for an individual blade control in the rotating frame attached to the rotor and, hence, it is known as individual blade control or IBC. Although HHC has already presented good results in both theoretical and experimental studies, it is recognized to lack the bandwidth to amply control the broad band spectrum of vibration that characterizes the operation of helicopter rotors in forward flight. The rotor hub reactions induced by the unsteady aerodynamic loads acting on the blades are the most important sources of helicopter vibration. In general, the vibration level is low in hover flight, increases in forward flight, and in fact limits the maximum speed of the modern aircraft. However, simple mathematical models are able to demonstrate that the segments of the spectrum of vibration located in the vicinity of integer multiples of the rotor spinning frequency are the most relevant regarding the dynamic excitation of the entire airframe. In particular, the first harmonic at *N/rev* (where *N* is the number of blades) has been identified as critical. Experimental results proved that overall reduction on the level of helicopter vibration is observed if determined blade modes are controlled in the rotating frame (Ref. 13). This observation stresses the efficiency of the IBC concept.

With the advent of the adaptive structure technology, the IBC concept must be reviewed since a superior authority over specific modes of the blades in the rotating frame is theoretically feasible (Ref. 14). Particularly attractive seems to be the application of the new technology to control the aeroelastic characteristics of the aforementioned modes. In fact, it is well known that rotor vibration suppression benefits from the so-called blade *aeroelastic detuning*.

The concept of smart structures not only involves the distribution of actuators and sensors to generate and measure internal strains but also the integration of controllers designed to work at the low and high authority levels. A true "smart rotor" would employ both. While *high* authority controllers optimize the overall performance of the rotor at different flight conditions, the *low* authority controllers provide the instantaneous or "involuntary" reaction to the blade dynamic excitation at the current flight attitude.

A recent paper by Chopra presents a review on the most important activities related to the development of the so-called "smart rotor" (Ref. 15). In summary, two strategies have been investigated in connection with the IBC philosophy. The first calls for embedding the adaptive material in the blade laminate in order to induce strain deformations that can be controlled externally. It not only has the advantage of being cleaner under the aerodynamic point of view, but it also allows the possibility of exploiting some excellent features of the distributed control theory, such as its inherent robustness and superior authority over the system's degrees of freedom. However, it now has been recognized that this solution leads to an overestimation of the adaptive material's capabilities to deliver strain deformations under the typical loads experienced in forward flight.

Since the introductory studies by Spangler and Hall (Ref. 16), who conducted tests in fixed wing models, the use of lumped control configurations has gained more interest. The solution calls for the introduction of a "smart flap" at the blade trailing edge. Feasibility studies have indicated that this technique is prone to produce more efficient actuation with the available smart materials. However, it is important to stress that

lumped control techniques are generally less robust because more modes than those considered in the controller's design are naturally excited by the actuator, causing spillover effects.

An alternative for the flap solution (but still a lumped control technique) has been proposed by Nitzsche, Lammering and Breitbach (Ref. 17). According to this solution, actuation is performed at the blade root, locally inducing torsion displacements which change the effective boundary conditions. Numerical simulations suggested that the solution is feasible and satisfies the power limitations of the available PZT. Further experimental tests are planned to confirm the analytical expectations.

7 CONCLUSIONS AND OUTLOOK

The use of new multifunctional material systems in connection with new adaptive control concepts based on digital filters have cleared the way for the establishment of a new structure related technology called adaptive, smart or intelligent structures. Current work and technology assessment studies give the highly interdisciplinary and system-oriented adaptive structures approach quite a promising forecast for future applications in a wide range of industrial branches. The result of recent investigations indicate that adaptive structures technology will be one of the most innovative disciplines in the future.

8 REFERENCES

1. ESA-ESTEC 1994, Technology Research and Development Programme for 1994-95-96.
2. Schütze R, German Patent P 41 35 695.025.
3. Schütze R 1986, 4th Int. Carbon Conf., CARBON, 30 June - 4 July 1986.
4. Lammering R 1991, The Application of a Finite Shell Element for Composites Containing Piezo-Electric Polymers in Vibration Control. *Computers & Structures*, 41, 1101-1109.
5. Lammering R, Jia J & Rogers CA 1994, Optimal Placement of Piezo-Electric Actuators in Adaptive Truss Structures, *Journal of Sound and Vibration*, accepted for publication.
6. Lammering R 1992, A Finite Shell Element for Composites with integrated Piezo-Electric Polymers, *Zeitschrift für angewandte Mathematik und Mechanik*, 72, T216-T220.
7. Melcher J 1992, Adaptive On-line System Identification of Aerospace Structures Using MX Filters. 12th IFAC Symposium, 7-11 Sept. 1992, Munich, Germany.
8. Melcher J 1994, MX-Filters: A New Tool for Performance Tests of Adaptive Structural Systems, 1994 Int. Conf. on Intelligent Materials, 5-8 June, 1994, Williamsburg, VA, USA.
9. Jackson LB, Lindgren AG & Kim Y 1979, Optimal Synthesis of Second-Order State-Space Structures for Digital Filters. *IEEE Transactions on Circuits and Systems*, Vol. CAS-26, No. 3, pp. 149-152, March 1979.
10. Nagle HT Jr. 1972, Survey of Digital Filtering, Final Technical Report, Contract NAS8-20163, NASA STAR, October 1972.
11. Vereshkin AE et al. 1968, Two New Structures for the Implementation of a Discrete Transfer Function with Complex Poles, *Automation and Remote Control*, pp. 1416-1422, Sept. 1968.
12. Melcher J 1993, Aktiv geregelte Modellhalterung im Deutsch-Niederländischen Windkanal, *DLR-IB 232-93C01*.
13. Ham ND 1987, Helicopter Individual Blade Control at MIT 1977-1985, *Vertica*, Vol. 11, No. 1/2, pp. 109-122.
14. Nitzsche F 1993, Modal Sensors and Actuators for Individual Blade Control, *Proceedings: AIAA/ASME/ ASCE/AHS/ASC 34. Structures, Structural Dynamics and Materials Conference,* AIAA, Washington, DC, 1993, Part 6, pp. 3507-3516.
15. Chopra I 1993, Development of a Smart Rotor, *Proceedings: 19. European Rotorcraft Forum*, Associazione Italiana di Aeronautica ed Astronautica, Cernobbio, Italy, 1993, pp. N6.1-N6.18.
16. Spangler RL Jr. and Hall SR 1990, Piezoelectric Actuators for Helicopter Rotor Control, *Proceedings: AIAA/ASME/ASCE/AHS/ASC 31. Structures, Structural Dynamics and Materials Conference,* AIAA, Washington, DC, Part 3, pp. 1589-1599.
17. Nitzsche F, Lammering R and Breitbach EJ 1993, Can Smart Materials Modify Blade Root Boundary Conditions to Attenuate Helicopter Vibration? Fourth International Conference on Adaptive Structures, DGLR Paper No. 93-04-12, Cologne, Germany, November 2-4, 1993 (to appear as Proceedings).

POLYMER ELECTROMECHANICS:MECHANICAL SENSING AND ACTUATION PROPERTIES OF ORGANIC MACROMOLECULAR SYSTEMS.

Danilo De Rossi

Centro "E. Piaggio" School of Engineering, University of Pisa, Italy

The recent upsurge of research activity in smart materials and structures stresses the interest in materials possessing both direct and inverse electromechanical transduction properties.
Three different classes of polymers appear to be particularly interesting in relation to their electromechanical properties: piezoelectric polymers, polyelectrolyte gels and doped electron conducting polymers.
In the last decade there has been an impressive growth in research and development in the field of sensor technology.
Some advances have also occured, albeit less substantial, in the field of actuation. Although the largest part of the new physical sensors and actuators make use of of inorganic materials as transduction elements, increasing attention is nowadays being paid to functional polymers.
In this paper the sensing and actuation properties of these polymers are briefly discussed.

1. PIEZOELECTRIC POLYMERS

1.1 Generalities

Three major mechanisms have been identified (1), being responsible of polymer piezoelectricity:

a) piezoelectricity caused by deformations at a molecular level
b) piezoelectricity caused by macroscopic deformations
c) piezoelectricity in systems with inhomogeneous material properties or containing trapped space charges.

Only the first two mechanisms are piezoelectric in a strict sense, since they imply the existence of crystalline or paracrystalline order. The third mechanism can operate also in amorphous systems,

0-8194-1700-9/94/$6.00

Only the first two mechanisms are piezoelectric in a strict sense, since they imply the existence of crystalline or paracrystalline order. The third mechanism can operate also in amorphous systems, and it is not piezoelectric in a narrow sense. We limit our discussion to the two first classes.
In a semicrystalline piezoelectric polymer some of the piezoelectric coefficients can be zero, depending anisotropy of mechanical properties and on the average orientation of the permanent dipoles which may originate particular symmetry conditions. Piezoelectricity in polymers is usually observed in oriented films; four different forms of the piezoelectric coefficient. matrix have been postulated and experimentally verified (2).
Piezoelectric polymers of synthetic origin which present a certain scientific and practical interest are some uniaxially oriented synthetic polypeptides, such as poly-benzyl glutamate (PBG) or polyhydroxybutirate (PHB) which present a D_∞ ($\infty 2$) symmetry class, or polyvinylidene fluoride (PVDF) and some of its copolymers, which upon uniaxial or biaxial stretching and poling respectively present a $C_{\infty v}$ (∞m) or C_{2v} (2mm) symmetry.

1.2 Mechanical sensing

In analyzing the sensing response of piezoelectric polymers the most important factors are selectivity to different components of the stress tensor, sensitivity and bandwidth.
The selectivity factor is governed by the structure of the piezoelectric coefficient matrix of the material and by the mechanical constraints and boundary conditions caused by sensor mounting.
In the usual configuration for PVDF (and related materials) samples, the electrodes are parallel to the film plane and orthogonal to the average orientation of the dipole moments. The voltage response is proportional to a linear combination of the three normal stress components acting on the sample multiplied by their respective piezoelectric coefficient d_{31}, d_{32}, d_{33}.
A much less utilized configuration is obtained by cutting a PVDF thick sheet along a direction perpendicular to the sheet plane and parallel to the drawing direction and then metallizing the resulting strip onto the cutting planes.
In this configuration the only non-vanishing component of the piezoelectric coefficient is d_{25}.
This configurationhas been rarely used, but it has been shown to be very effective and selective in measuring changes in the shear

stress component in a robotic tactile sensor during slippage of a grasped object (3). When using PBG or PHB in film form with the electrodes on the film major surfaces, the only active piezoelectric coefficient is d25 (= - d14), causing the film to respond only to the in-plane shear stress component.
The sensitivity of a piezoelectric polymer sensing elements is related to the values of their piezoelectric coefficients (ranging from 1 to 30 pC/N).
Usually the open-circuit voltage response is calculated, imposing the charge on the electrodes equal to zero.
In terms of temporal response of piezoelectric polymers, it is well known that piezoelectric sensors do not possess DC response.
The low frequency roll-off is determined by the souce time constant $\tau = \rho\ \varepsilon$. The typical figures of ρ (resistivity) = 10^{14} Ω-cm and ε = (dielectric constant) 138.85 = 10^{-12} F/m for PVDF sets τ = 115 s.
The high frequency cut-off a piezoelectric polymer working in a sensor mode is not determined, usually, by electrical factors, but by the mechanical resonant frequency of the sensor and its mounting.

1.3 Actuators properties

The use of piezoelectric polymers as actuators is limited because of the high driving voltages required to produce small strains (typically 2 KV for a 1 μ linear displacement of a 1 cm long sample) and the lack of a steady state response.
Nevertheless, they can be fast and highly reliable, and production technologies for piezoelectric polymers are quite advanced.
In order to produce useful displacements PVDF can be formed into a bimorph (4); to reduce the driving voltage, a stack configuration can be used.

2. POLYELECTROLYTE GELS

A polyelectrolyte gel is composed as minimal elements by a network of ionizable macromolecules swollen in a polar solvent, usually water. These gels rheologically behave as viscoelastic solids.
A necessary condition for the formation of a gel is the existence of a certain degree of cross-linking between the macromolecular chains; the crosslinks may be due to covalent bonds or physical interactions. The properties of a gel strongly depend upon the interactions between its solid and liquid components; the balance of the forces deriving from these interactions determine the state of equilibrium of the system as a whole.
The forces acting on an ionized gel originate from the rubber elasticity of the polymer network, from the polymer-polymer affinity and from the electrostatic interactions which involve the

fixed charges on the macromolecules and the mobile counterions in the interpenetrating liquid.
Any unbalance of these forces caused by an external stimulus causes the gel to rearrange its status reaching a different equilibrium volume through solvent intake or expulsion.
Temperature, pH, solute concentration changes in the solution, and mechanical stress acting on the solid component have been proved to be capable of causing gel swelling or deswelling.

2.1 MECHANICAL SENSING

Polyelectrolyte gels are capable of converting mechanical input energy into electrical signal mainly through two mechanisms (5,6). The first mechanism is related to the occurrence of streaming potentials when a relative motion between the solid and the liquid components of the gel in present.
Assuming a gel made by a polyacid partially dissociated carboxylic groups covalently bound to the polymer backbone hold a negative charge which is balanced by the positively charged mobile counterions when the gel is compressed, a liquid pressure gradient across the sample is induced producing fluid flow past the gel micropores; since the liquid holds a net charge, a spatial dishomogeneity of charge is created, originating the streaming potential which can be recorded across suitable electrodes. When the relative velocity between the liquid and the solid fractions goes to zero, the streaming potential also become zero; this sensing mechanism is, so, intrinsically dynamic.
A different mechanisms also operates in polyelectrolyte gels which may be used to detect mechanical signals of static nature (7).
In the case a mechanical load causes the solid polymer volume fraction in the gel to be perturbed from its initial, uniform state, the electrical charge density of the gel also becomes spatially inhomogeneous. In order for the conditions of electroneutrality and electrochemical equilibrium to be satisfied within the gels' interstitial fluid, the inhomogeneity in charge density must be accompanied by a spatial inhomogeneity in concentration of mobile ionic species.
In principle, these resultant concentration differences can be measured by using ion-selective electrodes.

2.3 Actuation properties

Recent work related to the development of new materials for actuation has focused on preparing stronger and faster polymer gels through chemical and physical processes.

A variety of gels differing in their chemical composition, degree of cross-linking, inter-link average molecular weight and other factors, can be used for actuation. An extensive review of chemomechanical materials has been given by Osada (8).

Recently, various research groups have synthesized and characterized hydrogels with the aim of obtaining high-performance actuation systems.

Umemoto et al. (9) have prepared fiber by spinning a copolymer of acrylamide and methacrylic acid, crosslinked with buthadiene diepoxy. These fibers showed rapid elongation and contraction upon solvent exchange (water-acetone).

Matsumura et al. (10) also used modified polyacrylonitrile (PAN) fibers as chemomechanical materials.

By heating the PAN fibers at 220°C and then hydrolyzing them in a concentrated NaOH solution, they obtained fibers with an amphoteric behavior; by changing the bath pH from alkaline to acidic and viceversa, a contraction ratio (under no load) of the order of 70% was observed.

Isometric force densities of 1 MPa or more were obtained with a time constant of the order of 2 seconds, using 30 μm diameter fibers.

Thermosensitive gel fibers have been prepared by Hirasa et al. (11), through γ-ray irradiation of polyvinyl-methyl-ether (PVME) under mild heating to obtain microphase separation.

Microporous fibers were obtained with an average diameter of 200 μm. Reversible contraction and elongation were observed upon changing temperature above and below 38°C respectively.

The time constant for length changes was of the order of 1 second and the generated force, for a single fiber, was about 0.3 m N.

Suzuki et al. (12) described the preparation of a tough hydrogel of polyvinil alcohol (PVA) and polyacrylic acid (PAA), made so by repetitive freezing and thawing and thus obtaining a macroporous structure.

Because of the cooperative hydrogen bonds among PVA chains, the tensile strength can be as high as 0.5 MPa. The material has reversible chemomechanical properties and high durability compared with other chemically cross-linked hydrogels. The contraction ratio strongly depends on the load; for example, 30% for no load and 10% for a load of 0.1 MPa.

The generated power density is found to be around 0.1 kW/kg for a 10 μm thick film, almost of the same order of that skeletal muscles.

Liquid crystalline gels have also been synthesized (13) with the aim of preparing ordered polymers to increase contraction force and speed through the cooperative action of oriented structures. These LC gels, however, only swell in organic solvents and no mechanisms for their electric drive has yet been suggested.

Some form of material structuring and modification is also required for the intimate contact between the contractile network and electron conducting materials delivering the electrochemical stimuli.

3. ELECTRON CONDUCTING POLYMERS

The most highly conducting polymers are those with π-conjugated electrons in the main chain backbone such as polyacetylene, polypyrrole, polyanilyne, polythiophene and their derivatives.
In their pristine undoped state these polymers are insulators, with conductivities of the order of 10^{-6} S/cm.
To render a polymer conductive, charge carriers are created in the polymer by reaction with a reagent with redox properties, or by electrochemical oxydation. In the latter case, a potential is applied between the polymer and an electrolyte containing the dopant in ionic form. Once charged, the polymer then absorbs a quantity of the ion that depends on the applied potential and the concentration of dopant. The ions act as local counter-ions, and render the polymer a semiconductor.
A large variety of applications has been proposed for conducting polymers ranging from batteries to chemical and biological sensors, electrocromic devices, EM shielding coatings and other. Much less attention has been given till now to their electromechanical transduction properties.

3.1 Mechanical sensing

Conducting polymer elements have been used in combination with interdigitated electrodes as strain sensors and are now commercially available (14).
Information on piezoresistitive properties of electron conducting polymers are scarce, mostly owing to the recent availability of materials possessing good mechanical properties. Polypyrrole doped with sodium benzensulfonate, prepared electrochemically (Lutamer from BASF AG) has been found to possess a gauge factor $GF=\Delta R/(R\varepsilon)$ of the order of 0.8 in its fully doped state and a GF of 0.4 when largely dedoped electrochemically (15).

3.3 Actuation properties

Conducting polymer (CP) have only recently been used for actuation, but have already have been shown to possess very high force generation capabilities [16] Π-electron conjugated polymers can exert tremendous forces, hundreds of times greater than those of muscles. In very thin CP fibers, where diffusion distances are minimized, response times can be of the order of milliseconds.

These fibers do, however, tend to have lower displacements (1-10 percent) than polyelectrolyte gels, but not as low as those of piezoelectric polymers. Pei and Inganäs [17] have investigated the mechanical properties of a bilayer CP strip of PPy.
On application of 0.8 V, the strip bent by 0.5 cm. The process was fairly slow, but reversible.
CPs are rather solid compact polymers, and it is this feature that limits the response times of anything other than very thin fibers or films.
To circumvent this limitation, a number of different approaches to designing CPs are being investigated. The synthesis of a polymer gel incorporating a CP backbone has been attempted [18]. However, this trial and error type approach may take several years before a useful polymer with adequate mechanical properties can be synthesized.
Alternatively, it may be possible to produce a microporous CP structures, rather than a gel, using a phase inversion spinning process.
This method would produce a polymer structure with a fast response time, at the expense of a slightly reduced force density.

REFERENCES

1) Y. Wada, R.Hayakawa: "Piezoelectricity and pyroelectricity of polymers", Jap. J. Appl. Phys., 15-2041, 1976

2) E. Fukada: "Piezoelectric properties of organic polymers", Ann. New York Acad. Sci., 38-7, 1974

3) C. Domenici, D. De Rossi, A. Bacci, S. Bennati: "Shear stress detection in an elastic layer by a piezoelectric polymer tactile sensor", IEEE Trans. Electr. Insul., 24-1077, 1989

4) M. Toda, S. Osaka: "Electromotional device using PVF_2 multilayer bimorph", Trans IECE of Japan, E61-507, 1978

5) D. De Rossi, A. Nannini, C. Domenici: "Artificial sensing skin mimicking mechanoelectrical conversion properties of human dermis", IEEE Trans. Biomed Eng, 35-83, 1988

6) D. De Rossi, L. Lazzeri, C. Domenici, A. Nannini, P. Basser: "Tactile sensing by an electromechanochemical skin analog", Sensors and actuators, 17-107, 1989

7) W. Kuhn, A. Ramel, DH Walters: "Conversion of chemical into mechanical energy by homogeneous and cross-striated polymer systems", in A. Wasserman (ed), Size and shape changes in contractile polymers, Pergamon Press, New York, 1960

8) Y. Osada:"Conversion of chemical into mechanical energy by sinthetic polymers (Chemomechanical systems)", Adv. Polym. Sci, 82-3, 1987

9) S. Umamoto, T. Matsumura, Y. Itoh, N. Okino, T. Sakai: "A study of mechanochemical gel fibers having high-tenacity and high-speed", Rep. Prog. Polym. Phys; Japan, 319, 1987

10) T. Matsumura, S. Umemoto, N. Okino, T. Sakai: "Mechanochemical behavior of ultrafine acrylonitrile gel fibers", Rep. Prog. Polym. Phys. Japan, 323, 1987

11) O. Hirasa, S. Ito, A. Yamauchi: "Thermoresponsive polymer hydrogel" in Polymer gels: fundamental and biomedical applications, D. De Rossi et al (Eds), Plenum Press, London, 1991

12) M. Suzuki, T. Teteishi, T. Ushida, F. Fujishige: "An artificial muscle of polyvinyl alcohol hydrogel composite", Biorheology, 23-874, 1986

13) Y. Osada, Y. Yasunaga: Kubunshi Rombunshu (in Japanese) 46-655, 1989

14) FSR (force sensing resistor), Interlink Electronics, Santa Barbara, Ca, U.S.A.

15) D. De Rossi, unpublished results

16) R.H. Baugham, L.W. Shacklette, R.L. Elsenbaumer, E. Plichta, C. Becht: "Conducting polymer electromechanical actuators", in Conjugated polymeric materials, JL. Bredas and RR Chance (Eds), Kluwer Acad. Pub, The Netherlands, 559, 1990

17) Q. Pei, O. Inganas: "Conjugated polymers as smart materials, gas sensors and actuators using hending beams" Synthetic Metals, 55/57 - 3730, 1993

18) K. Yoshino, K. Nakao, R. Sugimoto: "Poly (3 - alkylthiophene) gel and its properties", Jap. J. Appl. Phys, 28-490, 1989

INTELLIGENT MATERIALS FOR CIVIL ENGINEERING
-- PROPOSAL OF KEN-MATERIALS --

Hiroaki YANAGIDA*, Minoru Sugita** and Norio Muto***

*Professor, Faculty of Engineering, Director, Environmental Science Center, University of Tokyo, 7-3-1 Hongo, Bunkyo-ku, Tokyo 113 Japan
**Shimizu Corporation, Seavans South No.2-3, 1-chome, Shibaura, Minato-ku, Tokyo 105-07 Japan
***Sogo Security Services Co., Ltd., Engineering and Research Division, 2-14, Ishijima, Koto-ku, Tokyo 135 Japan

1 INTRODUCTION

Advanced technology has become too much complicated for general public to understand. Very limited expert can understand and treat this sort of complicated technology. Advanced technology is losing close contact to most people. The present speaker characterize this phenomenon as technomonopoly. Unless people accept and support technology, environmental issues cannot be solved. Intelligent materials have to be developed to simplify technology in order to recover friendship to general public. When general public understand technology, feel satisfied with technology and think technology of their own, technodemocracy is thus achieved.

2 ASPECTS OF SPAGHETTI SYNDROMES

Complicated features of technology are called as spaghetti syndromes. The word primarily came from the aspect of a patient entangled with many tubes and electric wires. The first aspect of spaghetti syndrome is the phenomenon itself difficult to find a key to unknitting. The second aspect is the way of thinking where additional parts are required for improvement. Thus technology becomes more complicated. The third aspect of spaghetti syndrome is misunderstanding, the more complicated the more advanced. The fourth aspect is focusing not to essential but to trivial. The last and fifth aspect is degradation of the performance. Many parts lead to higher probability of failures. The complicated feature segregate general public. Intelligent materials are to be developed to avoid this spaghetti syndrome of technology, but not to enhance.

Intelligent materials are required to develop to solve serious troubles arising from materials or technologies developed under guiding principles above mentioned. If intelligent mechanisms are put into materials by complicated ways suffering spaghetti syndrome, they are not friendly to people. If bridges are constructed with many sensors, the cost for sensors may exceed hat of bridges themselves. Sometimes week points are designed to assure effectiveness of sensors. This is the wrong way around.

3 INTEGRATION OF STRUCTURAL AND FUNCTIONAL PERFORMANCES IN KEN-MATERIALS

The intelligent materials proposed by the present author are without any additional sensors except structural materials themselves as will be discussed later upon the composite between carbon fiber and glass fiber to achieve self-diagnosis function. Structural materials are there functional materials at the same time. This may be more advanced than the method where intelligence is given with complicated design. To distinguish intelligent t materials with simple structure or design from intelligent materials with complicated features the present author uses the word "ken materials". Ken means wisdom, construction, health, saving, sensing, combination, and sphere all pronounced same way for their Chinese characters. Wise materials are intelligent materials with simple structures. Intelligent materials are not limited to tiny materials for electronics. Intelligence is also or more required for the construction

0-8194-1700-9/94/$6.00

materials used for large structures such as bridges or buildings. Healthy technology may be constructed with the ken materials. Health in technology means technodemocracy. Saving energy/resource is friendly to environment and saving complexity or avoiding spaghetti syndromes is friendly to people. Sensing is self-diagnosis within structural materials. Combination of structural and functional performance in identical materials is thus achieved. Finally sphere means "eco-", ecology conscious technology. Materials scientists and engineers are required to develop ken-materials for survival to 21st century with the philosophy based upon ken-materials. The present speaker and supporters have established recently "Ken-materials consortium" to enhance R & D activity and to help spread ken-materials and philosophy based there on.

The structural material with self-diagnosis function is considered as integration of structural and functional performances. This integration is the direction along which material scientists and engineers are requested to develop materials. Until very recently structural materials have been developed independently of functional materials. Diagnosis of structural materials is usually designed with additional sensors, which leads to the second aspect of spaghetti syndrome. We have to reconsider the way to obtain diagnosis without complexity. Only the way is to integrate structural materials and functional materials into integrated materials.

4 METHODS FOR ACHIEVING RELIABILITY

The method for achieving reliability of structure has been changing. It used to be to make thicker structure, consuming much amount of resources and leaving much waste. The next way is to make materials stronger. Unfortunately, the stronger materials fracture more suddenly. To improve reliability the way adopted is still to improve strength. Fracture of those materials take still place suddenly, whereas recycling of those materials too much strong is seriously difficult.

If we can notice some signals before fatal fracture takes place, we can repair or replace the materials. There are two different directions, one suffering and the other avoiding spaghetti syndromes of technology. Installing sensors at the points where fracture initiates looks reasonable. However, unless we know the points beforehand we cannot identify the places for applying sensors. If we do not know the places, we have to use many sensors to cover whole area of the structure. This is fourth aspect of the spaghetti syndrome. To minimize the number of sensors and to improve the performance of sensors the method frequently applied is to design some points where the strength is small. This is the fifth aspect of spaghetti syndromes, the wrong way around.

The best solution is to design the structural materials which can diagnose themselves.

5 DESIGN OF SELF-DIAGNOSIS

To avoid sudden fracture of the materials with high elastic modulus and small value of ultimate elongation, material A, usually applied is to hybrid materials with high tenacity and large value of ultimate elongation, material B. The present speaker's proposal is to apply a conductive material for the material A and an insulating material for the material B. Fracture of the material A is easily monitored by distinct increase of resistance. If the material is composed only of the material A, distinct increase of resistance corresponds to the death of the material. The presence of the material B keeps the hybrid material still alive although suffering from serious damage. This is not diagnosis of the death of the materials but that of suffering from a disease. Unless any remarkable increase of resistance is observed the materials are of no serious troubles. This is health diagnosis. A typical combination of materials A and B is carbon fiber and glass fiber. Carbon fiber and glass fiber reinforced plastic, CFGFRP, has primarily been developed by the people at Shimizu Corp. for an alternative of steel bars, the most serious disadvantage of which is to rust with salty water. The present speaker has considered the CFGFRP as the material of self-diagnosis.

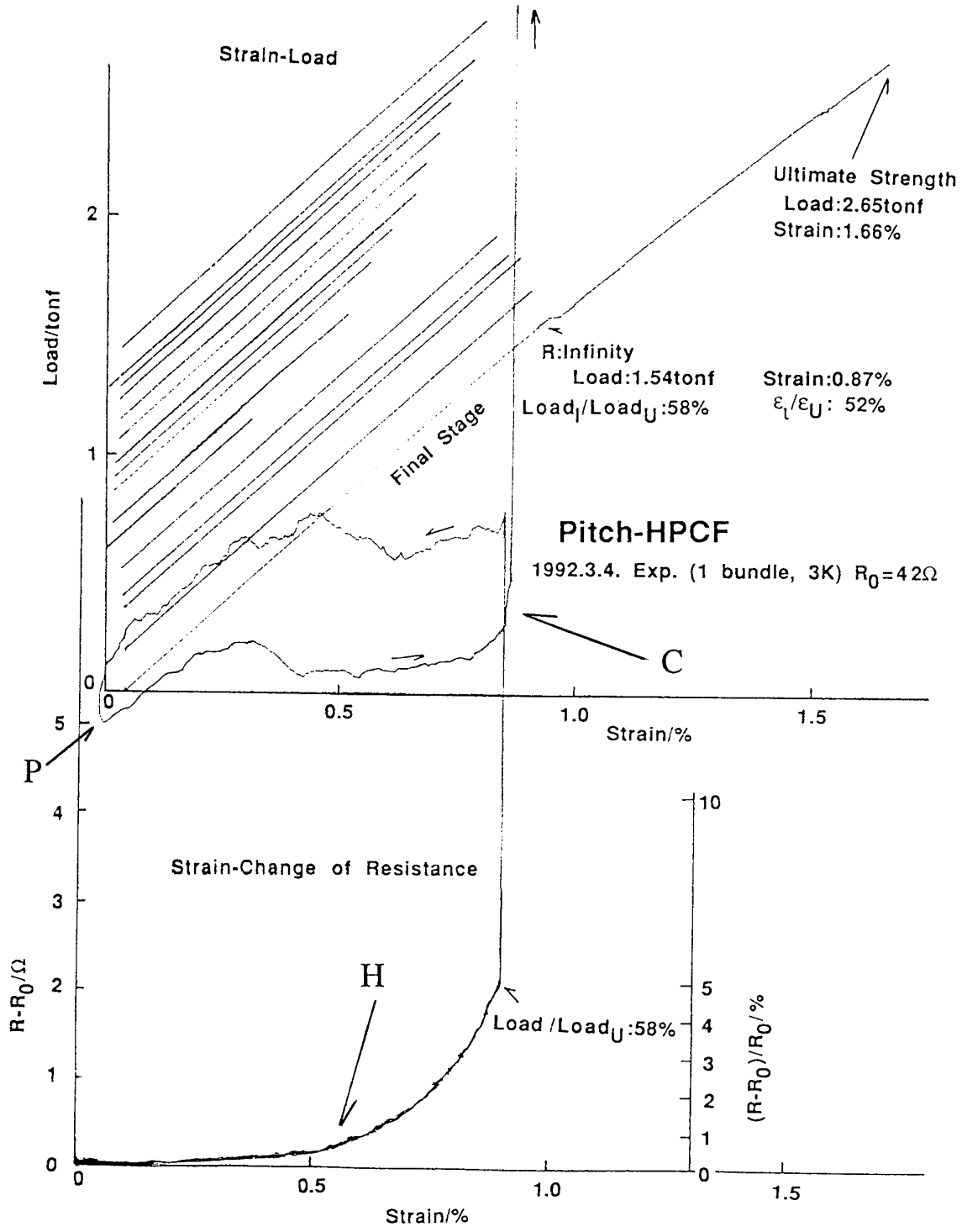

Figure 1 Changes of $(R - R_0)$, $(R - R_0) / R_0$ and load as a finction of strain for CFGFRP composites[4]

The relation between strain or and resistance upon the material is shown in Figure 1. In the region H the material is under healthy condition, in the region C it suffers from a serious damage although still alive with an allowance of 40% in the case, and the point P with zero load after the region C shows that the material has once suffered from a serious damage. This is a carte of the material. With use of ordinary sensors it is very difficult to have memory of damage. Very little residual strain is observed. Identification of damage is possible only under the criterion where one knows that a serious damage has once taken place. The damage appears apparent only under load. It disappears with unloading. The residual resistance at the point P is remarkable on the other hand. The very small residual strain by 0.04% is now easily noticed by observing the large residual resistance by 12.4% in the experiment.

6 APPLICATIONS OF MATERIALS WITH SELF-DIAGNOSIS FUNCTION

The material, CFGFRP, has important self-diagnosis functions, checking health, suffering from serious damage although still alive with much allowance until its fatal damage and memorizing the past maximum damage. Applications are expected very widely. The present speaker counts up those as in aircraft, automobiles, buildings, highways, guard walls etc. Especially checking latent damage after an earthquake with the material is very effective. Recent earthquake in Los Angels has raised necessity of this sort of concept and materials with self-diagnosis functions.

7 CONCLUSION

Intelligence of materials or technologies may be evaluated with a function,

$$Iw=(\text{Required merits})/(\text{Number of elements applied})^{n}$$

n greater than 1.

The higher the index, the familiar the technology to general public and environment.

REFERENCES

1) H. YANAGIDA, Intelligent Materials (Kodansha Bluebacks B-966, Jpn,1993)
2) H. YANAGIDA, Angewandte Chemie, **100**(1988) 553
3) Ken-Materials Consortium, Proposal and Proof of Intelligent(=Ken) Materials, (Ken-Materials Consortium, Tokyo, Jpn, February 7, 1994)
4) N. MUTO et al. Smart Mater. Struct. **1**(1992)324-329

Smart Hydrogels in Devices

Professor Neil B. Graham
Department of Pure and Applied Chemistry
University of Strathclyde, Glasgow, Scotland, UK

General

Hydrogels are materials which will swell in water but not dissolve. They are a large family of materials rather than a single entity. Indeed much of living tissue comprises hydrogel and the variety and function of this class presents the scope for the development of synthetic materials which can perform many so-called " Smart" functions. The action of muscles, the selectivity of membranes and the contraction and expansion of various sphincters and the control of blood flow in veins and arteries might all be simulated with synthetic analogues. Such materials are now being demonstrated and systems which undergo large dimensional changes with changes in hydrogen ion or other ionic concentration have been reported while hydrogels which bend when subjected to an electrical potential difference have been made. Hydrogels can be incorporated into devices which can act as transducers, as sensors and as accurately controlled timing devices for the release of drugs and in other potential applications. This paper will illustrate a selection of these applications utilising hydrogels developed in our laboratories and based on crosslinked poly(ethylene oxide). The dry form of the hydrogel will be referred to as a xerogel and the term hydrogel will refer to the material swollen to some degree with water.

Simple swelling devices controlling the release of contained drugs

When discussing "Smart" systems one can reasonably ask the question "How Smart is Smart?". If we take "Smart" to mean any system which responds in a desirable manner with respect to it's environment then simple xerogels which swell in an environment of water can be reasonably considered as "Smart". So most of the systems on which we have been working over the past twenty years would now be considered as "Smart", even though we didn't know they were at the time! The first of these(1) is a system to protect active drugs and to provide a desirable and largely constant rate of release when the containing xerogel device is immersed in an aqueous environment. This has just received it's clearance for marketing in the UK. It is a lozenge shaped piece of xerogel which contains 10mg of prostaglandin E_2. It is of dimensions such that it behaves approximately as an infinite flat slab. If the thickness of the slab of dry xerogel is in the order of > 0.5 mm then the release of the drug on immersing the slab in an aqueous environment is essentially constant for at least the first fifty percent of the release. This swelling along with the characteristics of the materials provides the "Smart" response which shows a dramatically improved zero order release profile compared with the reducing rate of release which is obtained from an initially fully swollen device. A generic drug delivery system is thus obtained

0-8194-1700-9/94/$6.00

which can be applied, in particular, to the delivery of many drugs in the form of inserts into bodily cavities such as the vagina and rectum. Thus work on the rectal delivery of a narcotic analgesic and the vaginal delivery of an antifungal agent have been reported(2,3).

Hydrogels as Precise timing devices

For some therapies it is desirable to have pulsatile rather than constant release
Diffusion is governed by a combination of thermodynamics and kinetics. It can be shown that diffusive events follow a precise pattern with regard to time. Though the swelling of hydrogels with changing dimensions and hydrogel/xerogel boundaries is a problem not easily amenable to clean mathematical solution it can be solved with the aid of computation and bond-graph theory. It can also be readily demonstrated experimentally(4) that the swelling of a block of hydrogel follows a precisely defined pattern with progressing time. The relationship obeyed is given in the equation below for the time (t) taken for a the xerogel-hydrogel boundary to move a distance (l).

$$t = K l^x$$

'K' and 'x' are constants for a given composition of xerogel.
This pattern of behaviour has been utilised by Polysystems Ltd and Scherer DDS (5,6) to develop an advanced precisely timed pulsed delivery capsule called Pulsincap™.
This "Smart" capsule is shown in Figure 1.

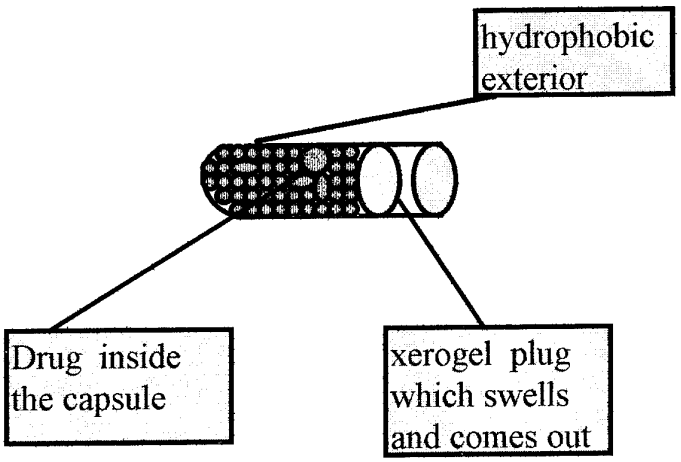

Figure 1. The Pulsincap™ Device

In this device the drug is placed inside a hydrophobic capsule which is the size of a conventional hard gelatine capsule. It is sealed in place with a short cylinder of hydrogel which when placed in an aqueous fluid begins to swell at a rate which is very precisely time defined by it's composition and dimensions. It begins to work it's way out of the hydrophobic shell like a cork coming slowly out of a champagne bottle and at a very precise period of time after it commences swelling separates from the capsule with the result that the contained drug is very quickly released thereafter. The device

can be made even "Smarter" by coating it with a pH sensitive enteric coating. This prevents the swelling of the xerogel plug until the drop of pH from around 2 to maybe 6.8 is encountered in passage through the pyloric sphincter on exit from the stomach. Depending on the particular disease state being treated either one or the other choice might be utilised.

Smart Transducers

The swelling of hydrogels in water is reversible and in reality depends on the chemical potential of the water in equilibrium with the xerogel/hydrogel. It is no surprise therefore that hydrogels can swell and deswell equally well in water vapour as in liquid water albeit more slowly in the former case. At 100% relative humidity the hydrogels will swell to the same degree as in pure water. The degree of swelling of the poly(ethylene oxide) based hydrogels are dependent on the temperature. The swelling decreases steadily with increasing temperature. These properties combined with the physical strength of the hydrogels allows them to be utilised as the transducing mechanism controlling a simple design of hydraulic valve which can control fluid flow directly or, in principle, indirectly via remote fluidic signalling. One design of such a valve is shown in the diagram below.

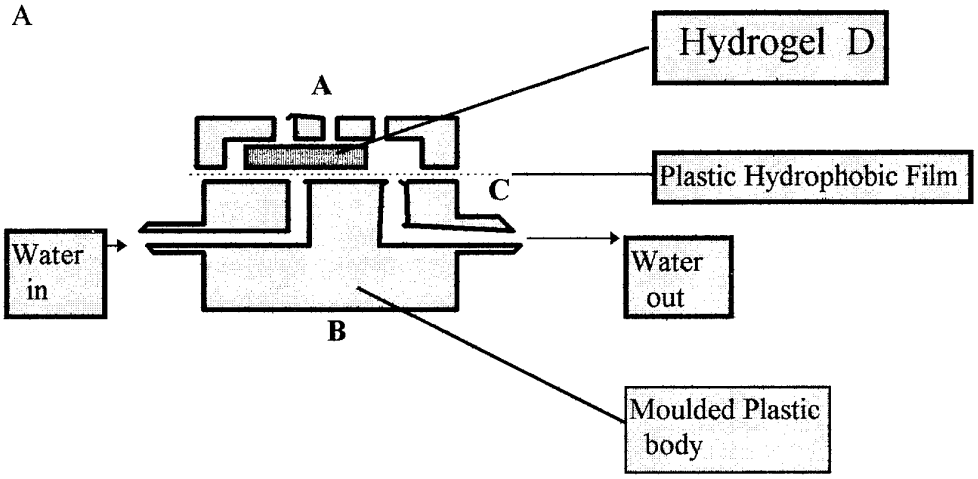

Figure 2. Hydrogel Actuated Controller Valve.

The valve above comprises four simple pieces. Two moulded plastic parts A and B comprising the top and the base of the main body of the device, a section of plastic film C separating the upper and lower body components and a small circular cross section slice of xerogel D. The gap between the upper and lower body parts is shown with a gap and each side of the plastic film for clarity but is in fact sealed. The flow of liquid water in the lower compartment is completely contained beneath the plastic film. The upper compartment is open to the surrounding environment . If the external environment is dry then the xerogel remains unswollen and the water flow in the lower compartment continues uninterrupted. If the exterior of the controller valve becomes immersed in liquid water or water vapour at high humidity, then the xerogel swells

with the water and in its swollen hydrogel form presses the film over the entrance hole for the water and cuts off the flow. A simple application for this device is the automatic watering of plants from a water supply. The valve is labour saving allowing labour free watering control and is efficient in water use. It is thus of potential utility in both the developed countries and the less developed countries where conservation of the water supply is of considerable importance. The changing response of this design of valve to temperature points to control of flow rates with temperature. They could conceivably be utilised to control the cooling water to a reactor where an increased flow of cooling water is required as the reaction temperature rises. The response time of these devices is currently minutes rather than seconds, which is perhaps slow for the rapid control of a reactor. A rather different potential use would be as a remote control detector of e.g. flooding or water level. The continuous flow through the device and associated tubing in a closed fluidic circuit can be monitored via the flow in the tube at some point remote from the tranducer valve. In the event that the valve is in contact with water the flow will cease and the condition may be detected at a distance. Alternatively the reverse process could be used to switch on a water supply when the conditions around the valve were dry. An example of such an application might be to automatically activate the watering systems on a golf course. Many other applications can be envisaged.

References

1. M.E. McNeill and N.B.Graham; Vaginal Pessaries from Crystalline/rubbery Hydrogels for the Delivery of ProstaglandinE_2, J.Cont. Release, 1,(1984) 99-117

2. C.D.Hanning, A.P. Vickers, G. Smith, N.B.Graham and M.E.McNeill; The Morphine Hydrogel Suppository- A New Sustained Release Rectal Preparation, B.J.Anaesthesia, 61,(1988) 221-227

3. L.Cole, C.D.Hanning, S. Robertson , and K.Quinn; Further Development of a Morphine Hydrogel Suppository, Br. J. Clin. Pharmacol.., 30(6), (1990) 781-786

4. M.E.McNeill and N.B.Graham, Properties Controlling the Delivery and Release of Water-soluble Solutes from Poly(ethylene oxide) hydrogels. 2. Dispersion in an Initially Dry Slab, J. Biomaterials Sci., Polymer Edition, (1990)

5. M.E. McNeill, A. Rashid and H.N.E. Stevens, International Patent Application, W090/09168

6. J.S. Binns, M. Bakhshee, C.J. Miller and H.N.E. Stevens, Application of a pH Independent PEG Based Hydrogel to Afford Pulsatile Drug Delivery, Proceedings of the 20th International Symposium on Controlled Release of Bioactive Materials, (1993) 226-227

SESSION 1

Fault Detection employing Transducer Optimisation Procedures

K. Worden , G.R. Tomlinson, A.P. Burrows
Dynamics and Control Research Group, Department of Engineering
University of Manchester, UK.

Abstract
This paper describes one possible way forward for smart structures in the domain of fault detection and classification using neural networks and genetic algorithms. Consideration is given to the incompatibility between numerical training data sets and real structures and how this may be ameliorated using optimisation procedures for determining the number and location of transducers required to locate and classify a fault.

1. Introduction
Structures which suffer from degradation due to faults such as cracks, corrosion, debonding etc. could benefit from procedures which provide optimal sensor distribution. It is well known that problems which have no well-defined solutions but produce characteristics that can be separated in pattern space are strong candidates for pattern recognition algorithms such as Artificial Neural Networks (ANNs).

These methods have found wide applications [1,2] and are becoming increasingly accepted by industry. However, we are still on a learning curve in terms of "best topology" for these algorithms, guidelines for the design of ANNs for particular applications and relating their internal structure to a mathematical framework.

Nevertheless, these procedures do offer a capability as described in earlier papers on fault detection and location [3,4]. In this work, finite elements (FE) were used to generate training data for supervised learning since it allows a large mapping space for simulated faults, boundary conditions, static/dynamic load cases and high spatial resolution. This can however, introduce its own problems as high spatial resolution cannot often be met in practice. As a result it may be necessary to optimise the number and location of sensors which can then be related to a finite element model for use with a neural network in fault detection.

This paper describes one approach to these problems by considering how to locate and classify the severity of a fault in a cantilever plate by optimising the sensor placement using various "fitness" measures.

2. Fault Location in a Cantilever Plate
A cantilever plate of dimensions 300 x 200 x 2.5mm was chosen as the basic structural model. A discretisation of 20x20 elements was used to generate the training sets for a neural network in which faults of different severity were simulated by "removing" small groups of elements. The 20x20 mesh size was sub-divided into a 4x4 grid, each grid bounding a group of 5 x 5 elements into which one of three fault severities could be introduced by deleting one, five or nine elements as shown in Figure 1. These are referred to as fault levels 1, 2 and 3 respectively.

Measurements were assumed to be available at only the nodes of the 4x4 grid as shown in Figure 2, thus creating a situation in which only a sub-set of the total information available from the finite element was being used.

The basic input/output topology of a neural network was therefore established in that the

0-8194-1700-9/94/$6.00

restricted set of measurements was chosen as the network inputs giving a total of 20 input nodes, the outputs of the network being selected to correspond to the transducer locations giving 16 output nodes.

The network was trained to respond in proportion to the severity of a fault which related to the area of the damage (see Figure 4), the desired outputs at each of the element locations being 0.1, 0.5 and 1.0 for the three fault levels. A single hidden layer was used with the final network structure resulting in a 20 : 18 : 16 architecture.

Training the network on the first mode shape data, a location matrix was obtained as shown in Table 1. The ability of the network to unambiguously detect the correct fault level and location would return a diagonal matrix (note that X's have been used to signify a 100% correct diagnosis). However, the network had difficulty in reporting accurately the lowest level of fault; the desired output of 0.1 being commensurate with the output variances of the network. This was due to the problem of small changes occurring in the mode shapes when the damage is located in the elements at the free end of the cantilever plate. Figure 3a, shows these effects where comparisons between the desired and actual network outputs over the whole training set are presented. In Figure 3b, corresponding to element 4, the level of variation is above the minimum value of 0.1 required to detect fault level 1. It is possible to minimise this insensitivity by weighting the modal responses for these elements to give more significance in the training data set; this was not investigated in this work.

Had the network been trained using the 20x20 mesh instead of the 4x4 mesh, improvements in the diagnostic procedure would have occurred. However, this highlights the problem of what is possible in practise in relation to the number of measurement points available compared with the data set available from an FE model, which can be orders of magnitude higher.

3. Sensor Placement

As already stated, using an FE model to generate a supervised learning data set for a neural network has few restrictions in terms of the number of data points (corresponding to computed displacements, strains etc). For the plate used in this work, the modeshapes were defined at twenty points (the actual number available was 400), which may be impractical from a modal test point of view. Thus the question arises as to how many sensors are necessary to produce a diagnostic network with a given probability of error and where the optimum positions of the sensors would be, assuming that the sensor positions allowed can only occur at the twenty locations shown in Figure 2.

The first approach taken was based on a defined "measure of fitness". The initial state assumes that all the sensor locations are occupied and that when a single sensor is removed, there remains twenty possibilities for nineteen sensor patterns. From these patterns the ability of the trained neural networks to locate/classify the fault are ranked according to the measure of fitness. The "fittest" is considered as the 'best' nineteen sensor distribution and the corresponding missing sensor is permanently deleted, leaving an array of eighteen sensor distributions which can be employed in a repeat procedure. Obviously this is a time consuming process and an automated procedure was used which allowed automatic fitting of many networks, using an input mask option which created a data file containing all possible input sets masked to inform the network program to train a specified subset.

As an example, if measurements from twenty sensors are available, and data from only three sensor locations, say 3, 10 and 17, is used the network program is passed the mask 00100000010000001000. This representation is used throughout this work.

In order to establish a measure of fitness a normalised mean square error (MSE) difference between the desired network responses y_i, and those estimated produced by the network after training, $\hat{y}_i$ was used defined as,

$$\text{MSE}\ (\hat{y}_i) = \frac{100}{N_t \sigma^2_{y_i}} \sum_{j=1}^{N_t} [y_i(j) - \hat{y}_i(j)]^2$$

i represents the i^{th} output neuron, N_t the training sets indexed by j. The network performance can be judged on the average value of the MSE over the whole set of outputs or the maximum of the set of output MSEs can be used.

Fault level three, and the first modeshape corresponding to unfaulted and fault cases were used to train the networks. In this case, noise was added to the computed (FE) modeshapes during the training phase. The fitness was established by ranking the networks according to the average and maximum error, number of misclassifications and awarding points accordingly. The overall results of applying the procedures are shown in Table 2.

In order to 'test' the answers, the best '10' sensor distribution was chosen and compared to ten randomly generated sensor distributions and ten distributions suggested by symmetry (sequential deletion of alternate sensors).

Table 3 shows these test results where it can be seen that the algorithmic approach produces the best results in terms of the lowest misclassifications and prediction errors. Figure 4 shows the best '10' sensor location from the algorithm.

Previous work had shown that the use of curvatures (or gradients) as training features for locating faults seemed to be more reliable than direct modeshapes [3]. Thus the procedure was repeated using gradients, calculated from the modeshapes for various fault levels.

In this case however, the fitness was judged on the average error, maximum error and probability of error and an additional strategy was assessed. This was an 'insert' strategy where the procedure starts with diagnostics generated for all one-sensor patterns. In this simulation the probability of error alone was used to determine fitness. The one with the lowest probability is carried forward to the next stage when another sensor is added, the process continuing until all twenty sensors has been added. The results are summarised in Figure 5 which shows the probability of error as a function of sensor number. It is interesting to note the similarity in the results indicating that the mixed fitness method offers no advantages over the insert sensor method. Further, to be sure of a greater than 99% chance of successfully locating the faults, a sensor distribution appears to be sufficient.

Sensor Placement using a Genetic Algorithm

For the sake of completeness, a brief discussion of genetic algorithms (GAs) will be given here, for more detail the reader is referred to the standard introduction to the subject [5]. The training data used for this section were the level 3 curvature data.

Genetic algorithms are optimisation algorithms which evolve solutions in a manner analogous to the Darwinian principle of natural selection. They differ from more conventional optimisation techniques in that they work on encoded forms of the possible solutions. Each possible solution i.e. each set of possible parameters in solution space is encoded as a gene. The most usual form of this gene is a binary string e.g. 00011010110. The first hurdle in setting up a problem for solution by genetic algorithm methods is working out how best to encode the possible solutions

as genes. In the case of the sensor location problem, a natural coding is provided by the input masks described earlier e.g. the gene 00100010000000001000 represents a solution in which transducers are placed at positions 3, 7 and 17.

Having decided on a representation, the next step is to generate, at random, an initial population of possible solutions. The number of genes in a population depends on several factors, including the size of each individual gene, which itself depends on the size of the solution space.

Having generated a population of random genes, it is necessary to decide which of them are fittest in the sense of producing the best solutions to the problem. To do this, a fitness function is required which operates on the encoded genes and returns a single number which provides a measure of the suitability of the solution. These fitter genes will be used for mating to create the next generation of genes which will hopefully provide better solutions to the problem. Genes are picked for mating based on their fitnesses. The probability of a particular gene being chosen is equal to its fitness divided by the sum of the fitnesses of all the genes in the population. Once sufficient genes have been selected for mating, they are paired up at random and their genes combined to produce two new genes. The most common method of combination used is called *crossover*. Here, a position along the genes is chosen at random and the substrings from each gene after the chosen point are switched. This is 1 point crossover. In 2 point crossover a second position is chosen and the gene substrings switched again. There is a natural fitness measure for the sensor location problem, namely the inverse of the probability of misclassification. This is modified here by the addition of a penalty function which suppresses solutions which do not have the desired number of sensors. A simple quadratic penalty function was used.

If a gene in a particular generation is extremely fit, i.e. is very close to the required solution, it is almost certain to be selected several times for mating. Each of these matings however involves combining the gene with a less fit gene so the maximum fitness of the population may be lower in the next generation. To avoid this, a number of the most fit genes can be carried through unchanged to the next generation. These very fit genes are called the *elite*.

To prevent a population from stagnating, it can be useful to introduce perturbations into the population. New entirely random genes may be added at each generation. Such genes are referred to as *new blood*. Also, by analogy with the biological process of the same name, genes may be *mutated* by randomly switching one of their binary digits with a small probability.

With genetic methods it is not always possible to say what the fitness of a perfect gene will be. Thus the iterative process is usually continued until the population is dominated by a few relatively fit genes.

One or more of these genes will generally be acceptable as solutions.

Note that the gene encoding used here is only suitable for numbers of sensors close to ten. This is because the number of distinct n-sensor genes is $\binom{20}{n}$ and this is very strongly peaked at ten. This means that genes introduced into the population by the various operations will have highest probability of having close to ten sensors. For this reason the GA was only used to generate distributions with 9 to 12 sensors. Fifty generations were used in each case, the GA used a single member elite and introduced five new blood at each step. The resulting probabilities of

misclassification for the fittest gene in each case are given in Table 1.

Number of sensors	Probability of error
9	0.0017
10	0.0017
11	0.0011
12	0.0016

Table 1 : Probabilities of error for the various GA-generated Sensor distributions.

Comparison with Figure 5 shows that the GA sensor placements outperform those from the heuristic method of the previous section. In fact, the results were quite close, the 10-sensor distribution from the insert strategy had eight sensors in common with that from the GA.

This is very much a preliminary study. Work continues using more complex gene encodings which do not bias the search towards the 10-sensor distributions.

References

[1] Advisory Council on Science and Technology, (ACOST), Cabinet Office, "Artificial Neural Networks", 1992.

[2] "Neural Networks, Neuro-Fuzzy and other Learning Systems", Proc. IT Workshop at Inst. Civil Engineers, April 1994.

[3] Worden, K., Ball, A.D. and Tomlinson, G.R., "Fault Location in a Framework Structure using Neural Networks", Smart Materials and Structures, **2**, p189-200, 1993.

[4] Kudva, J., Munir, N., and Tan P.W., "Damage detection in Smart Structures using Neural Networks", Smart Materials and Structures, **1**, p100-112, 1992.

[5] Goldberg, D.E., "Genetic Algorithms in Search, Learning and Optimisation", Addison Wesley, 1989.

Fault element	Output node															
	1	2	3	4	5	6	7	8	9	10	11	12	13	14	15	16
1	X	-0.2	-0.2	0.1	-	-	-	-	-0.2	-0.1	-	-	-	-0.1	-	-
2	-	X	-	-0.1	-	-	-0.2	0.1	-	-	-	-	-	-	-	-0.1
3	-	-0.2	X	0.2	-	-	0.1	0.1	-	-	-0.1	-	-	-	-0.2	-0.2
4	-	-0.3	-	X	-	0.1	-	0.2	-	-	-	-0.1	-	-	-0.1	-0.2
5	-	-0.2	-	0.1	X	-	-	-	-	-	-	-	-	-	-	-
6	-	-0.2	-	-	-	X	-	-0.2	-	-	-0.2	-0.2	-	-	-	-
7	-	-0.2	0.1	-	-	-	X	-0.1	-	-	0.1	-0.1	-	-	-0.1	-
8	-	-0.3	-	0.2	-	-0.1	-0.1	X	-	-	-	0.2	-	-	-	-0.2
9	-	-0.1	-	-	-	-	-	-0.1	X	-	-	-	-	-	-	-
10	-	-0.2	-0.2	-0.1	-	-	-	-0.2	-	X	-	-0.2	-	-	-	-
11	-	-0.3	0.2	-	-	-0.1	0.1	-	-	0.1	X	-0.2	-	-0.1	0.1	-0.1
12	-	-0.3	-	-0.1	-	-	-0.2	0.1	-	-0.1	-0.2	X	-	0.1	0.1	0.1
13	-	-0.1	-	-	-	-	-	-0.1	-	-0.2	-	-	X	-0.2	-	-
14	-	-0.3	-0.2	-	-	-	-0.2	-	-	-	-0.2	-	-	X	-	-0.1
15	-	-0.3	-0.2	-0.2	-	-	-0.2	-	-	-0.1	-	-	-	-	X	0.1
16	-	-0.3	-0.1	-0.1	-	-	-	-0.2	-	-	-0.1	0.2	-	-	-	X

Table 1: Location matrix from network trained on first modeshape

Fault element	Output node															
	1	2	3	4	5	6	7	8	9	10	11	12	13	14	15	16
1	400	-	-	-	-	-	-	-	-	-	-	-	-	-	-	-
2	-	400	-	-	-	-	-	-	-	-	-	-	-	-	-	-
3	-	-	387	-	-	-	13	-	-	-	-	-	-	-	-	-
4	-	-	-	373	-	-	-	4	-	-	-	1	-	-	-	22
5	-	-	-	-	400	-	-	-	-	-	-	-	-	-	-	-
6	-	-	-	-	-	400	-	-	-	-	-	-	-	-	-	-
7	-	-	9	-	-	-	373	-	-	-	17	-	-	-	4	-
8	-	-	-	36	-	-	1	237	-	-	-	122	-	-	-	-
9	-	-	-	-	-	-	-	-	400	-	-	-	-	-	-	-
10	-	-	-	-	-	-	-	-	-	400	-	-	-	-	-	-
11	-	-	-	-	-	-	13	-	-	-	373	-	-	-	14	-
12	-	-	-	17	-	-	-	60	-	-	-	303	-	-	-	20
13	-	-	-	-	-	-	-	-	-	-	-	-	400	-	-	-
14	-	-	-	-	-	-	-	-	-	-	-	-	-	400	-	-
15	-	-	-	-	-	-	-	-	-	-	9	-	-	-	391	-
16	-	-	-	46	-	-	-	1	-	-	-	7	-	-	-	346

Table 2: Classification matrix from network trained on first modeshape - noise RMS 0.001 (0.1% signal) - Fault severity 3.

Source of Pattern	Sensor Pattern	Average Error	Maximum Error	Failures
Algorithm	01010101011000011011	20.03	53.11	0
Symmetry	01010101010101010101	26.74	62.86	1
	10101010101010101010	31.66	72.26	1
Random	01101101000011001110	32.55	77.39	0
	11000100100111001011	29.80	73.85	0
	00010110001111100101	29.32	75.56	1
	01010101001000111101	25.45	67.05	1
	01110111000001101010	32.12	73.20	1
	00010111000110111100	30.12	78.86	1
	11101101110000101000	27.10	79.58	1
	11011101100100000101	29.06	78.79	2
	11011101110000100100	28.84	80.19	3
	11011101110010000001	28.07	78.25	2

Table 3: Test of 'optimum' 10 sensor pattern against random patterns; feature is first modeshape.

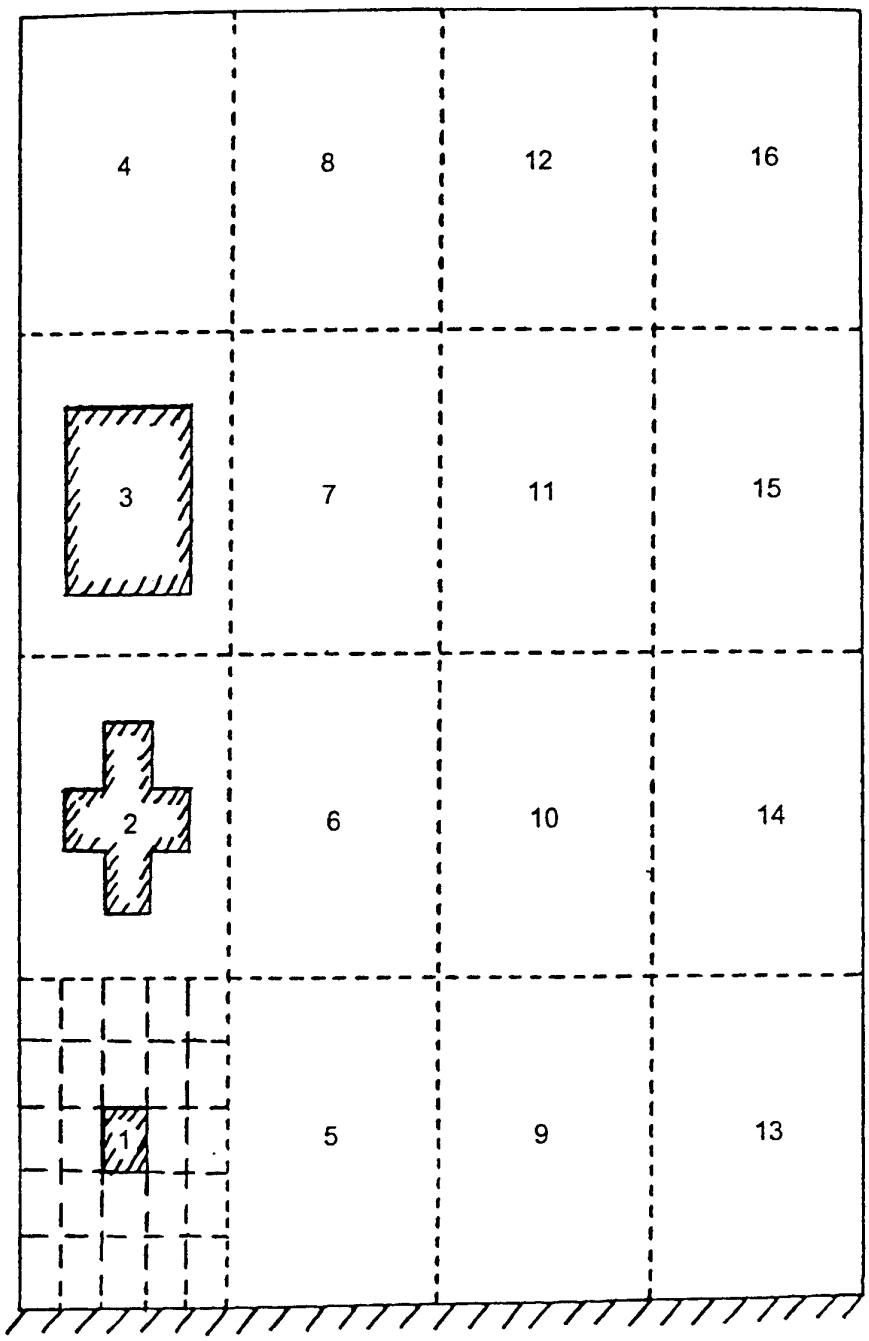

Figure 1 : Numbering system for fault locations and the three fault severity levels indicated by hatched areas.

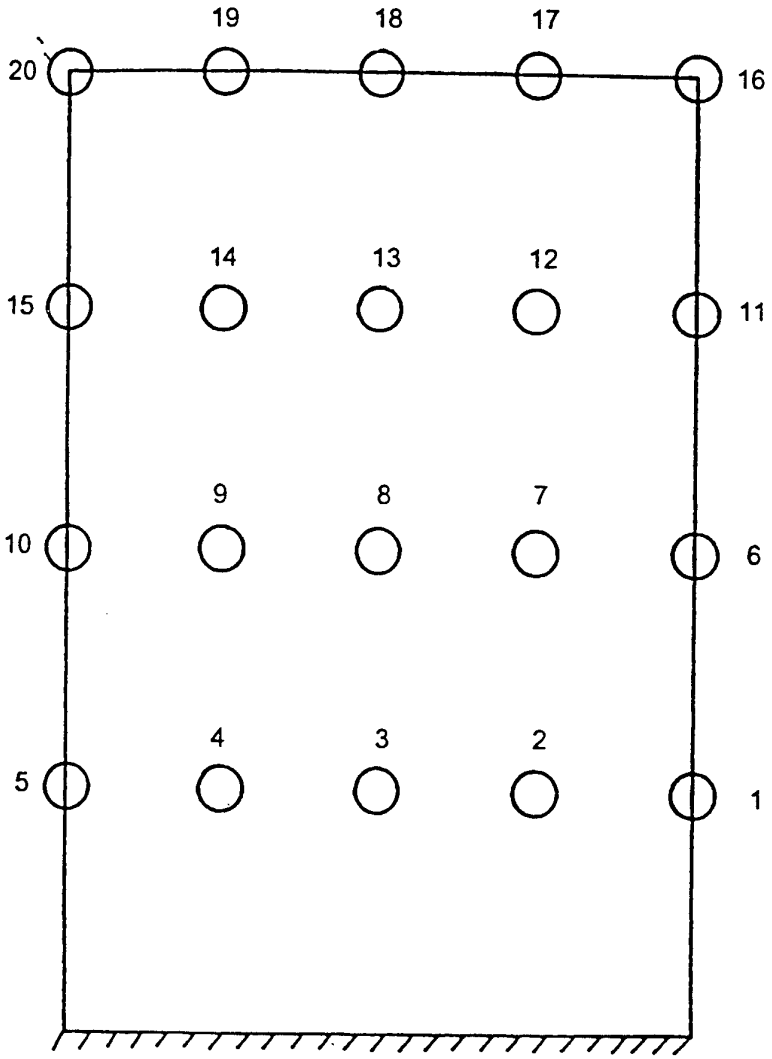

Figure 2 : Numbering system for sensor locations.

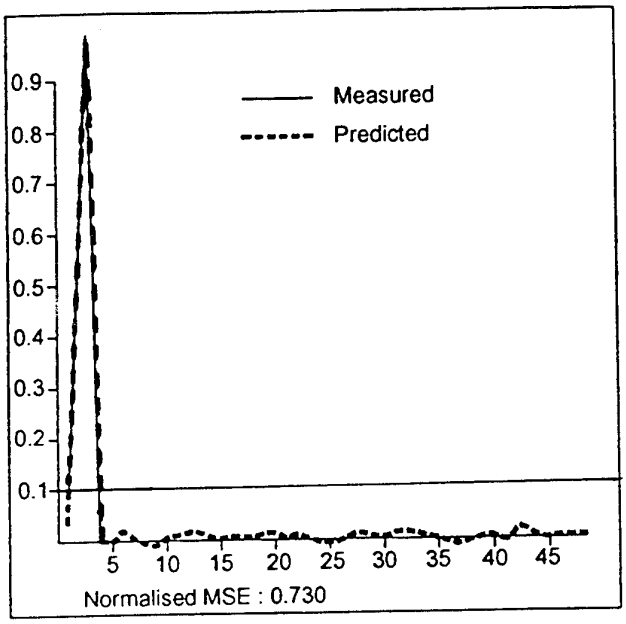

Figure 3 (a). Comparison between desired output 1 and network prediction for location/severity network trained on the first modeshape.

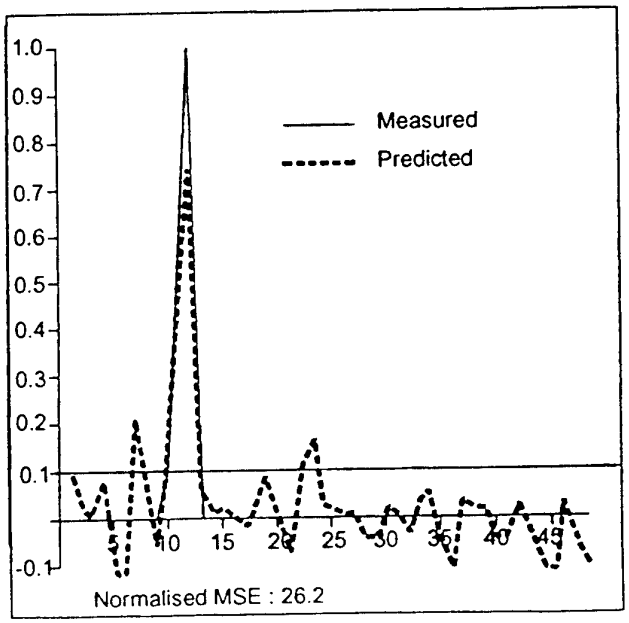

Figure 3 (b). Comparison between desired output 4 and network prediction for location/severity network trained on the first modeshape.

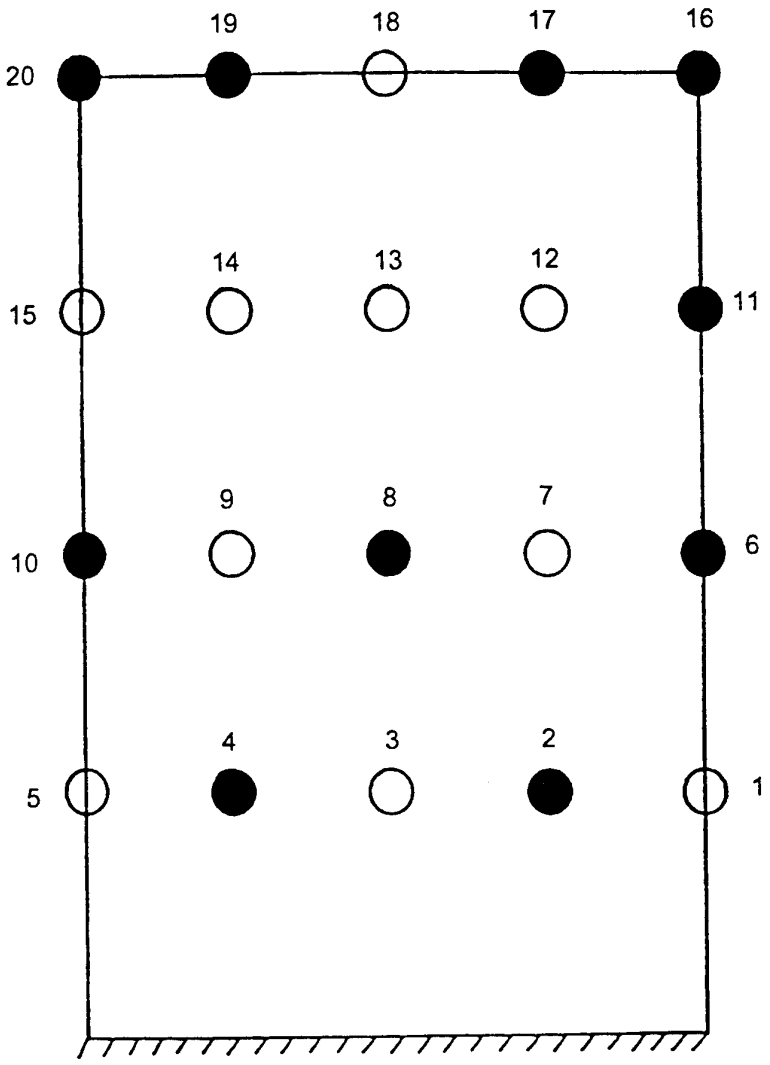

Number of sensors	:	10
Code	:	01010101011000011011
Network	:	10:12:16
Average error	:	20:03
Maximum error	:	53.11
Misclassification	:	0

Figure 4: Best 10-sensor pattern for modeshape diagnostic. Algorithm based on three separate fitness measures.

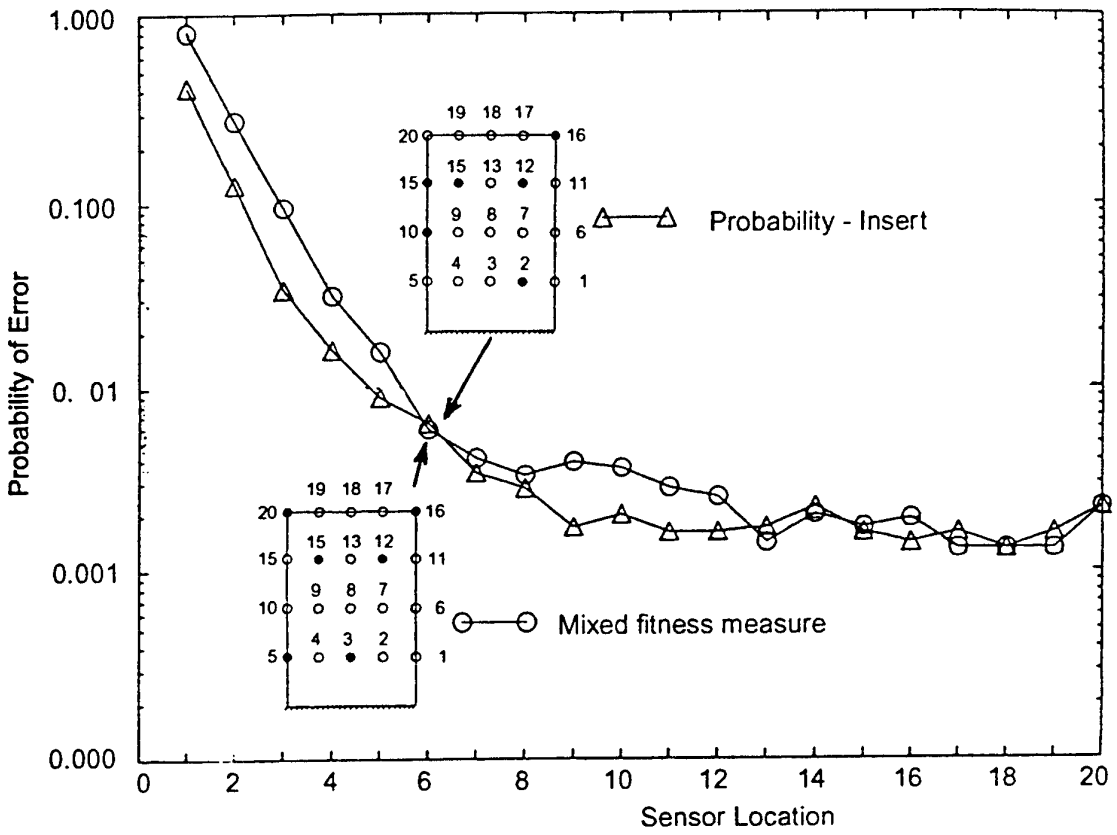

Figure 5 : Probability of error as a function of sensor number.

A Cellular Automaton Generating Topological Structures

Norio INOU, Naoko SHIMOTAI and Takefumi UESUGI

Tokyo Institute of Technology, O-okayama, Meguro-ku, Tokyo 152, Japan

Abstract: This paper describes a cellular automaton based on adaptive function of living systems. We simulated the behavior on a computer giving each cell local rules such as "death", "birth" and "division" like an organism. The computational results showed that the model generates a clear framed structure for a mechanical condition. We also reported on diverse topological structures inhered in the system.

1. Introduction

Living structure for supporting the body such as bone or wood has a function to adapt mechanical environment. In case of bone, it can change the shape or the inner structure. When a stress at a part of bone is not set up for a long time, the part is weakened by decreasing the bone density. Conversely, when a part of bone is highly stressed, the part is strengthened by increasing the bone density. As a result of the continuous process, the whole bone forms a proper structure to outer circumstance [1]. We call the phenomena functional adaptation or remodeling. From a viewpoint of engineering, remodeling can be explained as a congregation of local feedback mechanisms. If such a system was realized, it would self-organize a proper structure for a loading condition.

In the actual living system, the capability of remodeling is not so strong. It is difficult to synthesize such intelligent material in the near future. However, we can simulate the behavior of the system on a computer setting a characteristic of remodeling. We propose a distributed mechanical system for the simulation as shown in Fig. 1. The model consists of same elements which mechanically connect each other. Each element senses mechanical conditions and changes the material property itself.

This is a sort of a cellular automaton which consists of autonomous cells. The cellular automaton is generally known as a pattern generator. We expect that our model has a new feature to generate mechanical structures as it includes mechanical property.

In this paper, we focus on examining the performance of the model. First, we explain our simulation method. Second, we show the performance of the model giving each cell local rules like an organism. Third, we point out diversity of structures inhered in the same mechanical condition and evaluate the topological structures on a diagram with global criterions.

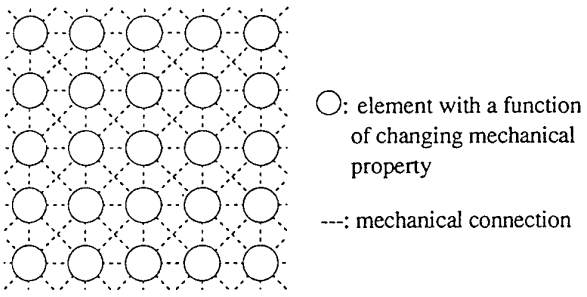

Fig. 1 Cellular automaton based on remodeling.

2. Simulation method

The simulation is executed by the following iterative process.

Step 1. Give an acting space of cells.
Step 2. Set loads and fixed conditions on cells.
Step 3. Calculate stresses in the cells.
Step 4. Evaluate the stresses.
Step 5. Change material property of the cells.
Step 6. Return to Step 2.

The above algorithm is basically same as Growing-Reforming Procedure [2] which reforms the shape of structure by partial modification. In our model, Young's modulus of each cell is changed. As far as the partial modification, there are many similar methods in the field of structural optimization. However, our method does not include any global estimation because of the cellular automaton although other optimal methods are based on sensitive analysis.

0-8194-1700-9/94/$6.00

Each cell changes the Young's modulus independently by the following equation.

$$E^{(t+1)} = E^{(t)}\{1 + a\,(\,\sigma/\sigma_c - 1\,)\} \qquad (1)$$

Where E: Young's modulus, t: iteration steps, σ: equivalent stress, σ_c: target stress value, α: constant value about 0.1.

The equation acts so that the difference between stress of each cell and the target stress at the each place gradually decreases. We expect that a condition to satisfy the relation $\sigma/\sigma_c=1$ for almost cells is formed by iterative calculations.

The simulation was executed on a personal computer (CPU:80486, 50MHz) with a batch program including several tasks. For the calculating stress of each cell, we used a finite element program called NISA II (EMRC) as a solver. After changing Young's modulus of each cell by local rules, we rewrote the data in the input file of NISA II. As the solver accepts about 320 kinds of Young's modulus, we provide a table of Young's modulus in advance and selected the nearest value among them after calculation of Young's modulus from the equation (1).

3. Behavior of the total system by local rules

Behavior of the proposed model is affected by local rules which each cell possesses. In this chapter, we report on this point.

3.1 Non-linear relationship in changing modulus

First, we examined the effect of change of Young's modulus on the total system. A change of Young's modulus of a cell means a change of density and strength. The relationship is important because the strength corresponds to the target stress value in equation (1). We expect that it has an effect on the self-organization of structure. In case of bone, the strength is proportional to the Young's modulus [3]. But it is very difficult to describe the relationship analytically because it depends on micro structure of material. In order to examine the effect, we set up two relationships as shown in Fig. 2. The non-linear relationship was defined by the following function.

$$\sigma_c = \sigma_{c0}\,[1+b\{\exp\,(a\,\frac{E-E_0}{E_0}) - 1\}] \qquad (2)$$

$$a = \begin{cases} a_1 \\ a_2 \end{cases},\quad b = \begin{cases} 2/\{\exp(2a_1) - 1 & (E \geq E_0) \\ 1/\{\exp(-a_2) - 1 & (E < E_0) \end{cases}$$

Where $a_1 = 7.5$, $a_2 = -10.0$.

We provided a problem as shown in Fig. 3 and simulated the model. Figure 4 (a), (b) are the simulation results which correspond to the relationships as in Fig. 2 (a) and (b) respectively. Right figures show the Young's modulus distributions and left are the histograms. The results show that the strong non-linear relationship as in Fig. 2 (b) is effective to self-organize a clear structure.

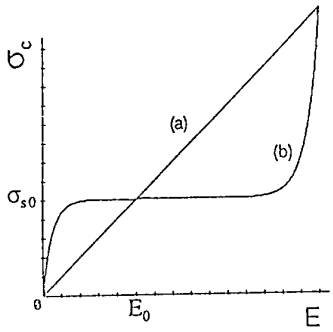

Fig. 2 Relationship between Young's modulus and target stress value. (a):linear, (b):non-linear.

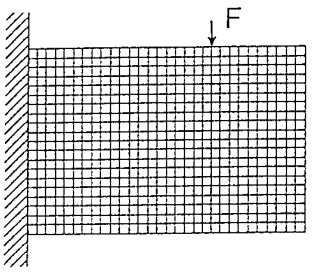

30 x 20 cells
(15 mm x 10 mm)
Load = 9.8 N
Young's modulus
$= 9.8 \times 10^4$ Mpa

Fig.3 Mechanical problem.

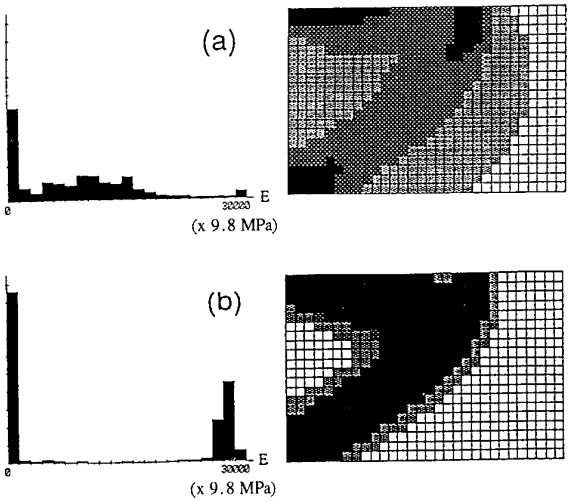

Fig. 4 Simulation results. (a):linear, (b):non-linear

3.2. "death" and "birth" rule

Although the non-linear relationship is effective for the formation of a clear structure, it is not enough for the formation when the applied load is small. Figure 5 (a) shows the result when the load decreases to 1/2 compared with the previous loading force. As some cells stay at low moduli, the structure is rather fuzzy.

To solve the problem, we added a local rule to the model. The local rule is : When Young's modulus of a cell decreases below a value, the cell dies (vanishes). Conversely, if a cell is highly stressed, a new cell is born at a vacant place near the cell.

The rule is similar to "life game" proposed by Conway [4]. Adding the "death" and "birth" rule to the model, we simulate the behavior of the system. The rule was applied when Young's modulus of a cell became 30% of the initial value. The simulation result is shown in Fig. 5 (b). A clear framed structure was formed.

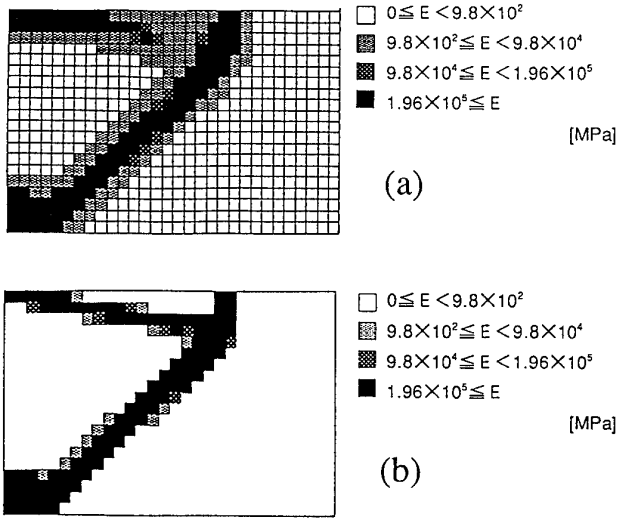

Fig. 5 Simulation results.
(a): without "death" and "birth" rule, (b): with the rule

3.3 "division" rule

If we desire a precise structure, we must provide many cells. However, it becomes difficult to execute the simulation because a required time for the stress analysis exponentially increases with the number of cells. To save the time, we proposed "division" rule. The rule is: Each cell split in several cells at a certain time when the total number of cells considerably decreased. In this two-dimensional problem, a cell splits in 4 cells when the number of cells decreases below 1/3.

Figure 6 is a problem for the simulation. The simulation result is shown in Fig. 7. A topological structure with holes was formed. Although the structure is rather complicated, it is a solution of the problem as the stresses of cells are almost same.

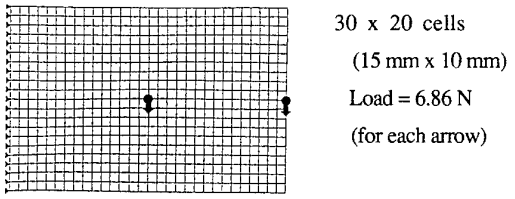

Fig. 6 Mechanical problem.

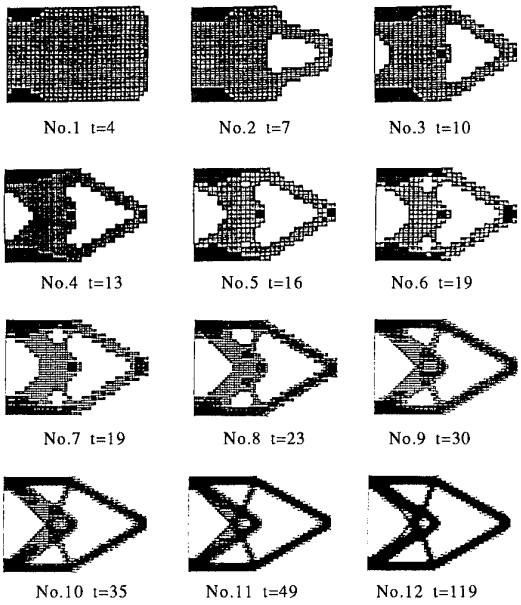

Fig. 7 Simulation results.
The "division" rule was applied at No. 7.

4. Topological structures and the comparison

A cellular automaton has potentiality to generate different patterns by altering the initial condition. In this study, it means that the model generates different topological structures. We examined the potentiality by altering initial Young's modulus.

Figure 8 is a problem for the examination. We provided several Young's modulus distributions as in the left side of Fig. 9. Young's moduli of the light dark areas are set as 1/2 compared with the dark areas. The simulation results are shown in the left side of Fig. 9. It should be noticeable that the topological structure with

holes was formed from even a homogeneous Young's modulus distribution. The structure No.1 is similar to a result obtained by a structural optimization method [5].

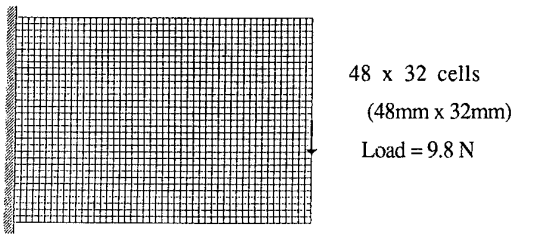

Fig. 8 Mechanical problem.

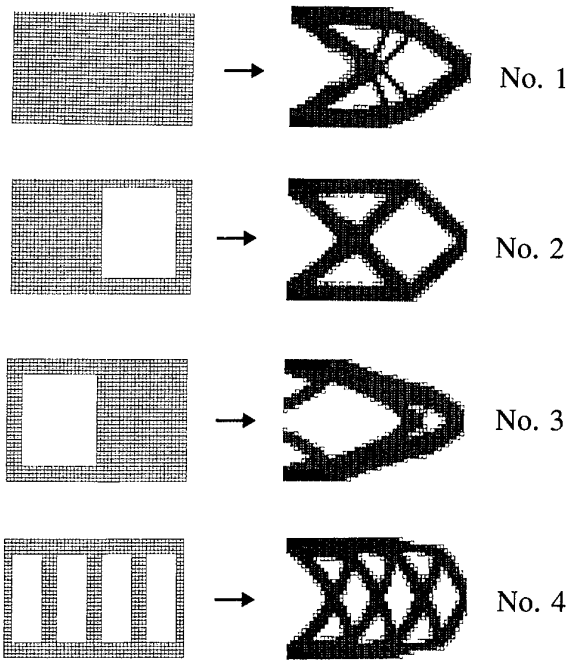

Fig. 9 Simulation results. Left sides are the initial conditions. Right sides are the final structures.

These results as in Fig. 9 are not guaranteed on the point of optimal design because our method is based on only local rules. We must make an estimation with global criterions for practical use. For the quantitative estimation, we standardized the structures. First of all we removed weak cells less than 4.9×10^4 MPa and next gave the same Young's modulus (2.94×10^5 MPa) to the remained cells. Finally we made the volume of these structures uniform as 1000 mm^2 changing the thickness of the cells for each structure.

After the standardization, we plotted them with other results on a diagram as in Fig. 10. The horizontal axis denotes the maximum stress and the vertical axis denotes the maximum displacement. We can say that a structure located in near the origin (more under side and more left side) is well-designed. The structure No.1 or No. 2 is mechanically superior to others under this situation.

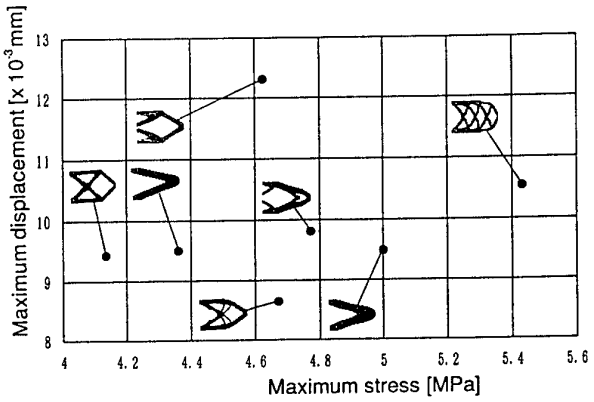

Fig. 10 Comparison of topological structures.

5. Conclusions

We proposed the cellular automaton based on remodeling of living systems. The computational results showed that the simple local rules such as "death", "birth" and "division" are effective to self-organize a framed structure and also showed that the model generates various topological structures by altering the initial condition. The proposed diagram gives us perspective for designing topological structure.

References

[1] Benno K. F. Kummer : BIOMECHANICS OF BONE, chapter 10 in BIOMECHANICS, Y.C.Fung, et al. eds., Englewood Cliffs, New Jersey (1972)

[2] Yoji UMETANI and Shigeoki HIRAI: Shape Optimization for Beams Subject to Displacement Restrictions on the Basis of the Growing-Reforming Procedure, Bulletin of the JSME, Vol.21, 1113/1119 (1978)

[3] S.A.Goldstein, D.L.Wilson, D.A.Sonstegard and L.S.Matthews: The Mechanical Properties of Human Tibial Trabecular Bone as a Function of Metaphyseal Location, J.Biomechanics, Vol.16, 965/969 (1983)

[4] Martin Gardner: MATHEMATICAL GAMES, Scientific American, Vol.223, 120/123 (1970)

[5] J.Fukushima, K.Suzuki and N.Kikuchi: Topology Optimization of a Car Body with Multiple Loading Conditions, The 33rd AIAA/ASME/ASCE/AHS/ASC Structures, Structural Dynamics and Materials Conference, 2499/2507 (1992)

Recursive Architecture for Large Scale Adaptive System

Kazuyuki HANAHARA and Yoshihiko SUGIYAMA

Department of Aerospace Engineering, College of Engineering,
University of Osaka Prefecture

1-1, Gakuen-cho, Sakai, Osaka 593, Japan

Tel. +81-722-52-1161 ext.2245
Fax.+81-722-59-3340

1 Introduction

'Large scale' is one of major trends in the research and development of recent engineering, especially in the field of aerospace structural system[1]. This term expresses the large scale of an artifact in general, however, it also implies the large number of the components which make up the artifact in usual. Considering a large scale system which is especially used in remote space or deep-sea, such a system should be adaptive as well as robust by itself, because its control as well as maintenance by human operators are not easy due to the remoteness. An approach to realizing this large scale, adaptive and robust system is to build the system as an assemblage of components which are respectively adaptive by themselves. In this case, the robustness of the system can be achieved by using a large number of such components and suitable adaptation as well as maintenance strategies.

Such a system gathers many researcher's interest and their studies such as decentralized motion control[2], configurating algorithm[3] and characteristics of structural elements[4] are reported. In this article, a recursive architecture concept is developed and discussed towards the realization of large scale system which consists of a number of uniform adaptive components. We propose an adaptation strategy based on the architecture and its implementation by means of hierarchically connected processing units. The robustness and the restoration from degeneration of the processing unit are also discussed. Two- and three-dimensional adaptive truss structures are conceptually designed based on the recursive architecture.

2 Recursive Architecture

The word 'recursive' indicates the self-similarity of the system, that is, a part of the system (referred to as a subsystem) has the same constitution as the original system. Examples of self-similarity can be easily found in natural systems, such as tree, blood vessel and coral reef which are referred to as the fractal geometry[5]. Based on such a constitution, a subsystem is expected to be also an independent system which is same as the original system except for its scale. The subsystem also has the sub-subsystems in the same manner. This 'recursive' characteristics is expressed in general form as

$$\boldsymbol{R}^N = \boldsymbol{R}(\boldsymbol{R}_1^{N-1}, \cdots, \boldsymbol{R}_M^{N-1}, \boldsymbol{S}^N) \tag{1}$$

$$\boldsymbol{R}^n_{i_{N-1}\cdots i_n} = \boldsymbol{R}(\boldsymbol{R}^{n-1}_{i_{N-1}\cdots i_n 1}, \cdots, \boldsymbol{R}^{n-1}_{i_{N-1}\cdots i_n M}, \boldsymbol{S}^n_{i_{N-1}\cdots i_n}) \qquad (n = N-1, \cdots, 2) \tag{2}$$

$$\boldsymbol{R}^1_{i_{N-1}\cdots i_1} = \boldsymbol{R}^1(\boldsymbol{X}_{i_{N-1}\cdots i_1}, \boldsymbol{S}^1_{i_{N-1}\cdots i_1}) \tag{3}$$

where the superscript n and the subscript string $i_{N-1}\cdots i_n$ describe the order (corresponding to the scale) and the index of the subsystem, the vectors $\boldsymbol{R}^n_{i_{N-1}\cdots i_n}$ and $\boldsymbol{S}^n_{i_{N-1}\cdots i_n}$ denote the status and environment values of subsystem $i_{N-1}\cdots i_n$ of nth order and $\boldsymbol{X}_{i_{N-1}\cdots i_1}$ is the control variable of primitive component $i_{N-1}\cdots i_1$, that is, the 1st order subsystem. The number of $(n-1)$th order subsystems under a nth order subsystem expressed as M is referred to as the coordination number and N is the order of entire system. The two functions R and R^1 describe the behavior as well as the characteristics of the system, that is, R is for $(2,\cdots,N)$th order subsystems and R^1 is for primitive components. The physical entity of the system is the assemblage of M^{N-1} primitive components.

0-8194-1700-9/94/$6.00

Paying attention to Eqs.(1) and (2), it is found that $\boldsymbol{R}$ is the only function which describes the behavior of the total system or any subsystem, except for primitive components. The description of the system based on the recursive architecture is achieved by specifying only two functions $\boldsymbol{R}$ and $\boldsymbol{R}^1$, in spite of the order of the system.

3 Adaptation Strategy

The adaptation of the system is formulated as the minimization problem of the criterion function which describes the degree of adaptation to the environment. For the system based on the recursive architecture expressed as Eqs.(1)–(3), the minimization problem is written as

$$\text{Minimize} \quad g \quad \text{with respect to} \quad \boldsymbol{X}_{i_{N-1}\cdots i_1}, \quad i_1,\cdots,i_{N-1} = 1,\cdots,M \tag{4}$$

where

$$g = g(\boldsymbol{R}^N) \tag{5}$$

is the criterion function defined for the system. In this study, the gradient procedure

$$\boldsymbol{X}_{i_{N-1}\cdots i_1} \leftarrow \boldsymbol{X}_{i_{N-1}\cdots i_1} - \Delta\boldsymbol{X}_{i_{N-1}\cdots i_1} \quad (i_1,\cdots,i_{N-1} = 1,\cdots,M) \tag{6}$$

$$\Delta\boldsymbol{X}_{i_{N-1}\cdots i_1} = \gamma\frac{\partial g}{\partial \boldsymbol{X}_{i_{N-1}\cdots i_1}} \tag{7}$$

is adopted for the minimization, where γ is the small coefficient for adaptation which denotes the alteration rate of control variables. The gradient $\Delta\boldsymbol{X}_{i_{N-1}\cdots i_1}$ is calculated from Eqs.(1)–(3) and (5) by applying the chain rule as

$$\Delta\boldsymbol{X}_{i_{N-1}\cdots i_1} = \gamma\frac{\partial g}{\partial \boldsymbol{X}_{i_{N-1}\cdots i_1}} = \Delta\boldsymbol{R}^1_{i_{N-1}\cdots i_1}\frac{\partial \boldsymbol{R}^1_{i_{N-1}\cdots i_1}}{\partial \boldsymbol{X}_{i_{N-1}\cdots i_1}} \tag{8}$$

$$\Delta\boldsymbol{R}^n_{i_{N-1}\cdots i_n} = \gamma\frac{\partial g}{\partial \boldsymbol{R}^n_{i_{N-1}\cdots i_n}} = \Delta\boldsymbol{R}^{n+1}_{i_{N-1}\cdots i_{n+1}}\frac{\partial \boldsymbol{R}^{n+1}_{i_{N-1}\cdots i_{n+1}}}{\partial \boldsymbol{R}^n_{i_{N-1}\cdots i_n}} \quad (n = 1,\cdots,N-2) \tag{9}$$

$$\Delta\boldsymbol{R}^{N-1}_{i_{N-1}} = \gamma\frac{\partial g}{\partial \boldsymbol{R}^{N-1}_{i_{N-1}}} = \Delta\boldsymbol{R}^N\frac{\partial \boldsymbol{R}^N}{\partial \boldsymbol{R}^{N-1}_{i_{N-1}}} \tag{10}$$

$$\Delta\boldsymbol{R}^N = \gamma\frac{\partial g}{\partial \boldsymbol{R}^N}. \tag{11}$$

Paying attention to these equations, the minimization of criterion function g in Eq.(5) by means of gradient procedure (6) can be performed by hierarchically connected processing units as shown in Fig.1. It is noted that this adaptation control based on the proposed strategy is realized by uniform processing units which perform only three kind of processes, that is, the process "CF" on criterion function g, the process "SS" on function $\boldsymbol{R}$ for subsystems and the process "PC" on function $\boldsymbol{R}^1$ for primitive components, in spite of the order(that is, the scale) of system. Because these processes require only calculation of the function values as well as the gradients, the modular neural network approach based on the alternative backpropagation[6] is also available for the processing units.

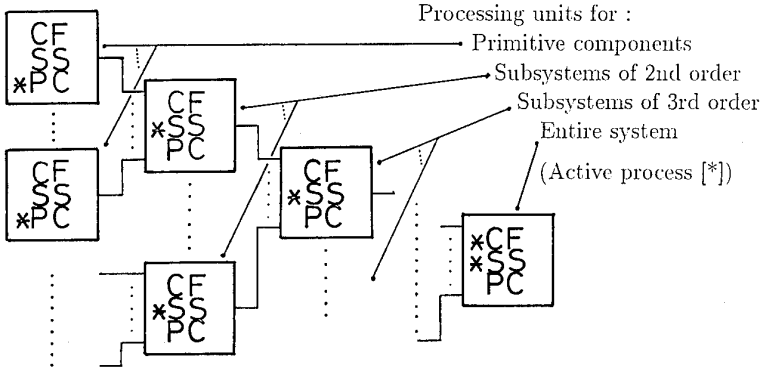

Figure 1: Hierarchically connected processing units for adaptation control

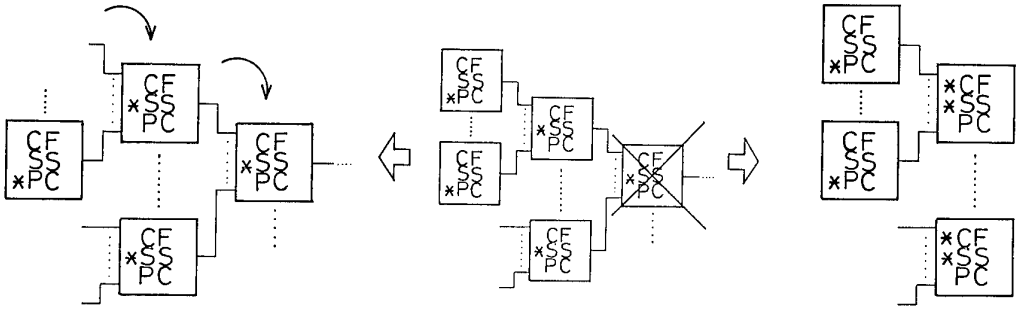

(a) Successive replacement (b) Independence of subsystems

Figure 2: Restoration from degeneration of processor

4 Robustness and Flexibility

The robustness of the system based on the recursive architecture is discussed from two kinds of viewpoints. One is the robustness against degeneration of the primitive component and the other is the robustness against degeneration of the processing unit for adaptation control.

Degeneration of a primitive component does not cause severe degeneration of the system essentially, because a large number of primitive components are participating the adaptation control respectively and the requirement of alteration for a primitive component is not affected by breaking down of other components.

There are two ways of restoration from degeneration of a processing unit. One is the successive replacements of degenerated or vacant processing units by the units for lower order subsystems as shown in Fig.2(a). This approach needs changeable connection among processing units, however, the adaptability deterioration of the system is suppressed to the level caused by degeneration of a primitive component. Independence of each subsystem under the degenerated processing unit shown in Fig.2(b) is the other approach. In this case, each subsystem become a new independent system by activating the process "CF" at the processing unit for its highest order.

The later approach of restoration from degeneration of processing unit also shows the scale changeability of the system based on the recursive architecture. That is, a system can separate into smaller systems, as well as, systems can unite to form a larger system, if the primitive components have the equipments to enable themselves to connect or disconnect with one another. Even in such a case, the adaptation strategy in the previous section is available for the smaller or larger system. This indicates that the scale of the system is flexibility changeable corresponding to the objective of the mission.

5 Adaptive Truss Based on Recursive Architecture

The recursive architecture is conceptually applied to the adaptive truss structure[7] which is expected to be used in various kind of future space mission. The adaptive truss is a truss structure which has a topology of statically determinate truss and actively length-adjustable truss members. It must be adaptive as well as robust by itself, because there is nothing but itself in the space where it exists, that is, the remote position from the earth.

The primitive components for two- and three-dimensional adaptive truss are shown in Fig.3(a) and Fig.4(a), that is, the triangle and the tetrahedron. The 2nd order systems are obtained by assembling them as shown in Fig.3(b) and Fig.4(b), and the 3rd order systems shown in Fig.3(c) and Fig.4(c) and the higher order systems are built in the same manner. The coordination numbers of these adaptive truss are 3 for two-dimensional truss and 4 for three dimensional truss. The proposed adaptation strategy is also available for these adaptive trusses. The objective of adaptation can be kinematic, static and dynamic characteristics.

6 Concluding Remarks

A large scale system should be totally as well as partially adaptive. In this article, the recursive architecture concept is discussed in order to realize such a large scale adaptive system. The architecture is formulated for general large scale systems in a mathematical manner, and the adaptation strategy based

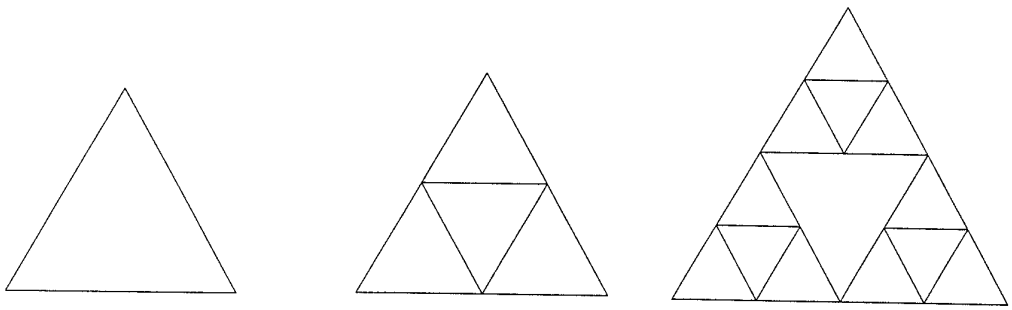

(a) Primitive component (b) 2nd order system (c) 3rd order system

Figure 3: Two dimensional adaptive truss based on recursive architecture

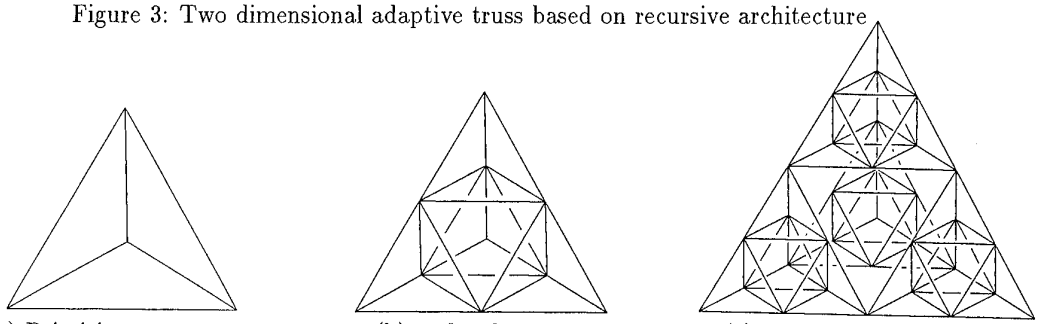

(a) Primitive component (b) 2nd order system (c) 3rd order system

Figure 4: Three dimensional adaptive truss based on recursive architecture

on the gradient procedure is proposed. It is also shown that the hierarchical connection of processing units is suitable for the proposed adaptation approach. The robustness against the degeneration is an another important topic for a large scale system. Based on the recursive architecture, the system which consists of a number of primitive components essentially has the robustness. We also proposed two types of restoration from degeneration of processing unit. The two- and three-dimensional adaptive truss structures are conceptually designed based on the recursive architecture.

Acknowledgement

The authors would like to express their appreciation to the Foundation of Shimano Cycle Development Center on the financial support.

References

1. Grandhi, R. V., et al., "Multiobjective Optimization of Large Scale Structures", AIAA Journal, Vol.31, No.7, 1993, pp.1329-1337.
2. Kokaji, S., "A Fractal Mechanism and Decentralized Control Method", Proc. USA-Japan Symposium on Flexible Automation, Vol.II, 1989, pp.1129-1134.
3. Fukuda, T. and Nakagawa, S., "Approach to the Dynamically Reconfigurable Robotic System", J. Intelligent and Robotic Systems, Vol.1, 1988, pp.55-72.
4. Tidwell, P. H., et al., "Kinematic Analysis of Generalized Adaptive Trusses", First Joint U.S./Japan Conference on Adaptive Structures, 1990, pp.772-791, Technomic.
5. Mandelbrot, B. B., The Fractal Geometry of Nature, 1977, W. H. Freeman and Company.
6. Tanaka, M., et al., "Configuration Control of the Truss-Type Parallel Manipulator by the Modular Neural Network Model", JSME International Journal Ser.III, Vol.35, No.1, 1992, pp.89-95.
7. Wada, B. K. et al., "Adaptive Structures", J. Intelligent Material Systems and Structures, Vol.1, No.2, 1990, pp.157-174.

FAULT DETECTION IN A MECHANICAL SYSTEM BY NEURAL NETWORKS

M.D. Thomas and S.J. Flockton

Royal Holloway, University of London, Egham, Surrey, TW20 0EX, England

ABSTRACT

Two possible neural network methods for fault detection in a vibrating mechanical structure, are presented. Results are given for preliminary tests carried out using data from a simple model of a clamped cantilever beam.

1. INTRODUCTION

The problem of fault detection in mechanical structures is a very important one in modern life. Safety often depends on structural integrity and large costs must be incurred taking the structures out of service to allow inspection. One obvious example is an aircraft structure. Mechanical tests must be regularly performed on the airframe to ensure passenger and crew safety, but current techniques require the aircraft to be grounded and the time consumed is very expensive to the airlines. A further difficulty arises with the increasing use of new composite materials. The failure modes of these materials may not yet be fully understood and dangerously fatigued structural elements may be missed by the tests used at present.

One possible solution to these problems could be to continuously monitor the dynamic behaviour of the airframe in operation. As the aircraft operates its structure undergoes complex vibrations providing a means of exploring the dynamics of the airframe without having to withdraw it from service and applying an artificial stimulus. Whilst knowledge of the nature of the forcing vibration is vastly reduced, a suitable analysis of the effects of such motion may still be able to provide an in-service indication of the structural integrity. This could eventually allow a relaxation in the maintenance schedule and thereby an increase in efficiency. In order to achieve such results, any candidate system must be able to distinguish the signs of fatigue from the normal working dynamics of the airframe by analysing signals from sensors attached to it. Obviously this is a hugely complex problem and preliminary investigations require a much simplified structure with which to explore possible techniques.

This paper describes work in progress using neural network methods to analyze the dynamics of a very simple vibrating mechanical structure - the clamped cantilever beam. The motivation for using neural networks lies in their ability to learn a complex rule from examples where the rule may not be apparent to the trainer. If trained successfully, such networks may be able to generalise to produce meaningful outputs when presented with input signals that were not in the training set. A basic introduction to two candidate neural networks is given in section 2. Section 3 includes some results obtained by using these networks. These are discussed in section 4. Section 5 outlines some of the future aims of the project.

The beam was modelled by simple numerical integration of the appropriate equations [1] with a random forcing vibration at the clamp. The output of strain sensors mounted upon the beam was simulated by recording the curvature at the desired locations. Damage to the beam was then simulated by reducing the elasticity modulus at one point close to the centre of the beam. This is a very crude model and is to be viewed only as a means of providing data for preliminary exploration of different network architectures.

2. THE NEURAL NETWORKS

There are many different types of neural network that have been developed for different tasks [2]. The two networks described in this paper are both *fully connected feed-forward* networks. These networks have a number of nodes in an input layer connected through weighted connections and any number of 'hidden' node layers to an output node layer. The state of the outputs is a function of the inputs, determined by the weights and the functions performed by the nodes. Training is achieved by adjustment of the weight values according to a training algorithm designed to cause the network to approximate the required function.

In the work reported here we wished to use a neural network to distinguish between sensor signals from an undamaged and damaged beam. The first network chosen to do this attempts to extract some characteristic

0-8194-1700-9/94/$6.00

property of the signals from an undamaged beam. By finding a sufficiently 'tight' description of these signals the network should be able to discern a variation in them caused by damage to the beam. Such a network would only need to be trained on data from an undamaged structure and would not need the trainer to provide examples of the many different possible types of damage that could occur.

The network used was derived from work on image compression by Cottrell et al. [3]. Image compression relies on reducing the number of variables required to store an image. Thus such a network must extract something of the nature of the data involved, which is the property we require. The *auto-associative* network is designed to achieve this. It consists of n input nodes, a single hidden layer of p hidden nodes and n output nodes. Data compression is caused by setting p<n and training the network to set the activations of the output nodes to be equal to the activations of the input nodes. This forces the information presented to the network in n variables to be stored by the network in p variables (the hidden node activations) in such a way that the original n variable values can be reconstructed at the outputs. Baldi and Hornik [4] have shown that such a network trains by extracting the first p principal components of the training data set into the weight connections between the input and hidden nodes.

The input patterns to be used were contained in a nine by nine array representing nine successive samples of the output from each of nine strain sensors, equally spaced along the beam. For this network the best results were achieved by using nine hidden nodes and using linear transfer functions in all of the nodes. In order to obtain an indication of the condition of a beam from which test input patterns are drawn, a measure of the accuracy of the network's attempt to recreate that pattern had to be found. The measure chosen was the sum of the squares of the differences in the activations of respective input and output nodes and this was taken as the overall output of the damage detection system. The aim was to train the network to produce a low output for patterns generated by the undamaged beam, upon which it had been trained, and therefore higher outputs for patterns from damaged beams that should have different characteristics. Some experimental results are given in section 3.

An alternative method is to train a network on data from both undamaged and examples of damaged beams using a *classifier* network. Whereas linear functions were used in the nodes of the auto-associative network, this network used sigmoid functions throughout. The training patterns for a network of this form were each given a label of zero or one depending upon whether they came from damaged or undamaged beams. The training algorithm attempted to teach the network to output the correct label for the training data in the hope that the network would also correctly classify, or *generalise* to, previously unseen input patterns.

The patterns to be classified were taken to be the coefficients of a 128-point fast Fourier transform of signals from one sensor, located at the centre of the beam. Since the sampling rate of sensor signals was ten times the frequency of the forcing vibrations, only the first thirteen coefficients contained meaningful data. These thirteen values were then used as inputs to the network, which also contained a single hidden layer of m nodes and one output node. The value of m was varied to investigate its effect. A large number of nodes allow the network to implement more complex functions, but networks with fewer nodes are easier to train and are often found to generalise more effectively [2]. The network was trained to produce output values of zero or one according to the classifications of the input patterns used in training. During testing a pattern was recorded as being correctly classified if the actual output of the network was >0.5 when the desired output was one, or <0.5 when the desired output was zero.

The training of this network aimed to use very slightly damaged and undamaged beam models to isolate the region of the input pattern space representing the undamaged case. Then the network should correctly classify more severely damaged beams without the need for training on patterns from these models. Again some experimental results are given in section 3.

Both networks were implemented using the Stuttgart Neural Network Simulator (SNNS) [5] and trained using the RPROP [6] algorithm. RPROP is designed to converge more quickly than the standard back-propagation algorithm [7] without the need for learning parameters to be set by hand.

3. EXPERIMENTAL RESULTS

The auto-associative network was trained using only data from the undamaged beam model. A sequence of 5555 input patterns was created from a single run of the model and 500 of these were selected at random from the first 2222 to form the training set. After training the whole data set was fed through the network in sequence

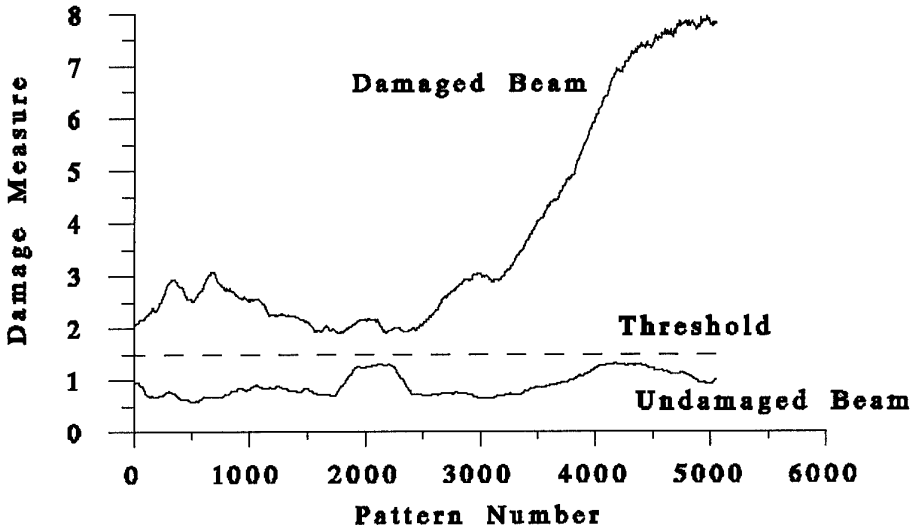

Figure 1. Output of Auto-associative Neural Network

as if the network were continuously sampling the signals from the beam sensors. The sum of the squared difference between input and output layers was recorded and smoothed by taking a 500-point running average. The results are shown as the lower graph in figure 1. This shows that the network performed with nearly equal effect on unseen data as it did on data from the training set. The upper graph in Figure 1 shows the result when similar data from a damaged beam was presented to the network. In this case the damage was a reduction of 90% in the elasticity modulus at a point near the centre of the beam. The dashed line indicates a threshold level that could be used to distinguish the two cases. Unfortunately it was not possible to find such a threshold for less severely damaged models.

Several classifier networks, each with a different number of hidden nodes, were trained using data from both damaged and undamaged beams. Initially an attempt was made to train the network to discriminate an undamaged beam from one with only a 10% reduction in elasticity modulus at the damage point. However, the network was not able to find a way of consistently discriminating between these cases. The networks were more successful when trained to detect a 30% reduction in elasticity modulus at the same point. Five networks with hidden layers containing 1, 2, 4, 8 and 16 hidden nodes were trained with 350 patterns from each of these beam models. 40 other patterns were available from each of these models and these were used as test sets to determine whether the network had learned the correct decision rule. Data from models with more severe damage were also used to test the network and the results are shown in Table 1.

	Number of Hidden Nodes				
Damage	1	2	4	8	16
0%-Training data	58.7%	85.4%	86.2%	76.8%	94.0%
30%-Training data	56.4%	33.3%	61.3%	76.4%	91.5%
0%-Test data	51.2%	92.6%	75.6%	58.5%	63.4%
30%-Test data	48.7%	25.6%	41.0%	59.0%	61.5%
50%-Test data	63.9%	43.6%	58.2%	69.3%	66.8%
70%-Test data	74.5%	51.9%	59.9%	71.1%	69.3%
90%-Test data	86.8%	71.9%	75.6%	89.7%	81.7%

Table 1. Percentage of patterns correctly classified by Classifier Network

4. DISCUSSION

The auto-associative network is a very crude system for damage detection. This is shown by comparison with the much more sensitive Fourier transform classifier network. However using the former technique, some damage could be detected without the network ever having to be trained with data from a damaged source. This may be very useful when the nature of possible damage is unknown. The classifier network was specifically trained with data from a very slightly damaged beam and tested using beams damaged in a more severe but similar manner. If such networks were actually applied to condition monitoring of airframes the auto-associative network could be trained using data from the specific aircraft it was to be installed on. This would not be possible with the classifier type network that would require examples of damage to the aircraft. This type of network would need training on data taken from typical examples of damaged and undamaged aircraft of a particular design. Slight differences in dynamics will exist even between aircraft of one type and this could reduce the ability of the network to detect damage to the airframe of any individual aircraft that did not have dynamics identical to those of the training data.

The results given in Table 1, obtained using the classifier network, illustrate how the number of hidden nodes affects learning and generalisation. Adding more hidden nodes will always increase the ability of the network to learn the training set (if the increase in training time due to the extra complexity is ignored) because the network can form more complicated decision surfaces. However there is an optimum number of hidden nodes beyond which the generalisation abilities of the network deteriorate. In this case the optimum number would probably be between 8 and 16. The network does not correctly classify every pattern presented to it probably because of the constantly changing frequency spectrum of the random forcing vibration of the beam model. A practical implementation of this technique would have to operate by using a sequence of sample data taken from the sensors on the structure. The percentage of these classified as indicating damage would then be a measure of the likelihood of actual damage being present. This interpretation is supported by the results in Table 1 that show that data from more severely damaged beams is correctly classified more frequently than data from beams that are less damaged.

5. CONCLUSION

The ability of neural networks to learn to detect damage in a structure has been clearly illustrated by this work. Further experiments with sensor arrangements and damage locations need to be carried out to give a more comprehensive assessment of the usefulness of these techniques. There are also many other forms of neural network that may prove more suitable to the damage detection task. In particular Radial Basis Function networks [8] might be used to create more suitably shaped decision boundaries than those formed by the classifier network reported here.

6. REFERENCES

[1] R. E. D. Bishop and D. C. Johnson, "Flexural Vibration of Uniform Beams," in *The Mechanics of Vibration*. Cambridge: Cambridge University Press, 1960, pp. 282-406.

[2] R. Hecht-Nielsen, *Neurocomputing*. Reading, MA: Addison-Wesley, 1990.

[3] G. W. Cottrell, P. Munro, and D. Zipser, "Learning internal representations from gray-scale images: An example of extensional programming," in *Proceedings - 9th Annual Conference on Cognitive Science*. Seattle, WA:, 1987, pp. 461-473.

[4] P. Baldi and K. Hornik, "Neural Networks and Principle Component Analysis: Learning from Examples Without Local Minima," *Neural Networks*, vol. 2, pp. 53-58, 1989.

[5] Stuttgart Neural Network Simulator, available via anonymous ftp from *ftp.informatik.uni-stuttgart.de*.

[6] M. Riedmiller and H. Braun, "A Direct Adaptive Method for Faster Backpropagation Learning - The RPROP Algorithm," in *Proceedings of the IEEE International Conference on Neural Networks*. New York: IEEE, 1993, .

[7] D. E. Rumelhart, G. E. Hinton, and R. J. Williams, "Learning internal representations by error propagation," in *Parallel Distributed Processing*, vol. 1, D. E. Rumelhart and J. L. McClelland, Eds. Cambridge, MA: MIT Press, 1986, .

[8] M. Servin and F. J. Cuevas, "A new kind of neural network based on radial basis functions," *Revista Mexicana de Fisica*, vol. 39, no. 2, pp. 235-249, 1993.

INTELLIGENT AIRCRAFT STRUCTURES- A TECHNIQUE TO VERIFY SENSOR INTEGRITY

Peter D. Dean

Lockheed Missiles and Space Co.
Research and Development Division, Palo Alto, California, USA

ABSTRACT

This paper describes the experimental verification of a technique to ensure that the raw sensor data base meets integrity confidence levels required for initiating critical operating decisions associated with aircraft structures. Neural Network techniques are used to characterize the spectral response of sensor arrays to known sensor faults, thus discriminating between structural and sensor anomalies

1. INTRODUCTION

A Structure is Smart only if it is capable, without human intervention, of 1) sensing its state or condition, then 2) determine a course of remedial action, and 3) performing that action. The concept of an Intelligent Structure is that it can perform the above when the sensed state or condition has not previously been known in the experience base. This implies the ability to learn, in addition to reason, i.e. to change code within the system, without human intervention. The first of this chain of events, the sensing of state, is the most important since the worth of the entire procedure hinges on whether the sensors are reporting the true state of the structure or not. It is just not acceptable to put human life and high value assets, such as aircraft, buildings, bridges etc., at risk from inaccurate data produced by transducer partial failures or out-of-calibration errors.

This paper describes a concept or technique that 1) improves the confidence level of sensor data by discriminating between sensor faults and structural faults, 2) characterizes these faults and 3) enables recovery through recalibration or other means. The technique used is based on the use of a Probabilistic Neural Network (PNN) to process the sensor data and perform the tests of reasonableness or not, and in the latter case to proceed further and categorize the errors or faults. This technique should be considered as a first data screen, before further processing is allowed.

2. APPROACH

In the most simple terms, we are performing a sensor failure analysis. Further, if we determine that a sensor has failed, this failure needs to be categorized as recoverable or not, and if so to initiate recovery. In the ideal real world, there will be available knowledge of the structural responses expected, as well as common sensor failure modes, thus a neural network approach is ideal as these training sets are in existence. Further, sensor recovery through recalibration, can be done using baseline training sets as a reference as well as the traditional technique of response to known stimulus.

Conventional algorithmic solutions could be adapted to achieve similar results in an expert system sense, however the use of the Neural Network has advantages in that it is computationally easy to do and offers the potential of being able to adapt to unknown failure modes not in the original training set.

The demonstration of the concept was performed on two types of sensors with dynamic response, viz., conventional foil strain gauges and unconventional strain sensitive piezoelectric crystal sensors. These were chosen based on the author's knowledge of both their failure modes and the spectral response from impact excitation. The training data required for the NN analysis was the relative amplitude and phase of spectral peaks obtained from the Fourier Transform of the time history of the impact response. Four sensors of each type were mounted on a cantilever beam (7076-T6 Aluminium, 1ins. x 0.1ins. crossection, 10 ins. long) under impact excitation from an in-house test system with rebound control and known impact energy levels.

0-8194-1700-9/94/$6.00

The experimental hardware is shewn in figure 1. The output of each sensor was digitally recorded for three impact positions on the beam, two energy levels and two damping levels. The basis of the training/diagnosis sets was limited to five characteristic frequencies, representing peaks in the spectral response. The logic behind this choice was the realization from basic physics that any sensor fault or structural change could be categorized uniquely from the impact frequency response.

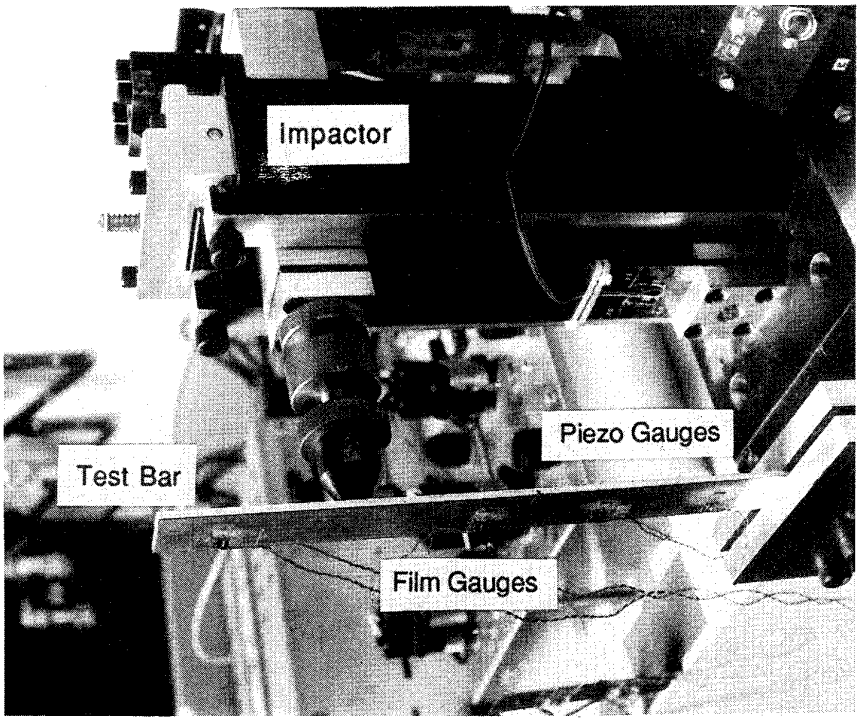

Figure 1. Impactor beam transducer test system

3. PROCEDURE

First, "good" baseline data was taken from the sensor array, then "failures" were introduced and failure training sets recorded. Five basic failure modes were used, based on the author's experience to be the most common observed in field installations. These were

- Degradation of the power supply
- Delamination or disbond of the sensor
- Temperature fluctuations (+/- 50 %)
- Partial electrical shorts to ground or intermittency
- Cracked sensor crystal

Two types of structural changes were also included in the training set. The first was a damping variation produced by a passive viscoelastic constrained layer system in tape form, while the second change was induced by a saw cut near the base of the bar that drastically changed the basis stiffness and resonant frequency. Figure 2 shows examples of impact time histories, both normal baseline and faulty. The NN was implemented on a 386 PC for convenience, however, the project ultimate goal is to implement this technique at the sensor site on a chip, possibly the sensor chip itself. The Neural Network software was developed in-house by Lockheed some years ago and is considered proprietary, however similar packages are becoming available commercially that should be easily adaptable to this technique.

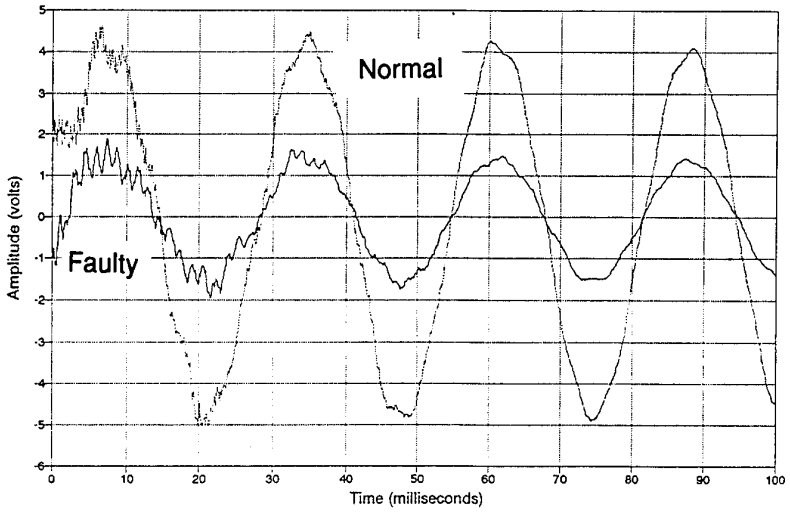

Figure 2. Time histories of two sensors, normal and faulty.

The training set was implemented and the network presented with an "unknown" set of data to analyze. This set included two known sensor error conditions as well as good data. Figure 3 shows a tabular summary of the test scores for twelve data sets. It can be seen that the network correctly categorized and detected both errors. The gauge peel-off condition is a prime candidate for recalibration, which in this case would be done by changing the scale constant using amplitude ratios of the baseline spectral information of neighboring sensors.

	Fault detected (% probability)		
Sensor Analyzed	Good data	Flaky Connect.	Impede. Change
Foil Ga. 1	92*	3	5
Foil Ga. 2	25	65*	10
Foil Ga. 3	15	13	72*
Foil Ga. 4	7	7	86*
Foil Ga. 5	85*	8	7
Foil Ga. 6	18	72*	10
Piezo Ga. 1	82*	2	16
Piezo Ga. 2	8	12	80*
Piezo Ga. 3	10	12	78*
Piezo Ga. 4	94*	2	4

Figure 3. Fault detection probabilities

Note: * denotes correct categorization. The allowable options in the above data set were simplified for this presentation to include only three categories thus the sum total of probabilities was forced to unity. In the more general case, more allowable categories would generate different probabilities.

4. CONCLUSIONS

A concept for monitoring sensor data integrity typical of smart structure systems has been described and successfully demonstrated. Sensor failures and structural anomalies were clearly discriminated on the basis of probability of being within a particular failure category. The technique resolves the classical dilemma "am I measuring real structural phenomena, or has my sensor degraded?". A critical element of the concept is the premise of an extensive array of dynamic sensors, which produce time histories of physical changes. The signal processing included spectrum analysis and probabilistic Neural Network categorization procedures. The demonstration was limited to the use of dynamic strain sensors, however the application can be applied to any array or combination of sensors. The most significant feature of the demonstration was the realization of the simplicity and power of Neural Networks. The transition from smart to intelligent now appears easily possible using this technique by exploiting regression and clustering adaptations that can deal with sensor failures not in the original data base but have similar but not exact features of failure.

5. FUTURE DIRECTIONS

The field of Smart Structures contains many examples of concepts proved feasible in laboratory environments. This demonstration by itself provides no guarantees that any industrial entity will exploit the concept. The author would like to make some observations concerning the transition of Smart Structures from laboratory to field use. These observation will be limited to aircraft applications. Currently there are four areas of emphasis: 1) crack detection, 2) corrosion monitoring, 3) battle damage assessment (military only!) and 4) cost reduction of composite parts (e.g. intelligent cure monitoring). The first is the result of fatigue damage, the second is environmentally induced, and the third ballistic or impact in origin. These four areas currently require experienced human experts, reliable instrumentation, lots of time for inspections and therefore lots of dollars.

The resistance to exploitation is not in the technology itself but rather in the implementation. Reliability and survivability are valued far more that five significant places in accuracy. Contemplating the use of an array of 1000 or more sensors on a structure implies cost per channel is a critical issue, with direct impacts on maintainability. It must be realized that, in the industrial real world, the measure of worth of these concepts is not in laboratory generated technical data, but rather in the ability of those with the technical knowledge to focus on and demonstrate these concepts in a way that meets the implementation issues head-on.

Finally, it should be realized that it is inevitable that the sensor site will contain not only the sensors, but also the signal processing for the spectrum analysis and NN categorization in the form of silicon based electronic chips. Further, there will be requirements for distributed high bandwidth data links, either on board (fiber-optic), or relayed to ground (wireless) as part of the system. These enabling technologies are already mature, thus the only obstacles to general use are 1) cost per channel and 2) confidence in the data and 3) a methodology of evaluating the data. These obstacles will only be overcome from widespread field use. The message is clear, focus on implementation, not performance issues, this technology is mature enough.

A FUZZY NEURAL NETWORK FOR IN-PROCESS ERROR COMPENSATION

Erping Zhou, *D.K. Harrison, *D. Link and R. Healey

Bolton Institute of Higher Education, Bolton, Lancs, BL3 5AB
**Staffordshire University, Stafford, Staffs, ST18 0AD*

ABSTRACT

In this paper, a fuzzy neural network applied to in-process error compensation on CNC machine tools is proposed. The system is designed by a linguistic rule-based fuzzy controller and trained by a back propagation neural network to adjust and develop the control rules.

1. INTRODUCTION

Essentially all intelligent control systems can be coded using only rules as a collection of "if ... then... else" statements [White, D.A. & Sofge, D.A. 1992]. The conventional knowledge-based control system is typically implemented using these statements by the concept of set inclusion (crisp set). In a crisp set, an element either belongs to a set or not. If more than one rule is suitable, then the most significant rule could be selected by using object-oriented systems. When there are no suitable rules existing, the control system fails to execute the inference.

Instead of using crisp set inclusion, the fuzzy set takes values in the range 0 to 1 to express the degree of belonging to a given set. The fuzzy logic control system tries to imitate the actions of an experienced operator via a collection of fuzzy rules. In the case of fuzzy control systems, the ranges of inputs and outputs are split into smaller and overlapping ranges or fuzzy sets. A fuzzy membership function is associated to each fuzzy subset. The mapping from the inputs to the outputs is achieved through these fuzzy rules, the membership functions and de-fuzzification procedure. Since ambiguous rules and approximate reasoning techniques are introduced, the system is able to perform inference much more flexibly.

The applications mentioned above have mainly concentrated on emulating the performance of a skilled human operator in the form of linguistic rules. However, the process of fine tuning the control rules to get the desired performance remains a time-consuming and tedious task [Berenji, H. R. 1992]. Secondly, to obtain satisfactory results careful setting of input and output membership functions is necessary. These membership functions can have different shapes depending on the designer's preference or knowledge or experience [Ramamoorthy, P.A. & Huang, S. 1991]. Obviously, the learning ability to adjust the fuzzy membership functions of the linguistic labels used in different control rules is important. Therefore, the neural network has been brought into the fuzzy control system.

A typical neural network has multiple inputs and outputs that are connected by many neurons via weights to form a parallel structure for information processing. The most attractive advantage of a neural network is its ability to learn through training. This ability means that only a minimum amount of information about the environment is required. However, the neural network has conventionally been applied independently of the knowledge base, so the already-known knowledge (for example the operator experiences) could not be used sufficiently.

By merging the advantages of the fuzzy logic system and the neural network, a more powerful and more flexible system for inferring and learning could be obtained. This potential feature has attracted many researchers recently. There are two major types of learning approaches involved in fuzzy neural network architecture. One approach is to extract automatically fuzzy linguistic rules from a trained neural network. The other is the development and fine tuning of the fuzzy memberships which are used in the control rules. The latter learning architecture is concentrated and applied in the in-process error compensation system. This paper

0-8194-1700-9/94/$6.00

describes a new fuzzy neural network model to control the error compensation system used on CNC machine tools. A rule-based fuzzy controller that uses qualitative linguistic rules obtained from human experiences has been designed and a multi-layer neural network trained by the supervised technique has been employed to adjust and adapt the control rules.

2. THE FUZZY NEURAL NETWORK MODEL

For simplicity, a multi-input and one output model is employed in the following example. Figure 1 illustrates this fuzzy neural network model which includes two systems, a fuzzy logic controller and a multi-layer neural network.

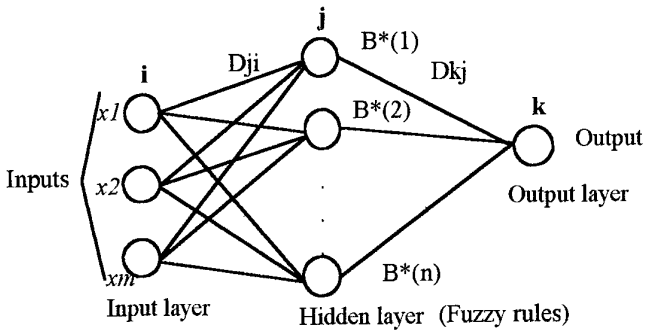

Figure 1. The Multi-layer Fuzzy Neural Network

Fuzzy Rules and Fuzzy Inference

The fuzzy controller consists of rules and these are described using linguistic terms. Let x_1 , x_2 , ... x_m be the inputs and y the output. Suppose that there are the following implications:

If x_1 is $A_{1\,1}$ and x_2 is $A_{1\,2}$ and ... and x_m is A_{1m} Then y is B_1
If x_1 is $A_{2\,1}$ and x_2 is A_{22} and ... and x_m is A_{2m} Then y is B_2

.

.

If x_1 is A_{n1} and x_2 is A_{n2} and ... and x_m is A_{nm} Then y is B_n

where n is the number of fuzzy rules. If x_1^*, x_2^* ... x_m^* are the readings taken by the sensor system for fuzzy variables X, then their truth values are represented by $\mu_{Aj1}(x_1^*)$, $\mu_{Aj2}(x_2^*)$, ..., $\mu_{Ajm}(x_m^*)$ respectively. Assuming that a minimum operator is used as the conjunction operator, the strength of rule j can be calculated by

$$w(j) = \min \{\mu_{Aj1}(x_1^*), \mu_{Aj2}(x_2^*), ..., \mu_{Ajm}(x_m^*)\} \quad (j = 1, 2, ..., n) \qquad \text{(Eq.1)}$$

Where $w(j)$ represents the degree to which rule j is satisfied by the input variables in set X. Then a fuzzy set B*(j) is formed as

$$B^*(j) = \min \{w(j), \mu_{Bj}(y)\} \qquad \text{(Eq. 2)}$$

and

$$B^*(y) = \max_j \{\min \{w(j), \mu_{Bj}(y)\}\} \qquad \text{(Eq. 3)}$$

The output from Eq.3 is a fuzzy set. As a process usually requires a non-fuzzy value of control, a "de-fuzzification stage" is needed. There are several ways of tackling this problem, the max-procedure is chosen in the control action y^* and the combined set of control rules is then calculated from

$$y^* = \max_{y \in Y} \{B^*(y)\} \qquad \text{(Eq. 4)}$$

Back Propagation Neural Network

The back propagation algorithm teaches the network by presenting an input pattern, and the network will produce an output by using the current weights and thresholds. An error function is then needed to represent the difference between the output pattern and the desired output pattern, or target. By adjusting the weights and thresholds to minimize the value of the error function, the system is converged to a set of weights and responds with the desired patterns. This algorithm is currently the most popular method for performing the supervised learning tasks in the neural network. It is therefore applied in this model.

If we set the sample sizes for training is P, there are P pairs of inputs and outputs (I_p , T_p), (p = 1, 2, ..., P). Here I_p represents the input for sample p, $I_p = (x_{p1} , x_{p2} , ...x_{pm})^T$, (m is the dimension of input nodes). T_p represents the target output for sample p, $T_p = (t_{p1} , t_{p2} , ... t_{pn})^T$, (n is the dimension of output nodes, n = 1 in this case), whilst O_p represents the actual output corresponding to I_p, $O_p = (o_{p1} , o_{p2} , ..., o_{pn})^T$. D_{ji} is the weight from node i to node j and D_{kj} is the weight from node j to node k.

In a traditional multi-layer neural network, the net input to each hidden layer unit j is

$$Net_{pj} = \sum_i D_{ji}\, o_{pj} \qquad \text{(Eq. 5)}$$

and similarly, the output from nodes in the hidden layer is fed into nodes in the output layer

$$Net_{pk} = \sum_j D_{kj}\, o_{pk} \qquad \text{(Eq. 6)}$$

In the fuzzy neural network model, the min for multiplication and max for addition are employed. Therefore, it might be called the max-min neural network [Hayashi, Y., Czogala, E. et al 1992] which is

$$Net_{pj} = \min \{D_{j1}\mu_{Aj1}(x_1^*), D_{j2}\mu_{Aj2}(x_2^*), \ldots D_{jm}\mu_{Ajm}(x_m^*)\} \qquad \text{(Eq. 7)}$$

where $\mu_{Aji}(x_i^*)$ (i = 1, 2, ..., m) represents the degree of membership of the input x_i in a fuzzy set of rule j. Then

$$Net_{pk} = \max \{D_{k1} B^*(1), D_{k2} B^*(2), ..., D_{kn} B^*(n)\} \qquad \text{(Eq. 8)}$$

Since the output o_{pk} is usually not the same as the target t_{pk}, an error function is defined

$$E_p = \frac{1}{2}\sum_k (t_{pk} - o_{pk})^2 \qquad \text{(Eq. 9)}$$

The error is then back propagated from nodes in the output layer to nodes in the hidden layer by using a gradient search method [Hou, T.H., Lin, L. et al 1993]

$$\Delta_p D_{kj} = -\eta \frac{\partial E_p}{\partial D_{kj}} \qquad \text{(Eq. 10)}$$

By applying Eq. 8 to Eq. 10 and using a few chain rules, we obtain

$$D_{kj}(t+1) = D_{kj}(t) + \eta \delta_{pk} \frac{\partial o_{pk}}{\partial D_{kj}} + \alpha (D_{kj}(t) - D_{kj}(t-1)) \qquad \text{(Eq. 11)}$$

where η is the learning rate and α is the momentum constant which are determined by the user and

$$\delta_{pk} = (t_{pk} - o_{pk}) \qquad \text{(Eq. 12)}$$

$$\frac{\partial o_{pk}}{\partial D_{kj}} = \begin{cases} y^*, \text{ if } D_{ki}^{-1}(o_{pk}) = D_{kj}, (y^* = \max \{B^*(y)\}) \\ 0, \text{ otherwise.} \end{cases}$$

As the error is back propagated from nodes in the hidden layer to nodes in the input layer, the similar equation could be achieved

$$D_{ji}(t+1) = D_{ji}(t) + \eta \delta_{pj} \frac{\partial o_{pj}}{\partial D_{ji}} + \alpha (D_{ji}(t) - D_{ji}(t-1)) \qquad \text{(Eq. 13)}$$

where

$$\delta_{pj} = \delta_{pk} \frac{\partial o_{pk}}{\partial Net_{pk}} \cdot \frac{\partial Net_{pk}}{\partial o_{pj}} \qquad \text{(Eq. 14)}$$

$$\frac{\partial o_{pk}}{\partial Net_{pk}} = \begin{cases} 1, \text{ if } o_{pk} = Net_{pk}, \\ 0, \text{ otherwise.} \end{cases}$$

$$\frac{\partial Net_{pk}}{\partial o_{pj}} = \begin{cases} D_{kj}, \text{ when } B^*(i)^{-1}(Net_{pk}) = o_{pj}, \\ 0, \text{ otherwise.} \end{cases}$$

$$\frac{\partial o_{pj}}{\partial D_{ji}} = \frac{\partial o_{pj}}{\partial Net_{pj}} \cdot \frac{\partial Net_{pj}}{\partial D_{ji}}$$

$$\frac{\partial o_{pj}}{\partial Net_{pj}} = \begin{cases} 1, \text{ when } o_{pj} = Net_{pj}, \\ 0, \text{ otherwise.} \end{cases}$$

$$\frac{\partial Net_{pj}}{\partial D_{ji}} = \begin{cases} \mu_{Aji}(x_i^*), \text{ when } D_{jk}^{-1}(Net_{pj}) = D_{ji}, \\ 0, \text{ otherwise.} \end{cases}$$

Equations (Eq. 11) - (Eq. 14) are the algorithm for the multi-layer fuzzy neural network shown in Fig. 1, in which the inputs and the outputs are fuzzy sets and the threshold functions for each layer are max-min functions.

3. APPLICATION OF THE FUZZY NEURAL NETWORK MODEL TO AN IN-PROCESS ERROR COMPENSATION SYSTEM

In-Process Measuring (IPM) or gauging is a sensor-based measuring system and measuring is carried out on the machine tool as part of the total machining cycle but not at the same time as cutting takes place. A typical IPM system normally consists of sensors, sensor interfaces, microprocessors or microcomputers, software measuring programs and compensation methodologies.

In machining and /or measuring operations on the machine tool, the accuracy of the workpiece dimensions is affected by the error of the relative movement between the cutting tool or the probe and the workpiece. Factors that influence measuring accuracy may be described as inherent geometrical errors of the machine tool, probe errors, process dependent errors and environmental errors. The main factors among them that affect the relative position are the geometric errors of the machine tool and the thermal effects on these geometric errors. The key issue involved is how many error items could be found by a Touch Trigger Probe (TTP) system and compensated through the IPM. It is difficult to understand the detailed and precise structure knowledge of the machining and measuring processes, since there is vagueness inherent in real practical systems and only a few aspects of the information can be detected by the TTP system. Thus, the fuzzy neural network model designed above has been applied.

In the error compensation system, the deviation of the measured value from the desired value can be expressed by the relative error (e_n). The change of error (ce_n) is defined as the difference of two adjacent errors e_n and e_{n-1} as follows:

$$e_n = v_m(\text{measured value}) - v_d(\text{desired value})$$
$$ce_n = e_n - e_{n-1}$$

The error compensation process could be expressed in the following linguistic terms

if error is PB and change of error is PM then compensation is NB;
if error is NS and change of error is NM then compensation is PB;
.....

where PB, PS, NM, and Z0 etc. represent Positive Big, Positive Small, Negative Medium, and Zero respectively. The fuzzy rule-bases and the membership functions can be determined. Then, these fuzzy variables are put into the fuzzy neural network model. Although changing the weights in the network does not create the new rules, the membership functions used in the control rules are to be fine tuned during the learning process and a rule could become ineffective since the weights can be reduced to zero.

4. CONCLUSIONS

A new architecture based on a fuzzy controller with fuzzy inputs for error and change of error, using a max-min neural network has been described. Since fuzzy logic and a neural network are employed the need for an exact mathematical relationship is avoided and thus the process evaluation is simplified. Therefore, a more powerful and more flexible error compensation system for inferring and learning can be obtained.

REFERENCES

White, D. A. & Sofge, D. A., 1992, Handbook of Intelligent Control: Neural, Fuzzy, and Adaptive Approaches. (Van Nostrand Reinhold, New York)

Berenji, H. R., 1992, A Reinforcement Learning - Based Architecture for Fuzzy Logic Control. International Journal of Approximate Reasoning, Vol. 6, No. 2, pp 267-292

Ramamoorthy, P.A. & Huang, S., 1991, Fuzzy Expert Systems Vs. Neural Networks - Truck Backer-Upper Control Revisited. IEEE International Conf. on Systems Engineering, Fairborn, OH, USA, pp221-224

Hayashi, Y., Czogala, E. and Buckley, J.J., 1992, Fuzzy Neural Controller, IEEE International Conf. on Fuzzy Systems, San Diego, CA, USA, pp197-202

Hou, T.H., Lin, L. and Scott, P.D., 1993, A Neural network-based automated inspection system with an application to surface mount devices. IJPR, Vol. 31, No. 5, pp1171-1187

ENERGY EVALUATION ON BOUNDED NONLINEAR CONTROL LAWS FOR CIVIL ENGINEERING APPLICATIONS

Vincenzo Gattulli

Dipartimento di Ingegneria Strutturale e Geotecnica
Universita' di Roma "La Sapienza"

1. Introduction

In the last decades researchers in the field of structural engineering have challenged the idea of facing natural hazard mitigation problems by adding to structures particular systems which are designed to protect buildings, bridges and other facilities from the damaging effects of destructive environmental actions. Among most protective systems and devices, active structural control, although having already reached the stage of full-implemented systems, still needs theoretical investigation to achieve a complete exploitation of its capacity in reducing structural vibrations.

In most of the operating systems (e.g. Soong and Reinhorn, 1993), linear control laws based on some quadratic performance function criteria are used since the design process for these linear strategies are fully developed and investigated. Moreover, the performances of structural systems controlled by linear techniques bring about some questions concerning the complete and wise utilization of the capacity of control devices. Indeed, some of these inefficiencies are evident such as the inability to produce a significant peak response reduction in the first cycles of recorded or simulated time histories. (e.g. Reinhorn et al., 1993).

Realizing that the expected maximum value for the required control force is a fundamental parameter in all processes to design the complete control system, in this paper it is shown that appropriate nonlinear control laws can significantly enhance the reduction of the system response under the same constraints imposed on the control force. Energy evaluation on the performance of different kinds of nonlinearities are reported such that a common base is built to perform comparative studies. These techniques have been successfully experimented on a structural model with ground excitations supplied by shaking table (e.g. Gattulli et al., 1994).

2. Basic Nonlinear Control Laws

The attempt of these studies is focused on basic principles regarding the class of oscillating systems controlled by nonlinear algorithms. Thus, it will be considered a linear single-degree-of-freedom (SDOF) structural system. The equation of motion in the state-space form is

$$\dot{z}(t) = Az(t) + w\ddot{x}_0(t) + bu(t) \tag{2.1}$$

in which

$$z(t) = \begin{bmatrix} x(t) \\ \dot{x}(t) \end{bmatrix}, \quad A = \begin{bmatrix} 0 & 1 \\ -\omega^2 & -2\xi\omega \end{bmatrix}, \quad w = \begin{bmatrix} 0 \\ -1 \end{bmatrix}, \quad b = \begin{bmatrix} 0 \\ b \end{bmatrix} \tag{2.2}$$

where $x(t)$ is the displacement of the mass relative to the base; ω and ξ are the natural frequency and damping ratio, respectively; $\ddot{x}_0(t)$ is the base acceleration input and $u(t)$ is the control force. It is well-known (e.g. Soong 1990) that classical linear quadratic regulator LQR will permit the conduction of feedback control design process in which the control force is linear in the state vector $z(t)$, i.e.,

$$u(t) = g^T z(t) = g_x x(t) + g_{\dot{x}} \dot{x}(t) \tag{2.3}$$

where the control gain vector **g** is the unknown design parameter evaluated by the approximated time-invariant Riccati matrix equation.

0-8194-1700-9/94/$6.00

The linear control law derived by this classical technique is effective in reducing the structural response in the time-averaged mean-square sense due to the fact that the designed feedback minimizes a quadratic functional of performance defined on the time interval of interest. However, the control law in Eq.(2.3) may not be effective for the peak response. Since peak response reduction is of practical importance in structural control, other forms of the control law may be more desirable. By comparing the performances of nonlinear control techniques with the linear one and having a level of performance always attainable by linear feedback, the alghoritms investigated in the following steps can be generally expressed as

$$u(t) = \boldsymbol{g}^T \boldsymbol{z}(t) + u_{nl}(t) \tag{2.4}$$

The nonlinear term $u_{nl}(t)$ will be chosen in the high-order functions of $z(t)$, so that the control acquires the possibility of giving more emphasis to large value of the response. Thus, proposed alghoritms result to be

Nonlinear Control Algorithm 1

$$u_1(t) = g_{\dot{x}}\dot{x}(t) + \alpha_1 g_{\dot{x}}\dot{x}^3(t) = g_{\dot{x}}(1+\alpha_1\dot{x}^2)\dot{x} \tag{2.5}$$

Nonlinear Control Algorithm 2

$$u_2(t) = g_{\dot{x}}\dot{x}(t) + \alpha_2 g_{\dot{x}}x^2(t)\dot{x}(t) = g_{\dot{x}}(1+\alpha_2 x^2)\dot{x} \tag{2.6}$$

3. Bounded Nonlinear Control Laws

The possibility of reaching a limitation in the control force requirement is a desirable condition to achieve the enhancement of the controlled system performance. However, the demand of control force for the two nonlinear control algorithms depends on the frequency content of the forcing term and on the amplitude of the external excitation. This second characteristic should not be suitable if it is related with the design of active devices in which one of the first concerns is the maximum force capability. Indeed, the difficulties to determine this quantity related with the stochastic behavior of the external excitation are increased by the nonlinearity of the controller. Moreover, the same reasons do not permit one to easily conduct comparative studies between the performance of nonlinear algorithms and the classical LQR.

The previous considerations and others, have introduced the idea of bounding the region of the control force requirement by a well-known level of achievable maximum value. Therefore, the following constraints will be added to each of the nonlinear control algorithms presented in section 2

$$\max|u(t)| \le u_b \tag{3.1}$$

Thus, in order to evaluate the performances of the nonlinear algorithms in the following calculations a reference level of performance for the system will be chosen attainable by a determinate level of the linear control (LQR). This performance level determines the peak value of the linear control force which is taken as the bounded value u_b for the nonlinear algorithms. This operation of bounding the maximum excursion for the control force, reaches the double goal to determine the main characteristic for the control device and to perform an easy comparison with the linear techniques.

Following the second objective a general result for the control algorithms *nonlinear1* is presented in Fig.(3.1) in which the maximum level for the control force is fixed on the maximum value required by the linear control (case ξ = 6.85%). The magnification factor β, numerically evaluated, is presented as an index of the system response and it is related with the generalized transfer function of the system, thus it is clear the effect of the nonlinear term. Moreover, the increment of the parameter α_1 results to be effective in order to reduce the β factor until a certain level after that the system seems to respond without considerable changes. This characteristic is confirmed also increasing the level of external excitation Γ. In Fig.(3.2) are shown similar results for the control algorithm *nonlinear2,* also in this case a certain level of reduction on the β factor is reached increasing the parameter α_2.

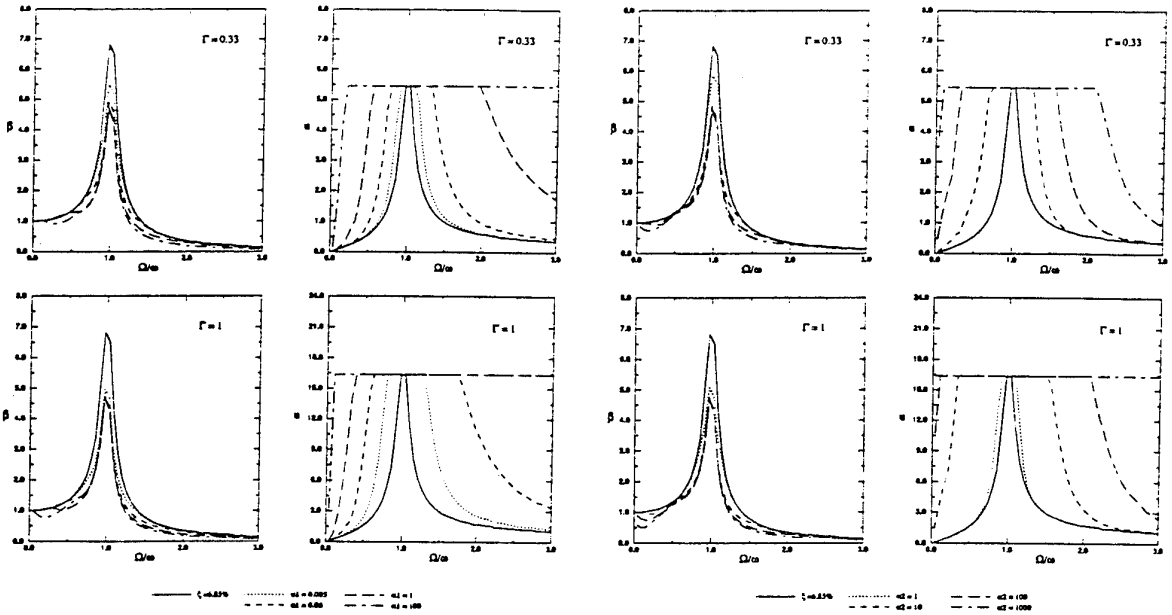

Figure 3.1 β factor for bounded control *nonlinear1*

Figure 3.2 β factor for bounded control *nonlinear2*

4. Frequency Domain Energy Evaluation

An energy representation for the actions of the control force in Eq (2.1) can be formed by integrating the control force term $mbu(t)$ over a determinate interval of the displacement history

$$E_c = \int mbudx \tag{4.1}$$

An approximate expression can be performed for the energy dissipated by the *nonlinear1* and *nonlinear2* control algorithms, although the nonlinear controlled structural system shall respond with induced oscillation not only in the frequency of the forcing term, the steady-state solution at least contains a periodic predominant term with the period of the forcing term. Thus, in order to evaluate the energy related with the nonlinear term it seems reasonable to take into account only the contribution furnished by the main periodic term considering less important the contribution of the sub and super-harmonic oscillation. Under this assumption the expression for the energy dissipated by the nonlinear control laws is found for the two cases *nonlinear1* and *nonlinear2* and it respectively yields

$$E_{c1} = 2\pi mbg_{\dot{x}}\Omega\Gamma^2\left|x_{0n1}\right|^2 + 2\pi mbg_{\dot{x}}\Omega^3\Gamma^4\left|x_{0n1}\right|^4 \tag{4.2}$$

$$E_{c2} = 2\pi mbg_{\dot{x}}\Omega\Gamma^2\left|x_{0n2}\right|^2 + 2\pi mbg_{\dot{x}}\Omega\Gamma^4\left|x_{0n2}\right|^4 \tag{4.3}$$

in which $\left|x_{0n}\right|$ is a generalized transfer function numerically evaluated for the different two nonlinear cases.

In order to compare the control energy evaluated for the nonlinear algorithms in which no restraints are added to the system with the case of bounded maximum force value, similar assumptions in the evaluation of this second case are introduced. Indeed, the bounded control force is also assumed periodic with the principal period equal to the period of the forcing oscillating term, thus knowing the value of the amplitude of this bounded force as shown in Figs.(3.1) (3.2) the energy integral in Eq. (4.2) can be evaluated in this case by

$$E_{cb1} = 2\pi mbu_{b1}\Gamma\left|x_{0b1}\right| \tag{4.7}$$

$$E_{cb2} = 2\pi mbu_{b2}\Gamma\left|x_{0b2}\right| \tag{4.8}$$

The results for *nonlinear1* control algorithms are presented in Fig.(4.1) in which on the left hand side there is the case without boundary restraints on the control force and on the right hand side there is the bounded one. A remarkable result is the shift towards lower frequency for the energy peak value increasing the influence of the

nonlinear term by increasing α_1 in the unbounded case. Moreover a lesser amount of energy is evaluated for the unbounded case compared with the bounded one but this result has to be considered also in relation with the fact that a larger maximum force is required in the first case which produces a greater reduction in the dynamic response.

In the second case for *nonlinear2* control algorithm the results are presented in Fig.(4.2) where now, for this second kind of nonlinearity the shift is towards higher frequency. Due to the fact that the demand of maximum control force is very high in this case, the energy level is still comparable with the bounded case also if the level of oscillation of the system is lower. However, a general result in both cases may be summarized saying that the energy dissipated by the introduction of a bounded nonlinear control force in the system is more sparse over the frequency range.

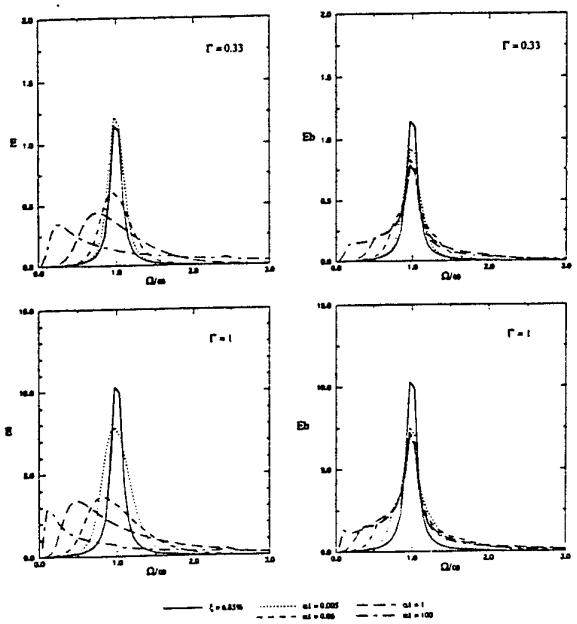

Figure 4.1 Energy distribution for *nonlinear1* control

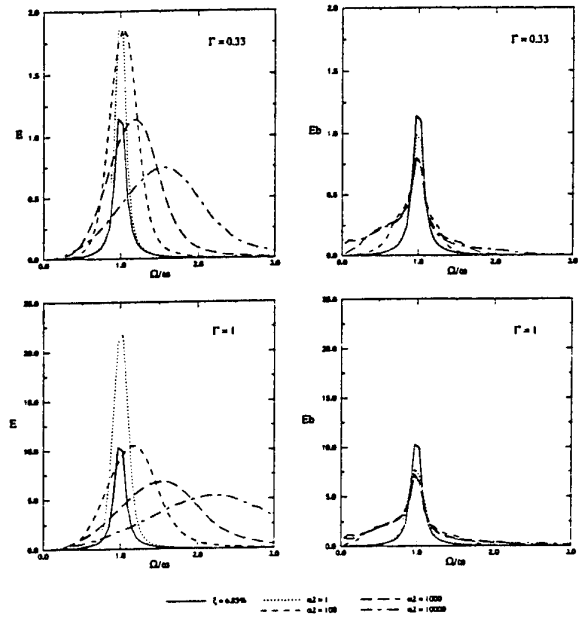

Figure 4.2 Energy distribution for *nonlinear2* control

5. Conclusion

The energy related to different nonlinearities in the control term has been evaluated such that a method to perform comparative studies can be followed. Thus, interesting results are found when a boundary for the nonlinear control laws are introduced such as the reduction achieved in the resonance range. These investigations permit one to have a better understanding of actual enhancement of structural control effectiveness reached in experimental testing.

Acknowledgments

The author would like to thank Prof. T.T. Soong for his encouragement and assistance.

References

Gattulli, V., R. C. Lin, T.T. Soong. "Nonlinear Control Laws For Enhancement of Structural Control Effectiveness." *Proceedings of Fifth US National Conference on Earthquake Engineering.* Chicago, Illinois, 1994.

Reinhorn, A.M., T.T. Soong, et al. "Full-scale Implementation of Active Control II: Installation and Performance." *ASCE Journal of Structural Engineering* 119 (1993): 1935-1960.

Soong, T.T. *Active Structural Control, Theory and Practice.* London and New York: Longman and Wiley, 1990.

Soong, T.T. and A.M. Reinhorn. "Observed Response of Actively Controlled Structures." *Structural Engineering in Natural Hazard Mitigation* (A.H.S. Ang and R. Villaverde, eds.). ASCE, New York, 1 (1993): 187-192.

On the Stress Distribution in a Simple Adaptive Structure Actuated in Bending Mode

Renato BARBONI, Paolo GAUDENZI, Giulio STRAMBI

Università di Roma "La Sapienza", Dipartimento Aerospaziale
Via Eudossiana 16, 00184 Roma, Italy

1. Introduction

Recently piezoelectric materials have been used as actuators or sensors in some simple adaptive structures. Thin polarized piezoceramics were bonded to the top and bottom surfaces of simple plate-like passive structures. The piezoelectric layers work as actuators or sensors by means of the converse or the direct piezoelectric effect. In both cases the interaction mechanism between the active layer and the passive structure plays a fundamental role in the response of the overall structure [1,2,3].

Aim of the present paper is to study the stress distribution that is generated in the interaction between a simple (plate) structure and a piezoelectric actuator. A closed form solution is obtained for a given displacement assumption, based on a power series technique. The displacement form allows the interlaminar stress continuity at the interfaces between the actuator layer and the structure [4].

2. Theoretical formulation

The case of a simple plate structure under bending actuating mode is considered. The structure, represented in fig.1, consists of two actuating piezoelectric layers perfectly bonded to a passive plate structure. For sake of simplicity the response of the system is studied in the bidimensional case, under the hypothesis of small displacements.

The piezoelectric part exhibits a coupled piezo-elastic constitutive behaviour in which the electric field is supposed to be given for each point of the material, namely a uniform and constant electric field is assumed. For this reason the actuation mechanism is represented in the model simply by applied actuation strain components.

In the following sections the mathematical formulation of the problem is described and the obtained stress distributions are shown and discussed.

2.1 *Kinematics*

Distinct displacement unknowns for the structure and the actuators are used with the following assumed form :

- passive plate structure

$$\begin{aligned} u^s(x,z) &= u^{1s}(x)\, z + u^{3s}(x)\, z^3 \\ w^s(x,z) &= w^{0s}(x) + w^{2s}(x)\, z^2 \end{aligned}$$

- upper and lower actuator

$$\begin{aligned} u^{a(u,l)}(x,z) &= \pm\, u^{0a}(x) + u^{1a}(x)\, z \pm\, u^{2a}(x)\, z^2 \\ w^{a(u,l)}(x,z) &= w^{0a}(x) \end{aligned}$$

2.2 *Constitutive relations*

- plate structure $\qquad z_s \in [-t_s/2;\ +t_s/2]$

$$\mathrm{T}^s = \begin{vmatrix} Q^s_{11} & Q^s_{13} & 0 \\ Q^s_{13} & Q^s_{33} & 0 \\ 0 & 0 & Q^s_{55} \end{vmatrix} \mathrm{D}^s$$

0-8194-1700-9/94/$6.00

- piezoelectric layer $\quad z_{a(u)} \in [t_s/2;\ t_s/2 + t_a]$ and $z_{a(l)} \in [-t_s/2;\ -t_s/2 - t_a]$

$$\mathrm{T}^{a(u,l)} = \left| \begin{array}{ccc} Q^a_{11} & Q^a_{13} & 0 \\ Q^a_{13} & Q^a_{33} & 0 \\ 0 & 0 & Q^a_{55} \end{array} \right| \left(\mathrm{D}^{a(u,l)} \mp \left| \begin{array}{c} d_{31} \\ d_{33} \\ 0 \end{array} \right| E^{el}_z \right)$$

where the top and bottom signs refer respectively to the upper and lower actuator.
$\mathrm{T} = \{\sigma_x;\ \sigma_z;\ \tau_{xz}\}^T$ and $\mathrm{D} = \{\epsilon_x;\ \epsilon_z;\ \gamma_{xz}\}^T$ are the stress and strain vectors, while E^{el}_z is the electric field component along the z axis.

2.3 *Continuity conditions*

At this stage continuity conditions have to be imposed at the upper interface (on the lower one they are automatically verified) both on displacements and on the out-of-plane stress components (that is the components that act in the direction normal to the middle plane of the structure). The top surface equilibrium condition for the shear stress is also imposed (the equilibrium on the bottom surface leads to the same equation in terms of displacement components).

- Displacement continuity at the interface.

$$\begin{aligned} u^{a(u)}(x, t_s/2) &= u^s(x, t_s/2) \\ w^{a(u)}(x, t_s/2) &= w^s(x, t_s/2) \end{aligned}$$

- Out of plane shear stress continuity.

$$\tau^{a(u)}_{xz}(x, t_s/2) = \tau^s_{xz}(x, t_s/2)$$

- Out of plane normal stress continuity.

$$\sigma^{a(u)}_z(x, t_s/2) = \sigma^s_z(x, t_s/2)$$

- Condition on the top free-load surface.

$$\tau^{a(u)}_{xz}(x, t_s/2 + t_a) = 0$$

By imposing these conditions the number of displacement unknowns reduces from 8 to 3, i.e. to the three functions $u^{1s}(x), u^{3s}(x), w^{0s}(x)$ that can be viewed as the generalized displacement components of the structure.

2.4 *Equilibrium equations*

In order to obtain the governing equations of the problem, the principle of the virtual work may be used. In absence of external applied loads the virtual internal load $\delta\mathcal{L}$ is equal to zero

$$\delta\mathcal{L} = \int_0^L \int_{-\frac{h}{2}}^{\frac{h}{2}} \delta\mathrm{D}^T \mathrm{T} dz dx = \int_0^L \left[\int_{-\frac{t_s}{2}}^{\frac{t_s}{2}} \delta\mathrm{D}^{s^T} \mathrm{T}^s dz + \int_{\frac{t_s}{2}}^{\frac{h}{2}} \delta\mathrm{D}^{a(u)^T} \mathrm{T}^{a(u)} dz + \int_{-\frac{h}{2}}^{-\frac{t_s}{2}} \delta\mathrm{D}^{a(l)^T} \mathrm{T}^{a(l)} dz \right] dx = 0$$

Following the classical techniques it is easy to obtain a set of ordinary differential equations with the variationally consistent boundary conditions.
The characteristic equation of the differential system is :

$$\phi^4 \left(C_1 \phi^4 + C_2 \phi^2 + C_3 \right) = 0$$

with the roots : $\phi_i = 0$ for $i = 1,2,3,4$, $\phi_{5,6} = \pm\sqrt{\alpha_1}$, $\phi_{7,8} = \pm\sqrt{\alpha_2}$.
The coefficients C_j are functions of the geometric and elastic characteristics of the structural system. The solution is therefore of the form

$$U_s(x) = \begin{vmatrix} u^{1s}(x) \\ u^{3s}(x) \\ w^{0s}(x) \end{vmatrix} = U_1 + U_2 x + U_3 x^2 + U_4 x^3 + U_5 e^{\phi_5 x} + U_6 e^{\phi_6 x} + U_7 e^{\phi_7 x} + U_8 e^{\phi_8 x}$$

The indipendent constants to be determined are obtained by imposing the boundary conditions of clamped edge in $x = 0$ and free edge in $x = L$.

From the closed form displacement solution the expression of the stress components can be easily derived.

3. Discussion

In fig.2 the inplane bending stress distribution along the thickness is shown for three different positions along the x axis, for the case $t_s/t_a = 5$ and $L/t_a = 50$. It is interesting to note that close to the free edge the plane-section hypothesis cannot be considered valid since curved configurations of the stress distribution are observed. The distribution of the interlaminar shear stress is reported in fig.3. An increase of the maximum values of the stresses occurs in the area close to the free edge. This effect can be also evaluated from a global point of view by examining fig.4 where the induced bending moment is illustrated along the x axis. In the diagram an edge effect can be easily recognized and also a reduction in the bending moment, compared to the Euler-Bernoulli prediction, can be observed also far from the edge. An improvement of the description of the edge effect can be obtained by taking higher order powers of z for the assumed displacement field.

References

1 Wada B., Fanson J. L., Crawley E. F., "Adaptive Structures".
in B. Wada editor, Adaptive Stuctures, (1-8), New York, 1989, ASME.

2 Crawley E. F., de Luis J., "Use of Piezoelectric Actuators as Elements of Intelligent Structures", *AIAA Journal*, 1987, 25 (10), pp. 1373-1385.

3 Anderson E. H., Crawley E. F., "Piezoceramic Actuation of one- and two-dimensional Structures", MIT Space Systems Laboratory Report 5-89, Cambridge, Massachusets.

4 Gaudenzi P., "A General Formulation of Higher-Order Theories for the Analysis of Laminated Plates", *Composite Structures*, 1992, 20, pp. 103-112.

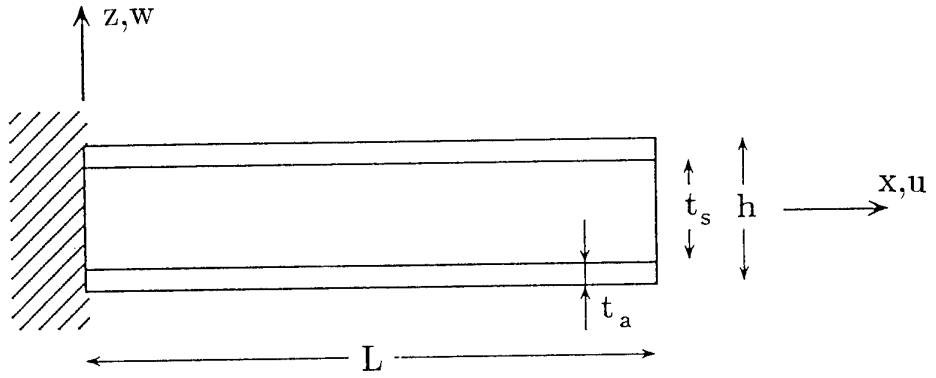

Fig.1

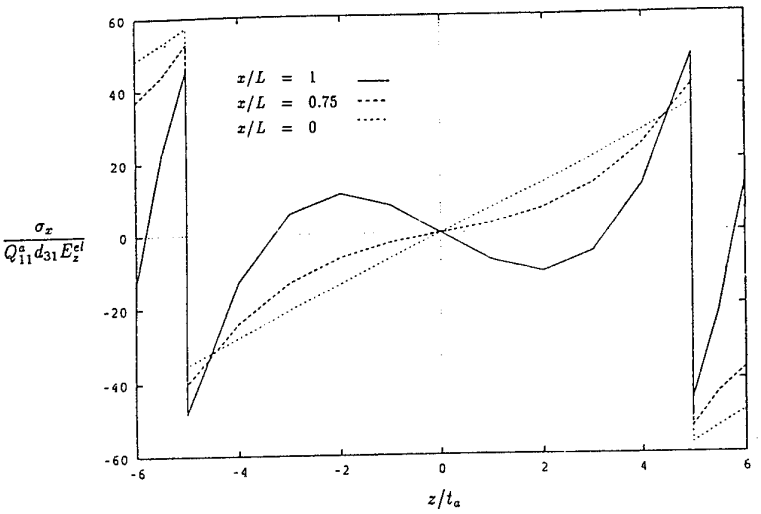

Fig.2 Distribution of stress component σ_x

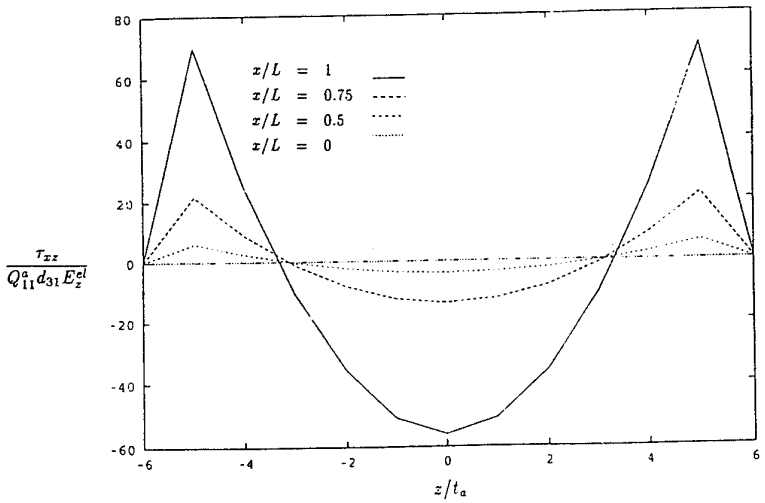

Fig.3 Distribution of stress component τ_{xz}

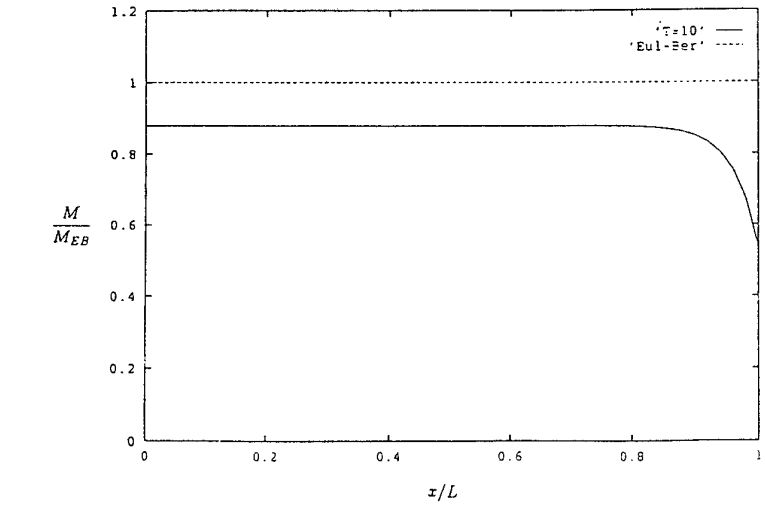

Fig.4 Normalized bending moment

ASYMPTOTIC ANALYSIS OF THIN SPACE STRUCTURES

Doina Cioranescu – Jeannine Saint Jean Paulin

We consider the linearized elasticity system for a class of periodic structures made by very thin bars (as cranes for instance). There are three small parameters which characterize these structures: their global width (or thickness) e, the size of the period ε and the thickness $\varepsilon\delta$ of the bars composing the structure.

More precisely, we consider a domain $\Omega_{e\varepsilon\delta}$ consisting of four vertical bars of length L and of cross section $e\delta/2 \times e\delta/2$. These bars are linked with horizontal thin bars of length e and cross section $e\delta/2 \times \varepsilon\delta$ and periodically distributed (with period ε) along the vertical direction.

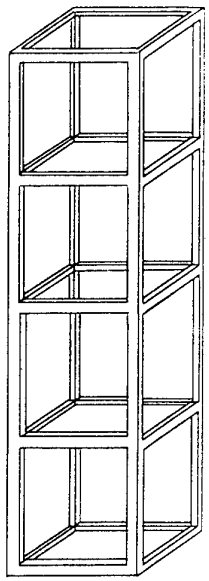

Figure 1

Let $u_{e\varepsilon\delta}$ be the displacement of the structure satisfying the system of linearized elasticity

$$\begin{cases} -\dfrac{\partial}{\partial x_j}\left(a_{ijkh}\dfrac{\partial u_k^{e\varepsilon\delta}}{\partial x_h}\right) = F_i^e & \text{in } \Omega_{e\varepsilon\delta} \\ a_{i3kh}\dfrac{\partial u_k^{e\varepsilon\delta}}{\partial x_h} n_3 = 0 & \text{on the top of the structure} \\ u_{e\varepsilon\delta} = 0 & \text{on the bottom of the structure} \\ a_{i\alpha kh}\dfrac{\partial u_k^{e\varepsilon\delta}}{\partial x_h} n_\alpha = G^{e\varepsilon\delta} & \text{on the rest of the boundary.} \end{cases}$$

0-8194-1700-9/94/$6.00

The elasticity constants a_{ijkh} satisfy the usual hypotheses of symmetry and coercitivity. For sake of simplicity we suppose that they are Lamé constants, i.e.

$$a_{ijkh} = \lambda\delta_{ij}\delta_{kh} + \mu(\delta_{ik}\delta_{jh} + \delta_{ih}\delta_{jk}).$$

Clearly, a direct computation $u_{e\varepsilon\delta}$ will be far too long and expansive because of the smallness of e, of the great number L/ε of cells (as ε is very small) and the small thickness of the bars. Therefore a natural question is : can one obtain an easily computable approximate solution u^*? Our aim is to give an answer to this question, that is to perform an asymptotic study of $u_{e\varepsilon\delta}$ when successively $e \to 0, \varepsilon \to 0$ and $\delta \to 0$.

We show that after appropriate rescalings, the limit displacement has the form

$$\begin{cases} u_3^\star = -z_1 \dfrac{\partial V_1^\star(z_3)}{\partial z_3} - z_2 \dfrac{\partial V_2^\star(z_3)}{\partial z_3} + V_3^\star(z_3) \\ u_\alpha^\star = V_\alpha^\star(z_3) \end{cases}$$

where $V_\alpha^\star$ and $V_3^\star$ are respectively solutions of the limit systems

$$\begin{cases} \dfrac{E}{2}\dfrac{\partial^4 V_\alpha^\star}{\partial z_3^4} = -\mathcal{F}_\alpha + \dfrac{\partial \mathcal{G}_\alpha}{\partial z_3} & \text{in} \quad (0,L) \\ V_\alpha^\star(0) = \dfrac{\partial V_\alpha^\star}{\partial z_3}(0) = 0 \\ \dfrac{\partial^2 V_\alpha^\star}{\partial z_3^2}(L) = \dfrac{\partial^3 V_\alpha^\star}{\partial z_3^3}(L) = 0 \end{cases}$$

and

$$\begin{cases} E\dfrac{\partial^2 V_3^\star}{\partial z_3^2} = -\mathcal{F}_3 & \text{in} \quad (0,L) \\ V_3^\star(0) = \dfrac{\partial V_3^\star}{\partial z_3}(L) = 0 \end{cases}$$

where E is the Young modulus

$$E = \frac{\mu(3\lambda + 2\mu)}{(\lambda + \mu)}$$

and $\mathcal{F}_\alpha$ and $\mathcal{G}_\alpha$ are limits of integrals of the given forces and of their first order moments.

Remark. We can apply the same technique to more complicate $\Omega_{e\varepsilon\delta}$. For instance, we can add in Figure 1 oblique bars.

Conclusion. We started with the real three dimensional system of linearized elasticity and after passing to the limit, we obtained simple differential equations on the interval $(0, L)$. In the first step, we make $e \to 0$ and we use plate or rod techniques to get second order and fourth order systems satisfied by the displacements. The following step, $\varepsilon \to 0$, is a classical homogenization process in perforated domains. The last step, $\delta \to 0$, gives the possibility to compute explicitely the overall coefficients which in this case are very simple, expressed only in terms of E.

Let us point out that our technique can be applied to thermal or elasticity problems for a very large range of structures: towers (where the material is disposed in very thin layers), gridworks or complicate truss structures. Different boundary conditions (as Neumann, Dirichlet or Robin) can be considered, as well as eigenvalue problems. In all these situations the above procedure ends up with overall coefficients which are simple algebraic expressions of the initial physical material coefficients.

Moreover, we show that the limit $u^\star$ is a good approximation of $u_{e\varepsilon\delta}$. More precisely, we prove that if data are sufficiently smooth, then we have error estimates of the following type:

$$\frac{1}{(\text{ meas } \Omega_{e\varepsilon\delta})^{\frac{1}{2}}} \quad \| u_{e\varepsilon\delta} - u^\star \|_{L^2(\Omega_{e\varepsilon\delta})} \quad \leq \quad C\,(\delta^{\frac{1}{2}} + \varepsilon^{\frac{1}{2}})$$

$$\frac{1}{(\text{ meas } \Omega_{e\varepsilon\delta})^{\frac{1}{2}}} \quad \| \text{ grad } u_{e\varepsilon\delta} - \text{grad } u^\star \|_{L^2(\Omega_{e\varepsilon\delta})} \quad \leq \quad C\,(\delta^{\frac{1}{2}} + \varepsilon^{\frac{1}{2}}).$$

Doina Cioranescu
Laboratoire Analyse Numérique - CNRS
4 Place Jussieu
75252 Paris Cedex 05
France

Jeannine Saint Jean Paulin
Université de Metz - Mathématiques
Ile de Saulcy
57045 Metz Cedex 01
France

SESSION 2

Paper presented at the Second European Conf. on Smart Structures and Materials, Glasgow 1994, Session 2

RESEARCH NEED FOR PIEZOACTUATORS IN ADAPTIVE STRUCTURES

P. Jänker, W. Martin

Daimler Benz AG, Research and Technology, 81663 Munich, Germany

ABSTRACT

Piezoelectric materials are highly attractive as actuator elements for Adaptive Structures since they have material-inherent actuatoric and sensoric functions and can easily be electrically controlled. This paper describes the possible fields of applications and deduces research needs.

1 INTRODUCTION

The key elements of Adaptive Structures are sensors to recognize internal or external stimuli, control units to process the information, and actuator mechanisms to react to the stimuli in an adequate manner. In practice, the adjustment capability of an Adaptive Structure is limited by the performance of the integrated actuator; thus, actuator materials play a major role in Adaptive Structures concepts.

While a great number of various sensors is commercially available, there has been an urgent demand for integratable materials which perform the mechanical actuatoric functions. Some of the currently most potential candidate materials to be used for actuation purposes are electric field induced actuator materials, and, in particular, piezoelectrics and electrostrictive materials. In a previous paper /1/, the different actuator materials which are being discussed for use in Adaptive Structures (SMA, piezoelectrics, magnetostrictives) have been evaluated by means of their specific actuatoric energy and compared with conventional actuator principles (hydraulics, electromagnets, human muscle). The study pointed out that each of these candidates has its special properties and thus its most suited fields of application.

2 FERROELECTRIC MATERIALS

Ferroelectricity, the fundamental phenomenon of piezoelectricity, has many fascinating scientific facets. Besides problems of enormous physical importance, ferroelectricity addresses a broad scope of sciences: chemistry, crystallography, mechanical and electrical engineering. There has been much research ranging from fundamental physical studies to problems of technical application.
The underlying effect of ferroelectric phenomena is **Spontaneous Polarisation.** In ordinary crystals such as quartz the electric polarisation P is proportional to the applied electric field. But there are many crystals which have polarisation in the absence of electric fields. This polarisation is called spontaneous polarisation. A crystal which shows spontaneous polarisation is called a pyroelectric crystal /2/. A ferroelectric crystal is defined as a crystal which belongs to the pyroelectric family and of which the direction of spontaneous polarisation can be reversed by an electric field.
Ferroelectric materials are able to interact in various ways with their physical environment. Consequently, a variety of specialised and optimised materials for different purposes have been developed. These materials are an attractive source for adaptive systems. Table 1 lists the most relevant effects, the corresponding actuatoric and sensoric functions, and exemplary materials.

0-8194-1700-9/94/$6.00

INTERACTION	Actuatoric	Sensoric
Mechanical	• E-induced change of shape • E-induced change of volume *PZT, PMN, PVDF*	• stress-induced polarisation *PZT, Quartz*
Thermal (infrared)		• pyroelectricity *SBN, TGS, PVDF*
Optical	• photostriction *doped PLZT* • E-controlled birefringence • E-controlled light scattering *PLZT*	photovoltaic effect *WO_3-doped PLZT*

Table 1. Useful ferroelectric phenomena and exemplary materials for adaptive structures.

Ferroelectrics are temperature-sensitive. Their electric polarisation can be switched, hence they have a memory and can be used to store information. The shape and volume of ferroelectric bodies can be changed by electric fields; and in turn they generate electric fields when they are mechanically stressed. There are transparent ferroelectric ceramics (PLZT) with electrically controllable photorefractive properties. These materials can be exploited for a wide range of electrooptic applications. Vice versa, many crystals are generating electric fields under optic radiation. For instance, doped (Nb, Ta, W) PLZT perovskites are photostrictive. Recently, K. Uchino /3/ succeeded in developing a photostrictive bimorph element.

From this short introduction we can see that ferroelectrics offer a lot of phenomena which could be used for adaptive structures. From an industrial point of view, the key targets of Adaptive Structure research activities are:

- self-diagnosis (structural health and usage monitoring systems)
- new actuation technologies
- active shape control
- vibration, anti-noise control
- in-service control of materials properties
- structure-integrated electronics/avionics (Smart Skins).

The objective of this paper is to focus on mechanical systems and infer research needs for piezoactuators. The first step we have to take is to describe the properties and limitations of today's available actuator materials.

2.1 PERFORMANCE AND CHARACTERISTICS OF AVAILABLE FERROELECTRIC ACTUATOR MATERIALS

Ferroelectric materials are of great attraction for mechanical adaptive structures because they are able to change shape or volume in electric fields. The underlying phenomenon is that polarisation is accompanied by a lattice deformation. In the following, the deformation behaviour of a ferroelectric material in an electric field is roughly outlined. Generally, in all isolating materials electrostrictive strain is induced:

$$S = Q P^2 \qquad (1)$$

Where S, Q, and P are the mechanical strain, the electrostrictive coefficient and the electric polarisation. In case of ferroelectrics, polarisation P consists of spontaneous polarisation P_S and induced polarisation P_i :

$$S = Q (P_S + P_i)^2 = Q P_S^2 + 2 Q P_S P_i + Q P_i^2 \qquad (2)$$

From that we can differentiate three terms of deformation. First, there is a field-independent polarisation deformation. Second, we can identify a field-proportional term, the piezoelectric deformation term. And, thirdly, there is a field-quadratic term, the electrostrictive deformation.

Today piezoelectric actuators are mainly based on PZT (lead zirconate titanate) ceramics. The invention of poled PZT ceramics in the 1950's /4/ was a real breakthrough since piezoelectric performance, especially piezoelectric strain ,was improved drastically. Like most of the useful ferroelectric materials, PZT-materials are ceramics of perovskite-type structure. Today, these materials are the main industrial piezoelectric product. They are based on compositions of ($PbZrO_3$) and ($PbTiO_3$). At a ratio of 53/47 there is a morphotropic phase boundary (MPB) where the structure can be considered to be transitional between tetragonal and rhombohedral phases. Thus the lattice may be changed between tetragonal and rhombohedral structures by an external field. That explains why PZT compositions near the MPB exhibit excellent piezoelectric properties.

Electrostrictive materials have vanishing remanent polarisation. According to formula (2) their strain behaviour is quadratic to the induced polarisation. Electrostrictive materials have played a minor role since the electrostrictive strain is strongly dependent upon temperature. In practice the operation of electrostrictive actuators is limited to a small temperature range of some 30 K.

The basic limiting data of piezoelectric materials with respect to mechanical applications are primarily active and passive strain. Table 2 lists the basic data for today's high-performance piezoelectric ceramic materials to give a rough overview.

• active strain	$2\ 10^{-3}$
• passive strain	
- loss of mechanical function	
tensile strength	10^{-3},
compressive strength	10^{-2}
- loss of piezoelectric function, depolarisation	10^{-3}
• Young's module	60 GPa
• energy conversion η	50 %
• mass density	7.8 kg/l

Table 2. Mechanical data of today's high-performance piezoelectric ceramics.

A piezoelectric actuator is an energy converter. Primary energy in the form of electrical energy is converted and stored by the piezoactuator as electrical and mechanical energy. In this context, the energy conversion efficiency η is important. The energy conversion efficiency η is deducible from the electro-mechanical coupling coefficient k:

$$\eta = k^2 \qquad (3)$$

The maximum converted mechanic energy density is some 70 J/l. It has to be noticed that, depending on the load conditions, only a fraction of the converted mechanical energy can be transferred to work.

2.2 GENERAL FIELDS OF APPLICATIONS

Due to the properties of piezoelectric materials some suitable fields of technical applications can be found. On account of the relatively small active strain the fields of applications are limited by small mechanical amplitudes. Nevertheless, the many outstanding properties of piezoelectric actuators make them attractive for adaptive structures:

- simplicity in design
- precision
- high forces
- good dynamic behaviour
- simultaneous sensoric & actuatoric functions
- can be easily integrated in complex structures

To find the most suitable field of application we have to answer the question: Where is fast reaction, high forces, good resolution found in piezoelectrics fundamental for an actuator?

The extremely high resolution of piezoelectric actuators is exploited by way of microelectronics fabrication equipment. In STM (Scanning Tunneling Microscope) devices extreme positioning resolution down to atomic scales is verified. An eye attracting feature is the outstanding dynamic force generation of piezoelectric ceramics. In this paper we would like to focus on and discuss dynamic adaptive solutions. As examples we have chosen (I) the piezoelectric driven fuel injector as a key element for future adaptive combustion engines and (II) Anti Noise Control structures (ANC). From the discussion of these exemplary applications we can infer general research needs.

3 EXAMPLE (I) FUEL INJECTOR

Fast electronically controlled fuel injectors are highly attractive for the automotive industry in order to reduce emission rates and fuel consumption considerably. The exact control of the fuel injection process in time and flow is essential to adapt the combustion process to the actual conditions of operation, i.e. to shape the fuel flow precisely. The direct injection of fuel requires very fast reaction times of approx. 0.2 ms. Additionally, time jitters have to be less than 50 µs. Fuel quantity requires an accuracy of ± 2 %. Electromagnetic actuators cannot meet these requirements. Piezoelectric actuators have the potential to overcome these limitations, but there are still some unsolved problems.

Stroke. Typically, the driver of a fuel injector has to perform a 0.1 - 0.3 mm linear stroke. To perform a 0.1 mm stroke directly with a longitudinal expansion actuator, a ceramic stack of some 100 mm in length is necessary using today's materials. In order to reduce volume and costs, recent development activities have been concentrated on stacks in combination with hydraulic stroke amplifiers. A smarter approach is to search for new materials with a significantly higher strain than 1000 - 2000 microstrain of current piezoelectrics. These materials would make it possible to simplify the injector design.

Research Need: *High-strain materials*
Suggestion: Polarisation-controlled high-strain ferroelectric materials,
antiferroelectric - ferroelectric phase-switching materials /5/.

Dynamics. In highly dynamic applications the piezoelectric elements are driven with very fast rise times, accelerating the material near to resonance frequency. A pulse-driven piezoelectric actuator swings over the mechanical state of equilibrium with an amplitude of the active strain. Thus strong dynamic tensile stresses arrive which make additional appliance necessary. Here is an urgent need for materials with a high tensile strength significantly greater than the maximum piezoelectric strain.

Research Need: *higher tensile strength*
Suggestion: structural ceramic concepts

Voltage Supply. In order to achieve compatibility to today's electronics, there is a clear trend towards reducing the voltage supply of piezoelectric actuators. However, it is not definitely clear what the optimal voltage level is optimal. As it appears, there is a lower voltage limit. Different aspects of materials and electronics have to be considered. It is clear that technical problems and costs of actuators increase as layer thickness decreases. With decreasing thickness the total electrode area and thus damage susceptibility increases. Last but not least, the functionality of very thin (< 10 μm) piezoelectric films is reduced in comparison to the thick bulk material .

Research Need: *low-voltage actuators*

Suggestion: monolithic multilayer actuators

Reliability. A lifetime of some 10^9 cycles has to be achieved. The fatigue behaviour of piezoelectric ceramics is a crucial point of large strain piezoelectric actuators. Mechanical loads and high electric fields stress the material and induce cracks. Besides mechanical fatigue, degradation of piezoelectric function is critical: polarisation and field-forced strains decrease with increasing cycles.

Research Need: *stability, fatigue mechanism*

Costs. The automotive market is a typical mass market. Hence, fuel injectors have to be cheap to have a real chance of market success. For a calculation the complete injector system has to be considered: piezo driver, stroke amplifier, and electronics. With respect to costs and operation voltage, only monolithic ceramic elements can be applied.

Research Need: *cost-effective actuators*

Suggestion: monolithic, structurally integrated actuators, power-efficient electronics

4 EXAMPLE (II) ANTI-NOISE/VIBRATION CONTROL (ANC)

The reduction of vibration and noise has been of continual increasing importance. ANC is an emerging technology which is led by the idea to cancel noise or vibrations by actively superposing mechanical waves of opposite phase. Actuators generating high forces and fast reaction are required to control the vibration of solid components. An ANC is principally a feedback loop consisting of a sensor, control algorithm, electronic amplifier, and actuator. Principally, piezoelectric actuators can perform sensor and actuator functions simultaneously. Due to the simple design of solid state actuators they can easily be integrated into structures. Hence they are highly attractive for ANC. ANC concepts are in an early stage of development and much fundamental work has to be done to establish optimal placement of actuators, sensors, and control technologies, electronics, and algorithms.

In recent years different prototypes have been developed. In adaptive truss structures active piezoelectric actuators are integrated as active struts generating forces (e.g. /6/). Other types of ANC structures are Adaptive Surfaces, i.e. piezoelectrically controlled surfaces. Piezoelectric patches are applied to the surfaces of plates for sensing and actuation /7/. These patches are inducing momenta working against and cancelling disturbing noise. B. Azvine et al. /8/ has suggested a combination of passive and active damping. In this work, a composite structure consisting of piezoelectric patches and a viscoelastic layer are attached to a beam. The piezoelectric patches are controlled in such a way as to enhance the shear generated in the viscoelastic layer to increase energy dissipation.

Strength. A principal problem arises from the fact that the mechanical strength of the piezoelectric materials is much smaller than that of common engineering materials like aluminium or steel. Hence, an improvement of the mechanical strength of piezoelectrics is needed to make them compatible with the structures.

Research Need: *higher tensile strength*

Suggestion: Concepts from structural ceramics.

Reliability. The highest operation frequency of an ANC is typically 1000 Hz. This is roughly one order of magnitude higher than the operation frequency of a fuel injector. Consequently, very high life time cycles are required. Another difference is that a fuel injector is pulse driven, whereas an ANC is operated with rather continuous signals. Hence dynamic forces are not so critical in comparison to the fuel injector.

Research Need: *high functional stability*

5 SUMMARY AND CONCLUSION

Adaptive Structure concepts are very attractive for a variety of industrial applications. From the examples discussed we can deduce that the present limitations of piezoelectric based actuator systems are due to insufficient functional and passive mechanical data of available materials. On the other hand, new materials are under development. Recent research on high-strain piezoelectric materials has demonstrated a piezoelectric strain of some 0.5 %. Such materials would be pioneering and of invaluable importance for adaptive technology. Integration technologies are essential for the construction of low-voltage multilayer actuators and further intelligent multifunctional elements. Can we learn from knowledge on structural ceramics to develop new concepts and improve mechanical strength and fatigue behaviour? From the examples discussed, (fuel injector and ANC) we can deduce the necessity of functional stability over very high numbers of load cycles and pulse rigidity of piezoactuators. Last but not least it takes the ingenious performance of the Smart Structure research community to overcome today's formidable technological problems.

REFERENCES

/1/ P. Jänker, W. Martin, Performance and Characteristics of Actuator Materials, 4th Conf. Adap. Struct., Köln, Nov. 2 - 4 (1993)

/2/ T. Mitsui, I. Tatsuzaki, and E. Nakamura, An Introduction to the Physics of Ferroelectrics (1976)

/3/ K. Uchino et al., Ferroelectrics 91, 281 (1989)

/4/ Jaffe et al., J. Appl. Phys. 25, 809 (1954)

/5/ W. Y. Pan et al., J. Appl. Phys. 66, 6014 (1989)

/6/ S. Shibuta et al., Adaptive Control of Space Truss Structures by Piezoelectric Actuator, 2nd Joint Jap./U.S. Conf. on Adapt. Struct., Nagoya, Japan, Nov. 12 - 14, 245 (1991)

/7/ J. D'Cruz, The Active Control of Panel Vibrations with Piezoelectric Actuators, Recent Adv. in Adapt. and Sens. Mat. and their Appl., Blacksburg, USA April 27 - 29, 665 (1992)

/8/ B. Azvine et al., Vibration Supression of Flexible Structures Using Active Damping, 4th Conf. Adap. Struct., Köln, Nov. 2 - 4 (1993)

Paper presented at the Second European Conf. on Smart Structures and Materials, Glasgow 1994, Session 2

RESULTS ON A DYNAMIC MODEL OF PHASE TRANSITIONS IN SHAPE MEMORY ALLOYS WITH NON-CONVEX LANDAU-GINZBURG FREE ENERGY

RUBEN D. SPIES *

Programa Especial de Matemática Aplicada PEMA
Instituto de Desarrollo Tecnológico para la Industria Química INTEC
Conicet - Universidad Nacional del Litoral
Güemes 3450
(3000) Santa Fe - Argentina

1. INTRODUCTION

The conservation laws governing the thermomechanical processes in a one-dimensional shape memory solid $\Omega = (0,1)$ with free energy potential Ψ, give rise to the following initial boundary value problem.

$$\begin{cases} \rho u_{tt} - \beta\rho u_{xxt} + \gamma u_{xxxx} = f(x,t) + \frac{\partial}{\partial x}\left[\frac{\partial}{\partial \epsilon}\Psi(u_x, u_{xx}, \theta)\right], & x \in \Omega, 0 \le t \le T, \\ C_v\theta_t - k\theta_{xx} = g(x,t) + 2\alpha_2\theta u_x u_{xt} + \beta\rho u_{xt}^2, & x \in \Omega, 0 \le t \le T, \\ u(x,0) = u_0(x), \quad u_t(x,0) = u_1(x), \quad \theta(x,0) = \theta_0(x), & x \in \Omega, \\ u(0,t) = u(1,t) = u_{xx}(0,t) = u_{xx}(1,t) = 0, & 0 \le t \le T, \\ \theta_x(0,t) = 0, \quad k\theta_x(1,t) = k_1\left(\theta_\Gamma(t) - \theta(1,t)\right), & 0 \le t \le T, \end{cases} \tag{1.1}$$

where u represents the displacement, θ is the absolute temperature, ρ the mass density, k the coefficient of thermal conductivity, C_v the specific heat, β is a viscosity constant, f the distributed body forces, g the distributed heat sources, u_0, u_1 and θ_0 are the initial displacement, velocity and temperature, respectively, θ_Γ is the external temperature, k_1 is a positive constant and T is a prescribed final time. The free energy potential Ψ, in general, is assumed to be a function of ϵ, ϵ_x and θ where $\epsilon = u_x$ is the linearized shear strain, and it is given in the Landau-Ginzburg form

$$\Psi(\epsilon, \epsilon_x, \theta) = -C_v\theta ln\left(\frac{\theta}{\theta_2}\right) + C_v\theta + C + \alpha_2(\theta - \theta_1)\epsilon^2 - \alpha_4\epsilon^4 + \alpha_6\epsilon^6 + \gamma\epsilon_x^2 \tag{1.2}$$

where α_2, α_4, α_6, γ, θ_1, θ_2, C are all nonnegative constants depending on the material under consideration. These nonconvex potentials give rise to hysteresis in the corresponding stress-strain laws in accordance with the experimentally observed behavior of Shape Memory Alloys. For details on the derivation of system (1.1) see for instance [**21**].

The boundary conditions in (1.1) mean that the body is clamped at both ends, thermally insulated at the left end and the rate of thermal exchange with the external temperature is prescribed at the right end. Other type of boundary conditions may also be considered. In particular, for the numerical experiments that we present in the following section, a symmetric tensile boundary stress is used. The partial differential equations appearing in (1.1) are coupled and nonlinear. The system can be regarded as a nonlinear beam equation in u coupled with a nonlinear heat equation in θ.

Initial bounday value problems of this type have been studied by several authors ([**11**], [**12**], [**17**], [**18**], [**19**], [**23**]; see [**21**] for a review). In particular, the proof of the following theorem can be found in [**21**].

THEOREM 1. *If the functions f and g and the initial and boundary data are sufficiently restricted (see [21] for details) then there exist $t_1 > 0$ such that the initial boundary value problem (1.1), with Ψ as in (1.2), has a unique classical solution on the interval $[0, t_1)$.*

An improved version of this theorem for less restricted initial data can be found in [**22**].

2. FINITE DIMENSIONAL APPROXIMATIONS AND NUMERICAL RESULTS

We consider the problem of developing approximations for the solutions of infinite dimensional systems of the type (1.1). We shall consider here the case in which a symmetric stress $\sigma_\Gamma(t)$ is prescribed as part of

*The work of the author was supported in part by the Argentinean National Council for Scientific and Technical Research CONICET and by the US Air Force Office of Scientific Research (AFOSR) under grant F49620-92-J-0078 and by the Institute for Mathematics and Its Applications of the University of Minnesota with funds provided by the Office of Naval Research (ONR) through grant N/N0014-93-1-0027 and by the National Science Foundation (NSF) through grant NSF/DMS-9023978 while the author was a postdoctoral fellow at the Institute for Mathematics and Its Applications of the University of Minnesota.

0-8194-1700-9/94/$6.00

the boundary conditions. In addition, for simplicity reasons we will take $\gamma = \beta = 0$ (i.e. no viscosity and no coupled stress are present). Under these assumptions, our initial-boundary value problem takes the form

$$\begin{cases} \rho u_{tt} - \frac{\partial}{\partial x}\left(2\alpha_2(\theta-\theta_1)u_x - 4\alpha_4 u_x^3 + 6\alpha_6 u_x^5\right) = f(x,t), & x \in (0,1), 0 \le t \le T, \\ C_v\theta_t - 2\alpha_2\theta u_x u_{xt} - k\theta_{xx} = g(x,t), & x \in (0,1), \quad 0 \le t \le T, \\ \theta(x,0) = \theta_0(x), \quad u(x,0) - u_0(x), \quad u_t(x,0) = u_1(x), & x \in (0,1), \\ \frac{\partial \Psi}{\partial \epsilon}(u_x,\theta) = \sigma_\Gamma(t), \quad k\frac{\partial \theta}{\partial \nu} = k_1(\theta_\Gamma(t) - \theta), & x = 0,1, \quad 0 \le t \le T, \end{cases} \tag{2.1}$$

where ν is the outward normal unit vector and $\sigma_\Gamma(t)$ is the applied stress at time t. We note here that it is not known if the initial-boundary value problem (2.1) is well-posed since we are considering here the case $\beta = \gamma = 0$ and slightly different boundary conditions for which Theorem 1 does not hold. However, as we shall see later, numerical experiments seem to suggest not only that the system is in fact well-posed, but also that physically reasonable solutions can be obtained for particular values of the model parameters.

We shall use a finite element scheme based on a weak formulation of (2.1) to investigate this system. Let us consider the approximations of u and θ given by $u^N(x,t) = \sum_{i=-1}^{N+1} a_i^N(t)\phi_i^N(x)$, $\theta^N(x,t) = \sum_{i=-1}^{N+1} b_i^N(t)\phi_i^N(x)$, where the ϕ_i^N's are the standard cubic B-splines in $(0,1)$, $a_i^N(t)$ and $b_i^N(t)$, $-1 \le i \le N+1$, are coefficients to be computed and $N+3$ is the order of the approximation. By using standard finite element techniques, which involve the weak formulation of the partial differential equations in (2.1) and orthogonal projections, the finite-dimensional approximating system associated with (2.1) can be written as the following initial value problem in the coefficients of u^N, u_t^N and θ^N.

$$\begin{cases} \frac{d}{dt}X(t) = AX(t) + N(X(t)) + F(t), \\ X(0) = X_0 \end{cases}, \tag{2.2}$$

with

$$X(t) = \left[a_{-1}^N(t)\dots a_{N+1}^N(t)\, a_{-1}'^N(t)\dots a_{N+1}'^N(t)\, b_{-1}(t)\dots b_{N+1}^N(t)\right],\ A = \begin{bmatrix} 0 & I_{N+3} & 0 \\ 0 & 0 & 0 \\ 0 & 0 & C_v^{-1}M^{-1}\left(-kS + \tilde{S}\right) \end{bmatrix},$$

$$N(X(t)) = \begin{bmatrix} 0_{N+3} \\ \rho^{-1}M^{-1}P(X(t)) \\ C_v^{-1}M^{-1}Q(X(t)) \end{bmatrix},\ F(t) = \begin{bmatrix} 0_{N+3} \\ \rho^{-1}M^{-1}(F_1(t)+F_2(t)) \\ C_v^{-1}M^{-1}(G_1(t)+G_2(t)) \end{bmatrix},\ \text{and}\ X_0 = \begin{bmatrix} M^{-1}U_0 \\ M^{-1}U_1 \\ M^{-1}\Theta_0 \end{bmatrix}$$

where M and S are the mass and stiffness matrices, respectively, associated with the ϕ_i's, I_{N+3} is the identity matrix of order $(N+3)$, $\tilde{S} = k_1 \begin{bmatrix} T & 0 & 0 \\ 0 & 0 & 0 \\ 0 & 0 & T \end{bmatrix}_{(N+3)\times(N+3)}$, $T = \begin{bmatrix} -1 & -4 & -1 \\ -4 & -16 & -4 \\ -1 & -4 & -1 \end{bmatrix}$,

0_{N+3} is an $(N+3)$-dimensional column vector of zeros, $P(X(t)) = \left[-\left\langle \frac{\partial \Psi}{\partial \epsilon}(u_x^N, \theta^N), \phi_j' \right\rangle_{L^2(0,1)}\right]^T_{-1\le j\le N+1}$,

$Q(X(t)) = \left[2\alpha_2 \left\langle \theta^N u_x^N u_{xt}^N, \phi_j \right\rangle_{L^2(0,1)}\right]^T_{-1\le j\le N+1}$, $F_1(t) = \left[\langle f(\cdot,t), \phi_j\rangle_{L^2(0,1)}\right]^T_{-1\le j\le N+1}$,

$F_2(t) = [\sigma_\Gamma(t)(\phi_j(1) - \phi_j(0))]^T_{-1\le j\le N+1}$, $G_1(t) = \left[\langle g(\cdot,t), \phi_j\rangle_{L^2(0,1)}\right]^T_{-1\le j\le N+1}$

$G_2(t) = [k_1\theta_\Gamma(0,t)\phi_j(0) + k_1\theta_\Gamma(1,t)\phi_j(1)]^T_{-1\le j\le N+1}$, $U_0(t) = \left[\langle u_0, \phi_j\rangle_{L^2(0,1)}\right]^T_{-1\le j\le N+1}$,

$U_1(t) = \left[\langle u_1, \phi_j\rangle_{L^2(0,1)}\right]^T_{-1\le j\le N+1}$ and $\Theta_0 = \left[\langle \theta_0, \phi_j\rangle_{L^2(0,1)}\right]^T_{-1\le j\le N+1}$.

The numerical results presented below are based on data reported in [7] and [8] for the alloy $Au_{23}Cu_{30}Zn_{47}$: $\alpha_2 = 24$ J cm^{-3} K^{-1}, $\alpha_4 = 1.5 \times 10^5$ J cm^{-3}, $\alpha_6 = 7.5 \times 10^6$ J cm^{-3}, $\theta_1 = 208$ K, $C_v = 2.9$ J cm^{-3} K^{-1}, $k = 1.9$ W cm^{-1} K^{-1}, $\rho = 11.1$ g cm^{-3}. We employed a sixth order Runge–Kutta–Verner method to integrate (2.2) for this data. We took $\theta_0(x) = 200$ K, $u_0(x) = 0$, $u_1(x) = 0$, $\theta_\Gamma(t) = 200$ K, $k_1 = 100$, $f = g = 0$, $T = 40 \times 10^{-3}$ sec., $N = 10$ and $\sigma_\Gamma(t)$ was defined to be a tensile load which was linearly increased until it reached 250 MPa at time $t = 10^{-3}$ sec., after which it was held constant at 250 MPa until $t = T$ (Figure 1). Figures 2.(a),(b) and (c) show the evolution of displacement (u), temperature (θ) and deformation (u_x), respectively, obtained with this data. Note that there is a phase transition front moving towards the center of the wire. At some points near this front, the temperature rose by more than 40° K. We should note here that this type of numerical experiment provides valuable data and information for the design of laboratory experiments to collect dynamic data for parameter identification purposes. For instance, the temperature evolution depicted in Figure 2.(b) provides important information about the possible location of sensors to detect stress-induced temperature increments. Figure 2.(c) shows that the deformation exhibits sharp edges along the phase boundaries due mainly to the absence of viscosity effects.

We observed in Figure 2.(b) that the temperature increased by more than 40° K due only to the applied stress. Experts in the field seem to agree on the fact that such an increment is too high for real materials. The coefficient that couples strain and temperature in our case is α_2 (see equation (1.2)). In the next experiment, we decreased α_2 by a factor of 10 and then by a factor of 100, keeping all the other parameters unchanged. When $\alpha_2 = 2.4$ (Figures 2.(d),(e) and (f)), the highest temperature increment observed was only of about 4° K (Figure 2.(e)). This lower temperature resulted now in larger deformations near the boundaries, in agreement with the fact that Shape Memory Alloys are more ductile at lower temperatures. When $\alpha_2 = 0.24$ (Figures 2.(g), (h) and (i)), the highest temperature increment observed was less than 0.5° K (Figure 2.(h)). Figure 3 shows a comparison of the different temperature evolutions obtained with the different values of α_2. Assuming that all the other estimates in [7] and [8] are accurate, this numerical experiment suggests that the value $\alpha_2 = 24$ for this alloy is probably too high. Consequently, it would be important to conduct an experiment to collect data in this case, for use in a parameter estimation scheme. We have also performed several additional numerical experiments with the remaining model parameters. Reports on these results will be published shortly elsewhere.

3. CONCLUSIONS

We have presented a mathematical model to describe the dynamics of Shape Memory Materials under certain distributed and boundary inputs. We have studied the influence of some of the model parameters on the evolution of displacement, temperature and deformation. The numerical experiments suggest that this model used in conjunction with the Landau-Ginzburg free energy (1.2) can provide intereresting qualitative information about the dynamics of phase transitions in materials with memory. The next step is to use dynamic experimental data to approximate the model parameters. This process is known as parameter identification and its implementation requires not only the design of adequate laboratory experiments but also the availability of efficient approximation schemes. This step will also determine whether this model can also provide relevant quantitative information to be used as a tool for control design. We are already devoting efforts into this area of research.

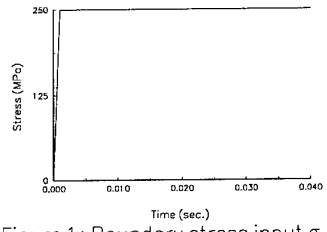

Figure 1 : Boundary stress input $\sigma_r(t)$.

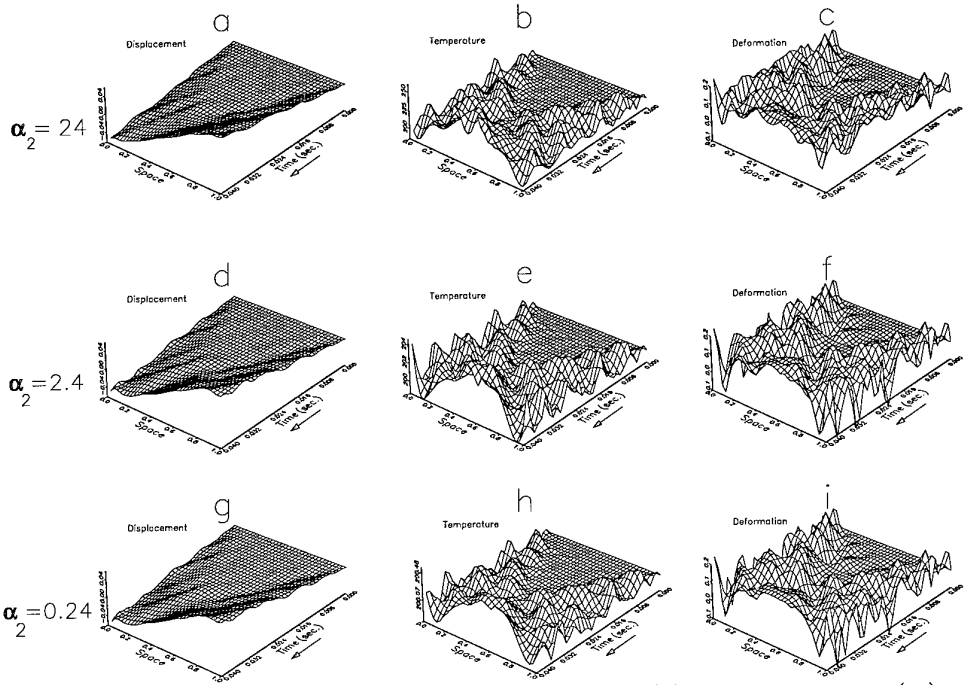

Figure 2: Evolution of displacement (u),temperature (θ) and deformation(u_x) for different values of α_2.

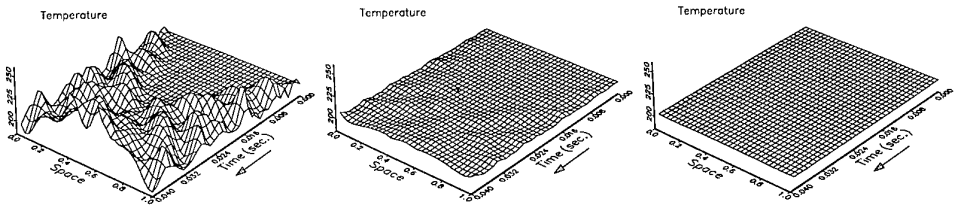

$\alpha_2 = 24.0$ $\alpha_2 = 2.4$ $\alpha_2 = 0.24$

Figure 3: Temperature evolutions obtained for different values of α_2.

References

[1] ACHENBACH, M. and MULLER, I., *"A Model for Shape Memory"*, Journal de Physique, Colloque C4, Supplément au No 12, Tome 43, décembre 1982, pp C4 163-167.

[2] ACHENBACH, M. and MULLER, I., *"Creep and Yield in Martensitic Transformations"*, Igenieur-Archiv, 53, pp 73-83, (1983).

[3] ACHENBACH, M. and MULLER, I., *"Shape Memory as a Thermally Activated Process"*, Plasticity Today: Modelling Methods and Applications, pp 515-531, Sawczuk and Bianchi.

[4] BURNS, J. A. and SPIES, R. D., *"Modeiling for Control of Shape Memory Alloys"*, 30^{th} IEEE Conference on Decision and Control, Brighton, England, 1991.

[5] FALK, F., *"Ginzburg-Landau Theory and Solitary Waves in Shape Memory Alloys"*, Z. Physik B-Condensed Matter 54, pp 177-185, (1983).

[6] FALK, F., *"Ginzburg-Landau Theory of Static Domain Walls in Shape Memory Alloys"*, Z. Physik B-Condensed Matter 51, pp 159-167, (1984).

[7] FALK, F., *"Model Free Energy, Mechanics and Thermodynamics of Shape Memory Alloys"*, Acta Metallurgica, Vol. 28, pp 1773-1780.

[8] FALK, F., *"One Dimensional Model of Shape Memory Alloys"*, Arch. Mech., 35, pp 63-84, Warszawa, (1983).

[9] FALK, F., *"Wie hãng die Freie Energie einer Memory-Legierung von der Verzerrung und der Teperatur ab ?"*, ZAMM 60 (1960), pp T 118- T 120.

[10] FUNAKUBO, H. (Ed.), *"Shape Memory Alloys"*, Precision Machinery and Robotics, Vol. 1, Translated from the Japanese by J. B. Kennedy, Gordon and Breach Science Publishers, (1987).

[11] HOFFMANN, K. H. and SONGMU, Z., *"Uniqueness for Nonlinear Coupled Equations Arising from Alloy Mechanism"*, Preprint 118, Institut für Mathematik, Ausburg, (1986).

[12] HOFFMANN, K. H. and SONGMU, Z., *"Uniqueness for Structural Phase Transitions in Shape Memory Alloys"*, Mathematical Methods in the Applied sciences, Vol. 10, pp 145-151, (1988).

[13] LOHMAN, R. and MULLER, I., *"A Model for the Qualitative Description of Martensitic Transformations in Memory Alloys"*, in Phase Transformations, Aifantis E. and Gittus J., pp 55-75.

[14] MULLER, I., *"A Model for a Body with Shape Memory"*, Arch. Rational Mechanics Anal., 70, pp 61-67, (1979).

[15] MULLER, I. and VILLAGGIO, P., *"A model for an Elastic-Plastic Body"*, Arch. Rational Mechanics Anal., 65 #1, pp 25-46, (1977).

[16] MULLER, I. and WILMANSKI, K., *"A model for Phase Transitions in Pseudoelastic Bodies"*, Il Nuovo Cimento, Vol. 57B, No 2, pp 283-318, (1980).

[17] NIEZGODKA, M. and SPREKELS, J., *"Existence of Solutions for a Mathematical Model of Structural Phase Transitions in Shape Memory Alloys"*, Mathematical Methods in the Applied Sciences, Vol. 10, pp 197-223, (1988).

[18] NIEZGODKA, M., SONGMU, Z. and SPREKELS, J., *"Global Solutions to a Model of Structural Phase Transitions in Shape Memory Alloys"*, Journal of Mathematical Analysis and Applications, Vol. 130, 1988, pp 39-54.

[19] SONGMU, Z., *"Global Solutions to the Thermomechanical Equations with Non-convex Landau-Ginzburg Free Energy"*, Journal of Applied Mathematics and Physics (ZAMP), Vol. 40, pp 111-127, January 1989.

[20] SONGMU, Z. and SPREKELS, J., *"Global Solutions to the Equations of a Ginzburg-Landau Theory for Structural Phase Transitions in Shape Memory Alloys"*, Physica D, Vol. 39, pp 59-76, (1989).

[21] SPIES, RUBEN D., *"A State-Space Approach to a One-Dimensional Mathematical Model for the Dynamics of Phase Transitions in Pseudoelastic Materials"*, Preprint # 1054, Institute for Mathematics and Its Applications, University of Minnesota, November 1992. To appear in the Journal of Math. Anal. and Applic.

[22] SPIES, RUBEN D., *"Local Existence and Regularity of Solutions for a Mathematical Model of Thermomechanical Phase Transitions in Shape Memory Mat ials with Landau-Ginzburg Free Energy"*, Preprint # 1166, Institute for Mathematics and Its Applications, University of Minnesota, September 1993. Submitted to the Journal of Smart Structures and Materials.

[23] SPREKELS, J., *"Global Existence for Thermomechanical Processes with Nonconvex Free Energies of Ginzburg-Landau Form"*, Journal of Mathematical Analysis and Applications, Vol. 141, pp 333-348, (1989).

[24] WILMANSKY, K., *"Propagation of the Interface in Stress-Induced Austenite-Martensite Transformation"*, Ingenieur-Archiv., Vol. 53, 1983, pp 291-301.

SMART STRUCTURES WITH SHAPE MEMORY ALLOY ACTUATORS

Rolf Lammering

Institute of Structural Mechanics, German Aerospace Research Establishment (DLR)
Lilienthalplatz 7, D-38108 Braunschweig, Germany

ABSTRACT

The physical basis of shape memory alloy (SMA) behavior is outlined and a general one-dimensional constitutive law is reviewed, which is incorporated into a finite element procedure. A demonstration of two applications is given: a SMA pipe connector and a composite beam with embedded SMA wires. Another example is concerned with the use of SMAs for active control of a magnetic mechanical spring system which is currently under investigation for vibration isolation purposes.

1 INTRODUCTION

The growing global interest in smart material and smart structure technology has prompted an increasing number of investigations of SMAs in the past decade. The result of this research has been increasingly information regarding the crystalline structure of SMA materials, a greater understanding of macroscopic SMA material behavior, the development of new alloys and processing techniques, and a dramatic increase in the number of applications studied, which now span a wide range of products and devices.

The remarkable features of SMA that make them especially suitable for active elements in actuators are their capacity for high forces, high displacement reliability with temperature control, and the potential to create compact powerful actuators. Moreover in contrast to piezoelectric or magnetostrictive materials, SMAs offer the advantage that they can exert large repeatable displacements at zero or constant load. Additionally, since SMAs are mainly manufactured as wires, a promising method of their integration into smart structures is to embed the wires into a composite sructure.

2 REVIEW OF SMA CONSTITUTIVE BEHAVIOR

The mechanical properties of SMAs depend upon internal crystalline deformations as functions of stress, temperature, and history of the material. At high temperatures under stress-free conditions, a SMA exists in the parent phase (austenite) and when cooled the material undergoes a transformation to the low temperature phase (martensite). In the stress-free state a SMA material can be considered to have four transition temperatures, M_f, M_S, A_S, A_f: martensite finish, martensite start, austenite start, austenite finish. Note that a change of temperature, T, within the range $M_S<T<A_S$ induces no phase changes.

When unidirectional stress is applied to the SMA material, there is a critical value, dependent on the temperature, at which the martensite variants begin a detwinning process that results ultimately in the material consisting of a single variant of martensite aligned with the axis of loading. Additionally, for material in the austenite phase prior to loading, there is likewise a critical stress value, dependent on temperature, at which the austenite undergoes a crystalline transformation to martensite and in fact, because of the presence of stress, to a single variant of detwinned martensite. In the transformation process to detwinned martensite with the application of load, the stress raises only slightly and a large, apparently plastic strain is achieved. If the material temperature is above A_f, this large strain will be recovered by unloading in a characteristic hysteresis loop since the martensite is unstable at such temperatures without stress. This overall loading and unloading effect is termed pseudoelasticity. If the material temperature is below A_S, a large residual strain remains after unloading, but may be recovered by heating the material above the austenite finish temperature. This behavior is generally termed the shape memory effect. The corresponding stress-strain curves as well as the critical stresses as functions of temperature are shown in Fig. 1.

0-8194-1700-9/94/$6.00

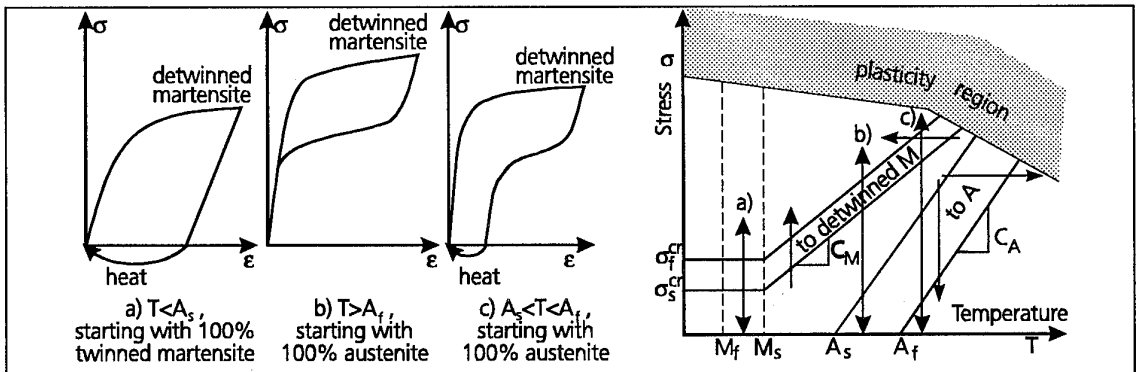

Fig.1: Schematic of stess-strain curves. The non-linear loading portion represents detwinning of martensite variants or transformation of austenite to martensite. The critical stresses as functions of temperature are also shown.

3 CONSTITUTIVE RELATIONS

The constitutive equation presented by Brinson [Ref. 1] is used for the subsequent finite element implementation. This constitutive description is derived on a thermomechanical basis, has a relatively simple mathematical expression, and includes only quantifiable engineering variables and material parameters in its expression. This one-dimensional constitutive law is given in the following form:

$$S - S_0 = D(\xi)E - D(\xi_0)E_0 + \Omega(\xi)\xi_S - \Omega(\xi_0)\xi_{S0} + \Theta(T - T_0) \quad .$$

where S is the 2nd Piola-Kirchhoff stress, T is the temperature, and ξ is an internal variable representing the stage of transformation. D denotes the modulus of the SMA material, Ω is considered the transformation tensor, and Θ is related to the thermal coefficient of expansion. The subscript 0 indicates the initial state or the initial conditions. The martensite fraction is additively decomposed into a stress-induced part, ξ_S, and a temperature-induced part, ξ_T: $\xi = \xi_S + \xi_T$. In accordance to experimental observations, a linear dependancy of the modulus on the martensite fraction is assumed: $D(\xi) = D + \xi(D_M - D_A)$ where D_A is the austenite and D_M the martensite modulus (twinned or detwinned). The transformation tensor is related to the modulus function by $\Omega(\xi) = -E_L D(\xi)$, where E_L is the maximum residual strain of a SMA and a material constant. In addition to the constitutive law , evolution equations for ξ_S, and ξ_T are necessary to complete the set of governing equations; they are not repeated here for brevity's sake.

4 FINITE ELEMENT FORMULATION

Given the variety of potential uses for SMAs and the high interest in developing new applications, the ability to accurately model and analyse structures containing SMA components via a finite element procedure is extremely attractive. Since the properties of a particular alloy can be easily and drastically altered in the manufacturing process, the properties of the SMA component in a given design can be varied systematically before production. This optimization procedure will enable use of SMA components with specifically tailored properties that will realize their full potential in each individual application.

A nonlinear finite element procedure has been developed which incorporates the constitutive law for SMA material behavior. Since SMAs exibit large strains, it is essential to introduce the non-linear Green-Lagrange strain tensor into the weak form of the mechanical balance equation. The solution for the geometrically and physically nonlinear problem is achieved by application of a Newton's method in which a sequence of linear problems is numerically solved. Due to consistent linearization, a quadratic rate of convergence is obtained. A comprehensive description is given by Brinson and Lammering [Ref. 2].

5 SMA PIPE COUPLING

One of the most established uses for SMAs is that of connectors for tubing. The procedure in these applications is to manufacture a ring of SMA that has a somewhat smaller inner diameter in the austenitic state than the outer diameter of the pipes to be connected. The ring is deformed at a low temperature such that its inner diameter exceeds slightly that of the tubing. The ring is placed over the pipes in this phase and then heated to the ambient temperature. As the transformation to austenite takes place, the material attemps to recover the initial residual strain. Being partially restrained, however, by the strenth of

the pipe material, the SMA ring subsequentely recovers only part of its residual strain and as a result builds up large internal stresses. Both of these effects together suberbly seal the connection.

The finite element procedure is utilized with two one-dimensional rings of truss elements linked together at the nodes: one ring of elements is of the shape memory alloy, the other of the pipe material. A schematic is shown in Fig. 2. The shape memory alloy is given an initial strain in the θ-direction at T_O= 20°C and then the structure is heated to various temperatures and the resulting stresses and strains calculated. The results of the circumferential stresses at the shape memory alloy - pipe interface are shown for a variety of strengths of the pipe material in Fig. 2 [Ref. 2]. It is clear that the results are converging with increasing pipe stiffness on the case of pure restrained recovery.

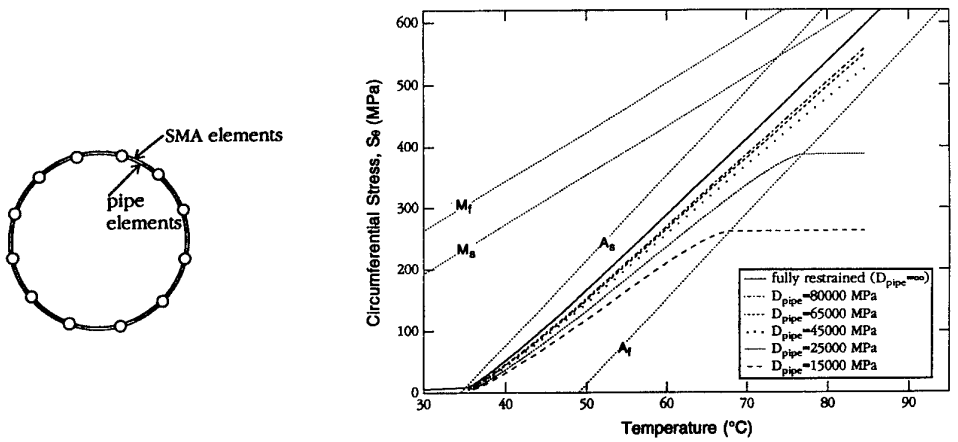

Fig. 2: Finite element discretization and circumferential interface stresses in a pipe coupling with various values of the Young's modulus for the pipe. Transformation regions for the SMA are also shown.

6 ACTIVE FREQUENCY TUNING OF A COMPOSITE STRIP

Although the use of SMAs is limited by the low frequency (maximum 2 Hz) at which they can be run, SMAs can be used in many dynamic applications. One possibility currently being researched is structures with embedded wires of shape memory material, activated by an electric current to vary the temperature. Active frequency tuning of this type can be used, for example to avoid resonances.

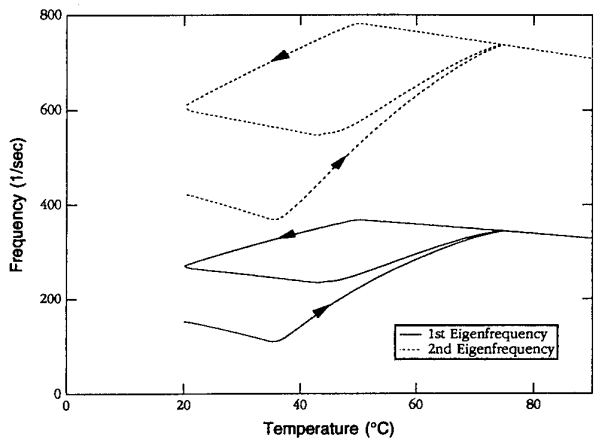

Fig. 3: Variance of eigenfrequencies of a composite beam with temperature (SMA wires with E_O=0.005).

The test specimen is a fiber-reinforced composite strip with a rectangular cross-section and eight embedded SMA wires in the neutral axis. The structure with a total length of 1m is clamped at both ends. The initial conditions are 0.5% residual strain of the SMA wires, no prestress and temperature 20°C. In the numerical experiment the first two eigenfrequencies are calculated as a function of temperature. The results are presented in Fig. 3. Since the material is restrained as the transformation to austenite occurs due to heating, and the shape memory alloy would recover the residual strain if unrestrained, extremely

large internal stresses are incurred. As the eigenfrequencies depend on the axial force of this structural system and the stress due to heating raises primarily within the temperature range from 35°C to 75°C (the region of martensite to austenite transformation), the change of the eigenfrequencies reflects this behavior. The slight decrease of the eigenfrequencies with increasing temperaure from 20°C to 35°C and above 75°C is explained by the compression force exerted by the composite strip (due to the constraint of normal thermal expansion) and cannot be compensated for by the shape memory alloy wires outside the transformation region. The hysteresis loop seen upon cooling is due to the transformation of the shape memory material to martensite. These results agree well qualitatively with experimental results on a similar system studied by Mooi [Ref. 3]. Direct comparison of numerical results is not possible due to the lack of detailed information on the material properties in the experiment.

7 VIBRATION ISOLATION USING MAGNETIC SPRINGS

A novel concept for the isolation of vibrations using magnetically adjusted springs is currently under investigation. Fig. 4 shows a schematic representation of the overall spring system. Component k represents a conventional suspension spring. Mounted in parallel is the magnetic spring MS, designed to effect a negative stiffness characteristic through operation around a point of unstable equilibrium [Ref. 4]. A linear damping element b appears likewise mounted in parallel to the primary suspension spring. Fig. 4 also shows the force-displacement curves for both of the springs and their combination. By judicious design of the individual spring components, a combined effective spring system characterized by an extremely flat force displacement curve results. Within this flat region, therefore, the magnetic-mechanical spring acts exactly as if it were an extremely soft linear spring.

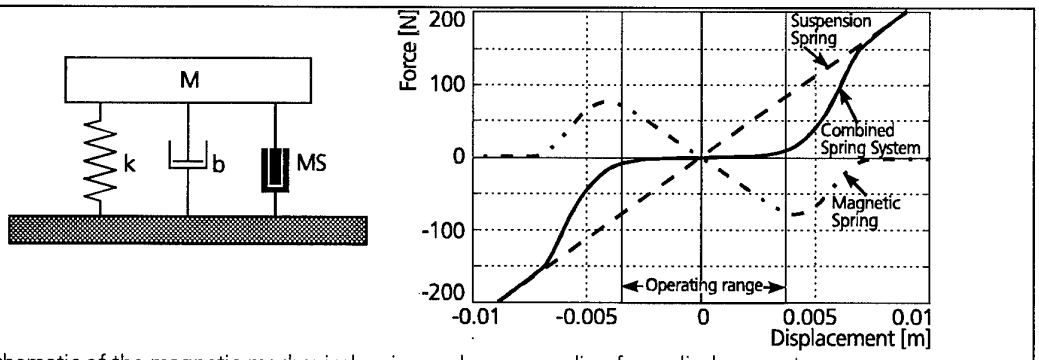

Fig. 4: Schematic of the magnetic-mechanical spring and corresponding force-displacement curve

The spring system is restricted in its operation to a region of displacement around its defined equilibrium point. If the magnetic spring can be constructed so that the region of linear operation for the combined system is large enough to accomodate all envisioned disturbances, and further assuming that the sensitive mass undergoes no change, than nothing further need be done and the system remain purely passive. This is not likely to be the case for most practical applications, however, and this necessiates the addition of an accompanying control system [Ref. 5]. The requirement is for a very low-bandwith position control action to keep the operating point centered around equilibrium. A simple position sensor is selected in order to monitor the offset from the zero-position and a bi-material composite arch consisting of an outer layer of carbon fiber reinforced plastic and an inner layer of aluminum is used as actuator. Due to electric heating this bi-material actuator produces the forces that are necessary to keep the operating point. Current investigations focus on the integration of a SMA based actuator into this spring system.

8 REFERENCES

[1] Brinson L C 1993, One-Dimensional Constitutive Behavior of Shape Memory Alloys, *Journal of Intelligent Material Systems and Structures,* 4, 229-242.

[2] Brinson L C & Lammering R 1993, Finite Element Analysis of the Behavior of Shape Memory Alloys and their Applications, *Int. J. Solids Structures,* 30, 3261-3280.

[3] Mooi H G 1992, Active Control of Structural Parameters of a Composite Strip Using Embedded SMA Wires. Diploma-Work, University of Twente , The Netherlands, and German Aerospace Research Establishment, Göttingen, Germany.

[4] Breitbach E. 1992, Federungssystem für ein Kraftfahrzeug, *European Patent No. 0 127 741.*

[5] Trimboli M S , Wimmel R & Breitbach E J 1994, A Quasi-Active Vibration Isolation Using Magnetive Springs, *1994 North American Conf. on Smart Struct. & Mat.,* Orlando, USA, Feb. 14-16, 1994.

Paper presented at the Second European Conf. on Smart Structures and Materials, Glasgow 1994, Session 2

THE CYCLIC RESPONSE OF SHAPE-MEMORY ALLOY 'SMART' COMPOSITE BEAMS

Clifford M Friend and Neil B Morgan

Smart Materials Group
Cranfield University
Shrivenham Campus
Swindon, UK

1. INTRODUCTION

'Smart' structures are an emerging technology which will provide the possibility of engineering structures with enhanced functionality for a wide range of applications. In most current Smart Structural Concepts a mechatronic or 'Frankenstein' approach is adopted where separate sensors, signal processing and actuators are 'bolted-together' to produce a 'Smart' system response. In the majority of these concepts the sensors and actuators are integrated within the host structure itself, and many of the sensor and actuator materials are familiar from other more conventional sensing/actuation applications. Amongst the materials used/proposed for actuators are Shape-Memory Alloys (SMAs) since these materials offer a range of attractive properties, including the possibility of high strain/stress actuation. The literature-base on the integration of SMA actuators into composite structures is not extensive. However, their use has been investigated for vibration [1], acoustic radiation [1,2], damage [3], buckling [1,2], and shape [1] control. An interesting feature of this work has been a heavy bias towards modelling, with only limited attempts to experimentally verify the calculated results. Previous work has also failed to produce a systematic database on one other key issue. This is the durability of SMA hybrid composites. The present work was therefore undertaken to provide a preliminary appraisal of the durability issues associated with the use of SMA hybrid composites. This work addressed a number of issues including (i) the effect of actuator fraction on strain outputs (ii) the effect of actuator fraction and maximum strain on the cyclic stability of shape changes, and (iii) the effect of these variables on damage accumulation within the hybrid structures.

2. EXPERIMENTAL DETAILS

The samples employed in this programme were small glass-fibre reinforced epoxy cantilever beams (145 x 20mm) which contained embedded Ni-Ti SMA actuators. The beams were constructed by hand lay-up and vacuum-bagging using Fibredux 913 unidirectional glass pre-preg. The actuators were present in the form of 300μm diameter wires with a transformation temperature of 60 ° C. In the reported work the actuators were orientated parallel to the fibre direction of unidirectional composite beams. The volume fraction of actuator was varied systematically in the range 0 to 2.5 vol %, and the level of memory strain introduced into the actuators was 6%. The beams were 6 ply in thickness with the actuators introduced between plies 2 and 3. The 6% strain was maintained on the actuators during composite cure which was carried out using a thermal cycle recommended by the pre-preg manufacturer. Once the cure cycle was complete the hybrid beams were removed from their fixing jigs. Prior to testing the actuators were constrained at the free ends of the beams, since preliminary tests showed that during actuation of unconstrained hybrid beams significant interfacial decohesion took place and resulted in poor cyclic actuation.

Since the actuators were off the beam's neutral axes bending was induced during actuation. Such deflections were used to characterise the mechanical responses of the hybrid beams. Measurement of these deflections (to an accuracy of $\pm$ 30 μm) was by means of a commercial non-contact optical displacement measurement system. This employed a laser and operated by means of simple triangulation. The actuators were activated electrically by means of resistive heating, and were connected in series to ensure that each volume element of actuator was subjected to the same heating current. During deflection testing the heating current was increased over a period of approximately 2 seconds and was then allowed to stabilise for one minute prior to measurements being taken. The heating current was therefore increased incrementally up to the maximum value for each cycle. The mechanical responses of the SMA hybrid beams were characterised by their deflection/ current characteristics, and optical and electron metallography was employed to investigate damage accumulation within the host composites.

0-8194-1700-9/94/$6.00

3. RESULTS AND DISCUSSION

With the Fibredux 913 pre-preg system there was a limit to the maximum drive current which could be applied to the hybrid composites. This was approximately 2A. At current levels above this value there was visible darkening of the composite around the actuators, and delamination was observed through the tansluscent resin. This restricted measurements to drive currents below this level. Figure 1 shows the effect of actuator fraction on the deflection characteristics of the cantilever beams. This response was not unexpected, in that as the fraction of actuator increased the maximum deflection of the cantilever increased. Such observations are important since they show that rather than overdriving a low actuator fraction beam and risking matrix degradation, similar deflection outputs can be achieved by the use of higher actuator fraction materials. However, this data does suggest that there is a decreasing return from such an approach and that there must be a level of actuator fraction beyond which there are no further increases in deflection output.

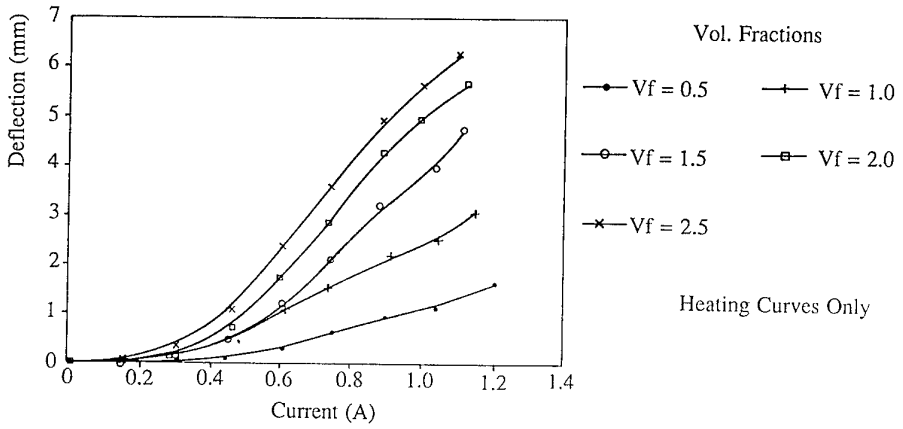

Figure 1 - Effect of Actuator Fraction on Deflection Response

Figure 2 shows both the heating and cooling stages of actuation cycles for some of the beams. This figure is interesting since it shows the significantly different hysteresis associated with actuation of higher fraction materials.

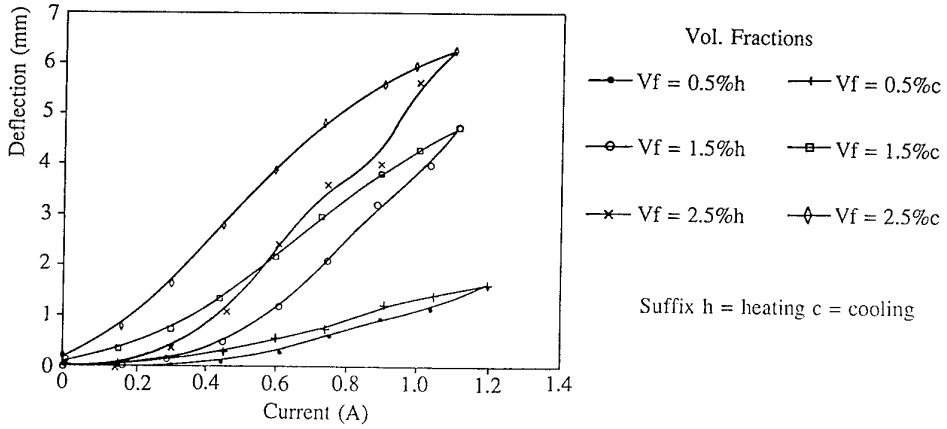

Figure 2 - Hysteresis Associated with Deflection Cycles

The hysteresis data is interesting since such differences are observed in more conventional SMA applications where actuators are employed against varying levels of external bias force. In such situations, operating a SMA against an increasing spring-rate (where the bias force increases as a function of actuation strain) results in decreased strain output, a lower temperature sensitivity of the strain output, and smaller forward/reverse hysteresis. Phenomenologically the observations in figure 2 appear similar, although the origin in this case is not as simple since the situation is complicated by the fact that the effective spring-rates of the laminates were approximately constant, but the volume fractions of actuator varied. Deflection output clearly increased with the level of actuation built into the hybrid composites and this also resulted in the higher sensitivity of the

deflection output (as a function of drive current). The origin of wider hysteresis at higher actuator fractions is not so clear. Currently it is not possible to provide a categorical explanation of this phenomenon, however, it is believed that it is associated with both the restoring force developed in the hybrid beams during actuation, and the effect of stress on the martensitic transformation within the actuators during reverse transformation. Because of their constant stiffness, the elastic restoring forces in the beams were greater at higher actuator fractions (due to their larger absolute deflections). This would at first sight be expected to assist reverse actuation of the SMA and thus result in narrower hysteresis. However, it is also important to note that when considering the effect of this restoring force, this must be done in terms of the effective actuator stress. Although the force was larger in the higher actuator fraction beams, this was distributed over a larger area fraction of actuator. Thus it is likely that when both factors are considered the higher restoring force of the high strain beams actually resulted in less influence on the reverse actuation and thus broader hysteresis.

The behaviour shown in figures 1 and 2 are the first cycle responses of the beams. However, when considering the durability of SMA hybrid materials it is perhaps more important to consider the longer-term stability of such behaviour. Figure 3 shows data of this type for one of the materials investigated in this work. This shows that there was some instability in the actuation response with changes over the first 5 cycles. After these initial cycles a more stable behaviour developed.

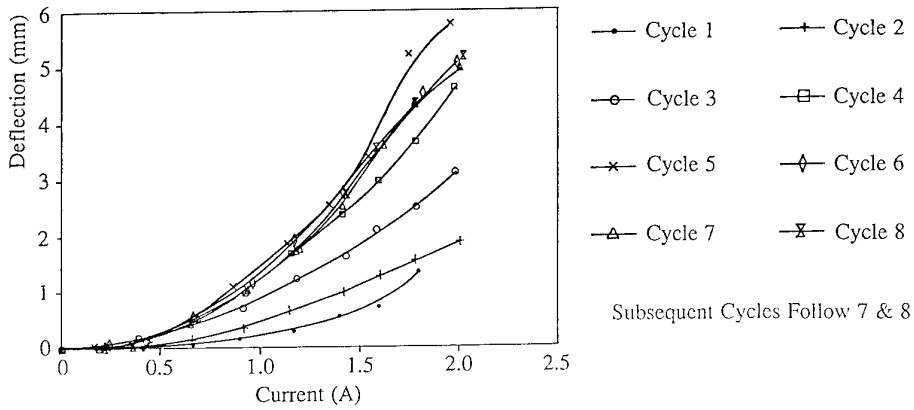

Figure 3 - Cyclic Data for 1 vol% Actuator

The origin of instabilities in deflection output were investigated in terms of damage accumulation within the cycled composites. This work was carried out on beams cycled to a maximum drive current of 2A. Microscopy showed that there was little damage accumulation during the first two actuation cycles. However, during subsequent cycles damage was initiated within the beams. This internal damage was in the form of interfacial breakdown between the actuators and host composite (figure 4). The actuator/composite interface therefore gradually degraded with each actuation cycle until cycle 6 where gross delamination was present. This is interesting since as shown in figure 3 this cycle coincided with the development of a reproducible deflection response. This suggests that during cycles one to five the interfacial contact gradually decreased until the actuators were completely delaminated within the host composite and acted on the beams only through the mechanical constraints at the free ends. Following cycle six no further delamination was possible and there were then no further changes in the deflection responses of the beams. It is also interesting to note that during this delamination the deflection ouput from the beams actually increased.

The data in figure 3 also suggests a further feature associated with the durability of these hybrid composites. Figure 3 shows that although the deflection outputs at lower drive currents were smaller than at higher values, they did appear to exhibit better reproducibility. This was confirmed by cycling beams to a lower maximum current. Typical data is shown in figure 5(a) and (b). Cycling to 1.1A resulted in reproducible behaviour with respect to both the forward and reverse actuation pathways. The deflection outputs were smaller than those obtained by cycling to higher currents, however, the absolute value could be maximised to some extent by selection of an appropriate actuator fraction.

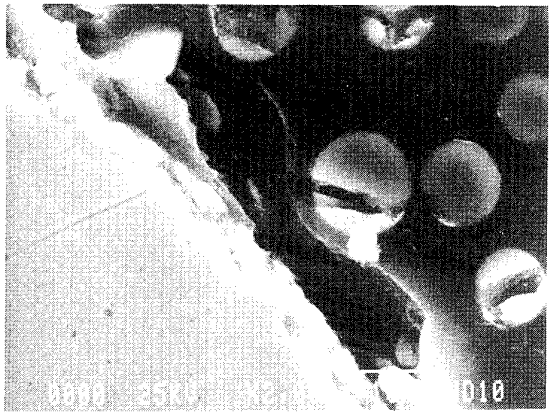

Figure 4 - Actuator/Host Interfacial Failure

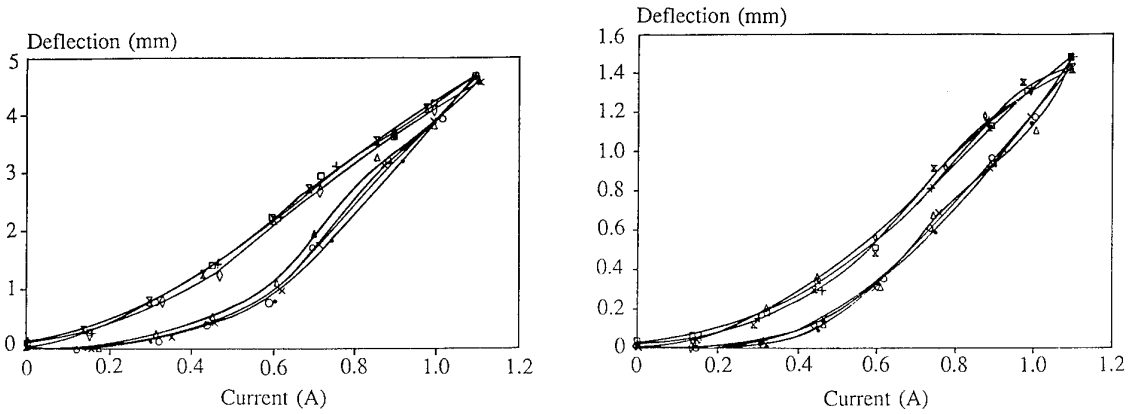

Figure 5 - Cyclic Data for (a) 1.5, and (b) 0.5 vol% SMA Hybrid Composites (maximum drive current 1.1A)

4. CONCLUSIONS

The results presented in this paper begin to address some of the durability issues associated with the use of SMA hybrid composite materials. It has been shown that as expected actuator fraction plays a significant role in controlling both the deflection response of these materials and the hysteresis associated with the forward and reverse actuation pathways. It has also been shown that during cyclic operation such hybrid composites can suffer from instabilities in deflection response. This appears to be associated with the accumulation of internal damage within the composites due to cycling close to the maximum drive current for these materials. However, it has also been shown that by careful selection of the maximum drive current and volume fraction of actuator, it is possible to achieve useable deflection outputs which are stable over many actuation cycles.

5. REFERENCES

1. C Liang, J Jia, C Rogers. Proc 30th AIAA/ASME/ASCE/AHS/ASC Structures, Structural Dynamics and Materials Conf. (AIAA, 1989) pp 1504 - 1513
2. DH Thompson, OH Griffin. Proc Conf Recent Advances in Adaptive and Sensory Materials and their Applications, Blacksburg, 1992 (Technomic, 1992) pp 377 -384
3. CA Rogers, C Liang, S Li. Proc AIAA 32nd Structures, Structural Dynamics and Materials, Baltimore, 1991

THE EFFECT OF PRESTRAIN ON THE ACTUATION PERFORMANCE OF EMBEDDED SHAPE MEMORY ALLOY WIRES

Conrad J Doran

Defence Research Agency
Farnborough, Hampshire, GU14 6TD
UK

INTRODUCTION

Among the potential materials for embedded actuators in composite smart structures are shape memory alloys (SMA). They have the advantage of being relatively high authority actuators and can be drawn into wires which may be aligned with fibres in a host composite. Interest has been shown in their use in variable geometry aerofoils/hydrofoils[1] and shape control of composite plates has already been investigated[2]. Preliminary studies have also been completed to assess the use of SMA in active damage control[3]. Although the results of these studies appear promising, the durability of the material has not been fully assessed. One aspect of durability which must be considered is the ability of the SMA wire to generate the same force each time it is actuated. The force depends on the amount by which the wire has been prestrained, and the optimum prestrain will be that which produces the maximum repeatable force without creating damage in the host composite. This paper describes the results of an initial study of the effects of prestrain on the performance of embedded SMA wires under repeated actuation cycles.

EXPERIMENTAL

The shape memory alloy wire was supplied by Thomas Bolton Ltd. It was a Ni-Ti alloy, 0.2 mm in diameter with a nominal A_f temperature of 70°C. Laminates in which the wires were embedded were made from Ciba 913 epoxy/E glass unidirectional prepreg. This material was chosen because its mechanical properties are well characterised. It was also transparent so that any debonding of the wire from the host laminate could be seen directly.

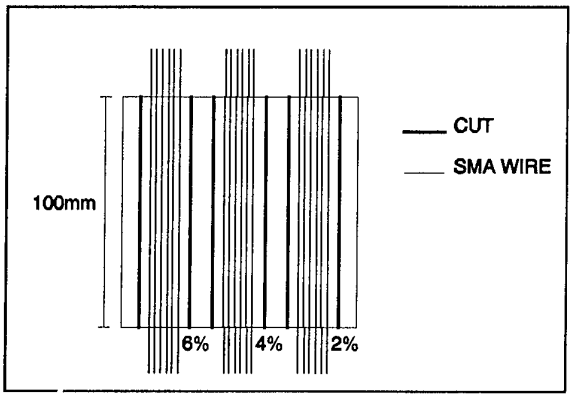

Figure 1 - laminate containing SMA wires

Lengths of SMA wire were firstly prestrained to the required levels of 2, 4 or 6%. In order to improve the surface properties the wires were then lightly abraded with fine SiC paper. They were then cut into 220 mm lengths of each prestrain and placed in groups of 6 between the central 0° plies in a quasi-isotropic $(90/+45/-45/0)_s$ laminate, parallel to the 0° fibres as shown in figure 1. Within each group the wires were placed at 2 mm intervals resulting in three 10mm wide sections of laminate containing SMA wire. As the actuation temperature range of the wires was below 70°C, the wires were restrained in a steel frame during the cure of the laminate to prevent premature actuation at the 120°C cure temperature. Once cured the laminate was cut into three 15 mm wide test pieces, each one containing a group of prestrained SMA wires as shown in figure 1. These will be referred to as the 2%, 4%, and 6% test pieces.

In order to measure the actuation strain, wire strain

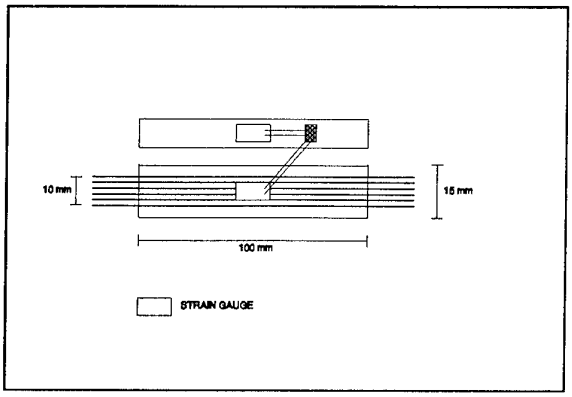

Figure 2 - Test piece with thermal strain compensation

0-8194-1700-9/94/$6.00

gauges were adhesively bonded to each test piece, parallel to the SMA wires using HBM Z70 acrylonitrile adhesive. The SMA was actuated by placing the test piece in an oven, and therefore a thermal compensating system was used to measure actuation strain. This involved bonding a second gauge to another test piece from the same laminate, with the gauge aligned in the same direction i.e. parallel to the 0° plies (figure 2). The two gauges were then connected in a half-bridge configuration so that any thermal expansion of the laminate containing the wires was compensated by the "dummy" gauge.

The test pieces were placed in an oven and heated from room temperature to 100°C at 3.5 °C/minute. The oven was then allowed to cool to room temperature. This thermal cycle was carried out 5 times. The temperature of the oven was measured using a thermocouple. Although in practice, the wires in such a system would be actuated by passing an electric current through them, this method was used so that the temperature of the wires was known.

After the first cycle, debonding was noticed between the SMA wires and the matrix at the ends of the test pieces. The debond length was measured for each wire within each test piece using an optical microscope and then measured after each thermal cycle. The position of the debonds are shown schematically in figure 3

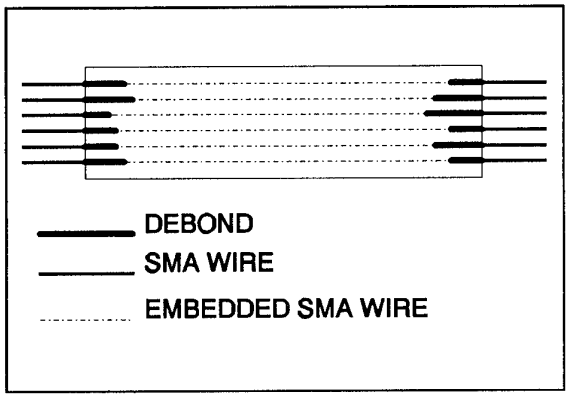

Figure 3 - Schematic representation of SMA debonds

RESULTS & DISCUSSION

The maximum strains obtained from each actuation cycle are shown in figure 4. The variation in actuation strain for each test piece obtained from each cycle is shown in figure 5.
From the data of figures 4 and 5 it can be seen that although the 6% test piece showed the highest initial actuation strains, during the first cycle (about 730με), the value fell with each successive cycle. By the fifth cycle the maximum actuation strain had significantly decreased to 40με. This loss of actuation strain indicated substantial loss of the memory effect or "ageing" of the shape memory alloy.

The 4% test piece showed a lower maximum actuation strain than the 6% test piece for the first three actuation cycles. The maximum strain produced in the first cycle was about 550με, falling to 300με for the third actuation cycle. The actuation strain for the fourth and fifth cycles appeared to stabilise at about 200με. This was in contrast to the 6% test piece which continued to show evidence of ageing for all actuation cycling.

The 2% test piece showed the lowest initial maximum actuation strain of 300με. The ageing observed in the 4% and 6% test pieces was not apparent in the 2% material. Despite variation in the maximum strain with cycling, by the fifth cycle the maximum actuation strain was about the same as the initial value.

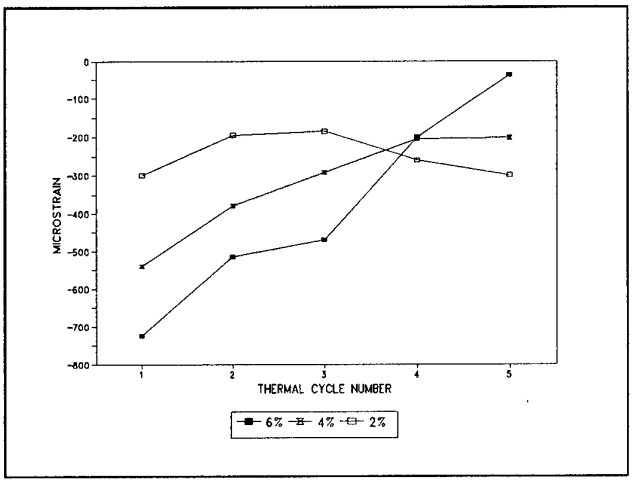

Figure 4 - maximum strain obtained from SMA wire actuation

Comparing the initial maximum actuation strain for each test piece, it can be seen that doubling the prestrain from 2% to 4% gives an increase in actuation strain from 300με to 550με i.e. less than double, and comparing the 2% to the 6% prestrain the increase from 300με to 730με is less than a factor of three. This would indicate that there is not a simple linear relationship between the wire prestrain and the resultant strain in the laminate.

Figure 5 - Variation in actuation strain with thermal cycling for SMA wires embedded in a GRP laminate

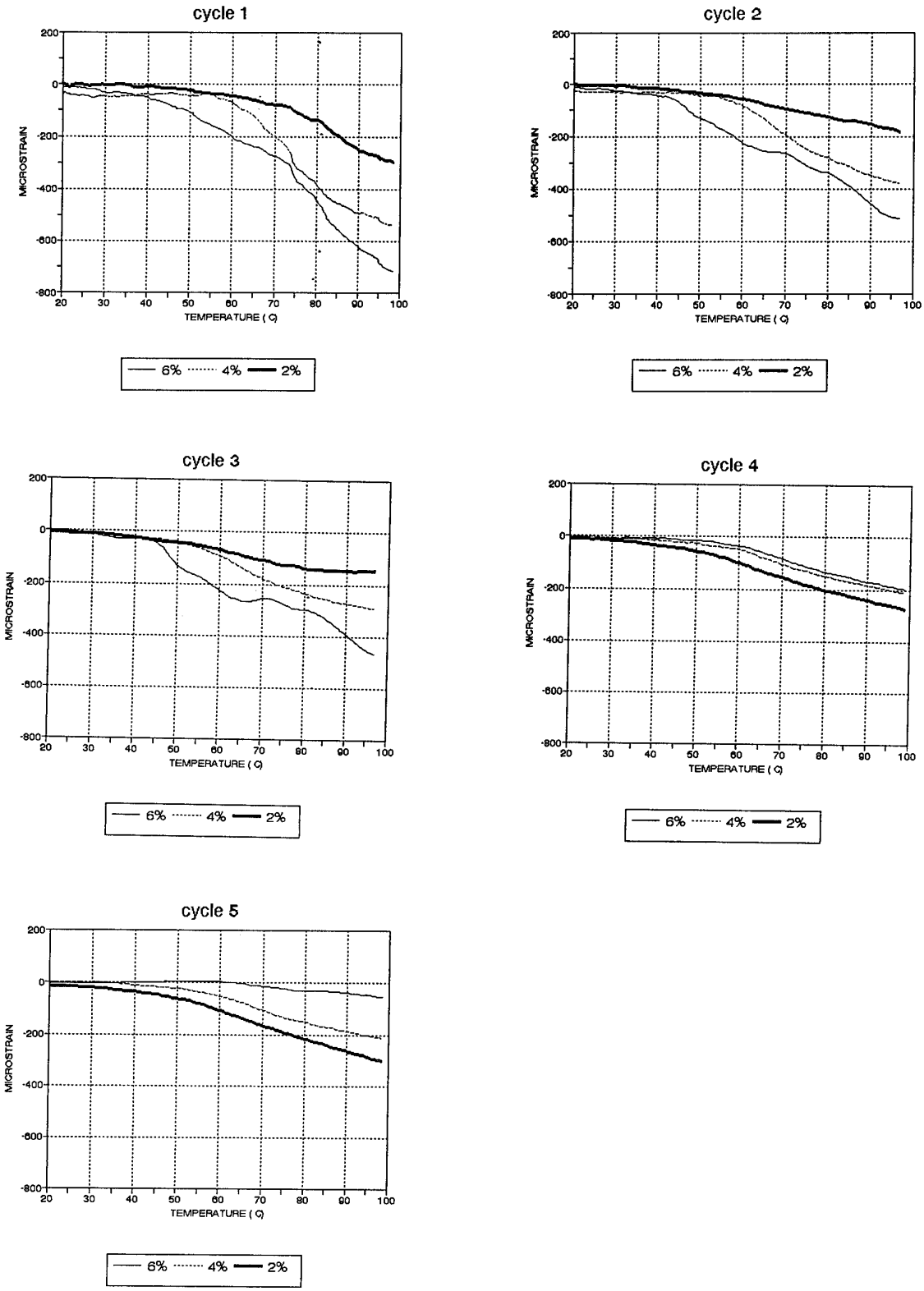

DAMAGE DEVELOPMENT

The effect of increased cycling on the propagation of the disbond between the SMA wire and the epoxy matrix is shown in figure 6. The mean length of disbond for each prestrain is calculated from a total of 12 embedded wire ends per test piece. The 6% test piece showed the most damage after the first cycle. The fact that little further damage was observed from cycle 3 onwards, but that a significant drop in the maximum actuation strain over the same cycling range occurred (cycle 3 = 500 με, cycle 5 = 40 με) suggests that the decrease in actuation capability is due to ageing rather than damage. This is supported by the observation that the debonds remained remote from the position of the gauges.

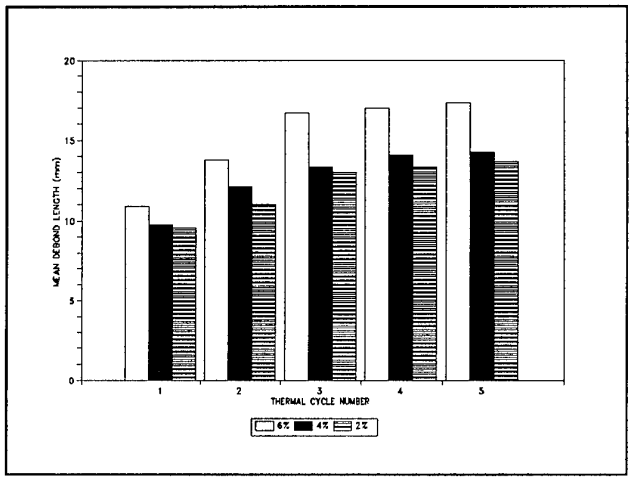

Figure 6 - Development of damage along SMA/laminate interface

Damage development for the 4% test piece and the 2% test piece were very similar although the 4% test piece showed slightly greater damage. The similarity in the damage development was not reflected in the variation in actuation capability of each material (figure 5) which suggested ageing of the shape memory effect has occurred. In a similar manner to the 6% test pieces the damage state appeared to stabilise after the third actuation cycle.

CONCLUSIONS

Increasing the prestrain of the embedded SMA wires, up to 6%, increased the maximum actuation strain obtained in the first cycle.

Increasing the SMA wire prestrain accelerated the ageing of the shape memory effect within wires.

Thermal actuation of the embedded SMA wires resulted in damage in the form of debonds propagating from the ends of the embedded wires along their length. This damage increased with increased prestrain. The damage appeared to stabilise after the third actuation.

REFERENCES

1. C.H.Beauchamp, R.H. Nadolink, S.C.Dickson, L.M.Dean. Proc. 1st European Conf. on Smart Structures & Materials, Glasgow, 1992 pp189-192

2. C.Liang, J.Jia, C.Rogers. Proc 30th AIAA/ASME/ASCE/AHS/ASC. Structures,Structural Dynamics & Materials Conf. (AIAA,1989) pp 1504-1513

3. C.A.Rogers, C.Liang, S.Li. Proc. 32nd Structures,Structural Dynamics & Materials Conf. Baltimore 1991 pp 1190-1203

The authors would like to acknowledge the Ministry of Defence for funding this project.

© copyright Crown / DRA 1994

Paper presented at the Second European Conf. on Smart Structures and Materials, Glasgow 1994, Session 2

CONTROL SURFACE MIRROR WITH LOCAL HEATERS

Vladimir V. Reznichenko, Valentina Kulagina,
Marina Lutinskaya, Yury Leonov

Reseach Center "S.I.Vavilov State Optical Institute"
Birzhevaya line, 12, St.Petersburg, 199034, Russia

INTRODUCTION

The majority of wavefront disturbances of space reflector and space telescopes are due to external thermal fields variations and the optical surface deformations. Two principal methods of disturbances compensation exist: a thermostabilization by temperature gradients decreasing and the mirror surface active thermodeformation. This can be accomplished only by some thermal methods: either by temperature gradients elimination or by keeping some given temperature field. The latter method is carried out by a system of heaters and sensors located on mirror elements /1,2/. Thermal deformation correction of distortions of optical and structural elements surface is possible, too, in accordance with control system responses.

A thermo-optical compensation system (TOCS) consists of individual control units which contain heaters and sensors fixed to respective mirror elements as well as electronic measurement and control units (MCU) interfaced to them Fig. 1.

The MCU are made constructively of unified printed circuit boards which can be functionally divided into various zones for interfacing of input/output, memory and supply circuits.

INTEGRAL AND MODAL CONTROL ALGORITHM DESCRIPTION

The heaters and sensors arrangement proposed provides stabilization of temperature gradients corresponding to seven fundamental modes or inherent functions of the system.

The algorithm proposed features by control signals generation

0-8194-1700-9/94/$6.00

according to orthogonal modes. Thus, manipulation of one of the modes values does not involve amplitude change of other modes. This feature ensures power consumption minimization and temperature field integral control by means of finite number of discrete heaters.

Furthermore, control is to be accomplished in real time. Therefore, thermal characteristics of control subjects are to be identified preliminary. Identification is carried out by complex calculation and experimental investigation of a real subject. A program for controllers functioning can provide possibility of an object identification repeating for the case of cosiderable change of operating conditions, however.

RESULTS

The flat monolithic mirror of 200 mm dia and 30 mm thick been mounted by central hole. While the mirror being warmed up or cooled down, changes of both the mirror temperature and deformation of the wave front reflected by the face surface have been monitored. The temperature response investigation has been carried out by means of the Zygo Mark 3 interferometer. High precesion surface testing is possible with the minimal perturbations even for this mirror made of fused silica being far from the best control subject.

Heat has been applied by means of the heaters mounted on the mirror back side. The investigation has included various modes , i.e. one heater mode, non-symmetrical heating mode and symmetrical heating one. The heating rate mean value has been set 0.3 gr/min. The power value applied to an individual heater has varied the in 0...4 W range at 1.5 V and 0.6 A current. The heating period has varied from 2 to 10 minutes.

The surface thermal response is equal 0.025 micron for this case. This values are increasing for metalic composit reflector and control surface few times easy.

Fig. 2 shows the temperature distribution while the local heaters functioning. Fig 3 shows distribution of the mirror surface deformation. Heating strenythening at the mirror edge results in decrease of the nearest sphere curvature radius.

The experiment results agree rather well with the numerical calculations of both temperature and surface deformations for various

modes. The surface deformation value has been obtained by means of the INTERF program complex while reconstructing from the interferogramms. Thus, the possibility of the fused silica mirror surface correction in small value range is provided both theoretically and experimentally.

Quasiperiodic heating mode has been investigated in this case , too, which allows to keep the mirror mean temperature at some given value and to provide minimal temperature drop by the mirror thickness. The heaters have been switched on and off in accordance with a cirtain regularity, which resulted in mean temperature value of 22.5 C and the temperature drop within 0.06 deg (see Fig.4). The surface RMS error, obtained by the monitoring results, provides to be practically at the initial level (see Fig.5). The mirror thermal stabilization algorithm is to be considered optimal if the heating and relaxation times are calculated for the specific mirror and controlled carefully.

CONCLUSION

The acceptable thermal response value provides the real possibility to develop an effective mirror temperature stabilization and surface deformation smart compensation and adaptive system.

ACKNOWLEDGMENTS

The authors wish to acknowledge and thank Dmitry Yeskov and Victor Kotov for their assistance during this program.

REFERENCES

1. R.Grenhalgh, L.Stepp, E.Hansen. " Gemini primary mirror thermal management system" SPIE vol. 2199 Advanced Technology Optical Telescopes V (1994).

2. V.Reznichenko, N.Yakovleva. "Mirror temperature stabilization and deformation by local heaters"SPIE vol. 2201 Adaptive Optics in Astronomy (94)

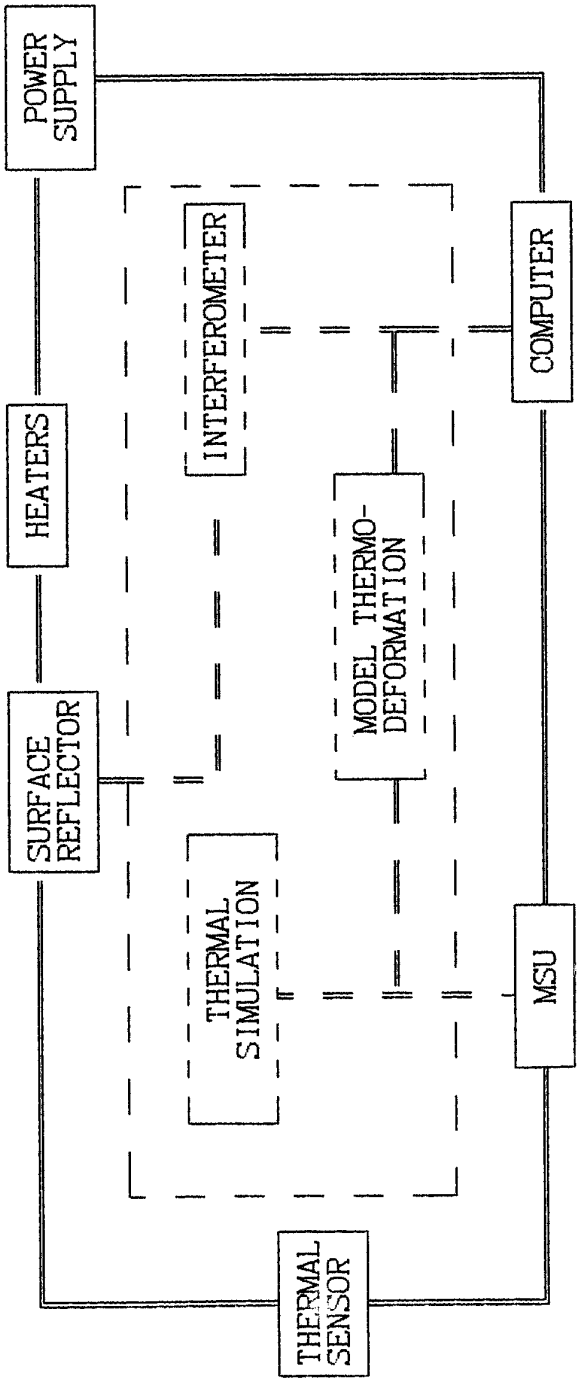

FIG.1 LAY - OUT OF CONTROL SURFACE MIRROR WITH LOCAL HEATERS

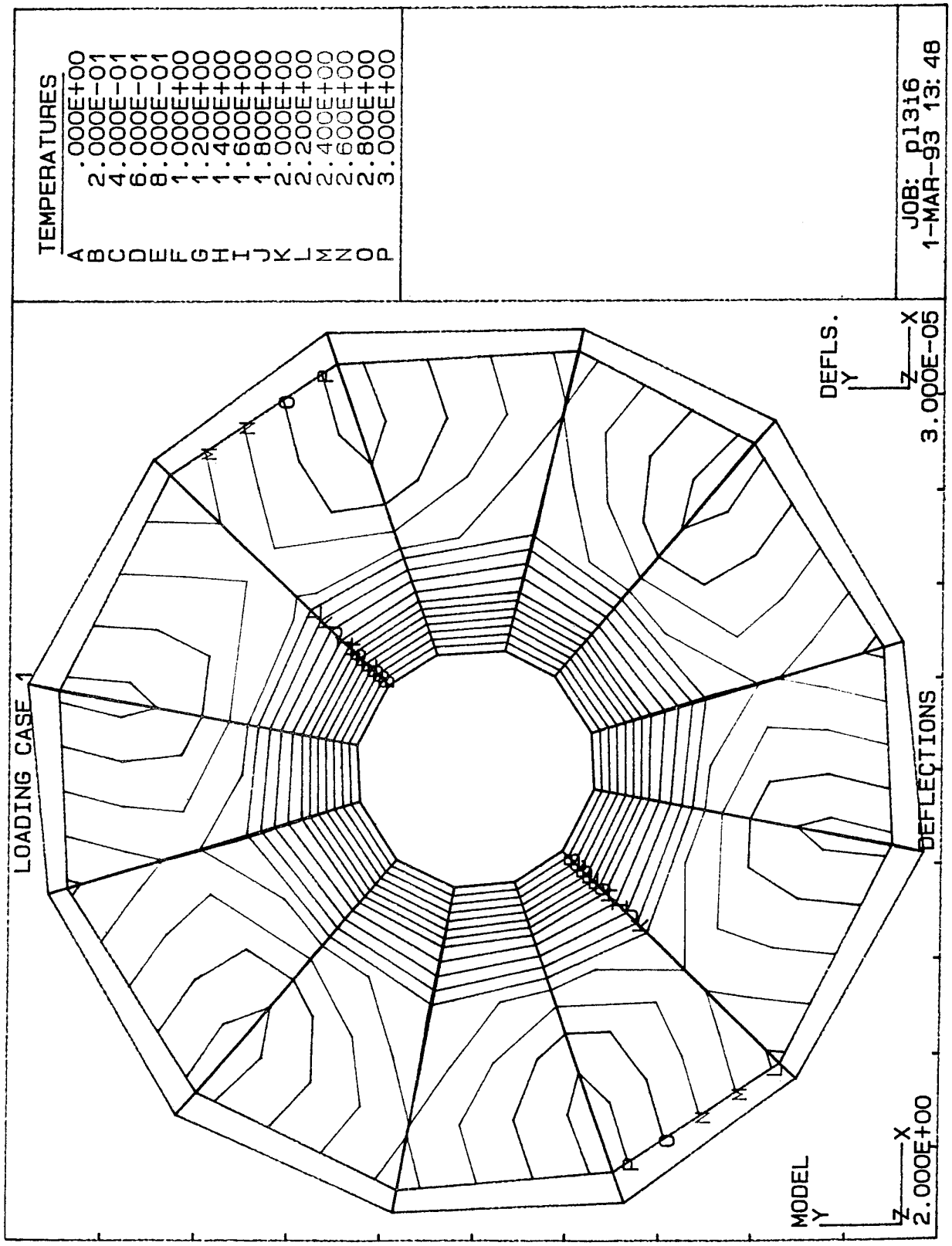
TEMPERATURES
A .000E+00
B 2.000E-01
C 4.000E-01
D 6.000E-01
E 8.000E+00
F 1.000E+00
G 1.200E+00
H 1.400E+00
I 1.600E+00
J 1.800E+00
K 2.000E+00
L 2.200E+00
M 2.400E+00
N 2.600E+00
O 2.800E+00
P 3.000E+00
JOB: p1316
1-MAR-93 13:48
LOADING CASE 1
DEFLECTIONS
DEFLS.
3.000E-05
MODEL
2.000E+00

FIG 2

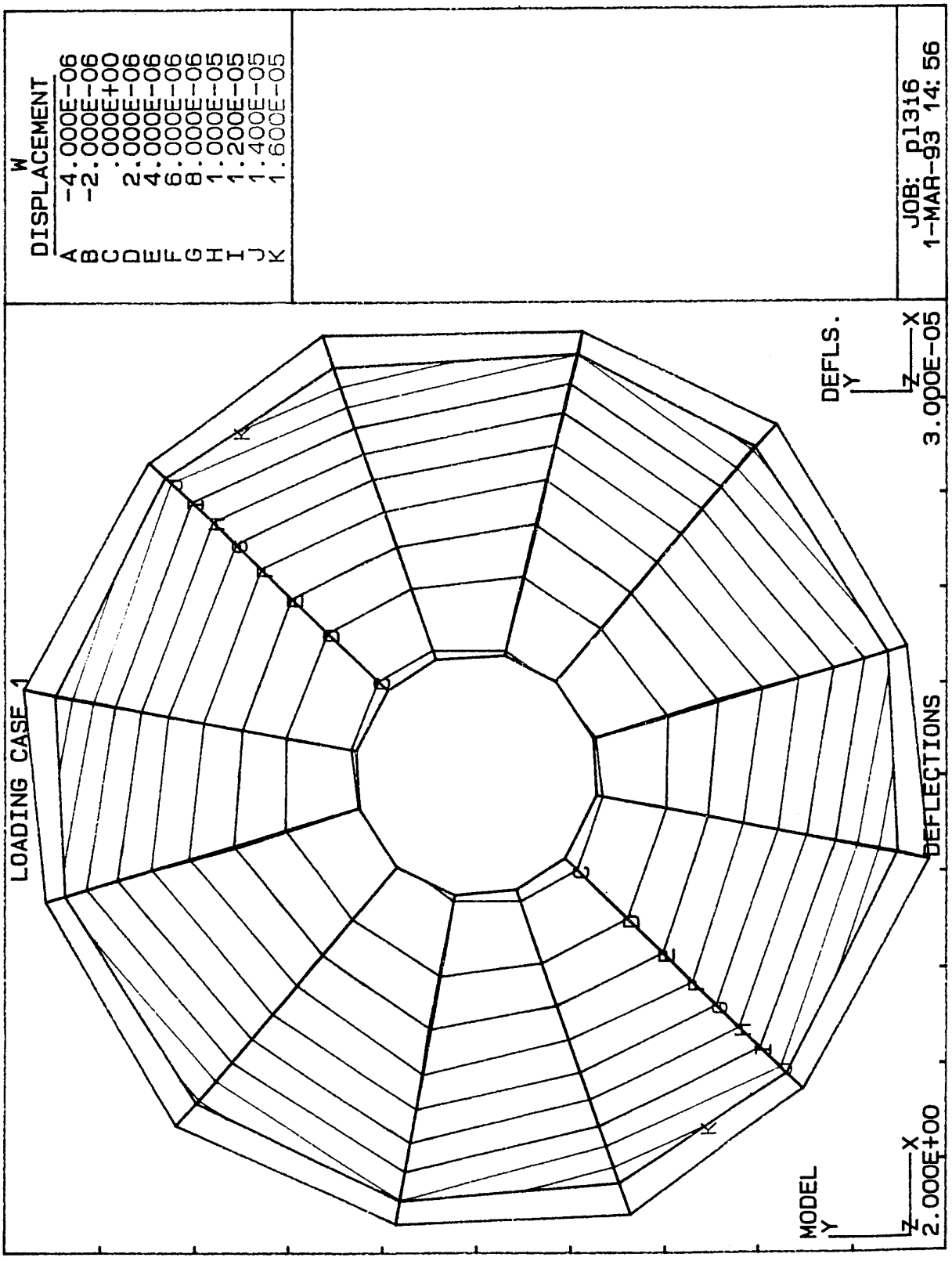
LOADING CASE 1
W
DISPLACEMENT
A -4.000E-06
B -2.000E-06
C .000E+00
D 2.000E-06
E 4.000E-06
F 6.000E-06
G 8.000E-06
H 1.000E-05
I 1.200E-05
J 1.400E-05
K 1.600E-05
JOB: p1316
1-MAR-93 14: 56
DEFLS.
Y
Z X
3.000E-05
DEFLECTIONS
MODEL
Y
Z X
2.000E+00

FIG 3

FIG. 4

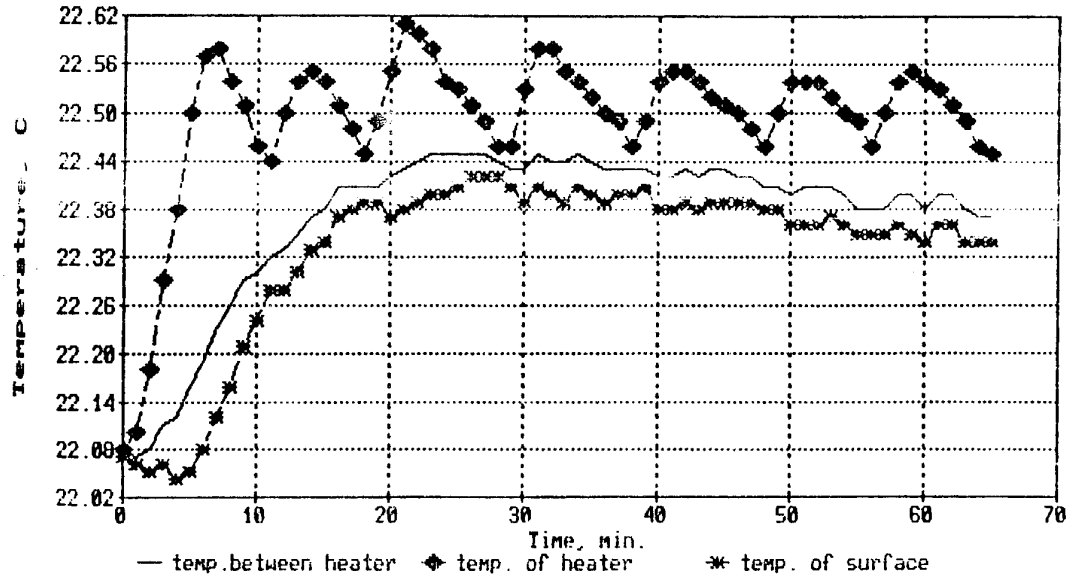
22.62
22.56
22.50
22.44
22.38
22.32
22.26
22.20
22.14
22.08
22.02
Temperature, C
0
10
20
30
40
50
60
70
Time, min.
temp.between heater
temp. of heater
temp. of surface

FIG. 5

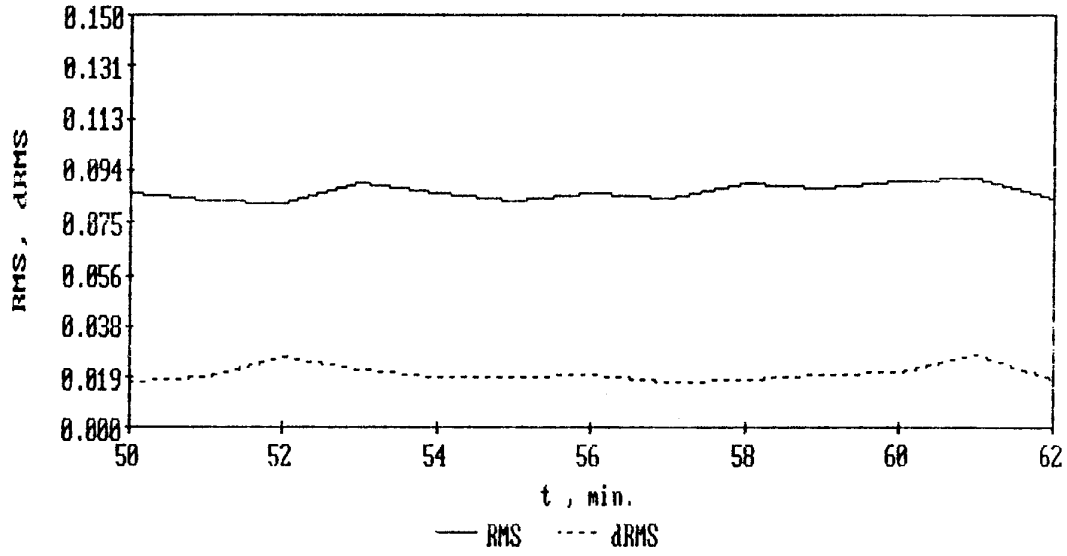
0.150
0.131
0.113
0.094
0.075
0.056
0.038
0.019
0.000
RMS, dRMS
50
52
54
56
58
60
62
t, min.
RMS
dRMS

CHARACTERISATION OF STATIC ACTUATION BEHAVIOUR OF ENCAPSULATED PZT

Conrad J Doran* & Raymond J Butler†

*DEFENSE RESEACH AGENCY - FARNBOROUGH, HAMPSHIRE, GU14 6TD, U.K.
†ADC LTD - NEWPORT PAGNELL, BUCKINGHAMSHIRE, MK16 OEP, U.K.

INTRODUCTION

Within the field of "smart" structures considerable interest has been shown in the use of piezoelectric materials both as sensors and actuators. One of the best characterised of these materials is the family of Lead Zirconate Titanate (PZT) based ceramics. The use of PZT in intelligent systems has been fairly widespread, the high modulus of the material gives high authority actuation, coupled with a wide operational bandwidth and relative ease of control by the application of an applied voltage. The linearity of the actuation response over a limited range has made PZT a popular choice for high precision, relatively low displacement applications.

A number of attempts have been made to utilise such actuators for aerospace, using both surface mounting[1] and embedding techniques[2,3]. The effects of actuators on aeroelastic performance has also been investigated for aerospace applications[4,5]. The current practical solution to this problem appears to be the use of spatially distributed actuators[6]. One of the practical limitations of this problem are the large number of actuators required to produce the required degree of static control. In order to ensure accurate shape control, measurements must be taken to ensure there are no significant difference in the actuator element properties due to factors such as batch processing variation. In the past this has proved difficult due to the extremely brittle nature of the actuator material. More specifically the requirement for thinner elements for use in embedded applications has increased this problem. A method by which the static performance of electroceramic actuators could be quickly established would therefore be desirable.

This paper presents the results of recent work to develop a test method to define the static electromechanical properties of encapsulated actuator materials in order to assess their suitability as static actuators for aerospace applications. Preliminary results using a standard PZT material are described.

PZT ACTUATOR PROPERTIES

The PZT material used for this work was US-DOD Navy type II or Vernitron PZT5A, 0.2 mm thick inclusive of nickel electrode coatings on each of the poling faces (through thickness).

To establish the electromechanical behaviour of the PZT actuator, strain gauges were attached to the surface of the material. A voltage ramp was then applied up to a maximum voltage of 250 volts. The characteristic "butterfly" strain response obtained is shown in figure 1. The non-linearity observed indicates the value of the strain coefficient d_{31} must vary with the applied field strength. This variation in d_{31} will be reflected in the obtainable force obtainable from the actuator (N_A).

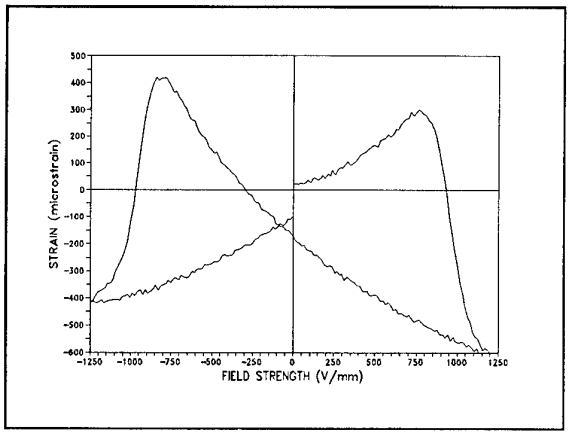

Figure 1 - voltage/strain response of PZT

It is a simple matter to calculate the relationship between the electric field strength (ϑ) applied across an actuator of thickness (t) and modulus (E), to the force per unit width (N/W) obtained:

0-8194-1700-9/94/$6.00

from basic Hookes law

$$\varepsilon = \sigma / E = N / W E t \qquad .....(1)$$

from the piezoelectric relationship

$$\varepsilon_{31} = d_{31}\vartheta \qquad .....(2)$$

combining the above gives:

$$N/W = d_{31}\,\vartheta\, E\, t \qquad .....(3)$$

EMBEDDED PZT ACTUATOR PROPERTIES

In order to confirm the calculated value for (N/W) shown in equation (3) it should be possible to predict the strain response of a laminate using by combining the value for actuation force with laminate plate theory[6]. A computer program has been written using a basic compiler which uses LPT combined with equation 3 to predict laminate actuation strains. The program calculates the compliance matrices of the laminate based on values of the transverse Young's modulus (E_2), the longitudinal Young's modulus (E_1), the shear modulus (G), the longitudinal poissons ratio (υ_{12}) and the orientation of each ply to calculate compliance matrices

$$\begin{bmatrix} a & b \\ b' & d \end{bmatrix} \begin{bmatrix} N_A \\ M_A \end{bmatrix} = \begin{bmatrix} \epsilon \\ \kappa \end{bmatrix} \qquad .....(4)$$

The (a) matrix corresponds to the extensional response of a laminate to actuation loads N_A and bending moments M_A. The (d) matrix is used to calculate the response of the laminate in bending. The b and b' matrices are used to calculate the extensional twist coupling and the bend twist coupling of the laminate respectively. For balanced symmetrical laminates like the ones used for this experimental study the b and b' effectively become zero so the actuation loads produce only extension and bending.

In order to calculate the resultant direct actuation strain (ε), and laminate curvature (κ), the values of the actuation force N_A (N/W) and actuation bending moment M_A must be calculated. The value of actuation force may then be calculated from equation 4 having calculated the relevant compliance matrices for the laminate including the effects on stiffness of the PZT actuator.

To assess the relationship, three laminates were fabricated using Ciba 913 epoxy/E-glass continuous fibre prepreg. Laminate 1 had a 90/0/90 lay-up. A portion of the 0° ply was removed and replaced by a single piezo actuator. Laminate 2 had a $(0/90)_s$ lay-up with a piezo actuator positioned between the central plies. Laminate 3 was of a $(45/-45/0)_s$ lay-up with the actuator again positioned between the central plies. An electric field was applied to the actuators in a similar manner to the initial test of the unembedded actuator.

The initial voltage/strain results of this analysis for three laminates containing PZT actuators are shown in figure 2. As each actuator was positioned on the neutral axis of the laminates only direct strain was assumed to have occurred ($M_A = \kappa = 0$). Agreement of the model with the experimental results can be seen to be fairly poor.

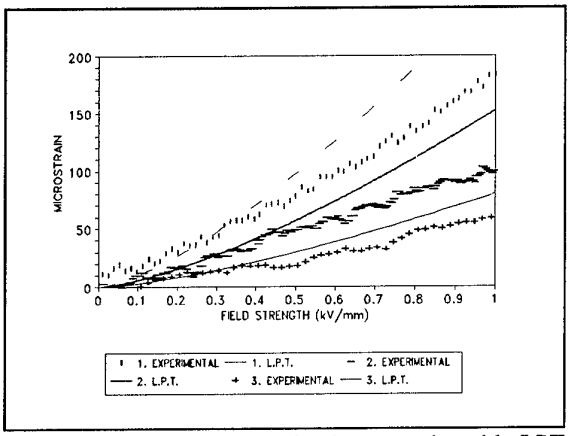

Figure 2 - Comparison of laminate strain with LPT theory

EXPERIMENTAL DETERMINATION OF ACTUATOR YOUNG'S MODULUS

One possible cause of error is the assumed value of the actuator Young's modulus. The literature[7] quotes a closed circuit value of 61 GPa measured at 4 kHz flexural resonance. For static loading this value may not be valid. It was therefore decided to

determine the mechanical properties of the actuator experimentally. To achieve this use was made of PZT actuators, encapsulated in GFP, previously developed by ADC Ltd. These are robust actuators with good resistance to arcing at high field intensities. The dimensions of the encapsulated PZT actuator are given in figure 3.

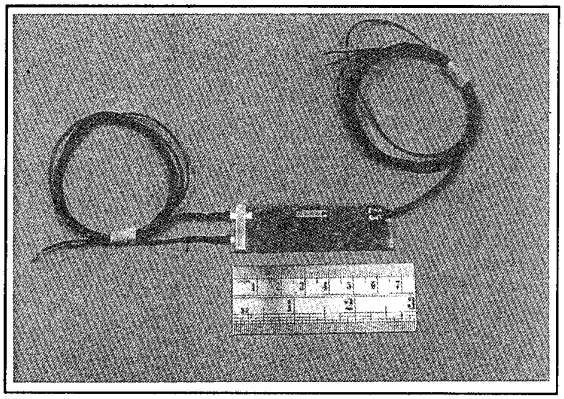

Figure 3 - Encapsulated PZT actuator

ADC designed a rig to directly measure the performance of the actuator. The rig is shown in figure 4 . The rig is designed to use either a LVDT or a load cell. The elements of the test set-up are shown in figure 5. The actuator was mounted in the test rig shown centre right. A simple Euler calculation indicated a possible buckling load of around 20N. This was thought to be a possible problem, although not very likely, even so the tests were carried out with lateral support blocks.

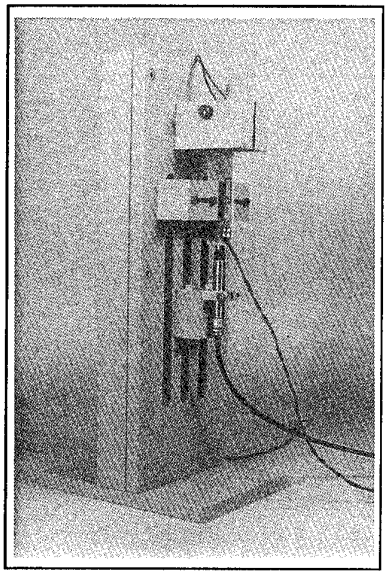

Figure 4 - Actuator test rig

The actuators were strain gauged with 120 ohm TML FLA-10-11 10mm gauges bonded with superglue. The gauges were connected to a 120 ohm full bridge with the other half of the bridge connected to a second dummy gauge mounted on an inactive actuator to provide temperature compensation. The LVDT was an RDP unit conditioned by a RDP E309 unit shown far lower right. The unit had a total stroke of 1 mm with a +/ 0.25mm linear range. The load cell was an Entran ELF-B26-50. This was a 50kN washer load cell with a centre button and a hole. The unit was designed to work in compression.

Experiments were carried out under static control measuring strain, load and displacement. The results of these tests are shown in figures 6 and 7. Figure 6 shows the displacement and strain behaviour of PZT. With a voltage amplitude range of 200 volts the displacement amplitude is 13.85 microns. With an actuator free length of 60 mm this implies a strain amplitude of 230με. The hysteresis is 21.3%. It is possible to compare this to the strain behaviour in the same test. At 200 volts range the strain amplitude is 240 με with a hysteresis of 20.1%. Good agreement thus existed between displacement and strain measurement. A strain of 240 microstrain from 200 volts implies an actuator gain of 1.2 με/volt and an effective d_{31} of 228 x 10^{-12} metres/volt as against a quoted value [7] of 171 x 10^{-12}.

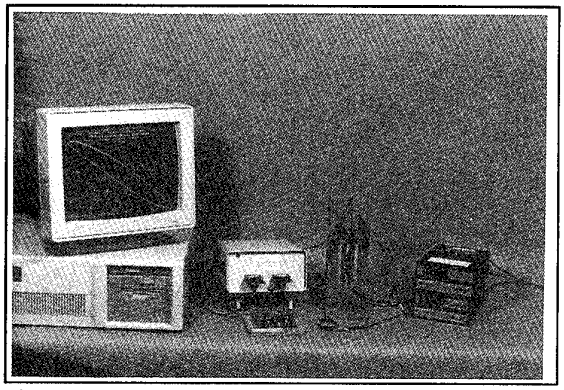

Figure 5 - Actuator testing experimental set up

The load behaviour of PZT is shown in figure 7. At 200 volts range the load range is 9.95 N with a hysteresis of 39.2%. This hysteresis was largely given by the load cell conditioning module. The compliance of the load cell resulted in the measured load not been completely blocked. A strain of 181.2 με was measured corresponding to the 9.95 N load. The load on the load cell is in fact equivalent to the blocked strain of the actuator, which is the difference between the strain range of the free actuator (240με) and the strain range of the "blocked" actuator (181.2με). From the blocked strain of 58.8 με giving a total load of 9.95 N we can deduce an effective Young's modulus for the actuator (closed circuit) of 46.6 GPa, based on the cross-section of the PZT. From this Young's modulus we can deduce a fully blocked load range of 40 N for a 200 volt load range.

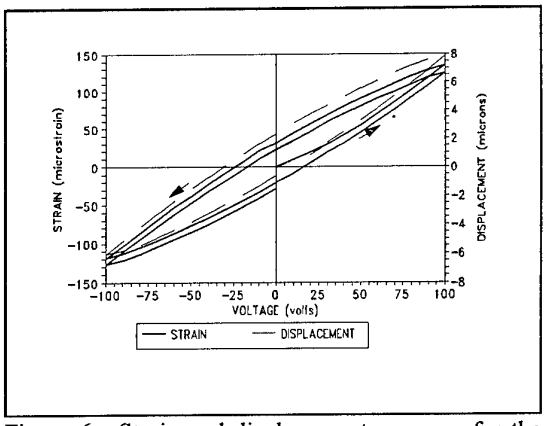

Figure 6 - Strain and displacement response for the encapsulated actuator

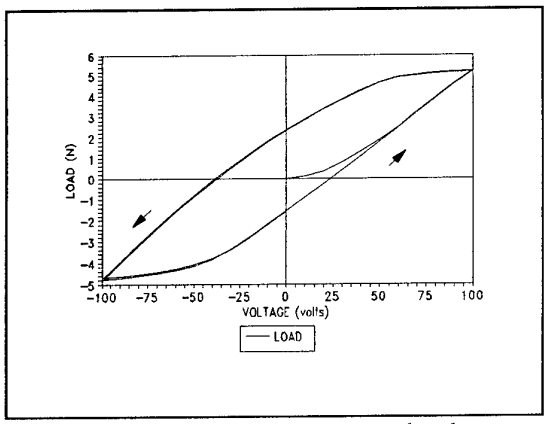

Figure 7 - Load response for the encapsulated actuator

In order to test the calculated value of Young's modulus the LPT analysis of the embedded actuators was repeated using the new value . The results of this analysis are shown in figure 8. The agreement between the LPT prediction can be seen to have improved significantly for the three laminates. It is probable that the agreement could still be improved however by the use of three dimensional LPT or finite element analysis with the associated decrease in the number of assumptions made.

CONCLUSIONS

The method of encapsulation enables the static electromechanical behaviour of actuators to be determined more readily. A rig has been designed which allows the testing of such an encapsulated actuator to determine the d_{31} coefficient and Young's modulus. The close agreement between the LVDT and strain gauge results suggests that in future strain gauging will not be necessary to measure strains saving time and expense. The experimental results of this rig have been shown to improve the agreement of LPT to the experimentally obtained data of embedded actuators.

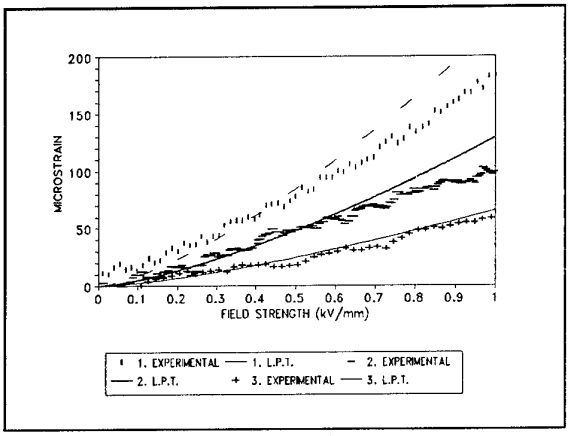

Figure 8 - Revised LPT prediction

REFERENCES

1. Barrett R. "Active plate and wing research using EDAP elements" Smart Materials & Structures 1 I(1992)
2. Bent A.A. Hagood N.W. Rodgers J.P."Anisotropic Actuation with Piezoelectric Fiber Composites" Proc. 4th International Conf. Adaptive Structures (1993)
3. Crawley E.F. De Luis J."Use of Intelligent Actuators as Elements in Intelligent Structures" J.AIAA 25 No 10 (1987)
4. Barrett R "Modelling Techniques and Design Principlesof a Low Aspect Ratio Active Aeroservoelastic Wing" Proc. 1993 North American Conf. on Smart Structures and Materials 1917-10
5. Ehlers S.M. Weisshaar T.A "Static Aeroelastic Behaviour of a Laminated Piezoelectric Composite Wing" Proc. 31st AIAA Structural Dynamics Conf. 90-1078 (1990)
6. Wang B. Rogers C.A. "Laminate Plate Theory for Spatially Distributed Induced Srain Actuators" J. Comp. Mat. 25 (1991) pp 433-452
7. "Modern Piezoelectric Ceramics" Morgan Matroc Ltd

The authors would like to acknowledge the Ministry of Defence for funding this project.

© copyright Crown / DRA 1994

CHARACTERIZATION OF ACTUATOR BASED MATERIALS USING OPTICAL FIBER SENSORS

David Sun, Mary K. Burford, Kent A. Murphy and Richard O. Claus
Fiber and Electro–Optics Research Center
Bradley Department of Electrical Engineering
Virginia Polytechnic Institute and State University
Blacksburg, Virginia 24061-0111

Jonathan A. Greene and Tuan A. Tran
Fiber and Sensor Technologies, Inc.
250 Arbor Drive
Christiansburg, VA 24073

G. P. Carman
Mechanical Aerospace and Nuclear Engineering Department
University of California, Los Angeles
Los Angeles, CA 90024-1597

1.0 INTRODUCTION

Piezoelectric/electrostrictive materials are a unique class of nonconducting, anisotropic materials which change in dimension due to the application of an electric field and thereby may be used as mechanical actuators [1]. The most widely used actuation materials for acoustic transduction applications [2] are piezoceramics, such as lead zirconate titanate (PZT) and lead magnesium niobate (PMN). Disadvantages of these materials include relatively high creep and hysteresis [3], the tendency of the ferroelectric dielectric material to retain electric potential after the alternating electric field to which it is subjected reverses polarity, thus causing electrostatic action to lag the applied voltage [4].

The need to study the geometrical, material, and time dependent nonlinear behavior, as well as the interaction effects between sensors and actuators, is increasingly apparent, although a unified approach for modeling the local and global response of a nonlinear active material system has not been accomplished. In this paper we discuss the use of optical fiber-based short gage length Fabry-Perot sensors to experimentally verify an analytical model and allow determination of the nonlinear behavior of actuator elements without affecting their material properties.

2.0 OPTICAL FIBER SENSING METHODS

Optical fiber sensors may be divided into two general classes: intensity-based devices which measure changes in received optical power, and interferometric devices which measure differential phase changes in multipath fiber geometries [5]. Fiber interferometers allow very high resolution but require relatively complicated signal processing to accomplish effective phase recovery [6]. Both sensor types allow operation without electromagnetic interference or radiation in relatively harsh environmental conditions. One such sensor, the extrinsic Fabry-Perot interferometer (EFPI), is formed along the fiber length and has been demonstrated largely as an optical fiber strain gage [7, 8] Laser light is input through a bidirectional coupler to an input/output single-mode fiber. The cleaved ends of this fiber and a second fiber supported in a hollow-core fiber tube form an air gap that acts as a low-finesse Fabry-Perot cavity. The Fresnel reflection from the glass/air interface at the front of the air gap and the sensing reflection from the air/glass interface at the far end of the air gap interfere in the input/output fiber. The reflector fiber is allowed to move longitudinally in the silica hollow core tube so that the length of the air gap can increase or decrease. The output intensity, I, of an EFPI sensor is described by the interference relation

$$I = I_{DC}\left\{1 + \cos\left(\frac{4\pi L}{\lambda}\right)\right\} \tag{1}$$

where I_{DC} is the DC offset of the intensity signal, L is the air gap length, and λ is the laser source wavelength. One period of this sinusoidally modulated signal is termed a fringe. Solving for the gap length, we find

0-8194-1700-9/94/$6.00

$$L=\frac{\lambda}{4\pi}\cos^{-1}\left(\frac{I-I_{DC}}{I_{DC}}\right). \tag{2}$$

For n fringes, the change in length of the air gap, ΔL, becomes

$$\Delta L=\frac{n\lambda}{2}. \tag{3}$$

The strain, S, on the hollow core tube of the sensor element is then related to ΔL as

$$S=\frac{\Delta L}{L} \tag{4}$$

where L is the gauge length defined as the distance between the attached ends of the two optical fibers.

3.0 EXPERIMENTAL ARRANGEMENT AND RESULTS

We discuss the use of such EFPI strain sensors for the analysis of three PZT/material configurations and one PMN actuator configuration, and describe one measurement here. These arrangements simulate the performance of an actuator by itself, in a stack, embedded in a composite and attached to a composite laminate. The first experimental analysis consists of a rectangular sheet of PZT material; strain induced in the PZT is given by the actuator equation

$$S=s^{E}T+dE \tag{5}$$

where s^{E} is the constant-field compliance of the PZT material, T the stress, d the piezoelectric constant and E the applied electric field. For a mechanically unconstrained actuator, T=0 and the free induced strain may be described by

$$S=\frac{Vd}{t} \tag{6}$$

where V is the applied voltage and t the thickness of the material. Due to the inherent nonlinear effects of PZT material, the strain coefficient increases with the electric field and is usually determined using an iterative method. [9]

The first configuration investigated is shown in Figure 1 where the EFPI is used to measure the free induced strain of the material in the 1 direction by an electric field in the poling direction. Figure 2 shows typical data indicating changes in applied PZT voltage and corresponding sensor output. It is significant that the experimentally obtained value of strain at 126 V is 2.5 times higher than the theoretical value of approximately 110$\mu\varepsilon$. This suggests a nonlinear response of the material due to an increasing strain coefficient. Figure 3 shows that disparity in strain paths between increasing and decreasing voltage. The gap between these curves shows a delay in recovery of strain with an aspect ratio of approximately 0.200.

The second configuration investigated is a cylindrical PMN actuator stack with an EFPI placed along the axis of the stack as shown in Figure 4. Actuation in this stack is based upon the second order electrostriction phenomenon of electromechanical coupling. Here the induced strain is described by its actuator equation as

$$S=s^{E}T+dE^{2}. \tag{7}$$

As before, the actuator was unconstrained causing the free induced strain to be described by

$$S=d\left(\frac{V}{t}\right)^{2}. \tag{8}$$

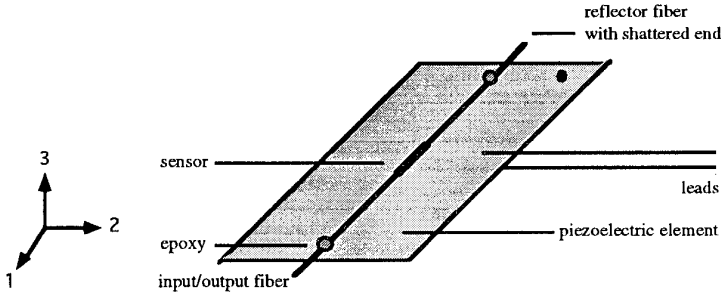

Figure 1. PZT with attached EFPI sensor and leads.

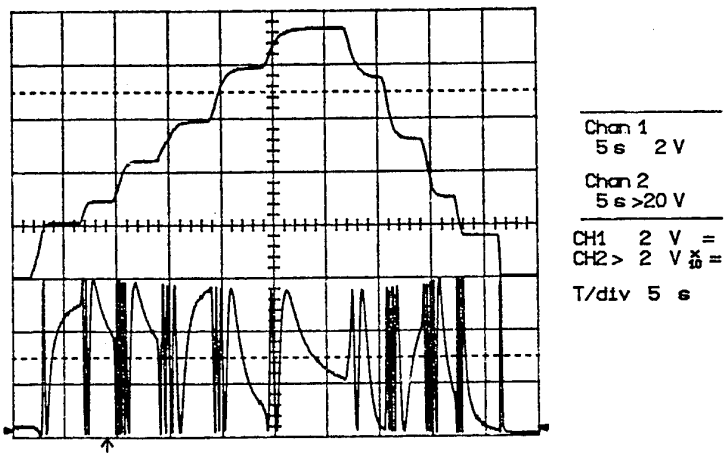

Figure 2. Typical data plot showing changes in applied PZT voltage and the corresponding sensor output.

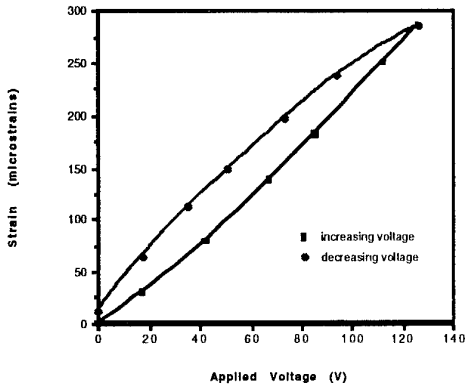

Figure 3. Measured hysteresis curve of a PZT element.

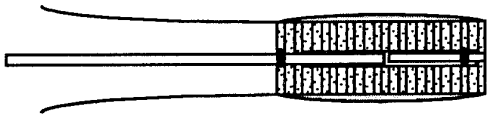

Figure 4. PMN stack with attached EFPI.

For this configuration, two types of hysteresis tests were performed. The first test is analogous to the PZT test in which the strain paths were determined. The results of this test appear in Figure 5. As can be seen, the aspect ratio of the actuator is approximately 0.0727, much less than that of the PZT.

The second test of the PMN involved exciting the actuator with square waves of different amplitudes to determine the displacements for increasing and decreasing fields and the residual strain in the actuator, as shown in Figure 6. Here,

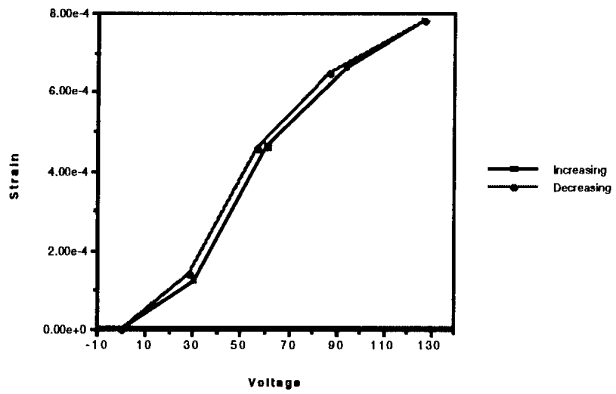

Figure 5. Measured hysteresis curve of a PMN element.

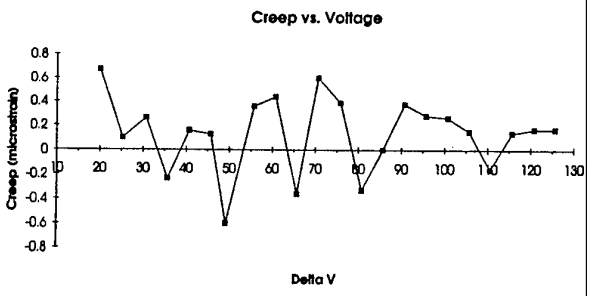

Figure 6. Measured residual actuator strain.

the residual strain in the actuator appears to be independent of applied field amplitude and the direction of residual strain independent of applied field.. The third configuration involves placing the piezoceramic between two single layer composite plies to simulate the performance of an actuator embedded within a composite. The graphite composite fibers and sensor are oriented parallel to the PZT. Here based on the simple actuation model, it is anticipated that the higher stiffness of the prepreg graphite fibers to diminish the ability of the "embedded" PZT to contract. Again, the hysteresis of the actuator is evident; however the aspect ratio has decreased to 0.123. This effect may be attributed to the effects of embedding the actuator in the composite. The final analysis incorporated a single layer composite ply cured with the PZT material. By clamping this specimen at one end, a unimorph beam arrangement is created. The sensor is placed so the cavity length is modulated as the PZT/composite element bends, producing strain shown that may be measured by the EFPI. Both of these final arrangements and results are discussed in the full version of this paper.

4.0 CONCLUSIONS

The feasibility of using extrinsic Fabry-Perot interferometer fiber sensors to experimentally investigate the effects of specific actuators on a composite material, and to determine the nonlinear behavior they exhibit has been investigated. Hysteresis curves are presented for three PZT/material configurations and one PMN configuration as the electric field applied to the actuator is varied. Differences in the peak amount of strain are observed.

5.0 ACKNOWLEDGEMENTS

The authors gratefully acknowledge the support of the Air Force of Scientific Research Contract No. F49620-93-C-0057, and appreciate the technical advice of Piezo Systems, Inc., and Mr. Jeff Paine in CIMSS at Virginia Tech.

6.0 REFERENCES

[1] C.A. Rogers, First European Conference Smart Structures and Materials, Glasgow, pp. 163-175, 1992.
[2] K. Yo, and S.B. Desu, Recent Advances in Adaptive and Sensory Mtls., Blacksburg, VA, pp. 157-168, 1992.
[3] J. West, "Electroactive Device Fundamentals", AVX Corporation Fundamentals Tutorial, 1993.
[4] R. P. Turner and S. Gibilisco, The Illustrated Dictionary of Electronics, Fourth Edition, 1988.
[5] R. O. Claus, Fiber Optic Sensor-Based Smart Materials and Strucutres, IOP Publishing Ltd., London,1992.
[6] A. Wang and K.A. Murphy, Smart Materials and Structures, pp. 5-7, 1992.
[7] J. Sirkus, SPIE/OE Fibers, Boston, MA, pp. 26-43, vol. 1588, 1991.
[8] K. A. Murphy, M.F. Gunther, A.M. Vengsarkar, and R.O. Claus, Optics Letters, Vol. 16, No. 4, 1991.
[9] E. F. Crawley and E. H. Anderson, J. Intell. Mater., Syst. and Struct., vol. 1, pp. 4-25, 1990.

PROGRESS TOWARDS A ROBUST, USER FRIENDLY, SYSTEM FOR ACTIVE STRUCTURAL DAMPING

S.S.J. Roberts#, R.J. Butler* and R. Davidson#

AEA Technology, B.528.9, Harwell, Didcot, Oxon., OX11 0RA, U.K.
* ADC Limited, 21 Silver Street, Newport Pagnell, Bucks, MK16 OEP

ABSTRACT

This paper details the progress made towards the realisation of a robust and user friendly system designed to damp vibration in composite structures. The system relies on polyvinylidene fluoride (PVDF) strain sensors linked to PZT actuators through a simple feedback signal inversion algorithm. The PVDF is coated to reduce charge leakage and the PZT ceramics are encapsulated to provide easy to handle, robust actuators that do not electrically short in CFRP based composites. Details of the system design are presented along with initial results showing vibration control of multimoded CFRP cantilevers.

1. INTRODUCTION

Unwanted vibrations in structures can frequently lead to problems in later life. In some cases, particularly for composite structures, solutions can be obtained by tailoring the composite design, in particular lay up and matrix characteristics. In other cases active damping solutions based on surface bonded or embedded sensors and actuators would appear to offer enhanced solutions[1-4]. The aim of this work is to improve on the enhanced damping capability for light weight structures already achieved through passive techniques[5]. The dimensions of a piezoelectric material change on the application of an electric field and such materials in film form can be used as either actuators or sensors operating at high frequencies and bandwidths. Typically, due to greater moduli combined with high d_{31} coefficients, piezoelectric ceramics offer better properties as actuators while the high g_{31} coefficients of piezoelectric polymers makes them more suited to sensing.

Much of the research and development work in active damping of composite structures has focused around the use of PVDF sensors and PZT actuators. Unfortunately the realisation of this work into usable practical applications has been very slow. One of the main reasons for this is the practical difficulty associated with handling the sensor and actuator materials and incorporating them into structural systems with the necessary interfacing electronic hardware and software control. This paper reports the progress made towards a simple and yet highly flexible and robust system that will have a widespread use for active vibration control.

2. SYSTEM OUTLINE

The operation of the system is frequency independent with no requirement for tuning to a given structural

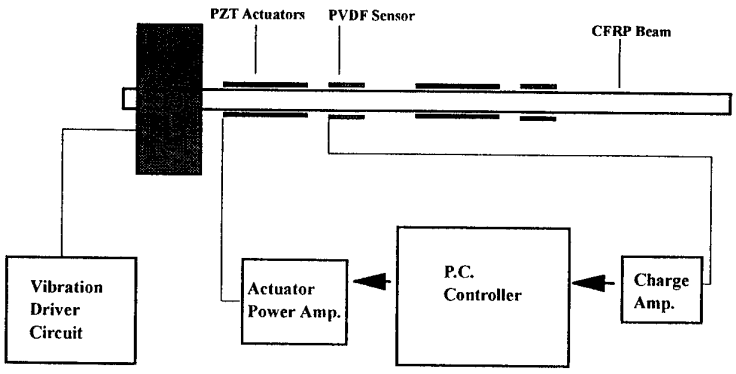

Figure 1. Schematic lay out of active damping system

0-8194-1700-9/94/$6.00

response. The lay out of the basic system is detailed in **Figure 1** and can be demonstrated using a cantilevered beam. The beam can be excited by either driving PZT actuators bonded to the root connected to a vibration driver circuit, or as for the work reported here, by applying impulsive loading to cause a lateral displacement. The system senses the resulting motion of the beam through polyimide coated PVDF sensors connected to screened cables leading to a charge amplifier. This can be displayed for convenience on the PC screen. The real time software loop which samples and damps operates at 450Hz on a 486DX33. This feeds an inverted output signal through appropriate amplifiers to PZT actuators located at the point of maximum strain energy for the particular mode of vibration. The resonant frequency is then successfully damped. The versatility of the system can be demonstrated by adding tip masses to change the resonant frequency of the beam which are also sensed and damped by the system.

3. ENCAPSULATED ACTUATORS

The actuators are encapsulated piezo-ceramic PZT wafers fitted with brass tags for electrical connection. The PZT is US DOD Navy type II, poled and nickel coated. These fragile wafers are then encapsulated in E-glass/epoxide providing electrical insulation and making the PZT actuator extremely robust for handling. The robustness of the encapsulated actuators results from the removal of the sensitivity of the ceramic PZT to surface crack formation and single crack catastrophic propagation[6]. This enables a greater volume of material to do work up to failure rather than a single flaw triggering total failure at an early stage The actuators employed for this demonstration had dimensions of 65mm x 20mm x 0.5mm. At 100V the actuators will generate approximately 20 N in-plane force when fully blocked or 8μm in-plane displacement when free. Temporary attachment to the structure can be achieved with small amounts of cyanoacrylate although for permanent installation epoxide adhesives are preferred. The measured properties of the actuators are shown below in **Table 1**.

Property	Value
Wafer Thickness	0.191 mm
Density	7.6 gcm^{-3}
Poissons Ratio	0.31
Curie Temperature	360 ^{o}C
Polarisation Field	2.4 MVm^{-1}
Approximate Capacitance	100 nF
Hysteresis	15 - 20 %
Youngs Modulus	46 GPa
Tensile Failure Strain (encapsulated)	0.25 %

Table 1. PZT Actuator Physical and Mechanical Properties

4. ACTUATOR POWER AMPLIFIER

The voltage amplifier is a four channel system specifically developed for structural control using piezo-electric actuators. It is driven by a set of four input signal voltages within the range of +10 volts to -10 volts. The input signals are then amplified with a fixed gain of 25 to produce a set of four output voltages within the range of +250V to -250 V. The unit also accepts a set of four feedback signals which it passes through from the structural sensors to the controlling computer. A simpler and cheaper form of the power supply is available which only offers the four driving channels without the feedback circuits being routed via this unit.

5. PVDF SENSORS

The sensors are constructed from polyvinylidene fluoride strips, oriented, poled and metallised by the suppliers Atochem. The as received material is coated in a polyimide film to reduce charge leakage. The film is then attached to shielded cable terminating in a mini RF plug for connection to the charge amplifier. The complete sensor can be attached to the structure, slightly forward of the optimal actuator position, with cyanoacrylate or epoxide. Correct sensor location is important in order to avoid positive feedback coupling which leads to dynamic instabilities.

6. CHARGE AMPLIFIER SIGNAL CONDITIONER

The signal conditioning is based on monitoring the charge on the sensor rather than the more conventional voltage. The charge conditioner works by the connection of a high precision capacitor in series with the piezo-sensor. This capacitor develops the same charge as the sensor and is used to monitor the activity of the sensor. In other work the precision capacitor is also used for control of piezo actuators. The significant advantage of this aspect of the system is that it operates at effectively zero volts and is thus relatively insensitive to stray electrical activity in the vicinity. The charge amplifier has been designed to give an output of 10 VnC^{-1} which has proved satisfactory for the control of this particular demonstrator.

7. CONTROL SOFTWARE

The damping software is written and compiled in Quickbasic. On execution, the programme zeros the 2 D/A's on the I/O card and then requests the required damping time. The signal input from the PVDF sensor is then sampled and plotted on screen. When damping is required, a value of the gain multiplier is input and the system damps the forced vibration for the specified duration. The control law is based on simple feedback signal inversion.

8. MULTIMODE BEAM DEMONSTRATOR

Vibrations in real structures contain complex combinations of a variety of modes. Initial steps towards controlling such a structure with our system have employed a multi-station approach enabling the first two modes of vibration in a CFRP cantilevered beam to be damped. Two stations were used for this demonstrator. Sensor (1) is located at the beam root and sensor (2) near the antinode of the second mode. The 900mm long, 25mm wide and 1mm thick beam is shown connected up to the control system in the photograph in **Figure 2**. Unlike earlier GRP beams the CFRP beam was found to act as an aerial and picked up mains 50Hz from the general laboratory environment. This was then transmitted to the PVDF sensor and hence into the system. This was solved by simply earthing the beam and increasing the shielding around the PVDF sensor.

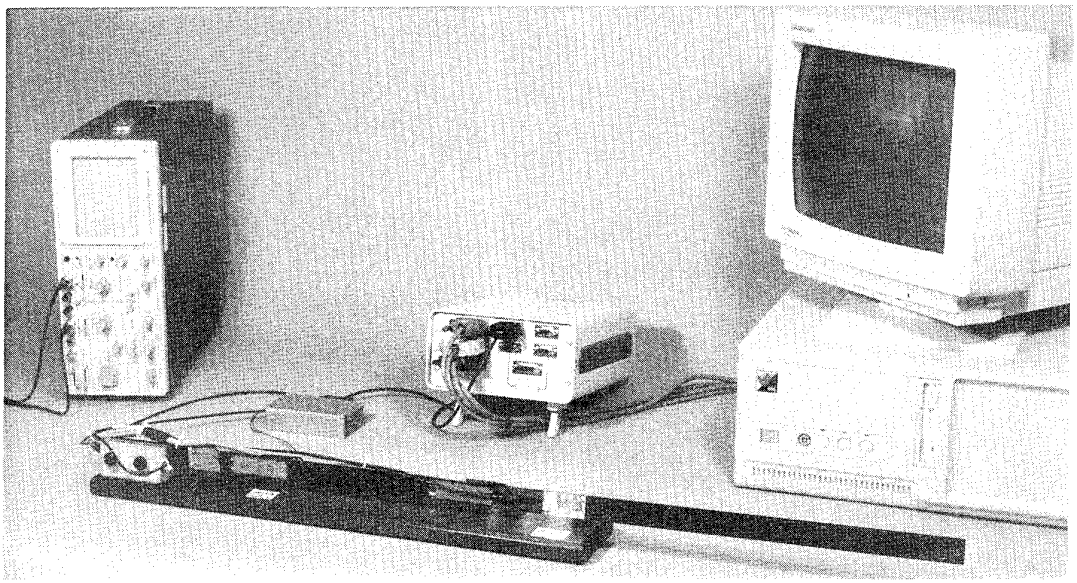

Figure 2. Active Damping Demonstrator

9. DAMPING PERFORMANCE

Figure 3a shows the un-damped characteristic vibration from the two sensors when the beam was excited with an impulse at approximately half way along its length. The increase in damping performance is shown in **Figure 3b**. Quantitatively, the damping ratio for the fundamental mode in **Figure 3a** is 2.7% whereas with active damping this increases to 10.1%.

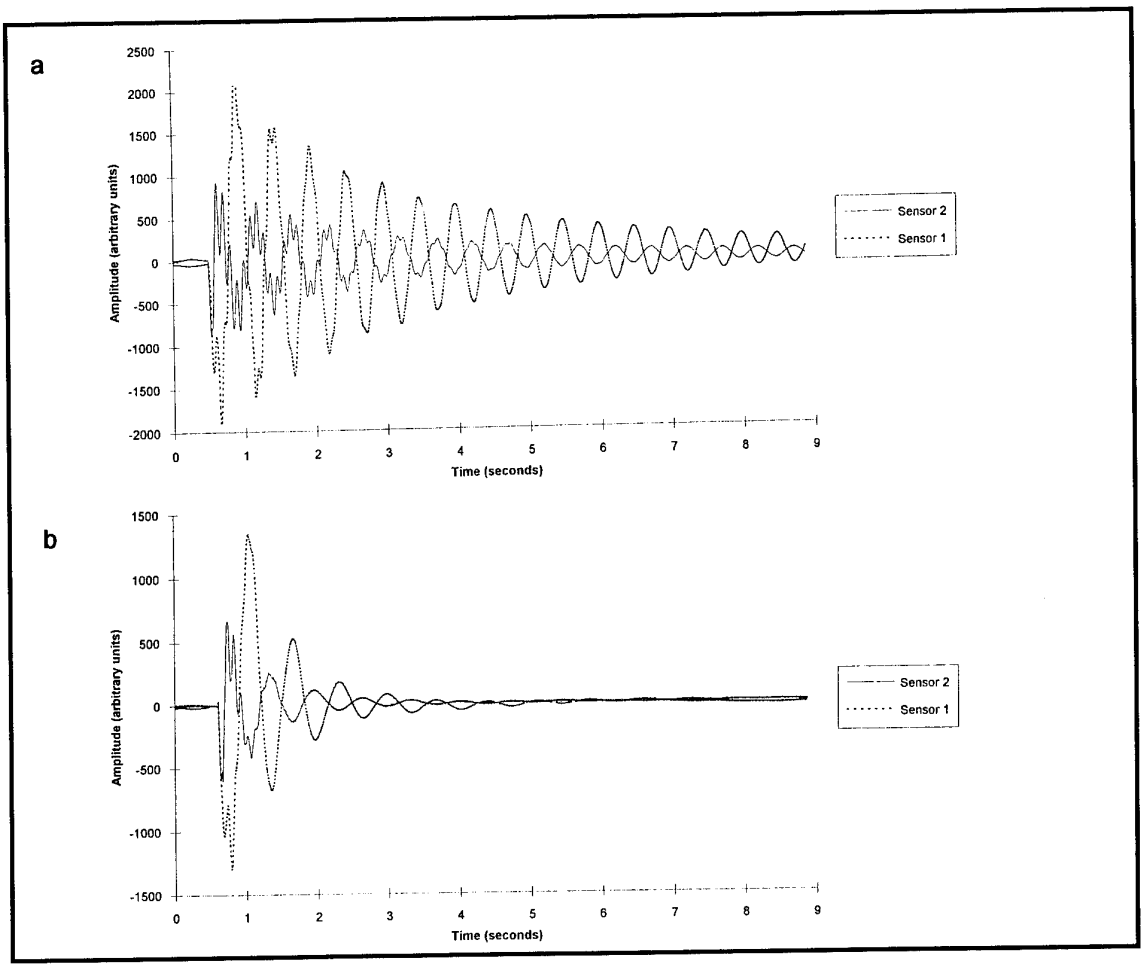

Figure 3. Damping Response of CFRP Beam (a) Open Loop and (b) Closed Loop

10. CONCLUSIONS AND FURTHER WORK

This active control system has shown significant increases in damping and is in the process of being applied to an automotive industrial robotic application[5]. Further work on the software will concentrate on automatic gain selection.

11. ACKNOWLEDGEMENTS

The authors gratefully acknowledge the financial support for this work from the AEA Corporate Investment in Research and Exploitation Programme.

12. REFERENCES

1. Bailey, T. and Hubbard, J.E., Distributed Piezoelectric-Polymer Active Vibration Control of a Cantilever Beam, J. Guidance, Vol. 8, No. 5 1985.
2. Forward, R., Electronic Damping of Orthogonal Bending Modes in a Cylindrical Mast - Experiment, J. Spacecraft, Vol. 18, No. 1, 1981.
3. Yang, S.M. and Lee, Y.J., Vibration Suppression With Optimal Sensor/Actuator Location and Feedback Gain, Smart Materials and Structures, Vol. 2, No. 4, pp. 232 - 239, 1993.
4. Zhang, H., Galea, S.C., Chiu, W.K. and Lam, Y.C., An Investigation of Thin PVDF Films as Fluctuating-Strain-Measuring and Damage-Monitoring Devices, Smart Materials and Structures, Vol. 2, No. 4, pp. 208 - 216, 1993.
5. Davidson, R., Roberts, S.S.J., Brabon S. and Yates, T., Vibration Reduction in Composite Structures, Proceedings of ECCM Smart Composites Workshop, pp. 89 - 94, Bordeaux, September 1993.
6. Butler, R.J. and Raymer, M.B., Static Stiffness and Strength of Encapsulated PZT Actuators, ADC Report ADC/I/1/94, 1994.

Shape control of an adaptive composite reflector panel

R. Paradies, W.J. Elspass, K.Schindler

Institute of Design and Construction Methods,
Swiss Federal Institute of Technology Zurich
ETH-Zentrum, Rämistr. 101, CH 8092 Zurich, Switzerland

ABSTRACT: This paper describes a manufacturing technique for active structures and a displacement measurement concept based on an embedded sensor system, which can both be used for the design of future active fibre reinforced reflector panels.

1. INTRODUCTION

One objective of the group for active functional design of the Institute of Design and Construction Methods at the ETH Zurich is the design and fabrication of an fibre reinforced reflector panel with an integrated sensor and actuator system. Since fibre reinforced composites enable the fabrication of thermal stable structures with high specific strength and stiffness, this material is used for active reflector panels. In addition the contour errors of the reflector panel due to manufacturing tolerances or acceleration loads can be reduced or even compensated by using an embedded actuator and sensor system.

2. IN-SITU FABRICATION OF ACTIVE LAMINATES BASED ON CARBON FIBRE REINFORCED THERMOPLASTICS

One disadvantage of fibre reinforced composites in general is the time and cost consuming fabrication process in the autoclave required for thermosetts. In case of in-situ fabricated laminates with embedded piezoelectric ceramic actuators (PZT's), where the temperature of the cure cycle have to be less than half of the Curie temperature, the cure time needed in the autoclave can take several hours. Using thermoplastic matrices instead of thermosetts, the production time can be cut down significantly to several minutes. However, the disadvantage of high performance thermoplastic composites (e.g. PEEK) is the fabrication temperature required, which is around 400°C and therefore well above the Curie temperatures of most piezoelectric ceramics (e.g. PXE 5 ≅ 285°C) [1].

The in-situ technique for glass fibre reinforced laminates with integrated piezoelectric actuators presented in [2,3] was modified for the embedding of standard PZT's into carbon fibre reinforced thermoplastics using the hot press technique. This fabrication process is followed by a repolarisation process of the embedded piezoelectric elements.

The grade of the PZT used is PXE 5 by Philips and the carbon fibre reinforced composite is APC2/IM8 by ICI. Since the embedded actuators would be electrically short-circuit by the conducting host material an insulating layer is placed between the actuator and the surrounding laminate. To ensure a stiff bond between actuator and the host structure either a ply of glass fibre reinforced thermoplastic fabric was used as an insulating layer or a 10μm thick Upilex film, which was bonded with an thermoplastic film (Litrex TK) to the actuator. To accomplish a laminate of homogeneous thickness holes of the same size as the actuators are cut in the plies that are to receive them. Furthermore, a standard copper tape of 50% of the single ply

0-8194-1700-9/94/$6.00

thickness, which is insulated by a high temperature resistant tape, is used for the electrical wiring. To avoid breakage of the brittle ceramics during the hot press cycle caused by a different laminate thickness near the electrical conductors, thin aluminium tape ($9\mu m$) replaces the copper tapes close to the ceramics. Furthermore this edge of the ceramic is insulated with a heat resistant plastic tape to avoid short circuits of the actuator (see Figure 2.1).

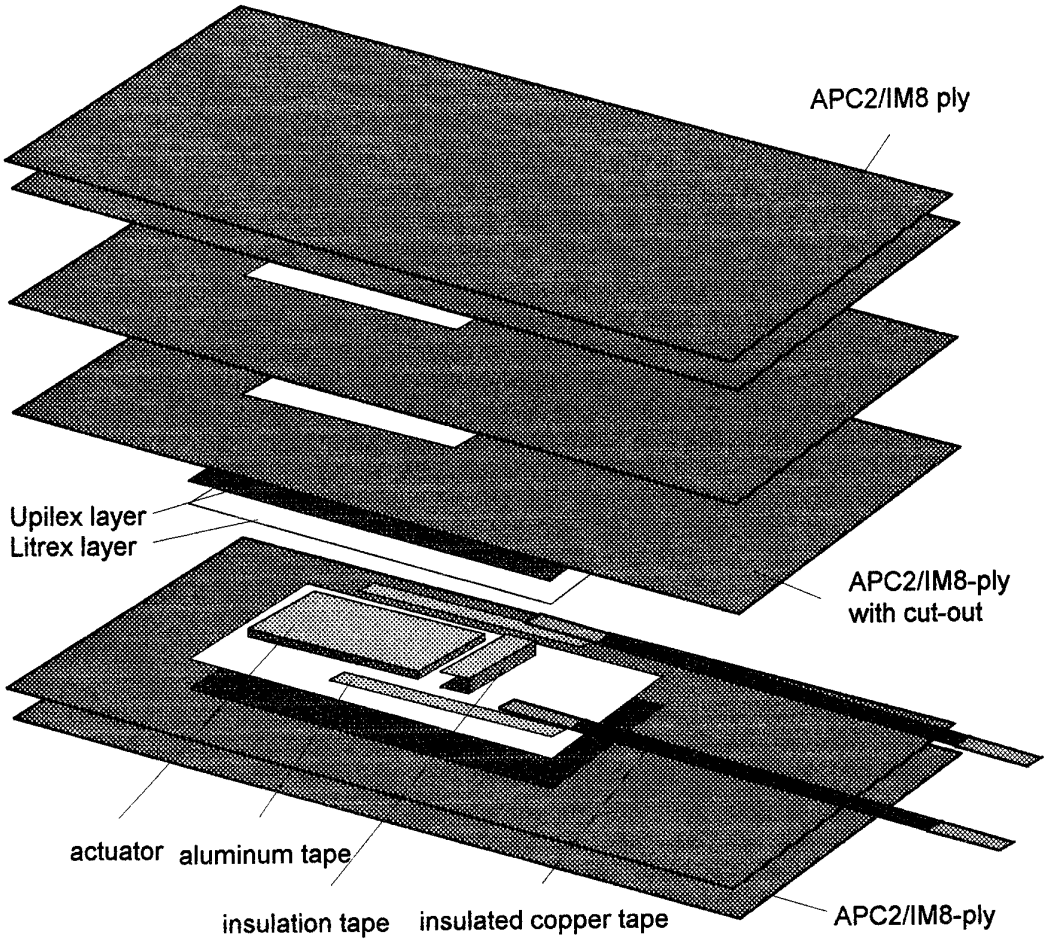

Figure 2.1. Piezoelectric actuator embedded in a carbon fibre reinforced thermoplastic prior to curing.

The parameter for the processing cycle of the laminate is given in Figure 2.2 and the parameter for the repolarisation of the embedded actuators is given in Figure 2.3.

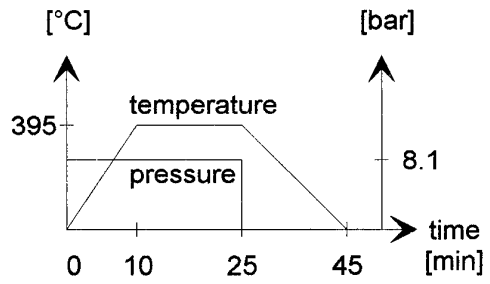

Figure 2.2. Cure cycle used for the thermoplastic composite with embedded piezoelectric ceramic.

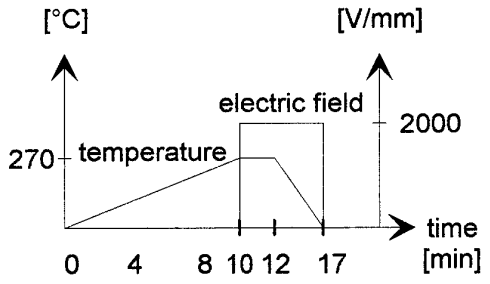

Figure 2.3. Repolarisation cycle used for the embedded piezoelectric actuators [4].

Since the heating and cooling rate of PEEK can be up to $700\,^{°C}/_{min}$ without any mechanical drawbacks [5] these parameters of the fabrication process strongly depend on the mould and hot press used. By using a high performance press the time of one cure cycle can be reduced to less than twenty minutes.

The piezoelectric properties of the ceramics during the fabrication process were checked by measuring the electric charge generated by the ceramic under compressive load. For this purpose single ceramics have been put through the same fabrication process as different specimens of embedded ceramics and tested prior to fabrication, after the hot press cycle and after repolarisation of the ceramics.

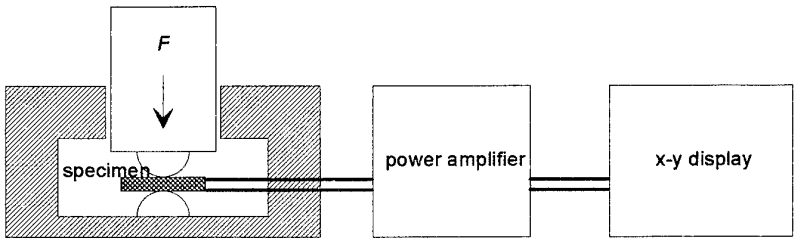

Figure 2.4. Quasi static measurement set-up of the electric charge generated under compressive load of the piezoelectric ceramic embedded in the specimen.

The quasi static test method given in Figure 2.4 indicates that the electric charge generated by the piezoelectric ceramics measured after repolarisation is of the same magnitude as before embedding. At the present time, the piezoelectric stability of the repolarised ceramics is going to be investigated.

3. EMBEDDED SENSORS FOR ACTIVE STRUCTURES

At this stage of the research, the composite mirror under investigation is a flat panel consisting of two face sheets, a foam core and a suspension [2,3]. One design objective is to gain the maximum bending moments induced by the piezoelectric actuators. Furthermore, the brittle ceramics should be protected from the surroundings and the surfaces of the structure should be

free of any components of the actuator-sensor system. Therefore, the actuators have been placed at the six radial positions from the centre to every corner of the hexagonal panel on top of the rear face sheet faced to the foam core (see Figure 3.5).

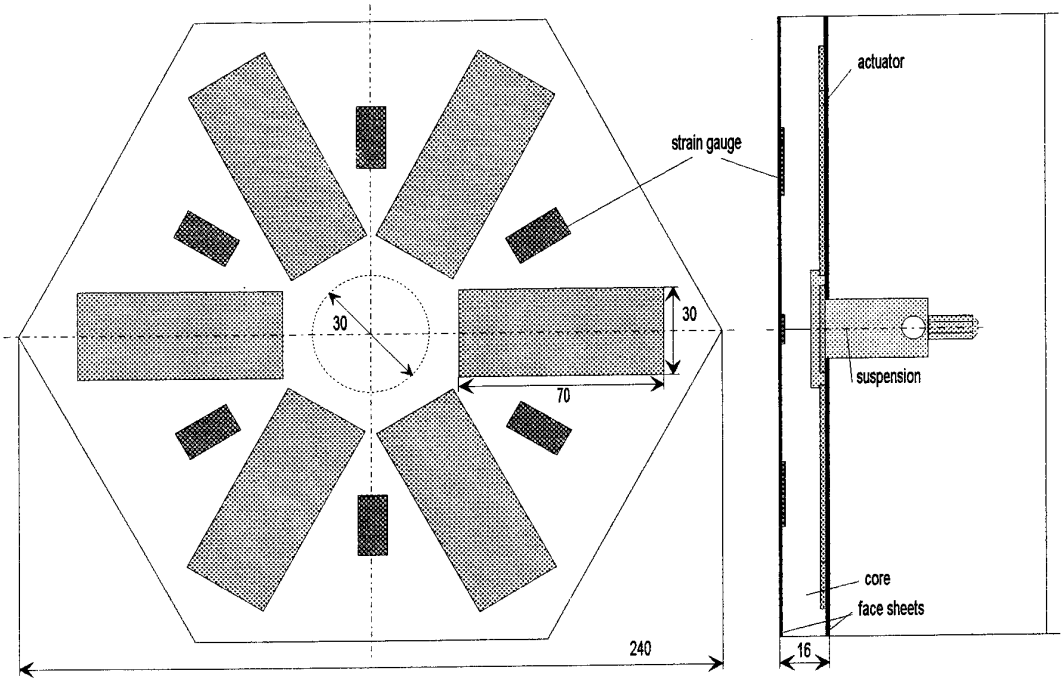

Figure 3.5. 240 mm flat panel with embedded piezoelectric actuators and strain sensors (Second face sheet, electric wiring and core are not shown in the front view).

Displacement sensors like hall sensors, laser displacement meters, etc. do require a reference plane presented by a backup structure. Because an additional backup structure should be avoided, investigations have been performed to describe the structural deformations of the panel based on embedded sensors. The signal obtained by sensors embedded or attached to the panel is a strain information. Therefore, an analytical model is required to calculate the state of deformation of the structure based on the strain information gained by the distributed strain sensors (see Figure 3.5). Assuming a linear strain distribution over the thickness of the sandwich and a constant curvature along the actuator the out-of-plane displacement along an active cross section, $w(r)$, is given by:

$$w(r) = \frac{\varepsilon_r - \varepsilon_f}{d} \cdot \frac{r^2}{2}$$

where r: radius
ε_r: radial strain component in the rear face sheet
ε_f: radial strain component in the front face sheet
d: distance of the strain gauges in z-direction

The displacement field of the reflector surface is approximated by polynomial functions, which are evaluated for different radius based on the extrapolated displacement profiles in the cross sections between two actuators. To verify the active concept presented various voltage steps

were applied to each actuator and the out-of-plane displacement of the panel was measured over the full surface of the structure. To avoid influence on the structure by external forces and having a reference system for the integrated sensor system two optical measurement systems were used. The phase shifted electronic speckle pattern interferometry (Speckle interferometry) [3,6,7] and a laser displacement meter. Furthermore, the experimental results were cross checked with a finite element model, in which the reflector panel is modelled by using triangular and quadrilateral linear membrane elements for the face sheets and the corresponding solid elements for the foam core. The piezoelectric actuators have been included in the laminate lay-up of the rear face sheet as an additional layer in the appropriate areas of the structure. Due to similar strain characteristics the analogy of the piezoelectric strain actuation to thermal expansion is used for the piezoelectric strain actuation.
A comparison of the displacement of the reflector surface evaluated by the different methods used is given in Figure 3.6 for the cross section $\theta = 0°, r \geq 0$.

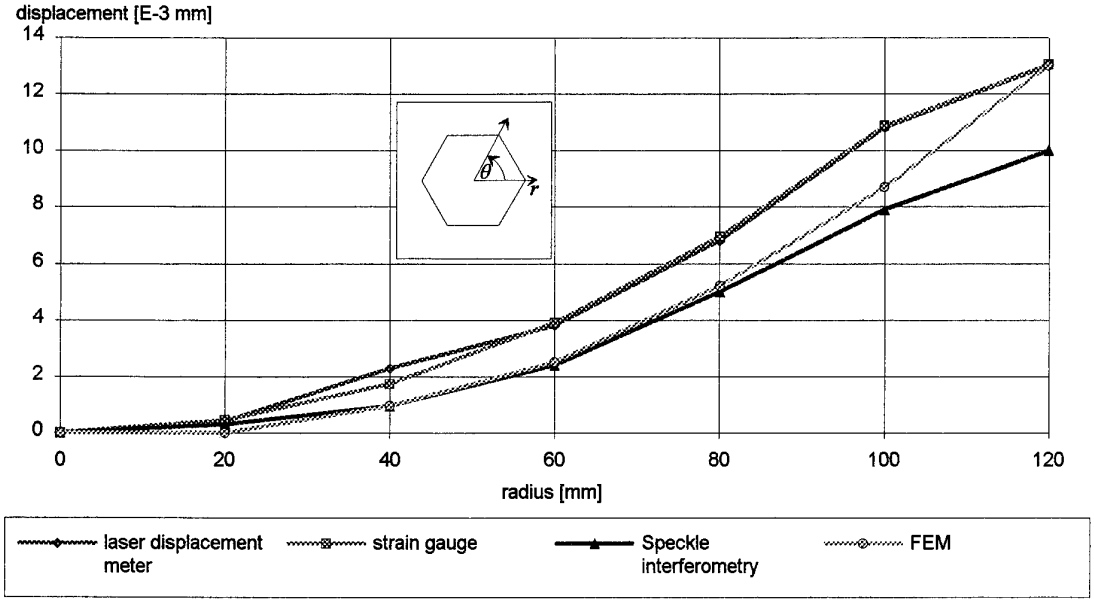

Figure 3.6. Comparison of the out-of-plane displacement along one radius of the panel [8].

The agreement between the methods used is fairly well. The discrepancies between the two optical measurement systems is based on small misalignments of the experimental set-up since both measurements can not be performed simultaneously. The displacement profile based on the strain gauge information and the displacement meter were measured simultaneously, which do agree for this special case of actuation extremely well. Although the finite element model consists of almost 8000 elements, the idealisation of this structure is still to simple. Additional refinements of the model close to the actuators should approach the experimental results closer.

4. SUMMARY AND CONCLUSIONS

The first part of the investigations summarised in this paper concentrates on the manufacturing process of active laminates. The modified in-situ manufacturing process presented for the embedding of piezoelectric actuators in carbon fibre reinforced thermoplastics is feasible. The main advantage of this fabrication process is a significant cut down in manufacturing time. Furthermore, the expensive autoclave technique can be replaced for simple structures by the less expensive hot press process. In future research the effects of this fabrication process onto the piezoelectric stability of the repolarised ceramics are going to be investigated.
It has been shown that the state of deformation can be measured by using integrated strain sensors in combination with an analytical model. The comparison of the out-of-plane displacements measured by an optical measurement system and based on the embedded strain sensors do agree well. Further investigations will be focused on the number of strain sensors and complexity of the analytical models required for the evaluation of the structural deformations.

5. ACKNOWLEDGEMENTS

This research presented has been supported by the Swiss National Funding for Scientific Research Grant No. 20-33680.92.

6. REFERENCES

1. J. Koch, 1988. "PIEZOXIDE (PXE) Eigenschaften und Anwendungen", Valvo Unternehmensbereich Bauelemente der Philips GmbH, Hamburg, pp. 14.

2. W.J. Elspass, R. Paradies 1994 "Design, numerical simulation, manufacturing and experimental verification of an adaptive sandwich reflector", North America Conference on Smart Structure and Materials.

3. R. Paradies, M. Hertwig 1993 "Reflector Panel designed as an Active Structure", Fourth International Conference on Active Structures.

4. U. Elkuch, 1994. "Integration von Piezokeramiken in faserverstärkte Thermoplaste", Project-report, IKB, ETH-Zürich, pp. 25,26.

5. W.J. Elspass, 1992. "Dimensionsstabile monolithische und hybride Bauweisen unter extremen Umgebungsbedingungen", IKB, ETH-Zürich, pp. 3.1-12.

6. R. Jones, C. Wykes, 1983. "Holographic and Speckle Interferometry", Cambridge University Press.

7. A. M. Maas, 1991. "Phase Shifting Speckle Interferometry", Ph. D. Thesis Techn. Universteit Delft.

8. K. Schindler, 1994. "Messung des Verformungszustandes aktiver Strukturen mit Hilfe integrierter Sensoren", Project-report, IKB, ETH-Zürich.

SESSION 3

Paper presented at the Second European Conf. on Smart Structures and Materials, Glasgow 1994, Session 3

ELECTRICAL POTENTIAL TECHNIQUES FOR DAMAGE SENSING IN COMPOSITE STRUCTURES

C Thiagarajan[1], I Sturland[2], D Tunnicliffe[2], P E Irving[1]

[1]Cranfield University, Cranfield, Beds.
[2] BAE Sowerby Research Centre, Filton, Bristol

(1) INTRODUCTION

Aircraft structures made of Carbon Fibre Reinforced Composites (CFRP) are susceptible to impact damage in service. If the damage is of sufficient size, strength and service durability of the structure are degraded. The size and location of the damage are only predictable in a statistical sense; leading to excessive conservatism in design strains. Statistical approaches (1) have been explored, but condition monitoring is increasingly seen as the way forward. Smart materials are an attractive route to condition monitoring, and in the past ten years there has been considerable work to develop optic fibre strain and damage sensing techniques for composites, together with similar work on compliance change, acoustic emission and acoustic injection techniques (2). All of these involve use of discrete sensors, manufactured integral with the composite laminate. Many of the difficulties associated with use of discrete sensors may be overcome by adoption of techniques which rely on changes in the physical properties of the composite as a consequence of damage. A prime candidate is the electrical resistance technique. This relies on changes in electrical resistance, or of potential distributions in the laminate to characterise the damage state.

(2) ELECTRICAL RESISTANCE TECHNIQUES OF DAMAGE SENSING

Previous work in this area (3-5) has exploited the technique as a laboratory tool for damage assessment during mechanical testing. Most commonly, the electrical resistance technique has been shown to detect fibre damage during tensile and fatigue testing, but there has also been work reporting its use to measure delamination crack growth rates. Use of the technique as a structural monitoring tool has been advocated (6-7).

The electrical conduction of unidirectional CFRP parallel to the fibres is due to current flow along the fibres. This can be modelled using the parallel resistance approach (5). The resistance of the composite R_C may be written as follows:

$$R_c = \frac{\rho_f L}{bdV_f} + R_e$$

Where ρ_f = fibre resistivity, V_f the volume fraction of unbroken fibres, L the length of specimen, b and d specimen width and thickness respectively, and R_e is the contact resistance. Fibre fractures, as shown in figure 1, will cause V_f to decrease hence increasing the sample resistance.

The conduction behaviour in the directions at 90° to the fibre orientation in a unidirectional laminate relies on fibre to fibre contact as shown in figure 2. The fibres are arranged randomly, and conduction occurs via continuous chains of carbon fibres arranged in random networks. Many of the chains are incomplete and there is no net conduction on these routes from one side of the laminate to the other. The number of complete chains is related to the volume fraction V_f of conducting fibres. Below a critical V_f, there will be no complete chains and conductivity falls rapidly to the level of the matrix. Achievement of complete conducting chains is called percolation, and has been studied extensively (4) for both conducting particles and conducting fibres in insulating matrices. For V_f values found in engineering composites (50-60%), percolation is always achieved. (8). Numerical models for transverse conduction via percolation have been developed (4) for hexagonal and for square arrays of carbon fibres, with random unoccupied sites in the lattice to

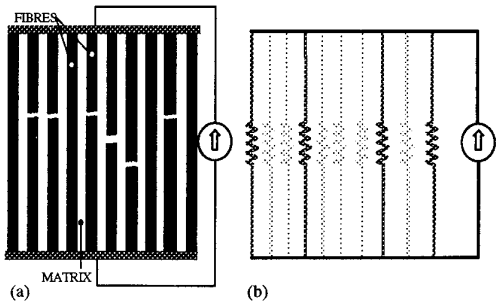

Fig.1. (a) Damage mechanism and (b) its electrical analogue (Fibre Breaks)

0-8194-1700-9/94/$6.00

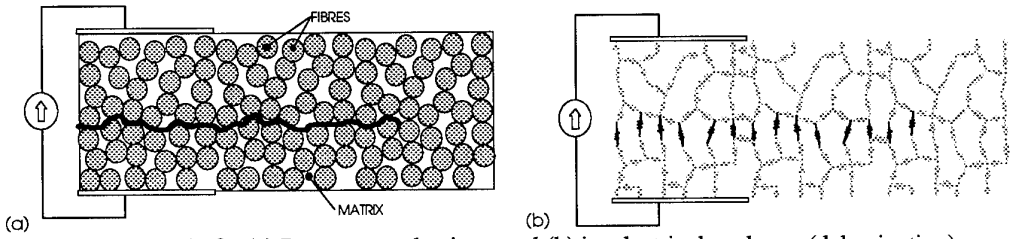

Fig.2. (a) Damage mechanisms and (b) its electrical analogue (delamination).

achieve the required fibre volume fraction. The lattice may be regarded as a network of resistors, and Kirchoffs laws may be solved iteratively to generate an effective resistance for the laminate. Figure 2 illustrates how matrix or delamination cracks can cause changes in the transverse conduction by cutting the resistive network. The models have been used to develop relationships between crack length and potential or resistance for use in delamination crack length measurement (4,8). In reality, a three dimensional model for current flow in these materials is required, as fibre to fibre contact is not uniform along the fibre length. Fibre contact occurs sporadically, as shown in figure 3, and conduction via percolation mechanisms is not adequately represented by 2-dimensional arrays. There will be many instances where conductive paths are not formed in a 2 dimensional slice, but will be formed in a three dimensional volume.

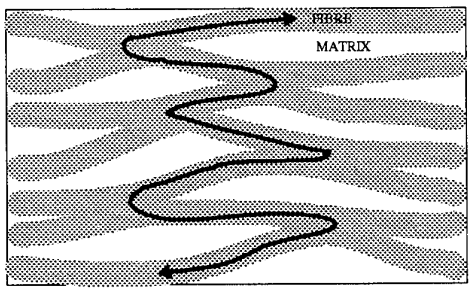

Fig.3. Transverse conduction due to fibre contacts

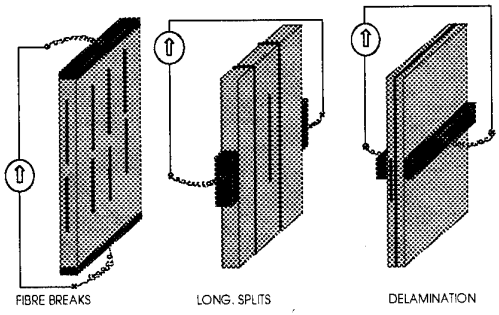

Fig.4. Damage mechanisms and electrode locations

2D models are useful for unidirectional material, damaged in ways for which a 2 dimensional model is an adequate representation. Real composite structures will consist of multidirectional laminates, in which the directional of electrical anisotropy will change in the through thickness direction. Such laminates will have complex failure modes such as fibre fracture, splits, delaminations and interface cracks between plies of different orientation. All of them reduce to the simple damage modes of fibre fracture, matrix cracking and inter ply cracking. Whether caused by impact, fatigue or any other damage mode, mechanical damage in cfrp can only consist of these mechanisms. All of them will influence potential distributions, providing the current flow is in a direction which can detect the anomalies. Current flowing in the fibres will be most sensitive to fibre breaks; delaminations and splits parallel to the fibre direction will require transverse current flow for their detection. Location of current introduction points is hence an important factor in determining damage sensitivity. Figure 4 shows the major damage mechanisms of cfrp and the electrode locations. For increased sensitivity to damage, the current flow should be perpendicular to the anticipated damage growth direction. For example if the current flows through the fibres in longitudinal direction will be sensitive to fibre breaks. Similarly longitudinal split growth will be easily detected if the current flows in the transverse direction. Electrode location could play a critical role in increasing the damage sensitivity of the technique. In the case of multiple damage mechanisms as found in real conditions, then changing the direction of current at different pairs of electrodes using a multiplexer would be necessary for complete characterisation of damage.

(3) ELECTRODE EFFECTS

Characterisation of damage using multiplexed systems will require detailed knowledge of electrode characteristics, contact resistance and models for current flow in composite samples. Even if the measurement technique records potential distribution rather than resistances, if more than one current input is used, then contact resistances must be either known or minimised. As part of a programme to investigate the electrical potential technique for damage sensing, a detailed study has been made of the resistance of contacts made using

a variety of techniques. Table I shows a selection of the techniques studied, together with relative values of contact resistance. Variations in resistance of up to a factor of 50 have been recorded. Many of these differences can be related to the efficiency of the electrode in electrically contacting all carbon fibres within its area, and the size of the laminate itself. The three dimensional nature of current flow in cfrp laminates also plays a role.

Because of fibre touching within the laminate, many of the non contacted fibres will play a role in current flow, providing the laminate is sufficiently long; anomalous conduction effects will occur at shorter laminate lengths, as individual fibres become isolated. This is demonstrated in figure 5 which shows the influence of sample length on the resistance of unidirectional cfrp parallel to the fibres. As laminate length is reduced to less than 200 mm, the relation between sample length and resistance becomes non linear. Between 200 mm and 50 mm the resistance increases slightly, prior to resuming a linear reduction. Further evidence of the role of fibre touching on conductivity is shown in figure 6 which illustrates the influence of sample length on the through thickness resistance. As the length is reduced, through thickness resistance is increased. Again, this may be explained by the isolation of fibres from the main conduction process as the length of the sample is reduced and regions of touching are eliminated.

(4) DETECTION OF FATIGUE DAMAGE

Fatigue testing of unidirectional specimens was carried out at various stress levels. The change in resistance of the unidirectional specimens with fatigue cycles is shown in Figure 7. Stepwise in crease in resistance was observed in specimens tested at stress level close to the ultimate tensile stress. At this stress level more fibre breaks are expected (10). The steps coincide with audible fibre breaks. It was observed that almost 40 to 80% of the increase in resistance occurs within 10 to 20% of life. At stress levels above 95% of static tensile strength, about 30-40% of the total eventual change in resistance had occurred by 10% of life. At stress levels below 95%, 60 to 80% of the eventual change had occurred by 10% of life. The result shows that there is a correlation between applied stress and the change in resistance. The resistance increases with increasing applied stress. It has been postulated by Barnard (10) that the number of fibre breaks will increase with applied stress. Hence it is expected that the change in resistance will be greater at higher stress levels. Fuwa et al (9) observed similar trends in acoustic emission counts with applied stress.

The change in resistance and of the stiffness with life of unidirectional specimen is shown in Figure 8. It clearly shows the correlation (correlation coefficient =0.97) between change in resistance and reduction in stiffness. As in the case of acoustic emission monitoring, the

Contact Preparation	Normalised Resistance
Mechanical Polish/Silver Epoxy	18.20
Saw cut/Silver Epoxy	13.84
Mechanical Polish/Cu. Coating	2.16
Mechanical Polish/Silver Paint	53.33

Table I. Influence of electrode type on normalised laminate resistance

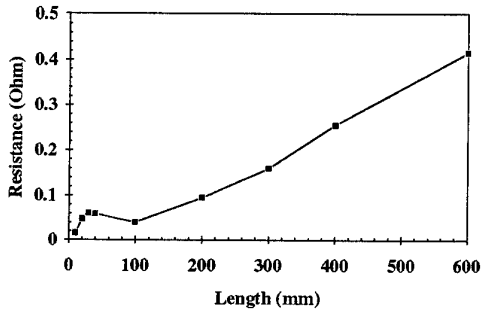

Fig.5. Dependence of longitudinal resistance on specimen length

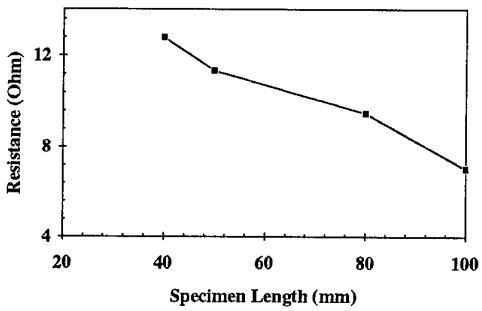

Fig.6. Dependence of transverse resistance on specimen length

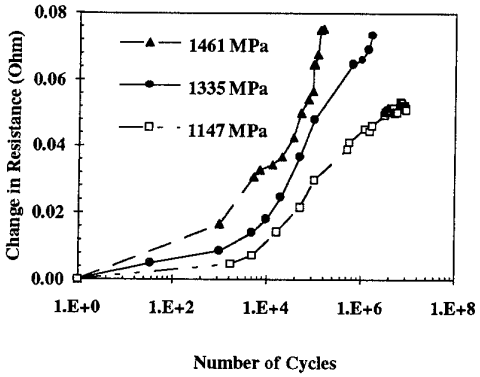

Fig.7. Dependence of resistance change on fatigue damage

electrical potential or resistance changes mirror those of the change in compliance. Initial cycling produces rapid changes in potential and sample compliance. The rate of change reduces after a few percent of life, and a pseudo plateau region is found. Further rapid changes ensue as final failure is approached. From the above results it is concluded that the major portion of damage due to fibre breaks occurs within 10% of total life. The rest of the life is used for propagation of other failure modes such as longitudinal splitting, not detectable by current parallel to the fibres, but detectable by the transverse configurations.

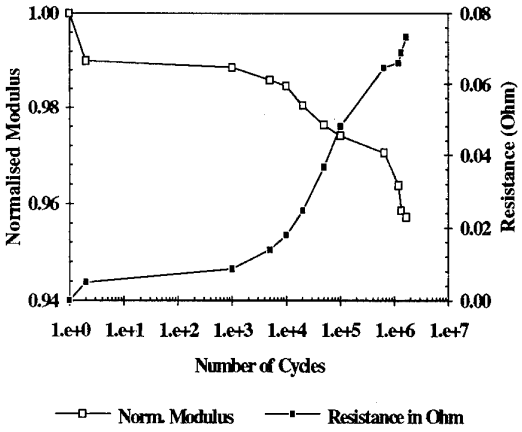

Fig.8. Fatigue damage and elastic modulus

(5) CONCLUSIONS

(a) Current flow in carbon fibre laminates is a complex three dimensional process in which fibre touching within the laminate plays a major role.
(b) Electrode type, area of contact and sample dimensions all influence the effective values of laminate resistance.
(c) Use of the electrical potential technique to monitor damage growth in fatigue of laminate samples, has shown that monitoring current flow parallel to the fibres is successful in detection of fibre breaks, but delamination and split growth parallel to the fibres are not detected. For the latter damage mechanisms, measurements perpendicular to the fibres are required.
(d) For detection of generalised damage in composites, a multiplexed system with current inputs in the three axes of orientation will be required.

ACKNOWLEDGEMENTS

The authors would like to acknowledge the financial support of the Indian Government and the Civil Aviation Authority, and British Aerospace for provision of laboratory facilities.

REFERENCES

(1) A J Rapoff, H D Dill, K B Sanger, " Certification of damage tolerant structure" Proceedings of 8th DOD/NASA/FAA conference on "*Fibrous composites in structural design*" (1990).
(2) Chr. Boller, R Dilger, "In flight aircraft structure health monitoring based on smart structures technology"; AGARD conference proceedings 531 "*Smart structures for aircraft and spacecraft*"; Lindau, Germany, Oct 1992.
(3) K Schulte, C H Baron; "Load and failure analysis of cfrp laminates by means of electrical resistivity measurements", Comp. Sci. & Tech. **36** (1989) 63-76.
(4) K Moriya, T Endo "A study of flaw detection method for cfrp composite laminates- the measurement of crack extension in cfrp laminates by the electrical potential method" Trans Jap Soc. Aero. Space Sci.; **32** (1990) 184-196.
(5) R Prabhakaran; "Damage assessment through electrical resistance measurements in graphite fibre reinforced composites", Exp. Tech. February (1990) 16-20.
(6) C Thiagarajan, P E Irving, "In Service Damage Monitoring techniques in polymer composites", Session 37, Aerotech 1994, Birmingham Jan (1994).
(7) N J Williamson, R M J Kemp, P T Curtis, "Development of self sensing smart composites using electrical resistance properties", paper 17, 6th Int. Conf. on fibre reinforced composites; FRC 94, Newcastle, (1994), pub Inst Mat. London (1994).
(8) Chr. Fischer, F J Arendts, "Electrical crack length measurement and the temperature dependence of the mode I fracture toughness of cfrp", Comp. Sci & Tech. **46** (1993) 319-323.
(9) M Fuwa, B Harris, A Bunsell; "Acoustic Emission during cyclic loading of carbon fibre reinforced plastics", J Phys. D: Appl. Phys. **8** (1975) 1460-1471.
(10) B M Barnard "Cumulative fatigue and life prediction of unidirectionally reinforced E glass epoxy composites" Ph D thesis Cranfield, 1986.

Paper presented at the Second European Conf. on Smart Structures and Materials, Glasgow 1994, Session 3

Applications of a New Solid-State Structural Health Monitoring Technology

L. D. Thompson and B. D. Westermo
Strain Monitor Systems, Inc.
San Diego, CA and Atlanta, GA, USA

Abstract

A new methodology has been developed for structural damage assessment and monitoring based on smart material sensors. The sensors transform to a ferromagnetic phase progressively as a function of strain. The solid-state phase transformation is useful in determining the local structural peak strains in monitored high stress sites. The technology is discussed with applications provided to illustrate the utility of the approach in addressing a range of engineering problems.

Introduction

Structural health monitoring of the aging infrastructure has become a major concern throughout the world. The desire to extend the lives of engineering structures beyond their intended design lifetimes has to be carefully weighed against the possible risks to public safety. Clearly, the economic reality is that most countries simply cannot afford to replace all of the structures which have reached the end of their respective design lives. With careful and cautious structural monitoring it is possible to safely extend useful service life well beyond the originally perceived limit.

A new solid-state technology has been developed to address this need. Strain Monitor Systems, Inc. (SMS) has commercialized an approach involving the site selective monitoring of the peak strains at key structural locations, in say, a bridge, highway overpass, or building. The attached sensor elements respond to structural straining by transforming from a nonferromagnetic parent phase to a ferromagnetic product phase. The ferromagnetic responses of the strategically positioned sensors can be correlated with the local peak strains. This information can be used in numerical models, either those generated as part of the original design or others more recently developed, to provide insight into structural stability and safety. The approach of monitoring the peak strains in key structural locations provides for an efficient methodology of assessing the damage throughout the structure, even at locations without sensors. In cases where the general cause of the damage is known, an analysis can provide a probabilistic estimate of the total damage and further progress. The inference of structural information from interstructural data relies on the detection of peak strains since the coupling is with structural instability as opposed to applied loads, although the stresses and applied forces are calculable as well. One important application of a structural health monitoring system is for post-earthquake damage assessment. Calculations of building response to earthquakes indicate that instrumenting as few as one-tenth of the potential damage locations can provide an overall confidence level of 95%, i.e., an overall estimate of error of 5% or less. A brief description of the technology follows with a section on applications to illustrate the widespread engineering appeal of the approach.

Strain Monitoring Technology

The structural health monitoring approach is based on the strain-dependent solid-state phase transformations experienced by a class of metastable alloy steels. The steels, known as TRIP (TRansformation Induced Plasticity) steels, were originally developed as ultra-high strength and fracture resistant materials about 30 years ago. [1, 2] TRIP steels are metastable and transform irreversibly during deformation from a nonferromagnetic, face-centered-cubic, austenitic parent phase to a ferromagnetic, body-centered-cubic, martensitic phase. The degree to which the transformation has occurred can be correlated with the strain necessary to trigger that extent of martensitic formation. TRIP steel sensor elements can therefore be used as mechanical "witnesses" to remember the peak structural strain in a monitored location even after all loads have been relaxed. [3-4]

0-8194-1700-9/94/$6.00

Figure 1 shows the stress-strain curves of two candidate sensor materials and their respective ferromagnetic responses as measured using a Hall effect sensor chip. The Hall chip provides an output voltage that increases as a function of the local increase in ferromagnetic material present in the gage section of a sensor element. Sensor elements in wire and ribbon form have been investigated and, in the simplest forms of application, the strain monitors have a configuration similar to that in Fig. 2 which shows a ribbon sensor element monitored by a Hall sensor.

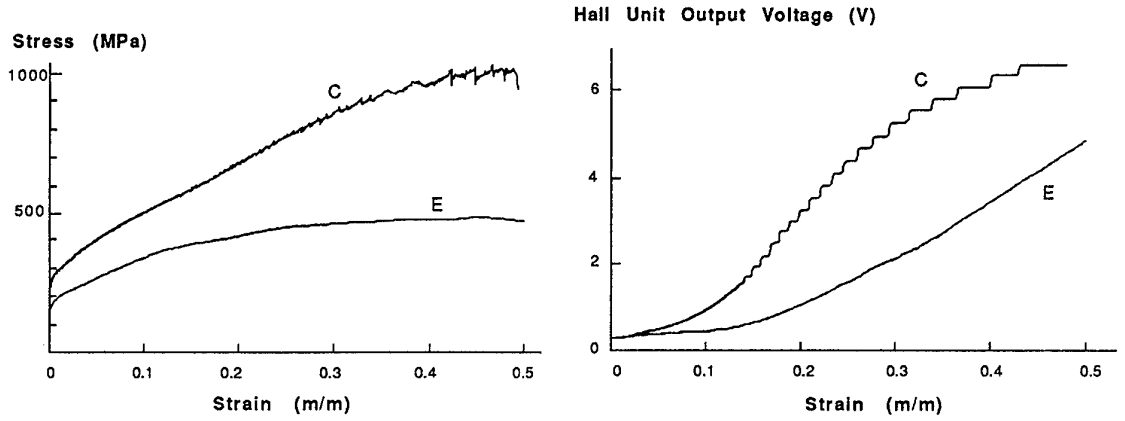

Figure 1. Stress and Hall Output vs. Strain for Two TRIP Alloys

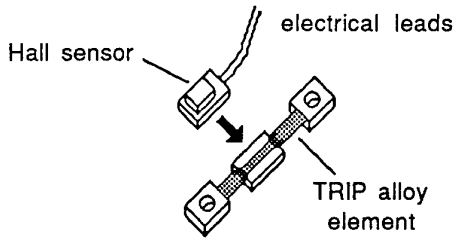

Figure 2. Schematic of Tensile Element Sensor

The monitors are strategically attached to the structure using attachment fixtures, the design of which depends on the specific geometrical constraints. The sensor elements can be fabricated with a convenient gage section length and geometry for the application. The detected structural strain can be significantly magnified by making the structural attachment span distance large as compared to the reduced sensor element gage length. The strain monitors behave entirely passively once affixed to the structure. Passive systems are ideal for the monitoring of earthquake-induced structural damage since the temperature is known and the strain rates can be accurately calculated from other data. The sensor material phase transformations are, to some extent, dependent on temperature and strain rates, as well as alloy chemistry and thermomechanical processing. The latter two parameters can be utilized to control the transformation response for a particular application as shown in Fig. 3. The incubation strain can be adjusted to a specific value or eliminated altogether depending on the needs. The sensitivity, i.e., the ferromagnetic response per unit strain, of the sensor material is determined by the slope of the transformation curve. The use of a sensor element prestrain once

the monitor is attached to the structure ensures that the element is functioning properly and that the optimum sensitivity in response is obtained.

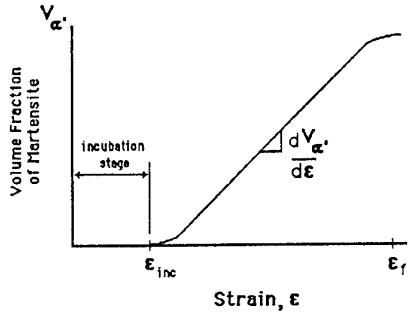

Figure 3. Volume Fraction of Martensite vs. Strain Behavior

SMS structural health monitoring systems have been developed for various applications along the logic illustrated in Table I. Smart systems are entirely passive and would be used in applications where wide variations in temperature and strain rate would not be expected, for example in mining structures. Smarter systems are semi-active and would be applied in situations where the range of temperature and strain rate are expected to vary significantly, for example certain bridges and highway overpasses. The smartest systems are fully active and can be integrated with real time ancillary safety systems which are set to be activated at a predetermined critical level of structural deformation, for example in a bridge equipped with a barricade designed to lower and stop traffic in the event of excessive deformation. The development of more sophisticated networked bridge monitoring systems with options regarding data acquisition, e.g., data telemetry and central station telemonitoring, has been the recent design focus.

Table I. SMS Smart Material Sensor Structural Health Monitoring Systems Description.

Operation Mode	Applications	Description
Passive (smart)	• Fairly constant T • Low strain rates • Periodically inspected structures • Provides indication of structural stability	• Array of gages or monitors • Interrogated during inspections
Semi-active (smarter)	• T, strain rate variations as f(t) • Data acquisition to be used for damage accumulation models	• Array of monitors • Data acquisition hardware for T and strain rate acquisitions • Low power requirements
Fully Active (smartest)	• Systems coupled with networking • Activation of secondary safety systems • Data transmission requirements	• Array of monitors • Data acquisition system • Secondary safety • Data transmission systems

Applications

The sensor materials were originally developed as structural materials and can be used for engineering components. Sensors and monitoring systems can be retrofitted to existing structures or incorporated as integral parts of new structures depending on the monitoring

requirements and level of sophistication desired. Table II lists some of the applications of the technology currently being investigated to illustrate some of these scenarios.

Table II. Examples of SMS Structural Health Monitoring Applications.

Application/Sponsor	Concern	Comments
1. I-95 Savannah Riv. Bridge/GA, US DOT	Excessive straining due to heavy truck crossings	100 μm/m strains detected
2. Mine safety sys./ U.S. Dept. of Interior Bureau of Mines	Delamination of mine roof rock strata and mine safety	Strain sensing structures; roof bolts, braided high-strength cable.
3. C-130 wing truss crack detection sys./ U.S. Air Force	Develop remote crack monitoring system to decrease inspection time	Conceptual design completed/ prototype construction/testing
4. Building /bridge safety systems/ NSF	Develop systems for post-earthquake damage assessment	Phase I design studies initiated/ conceptual designs completed
5. ARPA SBIR/ bridge safety	Design an active 9-bridge monitoring system	Phase II program will implement & evaluate Phase I design study

The monitoring approach was initially applied to detect and monitor overload strains associated with the transport of large reinforced concrete structures across the Interstate 95 Savannah River Bridge in Savannah, Georgia. The tensile strains in the lower flange of a steel I-beam and in the weld zone of plate web stiffeners were measured. Strains of 100-167 μm/m were detected corresponding to elastic stresses in the steel I-beam flange of 20-35 MPa, well under the elastic limit. The U. S. Dept. of the Interior, Bureau of Mines, is funding the development of passive monitoring systems to safeguard mining structures and to warn of structural instability. Mining roof bolts and cables are representative structures which will employ TRIP steels as the materials. The National Science Foundation is sponsoring the development of semi-active and fully active systems to monitor the safety of bridges and other civil engineering structures. The U. S. Air Force is funding the development of a remote crack detection system for the C-130 Hercules cargo aircraft wing truss assembly. In the latter application the inspection time required to detect crack initiation in the wing truss will be reduced from 200 person-hours to a matter of minutes by utilizing a semi-active monitoring system. The Air Force is also funding a feasibility study, in conjunction with E-Systems, Inc. of Dallas, TX, to investigate sensor embedment in advanced composite materials.

References

1. V. F. Zackay, E. R. Parker, D. Fahr and R. Busch, "The Enhancement of Ductility in High-Strength Steels," Trans. ASM, Vol. 60, 1967, pp. 252-259.
2. E. R. Parker and V. F. Zackay, "Strong and Ductile Steels," Scientific American, Vol. 219, 1968, pp. 36-45.
3. B. Westermo and L. Thompson, "A New Testing and Evaluation Technology for Damage Assessment and Residual Life Estimation in Aircraft Structures," Proceedings of the 14th Aerospace Testing Seminar, pp. 5-10, The Institute of Environmental Sciences and The Aerospace Corporation, Manhatten Beach, CA, 1993.
4. L. Thompson and B. Westermo, "A New Strain Measurement Technology for Material Damage Assessment," presented and published in proceedings of the North American Smart Materials and Structures Conference, Orlando, FL, Feb. 1994.

Paper presented at the Second European Conf. on Smart Structures and Materials, Glasgow 1994, Session 3

SELF-SENSING COMPOSITES FOR SMART DAMAGE DETECTION USING ELECTRICAL PROPERTIES

Dr Martin Kemp

Structural Materials Centre
Defence Research Agency
Farnborough
Hants, GU14 6TD

ABSTRACT

The concept is developed of a 'self-sensing' composite to enable 'Smart' damage detection. This approach involves monitoring the damage-induced change in a global physical property of a composite rather than the use of local sensors. The composite as a whole therefore effectively becomes the 'sensor'. Envisaged benefits of such an approach are reduced parasitic weight and increased reliability.
The concept has been examined in terms of monitoring the changes in electrical resitivity of a carbon fibre/epoxy composite due to impact damage. Preliminary results have shown that damage from a 6 Joule impact can be detected and located in a 2 mm thick laminate by an array of voltage sensing, point contacts. Changes in potential distribution have been interpolated as a potential difference surface to give a visual representation of the damage site. The inherent simplicity of the system promises a reliable technique for structural health monitoring.

INTRODUCTION

Carbon fibre/epoxy composite materials are used widely in aerospace applications due to their high specific strength and stiffness properties. Composites are highly damage tolerant with excellent crashworthiness, but damage can be sustained from low velocity impacts. In aircraft, impacts sustained from dropped tools, runway debris, and ground handling vehicles, can cause sub-surface 'barely visible impact damage' (BVID). By implication, the damage is difficult to detect by visual surface examination and must be located by detailed non-destructive examination during the maintenance inspection. This paper examines the concept of a 'self-sensing' composite skin which facilitates remote detection and location of damage. Composites have an inherent advantage over monolithic materials in that added functionality that can be 'built-in' to composite structures. The potential benefits of an in-flight health monitoring system have enormous implications in terms of reduced operating costs due to minimised down-time for structural inspection; increased safety due to improved damage detection; and reduced design safety factors allowing lighter, more efficient and lower-cost structures.

The application of 'Smart' concepts to damage monitoring has received widespread attention for a number of years, and laboratory techniques have been developed utilising optical fibres, piezo-ceramic and various other sensors which can detect damage. However, many of these techniques require complex and sensitive signal analysis equipment is not a feasible option for airborne use where parasitic weight and reliability are critical factors. In order to satisfy these requirements, the 'self-sensing' solution investigated here monitors damage-induced changes in a global physical property, ie electrical resistance. The aim is to reduce the number and complexity of the sensors. It has been shown that damage from static and dynamic loading has an effect on resistivity properties in uni-directional and mulit-directional composites [1,2,3,4]. These studies showed that the damage mechanism of fibre fracture had the greatest effect on the change in resistivity. The use of an alternating current introduces reactive capactitive and inductive components at high frequencies. These effects have been analysed in order to detect delaminations arising from impact damage [5]. Previous work [6] has shown that low frequency a.c. (1kHz) produces similar results to a d.c current with improvements in stability.

This paper presents preliminary work on a technique to detect impact damage using an array of sensing wires with interpolation to generate a damage map.

0-8194-1700-9/94/$6.00

EXPERIMENTAL DETAILS

The material used was a 16-ply carbon fibre/epoxy laminate of T800H-924C with a $[(0,90)_4]_S$ lay-up. The effects of a central sawcut were investigated using a panel of dimensions 300mm x 100mm with current input at the ends and 2 parallel rows of voltage sensing wires along the length of the specimen. The effects of multiple central impacts were investigated on a panel 300mm x 300mm having a 6x6 array of sensing wires as described elsewhere [6]. One face of each panel was lightly grit blasted to allow electrical contact to the carbon fibres. Sensing wires were attached on 1 face using silver dag and a protective coating of epoxy adhesive. Current input was through copper tags centrally positioned at opposite edges of the panel.

A 1 kHz alternating current was applied from an unamplified signal generator. The sensing wire voltages were monitored by means of a PC-based data logger featuring 12-bit sensitivity, independent variable gain controls for each input and a sampling rate of 50 kHz. A ground reference was taken from a current supply wire. For each set of data, 100,000 readings were captured and averaged from each sensing wire, and gain settings were continuously optimised by the software for each input. The ambient temperature was maintained at 20 ± 2 ^{o}C during measurements.

A sawcut slot was introduced in the 300 x 100mm panel from a central 1mm diameter drilled hole. Impact damage was introduced centrally in the 300 x 300mm panel by repeated impacts on the non-instrumented face. An instrumented falling weight impact machine was used with a mass of 2 kg and a hemispherical impactor tup of diameter 10mm. The impact energy was increased in 2 Joule steps from 2 to 8 Joules. The panel was supported on an annular anvil 100 mm internal diameter, 140 mm outside diameter, and was left unclamped to avoid damaging the surface wires.

RESULTS

The effect of a drilled hole and progressively increased slot length are shown in Fig 1 and Fig 2 respectively. The voltage difference results were averaged from the 2 rows of sensing points and computed as the difference between the initial and the damaged panel voltage readings. The effect of sensing point spacing is indicated in Fig 2 as central sensing points were omitted from the interpolated plot.

The effect of increasing impact damage is shown in Fig 3. For each data set, the maximum and minimum potential readings were found. These values were used to map the data set into the range 0 to 1, which normalised the data sets with respect to each other. The data sets from the undamaged panel were subtracted from the those of the damaged panel. This method allowed visualisation of the small changes in potential and removed any effects of drift in the supply current. The 36-point data sets had a spline-fitted surface applied to generate a finer grid, necessary to allow smooth contouring. It should be noted that this introduced considerable smoothing of the data presented. The plots of this data will be referred to as 'difference plots'.

DISCUSSION

This work and results reported previously [6] have shown that in a cross-ply laminate the in-plane current flow is essentially isotropic. Moriya [5] has explained this effect in terms of current flow between fibres and tows at discrete contact points. An estimate of the 'global' resistivity from the present tests indicated a value of around 75 μΩ.m. This is in general agreement with previously reported values of 25 - 150 μΩ.m [7]. The use of an a.c. supply rather than d.c. eliminated errors arising from thermal e.m.f's and reduced quantisation errors. Possible supply drift problems were obviated by the rapid sampling rate and the large number of averaged data readings.

The effect of fibre breakage in the form of a 1 mm hole produced a marked effect on the voltage distribution (Fig 1). Increasing the size of the slot produced an increase in the perturbation in the plot which implies that the detection limit is a function of damage level and sensing wire spacing. Increasing the sensing wire spacing for a fixed slot length is shown in Fig 2 where the sensing wire spacing either side of the slot was increased. The perturbation reduced as the spacing was increased, and a 1mm hole was not detected above a spacing of 100mm. This indicates that for fibre breakage or perforation damage, the sensitivity of this technique is high.

The effect of an increasing level of impact damage produced a detectable change in the potential distribution as shown in Figs 3a and 3b. The damage sustained after the 6 J and 8 J impacts was fairly severe, comprising fibre fracture, splitting and delamination, and this damage was readily detectable. Although it is not clear which component of the damage was responsible for the change, fibre fracture is the obvious candidate. At lower energy levels where delaminations predominated, the potential distribution did not appear to correlate with the damage site, although did it cause perturbations (Fig 3a). The cause of these perturbations was likely to be a reduction in the number of electrical conduction points between fibres due to ply separation (delamination), and it is unlikely that effects due to reactive components were responsible at the supply frequency used.

By superimposing a C-scan of the damage site onto the difference plot (Fig 4), a clear correlation is evident. Data processing and visualisation techniques can enhance the data analysis as shown by the 3-dimensional representation in Fig 5. The technique has therefore been shown to locate impact damage, and further work is required to ascertain the extent and type of damage.
The 'Smart' self-sensing composite using the electrical conductivity properties of carbon fibre is an attractive concept. A low voltage power supply is available on an aircraft, and if the number of sensing points is limited then the parasitic weight of the wires can be minimal. Data analysis can be performed on-board and the system is inherently rugged and hence reliable.

CONCLUSIONS

The feasibility of using changes in electrical potential to detect impact damage in a carbon fibre reinforced epoxy composite has been assessed. Damage in the form of a 1mm drilled hole was readily detected and the results indicated that a limiting voltage sensing wire spacing of ~100mm would detect this defect. A sequence of impacts of increasing energies (2, 4, 6 and 8 Joules), were performed on the same site on a 16-ply test panel. A 36-wire sensing grid detected the location of a 6 Joule impact site. This preliminary study has indicated that this method overcomes problems inherent in more complex Smart damage detection systems and is potentially applicable to aerospace structural health monitoring.

REFERENCES

1 Schulte K. Baron Ch. Comp. Sci. & Technol. **36** (1989) 63-76
2 Thiagarajan C. Irving P.E. 'Proc I. Mech. Eng. Conf. 'Aerotech '94'.
3 Prabhakaran R. Exp.Tech. Feb 1990 16-20
4 Wolfinger C. Drechsler K. Arendts F.J. Proc. Int Conf. on Advanced Materials, Nordwijk, Holland, 22-25 March 1994
5 Moriya K. Endo T. Trans. Japan Soc for Aero and Space Sci. **32**, Feb (1990) 184-196
6 Williamson N.J, Kemp R.M.J, Curtis P.T, Proc. Sixth Int. Conf. on Fibre Reinforced Composites, Newcastle, UK, March 1994, Paper 17. Institute of Materials.
7 Smithers B W, 'The electrical properties of carbon fibre composites', Culham Laboratory report (1981)

© British Crown Copyright 1994/DRA
Published with the permission of the Controller of Her Britannic Majesty's Stationery Office.

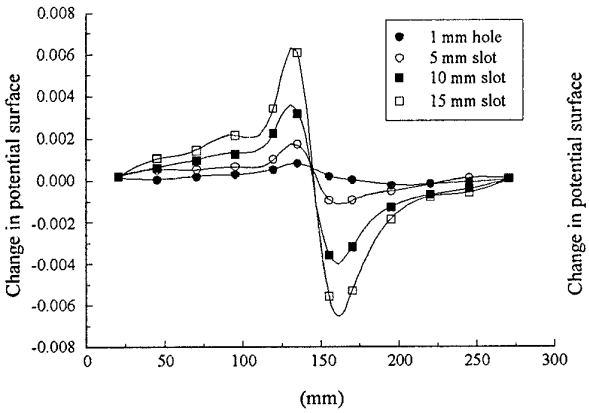

Figure 1 Change in potential along centre-line with increasing slot length

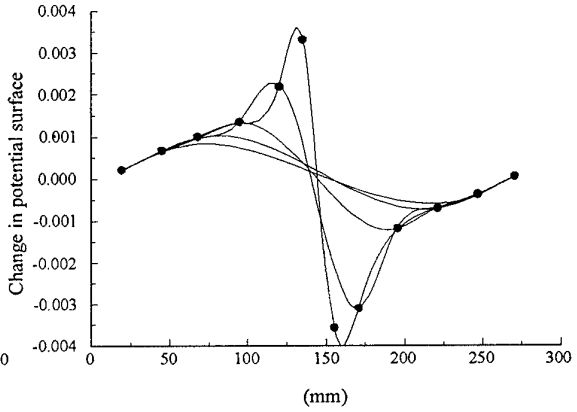

Figure 2 Change in profile with reduced data sets for 10mm slot

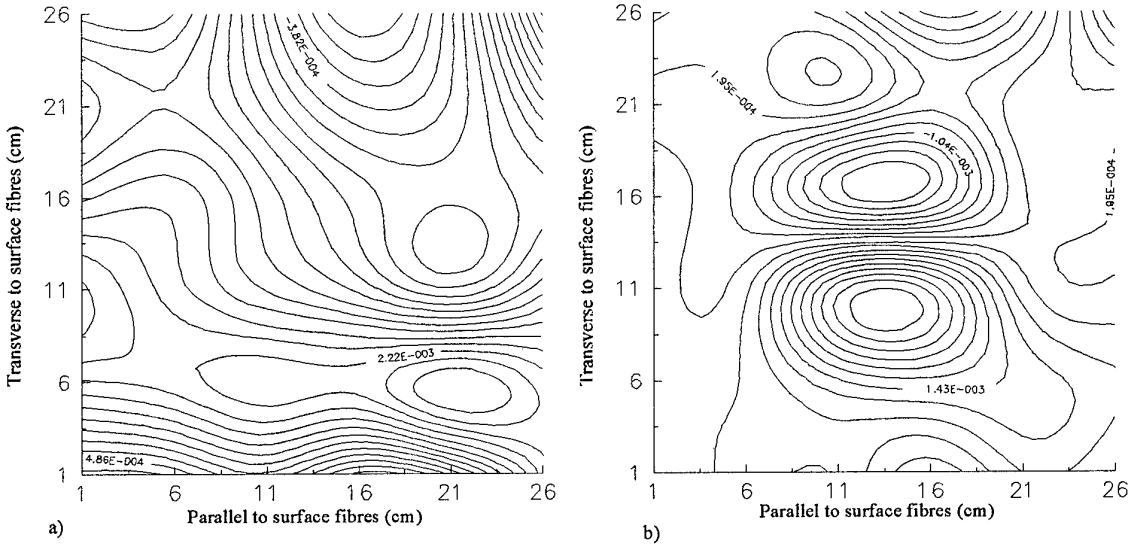

Figure 3 Effect of increasing impact damage on contour 'difference plot'. a) After 2J impact b) After 6J

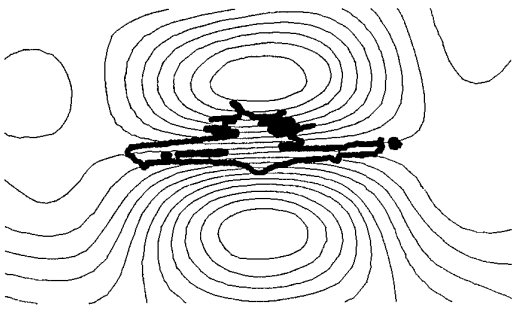

Figure 4 Outline of C-Scan overlaid on 'difference plot'.

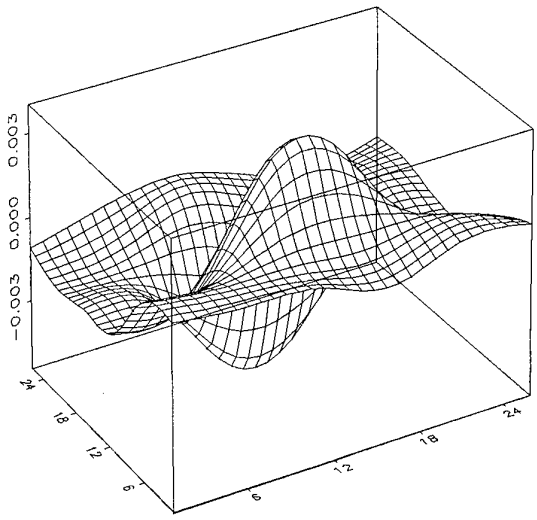

Figure 5 Surface 'difference plot' of post 8 J impact at 1kHz.

MONITORING VIBRATION OF SANDWICH PLATES AND DELAMINATION DETECTION WITH FIBRE OPTIC SENSORS.

Alf Egil Jensen[1], Helge Storøy[2], Fridtjov Irgens[2], Ole Johan Løkberg[2] and Gunnar Wang[1].

[1]Norwegian Defence Research Establishment, Div. for Electronics, P.O Box 25, N-2007 Kjeller, Norway.
[2]Norwegian Institute of Technology, University of Trondheim, 7034 Trondheim, Norway.

ABSTRACT.

The experimental feasibility study using fibre optic sensors, strain gauges and speckleinterferometry (ESPI), indicates that delamination in FRP-sandwich structures can be detected by monitoring changes in the vibrational resonance frequencies. The frequencies are also determined analytically.

1 INTRODUCTION

In the ongoing development of Smart Skins it is of interest to find areas where this technology could be of practical use in the future. One application would be monitoring of structural parameters in high speed marine vehicles. These vessels are made of composite materials, such as fibre reinforced plastics (FRP) and various sandwich structures. A problem that may occur in these vessels is delamination between the glass fibre laminas which the hull are being build of.

This paper presents a study of the possibility of using the changes in the natural frequencies of vibration in sandwich plates due to delamination, as key parameters in an NDT system for detecting delamination in sandwich structures. The natural frequencies were measured by both strain gauges and fibre optic sensors (Polarimetric sensors), and a Electronic Speckle Pattern Interferometry (ESPI) instrument was used to investigate the normal modes of vibration in the plates /1/. The purpose of using both strain gauges and fibre optic sensors was to see if the measurements from the two different techniques were in good agreement with each other. To avoid some of the difficulties by embedding optical fibres in the composite structure, the sensor fibres and the strain gauges were adhered on the outside of the skin of the sandwich plates. For practical use it is of interest to have a mathematical model that are capable of calculating the natural frequencies and the normal modes of vibration in sandwich structures. Such a model will make it easier to optimise where to attach the optical fibre to get maximum response. With relation to this, some results from a theoretical investigation of the mechanical vibrations in sandwich plates will be presented. In the investigation the general equations of vibration in a sandwich plate, based on J.M. Whitney's shear deformation theory /2/, are derived. The equations include the effects of shear deformation and rotatory inertia, and the implementation of the two effects follow Timoshenko /3/. As a part in a development of a fully theoretical model for the mechanical vibration in sandwich structures, which also must take temperature effects and damping properties of the material into consideration, it was of interest to investigate what influence the effects of shear deformation and rotatory inertia have on the natural frequencies of a sandwich plate. And specially to see if the effects of rotatory inertia could be neglected. To obtain analytical solutions from the general equations of vibration a plate subjected to cylindrical bending and simply supported along two opposite edges was chosen.

The ESPI instrument that were used could give maps of the phases and amplitudes of the normal modes of vibration and the natural frequency, and the test objects can be several square meters. The maps presented in this paper are photos using a scale from black to white, where black is representing zero amplitude and phase. Areas in the map that have the same grey-tone have either the same amplitude or the same phase. See figure 7a and 7b. The instrument was used for two reasons. The main reason was to find the lines and the points on the plate with zero amplitude for the different vibration modes. This was done to avoid attaching the strain gauges and sensor fibre on one of these lines and points. Because with such an attachment the strain gauges and fibre sensors will not measure the natural frequencies belonging to these modes. The second reason was to see if the delamination caused a change in the vibration modes compared with a plate without failures.

0-8194-1700-9/94/$6.00

2 EXPERIMENTAL SET-UP

Experiments were carried out on two rectangular sandwich plates, where one plate had a delamination covering 30-35 % of the plate area. The plates were simply supported along the two shortest edges and free along the other two. Figure 1 shows the geometry of the plates and where the delamination was located.

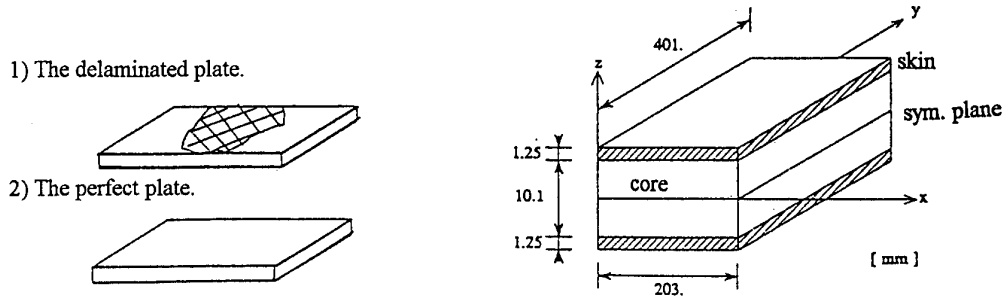

Figure 1 The geometry of the test plates and the location of the delamination.

The strain gauges and the polarimetric sensors were adhered to the plates by low viscosity cyanoacrylate. The locations of the strain sensors are shown in figure 2. The positioning are based on an investigation of the different vibration modes found by using the ESPI instrument . The instrument was a RETRA 1000 made by Conspec, Norway. By avoiding the lines and the points with zero amplitude, the positions of attachment are optimised to give the best response with relation to the first three or four vibration modes of the plate. The strain gauges system was coupled in a conventional Whetstone half bridge with two strain gauges attached at the opposite side of each other. The fibre sensor was a polarimetric sensor /4/, where a single birefringent fibre forms the sensing element. Light is launched in both polarisation modes of the fibre and since the fibre is birefringent, a phase difference will occur between the two components. This phase difference will vary if the fibre is strained, both because the light has to travel a longer distance in the birefringent medium, but even more for our bow-tie fibre because of the increased radial asymmetric pressure on the fibre core. This phase difference is then converted to an amplitude signal through an analyser oriented at 45 degrees with respect to one of the eigenmodes. The fibre optic system is shown in figure 3.

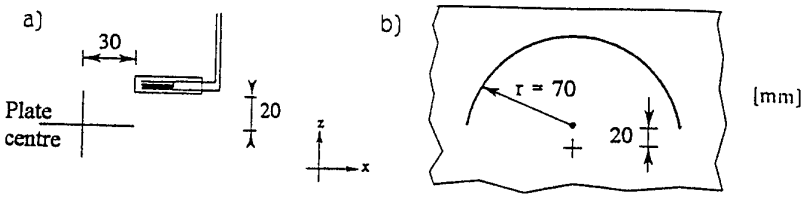

Figure 2. The position were the strain gauges and the polarimetric sensor fibre are adhered.

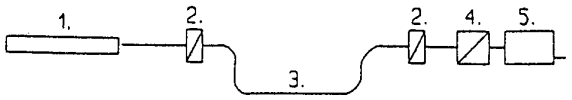

1. Pigtail laser
2. FC-connector
3. Sensor fibre
4. polarisator
5. Detector

Figure 3. The fibre optic system.

The light source was a pigtailed single mode diode laser at 780 nm (Sharp LT 027) and the sensor fibres were a York bow-tie fibre (HB 750). The signals from the detector were analysed using a Standford Research Systems, SR 770 spectrum analyser, which transforms the signals to frequency spectra of the vibration of the plate (See figure 5b). The vibrations of the plates were induced by dropping a coin from a height of approximately 5 cm.

3 RESULTS.

The vibration frequencies found with the strain gauges and the polarimetric sensor are in good agreement, see the figures 5a and 5b. The difference in noise level and peaks seen in the figures may partly be explained from the different nature of the two measurement techniques. The strain gauges give point measurements, while the polarimetric sensor give average measurements over the attachment length of the sensor fibre. The strain gauges will therefore be more sensitive to local disturbances.

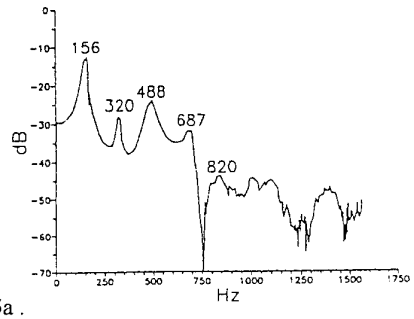

Fig. 5a .

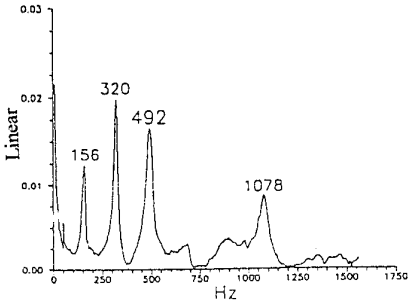

Fig. 5b.

The frequency spectra from measurements done by a) strain gauges and b) a polarimetric sensor. These measurements are taken from a plate that did not contain any failures.

As stated in the introduction, the purpose of the work is to see if a delamination in a sandwich plate caused a change in the natural frequencies of vibration. Since a delamination reduces the stiffness of a sandwich plate, a change in the natural frequencies would be expected. Figure 5b shows a frequency spectrum for a plate without a delamination, while figure 6 shows a frequency spectrum of a plate with a 30-35 % delamination in one of the skins. The dB-scale in figure 6 was chosen because the fundamental frequency at 156 Hz was very dominant, compared with the other peak values. A comparisation between the natural frequency of equal vibration modes revealed that, except from the fundamental mode the values of the natural frequency had been reduced due to delamination. The amount of reduction is also increasing for higher order of vibration modes. The second mode is reduced from 320 Hz to 309 Hz, while the third mode is reduced from 492 Hz to 406 Hz. Because the peak levels are decreasing with higher order vibration modes, delamination should be detected by using the higher order vibration modes that have a significant change in natural frequency value combined with a good peak level.

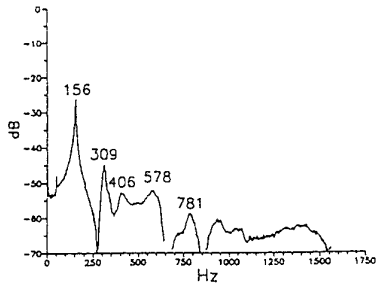

Figure 6. The frequency spectrum from measurements done by a polarimetric sensor on a plate having a 30-35 % delamination.

Figure 7a and figure 7b are showing photos of an identical vibration mode. This can be seen from the two phase maps which are almost identical to each other. From the amplitude map of the vibration mode in figure 7b, the delamination is clearly seen as a black spot down at the middle of the map. The line of zero amplitude at the right is also following the edge of the delamination. The natural frequency of vibration belonging to this vibration mode is reduced due to a delamination from 926 Hz to 747 Hz.

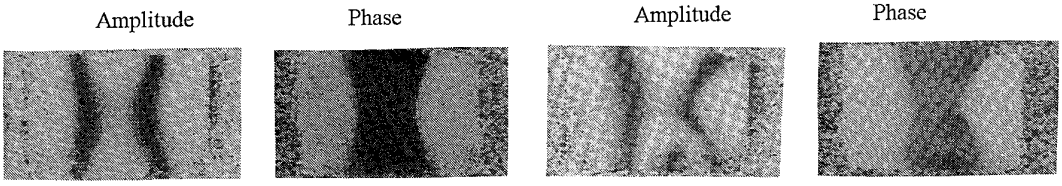

Fig. 7a. Fig. 7b.

Amplitude and phase maps for the same vibration mode in a) a perfect plate and b) a plate that contains a 30-35 % delamination in the skin.

From analytical solutions of the natural frequencies of vibration the first and third natural frequency were calculated. The geometrical values that were needed for the calculations are shown in figure 1. The two natural frequencies were calculated in three different ways. In the first case both the effects of shear deformation and rotatory inertia were taken into account, then only the effects of rotatory inertia was neglected and in the last case both effects were neglected. The calculated natural frequencies of vibration are shown in table 1 /5/.

Table 1.	First natural frequency.	Third natural frequency.
Both the effects of shear deformation and rotatory inertia are taken into account.	156 Hz	475 Hz
Only the effects of rotatory inertia are neglected.	156 Hz	475 Hz
Both the effects of shear deformation and rotatory inertia are neglected	180 Hz	720 Hz
Measured natural frequencies of vibration	156 Hz	485-495 Hz

From the frequencies in table 1 it is clearly seen that the effects of rotatory inertia are neglect able, and that the effects of shear deformation always have to be taken into account.

4 CONCLUSION.

* The natural frequencies of vibration in a sandwich plate, except for the fundamental frequency, are reduced due to a delamination in one of the skins. The frequency values for higher order vibration modes may then be used as key-parameters in a system for detecting delamination in sandwich plates. Further work with more realistic size sandwich structures have to be made.

* A SEPI instrument is well suited for monitoring vibration modes and where the delaminations are located in a sandwich structure.

* The results from the existing general equations of vibration in a sandwich plate was very promising, but to get a complete mathematical model of the mechanical vibration of a sandwich structure, the effects of temperature fluctuations and the damping properties of the material has to be included

5 LITERATURE.

/1/ Løkberg O.J. ESPI-The Ultimate Tool For Vibration Holographic Analysis?. J. Acoustic Soc. of America. vol. 75. 1783 - 1791. (1984).

/2/ Whitney J.M. Structural Analysis of Laminated Anisotropic Plates. Technomic Publishing Company, Inc. Pennsylvania. (1987).

/3/ Timoshenko S. Vibration Problems in Engineering, 3rd edition. D. Van Nostrand Company, Inc. New York. (1955).

/4/ Storøy H. Fibre Optic Strain Sensors for Smart Skins. Thesis at The Norwegian Institute of Technology, Trondheim. (1992).

/5/ Jensen A.E. Theoretical and experimental investigation of normal modes of vibration in sandwich plates. Thesis at The Norwegian Institute of Technology, Trondheim. (1993).

ACKNOWLEDGEMENT.

This paper is a part of a finale thesis of a Master of Science Degree at Norwegian Institute of Technology, University of Trondheim, Norway, 1993. The work was done with support from the Norwegian Defence Research Establishment (NDRE).

Paper presented at the Second European Conf. on Smart Structures and Materials, Glasgow 1994, Session 3

FIBER SENSORS FOR MONITORING STRUCTURAL STRAIN AND CRACKS

Karl F. Voss and Keith H. Wanser

Department of Physics, California State University Fullerton
Fullerton, California 92634, U.S.A.

Abstract: Recent structural failure and damage associated with earthquakes and pipeline failures have underscored the need for structural integrity monitoring systems using distributed fiber optic sensors. Such sensors must be low-cost, easily installed on new and existing structures, allow rapid assessment of structural integrity, and be capable of surviving and sensing large displacements associated with cracks and deflections in structural members. Experimental results for multimode fiber crack detection sensors based on the orientation angle approach are reported for both longitudinal and transverse crack displacements. In addition, we report results on a novel all-fiber sensor capable of sensing sub-millimeter cracks while surviving and sensing larger than 100% strains and cm level displacements.

1. Introduction: After the recent (1994) earthquake in Northridge California, building inspectors found cracked joints between beams and columns in at least 50 steel-frame buildings. Although no steel-frame buildings collapsed during the quake, the fractured joints have weakened some structures, reducing their safety in future shocks[1]. The large number of structures with damage and the resulting requirements for building inspections prevented many people from returning to homes and places of employment for a considerable period of time. Freeway bridge collapses caused severe traffic problems for more than two months following the quake. The extent of cumulative earthquake structural damage is largely unknown in areas inaccessible to inspection.

Pipeline failures can also have disastrous consequences. The 1992 San Diego California underwater sewer pipe failure[2] was an example of an economic, health, and environmental disaster that could have been avoided had a distributed fiber optic pipeline monitoring system been in place. This pipeline disaster caused approximately 180 million gallons a day of partially treated sewage to be dumped into the ocean less than three-quarters of a mile off shore of Point Loma in shallow water. Joints dislodged in 19 of the 25 foot long sections of 9 foot diameter concrete pipe, each weighing 30 tons. The disaster was blamed on a settling ocean floor and resultant pipeline sag. The repair costs alone were estimated at $10,000,000. In addition, there was a large economic loss to the local fishing industry, tourism, and severe environmental and health hazards. A similar underwater sewage pipeline extending from Hilo, Hawaii broke in 1987.

Many fiber optic sensors have been developed for sensing strain and displacement. Strain sensitivity levels below 1 μstrain have been achieved in interferometric, Bragg grating, and microbend based sensors[3,4], but unfortunately these devices are generally not able to sense strains larger than ~1% due to elastic limitations of fused silica. Hybrid fiber devices have been developed which sense large displacements but are not suitable for highly multiplexed structural monitoring applications where low-cost all-fiber devices are desirable. It is clear that sensors capable of monitoring cracks and crack growth must be able to sense local strains that are much larger than elastic limits of structural materials or brittle materials such as fused silica. A new type of fiber strain and crack monitoring sensor capable of covering reasonably large areas and with rapid, remote passive interrogation is required to solve structural monitoring problems such as those just described.

2. Kink Loss and Crack Detection with Multimode Fibers: Consider the detection of localized cracks by attaching an optical fiber to a metal (or other material) structure in a region of high stress concentration where cracks are likely or known to occur. Examples of such areas are numerous, and this is an important application for a fiber optic distributed sensing system with the capability of a large number of sensing regions. Statements like "a bridge may fail because a crack develops in a steel girder" and "the best systems would have to find small structural flaws like a hairline crack in a tension

0-8194-1700-9/94/$6.00

flange"[5], point out the need for a distributed fiber sensor system with millimeter or less crack resolution detection capability. On the other hand, a strain and crack monitoring system should be able to withstand large crack displacements and strains associated with cumulative structural damage. This requires new types of fiber strain sensors to be developed in order to respond to this range of structural monitoring concerns.

The first localized crack detection study using optical fibers and optical time domain reflectometry (OTDR) was performed by Vishlizki and Roberts[6], who pioneered the orientation angle approach and studied longitudinal crack separation. The method essentially induces a double kink type of deformation of the fiber axis as shown in fig. 1 a-b. We have extended their work by fabrication of a crack simulation test fixture which allows more rapid, repeatable, and controlled experiments to be performed[7]. Two micropositioners control movement both parallel and perpendicular to the line of separation, thus allowing study of shear effects as shown in fig. 1 c.

In spite of all the previous work on microbending loss in optical fibers, the theories all have several shortcomings when applied to practical sensors based on multimode fiber[7]. The most fundamental fiber microbend is a single kink, since an arbitrary fiber bend profile can be finite element modeled by a sequence of successive kinks. The first exact, all mode wave optics calculations for the transmission loss across a single kink in a highly multimode optical fiber as a function of kink angle are shown in fig. 2. The results for a single kink shown in fig. 2 show that crack detection sensors based on kink loss can be designed with excellent sensitivity. For example, since a 1° kink produces a loss of 0.43 dB and commercial OTDR instruments can measure changes of 0.02 dB reliably, kinks as small a 0.05° can be sensed with this measurement method.

Figure 3 presents the longitudinal and shearing response of a fiber optic crack detection sensor attached to the metal test fixture as shown in fig. 1. To our knowledge, these are the first reported results on both longitudinal and shear response of a fiber optic crack sensor. The distance between the bond sites was $d_o = 5$ mm, and the orientation angle $\theta_o = 45°$. The sensor was interrogated using an 850 nm Tektronix FiberMaster OTDR. Acrylate coated 50/125/242 μm (core/cladding/coating diameter), graded index fiber with an *NA* of 0.22 was used in all results reported here. Both the shear and longitudinal displacements had a reproducible resolution of 20 μm. After the initial shearing phase, the fiber follows a well-defined curve upon repeated cycling. A conservative 0.1 dB alarm threshold results for a 0.05 mm shear displacement, with a maximum sensing range of ~ 0.7 mm. It is interesting to note the sensor response in dB is proportional to Δs^3, where Δs is the shear displacement. The longitudinal response of the sensor also shows a two phase response which is repeatable upon cycling. The sensitivity of the longitudinal response is much lower than the shearing case, with a 0.1 dB alarm threshold of 0.6 mm, while the sensing range has increased to ~ 2 mm. In contrast to the shear response, the sensor response in dB is proportional to $\Delta l^{3/2}$, where Δl is the longitudinal displacement.

Figure 4 shows the angular response of a sensor identical to that in fig. 3, except that $d_o = 3$ mm. These data were obtained by simultaneously displacing the sensor a small amount parallel and perpendicular to the line of separation so that the desired angle was achieved. The figure shows a sensor response in dB that is proportional to $\Delta\theta^3$, where $\Delta\theta$ is the angular displacement from the orientation angle θ_o. The response is very reproducible. The fact that the loss is considerably less than the transmission loss for two kinks of the corresponding angle shown in fig. 2 is evidence that the "kinks" are not sharp but rather somewhat distributed. Computer modeling of this effect is currently in progress.

Although the sensor just described exhibits excellent shear response, it is not readily adaptable to surviving and sensing both large and small longitudinal displacements, and the attachment method is not practical for covering large areas. Shown in fig. 5 is the longitudinal response of a packaged all-fiber sensor based on the above results that overcomes these limitations. Note the excellent (sub-mm) response and large sensing range of 6 mm, corresponding to a strain of 110%. The longitudinal and transverse sensitivity, sensing range, and size for area coverage are flexible, and can be substantially varied to adapt to a variety of applications. Additional details of this sensor will be presented elsewhere.

Further refinements of the packaging and attachment of these sensors are in progress to allow numerous strain/crack sensors to be rapidly and inexpensively deployed in many structural monitoring applications.

3. Acknowledgments: This work was partially supported by G2 Systems Corp. under Dept. of Energy grant DE-FG49-93CE15547.

4. References:

1.) R. Monastersky, "Can Los Angeles ride out a stronger quake?", *Science News*, **145** (April 16, 1994) 244-245.
2.) M. Granberry, "San Diego Sewage Spill Grows", *Los Angeles Times*, p. A1, Feb. 6, 1992. Series of articles on this, p. A1, Feb. 7; p. A1, Feb. 8; p. A3, Feb. 9; Feb. 10; Feb. 11; and Feb. 19.
3.) T. G. Giallorenzi, *et al*, *IEEE J. Quant. Electron.*, **QE-18**, (1982) 626-665.
4.) A. D. Kersey, T. A. Berkoff, and W. W. Morey, *Opt. Lett.*, **18**, (1993) 1370-1372.
5.) P. Tarricone, "Bridges Under Surveillance", *Civil Engineering*, **60**, May (1990) 48-51.
6.) Vishlizki, Y., "Crack Detection with Fiber Optic Sensor: A Parametric Study of the Orientation Angle Approach", M. S. Thesis, Lehigh University, Pennsylvania (1992).
7.) K. H. Wanser, *et al*, *Applications of Fiber Optic Sensors in Engineering Mechanics*, F. Ansari, ed., American Society of Civil Engineers, New York, (1993), 303-327.

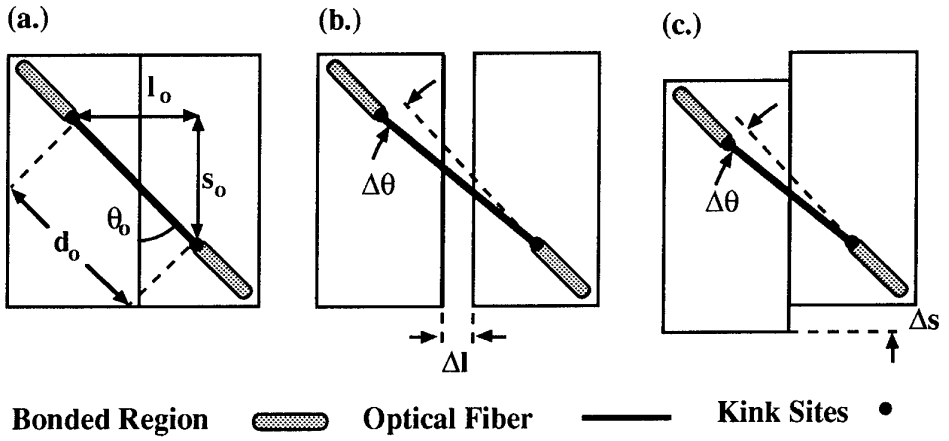

Figure 1. *Orientation angle approach to crack detection showing, a.) optical fiber attachment to surface, b.) longitudinal crack separation, c.) transverse shear crack displacement.*

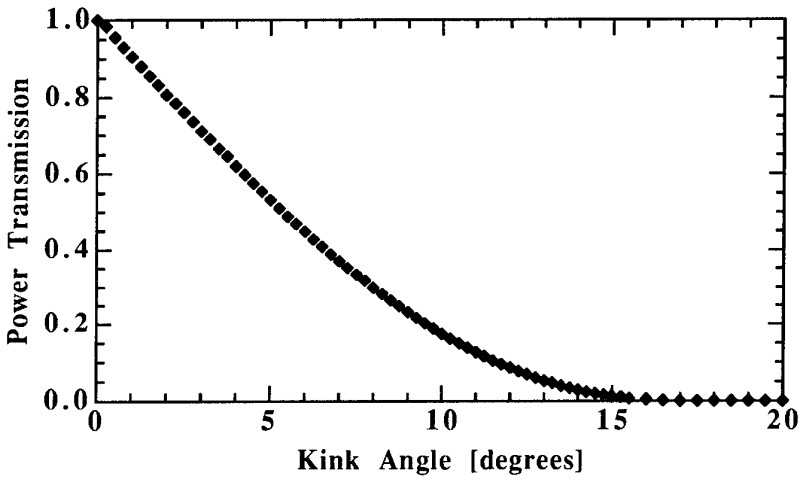

Figure 2. *All mode wave optics calculation of the transmission through a single kink in a graded index optical fiber at 850 nm, fiber NA = 0.22, core diameter = 50 μm.*

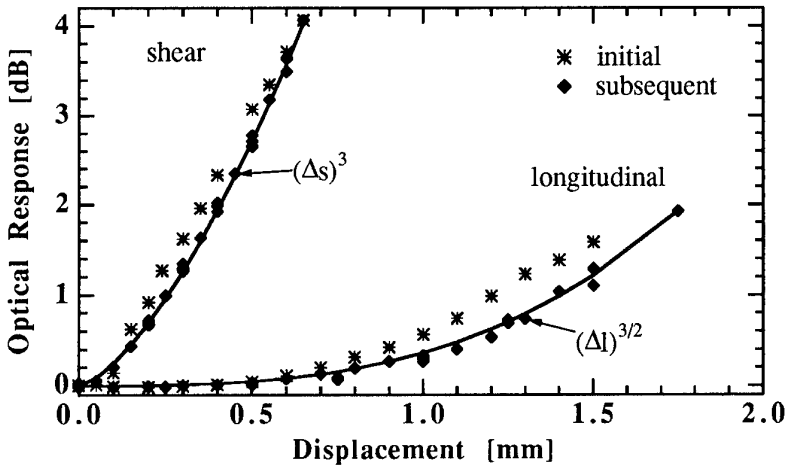

Figure 3. *Response of sensor to longitudinal and shear displacements shown in fig. 1b and 1c. Orientation angle $\theta_o = 45°$, distance between kink sites $d_o = 5$ mm. Note different fit line exponents.*

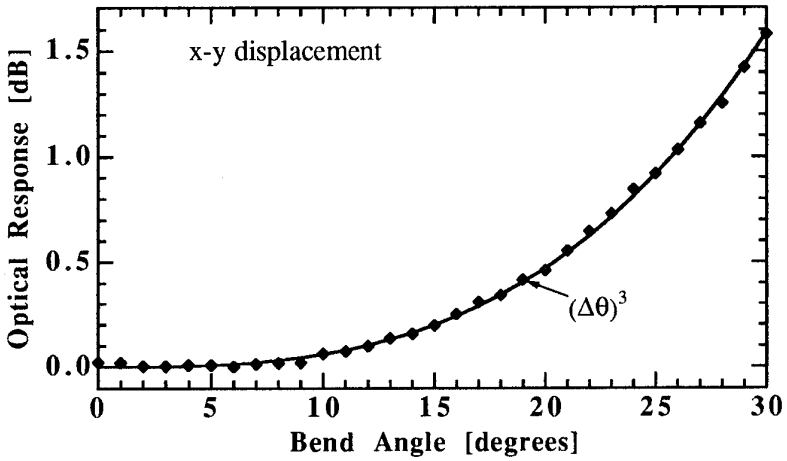

Figure 4. *Sensor response to angular displacement using x-y positioners. Angle $\theta_o = 45°$, distance between kink sites $d_o = 3$ mm. Note fit line has same power law exponent as shear fit in fig. 3.*

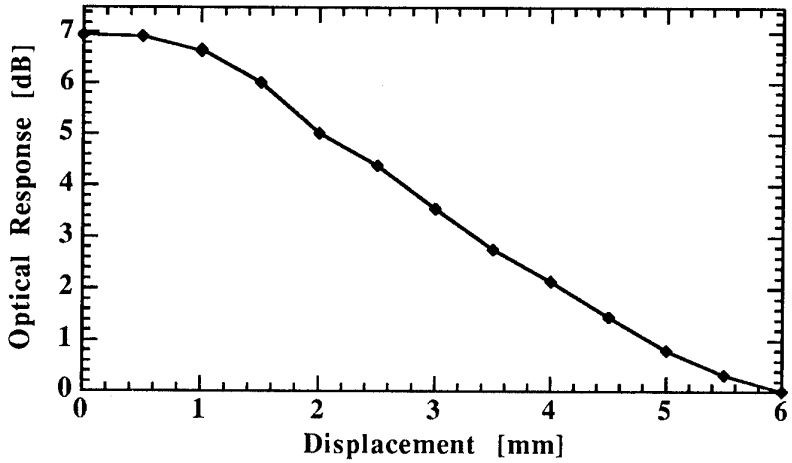

Figure 5. *Longitudinal crack displacement response of novel packaged sensor based on bend loss. Note large sensing range and improved optical response compared to longitudinal response of fig. 3.*

Remote Monitoring of Instrumented Structures Using the INTERNET Information Superhighway

Peter L. Fuhr
Dryver R. Huston
Timothy P. Ambrose

University of Vermont
Intelligent Structural Systems Research Institute
College of Engineering
Burlington, VT 05405

Correspondence:
Fuhr: telephone: (802) 656-1917, FAX: (802) 656-0696, email: fuhr@emba.uvm.edu

ABSTRACT

The requirements of sensor monitoring associated with instrumented civil structures poses potential logistical constraints on manpower, training and costs. The need for frequent or even continuous data monitoring places potentially severe constraints on overall system performance given real-world factors such as available manpower, geographic separation of the instrumented structures, and data archiving as well as the training and cost issues. While the pool of available low wage, moderate skill workers available to the authors is sizable (undergraduate engineering students), the level of performance of such workers is quite variable leading to data acquisition integrity and continuity issues - matters that are not acceptable in the practical field implementation of such developed systems. In the case of acquiring data from the numerous sensors within the civil structures which the authors have instrumented (e.g., a multistory building, roadway/railway bridges, and a hydroelectric dam), we have found that many of these concerns may be alleviated through the use of an automated data acquistion system which archives the acquired information in an electronic location remotely accessible through the Internet global computer network. It is therefore possible for the data monitoring to be performed at a remote location with the only requirements for data acquistion being Internet accessibility. A description of the developed scheme is presented as well as guiding philosophies.

1. Introduction

The recent advent of advanced materials with internal sensory and reaction capabilities, i.e. 'intelligence,' has opened the door for many useful applications in civil structures, e.g. bridges, buildings, dams, in contrast with aerospace structures. Structures built with intelligent materials will be able to sense external loads, assess the internal stresses and damage caused by the loads, and, if necessary, respond appropriately. Although relatively few structures are presently built with such materials, the potential market for the application of these materials can be quite large[1]. The most probable candidates for the initial application of these materials will be high-performance structures such as skyscrapers, including intelligent buildings, bridges, and those facilities where failure

0-8194-1700-9/94/$6.00

presents large safety concerns, such as nuclear waste containment vessels, bridge decks, dams, and structures under construction.

Large scale structures that have actually had fiber optic sensors embedded into them are still relatively few. Holst and Lessing[2] have installed fiber optic displacement gages in dams to measure shifting between segments. Fuhr et al.[3] report the installation of fiber optic sensors into the Stafford Building at the University of Vermont. Similar installations have been completed at the Winooski One dam in Winooski, VT[4], in the newly constructed physics building on the campus of the Dublin City University in Ireland[5], and in a railway overpass bridge in Middlebury, VT[6]. Researchers at the University of Toronto, in conjunction with City of Calgary (Alberta, Canada) officials, have embedded fiber optic strain gauges into the prestressed concrete support girders on a highway overpass[7].

A major challenge to building and using a comprehensive sensor system is that a variety of physical parameters must be measured using sensors that are often spatially distributed across the span of a large structure. The sensing and data processing requirements are complicated by most of the measurands exhibiting dynamic behaviors with time scales that vary over several orders of magnitude. An additional concern is that modern data acquisition hardware collects enormous amounts of data, only a small fraction of which may be useful.

In the case of an instrumented civil structure questions regarding the data acquistion and frequency of monitoring of the embedded sensors arise. In parallel, labor concerns ranging from training of sensor "inspectors" to who actually performs the processing and analyzing of the acquired data are legitimate matters in the practical field implementation of such developed systems.

2. Data Acquistion from Instrumented Structures

We have been concerned with the acquistion of data from embedded and surface attached sensors which are placed throughout a potentially large instrumented civil structure. Two issues predominate our activities: (1) collection of the sensors' data at a single central location within (or near) the instrumented structure; and (2) development of a method for remote monitoring of this sensor information. With respect to issue 1, we have proceeded to use radio telemetry for data acquistion and concentration at a single central location[8]. Issue 2's requirements are currently being met through the use of system software resources associated with the Internet global computer network. The Internet is actually a collection of approximately 30,000 computer networks. There is a vast array of network software utilities that manage and control network node-to-node communications. We have found that for simple data archiving and subsequent remote locale retrieval, the use of an "anonymous" File Transfer Protocol (FTP) site is optimal. This allows raw, time history data from each embedded sensor to be archived on an Internet networked computer in a file (or folder) that may be accessed using FTP. Information security may be obtained by requiring a password to access this data, or, complete world-wide Internet access may occur if the sensor data is archived in an anonymous FTP accessible file/folder. Power frequency data acquired from fiber optic vibration sensor #16, located within turbogenerator #3's support mount is displayed as Figure 1. This data was accessed remotely using a modem equipped Macintosh LCII microcomputer from the "WinOneDam@emba.uvm.edu" anonymous FTP data site located on a Sun Microsystems computer at the University of Vermont. A portion of the raw data is shown in this Figure as well as the associated frequency power spectra.

In conjunction with the monitoring of the status of the embedded sensors is the need to concurrently monitor the electric power generation status as well as the water level and flow rates. Two methods are used for this data acquistion: (1) traditional analog-to-digital (A/D) conversion of the electrical values associated with each turbogenerator's water flow rate, turbine rotation rate (RPM),

generation efficiency and generator output electrical power; and (2) simple TV camera video capture of the operator's consoles associated with each turbogenerator. In the first case, the acquired individual voltage levels are interfaced to a unique channel on a microcomputer's A/D board, sampled, scaled, time-tagged and stored in memory for transmission to the Internet host computer. This information is then formatted on the Internet-host and placed in an anonymous FTP account for worldwide Internet access. In the second case, the acquired video frames, (1 for each console display plus the outside camera) are transmitted to the Internet-host computer's "WinOne-video" Mosaic file for worldwide Internet access and viewing using Mosaic or a comparable video display program.

Point	fiber_freq.y	freqs.y
0	6.1583e-05	0
1	3.3713e-08	12
2	8.6179e-08	24
3	3.6841e-08	36
4	1.6613e-07	48
5	3.1326e-08	60

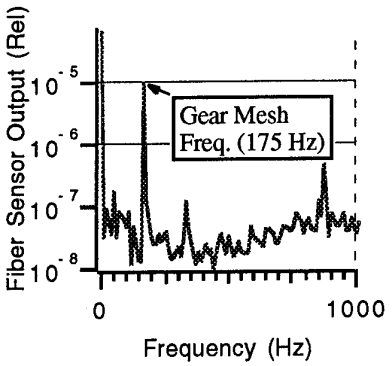

Figure 1. FTP accessed embedded sensor data obtained from the Winooski One dam.

In a manner somewhat similar to the FTP site, the use of the Internet network utility program "Mosaic" has been chosen for the visual display of video frames acquired from video cameras positioned at the Winooski One dam. Mosaic is an Internet-based global hypermedia browser that allows the user to discover, retrieve, and display documents and data from all over the Internet. It is part of the World Wide Web project, a distributed hypermedia environment originated at CERN and collaborated upon by a large, informal, and international design and development team. Mosaic, which can be copied for free from many Internet software archives, organizes information into a so-called "home page", which serves as a table of contents about a particular topic or group of topics.

In the context of instrumented civil structures information, we have configured a multimedia (video/audio) equipped microcomputer for acquiring and preprocessing of the video images obtained from the cameras located at the instrumented structure, in this case, the Winooski One hydroelectric dam. Near realtime video images are placed into the appropriate Mosaic source location home page. All video images are not archived, due to limited physical disk space, but rather have the last 30 frames temporarily stored. Viewing of the video frames is achieved using Mosaic on an Ethernet configured Internet accessible (IP - Internet Protocol addressed) microcomputer.

The images shown as Figure 2 represent the Mosaic video viewing of the Winooski One dam on April 6, 1994 at 2:20 PM EST. Specifically, Figure 2.a shows the outside video view of the water flowing over the dam at this time. Figure 2.b shows the associated video frame of the camera's view of the control monitor for turbogenerator number 2. From this frame the operational values and river level and flow rate data of this generator are readily apparent (please note that the full screen sized video frames have been reduced for this publication).

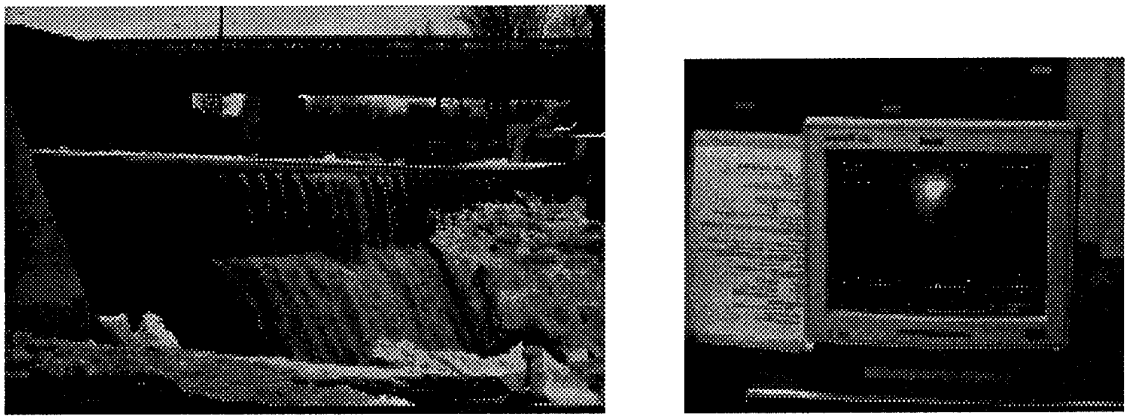

(a) (b)

Figure 2. Internet accessed, Mosaic displayed realtime "snapshots" of: (a) from an outside deck video camera showing the current water flow level at the Winooski One hydroelectric dam; (b) powerhouse control console associated with turbogenerator #2. The actual display has been reduced from its full screen size for this publication.

3. Summary

The requirements of sensor monitoring associated with instrumented civil structures poses potential logistical constraints on manpower, training and costs. The need for frequent or even continuous data monitoring places severe constraints on the monitoring performance given real-world factors such as available manpower, geographic separation of the instrumented structures, and data archiving as well as the training and cost issues. We have found that many of these concerns may be alleviated through the use of an automated data acquistion system which archives the acquired information in an electronic location accessible through the Internet. It is therefore possible for the data monitoring to be performed at a remote location with the only requirements being Internet accessibility.

4. References

1. D.R. Huston, Smart Civil Structures - An Overview, SPIE Paper No. 1588-21, Proc. SPIE Fibers '91 Symposium, Boston, MA, Sept. 1991.
2. A. Holst and R. Lessing, "Fiber-Optic Intensity-Modulated Sensors for Continuous Observation of Concrete and Rock-Fill Dams", Proc. 1st European Conf. on Smart Structures and Materials, Glascow, 1992, p. 223.
3. P.L. Fuhr, D.R. Huston, P.J. Kajenski, and T.P. Ambrose, "Performance and Health Monitoring of the Stafford Medical Building Using Embedded Sensors", J. Smart Materials and Structures, 1, (1992), 63-68.
4. P.L. Fuhr and D.R. Huston, "Multiplexed fiber optic pressure and vibration sensors for hydroelectric dam monitoring", J. Smart Materials and Structures, 2 (1993), 320-325.
5. B. McCraith, Dublin City University , Ireland, personal communication to P.L. Fuhr, 1993.
6. D.R. Huston, P.L. Fuhr, T.P. Ambrose, "Intelligent Civil Structures - Activities in Vermont", to be published in the J. of Smart Materials and Structures, 1994.
7. R. Measures, et al, "Strain gauge measurements obtained from an instrumented bridge girder", Smart Materials and Structures Conference 2, Orlando, FL, Feb. 1994.
8. P.L. Fuhr, D.R. Huston and T.P. Ambrose, "Interrogation of multiple fiber sensors in civil structures using radio telemetry", J. Smart Materials and Structures, 2, (1993), 264-269.

Paper presented at the Second European Conf. on Smart Structures and Materials, Glasgow 1994, Session 3

Smart Aircraft By Continuous Condition Monitoring of Aircraft Structures and Components

Daryoush Allaei, Ph.D., P.E.
QRDC Inc.
Box 562, Excelsior, MN 55331-0262, USA

ABSTRACT

There exists a need to have a reliable comprehensive software/hardware to monitor the condition of airframe structures and aircraft components. Failure of any structural parts of aircraft are often prohibitively costly and could even lead to loss of life. The existing technologies deal with the use of some of the characteristics of structural vibration and thus resulting in false detections. The use of complete vibration signature measured by an array of embedded (or attached) fiber-optic sensors, which are loaded with multiple laser beams generated by a single optical source, is the focus of this project. The hardware will be light weight, low cost, and effective for monitoring discontinuities, damages, and delamination in both composite and metal airframes.

INTRODUCTION

The goal of this project is to develop a real-time, aircraft or ground based Vibration-Based Condition Monitoring System (VBCMS) for predicting defects and damages in both composite and metal structural elements in aircraft. Fiber optic sensors embedded in or attached to the aircraft structure during maintenance or manufacturing are used to collecte the neceassary data. The collected vibration signal is then compared with the pre-flight calibrated, 'healthy' vibration signature to diagnose the condition of the aircraft structure using a knowledge-based expert system. The main contributions of this concept are: (1) the complete set of the vibration signature (natural frequencies, mode shapes, modal damping factors, and input force) are used in the evaluation procedure rather than just a portion of it (frequencies and modal damping), (2) optimal design based on the number and the location of the sensors, and (3) application of binary optics in vibration measurement. Since all structures have their particular vibration signature, the proposed concept is suitable (light weight, low cost, and effective) for monitoring discontinuities and impact damages in both composite aircraft structures and metal airframes. The use of an optimized array of embedded (or attached) fiber optic sensors makes it possible to directly and accurately measure the changes in mode shapes of the structure caused by various factors such as delamination of the bonded aluminum components and wear, for example. The same concept is also applied to monitor the condition of gearboxes and other aircraft rotating equipment.

As structures and engineering systems become more complex and costly, the need to measure, monitor, and control their dynamic performance and characteristics also becomes more important. Failure of aircraft structures can be prohibitively costly and deadly. Thus, a major effort has been directed by researchers toward a better understanding of vibration characteristics of structures and designing more advanced monitoring and control systems.

Vibration theories have always been important and unavoidable elements in engineering and design problems. It is well understood that the natural frequencies and mode shapes of vibrating systems are part of system property [1], and that they do not depend on external excitations. There has always been the question of how one can truly measure, understand, and control the vibration characteristics (natural frequencies and mode shapes) of a structure. Also, researchers have been looking for ways of utilizing the changes in the frequencies to predict things like shape, content, material properties, failure modes, life, and operating conditions of systems. The development of more effective, accurate and practical measuring methods and instruments is a prerequisite for any meaningful condition monitoring system to accomplish the above goals.

It is known that structures vibrate in three directions: One out-of-plane and two in-plane displacement vectors. Depending on the particular system and its operating range one, two or all three directions may

0-8194-1700-9/94/$6.00

be excited. It has also been known that the in-plane vibration is much more difficult to observe, measure and simulate than the out-of-plane motion. One of the benefits of this concept is that the developed vibration measuring system is capable of detecting in-plane as well as out-of-plane vibrations.

The outcome of this project will be the first step toward developing the next generation of condition monitoring expert systems suitable for aircraft damage identification. It will also result in better understanding of the vibrating systems, and therefore designing more advanced aircraft structures and monitoring / control systems.

MATHEMATICAL MODEL

The mathematical model, which is used to conduct the theoretical analysis during the course of this project, is composed of three distinct parts: the primary (or host) structure, its components (i.e., sub-structures, fasteners, and imbedded/attached elements), and interfaces between the components and the host structure. The main advantage of this approach is that the developed model for vibration analysis of airframe structures can be incorporated in any existing structural model. First, the dynamic characteristics of all the parts are assumed to be known in terms of their natural frequencies, mode shapes, and modal damping factors. Next, the interfaces between the components and the host structure and the interfaces between the components themselves are modeled by employing the receptance method. Finally, sub-structures are connected by the developed interface models to resemble the total airframe structure. The computer model will be composed of the theoretical model which is refined by utilizing the measured vibration signature of the healthy aircraft structure.

Figure 1 shows the basic concept of the model applied to a wing structure carrying sub-structures (i.e., lumped and distributed units) which have point, line, and/or surface contacts with the host structure (wing). The system is partitioned into three segments as shown in Figure 2. The receptance method is then utilized to connect the three segments in order to resemble the total structure. After the dynamic analysis of the structure is completed, the model is refined by incorporating the weighted measured vibration signature of the total structure. The latter is the vibration signature of the healthy structure.

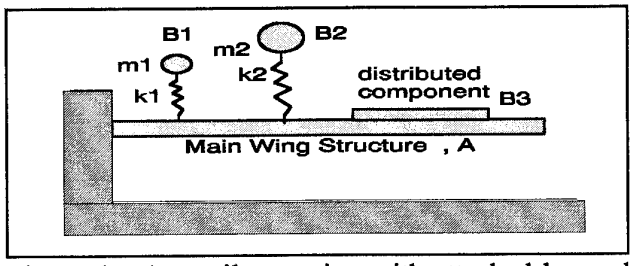

Figure 1 A cantilever wing with attached lumped and distributed components

The concept of a neural network (see Figure 3) will also be implemented in the computer model. Every time the program goes through the above mentioned steps, it keeps a record of the given conditions and the outcome of the analysis so that it can make recommendations on how to improve the condition evaluation procedure of the components, for example. The three segments of the model (main structure, interfaces, and attached components) are stored in the computer model in terms of their vibration characteristics which are natural frequency, mode shapes, and modal damping factors. This feature makes the model very flexible in interacting with other existing models of sub-structures since such vibration characteristics can be obtained by any method (i.e., FEMor closed form solutions).

Other advantages of the proposed approach [3] are in memory savings and computational speeds. There are neither any large stiffness, mass, and damping matrices, nor are there any geometric mesh matrices. The only required geometry of the sub-structures is their contact region. The latter reduces the degrees-of-freedom of the total structure by a large factor [3]. Such features will significantly decrease the memory requirement of the computer model. Also, the output of the analysis portion of the program are in terms of the vibration characteristics (natural frequencies and mode shapes) of the assembled structure. This data is then utilized to do a forced dynamic analysis of the total system. The author has shown [2-6] that such a process significantly increases the computational speeds of the computer model.

One of the significant contributions of this work is the application of line and surface receptances in the development of the proposed VBCMS. Point receptances have been extensively applied to various engineering problems [2-6]. However, line receptances have only been applied to a very limited cases. Surface receptances have not been yet appeared in the open literature. In this SBIR project, line and surface receptances will be developed for application to the proposed VBCMS. Fiber optic sensors, for example, need to be modeled as embedded (or attached) line elements in structural components.

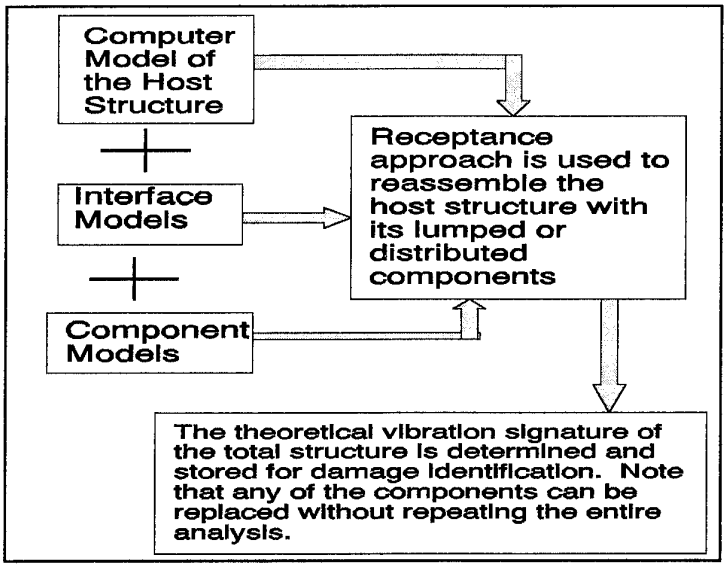

Figure 2 The vibration model of the segments of the proposed model

ADVANTAGES OF THE APPROACH

A summary of the advantages of the presented mathematical model, which is used to construct the theoretical vibration signature of the healthy structure, is given in this section.

Memory Requirement: The memory requirement is controlled by the number and type of the attached components rather than the complexity of the total structure. It has been shown [3] that the memory savings of the proposed sub-structuring concept based on the receptance method is 7 to 10 times better when compared with full FEM.

Computational Speed: The computational speed is significantly faster than the full numerical approaches, such as finite element method, since the analysis does not involve large matrix operations. The free vibration analysis of the sub-structures are performed only once and the results are input in the proposed interface model to study the assembled structure. The author has shown [2-6] that the receptance method increases the computational speed by a factor of 10.

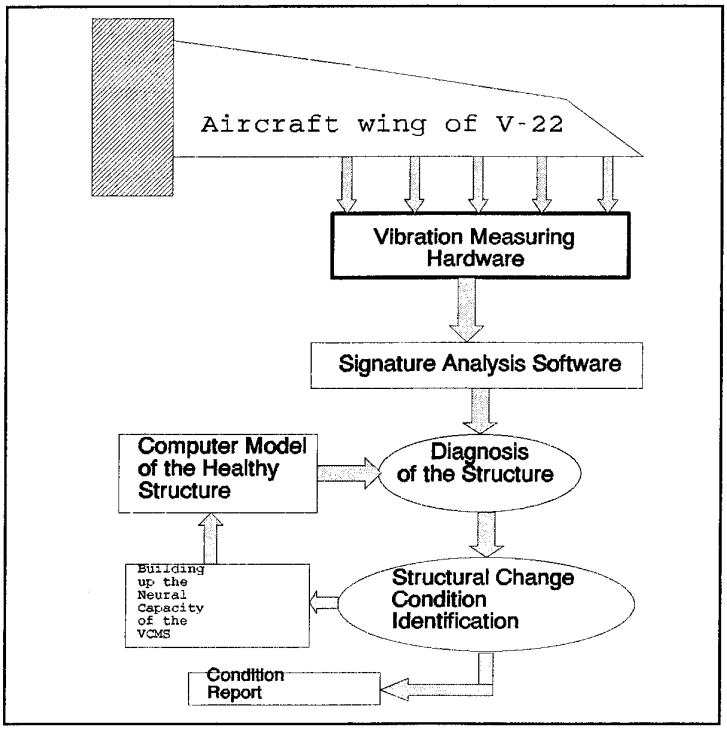

Figure 3 The VBCMS concept

Accuracy: The accuracy of the numerical results depends on the vibration characteristics of the sub-structures which are obtained independently by any suitable method. Assuming that the stored vibration characteristics of the sub-structures are within the acceptable accuracy range, the number of the required sub-structure modes should be double the number of modes of interest of the assembled structure [3] in order to have reasonable accuracy.

Reduced Condition Evaluation Formulas: In certain range of the system parameters, it is possible to reduce the equations to closed form formulas that can be used for simple parametric study and condition evaluation purposes.

Efficient Parametric Study: Since the host structure and its attached components are independently modeled and then connected via the proposed interface model, the parameters will be grouped in the three parts: host structure, attached elements, and the interface parameters. Dynamic models of host structures and individual components are covered in the open literature. Author's focus is on the development of effective, accurate, and efficient interface models.

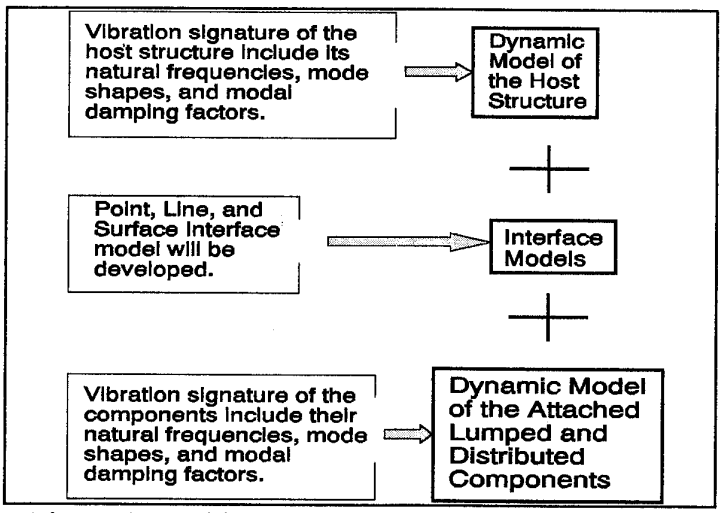

Figure 4 Partitioned structure into substructures with interaction forces

Sensitivity: As it was shown in reference [3], the natural frequencies appear in the denominator of the receptance and mode shape equations. Therefore, the inaccuracy of the higher natural frequencies of sub-structures generated by their independent dynamic models will not affect the calculated vibration characteristics of the assembled structure. Where as in conventional numerical models, such as finite element, the accuracy of the results depend on the number of degrees of freedom, the generated mesh, and the type of elements.

Rigid Body Modes: In order to trace the loosening effect of the attached or embedded elements, rigid body modes need to be incorporated in the model. The receptance method provides the capability of including the rigid body modes as well as the non-rigid body modes.

Compatibility with the Other Models: Since the three parts of the proposed model can be independently developed and only the vibration characteristics of the sub-structures are required, it will have full compatibility with other dynamic models of the sub-structures.

Efficient Replacement of Damage Components: After a damaged part is identified and recommended for replacement (or modification), only its vibration signature needs to be changed in the global computer model of the healthy structure. There will be no need for new data on the healthy portion of the system and therefore the vibration characteristics of the undamaged components remain intact. The same procedures will be followed if one or more parts of the total structure need to have a new design. In conventional numerical models, such as FEM, the total structure needs to be reevaluated if one (or more) component is replaced or modified. This feature makes the proposed VBCMS concept very flexible and efficient even for deep space applications and remote monitoring.

ACKNOWLEDGMENT
This work has been funded jointly by DOD (ARPA) and QRDC.

REFERENCES
[1]Dimarogonas, A.D., "The origins of vibration theory," Journal of Sound and Vibration, v 140 (2), 90.
[2] D. Allaei, W. Soedel & T.Y. Yang, "Vibration Analysis of Non-axisymmetric Tires", Journal of Sound and Vibration, Vol. 122, No. 1, pp 11-29, 1988.
[3] D. Allaei, "Application of Localized Vibration and Smart Materials in Controlling the Dynamic Response of Structures, Part II," Submitted to ARPA, October 1992.
[4] D. Allaei, "An Advanced Approach For Vibration Analysis of Nonuniform Tires," 11th Annual Meeting and Conference on Tire Science and Technology, Akron, Ohio, March, 1992.
[5] D. Allaei, "An Advanced Computational Method for Vibration Analysis of Structures Made of Composite Materials," Sixth Japan-United States Conference on Composite Materials, 1992.
[6] D. Allaei, "Vibration Monitoring Based on Frequencies and Mode Shapes," Recent Advances in Surveillance by Acoustical and Vib. Methods, SFM / Sfa, Senlis, France, 1992.

Paper presented at the Second European Conf. on Smart Structures and Materials, Glasgow 1994, Session 3

MONITORING OF BRIDGES SUBJECT TO TRANSVERSAL CRACKS

Charles Abdunur

Laboratoire Central des Ponts et Chaussées
58 Bd Lefebvre, 75015 Paris, France

ABSTRACT : In a bridge, flexure cracks can be spotted and their mechanical consequences estimated through the automatically measured redistribution of curvature variations under convenient loading and a quick chain application of the classical expression for bending moment in beams. The residual flexural stiffnesses are thus obtained and introduced into a specific structural analysis programme to define the new statical system of the bridge. More realistic stresses can then be predicted for any given live loads and at any time intervals.

1. INTRODUCTION

Flexure cracks are among the main structural defects observed while inspecting reinforced or prestressed concrete bridges. Up-to-date security precautions should mainly require a quasi-automatic detection and monitoring of these cracks and a reliable estimation of their influence on the local and general mechanical behaviour of the structure. For this purpose it is first necessary to explore the new structural system of the bridge. The corresponding live load stresses, the residual capacity assessment and the optimum needs for strengthening can then easily follow.

2. BASIC ASSUMPTIONS AND PRINCIPLE

As shown in figure 1, the cracked sections and their disturbed vicinities are assimilated to a series of elastic or plastic hinges (H), alternating with sound beam segments (B) and jointly setting up a new system in equilibrium.

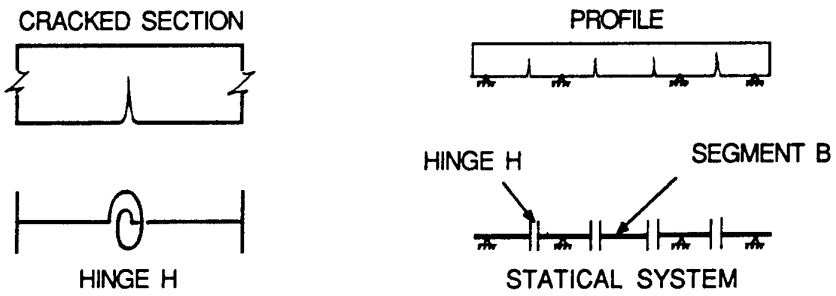

FIG. 1. Modelling assumptions of cracked sections of a bridge.

The main parameter is the residual flexural stiffness of each cracked section or hinge H. Its determination, for a quick and repeated access to the bridge new statical system, constitutes the main difficulty, especially in reinforced or prestressed concrete where several variables and assumptions are involved.

0-8194-1700-9/94/$6.00

An experimental method was developed, based on curvature redistribution measurements and on a chain application of the well known relationship between bending moment, stiffness and resulting curvature : M = EI.θ'

3. PROCEDURE

The bridge is equipped, throughout its spans, with prototype inclinometry instruments or optical fibres supplying curvature variation data.

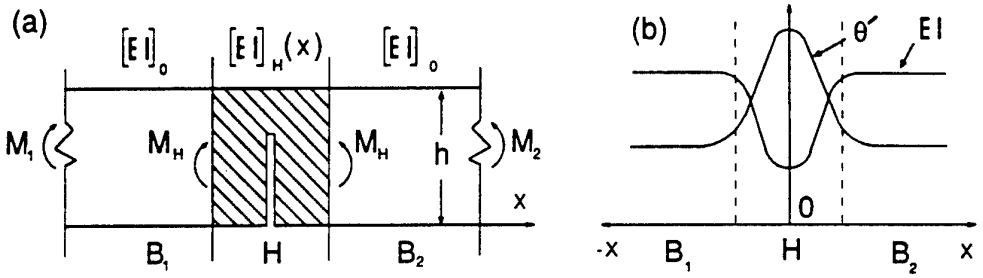

FIG. 2. (a) Moments *M* and stiffnesses *EI* in cracked sections H and sound segments B.
(b) Redistribution of curvature *θ'* and stiffness *EI*.

Under a convenient test loading, the measured curvature variation diagram θ' is plotted for the whole length of the bridge, detecting discontinuities and giving :

θ'_H (x) : the curvature over a cracked section or hinge H and its short influence zones

θ'_B (x) : the curvature along the sound beam segments B especially the parts close to the crack

The known initial stiffnesses $(EI)_0$ are assumed to be maintained in the sound segments B.

4. EVALUATION OF FLEXURAL STIFFNESSES

Figure 2 outlines the interpretation of results at a given crack or hinge H :

The plotted, load induced, curvature variation θ' (x) is cut into modules of different lengths each covering the hinge zone H and the near parts of both adjacent sound segments B_1 & B_2 (These conserving their initial stiffnesses $(EI)_0$).

For each module, the classical equation M = EI. θ' is now applied at conviently successive sections, but at a much closer pace in the hinge H zone where the moment M remains practically constant but EI and θ' considerably vary in opposite senses :

At any section over the H length : $(EI)_H . \theta'_H = M$

Through the close ends of segments B_1, B_2 : $(EI)_0 . \theta'_B = M$ also, H being very short and transmitting M anyway

from this identity :

$$\frac{[EI]_H(x)}{[EI]_0} = \frac{\theta'_B}{\theta'_H(x)}$$

$[EI]_H$ (x) is the only unknown at any value of x, so it can be determined and plotted to give the EI curve in fig. 2 (b) which is the required residual stiffness of the cracked section.

Sometimes the given initial $(EI)_O$ is not used and the relative residual stiffness $(EH)_H/(EI)_O$ or its inverse (fig. 3) are preferred to estimate the percentage remaining strength of the bridge.

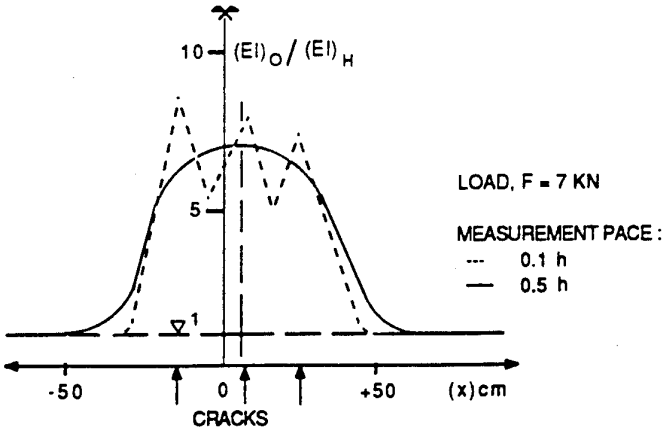

FIG. 3 Redistribution curve of the inverse relative flexural stiffness over a beam with three cracks.

5. THE NEW STATICAL SYSTEM

The relative or absolute stiffness function of each cracked or plasticised section H is automatically insert into a structural analysis programme.

The new actual statical system, thus defined, enables :

- The prediction of the real stresses under any given loading.

- The assessment of the load bearing capacity and optimum needs for strengthening.

The procedure can be repeated at any later stage to verify the effectiveness of eventual repairs or simply to follow up any time-dependent mechanical change.

6. IMPROVED CURVATURE MEASUREMENTS

The already accurate prototype inclinometry instruments are now being advantageously replaced by optical fibres, even for existing bridges. A small composite material beam, with known geometric and mechanical properties, is equipped with optical fibres at different levels of its section. It is firmly fixed on the bridge upper flange along the entire length (fig. 4). Under loading the measured curvature variations of the composite beam are supposed to be those of the bridge and lead, as already explained, to the new statical system.

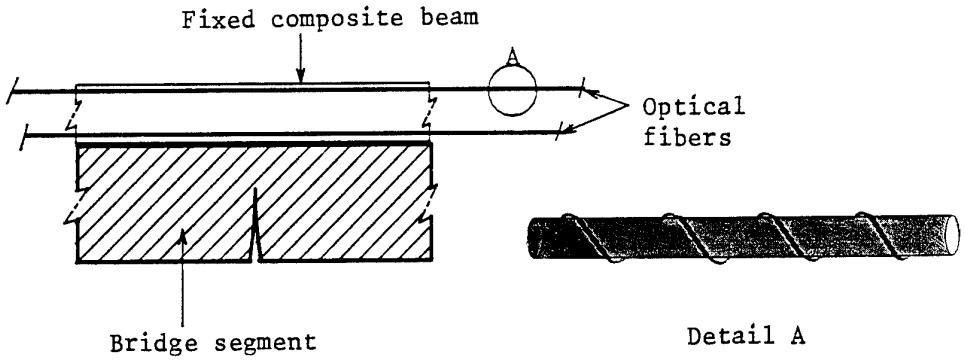

FIG. 4 : A beam of composite material, equipped with optical fibres, is firmly attached to the upper bridge flange to transmit load- induced curvature variations.

CONCLUSION

Concrete bridges, with potential or actual flexure cracks, can be reliably monitored through continuous data acquisition on their load-induced curvature redistribution diagram. Incorporated microbend optical fibres are now replacing conventional inclinometry. Data treatment can also give a quick access to the actual statical system and the corresponding live load stresses. This leads to a more realistic assessment of the bridge's structural capacity and its eventual needs for repairs. Continuity, quickness, instrument incorporation and adequate analyse, offer together a smart way of monitoring.

REFERENCES

[1] Chatelain, J., Bruneau, J. and Duchêne, J.-L., Estimation par des essais de chargement du défaut de résistance à la flexion de certains tabliers en béton précontraint. International Conference on Inspection, Maintenance and Repair of Road and Railway Bridges, Brussels Paris, 1981.

[2] Abdunur, C. and Duchêne, J.-L., Mesures de rotations pour le schéma statique d'un ouvrage fissuré. International Conference on Measurements and Testing on Civil Engineering, Lyon, 1988.

[3] Chatelain, J. and Godart, B., Evaluation de l'état mécanique réel de ponts en béton précontraint. IABSE Symposium, Helsinki, 1988.

SESSION 4

Bragg Grating Fiber Optic Sensing for Bridges and Other Structures

R. M. Measures, T. Alavie, R. Maaskant, S. Huang and M. LeBlanc

FIBER OPTIC SMART STRUCTURES LABORATORY
University of Toronto Institute for Aerospace Studies
4925 Dufferin St., Downsview, Ontario, CANADA

Abstract

We have demonstrated that fiber optic intracore Bragg grating sensors are able to measure the strain relief experienced over an extended period of time by both steel and carbon composite tendons within the concrete deck support girders of a recently constructed two span highway bridge. This is the first bridge in the world to test the prospects of using carbon fiber composite tendons to replace steel tendons. This unique set of measurements was accomplished with an array of 15 Bragg grating fiber optic sensors that were embedded within the precast concrete girders during their construction. We have also demonstrated that these same sensors can measure the change in the internal strain within the girders associated with both static and dynamic loading of the bridge with a truck. We are now studying the ability of Bragg grating fiber optic sensors to measure strong strain gradients and thereby provide a warning of debonding of any Bragg grating sensor from its host structure....one of the most important failure modes for any fiber optic strain sensor.

Introduction

The corrosion of steel within large concrete structures, such as bridges, is propting consideration of carbon fiber based composite material replacements for steel. In cold-climate countries this replacement is deemed to be even more important and urgent due to the greatly accelerated deterioration of steel reinforced concrete structures by the use of de-icing salts. Since composite materials are unproven in their substitution for steel in concrete structures there is considerable motivation to instrument test structures incorporating these materials in order to gain a better understanding of how well composite materials serve in this new challenging role.

Recent, developments in fiber optic sensors have made it possible to monitor the use of these advanced composite materials and attain a better understanding of their potential role in bridge: design, construction, maintenance and repair. In particular, fiber optic intracore Bragg gratings sensors are near ideal for strain sensing, [**Meltz et al. 1989**, and **Morey et al. 1989**] and the development of a passive method of wavelength demodulating these sensors, [**Melle et al. 1991**] leads to a practical sensing system. Excellent performance is possible when a sensing Bragg grating controls the wavelength of a tunable laser and the passive wavelength demodulation system determines the requiste measurand, [**Measures et al. 1992**]. We have shown that such a Bragg grating fiber laser sensor system may be packaged to form a compact, robust and sensitive sensing system with multiplexing potential, [**Melle et al. 1993** and **Alavie et al. 1993**].

In 1993 the city of Calgary commissioned the first highway bridge in the world to use carbon fiber composite prestressing tendons in 6 of the 26 precast, prestressed, bulb-tee deck support concrete girders. Carbon Fiber Composite Cable {supplied by Tokyo Rope Manufacturing Co. of Japan} was used to prestress 4 girders, while Leadline Rod {supplied by Mitsubishi Kasei of Japan} prestressed two. Steel prestressed the remaining 20 girders. We were asked to instrument each of

0-8194-1700-9/94/$6.00

the three types of precast concrete girders with fiber optic Bragg grating sensors in order to monitor the changes in their internal strain over an extended period of time and compare the performance of the different {steel and two types of carbon fiber composite} prestressing tendons. We also wished to ascertain if the embedded Bragg grating sensors were sensitive enough to detect the presence of vehicular traffic on the bridge.

Fiber Optic Sensing System

The development of the fiber optic sensing system for the Calgary bridge required us to address a number of issues: the load induced strains would generally be small {within 2500 μstrain} although, the prestressing tendons are subject to a tensile strain of around 8000 μstrain; the environment is harsh in terms of high moisture and large temperature excursions and the optical fibers were subject to rough handling. Installation of the Bragg gratings during the construction of the concrete girders was a crucial step and of the 18 embedded sensors, 15 survived and functioned correctly, [**Maaskant et al. 1994**].

A four-channel fiber laser demodulation system was specially developed for interrogating any four of these 15-fiber optic Bragg grating sensors. One semiconductor laser diode at 980 nm was demultiplexed to pump four independent erbium doped fiber lasers, each of which was tuned by one of the remote Bragg gratings that was embedded within a concrete girder. Because two intracavity connectors were interposed between each Bragg grating and its associated fiber laser the insertion loss and backreflection of the connectors had to be extremely low, **figure 1.** This was achieved with Angle Polished-Physical Contact {AP/PC} type connectors which had less than -60 dB backreflection and only 0.2 dB insertion loss. This demodulation system was: rugged, compact and able to work at the bridge construction site, see **figure 2,** *picture of Tino next to bridge* [**Alavie et al. 1994**]. It was also transportable and was taken several times from Tororto to Calgary by airplane in order to monitor the changes in the internal strain of the prestressing tendons over several months.

Each channel's strain response was characterized by connecting it to a Bragg grating that was mounted on a cantilever beam adjacent to a conventional resistive strain foil gauge. The cantilever beam was then loaded in flexure and both the foil strain gauge response and the filtered response of the optical system were recorded. This procedure was repeated for all four channels. The nonlinear behaviour of the spectral filter used in the passive wavelength demodulation system did not pose a serious problem as an electronic look-up table was employed. This prototype system had a strain measurement range of approximately 5000 μstrain and a resolution of a few μstrain [**Alavie et al 1994**]. A much improved system is now commercially available through ElectroPhotonics Corporation. Thermal apparent strain compensation was undertaken by using one Bragg grating within each girder exclusively as a temperature sensor.

Calgary Bridge Measurements

The fiber optic strain sensors that are embedded within the concrete girders and adhered to the prestressing tendons offer a direct measurement of the strain relief which occurs upon destressing of the precast girder. From the point of view of girder productivity it is desirable to destress and remove the concrete girder from its form as quickly as possible. This sometimes occurs while the concrete is not properly cured and this can lead to problems. The presence of these sensors could provide an opportunity to assess the condition of a girder and determine the suitability of scheduled events such as girder transportation and installation, deck pour and post-tensioning.

In the Beddington Trail Bridge project, an additional important motivation for the use of structurally integrated strain sensors was the desire to monitor the performance of the Tokyo Rope and Leadline carbon fiber composite prestressing tendons in relation to traditional steel strand

prestressing tendons. The long term characteristics of the tendon/concrete bond and the relaxation behaviour are required to allow an assessment of the appropriateness of these new materials in the present context. Some preliminary strain results are displayed in **figure 3**. The first set of strain data were obtained after the placement of the deck and immediately following post-tensioning of the girders. These measurements represent the stress relief in the tendons from the combined effects of destressing, concrete shrinkage, creep, dead loading of the bridge deck, and post-tensioning of the two spans. The second measurement was taken approximately one month after the bridge opening and shows some further relaxation of prestress for the carbon fiber composite prestressing tendons. However, the steel tendons show the opposite effect when proper allowance is made for the thermal apparent strain comensurate with the lower temperature in November.

Monitoring of: traffic usage, extreme load events and load history may also be possible with built-in fiber optic strain sensors. Such information may prove to be useful in bridge maintenance procedures and scheduling, in assessing bridge designs, and comparing actual loading to the design loads. This information might also be specified in bridge design codes and procedures. We have been able to demonstrate that our structurally integrated fiber optic sensors can measure the change in the internal strain within the deck girders arising from both static and dynamic loading of the bridge with a large truck [**Measures et al. 1994a**].

Bragg Intra-Grating Sensing

In most applications the Bragg grating is uniform and the strain gradient is assumed small in the vicinity of the sensor. However, this assumption may not always be valid and there are some occassions where it would be very desirable to ascertain the presence and extent of a strain gradient. This is particularly true when we realize that the most likely failure mode for embedded sensors is debonding from the host material. We have modelled Bragg gratings as a series of grating elements and have used a Transfer-matrix formalism based on coupled-mode theory to evaluate their reflection spectrum [**Measures et al. 1994b**]. This has enabled us to assess the consequences of strain gradients and sensor debonding on the sensor spectral response. Details of these calculations and their experimental verification will shortly be published [**Huang et al. 1994**].
Debonding of a fiber optic sensor from its host material represents one of the most probable modes of sensor malfunction and eventual failure. Since, debonding of the sensor would lead to the formation of local strong strain gradients this can be detected by the subsequent degradation of the form of the Bragg reflection spectrum. This is illustrated in **figure 4**, where we show three strain distributions corresponding to: fully adhered, partially debonded and fully debonded in **figure 4(a)**, and the corresponding Bragg reflection spectra in **figure 4(b)**.

Conclusions

We have installed a set of fiber optic Bragg grating sensors within a number of concrete deck support girders on a new two span highway bridge. We have developed a rugged and portable multichannel Bragg grating sensor demodulation system that has been taken out to the bridge site during construction and operation of the bridge. We have made the first measurements of strain relief associated with both carbon and steel prestressing tendons over an extended period of time using this sensing system. In addition we have demonstrated that this sensing system can measure changes in the internal strain resulting from both static and dynamic truck loading of the bridge.
We have modelled fiber optic intracore Bragg gratings by a series of elemental gratings and used T-matrix formalism based on mode-coupled theory to determine the effects of nonuniformity and strain gradients on their spectral response. We have shown that strong strain gradients can significantly degrade the Bragg reflection spectrum and provide a warning of debonding between the sensor and its host material.

Acknowledgments

We acknowledge support from the many agencies involved in this project. These include: Canadian Space Agency, City of Calgary, Institute for Space and Terrestrial Science, Natural Science and Engineering Research Council, Ontario Centre for Materials Research, and the Ontario Laser and Lightwave Research Centre. This project was greatly helped by the efforts of many members of the UTIAS Fiber Optic Smart Structures Laboratory, especially: G. Fishbein, S. Huang, S. Karr, D. Glennie and M. Ohn. The authors would also like to thank K. Hill of Communications Research Centre for providing the intracore Bragg gratings and D. J. DiGiovanni of AT&T Laboratories for the Erbium doped fiber, Dr. G. Tadros of Staight Crossings Inc., S. Rizkalla of the University of Manitoba and A. Guha-Thakurta and C. Wade of the City of Calgary for much help and guidance.

References

A.T Alavie, S.E.Karr, A. Othonos, and R.M.Measures, 1993, " Fiber Laser Sensor Array", SPIE-Vol., 1918, Smart Structures and Materials Conference, Albuquerque, February 1-4.

S. Huang, M. LeBlanc, M. Ohn and R. M. Measures, "Bragg Intra-Grating Structural Sensing," International Conference on Applications of Photonic Technology, 21-23 June 1994, Toronto.

R. Maaskant, T. Alavie, R. Measures, M. Ohn, S. Karr, C.Wade, G. Tadros and S. Rizkalla, 1994, "Fiber Optic Bragg Gratting Sensor Network Installed in a Concrete Road Bridge," SPIE-Vol., 2191-53, Smart Structures and Materials Conference, Orlando, 13-18, February.

R.M., Measures, S.M., Melle and K., Liu, 1992, "Wavelength Demodulated Bragg Grating Fiber Optic Sensing Systems for Addressing Smart Structure Critical Issues", Smart Materials and Structures, Vol.1., 36-44.

R. M. Measures, T. Alavie, R. Maaskant, S. Karr, S. Huang, L. Grant, A. Guha-Thakurta, G. Tadros, and S. Rizkalla, 1994a, " Fiber Optic Sensing for Bridges," 4 th International Conference on Short & Medium Bridges, Halifax, 8-11, August.

R. M. Measures, S. Huang, M. LeBlanc, M.Ohn and A.T. Alavie, 1994b, "Bragg Intra-Grating Sensing, Implications for Smart Structures," SPIE Vol. 2191, Smart Structures and Materials, Orlando, 436-445.

S.M., Melle, K., Liu and R. M., Measures, 1992 "A Passive Wavelength Demodulation System for Guided-Wave Bragg Grating Sensors", IEEE Phot.Tech. Lett. vol.4, 516-518.

S.M., Melle,T., Alavie, S., Karr, T., Coroy, K., Liu, and R.M. Measures, 1993," A Bragg Grating-Tuned Fiber Laser Strain Sensor System ", Photonics Technology Letts. Vol. 5, 263-266.

G. Meltz, W. W. Morey, and W.H. Glenn, 1989, "Formation of Bragg gratings in optical fibers by a transverse holographic method", Opt. Lett., Vol 14, 823-825.

W.W., Morey, G., Meltz and W.H., Glenn, 1989, "Fiber Optic Bragg Grating Sensors", SPIE Vol. 1169, Fiber Optic & Laser Sensors VII, 98-107.

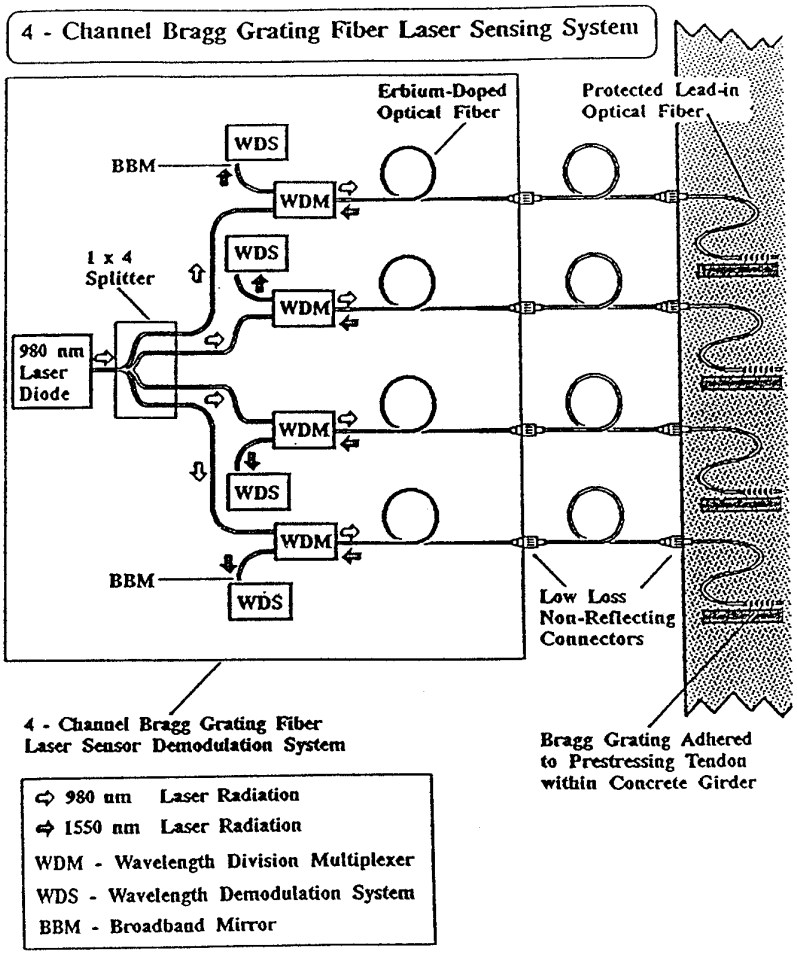

Figure 1. Schematic of a four-channel Bragg grating fiber laser sensing system based on passive wavelength demodulation and involving two low-reflection, low-insertion loss connectors in each laser cavity.

Figure 2. Photograph of portable 4-channel Bragg grating sensor demodulation system being used to test some of the instrumented precast concrete girders at the Beddington Trail bridge construction site.

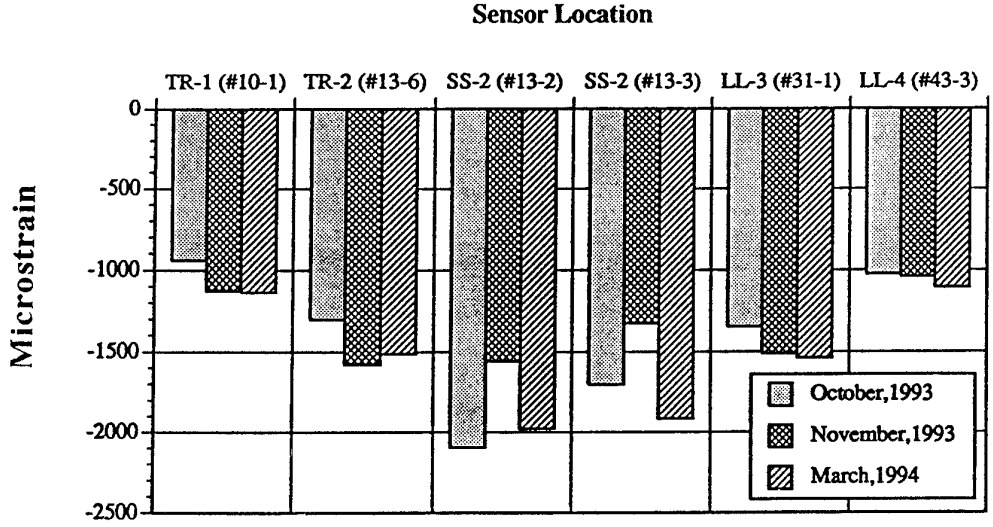

Figure 3. Preliminary internal strain measurements from the Beddington Trail Bridge revealing, the stress relaxation in the carbon and steel tendons from the combined effects of: destressing, concrete shrinkage, dead loading of the bridge deck, and the post-tensioning applied across the two spans. Sensor code: TR-Tokyo Rope, LL-Leadline and SS-Steel, tendons.

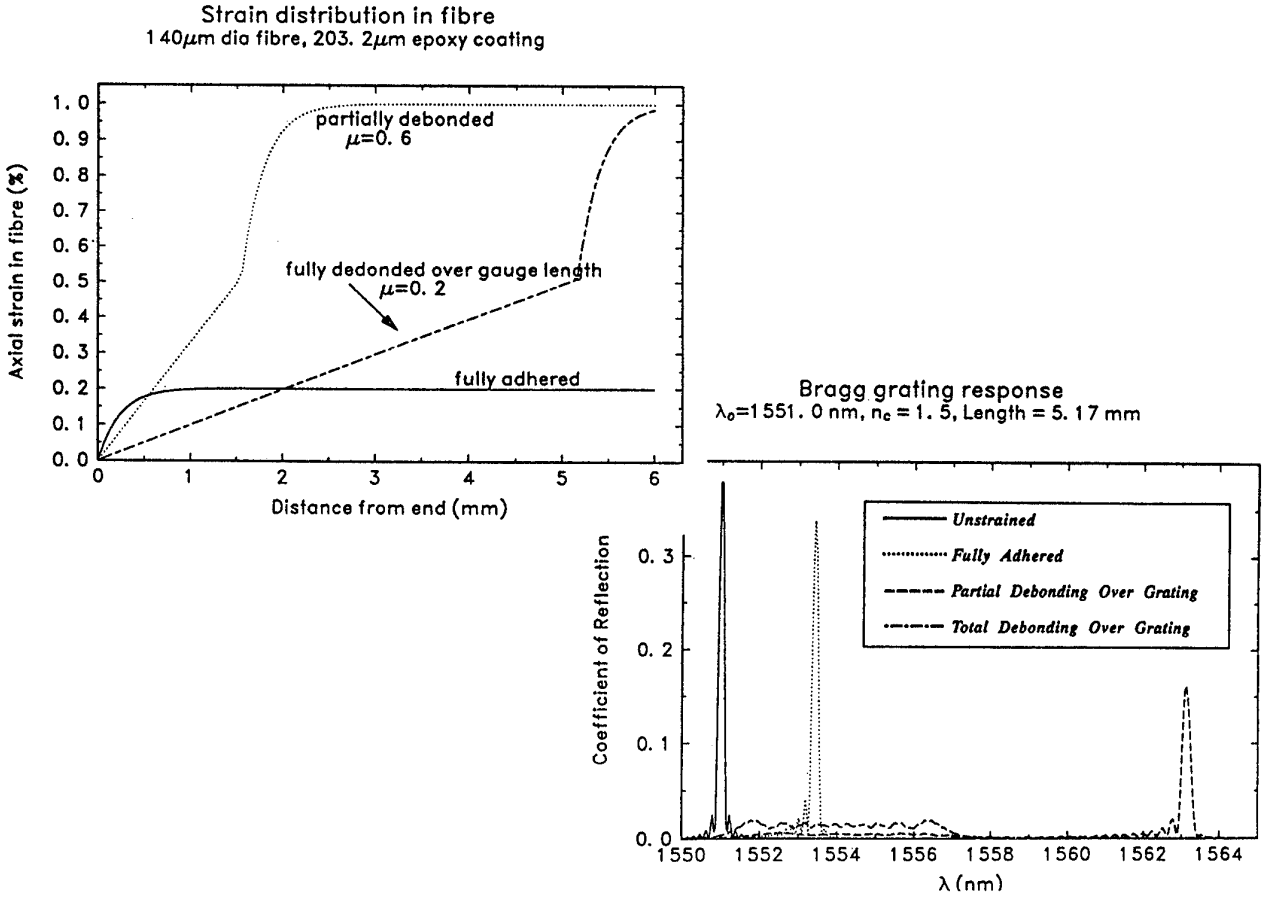

Figure 4. (a) Strain distributions corresponding to: fully adhered, partially debonded and fully debonded fiber optic Bragg grating sensors.

(b) Computed Bragg grating reflection spectra corresponding to the above strain distributions.

Paper presented at the Second European Conf. on Smart Structures and Materials, Glasgow 1994, Session 4

The Influence of concrete and alkaline solutions on different surfaces of optical fibres for sensors

Wolfgang R. Habel, Monika Höpcke, Frank Basedau, Helmut Polster

Institut für Erhaltung und Modernisierung von Bauwerken e.V. (IEMB), Berlin
(Institute for Maintenance and Modernization of Structures)
Plauener Str.163-165, D-13053 Berlin, ☎ +49 30/97 99 23 47, Fax: +49 30/9750524

Primarily coated optical fibres for non-destructive monitoring of structures were embedded in cement mortar bodies and, in a separate test series, exposed to concrete-specific chemical attacks. Microstructure studies after four weeks revealed the relative resistance of acrylate-coated and flourine polymer-coated fibres. Polyimide-coated fibres showed serious changes in the coatings after the exposure.

Introduction

By now, lightwave guides are used in civil engineering for measurement of strain and for indication and assessment of damages. Usually a direct contact of unjacketed fibres is avoided; the concrete's influence on fibres to be used as sensors has not yet been investigated systematically. Applied sensors are protected and merely fixed by special pins to the object of measurement at certain points /1/.

However, in some cases one cannot avoid contact of stripped fibres with concrete because of constructional conditions. For instance, some fibres of measuring rods of 2 m length were broken very close to the sensor, probably due to shock loads during strain measurements in a freshly concreted base plate of a final settling tank. There is reason to suppose that the merely coated fibres were affected chemically and/or mechanically during filling the rod mould with cement mortar /2/.

In order to determine deformation profiles exactly or to follow the settling process of concrete, up to detecting crack growing inside the body of a structure, a direct embedment of merely coated optical fibres in concrete components is desirable. To do this a continuously force-determining contact between sensor and object of measurement has to be ensured. The essential precondition for this is detailled knowledge of the processes in the fibre - concrete interface region; some results of guidance investigations at IEMB are presented.

Measuring task

When optical fibres are embedded in concrete they are mainly affected by the following:

- *mechanical attacks* as a time-limited occurence; due to aggregates during pouring of the fresh concrete and due to growing of cement stone crystals onto the fibres during the settling process
- *chemical attacks* during the whole life-span of the structure

The chemical attacks are changeable and manifold dependent on the concrete's composition and the period and kind of the structure's usage; the matter-specific alkalinity is always there. It is caused by calcium hydroxide which comes into being during hydration reaction of cement and which can also contain, dependent on the kinds of cement used, potassium and sodium hydroxide. Therefore the pH value of the fresh concrete can vary from pH = 12.4 to 14.0.

0-8194-1700-9/94/$6.00

In order to reduce the corrosive alkaline attacks on the glass fibres the cement matrix is modified, e. g. by means of adding pozzolanas or special Na_2O-SiO_2-ZrO_2 glasses /3/.

If, at present, you want to use glass fibres for structural monitoring, you firstly have to choose well-known optical fibres in order to ensure certain optical qualities and, secondly, you need to aim at a reduction of the attacks by an appropriate design of the interface region. In order to do this, knowledge of notch-unsensitive and alkaline-resistent coatings is indispensable. When designing the concrete - fibre interface region one has to pay attention to the concrete bond as well as to the load transfer onto the fibre. An additional layer around the sensor to guard against chemical and mechanical attacks must not lead to distortions in measuring the deformation.

The priority task of the investigations is the determination of suitable coating materials for a durable concrete contact. This necessitates, in addition to the matter-of-course rather "phenomenological" investigation of the long-term attenuation behaviour of embedded fibres, an analysis of micro reactions of the fibre components as well as of the micromechanical processes in the interface region. In /4/ Mendez et. al. address some problems that have to be solved and they suggest a special embedment technique. As yet, extensive investigations on concrete contact to optical fibres, as compared to /3/, have not been published. Escobar et. al. /5/ and Fuhr et. al. /6/ have reported their experience with the embedment of optical fibres in concrete, but without describing details of coating behaviour. We believe, that to ensure an efficient use of the fibres a microscopic proving of the long-term coating resistance is the first step and the coating optimization is the second step.

Experimental concept and specimen preparation

In order to separate the chemical influences from the mechanical ones different fibre pieces were embedded in cement mortar as well as directly exposed to attacks of chemical solutions. The fibres used are specified in table 1. For a separate assessment of possible attacks on coating and on glass the specimens were being prepared specifically. A stereo light microscope (125-times) of type Technival 2 (Jenoptik/G) and a scanning electron microscpe (SEM) op type BS 340 (Tesla/CS) were used . Two fibre ends were used for each specimen and each test series respectively.

Table 1: Specification of fibres used

Type No.	Dimensions Glass d_i/d_e	Coating		Remarks	
		Thick-ness	Material, Construction	Bonding Coating/Cladding	Removing
0-1 *	G 50/125 µm	62,5 µm	*Acrylate*-System (colour-coated)	very good	good (relatively soft)
0-2 *	G 50/125 µm	32,5 µm/ 30,0 µm	*Acrylate-System* (inside: soft/ outside: hard)	very good	good
0-3	S 9/125 µm	62,5 µm	*Acrylate*-System	very good	good
0-4	G 50/125 µm	7,5 µm	*Polyimide*	very good	bad, removed by Methylen-chloride
0-5 *	S 50/125 µm	14,8 µm	*Polyimide* (colour-pigmented)	good	bad
0-6	G 200/220 µm	11,5 µm	UV-hardened HPCS (*Fluorine-polymer*)	good (Coating's strength is very high)	good

* these types were embedded in concrete

Mechanical influence on fibres during embedment in cement mortar
The fibres chosen- all of which have merely got the primary coating - were embedded in a cement mortar body (rigth parallelepiped 160 x 40 x 40 mm^3, portland cement PZ 35 F, granularity 0 to 4 mm with a 4 mm-portion of ~ 15 %, water-cement ratio = 0,46) and tamped moderately. The fibres protruded at the body's end faces; it was stored for 28 days. The exposure of the fibres could be achieved by means of a PVC-shim which ended about 3 mm above the fibre line. After pulling out the shim the body was carefully splitted in two; the fibres could be analysed very well.

Chemical attacks on the optical fibres
The coatings were mechanically removed in a length of 20 mm. A check up by microscope confirmed the intactness of the glass surface. The coating of fibre type 0-4 was removed chemically by methylene chloride (separate protection of the remaining coating) and cleaned again with destilled water. The fibres were dipped into the alkaline solutions for about 60 mm and were analysed after one day, seven days, 21 days. The following solutions were chosen: aqueous, saturated concrete extract of pH = 11, saturated $Ca(OH)_2$-solution of pH = 12,4, soda lye and potash lye, both 3 per cent, pH = 14. All examinations were made at room temperature.

Results

In all solutions the **acrylate-coated fibre surfaces** showed slight reactions which started after some days. All specimens developed matt patches after 21 d; on some fibres (types 0-2, 0-3) the beginning of this effect could be discovered after 7 d. Type 0-3 did not show any reaction in potash lye; but it showed a uniform unsmooth surface ("sandpaper-effect) after 21 d in concrete extract. Type 0-2 showed the same effect. For the fibres of type 0-1 no changes could be discovered apart from the fact that the fibre's colour coding-layer softened in potash lye and that it could be slipped off. The underlying glass surface was intact. Only by SEM changes in the coating's general impression of type 0-2 exposed for 21 d in $Ca(OH)_2$-solution could be detected. However, it cannot be ruled out that this effect was caused by the conducting paste's solvent used for fixing the specimens on the supporting slide.
The fibres 0-2 with the sandpaper surface which developed after loading under concrete extract showed bad bonding to concrete *inside the mortar body*. The fibre's surface showed small scratches due to aggregates; the pulling out of the cement stone matrix was possible without great resistance. Some not wipeable matt patches were detected on the surface. Small fibre deflections caused by aggregates were obvious. Likewise, type 0-1 showed a weak bonding to concrete, but in this case cement matrix chips clinged to the colour layer around the coating. Pulling out the fibres, the colour layer was ripped off; no damages of or chemical influences on the glass could be observed.

No influence of any kind due to alkaline attacks was observed on **fluorine-thermoplastic-coated fibres** (0-6).

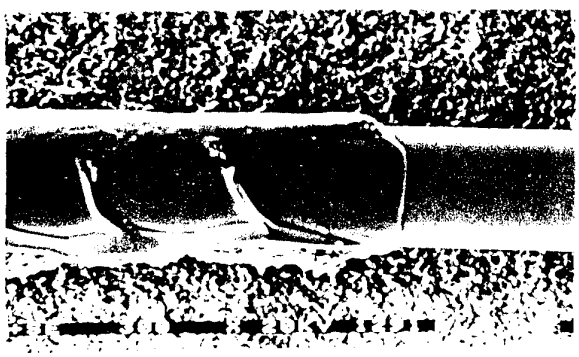

Fig. 1a. Type 0-5, soda lye, 7 d (x 300)

Fig 1b. Type 0-4, soda lye, 7 d, (x 500)

Polyimide-coated fibres showed serious changes. The reactions generally started in a period from 1 d to 7 d, with exception of soda lye and potash lye, where changes occured already after 24 hours. Type 0-4 showed no changes in the concrete extract and in the $Ca(OH)_2$-solution after 7 d. Type 0-5 showed occasional matt patches in the concrete extract. Fibre type 0-5 showed considerable impairments in potash lye and soda lye after 7 d. Fig. 1a shows the tearing off of the coating completely kept in soda lye, after it had been cleaned again with destilled water and had carefully been drawn through a moist cotton-wool pad. The coating portion which remained on the glass fibre formed crinkles. Fig. 1b shows a section of type 0-4 which was completely kept in soda lye for 7 d. The polyimide coating obviously softened and swelled up (forming crinkles, too). The coatings of fibre type 0-5 completely came off in potash lye after 21 days. In the lye - vapour phase interface area the coatings were nearly completely destroyed, while about 5 mm above the lye level the coating's swelling process led to crinkles. The same behaviour was observed in soda lye.

Fig. 2. Type 0-5, embedded in cement mortar, 28 d, (SEM - x 350)

The crinkles that could be observed in alkaline solutions also developed when the fibres were *embedded in cement mortar*. Fig. 2 shows an exposed fibre of type 0-5 after a curing period of 28 days. One can clearly see the cement stone crystals bonded to coating and grown in between the crinkles.

Conclusion

Optical fibres with different coatings kept over different periods of time in concrete-typical alkaline solutions were studied by SEM with regard to an attack of hydroxyl ions and several cations. Also, individual fibre types were embedded in cement mortar und investigated after 28 days by SEM. Both test series showed that the polyimide coatings changed seriously, so that their protective functions against moisture and OH^- got lost. Polyimide-coated fibres should not be used for an embedment in concrete. It needs to be investigated to what degree such crinkles could be generally helpful for load transfer from host material to sensor. Acrylate-coated fibres showed changes dependent on the charge. For one fluorine-polymer-coated charge a considerable resistance to all used solutions could be determined over the observation period.
Based on special-coated fibres the tests will be continued at IEMB in order to determine the durability of sensor fibres.

Acknowledgements

The SEM-photographs were made by Mr. K. Wehner, Dept. Building Chemistry, Building Material Examinations und Corrosion Prevention of the IEMB. The investigations were supported by the BMFT of the Federal Republic of Germany.

/1/ Referenzliste Überwachng mit Lichtwellenleitersensoren, SICOM GmbH Köln, Stand Febr. 1993
/2/ Technical report 4-30.93: IEMB Berlin, 1993
/4/ Majumdar, A.J.; Laws, V.: Glass fibre reinforced cement. BSP Professional Books, London 1991
/3/ Mendez, A: Applications of embedded optical fiber sensors for non-destructive testing of concrete elements and structures. Applications of Fiber Optic Sensors in Engieneering Mechanics. ASCE New York, 1993, S. 144-158.
/4/ Escobar, P.;u. a.: Fiber-optic interferometric sensors for concrete structures. 1st Europ. Conf. on Smart Structures and Materials, Glasgow 1992, S. 215-218.
/5/ Fuhr, P; u. a.: Stress monitoring of concrete using embedded optical fiber sensors. Preprint, Information by Dr. Fuhr, University of Vermont, Dept. of Elect. Engrg. 1993

Paper presented at the Second European Conf. on Smart Structures and Materials, Glasgow 1994, Session 4

DESIGN AND OPERATION OF A GALVANIC SENSOR FOR IN-SERVICE MONITORING OF THE CORROSION OF STEEL IN CONCRETE

N R Short, C L Page and G K Glass

Aston University, Department of Civil Engineering, Birmingham, UK

1 ABSTRACT

This paper describes the construction and operation of a galvanic sensor which responds to changes in the corrosion intensity of mild steel in carbonated mortars or concretes. The sensor is simple to construct and operate. It is robust and has potential for development as an inexpensive method for long-term, continuous non-destructive corrosion monitoring of steel in concrete. Its range of possible applications include laboratory and field studies of effects of environmental exposure conditions and cement matrix variables on corrosion rates of steel in reinforced concrete structures. Information derived from such investigations is needed to provide an improved basis for service-life prediction.

2 INTRODUCTION

Corrosion of reinforcing steel is one of the major causes of the premature deterioration of structural concrete. The kinetics of steel corrosion have usually been investigated by somewhat elaborate techniques, involving sophisticated electrochemical monitoring procedures. Although estimates of long-term integrated corrosion losses may be obtained by means of devices such as electrical resistance probes, these are incapable of providing information about short-term changes in corrosion rate in response to changing environmental factors. A simple sensor which can monitor the instantaneous corrosion rate of steel continuously over a long period of time would therefore be useful as a means of determining the effect of changes in environmental conditions and cement matrix variables both in the laboratory and for field studies. Successful monitoring should enable the determination of the initiation time to depassivation of steel, the subsequent rate of corrosion as a function of time and the tolerable amount of corrosion prior to cracking, for different environmental conditions and concrete qualities. This information would provide an improved basis for service life prediction.

The aim of the work described in this paper was to design and evaluate a galvanic sensor for monitoring electrochemical changes associated with the initiation and propagation of carbonation - induced corrosion. In particular it was required that the sensor should be sensitive enough to detect changes in corrosiveness of the concrete as a result of e.g. changes in moisture conditions and the presence of chlorides. It was also necessary that the sensor should be easy to construct, sufficiently robust for use in field studies, and that the associated instrumentation required for measurement should be simple.

3 EXPERIMENTAL

The galvanic sensor consisted of a disc of mild steel (anode) exposed through a hole drilled perpendicular to the axis of an austenitic stainless steel bar (cathode), as shown in Fig. 1. To insulate the mild steel from the stainless steel and to prevent crevice attack, the mild steel was covered by a thin layer of SBR modified cement paste, followed by heat shrink tubing. It was fixed within the stainless steel bar by an epoxy adhesive. A capillary salt bridge was mounted so that its tip was in close proximity to the exposed mild steel.

The sensor's primary mode of operation was as a galvanic couple, in which the current (Igalv) provided an index of the corrosiveness of the surrounding mortar. The device could also be used to form a cell subjected to polarisation by means of a potentiostat with the mild

0-8194-1700-9/94/$6.00

steel disc as working electrode and the stainless steel bar as counter electrode. This allowed the determination of polarisation resistance (Rp) and corrosion potential (Ecorr).

To ascertain whether any artifacts were associated with measurements made with the galvanic sensor, an alternative polarisation resistance probe was designed, consisting of a mild steel sheet of exposed area 2 cm^2, fixed parallel to a mesh counter electrode (titanium wire coated with an electrocatalyst) with a capillary salt bridge terminating in the space between them, see Fig. 2. In comparison with the galvanic sensor, the cell arrangement promoted a more uniform current distribution and the working electrode area was increased to facilitate accurate current measurement.

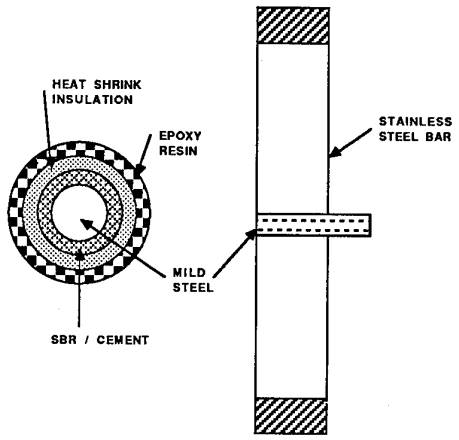

FIG. 1 CONSTRUCTION OF THE GALVANIC SENSOR

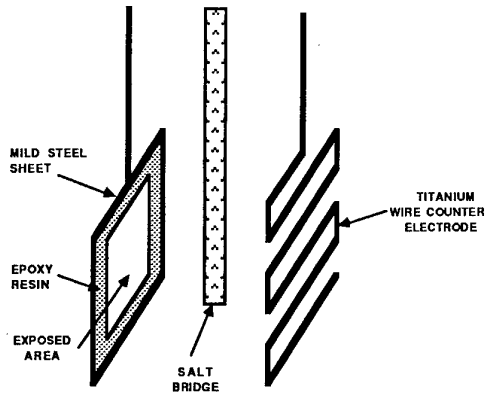

FIG. 2 CONSTRUCTION OF THE POLARISATION RESISTANCE SENSOR

Both types of sensor were then embedded in mortar cubes made using an Ordinary Portland Cement (OPC) and blends prepared from OPC and 65% ground granulated blastfurnace slag (GGBS) or 30% pulverised fuel ash (PFA). Mix design was such that the mortars had a relatively open pore structure to allow rapid carbonation and a fast response to changes in relative humidity (RH). Some specimens contained chloride, introduced by dissolving analytical reagent grade sodium chloride in the water prior to mixing, giving a chloride ion concentration of 0.4 or 1.0% by weight of the cement. An environmental chamber was used to carry out accelerated carbonation at controlled temperature / relative humidity, and subsequently for creating atmospheres of systematically varied relative humidity.

In the case of the galvanic sensor, the potentials of the stainless and mild steels were measured by means of a digital voltmeter. Galvanic current was determined by measuring the potential drop across a resistor of suitable value (« the electrolytic resistance of the mortars) after it had shorted the mild steel - stainless steel couple for 5 minutes.

For both types of sensor Rp values for the uncoupled electrodes were measured using methods described in more detail elsewhere(1). From the values of Rp obtained, corrosion intensities (Icorr) were calculated by means of the Stern-Geary equation:

$$Icorr = B / Rp$$

where $B = (\beta a \times \beta c) / 2.3(\beta a + \beta c)$. The anodic and cathodic Tafel coefficients, βa and βc, were both assumed to be 120 mV / decade, resulting in B = 26 mV. This has been found to yield acceptable agreement with gravimetric determinations for steel suffering active corrosion in concrete.

4 RESULTS

An example of the electrochemical response of a galvanic sensor embedded in an OPC mortar is shown in Fig. 3. Accelerated carbonation of the mortars commenced when samples were 62 days old (shown as zero time in Fig. 3) and continued for a period of 25 days. During the carbonation period, the RH in the tank was difficult to control and fluctuated between 63% and 79%, probably as a result of release of moisture during carbonation. The RH was then altered stepwise for successive periods as indicated at the top of Fig. 3a. The resulting changes in electrochemical response are shown for (a) the potentials (versus SCE) of the mild and stainless steel, (b) galvanic current (Igalv) of the mild steel - stainless steel couple, and (c) corrosion intensity (Icorr) of the mild steel calculated from measurements of Rp.

Carbonation penetrated to the level of the embedded sensors after an estimated 10 days at which time there was a marked decrease in the potential of the mild steel accompanied by increases in Igalv and Icorr. Thereafter the electrochemical behaviour followed changes in RH, so that a lower RH (e.g. 50% or 38-44%) produced smaller galvanic currents and corrosion intensities with less negative mild steel potentials, whilst the converse was true for a higher RH (e.g. 90-92% or 74-77%). Although fluctuations in stainless steel potential were observed, these were generally small in comparison with the changes in the potential of the mild steel.

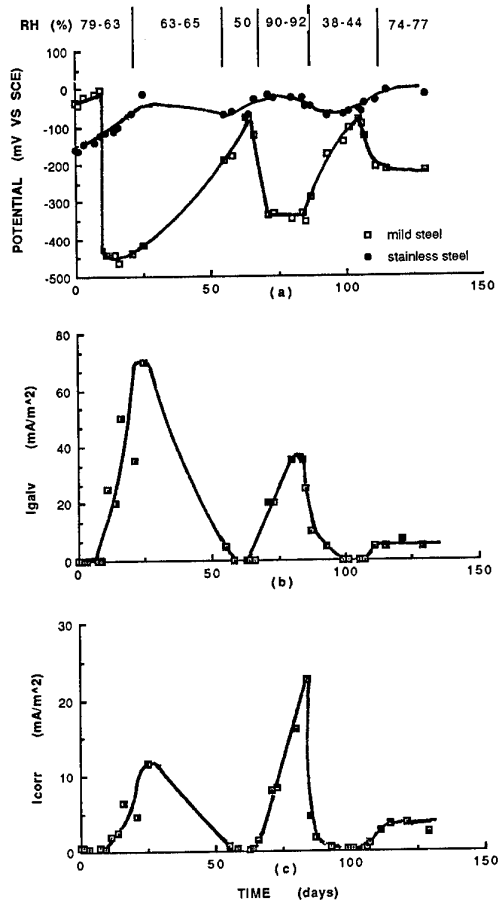

FIG. 3 CHANGES IN THE ELECTROCHEMICAL RESPONSE OF A GALVANIC SENSOR EMBEDDED IN AN OPC MORTAR:
(A) POTENTIALS OF MILD AND STAINLESS STEELS
(B) GALVANIC CURRENT, Igalv
(C) CORROSION INTENSITY, Icorr.

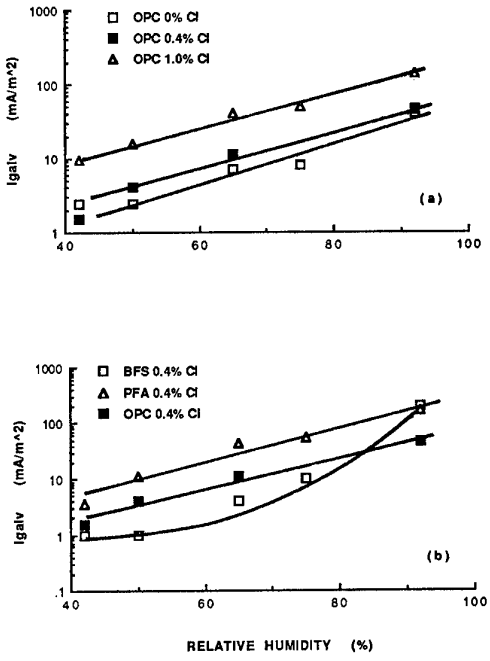

FIG. 4 VARIATION IN Igalv WITH RELATIVE HUMIDITY IN CARBONATED MORTARS:
(A) INFLUENCE OF CHLORIDES
(B) INFLUENCE OF BLENDED CEMENTS.

The reproducibility of results from galvanic sensors in identical mixes was generally very good and essentially similar trends to those presented in Fig. 3 were found for blended cement samples and for mixes containing 0.4 and 1.0% Cl. Using average values of Igalv from a number (~ 4) of sensors, regular trends in behaviour could be determined. For example, from the values of Igalv taken towards the end of a RH cycle when conditions had stabilised it was possible to demonstrate the sensitivity of the galvanic sensor to changes in RH (a regular increase in Igalv with increase in RH, Fig. 4a), the presence of chlorides (an increase in Igalv at any given level of RH, Fig. 4a) and the influence of blended cements, (Fig. 4b).

Changes in Ecorr and Icorr for the polarisation resistance probe embedded in the same mortar, followed exactly the same trends as for the galvanic sensor. It should be noted, however, that values of Icorr for this probe were lower than those for the galvanic sensor. This was also noticed when comparing the responses of the two devices in other mixes.

5 DISCUSSION

Comparing the results shown in Figs. 6b and 6c it is evident that the galvanic response of the simple sensor (Igalv) is related to the corrosion intensity of mild steel (Icorr) as measured by the more elaborate electrochemical technique of polarisation resistance determination.

The more complex polarisation resistance probe shown in Fig. 2, confirmed the trends in Icorr found with the galvanic sensor. Results obtained with the former device have been used as a means of more detailed elucidation of the mechanism of steel corrosion in carbonated concrete and these aspects of the work are reported elsewhere(2). Although the probe illustrated in Fig. 2 has some advantage with regard to its accuracy, it is less robust and requires more complex instrumentation than the galvanic sensor. It is therefore considered that the latter device is likely to be the more suitable one for prediction of relative corrosion rates in the majority of long term exposure tests and similar field applications.

In field studies it should be appreciated that, even if the sensors are embedded in close proximity to the reinforcing bars, the information obtained relates to the sensor itself and not the main steel. It cannot be assumed that the reinforcement will always behave in a similar manner to the sensor. Thus it would be necessary to determine a sensor 'constant' which correlates the values of Igalv to weight loss measurements of the adjacent reinforcing bar. Similarly a number of sensors would have to be installed to monitor a single structural member - the optimum number required being determined by experience. With this additional information, galvanic sensors should be helpful in establishing models for the prediction of corrosion behaviour of reinforced concrete structures.

6 CONCLUSIONS

A galvanic sensor has been devised which responds to changes in the corrosion rate of steel in carbonated mortars. The sensor is easy to construct and associated measuring instrumentation is simple. It is robust and has potential for development as an inexpensive method for long-term continuous non-destructive corrosion monitoring of steel in real structures.

7 ACKNOWLEDGEMENTS AND REFERENCES

The authors gratefully acknowledge financial support from the SERC and the BRE.

1. Short N R, Page C L and Glass G K, A galvanic sensor for monitoring corrosion of steel in carbonated concrete. Magazine of Concrete Research, Vol. 43, 1991, pp 149-154.

2. Glass, G. K., Page, C. L. and Short, N. R. Factors affecting the corrosion rate of steel in carbonated mortars. Corrosion Science,Vol. 32, 1991, pp 1283-1294.

Paper presented at the Second European Conf. on Smart Structures and Materials, Glasgow 1994, Session 4

Determination of structural parameters concerning load capacity based on Fibre-Fabry-Pérot-Interferometers

Wolfgang R. Habel, Detlef Hofmann

Institut für Erhaltung und Modernisierung von Bauwerken e.V. (IEMB), Berlin
(Institute for Maintenance and Modernization of Structures)
Plauener Str.163-165, D-13053 Berlin, ☎ +49 30/97 99 23 47, Fax: +49 30/9750524

Fibre optical sensors were applied on a cracked prestressed concrete bridge in Berlin to get the static and dynamic structure response under load. Interferometric sensors (extrinsic Fibre-Fabry-Pérot) were adhered on prestressing steels of a tendon opened inside the box girder; Intensity-modulated fibre sensors were tightened over the cracked concrete region. The very high resolution of interferometric sensors ($\varepsilon = \pm 0{,}024$ µm/m) simultaneously allowed to measure strain of tendon *and* dynamic (natural frequency) response. This bridge is the first prestressed concrete structure in Germany to have fibre optic interferometric sensors installed. The optimization of the adhesive bonding and embedment technique are problems that need to be addressed as part of the further development.

Introduction

In Germany traffic building are regularly being inspected on its stage of structure (observation and inspection of structures according to DIN 1076). In case the structure inspection should reveal cracks exact data concerning the strength-determining characteristics are necessary in order to assess the service quality (if need be, residual load capacity) and the life-span to be expected. To do this, in prestressed structures the vibration behaviour of a structure and the strain response of the tendons during a defined load (test load) are measured exactly. As sensors are generally being used: resistive strain gauges, acceleration sensors, inductive displacement transducers, vibration meters /1/.
Since the interferometric microsensors with high resolution are available, interesting uses in the field of structural diagnostics have become possible /2/. Favourable applicability of fibre sensors in civil engineering is to be exemplified using the case of deformation measurement in a prestressed concrete bridge.

Measuring task

A routine check of a motorway bridge in Berlin-Charlottenburg revealed a vertical crack at the outside of the bridge's box girder as well as several smaller cracks near the main crack. To assess the functional efficiency of the tendons, it was intended to carry out measurements concerning the vibration behaviour, the deformation and the behaviour in the crack region. As well as electrical sensors fibre optical sensors were to be used.

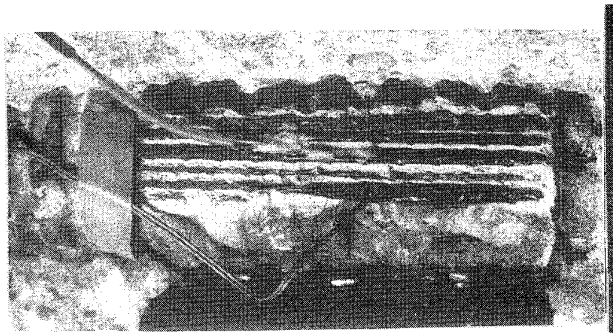

Fig. 1. Fibre optic sensor attached on the exposed prestressing steel

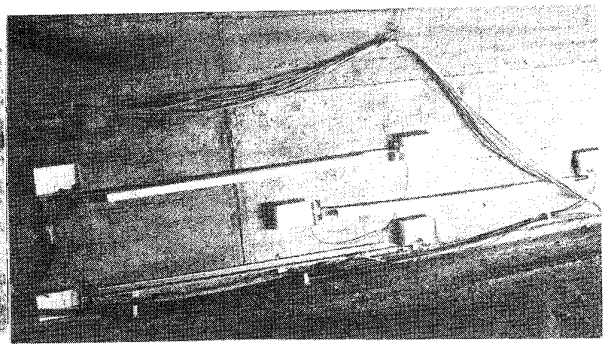

Fig. 2. Stranded fibres spanned on the concrete surface in the crack region

0-8194-1700-9/94/$6.00

For the test load a motor crane of DEMAG AC 435 -type (5 axles, uniform axle spacing of 1,5 m) with a total assets of 66 t, was used. The motor crane drove at different speeds (walking speed, 30 km/h, 60 km/h) on different lanes of the bridge. In addition typical traffic loads, including a high number of trucks, were recorded.
On both sides of the crack region one of the tendons was opened and a fibre -Fabry-Pérot as well as a resistive strain gauge were applied to an exposed prestressing steel (fig. 1). In addition, three stranded fibre sensors (of one meter length respectively) were spanned on the surface of the concrete wall's crack region (fig. 2).

Description of sensor technique

An extrinsic Fabry-Pérot-interferometer (manufactured by Fiber & Sensor Technologies, Blacksburg Virginia, USA) was used as sensor for the deformation measurement of the prestressing steel. The build up of the sensor is described in detail under /2/. In order to measure small changes in distance of opposed end faces by means of strain/contraction of the hollow tube the Fizeau-interference is used. The deflection of the fibre ends inside the hollow tube can be measured by means of assessing the changes in intensity (within an interference fringe) as well as by counting the interference fringes. This method is used to determine the strain of the prestressing steel and the vibration response of the bridge, including higher harmonic oscillations. In a special adhesion method the sensor element (hollow tube) was attached to the prestressing steel; the measuring basis (about 10 mm) is determined by its length.

Measuring parameters of interferometric micro-sensors:

Length of sensors (measuring basis):	ca. 10 mm
Sensor diameter:	< 1 mm
Connection cable:	Singlemode-fibre cable - diameter: 2,8 mm (Length about 40 m)
Measuring range (deflection):	< 50 µm (in relation to 10 mm meas. basis)
Strain resolution:	470 pm (in relation to 10 mm meas. basis)
Vibration limit:	80 kHz (for deflection < 10 µm)

The spanned fibres on the concrete surface consist of three stranded fibres (manufactured by SICOM GmbH Cologne, Germany) /3/. When there is an extension (or contraction) of the sensor this wire coil produces changes in local deformation of the fibres. This lead to changes in intensity of the light transmitted.

Installation

The microsensors were attached directly to the exposed prestressing steel. Pilot tests in the laboratory proved that a reproducible mechanical transmission of strain changes to the sensor can be guaranteed if one uses an appropriate adhesive /4/. The fixing of the stranded fibres was pre-fabricated in the laboratory, then attached to the concrete surface and - after a curing time of the adhesive of about 30 min. - biased in a defined value. The adhesive used was the 2-part-epoxy resin Silikal (manufactured by Silikal K. Ullrich GmbH, Mainhausen, Germany). The fixing of the optical connection cables was carried out in a usual manner, where necessary.

Measuring equipment and measuring program

The measuring signals of both sensor types were evaluated in separate receiving devices. For the microsensors a special bias and receiving device (manufactured by Fiber & Sensor Technologies, Blacksburg Virginia, USA) was used; the receiving device for the stranded fibre was developed and manufactured by the IEMB. The electronic signal was digitalized (A/D-transducer width: 12 bit) after having been converted and amplified. A generally available measuring program was used to record and to evaluate the measuring signals.

An uniterruptal power supply UPS (manufactured by Heinrich-Notstrom-Service, Hohenstein-Ernstthal, Germany) was connected with the supply circuit of the data recording equipment to guard against power failure (max. 3 hours) and voltage peaks. Data reduction and preliminary data editing were not intended, i. e. the measuring information was stored on the hard disk of the PC (486/ MHz, HD 240 MB) as original signal.

The interferometric sensors were sampled at 100 Hz for the test load and at 200 Hz for the traffic load. The stranded sensors and the sensors for temperature reference were sampled at 100 Hz. The recording was carried out during the measuring period only.

Results

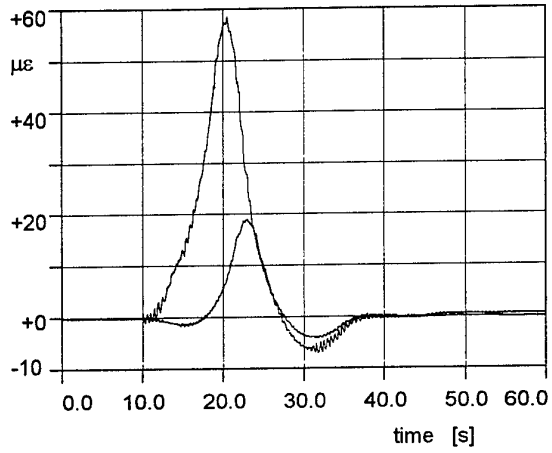

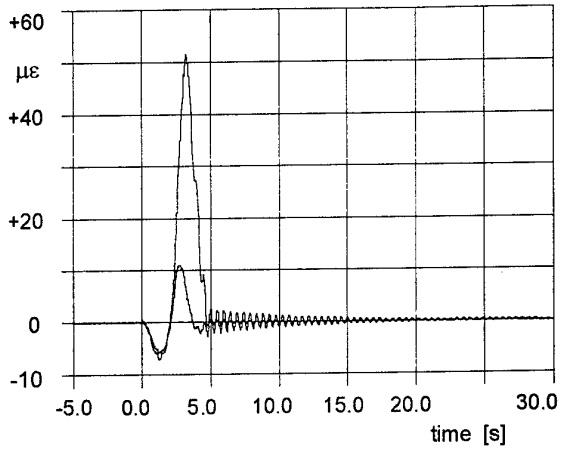

Fig. 3a. Steel strain during the test load (walking speed)

3b. Steel strain during the test load (60 km/h)

(smaller deflection: Sensor located at the calculated zero moment point of the bridge)

Following you can find an extract of the recorded data /5/. Fig. 3a and 3b show the strain of the prestressing steels at both measuring points, which are located in a distance of 7,60 m, at low and at high speed of the test vehicle. From them you can learn directly on the one

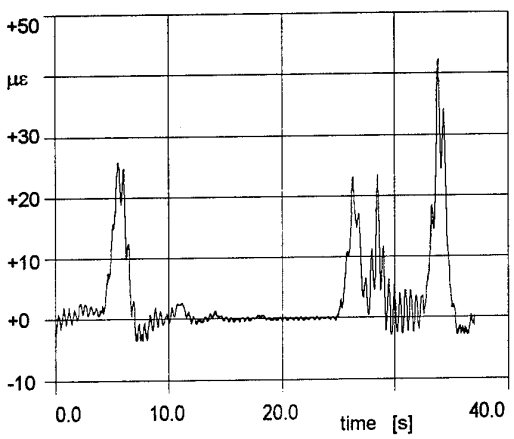

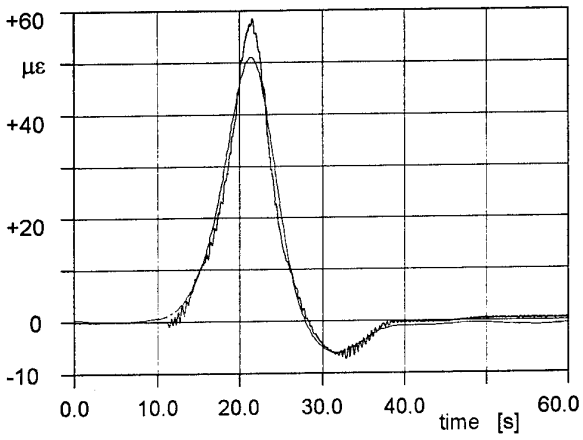

Fig. 4. Typical traffic load, including a high number of trucks (peaks allow to identificate the load of trucks)

Fig. 5. Comparison of steel strain and strain in the concrete wall near the crack region (smooth curve: stranded fibre sensor)

hand the various grades of deformation (in this case indicated by steel strain), which reflect the different moments of the bridge at the measuring points. On the other hand you can

learn the bridge's natural frequency under load (counting of modulated oscillations). The time lag in the recorded deflection peaks serves as a measure for the vehicle's speed. By looking at the final oscillation curve of the bridge at the moment of its being left by the vehicle (fig. 3b), one can learn the bridge's natural frequency of f_f = 2,10 Hz as well as the damping ratio of β = 1 %. The bridge's fundamental oscillations at times of a typical traffic load (fig. 4) is f_t = 2,06 Hz and is in a good keeping with the measured value of natural frequency without load. Fig. 5 shows comparison of both applied fibre optical measuring methods under condition of a test drive at walking speed. From this one can e. g. check the differences in the strain of the concrete and the prestressed steel section.

An additional FEM-simulation the static and dynamic behaviour of the prestressing concrete bridge resulted in a very good correspondence between the static (strain) and the dynamic (natural frequency) responses.

Conclusion

For the first time in Germany fibre optic interferometer sensors was used in a prestressed concrete structure to record the static and, at the same time, the dynamic behaviour of a bridge under test and traffic loads. The installation in the bridge's box girder proved to be unproblematic. The tiny dimensions of the sensitive elements as well as of the connecting cable ($\varnothing \cong 1$ mm) avoid the formation of cavities during the embedding of the sensors. Additional measurements, which may have to be carried out at later dates, can be made without a renewed opening of the tendon.

Existing strong electromagnetic interference near the measurement location perturbed the display unit during the data recording; however, the very small changes in measured values were recorded interference-free and without any noise in the signal. The S/N-ratio in the used data equipment was 63,2 dB. Based on these changes in strain (strain resolution) for short-term measurements the values could be resolved to 0,024 µm/m for the interferometers and to 4 µm/m for the stranded sensor fibres of 1 m length. The uncertainty of measurement independent of the used measurement system was $\pm$ 0,8 µm/m. The uncertainty of measurement caused by imponderablenesses in application technique (fastening sensors with adhesive) has not been fully validated by statistics; therefore it cannot be quantified. An exemplary investigation of the sensor attached to a steel bent bar in the laboratory resulted in an error of measurement of < 2 % as compared to the mechanically determined value. Even though the deflections were very small, an interference rejection and a measuring data correction were not necessary for an evaluation of the results.

For a wide usage of described sensors further investigations are necessary to ensure reproducibility and a construction-site-efficient application. Main problems that to have to be solved are: the choice of an adhesive, who's elastic modulus is matched to that of glass and steel as far as possible; the improvement of the measurement technique to detect the direction of changes (strain/contraction); the "storage" of the initial and/or instantaneous magnitude, which the sensor sees when the power supply is switched off.

Acknowledgements

The authors would like to thank the Berlin Senate Administration for Construction Engineering and Housing, department for bridges and engineering structures for supporting this work. The laboratory tests were supported by the BMFT of the Federal Republic of Germany. The FEM-calculations were carried out by Dr. Wagenknecht from IEMB.

/1/ Rösler, M.: Interaktion zwischen Brücke und Fahrzeug. Bautechnik Berlin 71(1994)1, 23-30.
/2/ Murphy. K. A.; u.a.: Extrinsic Fabry-Pérot optical fiber sensor. 8th Opt. Fib. Sens. Conf., Jan. '92 Monterey, CA. (USA). Conf. Proc. pp. 193-196.
/3/ Technical information paper. Sensors. SICOM GmbH Cologne, 1991.
/4/ Unpublished laboratory report. Fibre-optic laborytory, IEMB Berlin, 1993
/5/ Technical report 4-01.94: Strain measurements on a motorway prestressed bridge in Berlin-Charlottenburg by means of fibre sensors. IEMB Berlin, 1994

The authors would like to acknowledge the Ministry of Defence for funding this project.
© copyright Crown / DRA 1994

Strain measurements in reinforced concrete walls during the hydration reaction by means of embedded fibre interferometers

Wolfgang R. Habel, Detlef Hofmann

Institut für Erhaltung und Modernisierung von Bauwerken e.V. (IEMB), Berlin
(Institute for Maintenance and Modernization of Structures)
Plauener Str.163-165, D-13053 Berlin, ☎ +49 30/97 99 23 47, Fax: +49 30/9750524

In a reinforced concrete wall the deformation during concrete hardening was measured by means of embedded extrinsic fibre-Fabry-Pérot-interferometers. The sensors were specifically modified in order to provide a self-calibration cycle and to ensure the functional efficiency under adverse conditions at the building site. The installation was done in the wall's cage of reinforcement before its concreting. The measurement was carried out automatically over a period of 35 days. The measuring results are very satisfactory and give a resolution of 0,1 µm/m.

Introduction

Concrete in a young age is subjected to strain which does not normally lead to quality-reducing cracks. In large concrete structures new pouring sections have to be connected successively to already hydrated concrete sections. In such cases, additional stresses in young concrete during hardening caused by different temperature changes in both concrete sections can lead to cracks. These cracks, e. g. in the construction of sedimentation basins cause leaks, and thus have to be avoided.
In large concrete structures with special requirements the deformation behaviour during hardening is to be observed and usually recorded by resistive strain gauges. The usage of resistive strain gauges reaches its limits when one has to determine extremely small strain of less than 10 µε inside the concrete body. Especially in this field fibre interferometers offer new interesting possibilities for acquiring fascinating information about the concrete life.

Measuring task

In a new sewage treatment works which is being built, for the construction of the final settling tanks the reinforced concrete wall (tank wall) will be concreted upon the completely hydrated reinforced concrete base. To avoid cracks in the wall a special temperature control for both concrete sections in order to minimize strain during hydration will be tried out /1/. To verify the theoretical assumptions, the strain behaviour of the young concrete was to be observed by means of embedded resistive strain gauges and extrinsic fibre-Fabry-Pérot-interferometer sensors (EFPI). The assumed strain range is less than
10 µε. The sensors have to be installed as "lost" ones inside the bar reinforcing cage before concreting. They have to withstand the extremely high mechanical stress during the concrete distribution by means of a concrete pump. A container for installing the measuring equipment existed.

Description of sensor technique

The measuring path in the used interferometer sensor (fig. 1) is formed by two opposed end faces of fibres, which have smooth end faces broken perpendicularly. The fibre ends are framed in a hollow fibre piece; one of the fibres - a single-mode fibre - serves as connecting fibre, the other one - a multimode fibre - serves as a reflector /2/. The light transmitted

0-8194-1700-9/94/$6.00

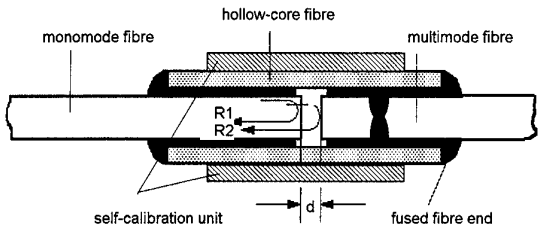

Fig. 1. Sensor head of an extrinsic Fabry- Pérot interferometer

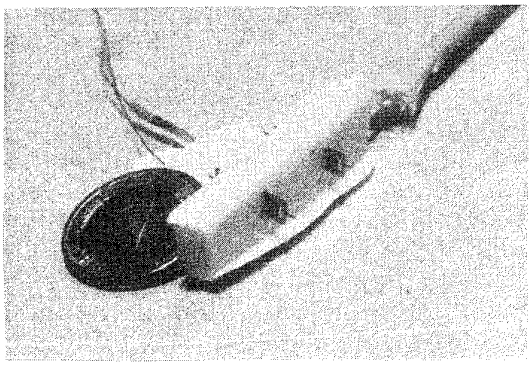

Fig. 2. Sensor head with "ears" embedded in a silicon rubber material

through the single-mode fibre, is partially reflected at the interface glass-air in the sensor head. The transmitted portion is only reflected at the end face of the multimode fibre. Both reflected components interfere and are re-transmitted to an optical detector through the single-mode fibre and through a coupler. The evaluation of the output interference signal allows the determination of an end face displacement value of about 0,5 nm. Considerable displacements are registered by counting the passing through of maximum/minimum values; small displacements are determined by the instantaneous output - to - maximum output - intensity ratio. In order to identify the interferometer's region of operation during the measurements, and to detect drifts and accidental errors a modification of the interferometer sensor was necessary. This was done by a forced displacement of the sensor end faces (see fig. 1), independent of the existing measurand (self-calibration cycle).

The used EFPI sensors were manufactured by Fiber & Sensor Technologies, Blacksburg Virginia, USA. The modified sensors were embedded in a protective material (silicon rubber). Two thin metal sheets ("ears") were attached to the sensor head´s body. The ears protruded from the silicon rubber (see fig. 2). This protected sensor was embedded in a cement mortar block (160 x 40 x 40 mm^3) to which its ears were clinged. The connected cable was protected by a flexible armour tube of steel (see fig. 3) to prevent damages during the pouring of concrete.

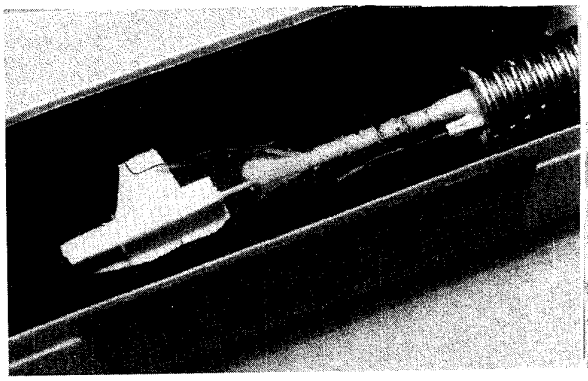

Fig. 3. Sensor before embedding in cement mortar body

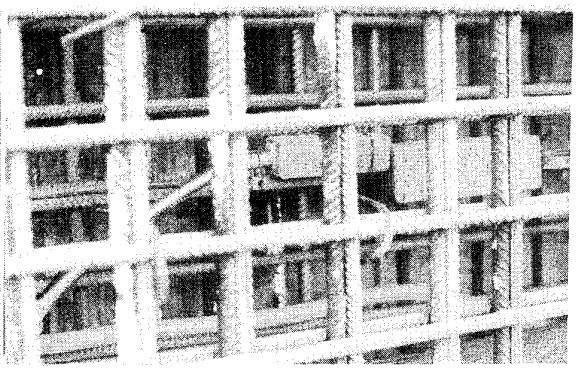

Fig 4. Fixing of the mortar body in the cage of reinforcement

Parameters of the EFPI sensor:

Length of sensors (measuring basis):	about 10 mm
Sensor dimensions (mortar block):	160 x 40 x 40 mm^3
Connection cable:	Single-mode-fibre cable - diameter: 2,8 mm (Length about 40 m)

Measuring range (deflection): < 50 µm (in relation to 10 mm meas. basis)
Strain resolution: 470 pm (in relation to 10 mm meas. basis)

Due to the long-term period of measurements (35 days) and the imponderablenesses in power supply on the building site (operation life of the laser diode) the maximum strain resolution was limited to 0,1 µε.

Installation

The assembled sensor body was delivered with a pig-tail cable of the required length. Fig. 4 shows the fixing of the cement mortar body on the inside of the reinforced cage. The connection of the sensor cable to the pig-tail fibre of the EFPI-device was done by a fusion splice in the measuring container. A succeeding check measurement served as initial adjustment of the sensor parameters (initial calibration curve, fig. 5). As a temperature reference ordinary semi-conductor temperature sensors were installed.

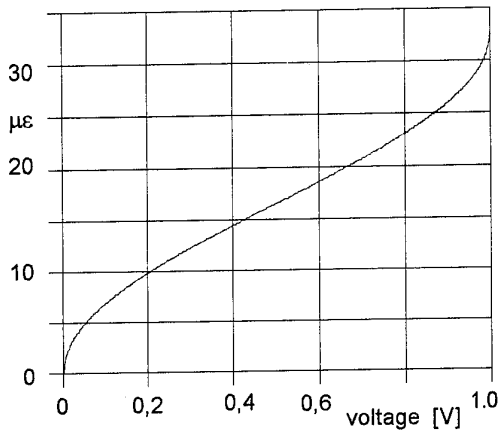

Fig. 5 Initial calibration curve

Measuring equipment and measuring program

To receive, convert and amplify the optical signals a special bias and receiving device (manufactured by Fiber & Sensor Technologies, Blacksburg Virginia, USA) was used. The electrical output signals of that device as well as the linearized and amplified signals of the temperature sensors were digitalized (A/D-transducer width: 12 bit) and recorded by a generally available measuring program. Data reduction and preliminary data editing were not intended, i. e. the measuring values were stored on the hard disk of the PC (Portable 486 DX2 - 66) as original signals. The measuring values were recorded in a density of one value per minute. Once every 6 hours a self-calibration cycle was carried out automatically; then the recording density was increased to 10 values per minute. Fig. 6 shows the measuring container on the building site.

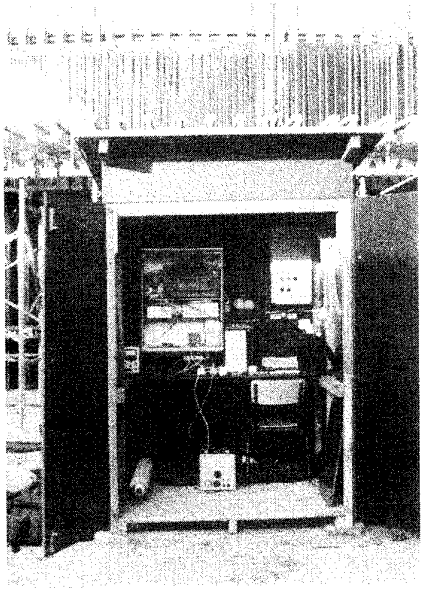
Fig 6. Measuring equipment

The period of measurement extended from January to March ´94; therefore a temperature controlled instrument box was used. In addition, an uninteruptable power supply USP (Heinrich-Notstrom-Service Hohenstein-Ernstthal, Germany) was used to tide over a failure in power supply for a maximum of 3 hours. Also special safety devices were used.

Results

The series of measurements was completed in March ´94. As a preliminary result you can see the EFPI-response during the pouring and during the first days of hardening of the concrete wall (fig. 7). A more detailed analysis will be conducted after a complete editing of all measured data /3/.

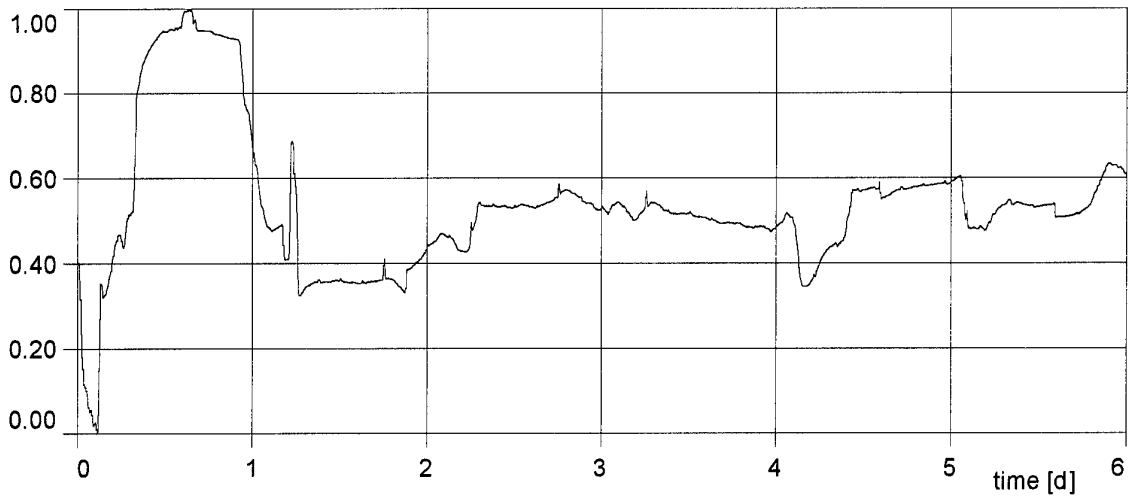

Fig. 7. Strain behaviour after pouring (arbitrary units, for 6 days)

Conclusion

Two extrinsic fibre-Fabry-Pérot-interferometers were embedded in a reinforced concrete wall - which will eventually form a final settling tank - in order to determine the strain behaviour during hardening of concrete. The experience gained confirms that this measuring technique is suitable for strain measurements inside concrete bodies as well as that an installation is possible under extremely adverse conditions.

Because of the very slow changes in strain/contraction a method for an automatic self-calibration cycle was developed. For this, the interferometer sensors were modified. The protection for the sensors used was sufficient; during formwork operations, pouring and hardening no failure or random perturbations were observed. Even though the measurements were carried out in close proximity to construction machines very small changes in the measured values were recorded interference-free and without any noise in the signal.

Such embeddable sensors can also be used for evaluating load-dependent deformations (e. g. filling of a tank) and, if necessary, for determining damages in a concrete wall.

Further investigations will have to address the following points: optimizing the embedding of the sensor head inside a cement mortar body; determining the influence of protective materials on load transfer from host to sensor; improving the mode of operation, especially the reliable indentification of the direction of changes (forward-backward-displacement); storing/re-identification of the reference basis when the power supply is disconnected.

Acknowledgements

The authors would like to thank Prof. Dierks (TU of Berlin, Dept. of Civil Engineering) for supporting the introduction of new measuring methods into the Construction Engineering and Prof. Claus, FEORC/University of Blacksburg, Virginia for providing the sensor probes.

/1/ Staffa, M.: Prevention of cracks in reinforced concrete walls due to hydration. Beton- und Stahlbetonbau Berlin 89(1994)1, 4-8.

/2/ Murphy. K. A.; u.a.: Extrinsic Fabry-Pérot optical fiber sensor. 8th Opt. Fib. Sens. Conf., Jan. '92 Monterey, CA. (USA). Conf. Proc. 193-196.

/3/ Technical report 4-17.94: Strain measurements in a reinforced concrete wall of a final settling tank during the hydration reaction by means of embedded fibre interferometers. IEMB Berlin, 1994

The authors would like to acknowledge the Ministry of Defence for funding this project.
© copyright Crown / DRA 1994

SESSION 5

Optical Fibre Grout Flow Monitor for Post Tensioned Reinforced Tendon Ducts.

W. Craig Michie[1], I. McKenzie[1], B. Culshaw[1], P. Gardiner[2], A McGown[3].

1.Optoelectronics Division, University of Strathclyde, 204 George Street, Glasgow G1 1XW.
2.Smart Structures Research Institute, University of Strathclyde, Glasgow.
3.Department of Civil Engineering, University of Strathclyde, Glasgow.

ABSTRACT.

We report on preliminary experimental trials aimed at assessing the suitability of a distributed water monitor as a means of determining the presence of grout in reinforced tendon ducts for civil engineering structures. This sensing capability is realised through a combination of Optical Time Domain Reflectometry (OTDR) and chemically sensitive water swellable polymers (hydrogels). This form of sensor cable can detect water as a function of linear position along its length with a spatial resolution of a few centimetres[1,2]. The experiments carried out here indicate that this approach has considerable potential as a means of providing quality assurance during the grouting procedure.

INTRODUCTION

The use of post tensioned reinforced concrete bridges has received a considerable amount of attention in recent years following the decision of the Department of Transport to impose a blanket ban of this method of construction. In such structures steel tendons located in ducts are used to apply a reinforcing compressive loading to sections of the structure. The ducts are then filled with a cementitious grout in order to provide a protective seal against influence from the environment. A major problem with this particular approach to construction is that there has been no effective means of assessing the status of the grout fill as a function of the position along the duct length and as a consequence the reinforcing tendons can be left exposed and prone to corrosion through moisture and chloride ion ingress. In extreme cases this could lead to the collapse of a bridge but more commonly it would require that expensive and time consuming repair procedures be undertaken. Fibre optic sensors are emerging as a key component in monitoring technologies for large civil engineering structures. In particular they have the benefit of being electrically passive and have the capability of providing information relating to particular events as a function of linear position. The present paper reports on the use of a fibre optic sensor to determine the position of grout along a tendon duct during the grouting procedure. Such a sensing approach would provide a unique and valuable means of quality assessment of the grouting procedure during construction.

PRINCIPLES OF OPERATION.

Measurement of optical back scatter as a function of position, Optical Time Domain Reflectometry (OTDR), is a well established test means for locating areas of high loss or fracture in optical fibre cables. Optical fibre sensors which modify the back scatter signal power in the presence of their target measurand can be readily interrogated using OTDR systems and are therefore a convenient means of enabling distributed measurements to be carried out. The present sensor employs a novel range of materials (hydrogels) as the active medium in the detection process to realise such microbending losses.

Hydrogels can be defined as polymeric materials which swell in aqueous media without dissolution[3]. The sensor cable prototype transduces the swelling action of the hydrogel material (which responds to the water content of the grout) into a loss of backscatter signal in an optical fibre which can be detected measured and located using an OTDR instrument.

Microbend Transducer Design.

Mechanical perturbations or bends in an optical fibre can cause modes which are guided within the fibre core to be coupled to the cladding where they are severely attenuated, this is revealed as a change in the back scatter signal strength at the location of the bend. Periodic perturbations (or microbends) can maximise this coupling between guided modes and radiative modes through resonant power transfer to produce a loss which may be calibrated to a particular force or pressure.

0-8194-1700-9/94/$6.00

Figure 1 shows a schematic representation of the hydrogel probe. Hydrogel polymer is dissolved in an alcohol based solvent and is deposited onto a central supporting former (a Glass Fibre Reinforced Plastic rod). The coated rod is then held in contact with an optical fibre by a helically wound Kevlar thread. When buried in grout hydrogel is exposed to water and swells to cause the fibre to deform locally by squeezing it against the thread. Light passing through the fibre at this point will therefore be attenuated through the microbending action of the thread and this loss can be used to indicate the presence of water at this location. The sensitivity of the sensor (the loss per unit length) can be tuned by varying the hydrogel thickness, the composition of the gel, the periodicity of the microbend inducing thread or the tension in the thread. To protect the sensor from perturbation or damage due to mechanical influences during handling or installation a cable arrangement was devised whereby the sensor was incorporated into a porous braided sheath. The arrangement was found to be sufficiently porous to enable the water content of the grout to be detected within seconds of grout being applied.

DEMONSTRATION OF SENSOR OPERATION.

Installation and experimental assessment was carried out on a 20 m long, 10 cm diameter duct containing 17 reinforcing tendons constructed at the Transport Research Laboratory (TRL) in Crowthorne. The sensor was installed by grouting contractors and TRL staff who then grouted the duct and introduced voids along its length. The sensor was then interrogated in order to assess the effectiveness of the grouting procedure. Determination of the wetted (grout covered) sections of the sensor was achieved by measuring the incremental loss of different sections along the fibre and comparing this to the response of the sensor in its ambient dry state. Positions of high signal loss were determined to be regions where the sensor had been wetted by the grout. In areas where a low loss was experienced it was concluded that the sensor was not covered in grout. After completion of the tests the duct was disassembled at various locations and the condition of the grout fill noted along its length. The data gathered was then compared with the information generated by the optical sensor. This data is presented graphically in Figure 2.

Examination of Figure 2 shows that the sensor identified clearly where it had not been covered in grout . Thus significantly voided regions (5,6,7,8,12) were detected. The amount of grout fill in each of these locations varies from around 30 % to 95 % of the area of the duct. In all cases the grout covering of the sensor was inadequate to induce the magnitude of loss that would be consistent with a totally wetted section and hence a void was assumed to be present. However the sensor has also indicated that a void exists at around section 10 where the cable appeared to be completely submerged in grout.

Sensor Sensitivity: Signal Processing.

While the results of the above trials are extremely encouraging, it is recognised that future work is required to develop this technique, particularly in the region of data acquisition and signal processing. Reliable repeatability tests have yet to be completed.

Presently the data are obtained by a sequential interrogation process and are manually logged. Automatic data logging and presentation would enhance the performance by enabling attention to be directly focused onto suspected problem areas. Automatic processing routines to carry out these tasks are now in an advanced state of development.

It may also be preferable to increase the sensitivity of the sensor such that greater losses are experienced locally to wetted portions of the cable. The present sensor was designed to have an attenuation characteristic of around 0.05 dB/m when wet. The minimum resolvable increment of backscatter signal in present day OTDR units is 0.01 dB^4 which means that the OTDR unit is easily capable of detecting the difference between an activated length of sensor and a deactivated length with a high degree of accuracy provided that the minimum resolvable event is around 1 m in length. While the OTDR is able to detect smaller events the effective signal to noise ratio is reduced and the probability of error increases. Increasing the sensor sensitivity can be readily implemented through adjusting the coating thickness of the hydrogel.

FUTURE SENSOR CONSIDERATIONS.

The above experiments have demonstrated the use of a distributed water monitor for detecting and locating grout in post tensioning tendon ducts during the grouting procedure. However an advantage of this particular

sensor cable design is that it is truly generic in nature and enables other chemical measurands to be targeted with appropriate selection of a hydrogel as the active component. Gels currently exist which swell in water only in the presence of a particular ion or if the water passes through a specific value of pH. Such gels have been manufactured within the University of Strathclyde and are wholly compatible with the processes used to construct the sensor cable[5]. Systems which are able to respond to pH changes would be of considerable value for long term monitoring of bridge structures as a means of indicating not only that water is present but also that the pH of the surrounding medium has dropped for example below pH 10, where the reinforcing tendons might be prone to corrosion.

CONCLUSIONS.

A generic form of fibre optic sensor, designed primarily as a water detector, has been used to determine the evolution of grout propagation during pumping into reinforcing tendon ducts. Preliminary evaluations of this technique have indicated that this method is extremely promising as a means of providing quality assessment of the grouting process. After installation, the sensor provides a long term monitoring facility capable of detecting future water ingress and can therefore provide a means of continuous monitoring for potential corrosion problems. While the current trials have concentrated on the evaluation of a simple water detection sensor, the cable construction enables other substances to be targeted with this approach by modifying the swelling response of the hydrogel. Such a measurement facility has enormous potential for a wide range of monitoring applications.

Acknowledgements.

The assistance of the Ericsson cable company in manufacturing prototype sample lengths of this sensor is gratefully acknowledged. The Secretary of State for Transport and The Scottish Office Industry Department acting through the Transport Research Laboratory are also acknowledged for providing the test facilities and financial support for these trials.

References.

1. Michie W C, Culshaw B, McKenzie I, Moran C, Graham N B, Santos F, Gardiner P, Bergqvist E, Carlstrom B. A Fibre Optic/Hydrogel Probe for Distributed Chemical Measurements, submitted to Optical Fibre Sensor 10, Glasgow 1994.
2. Michie W C, Culshaw B, Graham N B, Moran C, Gardiner P T. Fibre Optic Hydrogel Distributed Chemical Detector, UK Patent Application No. PCT/GB94/00292.
3. Peppas N A. Hydrogels in Medicine and Pharmacy, Vol II, Polymers, CRC Press, Boca Raton, FL, 1987.
4. Optoelectronics Inc. Product Data. Pico-second Fibre Optic System, Optoelectronics Inc., Unit 9, 2538 Speers Rd., Oakville, Ontario.
5. Moran C, Graham N B. Random Block Co-polymers, UK Patent Application. No. 9306887.2

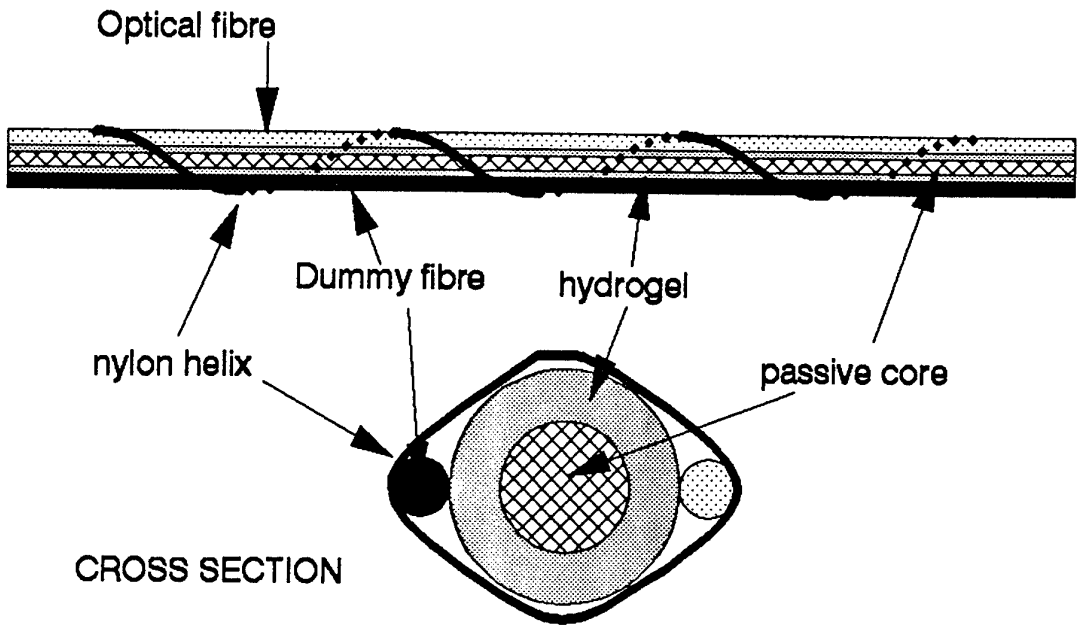

Figure 1: Schematic of Fibre Optic/Hydro Gel Distributed Water Detector.

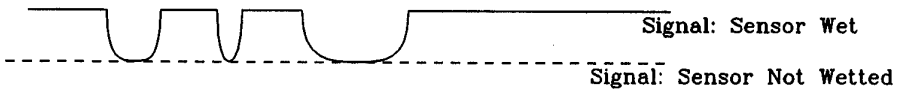

(a) Measured Signal Data

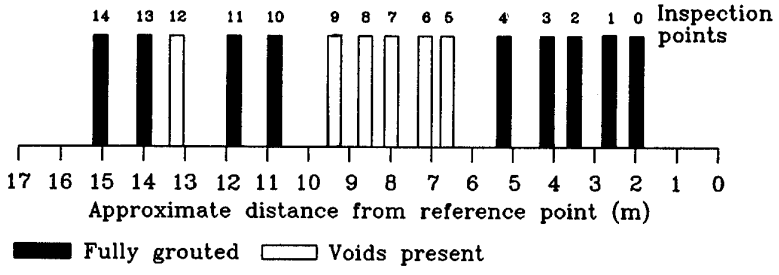

(b) Qualitative Assessment of Duct Grouting Condition as found from inspection

Figure 2: Void Detection in Tendon Duct Using Optical Sensor (including Void inspection data supplied by TRL).

Paper presented at the Second European Conf. on Smart Structures and Materials, Glasgow 1994, Session 5

ACTIVE RESPONSE CONTROL USING ROTOR FIN FOR WIND-INDUCED STRUCTURAL VIBRATIONS

Yoichi Mukai, Eizaburo Tachibana and Yutaka Inoue

Dept. of Architectural Engineering, Osaka Univ., Yamada-oka, Suita, Osaka 565, Japan

1. INTRODUCTION

Various types of active control systems have been proposed in order to reduce wind-induced structural vibrations. The objectives of this control are to keep structures safe from some distorting damages and to avoid sea sick of habitants. The typical type of those kinds of systems is so-called active mass damper system (AMD). This system aims to use controllable inertia forces of the AMD in order to reduce the structural vibrations. However, another problem may be arisen on the AMD system. It is that dead loads of structures obviously increase by introducing this system. Moreover, the AMD system needs large electric power to shake its additional mass. In order to solve those problems, an active fin system [1), 2)] is proposed by authors as an effective technique of the active control for wind-induced structural vibrations. The concept of this system is based on an idea to use wind force itself as effective damping forces. By changing the angle of the fin according to both wind direction and structural vibration direction, wind resistant forces can be generated arbitrarily. Moreover, the active fin system requires comparatively less electric power than that of the AMD system.

In this paper, the effectiveness of two different types of control devices of the active fin are investigated by experimental tests (a wind tunnel is used for this aim). One is a single-fin type and the other is a twin-fins type. Following three items are focused to investigate: 1) Composition of an effective control algorithm for the active fin system, 2) Comparisons of control effects in the case of using the single-fin type and in the case of using the twin-fins type, 3) Estimation for real wind resistance forces acting on the fins.

2. TESTING APPARATUS AND CONTROL DEVICES

In order to persuade experimental tests, CTAC system is adopted (CTAC means standard Compact Testing apparatus for Active Control systems developed in Osaka university).

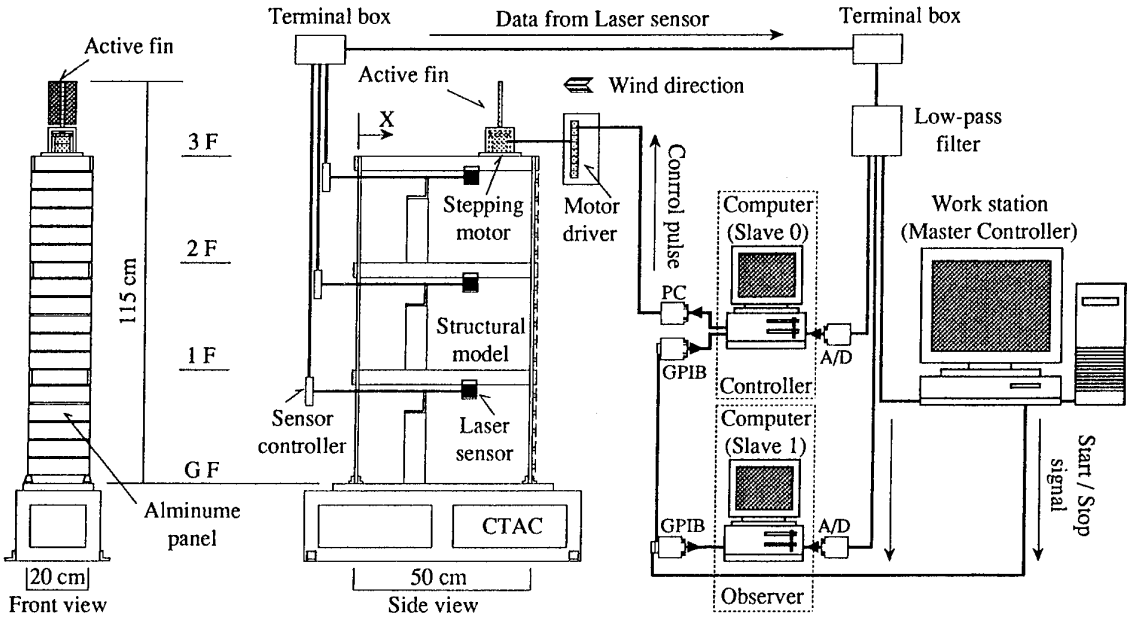

Fig. 1 Outlook of the CTAC

0-8194-1700-9/94/$6.00

The target structure which should be controlled is three-stories model (which can be includes three vibration modes). Relative displacements between each story are measured by three lazer sensors. The control of the active fin is operated by using those response data of the structural model, and the control movement of the devices are produced by rotating stepping motors. Fig.1 shows the outlooks of the CTAC. Two types of the control devices of the active fin are prepared for this investigation. The configurations of those devices are shown in Fig.2. Fig.2 (a) shows a single-fin type (TYPE II), and Fig.2 (b) shows a twin-fins type (TYPE II). Both devices are designed to have same area of 145cm^2 which is about 8% of the projected area of the structural model. The principal of the control algorithm of the active fin is very simple. That is, when the structure is moving against the wind flow, then to make the resistant forces enlarge. And, when the structure is moving to the same direction with the wind flow, then to make the resistant forces small. Those operations can be performed by changing the rotating angle of the active fins. In this paper, premier case for the configuration of the angle of the fins is called as a 'closed mode' (which is orthogonal to the wind flow), and the later case is called as an 'open mode' (which is pararel to the wind flow).

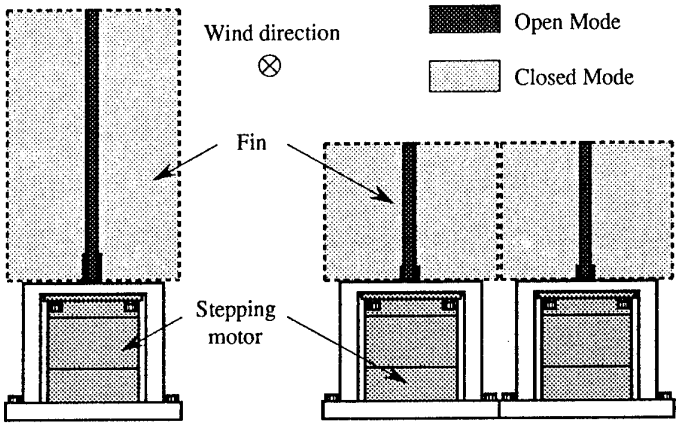

Fig. 2 Configurations of the active fin

3. DYNAMIC PROPERTIES OF STRUCTURAL MODEL AND PRELIMINARY TESTS

Static mechanical properties of the structural model are shown in Table 1. Dynamic properties are shown in Table 2. The natural periods are evaluated by both free vibration tests and numerical computations. A damping ratio is calculated by mean of logarithmic decrement. As can be seen in Table 2, numerical values of natural periods fairly coincide with experimental values.

Table 1 Static properties of structural model

	Mass (kgf)	Stiffness (kgf/cm)
First	13.0	1.95
Second	13.0	2.50
Third	14.0	3.15

Table 2 Dynamic properties of structural model

	Natural Period (sec) Experimental	Numerical
First	1.137	1.138
Second	0.379	0.376
Third	0.252	0.253
	Damping ratio (%)	
First	0.42	

* Natural preiod over the third order are omitted.

In order to estimate the control forces supplied to the structural model by the active fins, it is necessary to examine the wind resistant forces acting on the fins. Under laminar flow, by measuring the deformations of the structural model at the cases of the closed mode and the open mode, the wind resistant forces acting on the fins are estimated.

By using the least square method, the relation between the wind resistance force r (kgf) and the velocity of the wind w (m/sec) can be expressed as follows.

$$r = 0.0905 \cdot S \cdot w^2, \qquad (1)$$

in which the S (m^2) means the projected area of the active fins. The comparison of this relation and the experimental results are shown in Fig.3.

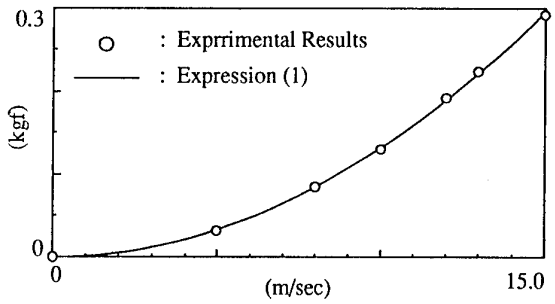

Fig. 3 Relation between resistant force and wind velocity

4. CONTROL ALGORITHM

The control algorithm adopted here is very simple. At each control step, the configurations of the active fins (changing to the closed mode or the open mode, or keeping the premier mode) are decided as following algorithm by using the direction of the velocity of the top floor. This judgement is operated as follows.

'If the velocity is nearly equal to zero, then let the active fin keep the premier mode,
else the direction of the velocity is against the wind flow, then let the active fin set the closed mode,
else the direction of the velocity is the same with the wind flow, then let the active fin set the open mode.'

5. EXPERIMENTAL RESULTS AND CONSIDERATION

At first, non-control tests are executed. A lattice grid is inserted in the wind tunnel in order to get semi-turbulent flow. Fig.4 and Fig.5 show displacements of the top floor. From those results, the responses of the structural model equipped the TYPE I are observed as to be a little larger than that of the TYPE II. However, for both cases, significant difference between the closed mode and the open mode can not be recognized in those figures.

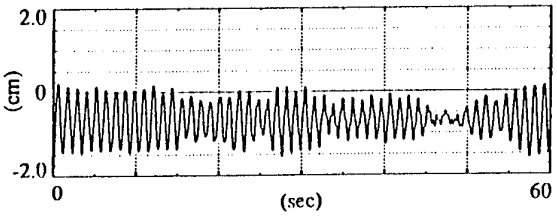

(a) Displacement of the top floor (Closed mode)

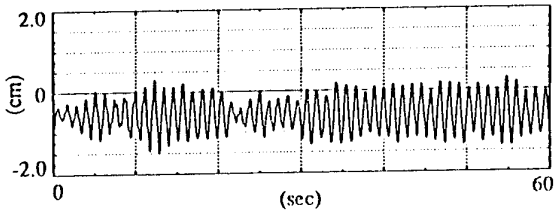

(b) Displacement of the top floor (Open mode)

Fig. 4 Cases without control (TYPE I)

(Mean of the wind velocity: 8.0 m/sec)

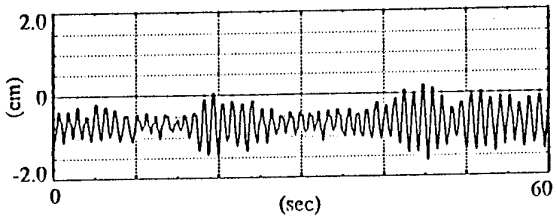

(a) Displacement of the top floor (Closed mode)

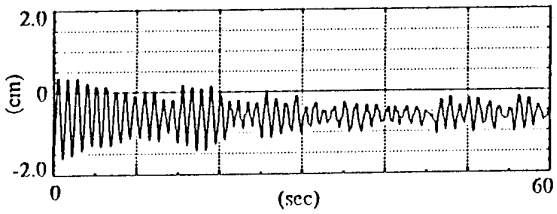

(b) Displacement of the top floor (Open mode)

Fig. 5 Cases without control (TYPE II)

By examining the non-controlled responses for the closed mode and the open mode, the wind resistant forces acting on the fins can be estimated as about 0.07 kgf. This value is the same for both cases of using the TYPE I and the TYPE II, and it has very good accordance with the numerical value (0.08 kgf) computed by ex.(1).

Next, the control effects of the active fin system are investigated by using the algorithm that is mentioned above. Displacements of the top floor are shown in Fig.6 and Fig.7. By comparing those controlled responses with the non-controlled responses (as seen in Fig.4 and Fig.5), good reductions of the responses can be observed by using either types of the active fin. From the comparisons of control effects by using the TYPE I and the TYPE II, more effective reductions of the responses can be gained at the case of using the TYPE II.

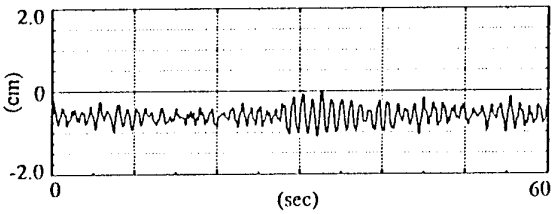

Fig. 6 Displacement of the top floor of Case for control (TYPE I)

(Mean of the wind velocity: 8.0 m/sec)

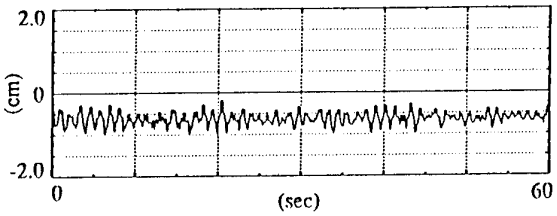

Fig. 7 Displacement of the top floor of Case for control (TYPE II)

The RMS values of the displacements of the top floor are shown in Table 3. The controlled responses are reduced into about 49% and 39% for the non-controlled responses by using the TYPE I and the TYPE II, respectively. This result shows that the control effects do not depend only on the total area of those fins.

Table 3 RMS values of the displacements of the top floor

		TYPE I	TYPE II
Non-control	Close Mode	0.325	0.422
	Open Mode	0.333	0.404
Control	Experimental	0.185	0.131
	Numerical	0.117	0.159

(cm)

6. NUMERICAL SIMULATION

The wind forces $\{f\}_{wind}$ acting on the structural model can be estimated by introducing the real responses to the equations of motions.

$$\{f\}_{wind} = [M]\{\ddot{x}\} + [C]\{\dot{x}\} + [K]\{x\}, \quad (2)$$

in which $\{\ddot{x}\}$,$\{\dot{x}\}$ and $\{x\}$ mean the response vectors of the structural model, and [M], [C] and [K] mean the mass, damping and stiffness matrices, respectively. The wind forces acting on the structural model are assumed as concentrated horizontal loads on each floor. Next, by using those simulated wind forces, numerical calculations for the control of the active fin are executed. According to the configuration of the active fin that is decided by the control algorithm, the value of the control forces are assumed as follows.

'When the active fin is kept the premier mode, the value of the control force is not changed,
when the active fin is set the closed mode, the value of the control force is changed to Δf,
when the active fin is set the open mode, the value of the control force is changed to zero.'

In which, Δf (0.07 kgf) means the measured value of the wind resistant force acting on the fins. The results of those simulations are shown in Fig.8 and Fig.9. The simulated responses for controlling are almost same as the experimental responses (as seen in Fig.6 and Fig.7). Moreover, the RMS values of the displacements of the top floor show good accordance with the real responses (as seen in Table 3). As the results, it is appeared that those simulations for the control of the active fin system are reasonable.

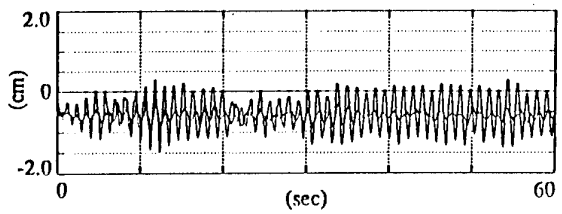

Fig. 8 Displacement of the top floor (TYPE I)

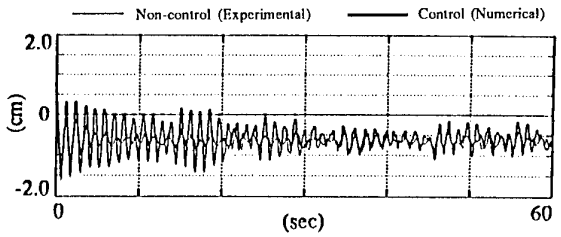

Fig. 9 Displacement of the top floor (TYPE II)

7. CONCLUDING REMARKS

As concluding remarks, it is considered that the active fin is very effective as the active response control system for the wind-induced structural vibrations. And, it is assured that the control effect do not depend only on the total area of those fins. Moreover, the practical control forces of the active fins can be estimated by using the wind forces simulated from structural responses.

ACKNOWLEDGEMENTS

The authors gratefully thank to Messrs. Kazutaka Igarashi, Yasushi Ujimoto and Naohiko Tsunashima for having cooperated in this experimental research.

REFERENCES

1) Mukai, Y., Kawakami, J., Tachibana, E., and Inoue, Y., "**Experimental Study of Active Control of Structural Vibrations**", *Proc. of the 12th Int. Conf on SMiRT*, Vol. A, Aug., 1993, pp. 249 - 254.
2) Mukai, Y., Tachibana, E. and Inoue, Y., "**Active Fin Control System Wind-induced Structural Vibrations**", *Theoretical and Applied Mechanics*, Vol. 42, Oct., 1993, pp. 209 - 218.

Paper presented at the Second European Conf. on Smart Structures and Materials, Glasgow 1994, Session 5

GLOBAL AND LOCAL HEALTH MONITORING OF CIVIL STRUCTURES USING SMART FERROELECTRIC SENSORS AND ELECTRONICALLY STEERABLE ANTENNAS

Vijay K. Varadan and Vasundara V. Varadan

Alumni Distinguished Professors of Engineering Science and Electrical Engineering
Research Center for the Engineering of Electronic and Acoustic Materials and Devices
Pennsylvania State University, University Park, PA 16802

ABSTRACT

In this paper, the global and local health monitoring of civil structures using RF antennas and ferroelectric sensors is presented. The sensors are fabricated with interdigital transducers printed on a piezoelectric polymer or ceramic type film. They in turn are mounted onto a ultra thin Penn State's novel RF antenna. The wave form measurements may be monitored at a remote location via the antennas in the sensors and an outside antenna.

1.0 INTRODUCTION

The global and local health monitoring of civil structures is challenging due to the physical size and structural complexity and useful life of the structures. These civil structures may include bridges, elevated highways, dams, homes, office buildings, airport buildings, etc. They are subjected to various kinds of loads and stresses due to rain, snow, earthquake, etc. Continuous monitoring of such civil structures is important for the safety of the people. Extensive arrays of conventional discrete sensors or new technologies using distributed sensors are being used for monitoring. Fiber optic and ferroelectric sensors such as PZT have been proposed recently for such instrumentation. For fiber optic sensors one needs a light source adjacent to or in the vicinity of the structure. In case of traditional ferroelectric sensors, the sensors are either distributed or discrete and have to be connected by wires to a power supply. Both these types of sensing systems may weaken the structure because of bonding problems between the structure and the optical fibers or the wires which will be running all over the structure. What is important and attractive is to develop a system which is ideal for both global evaluation (for e.g., structural integrity) and local evaluation (for e.g.., material integrity); which does not weaken the structure; and which is also cost effective. This may be achieved using Penn State's novel antenna architecture to interact with ferroelectric Surface Acoustic Wave (SAW) sensors with built-in- antennas that will be embedded into the structure. The type of sensor utilized for monitoring the structures is environmentally dependent, for example where high degrees of moisture are present. Our sensors are hermetically sealed with UV curable polymers which Penn State University CEEAM has developed.

Since microwave energy can penetrate concrete with relative ease, Penn State CEEAM electronically steerable antenna system using network analyzers and SAW sensors can be used to detect cracks and metal reinforcements in concrete. The detection of oxidization process also is possible due to the change in dielectric properties of the metal target.

2.0 FERROELECTRIC SAW SENSORS

At Penn State the SAW sensors had been developed for sensing and control of drag and skin friction in aerospace and underwater structures. Also their use for the remote monitoring of temperature, humidity and chemical changes in materials has also been investigated. The SAW sensors are fabricated with interdigital transducers printed on a piezoelectric polymer or ceramic type film. This is mounted onto a ultra thin Penn State's novel RF antenna. For local health

0-8194-1700-9/94/$6.00

monitoring of "previously known heavily stressed region" of the structure, the RF activated SAW sensor is usually small in the order of millimeters to centimeters. The global sensor which is in the order of inches to feet will provide quantitative information of the overall behavior of a civil structure during its life. It provides continuous monitoring of the entire structure. The global sensor and actuator systems also monitor the moving loads, ice formation and the corrosion. These can also be used to study the rotation or tilt of the structure. These sensors may be designed in such a way that both bulk waves, Love waves and surface waves can be launched onto the structure. They indicate stress and strain levels, predict crack formation and delamination in the structures. In addition, they can be used for controlling scouring and cavitation of concrete supports. Along with corrosion resistant UV curable polymer developed at Penn State's Center (CEEAM), these sensors and actuators also improve hydrodynamic performance near the pillar support and provide corrosion resistant surfaces. The wave form measurements also provide the amount of tilt or rotation of a bridge's pier or abutment, the amount of settlement and differential settlements of the bridge's foundation, and the deflection and rotation of the bridge's girders. These wave forms may be monitored at a remote location via the antennas in the sensors and an outside antenna.

A typical SAW device consists of an input IDT that generates a surface-acoustic-wave replica of the signal, a piezoelectric layer that acts as the propagation path for the waves, a substrate under the layer, and an output IDT that converts the delayed acoustic waves back into an electrical signal. The input and output IDTs each has an impulse response with a finite duration and the construction is such that the electrodes have a one-to-one correspondence with individual cycles in the impulse response. The impulse-response center frequency is set by electrode spacing and its envelope is set by the electrode length. The frequency dependent transfer function of each IDT is the Fourier transform of its impulse response. The delay line length of the sensor is proportional to the wavelength of the SAW.

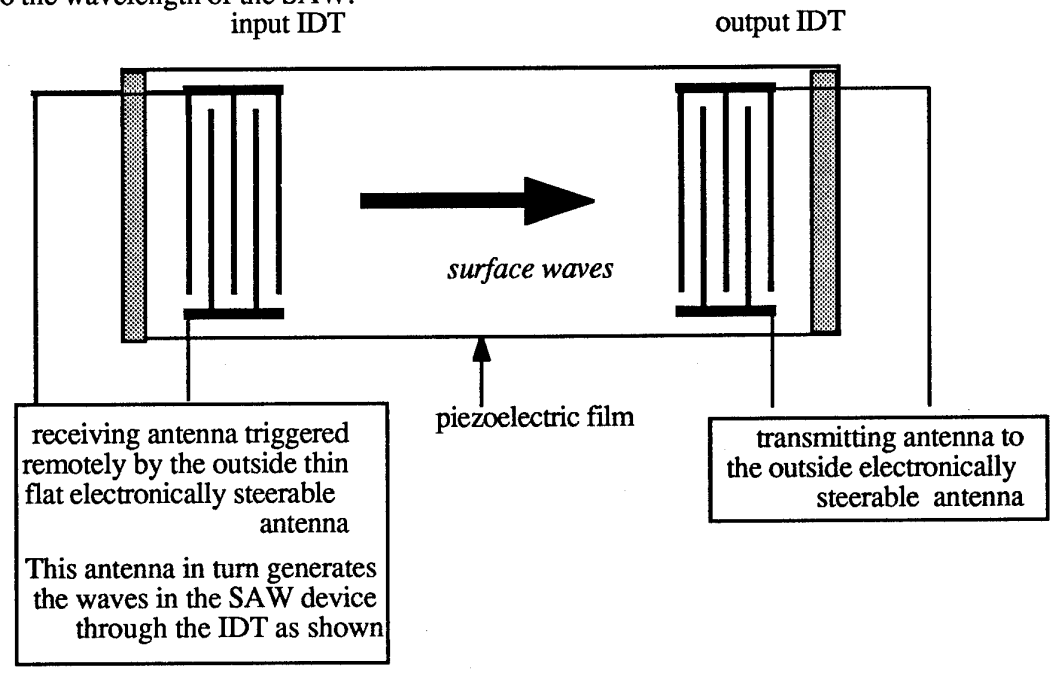

Fig. 1. Typical form of a SAW device.

The SAW sensor can be attached directly onto any surface without disturbing the structural surface shape. Restrictions concerning the surface geometry of the sensor and structures are largely

eliminated. Therefore, the SAW sensors offer promising new devices that accurately document the unsteady surface pressure, shear and surface friction development as a function of both time and space.

3.0 RF ANTENNAS

In this paper, both electronically steerable microstrip and leaky wave antennas using tunable ferroelectric material are presented. These are based on the Penn State CEEAM invention (PSU 92-1183; patent pending). These antennas are lightweight, thin, low volume, low profile and conformal. They have low fabrication costs and are easily mass produced. Linear, circular, and dual polarization are achieved with simple changes in feed position. Beam steering can be accomplished by varying the relative phase between radiating elements. In planar array, both horizontal and vertical beam can be combined to provide full scanning capabilities. Tunable ceramic phase shifters are used in these antennas. In microstrip antennas, they are deposited as thin films on the feed lines whereas in the leaky wave antennas they have been used as a traveling waveguide with a ground plane on one side and metallic periodic grating on the opposite side.

Microstrip patch antennas are placed in the vicinity of the structure to interface remotely with the antennas of the SAW devices, see Fig. 2. The power requirement is minimal and will be provided by high energy cells. SAW devices will be triggered by these microstrip antennas, see Fig. 1. The SAW devices themselves thus need not have power sources. Feed lines and matching networks are fabricated simultaneously. Commercially available electronically steerable microstrip antennas are bulky with PIN diode or magnetic ferrite phase shifters which require enormous amount of power. The Penn State novel antenna is ultra thin and the electronic steerability is obtained through ferroelectric thin film on the antenna feed line which requires just bias voltage only and thus very little power since the phase shifting does not require any current.

Microstrip antennas are easily fed by either a microstrip line or a coaxial probe, since they are located on one side of a dielectric substrate. Microstrip phased array antennas are fabricated by interconnecting individual patches with microstrip lines. These microstrip lines provide power splitting and phasing capabilities to produce the desired radiation pattern. Beam steering capabilities can be added to the array by inserting individual phase shifters on the microstrip feed networks. These phase shifters are in the form of thin film over which the strip line is printed. The printing of the microstrip lines can be done with ion printing with a resolution of a few mils. This helps one to develop antennas for a range of frequencies including the high GHz frequency range.

The leaky wave antenna is a traveling wave antenna characterized by a propagating wave along the antenna aperture. It is a guiding structure through which the guided waves travel and excite the leaky wave from perturbations to the structure. The perturbations can be intermittent electrodes on one surface, changing material properties, surface corrugations, etc. These leaky waves constitute the radiation into free space which, with proper design, form a very narrow beam. It is also possible to flush mount these antennas on a structure for conformal antenna applications. The main advantage is its capability to change the direction of the radiating beam by changing the guide wavelength. Because the leaky wave antenna is directly derived from the dielectric waveguide, it is easy to integrate it with the source and waveguide components. This integration reduces the size, weight and cost of the antenna system. The metal ground plane may also provide a heat sink and is convenient for dc biasing of integrated circuits. This antenna may find applications like automobile collision warning, intelligent high-way systems, aircraft smart skins and high-resolution radar. The Penn State CEEAM is working on many of these areas and a patent has been filed for some selected applications.

4.0 ELECTRONICALLY STEERABLE ANTENNA

The outside antenna can either be controlled by GPS or a central antenna at operating

stations located elsewhere. If GPS or a central antenna is not available or accessible, the sensor antennas may be connected to a cellular phone system for retransmission via cellular phone to the monitoring station, see Fig.2. A key issue is the reduction of false alarms in the systems. The remote system is designed to provide both remote operator prompts or collect time histories of the substructures they are monitoring. The system will ultimately be integrated into an automated system available to modem users. By integrating the system with currently available fuzzy logic detection systems software we believe that we can drastically reduce the occurrence of false alarms while still retaining a high level of diagnostic capability.

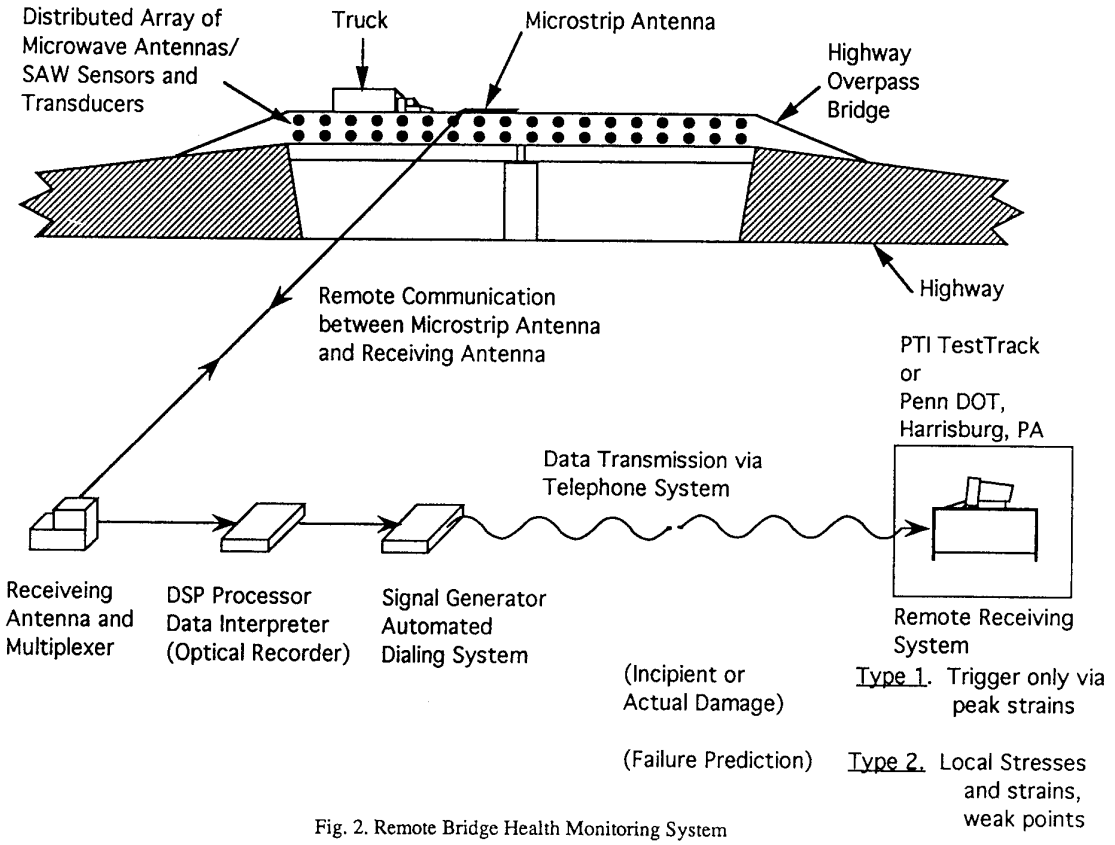

Fig. 2. Remote Bridge Health Monitoring System

Paper presented at the Second European Conf. on Smart Structures and Materials, Glasgow 1994, Session 5

VIBRATION AND NOISE CONTROL IN CIVIL STRUCTURES BY "SMART" DESIGN

Daryoush Allaei[1]
QRDC, Inc.
P.O. Box 562, Excelsior, MN 55331-0562, USA

ABSTRACT

In this paper, the results of a feasibility study for developing an efficient and effective design methodology to make systems "smart by design" is presented. The primary focus is on computer-aided structural design to implement the inter-coupling of modes of vibration and smart devices built in the original design of structures. The conventional add-on elements are replaced by built-in multi tasks components. First, structures are designed so that a major portion of their vibration energy is localized into their non-critical areas and thereby isolate and quieten critical areas. Next, multi tasks smart (components are integrated in the most critical locations of the system in order to monitor and maintain the designed vibration characteristics of the system.

BACKGROUND

Traditional techniques that have been used to reduce structural vibrations and noise fall into two categories: isolation and suppression (cancellation) methods. Furthermore, each of these techniques can be actively or passively applied to the system under consideration. Having flexible supports or adding passive and/or active damping systems to the path between the source and the receiver are two well known approaches used to isolate or suppress vibrations and noise. Passive methods have several drawbacks such as their very limited frequency range and restricted operating range. Active methods appear to be the dominating approach in recent years. They have been under constant improvement for more applications in the future. The goal is to make the systems "smart."

Vibration (or noise) control units are usually add-on elements which are attached to the primary vibrating system to reduce or isolate the transmission of vibrations without drastically altering the original specifications of the structure. The underlined key words designate the main drawbacks of these conventional approaches. First, since they are added to the primary structure, they increase the total weight of the system. Second, the interaction of the attached element unit with the structure not only modifies the system behavior but also augments the complexity of its dynamics. To have an effective active vibration (or noise) control system (for isolation or suppression), it is required to have smart devices which are optimally integrated in the original design of structures. The latter forms the basis for an ongoing funded research project that is briefly presented here.

In order to optimize the combination of the structure and the vibration control unit, an efficient and more accurate modeling methods are desired. Classical (closed form solutions), numerical (such as finite difference), and physical modeling (such as finite element) approaches have been extensively used to predict and analyze the dynamic characteristics of structures and machinery. However, the continuous demand for more precise systems with a minimum of undesired vibratory motion has forced researchers and engineers to search for more efficient and accurate computer models to investigate the dynamics of structures or machines with attached (or embedded) elements such as smart elements. Even though, the finite element method, the most applicable method for the majority of real life problems at the present

[1] Also, the Project Manager of the Sound and Vibration Engineering Technology Program at HTC, Hutchinson, MN.

0-8194-1700-9/94/$6.00

time, has been upgraded to accommodate new applications, it may not be the only answer to the complex structures of the future, such as those found in civil structure-smart element systems. In this work the most powerful numerical methods, such as finite element (FEM), boundary element (BEM), finite difference (FDM), and component-mode syntheses via receptance (CMS-R) methods are optimally combined to develop a much more efficient, accurate, and easy to implement numerical method to perform vibration analysis on civil structures and their attached subsystems (i.e., smart elements). Conceivably, the structures of the future, for example, could be designed with the aid of the proposed techniques to optimize the distribution of selected vibration modes away from certain regions. The integrated smart devices can then be applied to monitor and cancel the remaining vibrations to maintain the original design.

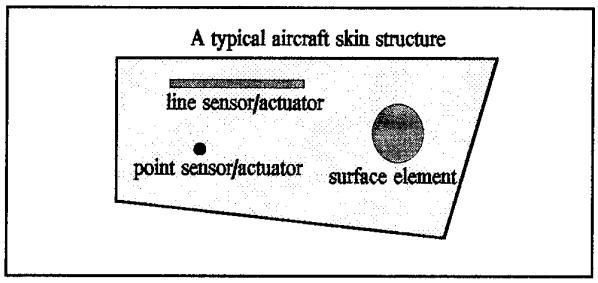

Figure 1 A structure with smart elements

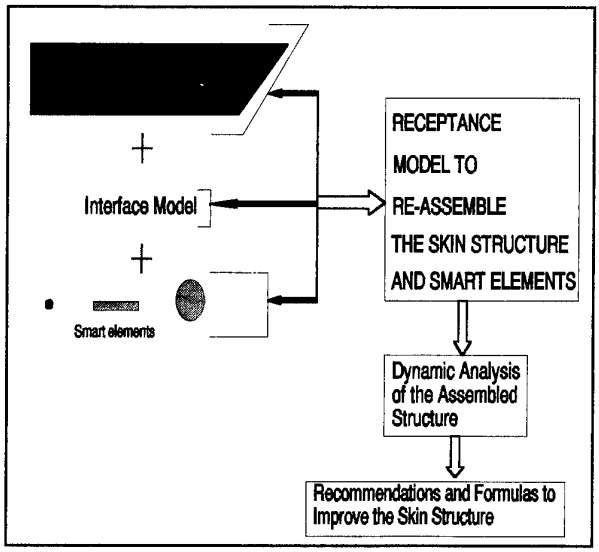

Figure 2 Partitioned structural components

DEMONSTRATION OF THE CONCEPT

The objective of this section is to demonstrate the feasibility of developing an efficient and effective mathematical model capable of incorporating the dynamic characteristics of smart elements-host structure system. A preliminary computer model based on the proposed concept is developed. The attached or embedded smart elements, their interfaces, and the host structure are separately modeled by employing the component-mode syntheses via receptance (CMS-R) method. It is shown that the application of CMS-R method to the dynamic analysis of smart structures is effective and efficient. In particular, it is an excellent tool to demonstrate the concept of "smart" by design (SBD). It is shown that this model results in significant gain in computational speed and improvement in accuracy of the numerical results. The inclusion of the effect of attached or embedded smart elements on the occurrence of vibration phenomenon, such as loci veering and modal energy localization (MEL), is also investigated.

Modeling Approach: The proposed mathematical model is composed of three distinct parts: smart elements, their interfaces with the host structure, and the host structure. Two main advantages of this approach are: (1) the developed prediction model can be incorporated in any existing structural model and (2) rigid body modes can be added to the model in order to account for the loosening of the smart elements. The dynamic characteristics of smart elements and the civil structural components are assumed to be known in terms of their natural frequencies and mode shapes. Next, the interfaces between the smart elements and the structural components are modeled by employing the CMS-R method. Finally, the smart elements and the structural components are connected by the developed interface models.

For demonstration purposes, a plate structure is considered. Figures 1 to 2 show the basic concept of the proposed model applied to a plate structure. The structure is partitioned into three segments as shown in Figure 2. The receptance method is then utilized to connect the three segments in order to resemble

the plate structure plus the attached smart elements. The two segments, the plate and smart elements, are stored in the computer model in terms of their dynamic characteristics which are natural frequency, mode shapes, and modal damping factors. This feature makes the model very flexible in interacting with other existing sub-structuring models since such vibration characteristics can be obtained by any method (i.e., finite element, vibration testing, or closed form solutions in the case of simple models).

Other advantages of the proposed approach are in memory savings and computational speeds. There are neither any large stiffness, mass, and damping matrices, nor are there any geometric mesh matrices. The only required geometry of the sub-structures is their contact regions. The latter has shown to reduce the degrees-of-freedom of the total structure by a large factor. Such features significantly reduce the memory requirement of the computer model. On the other hand, the first output of the analysis portion of the program are in terms of the vibration characteristics (natural frequencies and mode shapes) of the assembled structure. This data is then utilized to do a forced dynamic analysis of the total system. The results of this study has confirmed the findings of the author [3] that such processes significantly increase the computational speeds of the computer model.

SUMMARY AND CONCLUSIONS

The main concept and general modeling approach of "smart" by design (SBD) were presented in this paper. In the first part, preliminary computer models was described. In the second part, the CMS-R methods was applied to a typical civil structure with attached smart elements. The computer model was then expanded can easily be extended to include N lumped and continuous smart elements. Using the CMS-R method, the characteristic equations, whose roots were the natural frequencies of each of the above mentioned system, were developed.

Among the disadvantages of certain other methods (Finite Element method, for example) are the necessity for large stiffness, mass, damping, and geometric mesh matrices. Such methods require large memory capacity and large amount of matrix manipulations resulting in significantly large amount of computational time. As it was pointed out in the previous section, the computations of the CMS-R method involve only the symmetric receptance matrix. Furthermore, there is no need for the geometry of the structure to be stored in the computer. The only required geometry of the fasteners is their contact region. This feature reduces the degrees-of-freedom of the total structure by a large factor and significantly reduces the memory requirement of the computer model. Thus, two of the advantages of the proposed approach include memory savings and increased computational speeds.

The natural frequencies appear in the denominator of the receptances (Eqs 9-10) and the mode shape formulas (Eq. 16) of the assembled structure. Assuming that the natural frequencies of the assembled structure are not significantly different from the frequencies of the host structure, both formulations can be reduced to two single-term series solutions which involve their corresponding dominating modes. Such reduced formulations can be used for simple parametric study and evaluation purposes. On the other hand, the full solution (frequencies and mode shapes of the assembled structure) has very low sensitivity to the accuracy of the higher modes of the sub-structures. So the propagation of the numerical error of the higher frequencies, that are due to inaccurate models of sub-structures, do not have a significant effect on the numerical results of the lower modes of the assembled structure.

This unique smart structure concepts have been funded by SBIR-ARPA since 1991. Applications of this concept to both military and commercial industry are pursued. The following features make the presented smart structure technology unique.

(1) Smart-By-Design (SBD): Our concept has been to make structures or systems smart (or the smartest) at their design stage rather than designing "dumb" structures and than attempting to make them smart after they are designed and put in operation. The latter is costly and sometimes impractical. QRDC's concept is based on the modal energy localization (MEL) phenomenon that has proven to be an effective method to optimize a structure to withstand dynamic loads.

(2) Generic Smart Devices (GSD): QRDC's concept has been to develop smart devices that can be integrated in a wide range of existing structures to better control their vibration and noise responses.

(3) Multi-Tasks Smart Components (MTSC): Our concept has been to make all the existing components and sub-components (such as fasteners) smart in order to avoid or minimize add-on elements to the system. It is known that add-on elements, no matter how small, modify the dynamic behavior of structures. Furthermore, add-on elements also increase the complexity of the vibration response of the structure. QRDC's MTSC concept is being applied to fighter aircraft (F-15 at this time) through a project funded by the U.S. Air Force. The results have been very promising.

(4) Optimized Sensors and Actuators (OSA): Our smart structure technology is based on the optimized number of sensors/actuators located in the critical regions of the system. Such critical regions are identified in our smart design process. At this time, our sensors and actuators are an optimum combination of laser-based optics, PZT and PMN ceramics, and shape memory alloys.

ACKNOWLEDGMENT

This work has been funded jointly by Defense Advanced Research Project Agency (ARPA) through QRDC, Inc. Their continuous and dedicated support is acknowledged.

REFERENCES

[1] O.C. Zienkiewicz, "The Finite Element Method," London: McGraw-Hill, 1977.

[2] D. Allaei, "Application of Localized Vibration and Smart Materials in Controlling the Dynamic Response of Structures, Part I," Submitted to Defense Advanced Project Agency, 1992.

[3] D. Allaei, "Application of Localized Vibration and Smart Materials in Controlling the Dynamic Response of Structures, Part II," Submitted to Advanced Project Agency, 1992.

Paper presented at the Second European Conf. on Smart Structures and Materials, Glasgow 1994, Session 5

I.L.Curtis (Contracts and Marketing Manager) & M.J.Dill (Technical Manager)
Laing Technology Group :Structural Monitoring and Testing Service.

MONITORING TECHNIQUES FACILITATING THE LONG TERM ASSESSMENT OF STRUCTURES

SYNOPSIS.

This paper looks at the real problems facing engineers today when assessing the durability of structures. The role of monitoring structures to assess their current and long term behavioural characteristics and the enhancement of the safe use of structures is discussed. The capability of existing sensor systems to enable structures to inform engineers as to the onset of problems occurring is highlighted, thus establishing the advent of Smart Structures as a reality of today, rather than an idea of the future.

MONITORING STRATEGY

Monitoring, when used in conjunction with structural rehabilitation, should be deemed part of a global strategy for the structure under review. To ensure that the long term behavioural characteristics of the structure have been enhanced by the repair measures undertaken some kind of monitoring should be implemented. In the case of a heavily chloride contaminated structure that requires conventional repair techniques such as concrete replacement and re-waterproofing, it is important to ensure that the remedial measures have been successful in their attempt to arrest the deterioration of the structure.

A comprehensive permanent monitoring system must be able to provide specific information that will enable the structure to be monitored over a long period with the facility to provide remote interrogation of records from the instrumentation. A combination of monitoring techniques to include measurements of stress, strain, chemical environment within the concrete and corrosion rate of the reinforcement, will be required to enable a continual global analysis to be made of the structure so that a check on the long term durability and safe usage will be provided.

A monitoring system is also required as part of a design assessment, to decide the short term integrity of a structure, that will be used ultimately as a guide to the overall durability and service life recommendations for the structure. Monitoring is the only way to establish the actual response of a structure whilst under a test load or service conditions. This data can then be used to help in the comparison between the actual and assumed characteristic of the structure as used in the design assessment. Thus, working in conjunction with the assessment engineers, the monitoring data will provide detailed serviceability information and maximise the safe use of the structure.

0-8194-1700-9/94/$6.00

Benefits of monitoring

Long term monitoring:-

- Provide data as to the serviceability characteristics of the structure.
- Provide early warning as to the onset of structural problems at a stage when minor repairs will enhance durability.
- Provide an early warning system to maximise the safe use of the structure.

Short/Medium term monitoring:-

- Provide data on the actual structural behaviour of the bridge whilst under service or test load conditions.
- Provide the only way to compare actual structural responses and characteristics with assumed values used in design assessments.
- Provide an early warning system to maximise the safe of the structure.

STRAIN MONITORING

Conventional strain monitoring sensors, commonly used in structural monitoring, have a measuring capacity limited to point by point measurement, less than ideal when critical sections are not precisely known. Where the critical sections are known then the use of Electrical Resistance Strain Gauges (ERSG's), Vibrating Wire Gauges (VWG's) or Linear Variable Displacement Transformers (LVDT's) can be used to monitor local strains very effectively. The ability, however, to monitor large areas is of upmost importance when assessing the condition of large structures, such as bridges, before any critical sections have been established. Any monitoring system must be capable of providing reliable, accurate and permanent readings over a long period of time in order to ensure that structures are being used to high degree of safety. With such a monitoring system installed any structural problems can be highlighted at an early stage enabling the decision to be taken as to the repair works necessary to ensure the continued safe use of the structure. This allows for optimisation of property management to minimise life costs.

OPTICAL FIBRE SENSORS

Optical fibre sensors use two physical parameters of an optical fibre to produce movement gauges.

Stranded Optical Fibre Sensor (SOFS).

The first of these parameters is the measurement of light being lost, or attenuated, from a fibre that is wound in such a way as to create areas of microbending. Comparison of the intensity of light emerging from the sensor as it is strained, or relaxed, to the light supplied enables the change in the length of the sensor to be determined. This sensor is known as the Stranded Optical Fibre Sensor.

The light attenuation method of measurement has a resolution of ± 0.02mm, independent of gauge lengths from 2.0m upto a maximum of 15.0m, corresponding to ± 10 microstrain and ± 1.3 microstrain respectively. The long term accuracy of the system based on the initial datum is ± 0.1mm, however the resolution is maintained when measuring response to any movements occurring due to short term effects. This method however does not provide information regarding the distribution of strain in the sensor ie; where the strain is actually occurring. This information can be obtained, however, by using Optical Time Domain Reflectometer equipment (OTDR). The OTDR equipment transmits light pulses, at nano-second intervals, into the sensor and measures the transit time of light echoes from reflections occurring at the positions of attenuation. These reflections, or backscatter, of the light impulses allow the positions of the attenuation to be located, within ± 0.75m, thus providing a distribution of the major strain changes along the sensor.

Multi Reflection Sensor (MRS).

The second response parameter is based on the transit time of light to pass along a sensor to a partial mirror and be reflected back to the source. OTDR equipment is again used for carrying out the measurements but for the multi reflection sensor (MRS) a peco-second equipment is required to obtain the desired accuracy. A number of mirrors can be placed along a sensor and the position of each of these mirrors can be determined. The accuracy to which the positions of these reflectors can be measured is ± 0.15mm, this being constant for either long or short term measurement. A possible application of these sensors is to monitor distribution of strain within a prestressing strand by replacing the central wire of a seven wire prestressing strand, this strand is known as the "intelligent strand". The element applying the force to the structure now has its own measuring device built in allowing the tendon, in which the strand is an integral part, to be monitored along its whole length throughout its service life. Testing is being carried out at present on the Intelligent Strand and it is hoped that an experimental application of the system will be carried out in the near future. There is no limitation, within practical terms, to the length of the multi reflection sensor. The only limitation with this sensor is the number of reflectors that can be accommodated, at present the experiences of using the sensor limit the number to 12, when measuring from one end of the sensor only. If it is possible to monitor the sensor from both ends upto 24 reflectors can be used.

CONTROL AND DATALOGGING OF THE MONITORING SYSTEM.

All the instrumentation outlined above, except the MRS, can be controlled by the use of datalogging equipment to facilitate the operation of a long-term, permanent monitoring. The provision of an intelligent monitoring system provides comprehensive information on the day to day serviceability performance of a structure including dead load and temperature responses which are important factors when assessing the overall performance of a structure. Traditional dataloggers recording at set intervals, eg hourly, may mean that specific events, such as sudden strains occurring due to failure of wires within a prestressing elements, could go undetected. However by taking readings more frequently, for example at 5 minute intervals, such events should be recorded.

The datalogging equipment can been programmed to process information on site by making use of an intermediate storage facility contained within the equipment. For example the readings taken every 5 minutes are stored in the intermediate storage area and any changes are compared to a prescribed value. If the prescribed value is exceeded the datalogger would automatically transfer all of the 5 minute readings for the previous hour together with the next 2 hours of readings in to the final storage area. Under normal conditions, the datalogger would only store the reading taken on the hour in the final storage area. This latter information being used for the final data processing in the design office.

The prescribed value for the detection of possible structural problems occurring with the bridge eg: a sudden increase in strain, will be set at a level established by the design engineers. A period of monitoring would be required to establish a serviceability fingerprint which would enable refinement of this assessment to be highlighted against the assumed behaviour pattern.

If required the datalogger could be programmed to set off an alarm signal that notifies the engineer that a significant event has occurred on the bridge. This alarm system would be activated when any prescribed sensor reading was exceeded. At this point the datalogger would automatically send a signal, over a telephone modem line or RF transmitter, to a computer, in the office of the supervising engineer, that would alert them to a possible problem with the structure. This would then provide the structure with a certain degree of intelligence thus allowing it to inform the Engineer when problems start occurring.

CONCLUSION.

The application of a monitoring systems can enable structures, that have long term integrity doubts, to remain in service whilst at the same time maximising public safety. This will result in considerable saving in avoiding the costs associated with the only other solution to the problem which would be to demolish such structures. Optical Fibre Sensor systems have been used for some eight years for monitoring bridges, dams, rock and ground anchors in Germany, Austria and France and are now being used for the monitoring of structures in the UK. The Optical Fibre Sensor systems have been applied to structures in order to detect strain changes, due to problems occurring with the structures. In the applications to date undertaken on post tensioned structures, these systems were chosen to monitor beam soffits due to their capability of monitoring over their full gauge length, up to 15.0 m for a single gauge, as there was no way of predicting the actual position of a possible failure with this mode of construction. The development of these sensors has enabled this type of structure to be monitored comprehensively for the first time. The advancements of the electronics industry together with the further use of Optical Fibres in the communications industry will mean that the new applications will be discovered for this highly innovative and adaptable technology. The technology outlined in this paper is available to the Engineer today. It will, when combined with instrumentation to monitor chemical environment within the concrete and corrosion rate of reinforcement, enable a structure to have a limited amount of intelligence thus enabling a Smart Structure to be a reality providing a new outlook in the management of structures.

Paper presented at the Second European Conf. on Smart Structures and Materials, Glasgow 1994, Session 5

APPLICATION OF FUZZY LOGIC TO ACTIVE STRUCTURAL CONTROL

F. Casciati, L. Faravelli, and T. Yao [1]

Dept. of Structural Mechanics, University of Pavia, 27100 Pavia, Italy

1 INTRODUCTION

Severe environmental loads acting upon civil engineering structures can provide a significant hazard. Structural control, first formalized by Yao [10], is one tool that engineers today can use, especially in the retrofit of older existing structures that have been found to be deficient. Few active control strategies, however, can deal adequately with a lack of exact knowledge of system parameter values or nonlinear behavior.

One strategy that appears to be effective is fuzzy logic control. Imprecise linguistic descriptions of system conditions (e.g., the velocity is slightly negative and the displacement is somewhat positive, so apply a small force in the negative direction) can be used as the basis for activating control forces through the mathematical rules created by Zadeh [11].

In this paper, we discuss some aspects of the application of fuzzy control to civil engineering problems and we present results from the control of linear, two-degree-of-freedom systems that are subjected to simulated seismic excitation.

2 ACTIVE STRUCTURAL CONTROL

Ideally, the requirements of active control of civil structures can be defined by the following:

- identification of changes to the current state due to modifications of systems parameters and to external disturbances such as earthquakes, or winds;
- compensation for internal and external disturbances;
- learning and reasoning; the reaction strategy is updated on the basis of past successes/failures.

In order to provide a structure with such capabilities, a number of sensors must be incorporated into the structure to monitor the deflection and acceleration at joints or the strain at internal points. Actuators, tendons or other control devices can be used to actively modify the stiffness and damping characteristics of the structure.

A control unit must eventually use the sensor readings to manipulate the actuators to modify in real time the behavior of the structure subjected to a dynamic action. An active control system consists of these four stages:

1. gathering the sensor data;
2. assessing the structure state on the basis of the sensor data;
3. determining an appropriate set of control forces;
4. driving the actuators.

3 FUZZY CONTROL

Control literature in civil engineering is very rich in algorithms [4] [8] [9] to solve the equations that govern the system behavior. Many of these algorithms, however, require an exact knowledge of the system. As an alternative that is especially appropriate in the presence of an imprecise description, the Fuzzy Logic Controller (FLC) converts a linguistic control strategy, based upon expert knowledge, into an automatic control strategy [6]. The operations of a fuzzy controller comprise four parts:

1. *fuzzification interface*: the state variables to be monitored during the process must be measured. These values are fuzzified using fuzzy linguistic terms defined by the membership functions of the fuzzy sets, which are defined on an appropriate universe of discourse;

[1] Visiting Researcher

0-8194-1700-9/94/$6.00

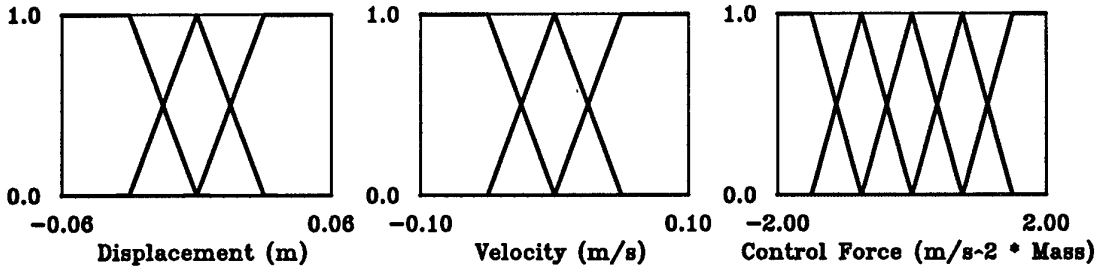

Figure 1: Membership functions

2. *knowledge base*: these linguistic terms are then used in the evaluation of the fuzzy control rules
3. *decision making logic*: the result of the application of these rules is a fuzzy set defined on the universe of possible control actions
4. *defuzzification interface*: the crisp control action is produced.

To design a fuzzy controller, we must specify the fuzzy sets and define their membership functions for each of the input and output variables. We employ triangular and trapezoidal membership functions for simplicity.

We can then compile the heuristic control and determine a method for selecting a crisp output action.

The fuzzy values of the output variable that are generated by the complete set of rules are combined by a union operator to derive the final fuzzy value of the output. This is defuzzified in our case by the center of gravity method (COG). The crisp value of the output in this method is computed as the center of gravity of the constituent membership function areas.

4 NUMERICAL EXAMPLES

The numerical example is a linear, two-degree-of-freedom (2DOF) system subjected to simulated seismic activity. The emphasis of this example is upon successful implementation of the fuzzy controller for a multi-degree-of-freedom (MDOF) system. The loading is a seismic-like simulated time history record consisting of a Kanai-Tajimi filtered white noise without time modulation.

Computations were performed upon a 486DX2-66MHz PC using PC Matlab 4.0. Routines from the MathWorks Control Toolbox [3] and the Delta Toolbox, were used to solve for the system response; and the Fuzzy Inference Systems Toolbox [7] provided the basic routines for performing the fuzzy calculations. Although computations were too slow with this setup to be used in an actual applications, there exist hardware implementations of fuzzy controllers that make fuzzy control feasible for real-time control.

The fuzzy control covers two input quantities (displacement and velocity) and one output (the control force) for each degree of freedom for a total of six fuzzy variables. We consider three descriptive fuzzy subsets for each of these: NE (negative), ZE (zero), and PO (positive). NL (negative large) and PL (positive large) are added to the control force variable. Trapezoidal membership functions map these fuzzy subsets to the appropriate universe of discourse. The combinations of input membership functions then yield eighteen fuzzy rules. Figure 1 shows the membership functions.

This approach, while cost effective, assumes that there is no explicit interaction between the actuators acting upon each degree of freedom (DOF); i.e., we assume that the state of one DOF does not directly influence the computation of the fuzzy control force of the other DOF. For this example problem, the other approach would require 81 rules to be complete. It is not easy to tune the membership functions or to determine the extent of coverage of each membership function within the domain of the universe of discourse.

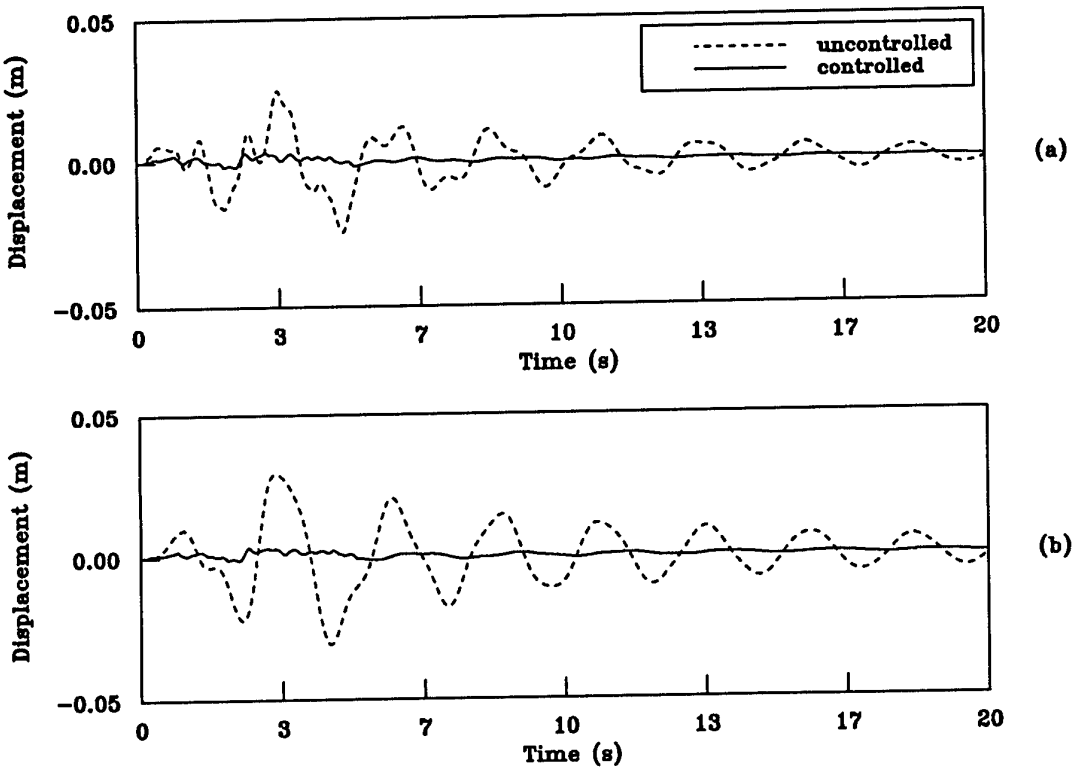

Figure 2: Comparison of controlled and uncontrolled displacement and velocity time histories, linear example: (a) first story displacements; (b) second story displacements.

Larsen's Product Rule in GMP is used to perform the fuzzy inference. This scales the membership function of the output variable by the rule premise's computed degree of truth. The defuzzification is accomplished through use of the center of gravity method.

The dynamic behavior of the two-story plane frame is defined by the mass ratio of its stories (1.0), natural frequencies (2.6 rad/s and 6.7 rad/s) and damping ratio (0.0355), and it is influenced by the intensity of the simulated seismic excitation (0.9 m/s^2 peak acceleration of the underlying white noise). The load duration is 5 seconds.

The universes of discourse are defined to be from -0.06 to 0.06 m for the displacement and from -0.1 to 0.1 m/s for the velocity for both degrees of freedom. Both story's universes of discourse range from -2.0 to 2.0 m/s^2 ($\times$ the mass of the appropriate story of the plane frame) for the control force.

Figure 2 shows a comparison of the controlled and uncontrolled displacement time histories for the two degrees of freedom.

5 CONCLUSIONS

Qualitatively, this simple example demonstrates some of the potential power of fuzzy control as applied to a civil engineering problem. Note that only three fuzzy subsets were used to describe each input and five fuzzy subsets to define the output variable in the control. Further refinement would likely improve the results, though it would increase the computational cost. Tuning the existing membership functions and possibly coupling the controllers for each story through additional rules would probably also improve the performance.

The tuning of fuzzy controllers (generally accomplished through adjustments to the membership functions) is not always intuitive and would likely benefit from automatic processing by neural networks [5] or genetic algorithms [2].

Future research will focus on extension of the MDOF example to include hysteretic behavior [1]. There will also be an investigation into efficient means of tuning the FLC and the interaction between the fuzzy controllers.

Acknowledgements

This work has been supported by grants from the Italian National Research Council (CNR) and the Ministry of University and Scientific and Technological Research (MURST).

References

[1] F. Casciati, L. Faravelli, and T. Yao. The effects of nonlinearities upon fuzzy structural control. In *Fifth Conference on Nonlinear Vibrations, Stability and Dynamics of Structures*, June 1994. (to be presented).

[2] Mark G. Cooper and Jacques J. Vidal. Genetic design of fuzzy controllers. In *Proceedings of the Second International Conference on Fuzzy Theory and Technology*, 1993. Durham, NC, October 1993.

[3] Andrew Grace, Alan J. Laub, John N. Little, and Clay M. Thompson. *Control System Toolbox for use with MATLAB.* The Mathworks, Inc., Cochituate Place, 24 Prime Park Way, Natick, MA 01760, July 1992.

[4] G.W. Housner, S.F. Masri, F. Casciati, and H. Kameda, editors. *Proceedings of the U.S.-Italy-Japan Workshop/Symposium on Structural Control and Intelligent Systems.* University of Southern California Press, October 1992.

[5] Jyh-Shing Roger Jang. Anfis: Adaptive-network-based fuzzy inference system. *IEEE Transactions on Systems, Man and Cybernetics*, 1992.

[6] Chuen Chien Lee. Fuzzy logic in control systems: Fuzzy logic controller, parts 1 and 2. *IEEE Transactions on Systems, Man and Cybernetics*, 20(2):404–435, March/April 1990.

[7] A. Lotfi. *Fuzzy Inference Systems toolbox for MATLAB (FISMAT).* Department of Electrical and Computer Engineering, University of Queensland, 1994.

[8] T.T. Soong. *Active Structural Control: Theory and Practice.* Longman Scientific and Technical, 1990.

[9] Y.K. Wen, editor. *Intelligent Structures 2: Monitoring and Control*, June 1991. Proceedings of the International Workshop, Perugia, Italy, 27-29 June 1991.

[10] James T-P. Yao. Concept of structural control. *Journal of the Structural Division, ASCE*, 98(7), 1972.

[11] Lotfi Zadeh. Fuzzy sets. *Information and control*, 8, 1965.

Paper presented at the Second European Conf. on Smart Structures and Materials, Glasgow 1994, Session 5

A Fiber Optic Smart Structure System for Natural Structures

Eric Udd
Blue Road Research
2555 N.E. 205th Avenue
Troutdale, Oregon 97060

Abstract

A fiber optic smart structure system is proposed for monitoring earth motion that has the potential to substantially enhance our understanding of earthquakes, and volcanic activity through the use of long gauge length strain sensors.

Introduction

One of the ways to try to understand the behavior of earthquakes and volcanic activity is to monitor strain build up. Currently the main methods that are used to monitor earthquake prone regions are satellite mapping, usage of the Global Positioning Satellite, and a few line of site laser systems placed at key locations. Satellite mapping can be used to locate major events for more detailed study. The Global Positioning Satellite system may be used to locate the position of two points to about a cm after a day or two of integration time. Only the line of sight laser systems offer real time measurement of displacement between two points. These systems are generally expensive and have been used in a limited number of locations. What is needed is a system that allows broad coverage of sites that are subject to earth movement to provide a data base on which future predictions and forecasts of earthquakes and volcanic activity may be made. Figure 1 illustrates the location of all historically recorded earthquakes in the United States that caused moderate to severe damage [1]. The scale of the problem is such that a cost effective system offering coverage over millions of square kilometers would be needed to provide coverage of particularly hazardous regions in the United States.

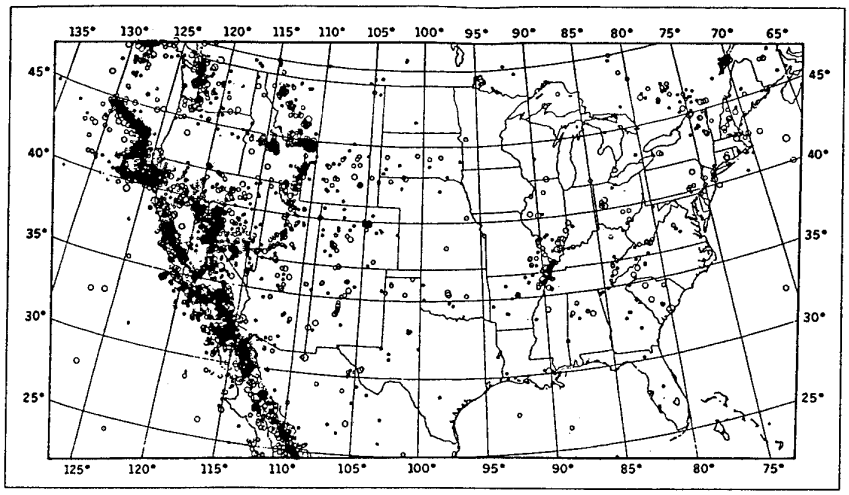

Figure 1. Locations of historical earthquakes with magnitude >3.5 producing moderate to severe damage after reference 1.

0-8194-1700-9/94/$6.00

Fortunately millions of kilometers of telecommunication grade fiber optic cables have already been installed into national networks and plans are in place to greatly expand the system into regional and local networks and eventually to fiber to the home. Long gauge length fiber optic strain gauges could be used in conjunction with national, regional and local fiber telecom systems to provide detailed strain information on hazardous natural formations. Figure 2 shows a fault line where two parts of the earth crust are moving in opposite directions. Before slippage and an earthquake occurs there is substantial build up of strain. The system would consist of long gauge length fiber optic strain sensors that are placed either directly into the wall of newly buried telecommunication cables or separate fiber strain sensor cables that fan out from break points in the telecom cable. The information would then be processed and placed as a data stream into the telecom cable for routing to a central processing area where strain build up and ground motion would be monitored.

System Details

The key sensing element of the system is a fiber optic strain sensor that offers low cost, compatibility with standard telecom fiber cables, and the ability to have extremely long gauge lengths. While many types of fiber sensors have very long gauge lengths [2-4] the Sagnac interferometer based strain sensor has the potential to meet all the criteria for a successful system [5]. Early demonstrations [6] showed that displacements on the order of 100 microns could be measured over a distance of 150 meters using bulk optic components operating at 0.8 microns. By using modern components operating at 1.3 microns the system could be extended to 10 km or more with similar sensitivity. By using polarization scrambling techniques conventional single mode optical fiber may be used allowing "dark fiber" in the telecom cables to be used as part of the sensor. Figure 3 illustrates a Sagnac strain sensor. A light source which may be a light emitting diode or for systems operating over very long lengths (10s of kilometers) a fiber laser is used to generate counterpropagating light beams in a Sagnac loop. A frequency shifter is placed in the loop so that a net frequency difference of F exists between the counterpropagating light beams but both light beams are shifted by the frequency F so that when they return to the central beamsplitter the

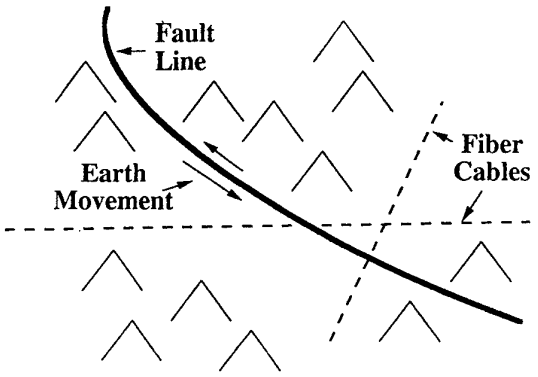

Figure 2. Usage of long gauge length fiber strain sensors in combination with standard telecom cables to produce an earth movement detection system.

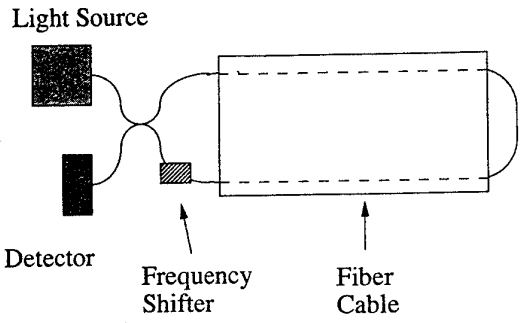

Figure 3. A Sagnac interferometer based long gauge length strain sensor.

frequency is matched and they can be compared in phase using standard techniques associated with fiber optic gyros. If the frequency shifter operating frequency is adjusted to hold the relative phase between the counterpropagating light beams constant then a change in length dL results in a frequency shift dF=-FdL/L where L is the length of the Sagnac loop.

Most telecommunication cables that are currently in operation are designed so that the optical fibers are strain relieved. Thus in order to implement this system new cables would have to be designed that incorporate optical fiber into the housing of the cable to measure strain or separate fiber cables that fan out from fiber cable at convenient locations would be used.

The support electronics for the sensor would be located at central nodes that ideally would be collocated with the fiber telecom repeater locations. The sensor information would be processed locally formatted into digital data and injected into the data stream for processing at a regional or national central location.

Related Applications

In addition to monitoring earthquakes and volcanic activity it is also possible to use similar systems to monitor stress on power lines that may increase or decrease with earth motion. This could be done by burying the optical fiber strain gauge directly into the power line as in Figure 4.

Another application area would be to monitor the relative position of oil platforms at sea as in Figure 5. Some of these platforms may move due to strong currents or winds and long gauge length fiber optic strain sensors could be used to monitor their location and provide information necessary for active control. By linking the data to telecommunication fiber systems the information could be processed in a central location.

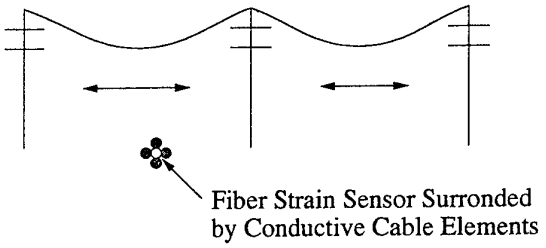

Figure 4. Usage of embedded fiber optic strain sensors to monitor strain on suspended power lines.

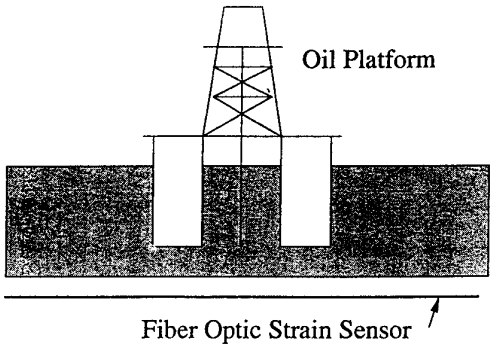

Figure 5. Usage of long gauge length strain sensors to monitor the position of an oil platform.

Summary

A system has been described based on long gauge length fiber optic sensors that has the potential to reduce hazards due to earthquakes and volcanic activity by providing a data base for predictions of these events. Systems may also be implemented to provide strain monitoring systems for power lines and to monitor the position of oil platforms.

References

1. W. L. Ellsworth and T. H. Heaton, "Real-Time Analysis of Earthquakes: Early Warning Systems and Rapid Damage Assessment", Sensors, Vol. 11, No. 4, p. 27, 1994.

2. E. Udd, Editor, *Fiber Optic Sensors: An Introduction for Engineers and Scientists*, Wiley, New York, 1991.

3. J. Dakin and B. Culshaw, *Optical Fiber Sensors: Principals and Components,* Artech, Boston, 1988.

4. B. Culshaw and J. Dakin, *Optical Fiber Sensors: Systems and Applications,* Artech, Boston, 1989.

5. E. Udd, R. Blom, D. Tralli, E. Saaski and R. Dokka, "Applications of the Sagnac Interferometer Based Strain Sensor to an Earth Movement Detection System", SPIE Proceedings, Vol. 2191, 1994.

6. R. J. Michal, E. Udd, and J. P. Theriault, "Derivative Fiber-Optic Sensors Based on the Phase-Nulling Optical Gyro Development", SPIE Proceedings, Vol. 719, p. 150, 1986.

SESSION 6

Paper presented at the Second European Conf. on Smart Structures and Materials, Glasgow 1994, Session 6

LOW COHERENCE INTERFEROMETRY FOR THE MONITORING OF CIVIL ENGINEERING STRUCTURES

Daniele Inaudi[1], Adil Elamari[2], Samuel Vurpillot[1]

[1] IMAC, Laboratory of Stress Analysis, Swiss Federal Institute of Technology, Lausanne, Switzerland
[2] GAP, Group of Applied Physics - Optical Section, Geneva University, Switzerland

ABSTRACT

A measuring system adapted to the needs of civil engineering structural monitoring is presented. It is based on low coherence interferometry in standard singlemode fibers and has a resolution of 5 μm, an operational range of 7 cm, stability over long periods (at least 1 year) and insensitivity to variations of the fiber losses. The portable reading unit doesn't need to be connected to the sensing fibers permanently and can thus be used to monitor multiple structures reducing the costs of the instrumentation.
This paper presents the operating principle of this system and different techniques used to install the sensing fibers in large concrete structures, timber and mixed timber-concrete structures as well as on metals.

INTRODUCTION

The FORMOS project (Fiber Optic aRray for the Monitoring Of Structures) aims to the observation of civil structures (1 m to 1 km in size) over their whole lifespan, which can extend to more than 100 years in the case of a bridge. The monitoring of such constructions requires a measuring technique with high accuracy, stability and reliability over long periods. It has to be independent of variation in the optical fiber losses and adapted to the adverse environment of a building yard. To reduce the costs of the instrumentation it is furthermore desirable to use the same portable unit for the monitoring of multiple structures. We describe here a system based on low coherence interferometry in standard telecommunication fibers responding to all these requirements.

Besides the design of the optical setup, the effectiveness of such a measuring system relays on the technique used to install the optical fibers in the structures itself. Two contradictory requirements need to be satisfied: on one side the fibers have to survive the adverse conditions during fabrication and service, on the other the sensors need to be in contact with the quantity to be measured (mechanical contact to measure deformations, chemical contact to measure the penetration of harmful products, thermal contact to measure temperature, ...). Contrary to the optical reading unit that is usually the same for different applications, the installation procedure has to be tailored to the specific host structure. Different materials such as concrete, steel or timber, require different approaches. In many cases further parameters such as accessibility of the structure, week or strongly charged points to be avoided, coordination with other installed sensors or even esthetic consideration need to be taken into account during the planning of a fiber optic monitoring network. Our group has gathered an important experience in installing deformation sensors for different civil applications including concrete slabs and beams, projected concrete for tunnel walls, rails, multilayer timber, mixed timber-concrete and steel-concrete slabs, anchorage or pre-stressing cables and crack opening measurements. The lessons learned from these tests are discussed in the second part of the paper.

OPTICAL SETUP

The optical arrangement consists in a low coherence double Michelson interferometer in tandem configuration (see figure 1) [1]. The two arms of the first interferometer are mounted in the structure, one in mechanical contact with the structure (measurement arm) and the other placed loose in a neighboring pipe (reference arm) in order to compensate the variations of the refractive index of silica fibers induced by temperature changes. The second "analyzing" interferometer consists in a portable single-mode Michelson interferometer with an arm ended by a mobile mirror mounted on a computer-controlled micrometric displacement stage [2]. When the arm unbalancing in the reading interferometer corresponds to the one in the measurement fibers, interference fringes are detected. A

0-8194-1700-9/94/$6.00

deformation of the host structure will stretch the measurement arm only and will require a different compensation in the reading unit in order to obtain interference, again. By measuring at different times the mirror position balancing the two Michelsons, one can then reconstruct the deformation undergone by the structure. No continuous measurement is required and the same portable reading unit can be used to monitor multiple fiber sensors. A detailed discussion of this technique can be found in [1].

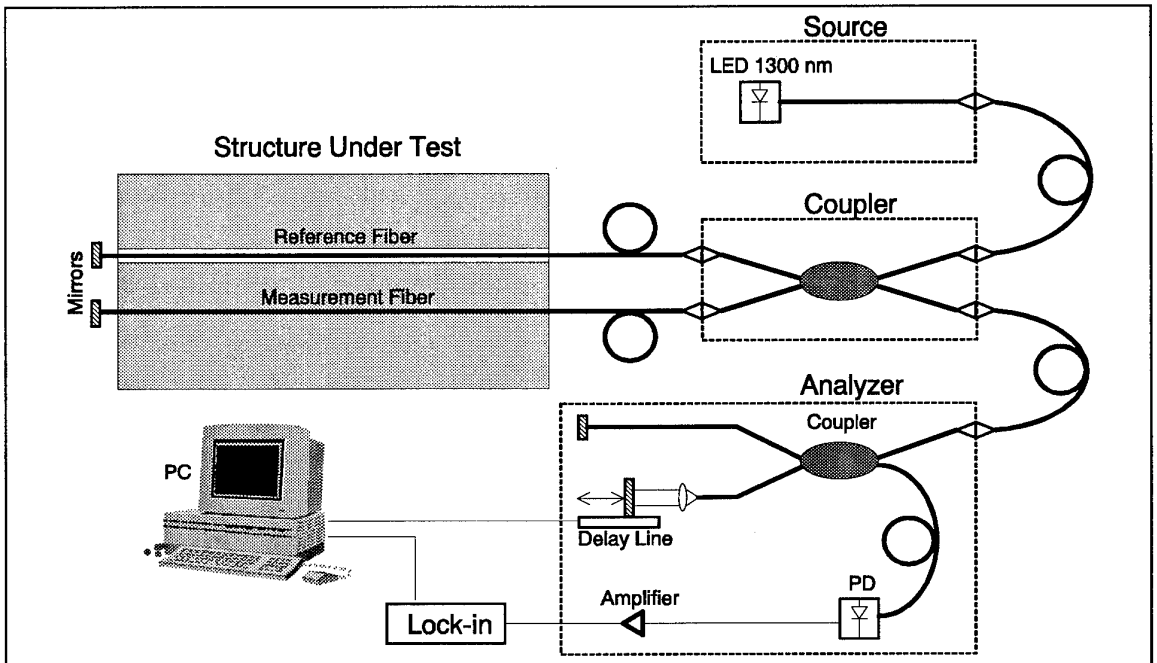

Figure 1: Experimental setup of the low coherence double Michelson interferometer used in the experiments.

The precision of the system is 5 µm with an operational range of 70 mm and a dynamic range of about -40 dB. The stability has been tested during 18 month on a 20 m long concrete slab without any noticeable drift [1,3]. The system has been used with sensing length between 50 mm and 60 m and in a temperature range between -25 °C and +150 °C.

FIBER INSTALLATION

Since the measuring system responds to variations of the total optical length of the sensing fibers, two installation approaches can be followed to couple the fiber to the structure: local and full-length coupling. In the first case the fiber is fixed to the host structure at two points, only. In order to follow both elongation and shortening, the fiber must be tighten during installation. In the case of full length coupling the fiber is attached over the whole sensing length. The characteristics of the fiber coating and, in the case of surface mounting, of the glue, can have in this case an important influence on the sensitivity of the sensor. These effects are often hardly solved by a numerical approach and calibration is required for every new host material, coating or glue. This approach is however interesting since the extended coupling length allows good measurements even if the mechanical contact between the fiber and the structure is rather weak. The two approaches give different results if deformation components perpendicular to the fibers are present, too. We have tested both approaches on different structures and found that in many cases the local coupling offers advantages over the full-length coupling.

a) Concrete structures

Most of the modern civil structures are made of reinforced concrete, this material is therefore the most attractive candidate for the application of fiber sensors. Interesting parameters to be monitored include shrinkage, elastic and plastic deformations due to pre-stressing, crack opening, temperature and long time deformations of large structures

such as bridges, tunnels and dams. The conditions in a real building yard are however so hostile that even a coated fiber can hardly survive the concreting process. The fibers have than to be protected without reducing their mechanical contact with the structure.

Our first approach to this problem was to install empty pipes and add the fibers after the setting of concrete. The fibers were then glued at the surface of the slab [1]. Although the results obtained with this technique were highly satisfactory, the gluing process and the assembly of connectors proved to be unsuited to building yard conditions.

The full length approach was also attempted. Since optical fibers are extremely fragile when bent, one has to avoid this type of deformation during the pouring of concrete. This was obtained by mounting the sensing fiber (with a 0.8 mm nylon coating) on the external face of a plastic pipe. A rubber band every 20-30 cm was used to hold the slightly tightened fiber on the pipe. The sensing fiber can re-enter the pipe a few centimeters before reaching the concrete surface. This technique seems very promising, but the preparation of the pipe was very time consuming.

After these first experiences it seemed that the number of operation to be performed at the building yard had to be reduced as much as possible. A new sensor design based on local coupling allows all critical operations (such as connector assembly, mirror deposition, fiber gluing, and so on) to be accomplished in laboratory conditions. The bare fibers are installed in small plastic pipes (6 to 8 mm external diameter) over their full length from the connector box to the mirrors. At the two measuring points a steel nail runs through the pipe, at this point an epoxy glue is injected inside the pipe through a tiny hole (see figure 2a). This sensor is than installed in the form, tightened to about 0.5% and tied to the reinforcing bars. During the setting process the concrete envelops the nail and the pipe realizing the desired mechanical coupling with the fiber. This system is extremely easy to install and gives reproducible results for both elongation and shortening. Even strong cracking does not usually affect the measurements.

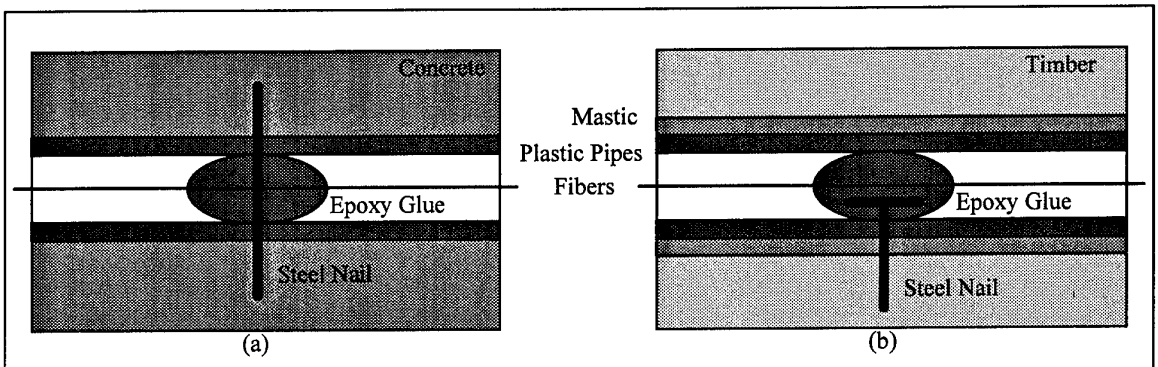

Figure 2: Installation techniques in concrete and timber. The optical fiber is protected inside a 6 mm plastic pipe. The mechanical contact between the fiber and the structure is realized by the steel nail and the epoxy glue.

Projected concrete represents a special case. It is mainly used to case the walls of tunnels. We have installed optical fibers with 0.8 mm nylon coating in a 1 m long sample projected in real tunneling conditions. A 5 cm layer of concrete was first projected, the fibers were than laid on this soft surface and some were protected with a plastic half-pipe. All of the 10 fiber (protected or not) survived the projection of a second 4 cm layer of concrete. The increase in the scattering losses was small and the microbend induced back-signal was at least -15 dB from the transmitted signal. By providing external reference fibers of the same length measurements could be performed normally.

Another important aspect of concrete mechanics is cracking. We were able to measure crack opening with 10 cm long sensors applied both on the surface of the structure (were a crack was observed) or inside. In this second case the sensing fiber was installed near a transverse steel bar were cracks usually appear. The results of the surface mounted sensors were in very good agreement with the ones obtained by standard Ω gauges.

b) Timber structures
Timber is a very interesting building material, its characteristics are however less understood than those of concrete and metals and present often a wider spread between different samples. This aspects make them ideal candidate for smart structure applications. Besides deformation in a full scale timber structure it is often interesting to measure internal deformations in multilayer beams, in this case bare fibers are installed between the wood layers during assembly.

We have installed optical fiber sensors in a 13 m long mixed timber-concrete slab in order to determine its neutral axis and to study the adherence between the two materials. The installation technique in the concrete part was the same as shown in figure 2a. On the timber beams a groove was first cut and the 6 mm pipe was than held in the desired position with mastic. The nail was pushed in a drilled hole filled with epoxy glue (see figure 2b). The beams were than assembled so that the pipes were surrounded by wood in all directions.

c) Anchoring cables
To monitor the deformations of both the free and anchored parts of an anchoring cable, optical fiber are often the only available sensors. A test was performed on eight 25 m long cables installed in a 250 m wide rockslide. The fibers were protected by 8 mm plastic pipe and mounted together with the steel cables. Since the needle technique was not adapted to this application, a mechanical piece was specially designed to insure the mechanical coupling between fibers and grout. A similar piece was used at the anchoring head. This same technique was used to fabricate a fiber rock-meter. In this case the pipe bundle is pushed in a hole drilled in the sliding wall and grout is injected to fill the empty spaces and couple the system to the rock.

d) Rails
Because of their immunity to electromagnetic interference, fiber sensors are very attractive for railway monitoring. Thermally induced deformations of a 1 m long rail sample were measured between 20°C and 150°C to prove the effectiveness of our sensors for this application and their insensitivity to temperature variations. The bare fibers were installed on the rail surface with epoxy glue. Both the local as the full length coupling were attempted, the first giving better results consistent with the thermal expansion coefficient found in the literature.

CONCLUSIONS

A measuring technique based on low coherence interferometry and adapted to the needs of civil smart structures was presented. Different techniques used to install optical fiber sensors in many building materials were discussed. The arrangements based on local coupling between the structures and the sensing fibers seem better adapted to the hostile environment of a building yard. Full length coupling can however be interesting in particular cases and for material research porpoises.

ACKNOWLEDGMENTS

The authors are indebted to Prof. L. Pflug, Dr. N. Gisin, Ing. P. Colombo, Dr. M. Pedretti, Ing. R. Passera, Dr. P. Jaquot, Dr. P. Rastogi, Dr. J. Breguet, Dr. R. Passy, P. Mivelaz, R. Emery, Dr. J. Piffaretti, Ing. D. Cilloni, R. Delez and the whole IMAC, GAP and IMM teams for their help, encouragement and helpful discussions. We are also thankful to Cabloptic in Cortaillod (Switzerland) for supplying all the optical fibers used in the experiment. The FORMOS research project is performed with the financial support of CERS (Commission pour l'Encouragement de la recherche Scientifique, Switzerland).

REFERENCES

[1] D. Inaudi, A. Elamari, L. Pflug, N. Gisin, J. Breguet: Low Coherence deformation sensors for the monitoring of civil engineering structures, to be published in Sensors and Actuators A, 1994
[2] N. Gisin, J.-P. Von der Weid, J.-P. Pellaux: Polarization mode dispersion of short and long single-mode fibers, Journal of lightwave technology, Vol 9, No 7 (1991), pp. 821-827
[3] L. Pflug, M. Pedretti: Construction of a 100-tons holographic table, IS&T/SPIE International symposium on Electronic Imaging, San Jose, 1993

Thermal expansion measurements of a concrete structure by embedded fiber-optic: an effective example of simultaneous strain-temperature detection

Valeria Gusmeroli, Mario Martinelli (*), Angelo Barberis,
Priscila Escobar and Paolo Morabito (**)

CISE Tecnologie Innovative, POB 12081, 20134 MILANO, Italy

Abstract

The measurement of thermal expansion of a 5 meter length concrete beam by embedded fiber-optic interferometric sensors is reported. The measurement has been done by a scheme which permits to solve the fiber strain-temperature cross-sensitivity by a contemporary reading of both the optical path length and the dispersion parameter of the fiber. The reported experimental data confirm the suitability of the technique for simultaneous detection of absolute strain and temperature.

Fiber-optic interferometric sensors have been recognised a suitable technology for the monitoring of large civil structures. In effect fiber sensors present some peculiar characteristics that make them suitable for that application. Over the electromagnetic immunity, the high sensitivity and robustness, optical fiber sensors present a unique general geometry that allow both the use of very long measurement bases and the development of sensors networks. The suitability of the technology in terms of sensor resolution, dynamic range long life term has been already proved [1], as well as the availability of sensor topologies adequate for the evaluation of the mode shape [2]. However a drawback limits the full exploitation of fiber sensors, especially in field applications: the high imprecision of the static strain measurement due to the fiber sensitivity to temperature. At the same time long-term, static-strain measurement are the main notification of the integrity and safety of a structure and material characterization often requires a precise measurement of both strain and temperature. The recovery of both the above parameters by a single fiber-optic sensor would allow the measurement of an important material characteristic like the thermal expansion coefficient.

A recent proposal suggests a solution for the "static" measurement: the contemporary evaluation of fiber optical-path and dispersion realised with very-high accuracy by an interferometric scheme. Both optical path and dispersion are dependent on temperature and strain, but with a different sensitivities. Hence, a couple of independent equations are available and permit to extract the "absolute" temperature and strain values.

The aim of this communication is to present a first example of simultaneous measurement of temperature and static strain by means of a fiber-optic interferometric sensor embedded in a 5- meter reinforced concrete beam. The measurement leads to a direct evaluation of the concrete-beam thermal expansion.

In fig.1 a picture of the measurement brass-board developed on the base of the above quoted method [3] is shown. The instrument is based on a white-light interferometric architecture where the sensor-fiber is arranged in a Fabry-Perot structure (with length equals to the structure, e.g. 5 m). The source is a 830 nm central-wavelength, 20 nm bandwidth, superluminescent diode. The light returning from the sensor feeds the brass-board receiving interferometer. In order to compensate the Fabry-Perot sensing cavity, one arm of the receiving interferometer is realised by a coil of optical fiber, thermal stabilised , plus an additional air path whose length is precisely adjusted by a moving stage . A couple of Bragg-cells give to the scheme the carrier (4 Khz) that allows a hetherodyne detection. The interference signal is simultaneously detected through 4 optical filters whose central wavelengths span within the source bandwidth. Each couple of filters allows the measurement of the group velocity associated to the respective section of the source spectrum along with the non-incremental optical path value [4]. Hence, the measurement done on the double couple of filters allows the extraction of the dispersive parameter and optical path parameter as a function of the perturbation acting on the sensor fiber.

0-8194-1700-9/94/$6.00

The Fabry-Perot sensor cavity is obtained by means of retroreflective dielectric depositions grown on the polished end-faces of the fiber itself. The fibres used have been prepared for the embedding with a teftzel coating.

The measurement is done on a concrete reinforced beam of cross-section 25x16 cm and 5 meter length (Fig.2). The beam has been casted by Ordinary Portland Cement and reinforced by 10 tendon. The sensor-fibres have been drawn along the longitudinal axis of the beam and embedded during the casting operation.

In order to measure the material thermal expansion coefficient, the beam has been heated by means of an heating ribbon wrapped around and able to dissipate a power of about 1 KW. Five electrical thermocouples embedded along the beam allow the control of the average temperature of the material. Then, the concrete beam has been submitted to slow thermal cycle from 10°C to 40°C.

The embedded sensor-fiber allows to recovery the data of temperature along with the integral of the axial strain. The results of the measurement are reported on Fig.3 a) and b). In the upper graph, the measured temperature is reported versus the imposed temperature: the slope of the best-fit line is .99 which confirms the precision of the measurement processing. The lower graph gives the measured strain versus the imposed temperature. The slope of the best-fit line is 11 μm/°C› in agreement with the expected value of the thermal expansion coefficient for the reinforced concrete.

In conclusion, a first example of simultaneous and non-incremental measurement of both temperature and strain by an embedded fiber-optic interferometric sensor has been reported. The experiment leads to the direct measurement of the thermal expansion of the concrete structure and outlines the possibility of a great number of "absolute" measurements useful to the diagnostic and monitoring purposes of large concrete structures, e.g. the monitoring of the hydration heat effects which follow the cast procedures of the concrete.

The work has been done in the framework of the CEMOPT Contract and has been entirely supported by ENEL-CRIS, to whose Direction the Author wish to express acknowledgements for the given permission to publication.

(*) Now with: Dpt Elettronica ed Informazione, Politecnico di Milano, Milano, Italy.

(**) With ENEL- Centro Ricerca Idraulica e Strutturale, Milano, Italy.

References

(1) P.Escobar, V.Gusmeroli, M.Martinelli, I.Lanciani, P.Morabito: "Fiber-optic interferometric sensors for concrete structures", Proc. of the 1st Europ. Conf. on Smart structure, Glasgow (1992)

(2) A.Barberis, P.Escobar, V.Gusmeroli, C.Mariottini and M.Martinelli : " Elastic curve recovery by a quasi-distributed polarimetric fiber-optic sensor", Proc. of the 1st Europ. Conf. on Smart structure, Glasgow (1992)

(3) V.Gusmeroli, C.Mariottini, M.Martinelli : "Absolute and simultaneous strain and temeperature measurement by a coherent optical fiber sensor" submitted to OFS-10.

(4) V.Gusmeroli, M.Martinelli : " Two wavelength interferometry by superluminescent source filtering" Optics Communic. 94, 309, (1992).

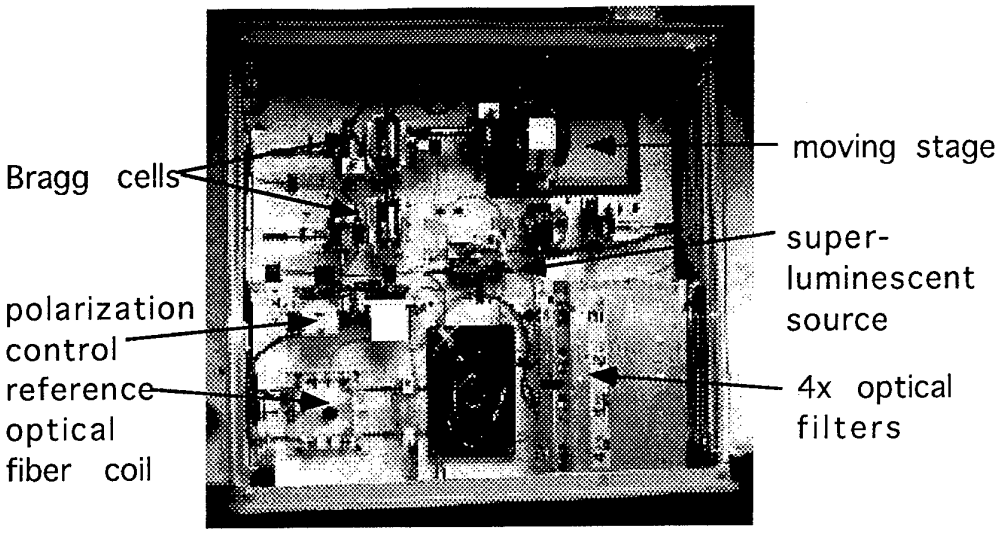

Fig.1. The brass-board of the optical processing unit: a novel interferometric scheme allows the simultaneous measurement of the temperature and of the strain by a single fiber sensor.

Fig. 2 . The 25x16x500 cm reinforced concrete beam. The fiber-optic sensors embedded-in, configured like a Fabry-Perot cavity, allow the measurement of the thermal expansion coefficient of the beam.

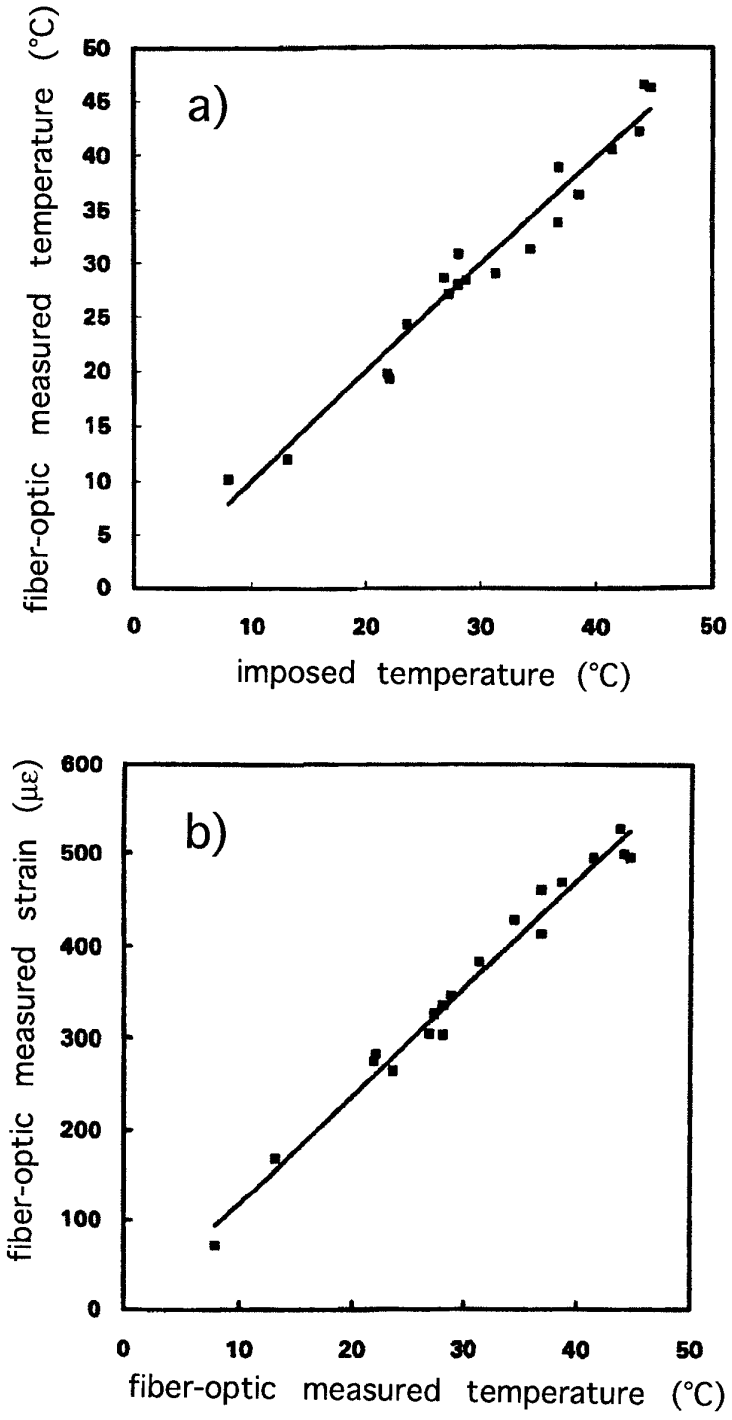

Fig.1a). The temperature measured by the embedded fiber-optic sensor versus that one imposed by heating.
Fig.1b). The strain versus temperature measured by the single embedded fiber-optic sensor: the slope of the best-fit line (the thermal expansion coefficient) results 11 μm/°C.

EMBEDDED OPTICAL FIBRE STRAIN GAGES FOR CIVIL ENGINEERING : APPLICATION TO CONCRETE MONITORING

J.J. GUERIN, M. LEQUIME

BERTIN & Cie, B.P. 22000, 13791 AIX-en-PROVENCE Cedex 3 FRANCE

Phone : (33) 42 60 46 00 Fax : (33) 42 60 00 13

E. TOPPANI, M. LEYGONIE

EDF/Direction de l'Equipement/TEGG, 905 Avenue du Camp de Menthe B.P. 605

13093 AIX-en-PROVENCE Cedex 2 FRANCE

Phone : (33) 42 95 95 95 Fax : (33) 42 95 95 00

D. CHAUVEL

EDF/Direction de l'Equipement/SEPTEN, 12-14 Avenue Dutrievoz 69628 VILLEURBANNE FRANCE

Phone : (33) 78 94 44 44 Fax : (33) 78 94 49 99

1. INTRODUCTION

Intrinsic Optical Fibre Sensors (OFS), in which the fibre is the transducer, are now recognized as good candidates for distributed or quasi-distributed sensing applications. In the particular field of Civil Engineering, this concept will provide powerfull means for global and real time monitoring of the structure integrity. Natural phenomena like earthquakes, wind, atmospheric pollutions but also more insidious internal effects such as chemical attack (Alkali problem) yield consequent internal damages for which the embedment of sensor arrays could be of great interest.

In our application, the transducer scheme is based on a polarimetric approach in which the two modes of a high birefringent fibre are used to measure a phase shift proportional to the strain state. A quasi-distributed measurement is performed by using the low coherence "White Light Interferometry " (WLI) to separate the information provided by a linear sensor arrangement. Along the fibre, the sensors are separated each others by intrinsic mode couplers [1,2].

In this paper, we report some experimental results of strain states obtained with concrete test structures. The sensors were embedded in the structure during its manufacturing and tests of elongation and compression were performed.

2. PRINCIPLE

The WLI is used to multiplex the different signals coming from the sensors. A schematic drawing of our arrangement is depicted in Figure 1. A pigtailed SLD light source, emitting at 830 nm, is launched into one of the polarization modes of the sensing fibre. In order to control the input polarization state, an optical fibre polarizer is added between the light source and the sensor. At the output of the sensor, an analyzer oriented at 45° with respect to the fibre axes allows to get the polarization condition necessary to recover the interferences after passing through a Michelson interferometer. The Optical Path Difference (OPD) associated to the sensing zones defined along the fibre are greater than the coherence length of the light source in order that the low coherence demultiplexing method may be used [3,4]. For demultiplexing, we use a specific multi-mirror Michelson [5] designed to generate several OPDs simulteneously which match the OPDs provided by the sensor zones localized along the fibre. In our experiment, the OPD between two adjacent mirrors is 150 µm. These developments have been achieved in the frame of the European Project *OSTIC BRITE N° RI1B0173-C(CD).*

0-8194-1700-9/94/$6.00

The intensity of the detected signal coming from the i^{th} coupler (i^{th} sensor zone) is given by :

$I=I_0(1+K_i\, m_0 \cos\Phi_i)$ with :

K_i : amplitude coupling coefficient m_0 : interferometer efficiency

Φ_i : phase corresponding to the i^{th} sensor zone

The expression of the phase is :

$\Phi_i=2\pi/\lambda(OPD_r-\Delta_n\, l_i)$

λ : wavelength (0.83 µm) Δ_n : birefringence ($5.5\ 10^{-4}$)

l_i : length between the i^{th} coupler and the fibre end OPD_r : Optical Path Difference in the receiver

When the interferometric receiver matches all the signals generated by the sensing fibre, the phase delay $\Delta\phi_i$ between two successive signals (corresponding to couplers i^{th} and $i\text{-}1^{th}$) can be measured :

$$\Delta\Phi_i = 2\pi/\lambda\, \Delta_n\, (l_i - l_{i-1})$$

and provides information upon the variations of the sensing zone lengths that are directly related to the strain distribution along the OFS.

3. SENSOR DESCRIPTION

The optical fibre used for our application is a Polyimide coated Hi-Bi fibre from FIBERCORE. For these trials, the optical sensor is limited to a single sensing zone defined between two coupling points, separated by a length L. The fabrication of the couplers consists in modifying locally the birefringence, by controlled heating using a standard splicer. It could be obviously possible to use photoinduced gratings to get the same effect [6].

The length between two couplers is defined by the following relation ship : $L = OPD_r/\Delta_n$ L = 272 mm.

The optical fibre must be protected by a sheath before embedment into concrete. The purpose of this protection is to reinforce the mechanical strength of the embedded fibre, to prevent from chemical agression, and to avoid the creation of parasitic coupling points which may be generated by the material grain. This mechanical protection of the fibre has been made by using a stainless steel thin tube.

The mechanical bond between the fibre coating and the metallic tube has been made by gluing. The Figure 2 shows the sensor structure.

4. TEST STRUCTURES DESCRIPTION

Two types of test structures have been manufactured. The first one of rectangular shape has been used for strain measurements. A schematic drawing of this test structure with armatures is shown in Figure 3. The length of the test structure was 800 mm and the optical fibre sensor was placed in the center of the test structure at 50 mm of its bottom.

The second one, of cylindrical shape, does not contain any armature. It has been used for pure compressive measurements. The optical fibre sensor is placed in the center (Figure 4).

The concrete used for the test structure fabrication has a breaking resistance of about 30 MPa. During their process, the test structures have been vibrated with a needle. Trials have been started after a delay of 28 days (time necessary for concrete drying).

The test structure have been intrumented with classical strain gages bonded on the surface, to get reference measurements.

5. EXPERIMENTAL RESULTS

5.1 Three point bending

Mechanical sollicitations have been applied through a 3 point bending configuration, the distance between points being about 500 mm. Because the OFS is located in the bottom part of the test structure, the mea-

surements that we describe here after are related to an elongation of the sensor.

Several load rises have been performed with this test structure. For a load of 160 kN, the strain value given by the reference strain gage was 1035 με and the differential phase variation provided by the OFS was 10.55 rd. The derived optical sensor sensitivity is 10.2 mrad/ με. For four successive load rises, the sensitivity repeatability was ± 0.22 mrad/ με.

Considering the measure integration on a length of 272 mm (length of one sensing zone), we can deduce a linear sensitivity of 37.5 mrad/ με/m.

The Figure 5 shows compared responses of the reference conventional electrical strain gage and of our optical fibre sensor. The good linearity of both gages is to be underlined.

5.2 Compression

The results for three successive compressions were the following. Under loading of 400 kN the value of strain provided by the strain gage was 263 με, and the phase variation was 6.61 rad. The derived sensitivity of the optical sensor was then 25 mrad/ με. For three successive load rises, the repeatability was ± 1.6 mrad/ με. The linear sensitivity was 92 mrad/ με/m. The Figure 6 shows the responses of both electrical and optical strain gages.

6. EXPERIMENTAL RESULT ANALYSIS

It is to be noted that the sensitivity of the OFS calculated from the three point bending experiment is 2.5 times lower than that found for compressive tests. This difference in sensitivity can be explained by the fact that, in the case of the bending test, the test structure is inhomogeneous due to the reinforcement. Consequently, the strain imposed to the mean fibre of the test structure, the strain imposed to the OFS and the strain measured by the reference strain gage bonded on the bottom surface were not physically identical.

In the compressive test case, the sensitivity of the OFS derived from the measurements is comparable to the one obtained with composite materials (*OSTIC*, 100 mrad/ με/m).

7. CONCLUSION

These first trials have shown it is possible to get information of concrete structure strain by using embedded OFS. The use of a thin metallic tube as sensor sheathing has been experimented with success. Further experimentations devoted to cracking analysis over several multiplexed sensing zones are now in progress and the corresponding results will be presented in the oral communication.

8. ACKNOWLEDGEMENTS

This work was supported by EDF/Direction de l'Equipement/SEPTEN, and achieved in cooperation with EDF/Direction de l'Equipement/TEGG.

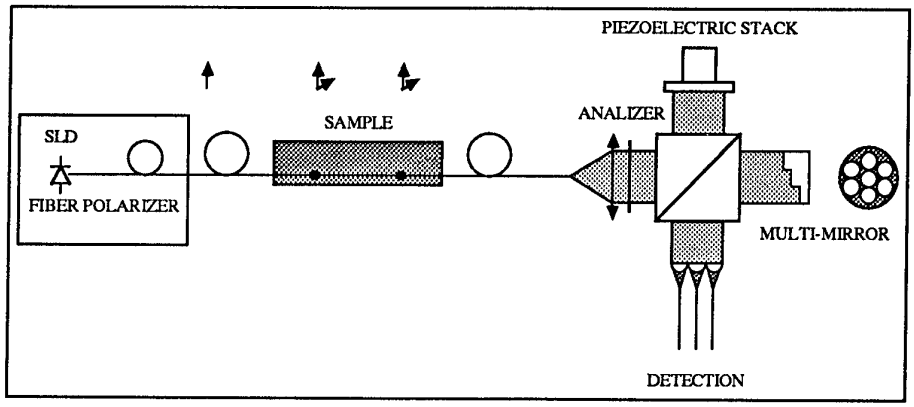

FIGURE 1 : Experimental setup

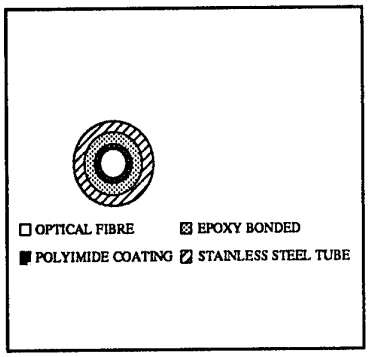

FIGURE 2 : Optical fiber sensor with tube

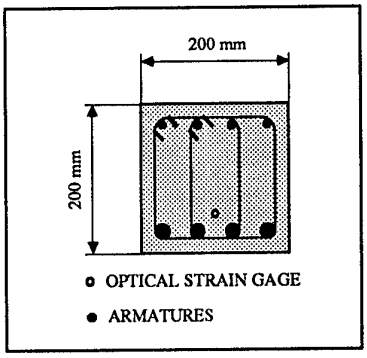

FIGURE 3 : Test structure for elongation

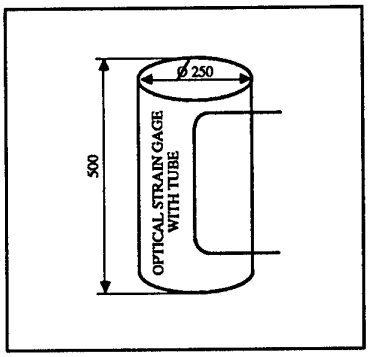

FIGURE 4 : Test structure for compression

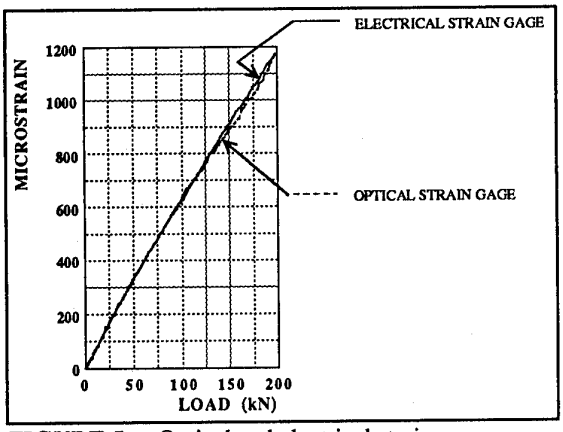

FIGURE 5 : Optical and electrical strain gages in extension

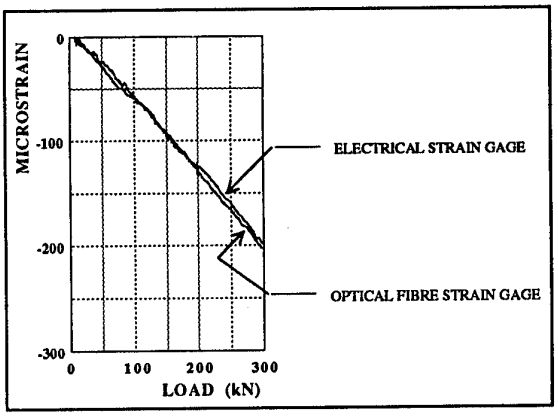

FIGURE 6 : Optical and electrical strain gages in compression

8. REFERENCES

1 M. TURPIN, D. ROJAS, C. PUECH, "Nouveau Concept de Capteurs Répartis Tout Fibre", MESUCORA Conference, PARIS, 1988.

2 V. GUSMEROLI, P. VAVASSORI, M. MARTINELLI, "A Coherence Multiplexed Quasi Distributed Polarimetric Sensor Suitable for Structural Monitoring", Springer Proceedings in Physics, 44, Optical Fiber Sensors OFS'6 Conference, PARIS, 1989.

3 P. SANSONETTI, J.J. GUERIN, M. LEQUIME, J. DEBRIE, "Mesure Polarimétrique Quasi-Répartie en Lumière Blanche au Long d'une Fibre Optique Biréfringente et Application à la Mesure de la Déformation de Matériaux Composites", Douzièmes Journées Nationales d'Optique Guidée, PARIS, 1992.

4 B. FORNARI, J.J. GUERIN, P. SANSONETTI, M. LEQUIME, G. ROMEO, "Strain Measurement of Carbon/Epoxy Composite Fibre Optics White Light Quasi Distributed Polarimetric Sensor", AGARD Conference Proceedings 531 Smart Structures for Aircraft and Spacecraft, LINDAU, 1992.

5. P. SANSONETTI, J.J. GUERIN, M. LEQUIME, J. DEBRIE, "Parallel Coherence Receiver for Quasi-Distributed Opical Sensor", SPIE Conference vol. 1588 Fiber Optic Smart Structures and Skins IV, BOSTON, 1991.

6 J.J. GUERIN, J.M. MAILLARD, P. SANSONETTI, "Polarization Mode Couplers Made by Photoinduced Grating for White-Light Quasi-Distributed Polarimetric Sensor", Optical Fiber Sensor OFS'8, MONTEREY,1992.

Demonstration of twisted polarimetric optical fiber sensor embedded in carbon-epoxy composite

Henrik D. Simonsen
Per Udsen Co. Aircraft Industry A/S
Fabrikvej 1, 8500 Grenaa, Denmark

ABSTRACT: The polarimetric fiber optic sensor is embedded in an 8 ply carbon/epoxy composite. The test specimens are exposed to different load conditions such as 3-point bending test. It is demonstrated that if the embedded optical fibers are twisted, the sensitivitity to stress transverse to the fiber will decrease.

1. INTRODUCTION

The fiber optic polarimetric sensor described in this paper is based on the fact, that light from a polarized laser is coupled into a polarization maintaining fiber so that the two orthogonal polarization modes are excited. If the fiber is subjected to changes in e.g. strain, pressure or temperature, the relative phase between the two modes will change along the fiber. By analyzing the polarization of the light coming out of the fiber, a sinusoidal signal will be seen where the phase is dependent on the measurand. This sensor can be embedded in a composite structure to monitor the strain. The sensor is an integrating sensor along its length so that the longer the sensing fiber is, the more sensitive it will be. It might be an disadvantage that it is sensitive to both longitudinal strain and strain transverse to the fiber. It is desirable to get a sensor signal, that unambigously measures the strain in only one direction, like the conventional resistance strain gauges.

2. EXPERIMENTAL BACKGROUND

The strain sensitivity for the polarimetric sensor can be found to be (Sirkis, 1991):

$$\Delta\phi = -\tfrac{1}{2}\beta_0 n_0^2 (P_{11}-P_{12}) \int_\Gamma \left[(1-\varepsilon_z^r)(\varepsilon_x-\varepsilon_y) - \varepsilon_z(\varepsilon_x^r-\varepsilon_y^r) \right] ds \qquad (1)$$

where $\Delta\phi$ is the phase difference of the light in the two eigenmodes when it is leaving the fiber, the x and y axes are oriented along the orthogonal eigenaxes in the fiber and z is oriented along the length of the fiber, β_0 and n_0 are the propagation constant and the effective refractive index of the fiber, P_{11} and P_{12} are the Pockel's strain optic constants; 0.113 and 0.252 respectively, (Bertholds *et al*, 1988), ε_j is the strain along the x,y or z axis, ε_j^r is the reference strain state and Γ is the fiber path. From the equation above it can be seen that the detected signal is dependent on the transverse strain. Moreover the sensor contribution from side stress is proportional to the strain difference between the two axes of polarization. This means that a uniform radial pressure along the fiber ($\varepsilon_x = \varepsilon_y$), will only affect the sensor with strain in the longitudinal direction. It is desirable to get a sensor that unambigously measures the strain in only one direction. For that reason, some of the fibers will be embedded so the condition $\varepsilon_x = \varepsilon_y$ is satisfied. This is done by twisting the fiber around its own axis. The pressure on the fiber will then be distributed evenly around the fiber, when it is averaged on a larger length.

The optical fibers to be investigated are HB-750 from Fibercore Limited and the light source is a HeNe-laser at 632.8 nm. Unfortunately the HB-750 fiber has a cut-off wavelength of 664 nm, which means that the fiber is two-mode, at the laser wavelength. However, the fiber works well as a single

0-8194-1700-9/94/$6.00

mode polarimetric sensor without spatial filtering. The fiber has a cladding and a coating outer diameter of 125 and 140 μm respectively. The coating is polyimide that can withstand curing temperatures up to about 390°C. Compared to conventional acrylate coated fibers, the coating is relatively thin and has a high E-modulus. In that way the polyimide fiber will be more sensitive to side stress.

The composite material is Fibredux 920-CTS-5-42%-125°C from Ciba-Geigy and is a prepreg consisting of carbon fibers in epoxy resin. The test specimen is made up of 8 layers of prepreg with the following orientation {90,0,0,90,90,0,F,0,90}, where F denotes the optical fiber. The optical fiber is parallel to the 0° layers. This means that the optical fiber is placed 50% from the neutral axis in the specimen. The fiber is thus protected by the composite layers, and by not placing them on the neutral axis it is also possible to expose the sensor to strain when the specimen is bent. The length and width of the test specimen is 200 and 40.0 mm respectively, and the thickness is measured to 1.27±0.02mm. Six polyimide fibers are each embedded in a test specimen, where three of them are twisted and the three others are not. The twisted fibers have a pitch length of 12.5 mm. The polarization axis orientation of the un-twisted fibers was not known during the embedding.

A conventional resistance strain gauge is used to measure strain in the longitudinal direction. It is placed in the middle of the specimen related to the specimen's longitudinal direction.

The test specimens are tested so that it is possible to obtain information about the sensitivity of the optical sensors partly in the longitudinal direction and partly from the lateral direction.

3. EXPERIMENTS

Fig. 1 shows the test set-up for the 3-point bending test. Two tests on each test specimen are performed; in the first test the specimen is bent 10000 μm, and and in the second one it is relieved by the corresponding 10000 μm.

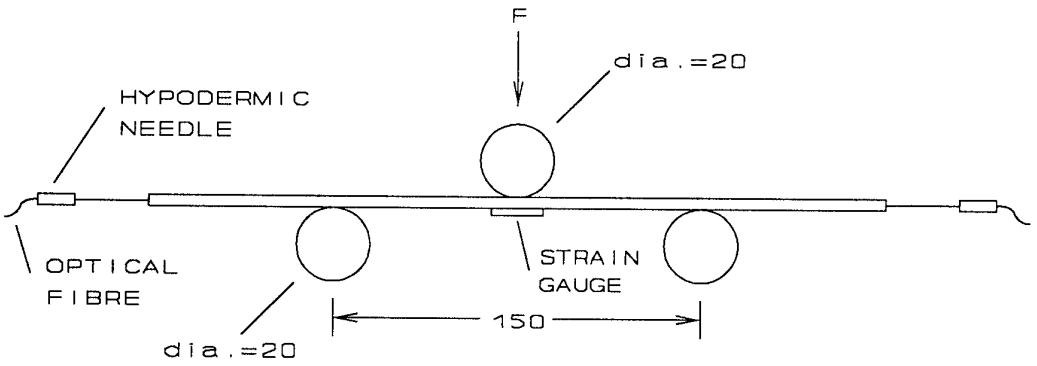

Fig. 1 Test set-up for 3-point bending test.

By assuming that the test is performed on a simply supported beam, the formulas for deflection of simple beams [TIM] can be used to give the following expression:

$$\varepsilon_z(z) = \frac{24 D z \Delta d}{L_1^3} \tag{2}$$

where D is the deflection of the central load cylinder, Δd is the distance from the neutral axis to the fiber, L_1 is the distance between the supporting cylinders, and z is the distance from one supporting cylinder in the direction of the central load cylinder. The integrated longitudinal strain seen by the fiber optic sensor can then be found to:

$$L_1 \bar{\varepsilon}_z = \frac{6D\Delta d}{L_1} \tag{3}$$

By using eq. 2, the strain measured by the strain gauge can be found to be :

$$\varepsilon_{sg}(L_1/2) = \frac{12D\Delta d_{sg}}{L_1^2} \tag{4}$$

where Δd_{sg} is the distance from the neutral axis to the strain gauge. During the test a phase shift occurs on the optical sensor, which is an expression of the amount of integrated strain. Meanwhile a strain change $\Delta\varepsilon_{sg}$ occurs on the resistance strain gauge. The optical sensor's strain sensitivity per unit length can be written as an expression where the measured strain gauge signal is included:

$$\frac{\Delta\phi}{\Delta(L_1\bar{\varepsilon})} = \frac{\Delta\phi}{\Delta(\varepsilon_{sg})}\frac{\Delta\varepsilon_{sg}}{\Delta(L_1\bar{\varepsilon})} = \frac{\Delta\phi}{\Delta(\varepsilon_{sg})}\frac{2\Delta d_{sg}}{L_1\Delta d} \tag{5}$$

The specimens are also tested as a cantilever beam in two test set-ups. In the first set-up, the sensor fiber is exposed to tension when the test specimen is bent and in the other set-up it is exposed to compression. As in eq. 5 an analytical expression for the fiber sensor can be found for the cantilever test (Simonsen, 1993). The specimen is also set-up in fixtures to expose it to flatwise and sidewise compression and to a tensile test in the lengthwise direction of the specimen. In the sidewise and flatwise compression tests and in the tensile tests the maximum force is 5 kN.

The sensitivity for the un-embedded fiber is found to be $1069 \cdot 10^{-6}$ rad/(cm·με). In table 1 and 2 the experimental results is shown. As seen on the table the un-twisted polyimide fibers have large variations in sensitivity as opposed to the twisted ones. This must be due to the fact that the un-twisted fibers are more sensitive to side stress, and the orientation of the fibers is unknown. The side stress that occur in the fiber is due to the loading conditions and to the stress induced in the fiber during the curing of the specimens. The sensitivity of the twisted fibers is measured to be close to the sensitivity of the un-embedded fiber.

	POLYIMIDE UN-TWISTED (HB-750) 10^{-6} [rad/(cm·με)]	POLYIMIDE TWISTED (HB-750) 10^{-6} [rad/(cm·με)]
3 POINT BENDING TEST	562±471	1073±26
CANTILEVER TENSION	563±452	1166±15
CANTILEVER COMPRESSION	607±404	1180±88
TENSILE TEST	496±505	1187±89

Table 1. Sensitivities for embedded sensors. The figures after '±' are the standard deviation.

The flatwise and sidewise compression tests show that the sensitivity from side stress is in the same order of magnitude as the longitudinal sensitivity. The stress sensitivities are shown in table 2. As expected, the un-twisted polyimide fibers are very sensitive to side stress and the standard deviation is large because of the unknown orientation of the polarization axes. The twisted fibers have a

sensitivity for side compression that is only 8% of the un-twisted ones. This means that the twisted polyimide fibers do not just give a more homogeneous strain sensitivity, but they are also far less sensitive to side compression.

	POLYIMIDE UN-TWISTED (HB-750) 10^{-9} [rad /(cm·Pa)]	POLYIMIDE TWISTED (HB-750) 10^{-9} [rad /(cm·Pa)]
FLATWISE COMPRESSION	277±252	222±96
SIDEWISE COMPRESSION	52.3±8.6	4.1±3.0
TENSILE TEST	9.1±9.6	21.7±2.2

Table 2. Sensitivity from stress in different directions. The figures after '±' are the standard deviation.

During the tests a small periodic noise signal mixed with the detected optical signal was detected. This noise is due to the Fresnel reflections at the fiber ends, so that each of the two polarization modes constitutes a Fabry-Perot interferometer. As an example the optical period related to the deflection (D) in the 3-point test is measured to 23.0±0.7 μm. If the period is related to the elongation of the optical fiber only, the period can be found to be $292 \cdot 10^{-9}$ μm (eq. 3) for the 3-point bending and $291 \cdot 10^{-9}$ μm for the cantilever beam. In (Sirkis, 1991) an expression for the strain sensitivity of the Fabry-Perot sensor is derived. If the influence from side stress is omitted the optical period can be calculated to be $296 \cdot 10^{-9}$ μm. In that way way it can be seen that optical fiber is close to 50% from the neutral axis.

4. CONCLUSION

It is demonstrated that it is possible to reduce the transverse strain sensitivity for polarimetric sensors embedded in composites. This is done by using twisted optical fibers. The results are compared with fibers that were not twisted. The orientation of the polarization eigenaxes was not known for the fiber that was not twisted. For that reason they had different sensitivities for strain in the longitudinal and transverse direction. Because of the Fresnel reflection at the fiber ends, a Fabry Perot interferometer was also constituted by the sensor. In that way it has been possible to see how far the optical fiber is from the neutral axis.

5. REFERENCES

Bertholds, A. & Dändliker, R., "Determination of the individual strain optic coefficients in single-mode optical fibers", Journal of Lightwave Technology, Vol 6, No 1, 1988, pp 17-20.

Simonsen, H.D., "Fiber optic sensors for smart composite structures", Ph.D. Thesis, Danish Academy of Technical Sciences/Per Udsen Co, 1993.

Sirkis, J.S., "Phase-strain-temperature model for structurally embedded interferometric optical fiber strain sensors with applications", Proceedings: Fiber Optic Smart Structures and Skins IV (Boston, MA), SPIE Vol 1588, 1991, pp 26-43.

Timoshenko,S.P. & J.M. Gere, J.M., "Mechanics of materials", Van Nostrand Reinhold Company, 1979.

Paper presented at the Second European Conf. on Smart Structures and Materials, Glasgow 1994, Session 6

AVERAGE STRAIN MEASUREMENT IN A STRUCTURE BY BEAT LENGTH DETERMINATION IN HOMOGENEOUS ZONES

S. Téral*, J.M. Caussignac, A. Tardy and M. Jurczyszyn*****

* Alcatel Cable, 30 Rue des Chasses, 92111 Clichy Cedex ,France,
** Public Works Research Laboratory (LCPC), 58 Bld Lefebvre, 75732 Paris Cedex 15, France,
*** Alcatel Alsthom Recherche, Route de Nozay, 91460 Marcoussis, France.

ABSTRACT: Different methods using optical fibers for real time inspection of concrete buildings and structures have already been investigated. According to recent progress it becomes more and more possible to obtain reliable punctual strain measurements with sophisticated techniques based on light polarization analysis. Based on knowledges about birefringence measurements in single-mode fibers which shows a fullness of information, this paper presents the difficulty of average strain measurement interpretation from beat length determination in homogeneous zones.

1. INTRODUCTION

The first concept of optical fibers applications was telecommunications but rapidly, in sequence with different demands, the progress enhanced knowledges and led to be thinking of doing every kind of measurements with these fibers in order to improve the current technologies, to replace or to complement them.
Depending on technical advantages over available techniques, accuracy, sensitivity and robustness, we can find the right optical fiber sensor for the right application, it has to be cost competitive.
There is a field where the theoretical limits in terms of material improvements have been reached: concrete buildings and structures. A complementary technology for periodic inspection or real time metrology is needed and optical fibers seem to be the most appropriate components.
The simplest way to use optical fibers as a sensor which appeared during the seventies, was intensity or amplitude changes detection proportional to a known perturbation [1]. Based on this principle several systems have been developed for smart structures like load measurements in bridges [2]. The most sophisticated way to sense various physical perturbations consists of light polarization analysis in single-mode optical fibers [3]. Before 1980 it was very difficult to use the phase or the polarization state in a fiber because of the lack of technology. The eighties showed a great revolution in this field [4] with a better understanding of this complex phenomenon and the apparition of devices like polarization maintaining fibers [5], polarizers/depolarizers, polarization controllers, rotators, isolaters ...
In this paper, we discuss in detail beat length measurements from single-mode fibers embedded in concrete for average strain determination. By applying Faraday effect, we characterize the fibers in terms of beat length before achieving specific sensing structures designed for civil structure applications and we review the state of the art with sophisticated apparatus currently available.

2. BEAT LENGTH MEASUREMENTS

In an ideal fiber with perfect rotational symmetry, both modes $HE11_x$ and $HE11_y$ are degenerated (kx = ky) and any polarization state injected into the fiber would propagate unchanged.
In practical single mode fibers, structural defects and imperfections break the circular symmetry of the ideal fiber and lift the degeneracy of the two modes. They propagate with different phase velocities and the difference between their refractive indexes is the BIREFRINGENCE: B = ny - nx.
When both modes are excited in a single mode fiber, there is a phase shift between them. When this phase difference is an integral number of 2π, the two modes will beat and at this point, the initial polarization input is reproduced. The length over which this beating occurs is called BEAT LENGTH: $Lb = \lambda/B$

The best solution to achieve such a beat length measurement is obtained by launching a linear polarized light at 45° to the fiber neutral axis and to observe the evolution of the output intensity also at 45°.
Birefringence can be expressed as: B = Bi + Be where Bi and Be are the birefringences produced by respectively intrinsic and extrinsic factors along a length z and the observed output intensity is: $I \# I_0\cos^2(2\pi z/\lambda o(Bi + Be))$.

0-8194-1700-9/94/$6.00

Generally for Bi or Lb measurements this principle requires an external perturbation (distributed or localized) modifying the intrinsic birefringence in a known way (Be is known).
The method currently used at Alcatel Alsthom Recherche is based on Faraday effect. In the presence of a transverse magnetic field H, a linear polarized light propagating along the z axis will rotate of an angle ξ proportional to the Verdet constant ($V = 1.8\ 10^{-6}/\lambda^2$ for silica). The birefringence induced is: $Be = \xi(\lambda,T).\lambda/\pi$.
Before any applications, all fibers and sensing structures are characterized with this method.

3. SENSING STRUCTURE AND INSTALLATION

The sensitivity to environmental perturbations of the polarization in a single-mode fiber is given by specific structure parameters. After embedding a single-mode fiber into a concrete structure we can define a intrinsic birefringence Bis = Bi + Bs for this system where Bs is the birefringence brought by the structure itself depending on the strain distribution. When different evolutions occur inside this structure (ageing) the global birefringence is B = Bis + Be where Be is the unknown parameter to be determined, localized and correlated with a load. The main parameters to take into account in order to assess Bis are:

1) Bi which depends on the core/cladding radius of the fiber, the core ellipticity of the fiber, the thermal expansion coefficients of the core/cladding and the relative photoelastic constant $C = n^3(P_{11} - P_{12})(1 + \nu)/2E$ where n is the refractive index of the silica, P_{11} and P_{12} are the photoelastic coefficients of the silica, ν is the Poisson's ratio and E the Young's modulus of the fiber [5] [6] [7].

2) The homogeneity of Bi for a given fiber length, the Fig.1 shows non-homogeneous birefringences measured on a standard single-mode fiber (SSMF) measured by the method described above.

3) Bs induced by the strain distribution inside the material which constitutes the structure including the way the fiber is installed (orientation, twist, bending).

4) The influence of the coating effects.

Depending on the magnitude of the pressure to be measured but also on installation, the type of the single-mode fiber can be chosen; two possibilities appear : fiber alone or sensing structure.
If the fiber is directly embedded into a girder, a Hi Bi fiber (Fig. 2-a) might be the best choice because of its distribution of stress in the cross-sectional area which makes it unsensitive to weak external perturbations.
The drastic limitation is axis orientation during installation, twist and bending have to be eliminated.
In our experimentations, low birefringence fibers (LBF) and SSMF have been embedded between two metallic ribbons under strain which give a uniform structure birefringence (Fig. 2-b). Our studies show an interesting result: SSMF with non uniform birefringence but approximate beat length of 1 m embedded into a structure which generates a birefringence ten times higher allows a constant and uniform neutral axis orientation. This facilitates installation in concrete or civil structures.

4. STRAIN MEASUREMENTS IN A CIVIL STRUCTURE

Beat length measurement can be done by reflection (reflected light) or transmission. By arranging a reflective extremity, reflected light analysis represents a very attractive method because it gives a phase information increased by a factor two due to the go and return (2ϕ) and the rotator normally used at the output can be suppressed.
For strain measurements in a structure by beat length determination in homogeneous zones, the observation of polarized Rayleigh lateral scattering light from a Hi Bi fiber [8] which has good polarization properties seems to be the most appropriate method but requires a high excitation power due to the low level of the scattered signal [9].
The principle is based on the fact that the backward Rayleigh scattered light (Fig.3) in a single mode fiber contains additional information about variation of the polarization state along the fiber. The beat length corresponds to the period of the interference fringes generated along the fiber axis.
Nevertheless, another limitation appears: in comparison with the Faraday's method the evolution of the measurand that induces Be and converts it into an amplitude variation is not distributed and is difficult to detect without any time reference. The sophistication of this principle leads to a polarimetric extension of conventional Optical Time Domain Reflectometry (OTDR) which is called POTDR (P for polarization).

That is very attractive and more powerful but possesses two drawbacks: it needs very fast signal provessing and the contrast fluctuates according to the magnitude of the measurand (the highest the magnitude, the weakest the contrast is). In fact, the relative fluctuation power occupied in total scattered power increases with the decrease of the pulsewidth and the increase of the birefringence. To illustrate this phenomenon, Fig. 4 shows an analysis by POTDR of 24 m single-mode fiber trunk before and after modified birefringence.
Nowadays POTDRs commercially available have a limited spatial resolution of 1 m corresponding to 10 ns in time. According to different trial measurements [10] already done in our laboratories, a strain variation of 0.1 MPa gives approximately an equivalent beat length of 3 m. For higher strain variations, more than 0.5 MPa, information is missing.
Therefore, even if we use a sensing structure with an intrinsic beat length of 100 m, depending on the analyzed zone length, the resulting dynamic range would not be very high. Similar considerations have been done in [11]. The birefringence of a Hi Bi fiber with a beat length of 1 mm has been analyzed by backscattered method and the frequency obtained was quite high: 100 GHz.

CONCLUSION

The birefringence B is a resultant of intrinsic and extrinsic factors, that means before embedding optical fibers for external perturbation measurements it is primordial to know exactly its intrinsic birefringence plus its homogeneity. Except for special single-mode fibers like LBF or Hi Bi, birefringence parameter or beat lenght does not belong to a current specific procedure of characterization.
These typical fiber parameters taken into account in addition with the order of measurand magnitude, average strain measurement in a structure by beat determination with generated variations not greater than 1 m is achievable. A compromise has emerged in terms of right sensing structure for ad-hoc corresponding measurements.
POTDR seems to be the most promising method but requires some signal processing improvements for full measurand analysis and particularly ; for more accurate average strain measurement in a structure.

REFERENCES

[1] G.B. Hocker, "Fiber optic sensing of pressure and temperature", App. Opt., Vol. 18, pp. 1445-1448, 1979.

[2] J.M. Caussignac, A. Chabert, G. Morel at al, "Bearings of a bridge fitted with load measuring devices based on an optical fiber technology", Proc. 1st, European Conference on Smart Structure and Materials, Glasgow, 1992, pp. 207-210.

[3] S.C. Rashleigh, "Origins and control of polarization effects in single-mode fibers", J. Lightwave Technol., Vol. LT1, n° 2,pp. 312-331, 1983.

[4] J. Noda, K. Okamoto and Y Sasaki, "Polarization-Maintaining Fibers and their applications", J. of Lightwave Technol., Vol. LT-4, n° 8, August 1986, pp. 1071-1089.

[5] J.I. Sakai and T. Kimura, "Birefringence caused by thermal stress in elliptically deformed core optical fibers", IEEE J. of Quantum Electronics, Vol. QE-18, N° 11, Nov. 1982, pp. 1899-1909.

[6] S.P. Timoshenko, J.N. Goodier, "Theory of elasticity", New York: McGraw-Hill, 3rd ed. 1970.

[7] P.L. Chu, R.A. Sammut, "Analytical method for calculation of stresses and material birefringence in polarization-maintaining optical fibers", J. of Lightwave technology, Vol. LT-2, N° 5, Oct. 1984, pp. 650-662.

[8] M. Nakazawa, "Theory of backward Raleigh scattering in polarization maintaining single-mode fibers and its application to polarization optical time domain reflectometry", IEEE J. of Quantum Electronics, Vol. QE-19, N° 5, May 1983, pp. 854-861.

[9] R. Calvani, R. Caponi and F. Cisternino, "Polarization measurements on single-mode fibers", J. of Lightwave Technol., Vol. 7, N° 8, August 1989, pp. 1187-1196.

[10] A. Tardy, M. Jurczyszyn, J.M. Caussignac, J.M. Morel & G. Briant, "High sensitivity transducer for fiber-optic pressure sensing to dynamic mechanical testing and vehicle detection on roads", Springer Proceedings in Physics, Vol. 44, 1989, pp.215-221.

[11] A.J. Rogers, "Distributed optical fibre sensing", SPIE Vol. 1511, Fiber Optic Sensors: Engineering and Applications (1991), pp. 2-24.

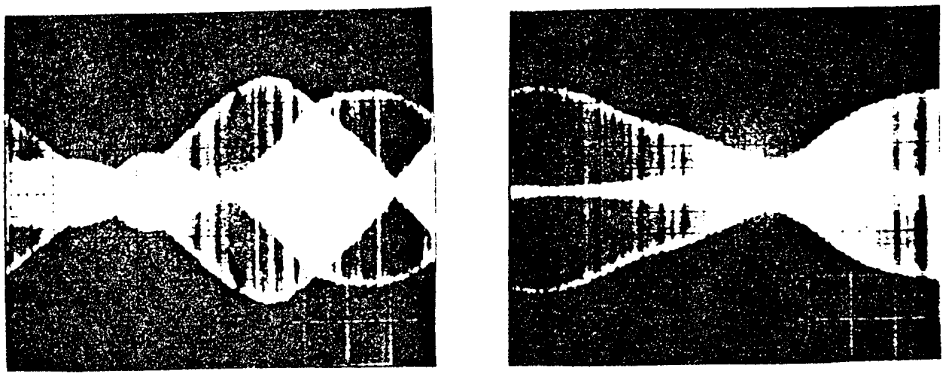

Fig.1: Beat between the HE11x and HE11y in a single-mode fiber observed on a oscilloscope screen for 2 m fiber sample at both extremities of the same coil

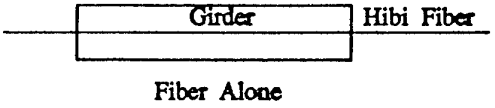

Fiber Alone

Fig. 2-a: fiber alone directly embedded in concrete

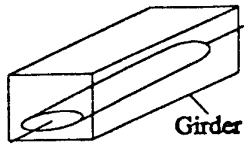

Embedded Fiber

Fig. 2-b: sensing structure.

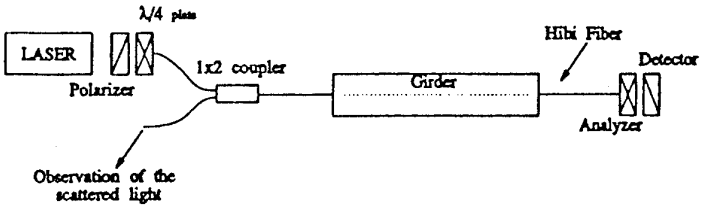

Fig.3: Strain measurement configuration with backward Rayleigh scattering method.

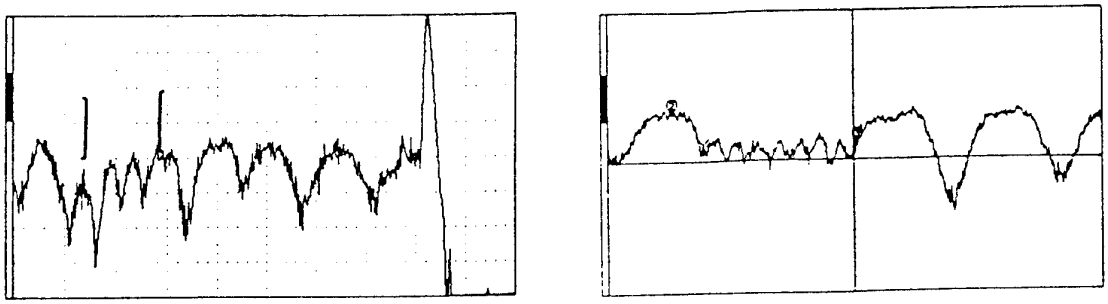

(a) (b)

Fig 4: Analysis by POTDR of 24 m single-mode fiber trunk with (a) initial beat length of 16 m and (b) after perturbation a beat length of 6.8 m.

MICROWAVE SUBCARRIER OPTICAL FIBER STRAIN SENSOR.

B.Noharet*, M.Turpin*, J. Chazelas ', P.Bonniau ', D.Walsh, W.C.Michie, B.Culshaw

* Thomson-CSF LCR, Domaine de Corbeville, 91404 Orsay Cedex, France
' Thomson-CSF RCM, La clef de St Pierre, 1 Bd Jean Moulin, 78852 Elancourt Cedex, France
Dept. E.&E.E., University of Strathclyde, 204 George St., Glasgow G1 1XW, Scotland

1- Introduction:

At present, there is an acute need for techniques in monitoring civil engineering structures, and optical fiber sensors are acknowledged to be amongst the best candidates. For more than ten years, interferometric optical fiber sensors have been widely investigated and now provide a rich extended basis for measuring strains experienced by structural elements. However, because of their periodic response, those sensors need extending measuring techniques to fulfill civil engineering requirements. Amongst different methods, Thomson-CSF and the University of Strathclyde have recently employed a microwave subcarrier system [1]. A specific sensor dedicated to the arena of large civil engineering structures has been designed and tested.

2- Principle:

As an optical fiber is elongated, the phase of a propagating lightwave is shifted. This phenomenon is related to three effects:
- the physical change of the fiber length.
- the photoelastic refractive index variations due to axial and transverse strains.
- the waveguide mode dispersion.

It has been theoretically and experimentally shown that the so-called "dispersion effect" can be neglected if we use classical single-mode fibers [2-3].
The phase shift can therefore be written as:

$$\Delta\phi = 2\pi/\lambda\ n\ [1 - n^2/2\ p_{12} + n^2/2\ (p_{11} + p_{12})\ v]\ \Delta L$$

where p_{11} and p_{12} are the Pockels constants
n is the unstrained refractive index
v is the Poisson ratio of SiO_2 fiber
ΔL is the elongation.

Taking $\lambda = 1.3\ \mu m$, the strain sensitivity of an optical fiber is: $1/L\ \Delta\phi/\Delta\varepsilon = 5.5\ rad/\mu\varepsilon.m$
Notice that the strain sensitivity is directly proportional to the optical frequency, as long as the lightwave is used as the sensing signal.
Now, consider the case of sinusoidal modulation of the intensity of the lightwave transmitted in the fiber, at a frequency around 1 GHz . As the fiber is strained, the generated 1GHz subcarrier is also delayed (see figure 1) and its phase shift is related to the "optical" one by: $\Delta\phi_{RF} = \lambda_{RF}/\lambda_{OPT}\ \Delta\phi_{OPT}$

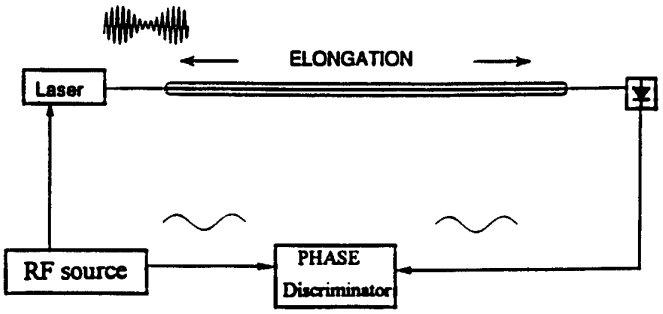

Fig.1: Schematic description of the microwave phase shift measurement.

* Present address: Bertin & Cie, 230 rue F.Joliot, BP 22000, 13791 Aix-en-Provence Cedex 03, France

0-8194-1700-9/94/$6.00

A microwave phase discriminator provides the phase information between the RF source and the detected light intensity from the fiber output.
Consider a 1GHz modulation frequency. The resulting strain sensitivity is consequently :

$$1/L\ \Delta\phi/\Delta\varepsilon = 23.9\ \mu rad/\mu\varepsilon.m$$

Thanks to the proportional relationship between frequency and phase shift, we can obtain the appropriate extended measuring range needed for monitoring large civil engineering structures (several tens or hundreds meter long) by choosing the modulation frequency.

3- Sensor design:

Surface-mounted or embedded fiber optic sensors require specific protection to become robust and reliable products dedicated to civil engineering applications.
Therefore, a pultruded E-glass and epoxy overcoating was added to the optical fiber. Figure 2 provides a physical description of the sensor:

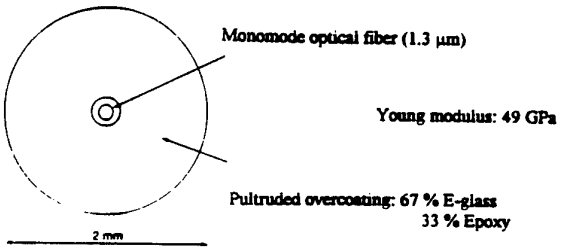

Fig.2 : Physical features of the pultruded rod.

In paragraph 2, we have neglected the influence of the fiber coating and considered only the average axial strain over the active length of the fiber. However, the influence of the pultruded structure on the fiber in terms of strain sensitivity can be evaluated. The expression of the strain-induced phase-change becomes:

$$\Delta\phi = 2\pi/\lambda\ n\ [1 - n^2/2\ p_{12} + n^2/2\ (p_{11} + p_{12})\ (-\varepsilon_R/\varepsilon_Z)]\ \Delta L$$

where ε_R is the radial strain in the fiber
ε_Z is the axial strain in the fiber.

By using the generalised mathematical plane strain model (no shear stresses at the interfaces) and the Lamé solutions for axisymmetric load on a multilayer structure [4-5], we found that the difference between $(-\varepsilon_R/\varepsilon_Z)$ and the Poisson ratio ν (silica) is less than 0.1%.
The phase-strain relation is therefore not significantly affected. The direct calculation of ε_Z is consequently possible from the measurement of $\Delta\phi$.

4 - Experimental results:

4.1- Strain sensitivity:

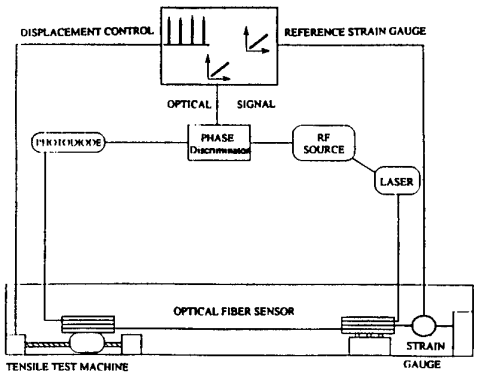

Fig. 3: The experimental system.

The experimental system is depicted on figure 3. A laboratory tensile test machine allowed us to obtain continuous strains integrated over 6m of pultruded rod. Strain gauge and displacement sensor were implemented to provide references.
Figure 4 shows a comparison of the output signals coming from the strain gauge, the displacement sensor and the optical fiber sensor. Non linearity of the electrical strain gauge signal for high loads, which corresponds to its limited range, can be observed on the recording.

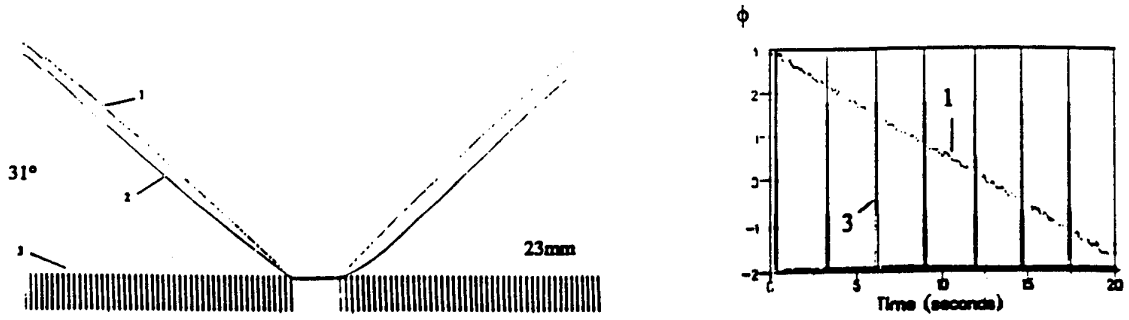

Fig.4 : Experimental comparison of the optical sensor response with reference sensors.
1: optical sensor response.
2: strain gauge response
3: displacement control (each step is equivalent to a 0.5 mm elongation)

In our implementation, the modulation frequency of the laser source driving current was 1 GHz. The strain sensitivity was experimentally determinated to be 23.5 +/- 0.4 μrad/με.m. This value has to be compared to the theoretical one calculated in paragraph 2. The good agreement between those values indicates clearly the full transfer of strain across the various interfaces of the sensor.

4.2 - Structure monitoring:

The control of a steel ground anchor was conducted with Strathclyde University at Dywidag test site in Germany [6]. The spatial location of the integrated strain was provided by the adhesive used to bond the pultruded rod to the steel tendon (1.7m long, 32mm diameter). The active length of the pultruded sensor was 87.5 cm. Strain references were provided by the extensometer from the tensile tester, and also by attaching strain gauges on the tendon surface and on the sensor surface. During the test, the load was increased up to 750 kN (equivalent to a 0.45% elongation), which was close to the test load of the ground anchor. Figure 5 displays the various output signals. The strain transfer losses were experimentally found to be around 5% and attributed to the low Young modulus of the adhesive.

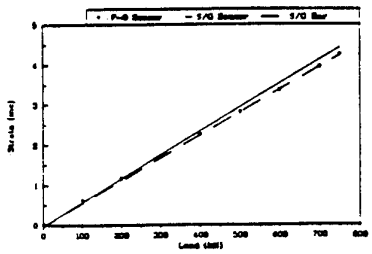

Fig.5 : Comparison of the strain experienced by the pultruded rod sensor and the reference strain gauges.

5 - Discussion:

Phase measurements are scalar by nature: thus, the optical sensor has to be conditioned to be sensitive to εz and insensitive to any other parameter. If we consider the influence of temperature in terms of phase shift, an elongation of 10με is equivalent to a temperature increase of 1°C. Therefore, a compensating system which used a second optical fiber for common mode rejection has been tested and is presented on figure 6.

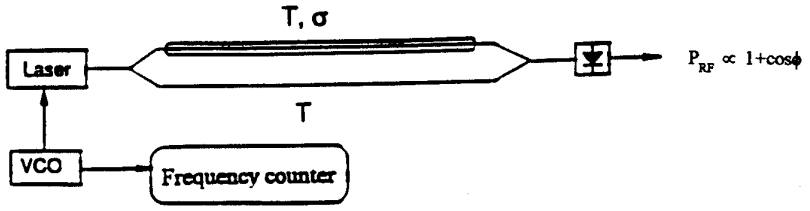

Fig.6: Temperature compensating system.

An optical fiber coupler separates the intensity modulated optical beam: half of the intensity is coupled into the strain sensing fiber while the other part is propagating across a reference fiber. The reference fiber length is also used as a delay line in order to combine incoherent optical beams in a second optical fiber coupler and create interferences between the microwave subcarrier signals. After quadratic detection, the interferometric microwave signal is filtered and recorded. The strain measurement technique is sequentially described by the following steps:

1 - recording of the microwave interferometric signal power level as a reference.
2 - elongation of the optical fiber sensor.
3 - comparison of the microwave interferometric signal power level with the reference.
4 - increase of the modulation frequency delivered by the voltage controlled microwave oscillator until the microwave interferometric signal power level comes back to its reference level.
5 - measurement of the frequency variation and calculation of the axial strain given by:

$$\varepsilon z = 1 / [1 - n^2/2\, p_{12} + n^2/2\, (p_{11} + p_{12})\, v]\ \ \Delta L/L\ \ \Delta f / f{+}\Delta f$$

where ΔL is the length difference between the two fibers
Δf is the frequency excursion
L is the sensing fiber length.

Compared to the previous phase measurement technique, the frequency measurement method provides a better resolution. Experimentally, we used minima of the interferometric $1+\cos\phi$ power function as reference level (see figure 7). Well-balanced microwave signals provide a high contrast ratio of the interferometric power signal: we obtained 40dB. Resolution was then limited by the uncertainty in the localisation of such a minimum and estimated to be $\Delta f/f \approx 0.0001$. However, a submicron resolution is obtained over a 1cm range. An electronic control loop can be implemented on the detection system in order to track the minimum and complete a fully automatic measurement of the axial strain [7].

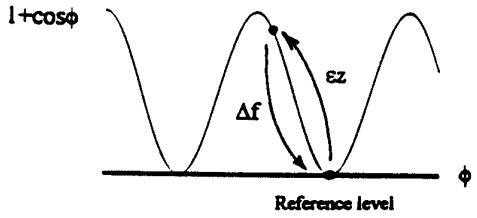

Fig.7 : Frequency shift technique.

6 - Conclusion:

The design of a rugged and reliable fiber optic sensor has been presented. A RF modulation system has led to experimental detection of strain-induced phase without any problem of nonuniqueness. An alternative detection system has also been tested to overcome temperature effects and improve resolution, and further implementations are under investigation to take fully advantage of the microwave subcarrier technique.

This work was financially supported by the OSMOS project, a Basic Research in Industrial Technology for Europe (BRITE) program.

References:

[1] B. Noharet, M. Turpin, J. Chazelas, P. Bonniau, J.P. Le Pesant, "Capteur d'élongation en optique hyperfréquence", *OPTO* Paris, April 1994
[2] C.B. Butter and G.B. Hocker, "Fiber optics strain gauge", *Applied Optics*, No.17, pp 2867-2869, September 1978
[3] J. Sirkis and H.W. Haslach, "Complete phase-strain model for structurally embedded interferometric optical fiber sensors", *SPIE* Vol. 1370, 1990.
[4] S.P. Timoshenko, "Theory of elasticity", Mc Graw-Hill, New-York, 1970
[5] H.W. Haslach and K.G. Whipple, "Mechanical design of embedded optical fiber interferometric sensor for monitoring simple combined loads", *Opt. Eng.*, Vol. 32, No. 3, pp 494-503, March 1993.
[6] D.Walsh and al. , "Radiofrequency subcarrier encoded fiber optic strain gauge for ground anchor", *ICAPT* Toronto, June 1994
[7] C.A. Wade, J.P. Dakin, J. Croft, J. Wright, "Optical fibre displacement sensor based on electrical subcarrier interferometry using a Mach-Zehnder configuration", *SPIE* Vol. 586, 1985.

SESSION 7

Overview of Smart Structure Concepts for Helicopter Rotor Control

J.P. Narkiewicz, G.T.S. Done
City University, London, UK

1. Introduction.

The crucial components on which helicopter performance and handling qualities depend are the main and tail rotors, which are also strong contributors to the noise and vibration levels. Improvement of these elements leads to an enhancement of the overall rotorcraft quality.

In this paper the aspect of smart structures applications chosen for consideration is that of control design concepts, leaving aside the areas of materials, sensors/actuators design, control algorithms, etc.

Various design concepts of helicopter rotor control currently under consideration are reviewed, thereby indicating that rotorcraft technology is an area in which research into the application of smart structures may lead to significant improvements.

2. Rotor control systems.

The flow condition over the rotor disc in forward flight is unsymmetrical. In order to achieve trimmed steady and manoeuvring flight the rotor blade has to adapt to the flow environment to achieve the required forces and moments at the rotor head. The established way of doing this is by changing the pitch angles of the blades relative to the plane of rotation.

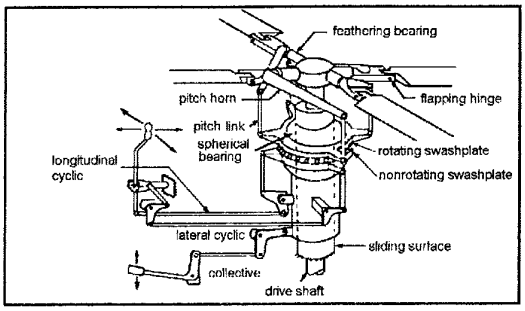

Fig.1. Swash-plate rotor control [1].

These angles are varied cyclically i.e once per rotor revolution in a controlled way. The most common form of rotor control system has remained basically unaltered for many years and relies on a swash - plate connected to the blade through pitch links. This facilitates the changing of the rotor blade angles of incidence in a collective or/and a first harmonic (cyclic) manner (Fig.1).

This kind of control, which enables the trim and required flight state (including manoeuvres to be achieved) is called "primary control". Flight safety depends absolutely on the reliability of this control.

The propulsive force required for steady translational flight and moments about the rotorcraft centre of mass required for manoeuvring flight are achieved by an overall rotor disc tilt, which stem from cyclic pitch changes. As a result, the rotor hub i.e. the area of the blade attachment to the rotor shaft, may utilise a series of hinges in a classical design or, in more modern designs, the hinges may be replaced by flexible structural elements.

3. Active rotor control.

Movements of the blades within a rotating frame of reference give rise also to undesired variable dynamic and aerodynamic loads. Additionally, there are other sources of disturbance such as gusts, turbulence and aerodynamic interference with other parts of the rotorcraft. All of these contribute to forced excitation of the rotor, which can under certain conditions, even become unstable.

As well as the need to ensure freedom of the rotor from instabilities there are also requirements for rotor behaviour enhancement, which continuously stimulate technology development. These are, for example, the improvement of performance by the elimination of flow stall regions, the alleviation of response to gusts and turbulence, the suppression of rotor and fuselage vibration and the reduction of noise. In pursuing the achievement of these goals, additional rotor control, usually active, has been introduced and is under development.

Research into the improvement of rotor quality by active control has led to the concepts of Higher Harmonic Control (HHC) and Individual Blade Control (IBC). Both are based on utilizing the existing swash-plate primary control systems but with additional control activity which imposes higher harmonics on the blade pitch angle.

Although the main objective of improving rotor behaviour may be achieved in this way, these

0-8194-1700-9/94/$6.00

systems can cause increasing power consumption, control system weight, blade vibratory loads and possible extra blade instabilities.

A new approach which provides prospects for avoiding some of the disadvantages of HHC and IBC systems is represented by smart structure technology.

4. Smart structures for rotor improvement.

A long term goal of the application of smart structures to rotorcraft is the designing of an integrated system which would perform simultaneously primary and additional rotor control, eliminating the existing swash-plate mechanism. This system would influence both aerodynamic and dynamic loads basically in two ways either by adapting the blade shape to the ambient flight conditions, or by operating some additional device mounted on the blades [2-5]. As further possibility would be to control just the dynamic properties of the rotor, such as the stiffness and damping of blades as function of time.

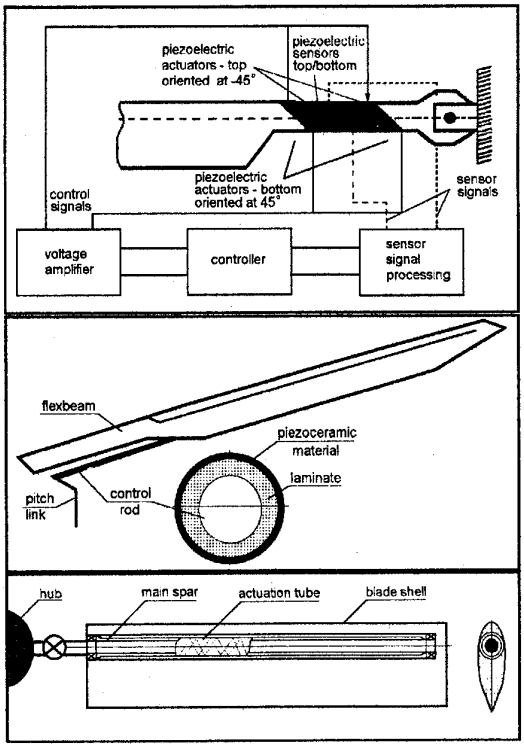

Fig.2. Controlling blade twist: blade root [3], control rod [3], actuator tube [4].

Recently several different concepts of smart blades have been investigated, from which some predictions can be made concerning future prospects of applications. The evaluation of these concepts is based on the current level of technology, and mainly depends of the properties of existing smart materials.

In the following these design concepts are briefly described, specific details being found in the references. They are classified as: shape adaptive blades, controlling dynamic properties and additional control surfaces.

5. Shape adaptive blades.

Under the heading of shape adaptive blades can be considered the variation of blade twist, the deflection in and out of the plane of rotation and the change of shape of the blade cross-section.

5.1. Controllable twist.

The blade may be either twisted at the root or throughout its length. Variation of the blade twist allows control of the local angle of incidence. It is a straightforward way of obtaining the desired aerodynamic loads as the aerodynamic environment is influenced directly by aerofoil angle of incidence. Root torsional actuators cause the blade angle of incidence to change by the same increment along the blade. Feasibility studies of blade root torsional actuators (Fig.2) have been performed using piezoelectrics [3], and shape memory alloy (SMA)

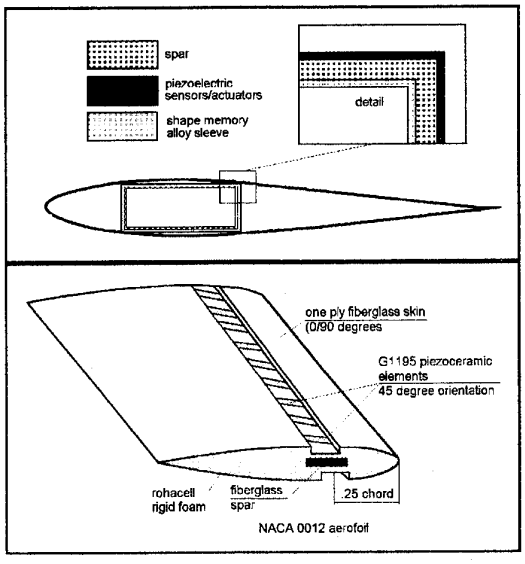

Fig.3. Distributed blade twist: adaptive spar [4], embedded elements [7].

materials [6] for twisting the blade root directly, or by a control rod [3]. Another method of introducing control via twist which allows a greater magnitude

of twist angle to be obtained is by using a torsionally actuated tube situated inside the blade main spar, or by a controlled active pitch link between the blade and the swash-plate (not ilustrated).

Distributed blade twist (Fig.3) can be achieved using an adaptive blade spar [4], which has smart material distributed along the span and embedded into the spar structure, or by placing piezoelectric actuators in the blade skin [7].

5.2. Bending deflection.

The two basic modes of deflection of a rotor blade are bending perpendicular to and in the plane of rotation. The method of directly controlling the instantaneous position of a rotor blade within and normal to the plane of rotation (Fig.4) is by amplifying and/or suppressing the blade bending modes. In [3] lag-wise excitation was suggested at the blade root and/or along the span using

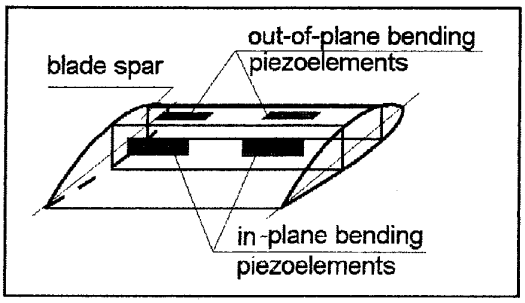

Fig.4. Blade bending.

piezoelectric actuators. In [8] a rotor Froude scaled rotor model having piezoelectric elements distributed along the blade was controlled by a closed-loop feedback system, leading to a reduction of flapwise vibration.

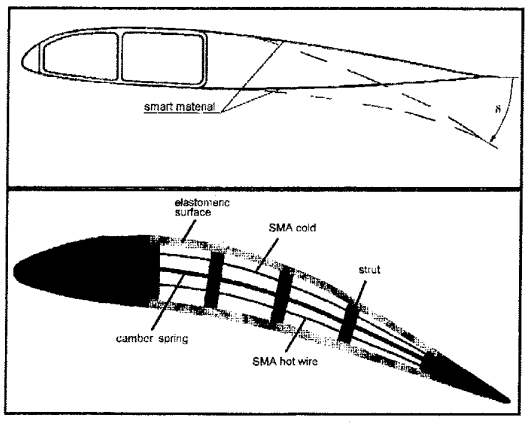

Fig.5. Controlling aerofoil camber: trailing edge [4], mean line [8].

5.3. Aerofoils of variable geometry.

A method of achieving changes in aerodynamic loads is by varying the aerofoil shape. In this case the main factor influencing the magnitude of aerodynamic forces is aerofoil camber.

The camber of rotor blade sections can be effectively changed (Fig.5) by deflecting the trailing edge using piezoelectrics [4], or by using SMA materials [8]. An analytical study of the influence of changing aerofoil shape was reported in [8], but practical application to full scale rotors is not yet feasible.

Summing up the shape adaptive blade concepts it would appear that application directly to full scale rotors is not currently possible, because existing piezoelectric materials are unable to achieve sufficient actuating power and reliability.

6. Blades with controlled dynamic properties.

The changing of blade damping and stiffness in a controlled way can lead to the tuning of beam dynamic characteristics to required values. This can be achieved by embedding smart materials into the blade. This approach is similar to that of adaptive shape, but with different control algorithms; it can also be realized by the application of different types of smart materials, for instance piezoelectric gels.

Research outside of helicopter applications [9] into similar concepts applied to beam-like structures continue to show promise of in the area of actively controlled damping or stiffnes The concept of a additional device influencing only dynamic loads has been explored in [10]. This is a controlled bender embedded inside the blade, which suppresses vibration of the blade by acting as a actively controlled anti-resonance device.

7. Additional control surfaces.

The control of local aerodynamic loads on rotor blades can also be achieved by using additional leading or trailing edge flaps or control surfaces.. The idea of using a control surface on a rotor blade however it may be actuated, is relatively unusual; however the use of blade trailing edge flaps for primary control has been successfully implemented by Kaman in their products, most recently on the K-Max helicopter.

Generally the trailing edge flap design concepts using smart materials concern different driving mechanisms, as the key factor (Fig.6). In [11] a piezoelectric bender was used for controlling a tab mounted on a non-rotating, non-scaled rotor blade.

Tabs driven by piezoelectric benders were tested experimentally in [12] on a rotor model. In [4] a piezoelectric stack operating in resonance with a gear type mechanism to drive a servo flap was considered. In [13] blade mounted mounted magnetostrictive actuators were suggested to drive several trailing edge tabs. Other concepts of tab operation include a torque tube and a special multi-element driving system.

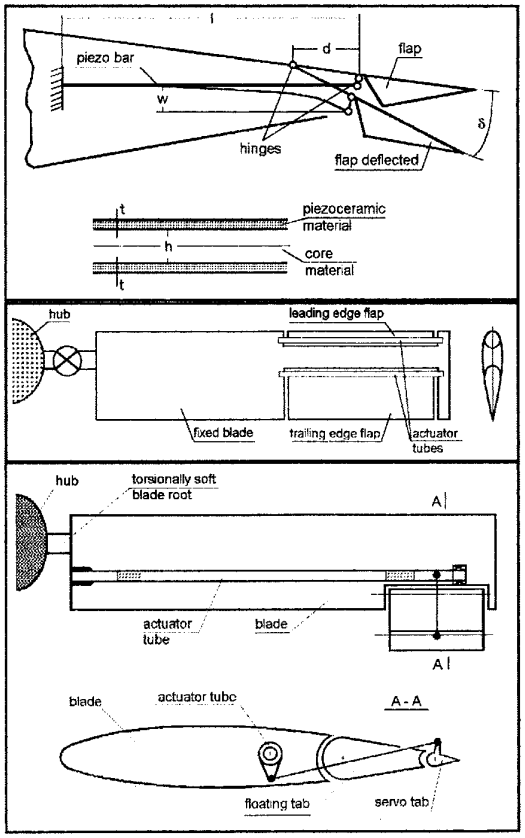

Fig.6.Driving mechanisms for blade flaps: elastic bender [4], torque tube [5], two-element flap [5].

Several analytical studies have been carried out to obtain insight into different aspects of the application of a trailing edge tab. Studies of the use of tabs for primary control were carried out in [14], for vibration suppression in [15], for blade vortex interaction reduction in [16] and for rotor performance optimisation in [17].

It would appear that there is ample scope for future study of the application of the trailing edge tab as a primary control device, and indeed this additional control concept may be the first to emerge in future rotorcraft designs.

Conclusions.

The use of smart structures in rotorcraft technology has attracted considerable attention. Studies and investigations are likely to continue until the most successful and practical solutions emerge, which will embody not only the configuration and mechanisms but also the necessary control algorithms. What can be observed now is the lack of an immediately feasible concept for replacing the primary control. However the application of smart structure technology concept as means of additional control appears more promising.

References.

1. Prouty R.W., "Rotor & Wing Helicopter Aerodynamics", PJS Publications, 1986.
2. Ormiston R.A., "Can Smart Materials Make Helicopter Better?", Fourth Workshop on Dynamics and Aeroelastic Stability Modeling of Rotorcraft Systems, The University of Maryland, November 19-22, 1991.
3. Strelhow H., Rapp H., "Smart Materials for Helicopter Rotor Active Control", AGARD/SMP Specialist's Meeting on Smart Structures for Aircraft and Spacecraft, 1992, Lindau, Germany.
4. Straub F.K.,"A Feasibility Study of Using Smart Materials for Rotor Control", 49th AHS Forum, St.Louis, Mo, May 1993.
5. Chopra I.,"Development of Smart Rotor", Pap. No. N6, XIX European Rotorcraft Forum, Como, Italy, September 1993.
6. Schmidt W., Boller Chr., "Smart Structures - A Technology for Next Generation Aircraft", AGARD/SMP 75th Meeting Of The Structures And Materials Panel, 1992, Lindau, Germany.
7. Barret R., Chopra I., "Inteligent Rotor Blade Actuation through Directionally Attached Piezoelectric Crystals", 46th AHS Forum, Washington D.C., May 1990
8. Hanagud S., Roglin R.L., Nagesh Babu G.L., "Smart Airfoils for Helicopter Control", Pap. No. 119 (H04), XVIII European Rotorcraft Forum, Avignon, France, September 15-18, 1992.
9. Bailey T., Hubbard J.E Jr.,"Distributed Piezoelectric - Polymer Active Vibration Control Of Cantilever Beam", Journal of Guidance and Control, Vol.8, No.5, Sept-Oct 1985
10. Narkiewicz J.P., Done G.T.S., "Smart Internal Blade Vibration Suppressor -A Feasibility Study", paper submitted to XX European Rotorcraft Forum, Amsterdam, October 1994.
11. Spangler R.L. Jr, Hall S.R., "Piezoelectric Actuators for Helicopter Rotor Control", AIAA Pap. 90-1076-CP, 31st AIAA Struct., Struct. Dyn. and Mat.l Conf., 1990.
12. Chen W.P., Samak D.K., Chopra I." Development of Scaled Rotor Using Smart Structures Technology", Fourth Workshop on Dynamics and Aeroelastic Stability Modeling of Rotorcraft Systems, The University of Maryland, November 19-22, 1991.
13. Fen R.C., Downer J.R., Bushko D.A., Gondhalekar V., Ham N.D.,"Magnetosctrictively Driven Flaps for Helicopter Vibration Reduction", Fifth Workshop on Dynamics and Aeroelastic Stability Modeling of Rotorcraft Systems, Troy, N.Y., 1993.
14. Yillikci Y.K.,"Aeroelastic Analysis of Rotor Blades with Flap Control", Paper No. E04, XIX European Rotorcraft Forum, Avignon, September 1992.
15. Millot T.A., Friedmann P.P., "The Practical Implementation of an Actively Controlled Flap to Reduce Vibrations in Helicopter Rotors", 49th AHS Forum, May 1993, St.Louis, USA.
16. Straub F.K., Robinson L.H., "Dynamics of a Rotor with Nonharmonic Control", 49th AHS Forum, St.Louis, May 1993.
17. Narkiewicz J., Rogusz M., "Smart Flap for Helicopter Rotor Blade Performance Improvement", XIX European Rotorcraft Forum, Cernobbio (Como), Italy, September 1993.

Paper presented at the Second European Conf. on Smart Structures and Materials, Glasgow 1994, Session 7

Modal Parameter Identification of Controlled Flexible Space Structures

T. Kasai, K. Komatsu and M. Sano
National Aerospace Laboratory, Japan
7-44-1 Jindaiji-Higashi, Chofu,Tokyo 182

ABSTRACT

A method for using the extended Kalman filter to identify the modal parameters of vibration controlled structures has been developed and demonstrated. The closed-loop structural vibration system is excited by a known or unknown excitation signal and the resulting time histories of the closed-loop system response are analyzed. The present method has the advantage that the physical parameters of the system are directly estimated. The numerical examples showed excellent results and it is expected that the present method can be applied to the on-orbit modal testing of controlled space structures.

1. Introduction

To evaluate the modal parameters of large space structures is essential for the controller design of the attitude control[1,2]. Although the finite element analysis for dynamic characteristics must be verified by tests, the gravity and the atmospheric effects can not be removed in the ground vibration test. Therefore on-orbit modal identification is absolutely necessary for a high performance control design[3,4].

In on-orbital modal testing, the attitude control system and reboost thrusters are the most suitable available excitation sources, it is not practical to directly measure the input force, which is essential in calculating frequency response functions (FRFs). Moreover for the attitude controlled space structures, the traditional modal analysis method based on the FRFs can not be used without modifications.[5,6]

In this paper, the extended Kalman filter (EKF) technique[7,8] is applied to evaluate the modal parameters of the closed-loop systems. This method has the advantage that the physical parameters of the system are directly estimated. The unknown parameters consist of eigen frequencies, damping ratios, modal masses, and modal shapes of the controlled flexible strucuture. Extensive prelaunch analysis and ground vibration tests will offer good initial values for the EKF analysis. Several numerical simulations are conducted and the modal parameters extracted from the time series of the controlled structure show excellent results comparing with the exact values.

2. Identification Method

When the structure is subjected to the external force $u(t)$, the vibration equation is expressed by the modal coordinate system q as

$$\tilde{M}\ddot{q} + \tilde{C}\dot{q} + \tilde{K}q = \Phi^T u \qquad (1)$$

where $\tilde{M}$,$\tilde{C}$,$\tilde{K}$ are $n \times n$ diagonal matrices whose elements are modal mass, modal damping, and modal stiffness respectively. Φ is $p \times n$ modal matrix

$$\Phi = [\phi_1, \ldots, \phi_i, \ldots, \phi_n]$$

and ϕ_i denotes the i-th eigen vector normalized to set the modal mass equal to unit. The above equation is transformed into the state equation

$$\dot{x} = A(\theta)x + B(\theta)u \qquad (2a)$$

$$y = C(\theta)x \qquad (2b)$$

where the state vector x consists of $(q, \dot{q})^T$ and y is the observation vector, u_t the force vector. θ is a modal parameter vector defined as

$$\theta = \{\zeta_1, \ldots, \zeta_n, \omega_1, \ldots, \omega_n, \phi_1^T, \ldots, \phi_n^T\}^T \qquad (3)$$

where ω_i and ζ_i are the i-th eigen angular frequency and modal damping ratio respectively. Then A,B are

$$A(\theta) = \begin{bmatrix} 0 & I \\ \mathrm{diag}(-\omega_i^2) & \mathrm{diag}(-2\omega_i\zeta_i) \end{bmatrix}$$

$$B(\theta) = \begin{bmatrix} 0 \\ \Phi^T \end{bmatrix}$$

Matrix C can be expressed according to the observation configulation, for example, when the system is observed by displacement

$$C(\theta) = \begin{bmatrix} \Phi & 0 \end{bmatrix}$$

0-8194-1700-9/94/$6.00

Assuming the unknown parameter θ is independent of time and introducing system noise w_t and observation noise v_t, the discrete state equation can be written (Fig.2)

$$x_{t+1} = A_d(\theta)x_t + B_d(\theta)u_t + D_d(\theta)w_t \quad (4a)$$

$$y_t = C(\theta)x_t + v_t \quad (4b)$$

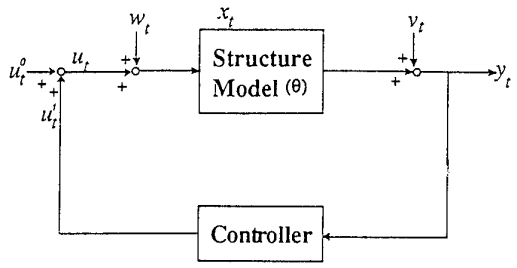

Fig.1 Closed-Loop System

where u_t^0 is an external force, u_t^1 admissible control force, w_t and v_t are system noise and observation noise respectively. w_t and v_t are zero mean stationary white noise processes with covariance given by

$$E[w_t] = 0 \quad , \quad E[v_t] = 0$$

$$E[\begin{pmatrix} w_t \\ v_t \end{pmatrix}\begin{pmatrix} w_s^T & v_s^T \end{pmatrix}] = \begin{bmatrix} Q_t & 0 \\ 0 & R_t \end{bmatrix}\delta_{ts}$$

$$E[w_t x_s^T] = 0 \quad , \quad E[v_t x_s^T] = 0 \quad \text{for} \quad t \geq s$$

Matrices A_d,B_d,D_d are obtained with a sampling rate Δt as

$$A_d = \begin{bmatrix} A_d^1 & A_d^2 \\ A_d^3 & A_d^4 \end{bmatrix} \quad (6)$$

$$A_d^j = \mathrm{diag}(a_i^j) \quad \text{for} \quad j = 1,2,3,4$$

$$\text{and} \quad i = 1,2,\ldots,n$$

$$a_i^1 = e^{-\zeta_i\omega_i\Delta t}[\cos(\omega_i\sqrt{1-\zeta_i^2}\Delta t) + \frac{\zeta_i}{\sqrt{1-\zeta_i^2}}\sin(\omega_i\sqrt{1-\zeta_i^2}\Delta t)]$$

$$a_i^2 = \frac{e^{-\zeta_i\omega_i\Delta t}}{\omega_i\sqrt{1-\zeta_i^2}}\sin(\omega_i\sqrt{1-\zeta_i^2}\Delta t)$$

$$a_i^3 = -\frac{e^{-\zeta_i\omega_i\Delta t}}{\omega_i\sqrt{1-\zeta_i^2}}\sin(\omega_i\sqrt{1-\zeta_i^2}\Delta t)$$

$$a_i^4 = e^{-\zeta_i\omega_i\Delta t}[\cos(\omega_i\sqrt{1-\zeta_i^2}\Delta t) - \frac{\zeta_i}{\sqrt{1-\zeta_i^2}}\sin(\omega_i\sqrt{1-\zeta_i^2}\Delta t)]$$

$$B_d = \begin{bmatrix} B_d^1 \\ B_d^2 \end{bmatrix}$$

$$B_d^1 = \{b_{ij}^1\} \quad , \quad B_d^2 = \{b_{ij}^2\}$$

$$\text{for} \quad i = 1\ldots n \text{ and } \quad j = 1\ldots p$$

$$b_{ij}^1 = \frac{\phi_{ji}}{\omega_i^2}[1 - e^{-\zeta_i\omega_i\Delta t}\{\cos(\omega_i\sqrt{1-\zeta_i^2}\Delta t) + \frac{\zeta_i}{\sqrt{1-\zeta_i^2}}\sin(\omega_i\sqrt{1-\zeta_i^2}\Delta t)\}]$$

$$b_{ij}^2 = \frac{\phi_{ji}}{\omega_i\sqrt{1-\zeta_i^2}}e^{-\zeta_i\omega_i\Delta t}\sin(\omega_i\sqrt{1-\zeta_i^2}\Delta t)$$

$$D_d = \begin{bmatrix} D_d^1 \\ D_d^2 \end{bmatrix}$$

$$D_d^1 = \{d_{ij}^1\} \quad , \quad D_d^2 = \{d_{ij}^2\}$$

$$\text{for} \quad i = 1\ldots n \text{ and } \quad j = 1\ldots p$$

$$d_{ij}^1 = \frac{\phi_{ji}}{\omega_i^2}[1 - e^{-\zeta_i\omega_i\Delta t}\{\cos(\omega_i\sqrt{1-\zeta_i^2}\Delta t) + \frac{\zeta_i}{\sqrt{1-\zeta_i^2}}\sin(\omega_i\sqrt{1-\zeta_i^2}\Delta t)\}]$$

$$d_{ij}^2 = \frac{\phi_{ji}}{\omega_i\sqrt{1-\zeta_i^2}}e^{-\zeta_i\omega_i\Delta t}\sin(\omega_i\sqrt{1-\zeta_i^2}\Delta t)$$

And let the augmented state space vector be a form

$$z_t^T = (x_t^T, \theta_t^T) \quad (7)$$

then the linear stochastic system including the unknown parameter θ is expressed by the following nonlinear stochastic system as

$$z_{t+1} = f(z_t, u_t, w_t)$$

$$= \begin{bmatrix} A_d(\theta_t)x_t + B_d(\theta_t)u_t \\ \theta_t \end{bmatrix} + \begin{bmatrix} D_d(\theta_t)w_t \\ 0 \end{bmatrix} \quad (8a)$$

$$y = h(z_t, u_t, v_t)$$

$$= C(\theta_t)x_t + v_t \quad (8b)$$

Now z_t can be estimated by the EKF

$$\hat{z}_{t+1/t} = f(\hat{z}_{t/t}, u_t, 0) \quad (9a)$$

$$\hat{z}_{t/t} = \hat{z}_{t/t-1} + K_t[y_t - h(\hat{z}_{t/t-1}, u_t, 0)] \quad (9b)$$

$$\hat{z}_{0/-1} = E[z_0]$$

$$K_t = P_{t/t-1}H_t^T[H_tP_{t/t-1}H_t^T + \bar{R}_t]^{-1}$$

$$P_{t+1/t} = F_tP_{t/t}F_t^T + \bar{Q}_t$$

$$P_{0/-1} = E[z_0z_0^T]$$

$$P_{t/t} = P_{t/t-1} - P_{t/t-1}H_t^T$$

$$[H_t P_{t/t-1} H_t^T + \bar{R}_t]^{-1} H_t P_{t/t-1}$$

$$F_t = \frac{\partial f(z_t, u_t, w_t)}{\partial z_t}|_{z_t=\hat{z}_{t/t}, w_t=0}$$

$$H_t = \frac{\partial h(z_t, u_t, v_t)}{\partial z_t}|_{z_t=\hat{z}_{t/t-1}, v_t=0}$$

$$G_t = \frac{\partial f(z_t, u_t, w_t)}{\partial w_t}|_{z_t=\hat{z}_{t/t}, w_t=0}$$

$$J_t = \frac{\partial h(z_t, u_t, v_t)}{\partial v_t}|_{z_t=\hat{z}_{t/t-1}, v_t=0}$$

$$\bar{Q}_t = G_t Q G_t^T \quad , \quad \bar{R}_t = J_t R J_t^T$$

where $\hat{z}_{t/t-1}$ denotes the predicted value of $z(t)$ and $\hat{z}_{t/t}$ denotes the filtered value.

3. Numerical Example

A satellite with flexible solar panels shown in Fig.2 is taken as an example. The LQ regulator control law is applied to the model. The model is analyzed as a two-dimensional plate-beam structure, and the lower three modes ($n = 3$) are adopted as our identification model.

The actuator is located at the center. And the response time series at 18 nodes ($p = 18$) are calculated by the mode superposition method setting $\Delta t = 0.05$sec. Therefore the total number of the unknown modal parameters is $(2+p)\times n = 60$ (cf. equation (3)) in this example.

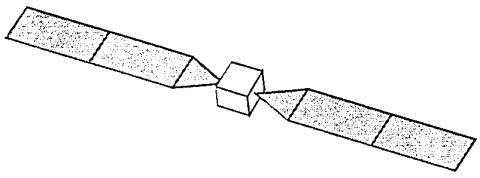

Fig.2 Numerical Model

The exact values in the numerical simulation are shown in Tables 1 and 2 with the initial values that are more than 20 % deviated from the exact values. In the first case, where the system is excited by the external force u_t^0 with the system noise w_t , the estimated parameters identified at various time $N\Delta t$ (N is time step number) are shown in Table 1(a) for eigen frequencies and Table 1(b) for damping ratios. In this case, w_t is set as

$$\frac{E[|w_t|^2]}{E[|u_t^0|^2]} = O(10^{-4})$$

The eigen frequencies converge to the exact values at $N = 500$, and for the estimated damping ratios, whose initial values are zeros, reasonable agreement with the exact values is apparent, though $N = 48000$ are needed to converge within 0.3 percent error for the first damping ratio. Identified mode shapes are illustrated in Fig.3.

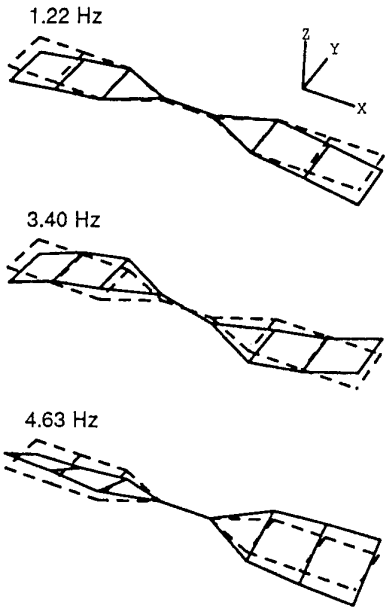

Fig. 3 Estimated Mode Shapes

In the second case where the system is excited only by the noise w_t, the estimated values are also shown in Table 2. The convergence for damping ratios is also shown in Fig.4. This is the possible worst case and the convergence is not so good as in the first case, especially for the damping ratios.

Even though, the EKF gives almost the same parameters with the exact value after sufficient time steps.

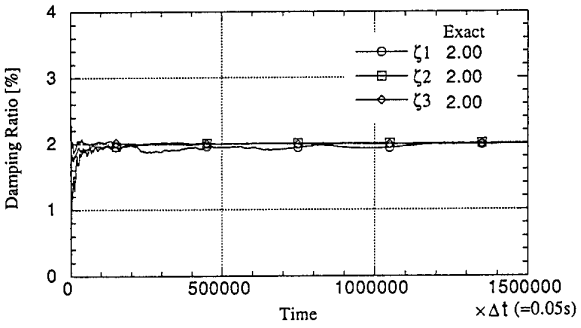

Fig.4 Convergence of damping ratios

Table 1(a) Estimated Eigen Frequencies (excited by external force and noise)

	frequency (Hz)		
mode	1	2	3
exact	1.22	3.40	4.63
initial	0.98	2.72	3.71
100	1.22	3.41	4.62
N 200	1.22	3.40	4.64
500	1.22	3.40	4.63

time=$N \times \Delta t$

Table 1(b) Estimated Damping Ratios (excited by external force and noise)

	damping ratio (%)		
mode	1	2	3
exact	2.00	2.00	2.00
initial	0.00	0.00	0.00
100	1.81	2.27	1.46
500	1.92	1.99	1.97
N 1000	1.98	1.99	1.97
2000	1.98	2.00	2.00
48000	2.00	2.00	2.00

Table 2(a) Estimated Eigen Frequencies (excited by noise)

	frequency (Hz)		
mode	1	2	3
exact	1.22	3.40	4.63
initial	0.98	2.72	3.71
100	1.18	3.45	4.66
500	1.24	3.42	4.65
N 1000	1.24	3.41	4.66
5000	1.22	3.40	4.63

Table 2(b) Estimated Damping Ratios (excited by noise)

	damping ratio (%)		
mode	1	2	3
exact	2.00	2.00	2.00
initial	0.00	0.00	0.00
100	0.04	0.56	1.51
1000	0.74	1.28	2.09
N 5000	1.01	1.83	2.02
48000	1.87	1.90	2.01
150000	2.00	2.00	1.99

4. Conclusions

The extended Kalman filter technique is applied to evaluate the modal parameters of the controlled flexible structures. This method has the advantage that the physical parameters of the system are directly estimated, and its initial values can be given by the finite element analysis or by the ground vibration test. The numerical examples showed excellent results and it promises that the present method can be applied to the on-orbit modal testing of controlled space structures.

References

[1] Quinn,R.D. and Yunis,I.S. : Control / Structure Interactions of Space Station Solar Dynamic Modules, J. Guidance, Control, and Dynamics, 16-4 (1993) 623-629.

[2] Sparks Jr,D.W. and Juang,J.-N. : Survey of Experiments and Experimental Facilities for Control of Flexible Structures, J. Guidance, Control, and Dynamics, 15-4 (1992) 801-816.

[3] H.M.Kim and H.H.Doiron:On-Orbit Modal Identification of Large Space Structures, Sound and Vibration (1992/Jun) 24-30.

[4] J.E.Cooper and J.R.Wright:Spacecraft In-Orbit Identification Using Eigensystem Realization Methods,ibid, 15-2 (1992) 352-359.

[5] C.-W. Chen and J.-K.Huang:Integrated System Identification and State Estimation for Control of Flexible Space Structures, ibid, 15-1 (1992) 88-95.

[6] J.-N. Juang and M. Phan:Identification of System, Observer, and Controller from Closed-Loop Experimental Data,ibid, 17-1 (1994) 91-96.

[7] Hoshiya,M.and Saito.E.:Structural Identification by Extended Kalman Filter,J.of Engineering Mechanics,ASCE, 110-12 (1984) 1757-1770.

[8] Bao,Z.-W. and Shi,W.-Y.:Parameter Identification of Structural Models by means of Extended Kalman Filter Algorithm,Proc. 7th IMAC (1989) 1554-1560.

Feedback Controllers for Broadband Active Noise Reduction

Benoît PETITJEAN, Isabelle LEGRAIN
ONERA, BP 72, F-92322 CHATILLON CEDEX, FRANCE

The aim of the present paper is to demonstrate the efficiency of an LQG-based controller for the active control of the acoustic field radiated by a rectangular panel. This topic has been of interest for numerous researchers in the past 10 or 15 years, but very little attention has been paid to broadband disturbances occurring in a relatively high frequency range. These are unfortunately common features of noise perturbations in realistic structures such as airplanes or helicopters. The few articles that deal with this problem provide very scarce experimental results and are related to frequency bands where the structure dynamics is rather poor.

From the outset, the problem at hand involves numerous difficulties, such as the modeling of the active structure itself and the possible large size of the controller. In the following, the experimental setup is described, then the controller design procedure is developed and finally some experimental results are shown that prove the efficiency of the method.

▷ Experimental setup ◁

The experimental testbed consists of a steel rectangular plate suspended by four elastic attachments that simulate free boundary conditions. This plate is excited by a B&K shaker in the 0 to 2500 Hz range. PVDF patches are bonded on both sides to be used as sensors (side B) and actuators (side A). The plate is 1.5 mm thick, 0.2 m wide and 0.3 m long and has 15 PVDF patches on each side :

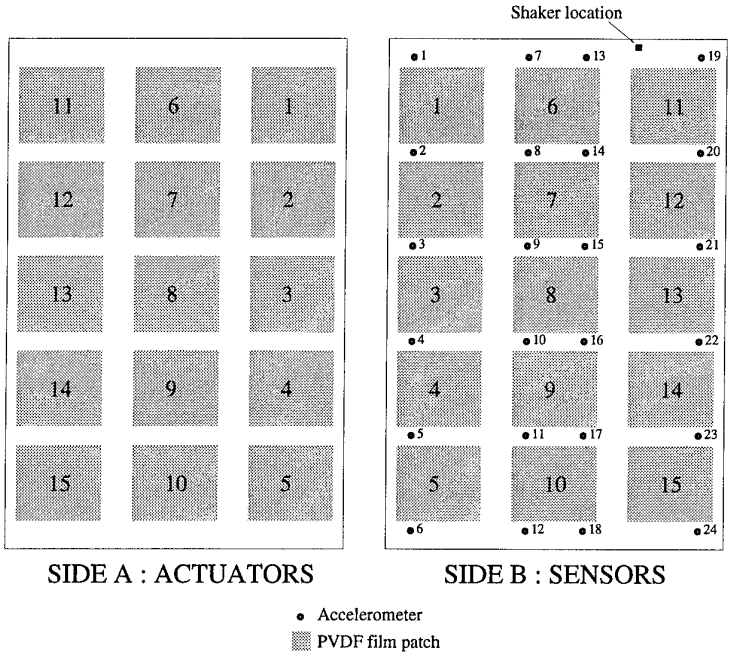

The 'neutral' layout of patches provides an interesting flexibility in the selection of efficient sensors and actuators. The digital controller is made up of two DSPs (Motorola 96002) and 8 analog input/output devices with standard DA and AD converters. The whole equipment is placed in a pseudo-anechoic chamber and a semi-circular array of microphones is employed to measure the radiated acoustic field. This array may be rotated around the plate in such a way that a fine mapping of the radiated sound field in a half space can be achieved.

0-8194-1700-9/94/$6.00

▷ Controller design ◁

The LQG procedure provides a natural framework for our design goals, because it assumes a white noise perturbation, and allows a targeted control performance through the cost functional.

The active structure is modeled using finite elements, leading to an usual time-domain state-space representation of the form :

$$\begin{cases} \dot{X}(t) = \mathbf{A}X(t) + \mathbf{B}_1 w(t) + \mathbf{B}_2 u(t) \\ y(t) = \mathbf{C}_2 X(t) \\ z(t) = \mathbf{C}_1 X(t) \end{cases}$$

where z is the pressure output, y the observation vector, u the input vector, w the shaker perturbation, and X the state vector made up of the plate modal displacements and velocities. As mentioned earlier, the plate is excited in the [0, 2500] Hz range. It exhibits a rich dynamics in this range, with more than 40 modes of vibration. The aim of the control is to reduce the sound radiation in a subset of this range, namely the [1000, 2000] Hz band, which includes 15 of the natural frequencies.

There is no point here to recall the LQG method, which has been a common design tool for at least 2 decades [1]. We want to focus more specifically on the difficulties encountered in this particular work.

a/ **Cost functional**

The radiated acoustic field has been both experimentally measured, using the microphone array, and numerically calculated. An efficient software called HEABF was used to this end, that solves the entire coupled fluid-structure equations for volumic or thin structures. One should indeed bear in mind that the free boundary conditions do not allow the use of simple Rayleigh integral representations of the radiated acoustic field, but that the parietal pressure distribution must be computed first.

It turns out in our case that the plate response, driven by resonance phenomena, is the very source of the radiated field. More precisely, the radiated energy spectrum follows that of the plate kinetic energy. Following this observation, it was decided to base the cost functional directly on the plate modes.

Moreover, the plate coïncidence frequency is about 7500 Hz, and care must be taken that the control do not excite more radiating modes ('spillover' effect). We used low pass filters between the DA converter and the actuators in an attempt to reduce this effect and included them in the controller design in order to account for the resulting phase shift.

b/ **Controller reduction**

The size of the controller issued from the LQG method is often felt as a definitive pitfall of this procedure. Nissim [2] has proposed a simple and sound way to reduce this controller that can be summed up as follows:

- decouple the observer states

- evaluate the rise of the cost functional that results from the omission of each observer state in turn

- select and keep the most important states to build the reduced controller.

Using this method allowed us to bring down the controller size to a large degree. A careful coding of the controller equations on the DSP makes it possible to deal with an 8-input 8-output 64-state LQG regulator (at most) with a sampling frequency of 10 kHz.

▷ Experimental results ◁

A characteristic example is selected here as an illustration of the method. Two controllers are designed and compared. The first one is based on a full plate model. We selected 32 modes, covering the range [400, 2400] Hz, so as to be able to run the resulting 64 state controller on the DSPs.

Then the reduction procedure was carried out. It was observed that choosing the cost functional so as to focus the control efficiency on the frequency range of interest ([1000-2000] Hz) seems to fool the reduction method, in that it tends to select the modes having the largest cost. Therefore, in this example, we used an uniform cost function.

The controller size drops from 64 to 38. There is far enough space left to add states that account for the phase shifts due to the low pass filters. Figure 1 shows the controller transfer function between input 1 and output 1 (first sensor/actuator pair) for both full (solid line) and reduced (dashed line) controllers. The control efficiency can be viewed in Figure 2, for the two configurations. This plot shows the acoustic pressures averaged over the hemisphere, in dB. Reductions as large as 10 dB are obtained. The solid line is for the uncontrolled system, the dashed line for the full controller and the dotted line for the reduced controller.

In both cases, actuators # 1 to # 8 and sensors # 1 to # 8 are used in the feedback loop, having proven very efficient in contrast to other configurations. However, some developments are currently in progress in order to optimally choose the sensors/actuators set.

▷ Conclusion ◁

We demonstrated the feasibility of broadband acoustic attenuation using a simple design tool. A salient feature of this work is the fact that the controller is designed from raw numerical models, where only the resonant frequencies have been taken from actual measurements. Nevertheless, the final reduced controller has sufficient robustness properties in relation to model uncertainties.

The reduction method allows extra space needed to model low-pass filters for example, but above all it makes possible the design of efficient controllers from state-space models that would lead otherwise to controllers that exceed the on-line computing capabilities.

There is still some work ahead : one has to make sure that this controller really outperforms simple active damping loops taking advantage of the co-located nature of the sensor/actuator pairs. Simulations and experiments are carried out and will be reported in the very near future to this end. In addition, some other design methods, like robust control strategies, must be tested so as to get a better understanding of the different characteristics of these various methods.

A further step will involve the treatment of higher frequency bands, where the modal representation no longer holds.

▷ References ◁

[1] KWAKERNAAK H., SIVAN R. : *Linear Optimal Control Systems*, Wiley Interscience, New-York 1972.

[2] NISSIM E. : Order Reduction of Linear Quadratic Gaussian Designed Controllers, *AIAA Journal of Guidance, Control and Dynamics*, 1993, **16**(6), 1154–1161.

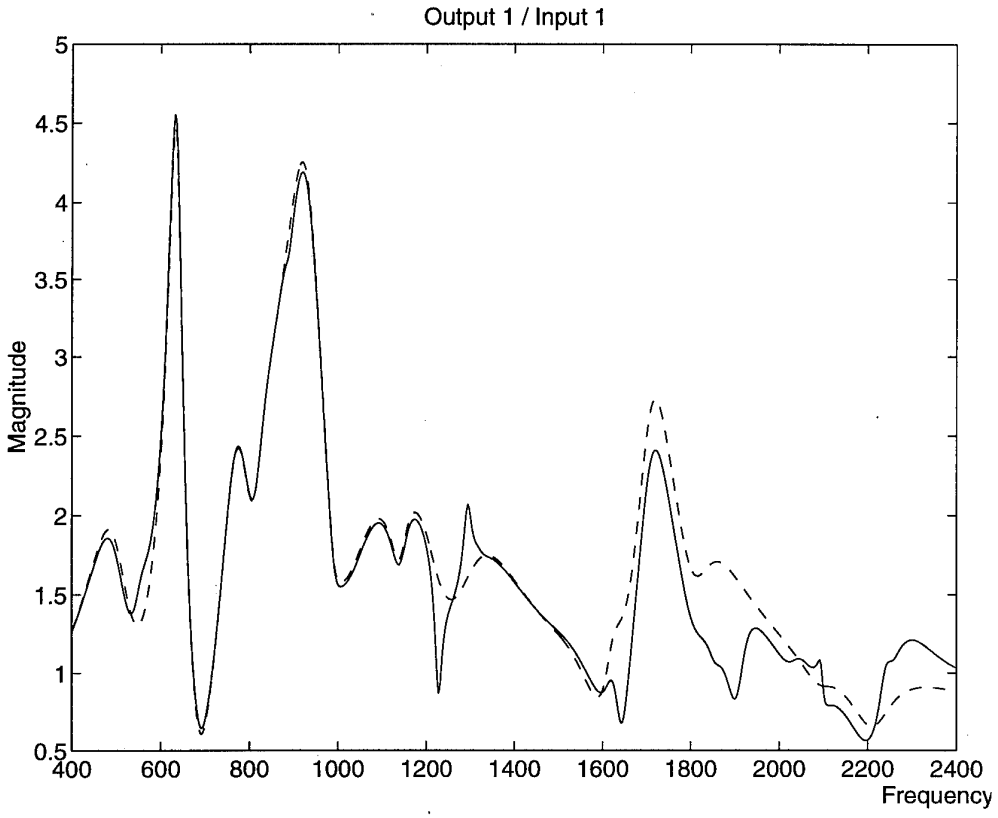

Figure 1 : controller transfer function

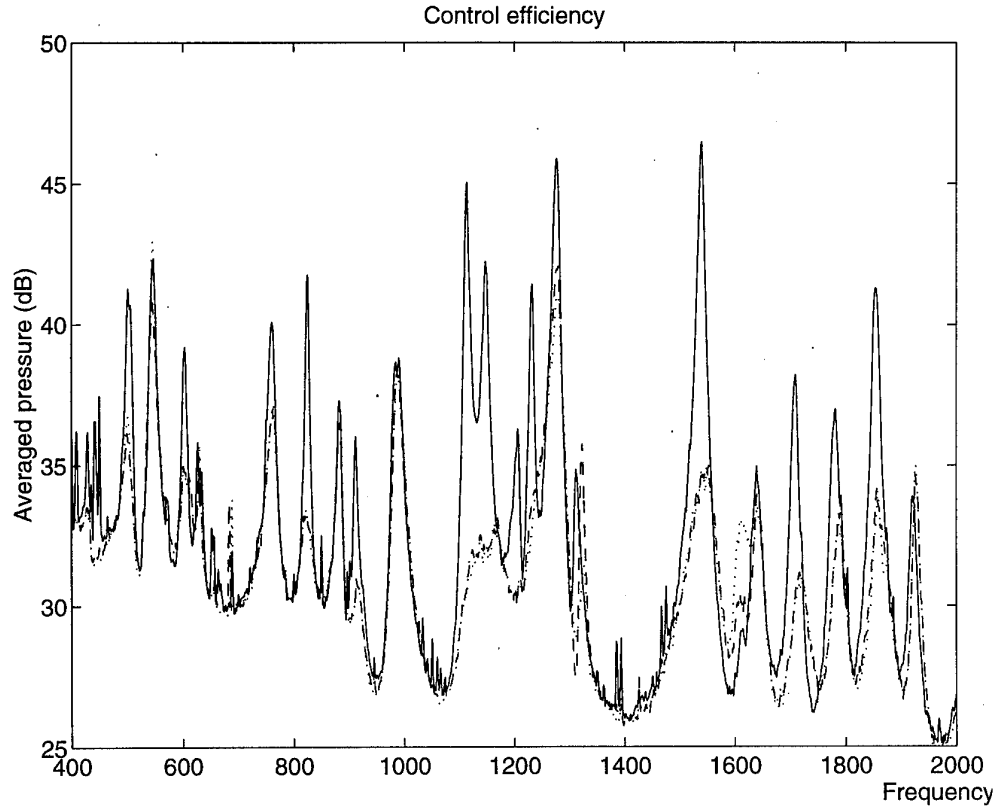

Figure 2 : uncontrolled and controlled system output

Paper presented at the Second European Conf. on Smart Structures and Materials, Glasgow 1994, Session 7

ACTIVE DAMPING CONTROL SYSTEMS FOR SATELLITES

C. R. Pietsch H. Baier

Dornier GmbH, D-88039 Friedrichshafen, Germany

ABSTRACT

The potential of Active Damping Control Systems (ADCS) is demonstrated for several satellite applications where active control of satellite disturbances is required. Test results of damping large satellite appendages like solar arrays will be presented.

1. INTRODUCTION

Space missions of earth observation, scientific or communication satellites require steady increasing performances of their payloads and instruments. They result from stronger requirements of the scientific community or from new space communication scenarii as e.g. the inter-orbit links via optical communication.

As a consequence this leads to the use of advanced systems allowing to realize these increasing demands. One interesting aspect is to actively control disturbances which react on a satellite structure either due to attitude and orbit control manouevers or due to the vibrations of reaction wheels, gyroscopes or stirling coolers. Also the orbiting of the spacecraft itself (sunlight, eclipse) creates thermal shocks, which can result in unforeseen vibrations of satellite equipment. The unexpected solar array vibrations of the Hubble Space Telescope with the corresponding consequences are a good example for this effect.

The low frequencies of these vibration sources generate relatively great amplitudes especially on large satellite appendages. Due to the low damping characteristic of such lightweight structures, the vibrations exist for a long time before achieving a balanced situation with a deflection close to zero. Therefore active control of the disturbances is necessary . This can be realized by implementing Active Damping Control Systems between satellite components to aim a structural decoupling of them. Functional models of such discrete mechanisms have been developed and tested, demonstrating high damping capability.

2. APPLICATIONS FOR ACTIVE DAMPING CONTROL SYSTEMS

The purpose of ADCS is to improve the dynamic behaviour of satellite structures and payloads with low eigenfrequencies and damping behaviour by a structural decoupling of pertubating and pertubed structures and by superimposing controlled forces. A characteristic task is the active damping of solar array vibrations. Further applications are the multi-axial damping of large satellite booms, platforms for optical communication or interferometry, high accurate telescopes, large reflectors for astronomy, earth observation instruments, communication devices, gyroscopes and actuators as reaction wheels or stirling coolers. **Figure 1** illustrates some important applications for ADCS using the FIRST satellite as reference configuration.

Some interesting system aspects also plead for the use of ADCS in satellites. First, relaxed demands exist for the Attitude and Orbit Control System (AOCS), because AOCS manoevers can mostly be executed independently from structural constraints. Also, dynamic aspects can be minimized, because an unwanted feedback of the satellite structures is mainly reduced. Furtheron, the compliance effects of deployment and pointing mechanisms can be compensated. With adaptive controllers the possibility exists to get optimized structural behaviour with increasing orbit time. Finally, ADCS support the increase of satellite life time in orbit by increasing the reliability of satellite parts due to the reduction of their dynamic loads.

0-8194-1700-9/94/$6.00

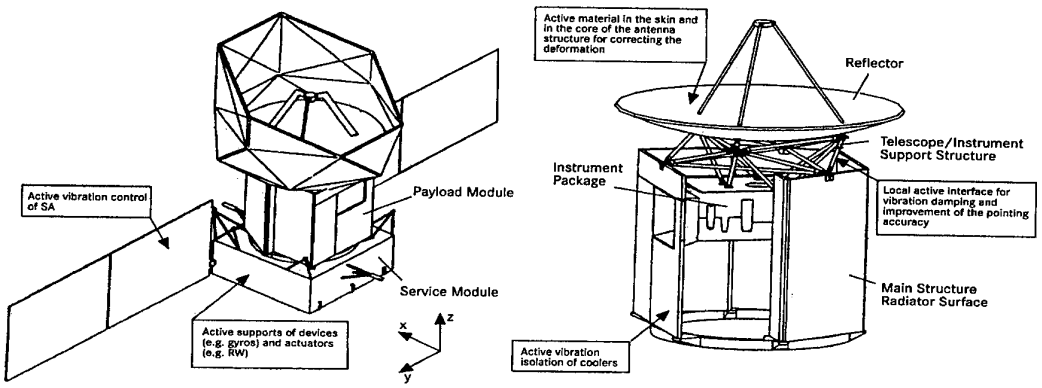

Fig. 1: Some Applications for Active Damping Control Systems

The realisation of ADCS implies the use of active structure technology, because passive devices can not be used in this low frequency range. The concept of active structure technology is, that disturbances acting on a mechanical structure will be measured by attached sensors. These sensors provide signals to the responsible controller which computes the necessary actuator forces. The actuators receive the controller commands and carry out the necessary reaction-forces. The principle of active structure technology is demonstrated in **Figure 2** using the vibration attenuation of solar arrays as reference application.

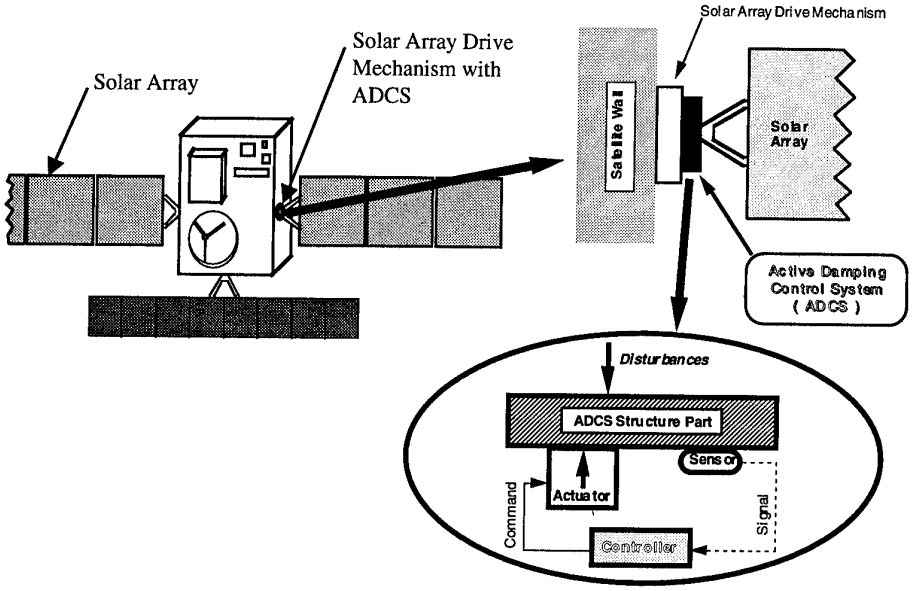

Fig. 2: Principle of Active Structure Technology

The main characteristics of Active Damping Control Systems are low mass and volume data, low power consumption, compact design and low complexity impact on satellite configurations. Besides high reliability, the passive behaviour of the actively damped system will not be deteriorated in case of a failure of the ADCS.

3. ACTIVE DAMPING CONTROL SYSTEMS FOR SOLAR ARRAY VIBRATION ATTENUATION

Acting as local active systems for minimization of dynamical loads, a mainly interesting application is the use of an ADCS as an assessory unit between the solar arrays and the solar array drive mechanism. This allows on the one hand a simplification of the AOCS, because the AOCS layout has not furthermore to consider structural constraints as e.g. eigenfrequency ranges of the solar arrays. On the other hand, the rejection of the disturbances from the solar arrays to the remaining satellite will be avoided.

Two different possibilities exist for positioning the ADCS between the solar array and the satellite. A position between the satellite and the solar array drive mechanism facilitates the work of the drive mechanism, because no additional inertia has to be brouht up, but the ADCS and the solar array coordinate axes are different. This complexes the layout of the ADCS controller. Therefore, a position between the drive mechanism and solar array is the better one, because the controller of the ADCS has not to consider the orientation of the solar array.

For the development of ADCS for solar arrays, a breadboard model has been built. In **Figure 3** the test configuration is demonstrated. The test set-up consists of three main components: the ADCS breadboard device, the Solar Panel Simulator (SPS) and the belonging controller unit (not shown).

The ADCS is fixed to the laboratory wall in a height of about 6 m and connected with a 5.6 m long SPS, which is free movable in horizontal direction at the free end . As shown in **Figure 4**, the piezo-sensor and actuator are collocated above each other. The lever action between the ADCS simulator and the SPS free end results in actuator forces lower 1 N and in strokes lower than 10 µm. Due to the very small amplitudes and the low frequency range, only a force measurement with a sensor system of high stiffness is usable. The sensor signal will be amplified by a PI-controller and submitted to the piezo actuator. The defined controller has been built to allow aperiodic damping in orbit. A space qualified mechanism and controller system would have the dimensions of a cigarette box, each with a total mass below approximately 1 kg.

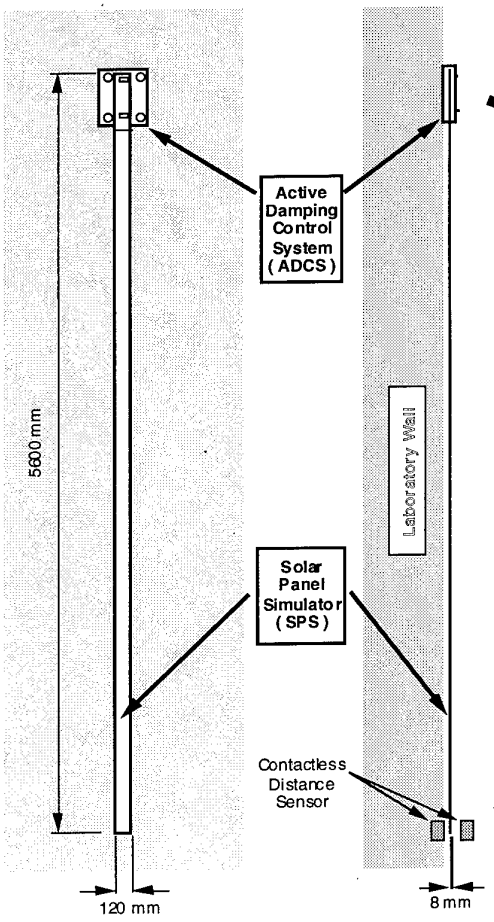

Fig.3: Configuration of the Test Set-up

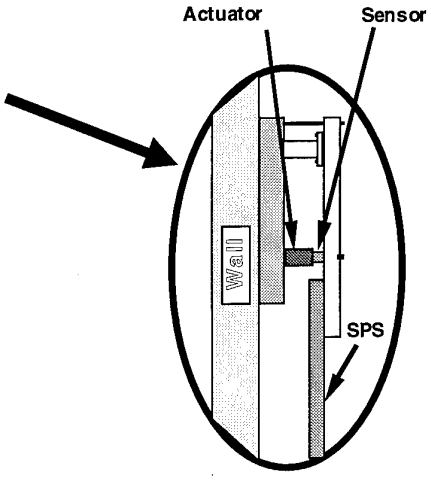

Fig. 4: Side-view of the ADCS Breadboard Device

The Solar Panel Simulator possesses a representative mass and stiffness. The aluminium structure has a length of 5.6 m, a cross section of 120 mm x 8 mm and a mass of 15 kg. The measured relative damping of the SPS is about 0.1 %. Without considering the gravity influence the dynamic analysis shows the first mode as a symmetric bending along the SPS longitudinal axis at 0.21 Hz and the second mode at 1.22 Hz (asymmetric bending). Due to the mass impact of the SPS, the first eigenfrequency rises from 0.21 Hz to 0.32 Hz. This value has been confirmed by the performed test.

The power consumption for the actual test set-up is about 5 W with an input voltage of +/-15 V, but this would be lowered with a miniaturized electronic.

The test results are very impressive. **Figure 5** demonstrates the effect on the deflections without and with an ADCS. The deflections were measured at the free end of the SPS by contactless distance sensors. The left picture shows, that without an ADCS the damping is very low and the deflections occur nearly half an hour for reaching one tenth of the original deflection. With the ADCS the pertubation can be brought to a very low value within less than half a minute. Compared to the undamped SPS, the vibration duration is reduced by a factor of more than 60 ! Regarding the 1g effect, this factor will be considerable increased in orbit!

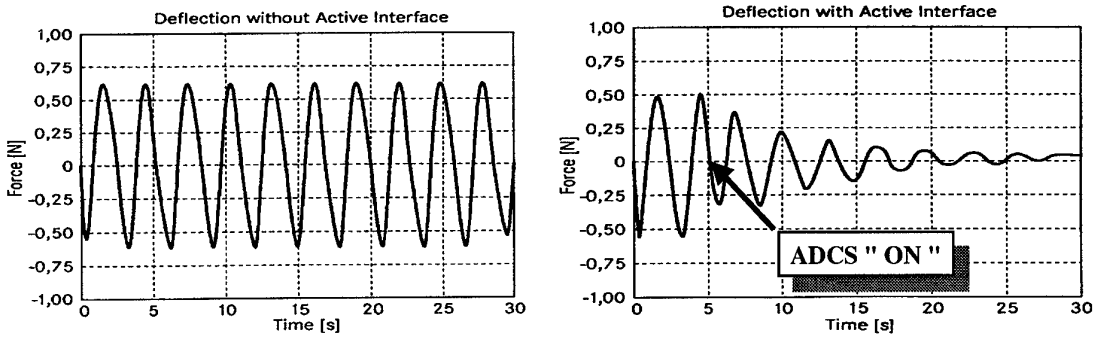

Fig.5: Measured Deflections without and with Active Damping Control System

The breadboard model of an ADCS demonstrates impressively the function of active vibration damping in general. Further investigations aim towards space qualified ADCS. Finally, for simplification reasons a combined system of the Solar Array Drive Mechanism and ADCS should be envisaged.

4. ACTIVE DAMPING CONTROL SYSTEMS FOR OPTICAL COMMUNICATION SYSTEMS

Extremely high pointing requirement data in the range between 0.1 µrad and 1.0 µrad as they exist e.g. in the optical space communication are only managable with active damping control systems. They filter pertubations on the high precision payload module and provide an augmentation of the pointing stability. A further significant advantage is the simplification of the whole tracking system. As shown in **Figure 6** the ADCS systems can be used as discrete mechanisms below the optical head or as structure integrated devices. Both possibilities provide low mass and volume impacts and require only a small amount of electrical power.

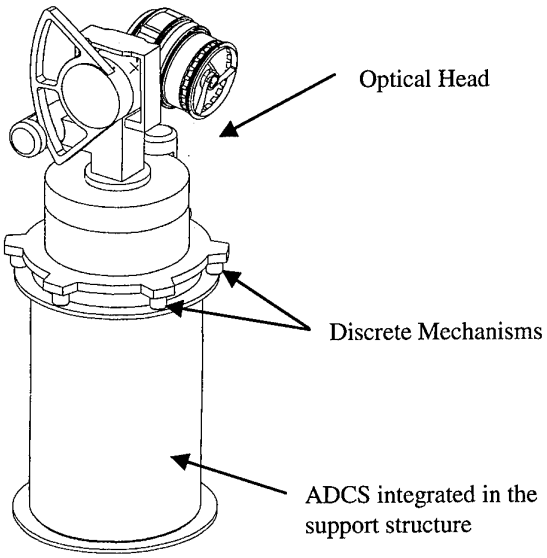

Fig. 6: Active Damping Control Systems for Optical Communication System

5. CONCLUSION

Active Damping Control Systems mean a step towards more precision of satellite payload modules with only a minimal impact on system key data like mass,volume or power demand. The great potential of active vibration damping has been demonstrated. Future steps aim to space qualified systems. This implies to develop flight experiments to check the influence of the earth gravitation onto the ADCS and to optimize their controller strategies. Also the development of existing solar array drive mechanisms with active damping systems can provide more effective systems in total.

REFERENCES

1. Aktive dimensionsstabile Strukturen und Mechanismen - W. Charon, R. Sippel, R. Veigel, B. Kettner - Internal R&D Documents, 1992 and 1993

2. Active Mechanical Components as a Step Towards Adaptive Structures in Space - W. Charon, H. Baier Proc. of the 'Fourth International Conference On Adaptive Structures', Cologne (FRG), Nov. 2-4, 1993

3. Active Damping and Compensation of Satellite Appendages - W. Charon, H. Baier - Proc. of the ' International Astronautical Federation ', Graz (Austria), 1993

MACHINE TOOL CHATTER REDUCTION VIA ACTIVE STRUCTURAL CONTROL

S. O'Regan[1], J. Miesner[1], R. Aiken[2], A. Packman[3], E. Unver[1], S. Akerley[3]

ABSTRACT

A proof of concept for the applicability of active structural control on a Vertical Turning Lathe was demonstrated. The effort proved that active damping can reduce chatter in a production machine tool when machining tough materials like nickel. Significant vibration reductions and surface roughness improvements were achieved.

1. Introduction

Today's machining applications require the development of modern machine tools with higher power, working speeds and accuracy. This requires machine tool manufacturers to produce structurally more robust machines so that undesired vibrations are minimized. Machine tool vibrations significantly limit process throughput and quality. High installed power allows machining processes to use a diversity of tools and cutting regimes but the benefits are limited by the onset of severe vibrations called chatter.

Past efforts have tried to prevent chatter by means of passive control. Having applied passive techniques to the fullest practical extent with only modest success, the machine tool industry is now looking toward active solutions.

This work features a feasibility demonstration of the applicability of active structural control (ASC) technology on reducing chatter from machining operations on a Vertical Turning Lathe (VTL). This work was funded by the Advanced Research Project Agency (ARPA) and managed by the USAF Wright Laboratories Manufacturing Technology Directorate, Contract No. F33615-92-D-5812.

2. Active Control Strategy

The VTL configuration is depicted in Figure 1. The cutting tool generates a compressive force when it engages the workpiece. This cutting force causes both the ram and the workpiece to vibrate. Forces from the

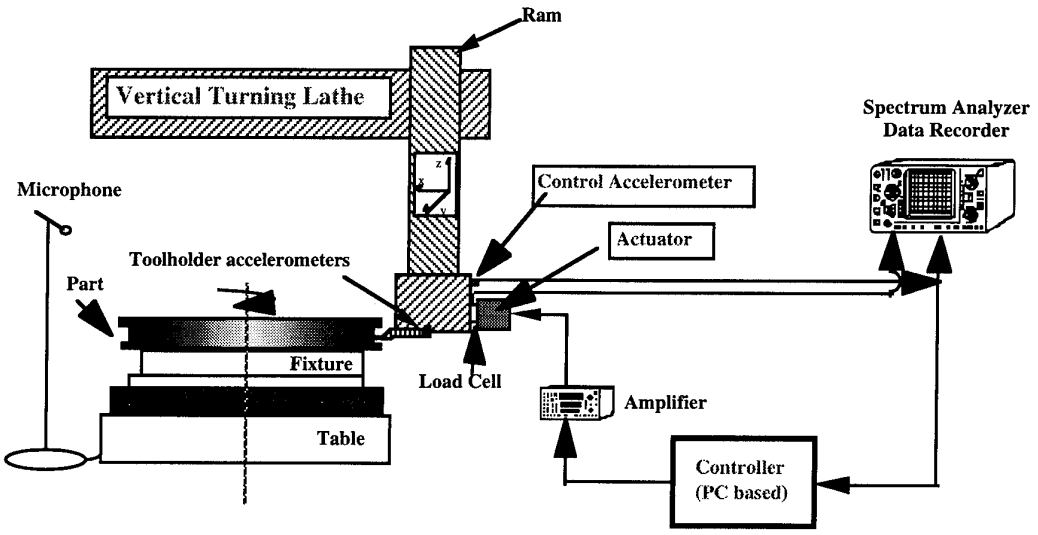

Figure 1. ASC-VTL Configuration

[1] AT&T- Advanced Technology Systems, Arlington, VA, USA
[2] AT&T - Advanced Technology Systems, Whippany, NJ, USA
[3] United Technologies Pratt&Whitney, East Hartford, CT, USA

0-8194-1700-9/94/$6.00

ram support structure propagate downward to the cutting tool and cause additional vibrations. These vibrations cause the cutting depth to vary. Uncontrolled, the vibrations build up and chatter occurs, leaving visible marks on the workpiece.

Our control scheme employs the active damper concept. An actuator is attached to the end of the ram on the opposite face of the cutting tool. Ram acceleration, measured by a sensor positioned near the actuator, is fed into a controller. The controller integrates the acceleration signal, multiplies it by a pre-determined gain and passes it through a bandpass filter to produce a modified velocity signal. The bandpass filter focuses the signal on the frequency band containing the detrimental chatter frequencies. The modified velocity signal then drives the actuator which delivers a force to the ram. The ram works against this actuator force, causing the ram's mechanical power to dissipate, thus drawing down the ram vibrations.

A signal flowchart of the cutting process under active control is shown in Figure 2. U_O is the desired cutting depth (feedrate), U is the actual cutting depth, E is the cutting depth error, X_W is the workpiece displacement, X_S is the ram displacement, F_C is the cutting force, F_n is the foundation force acting on ram, F_a is the actuator force, $T_{turning}$ is the turning period, $\mu_{turning}$ is the overlap factor, H_S is the cutting force-ram displacement transfer function, H_W is the cutting force-workpiece displacement transfer function, G is the feedback gain, K_C is the cutting stiffness, f is frequency and $j = \sqrt{-1}$.

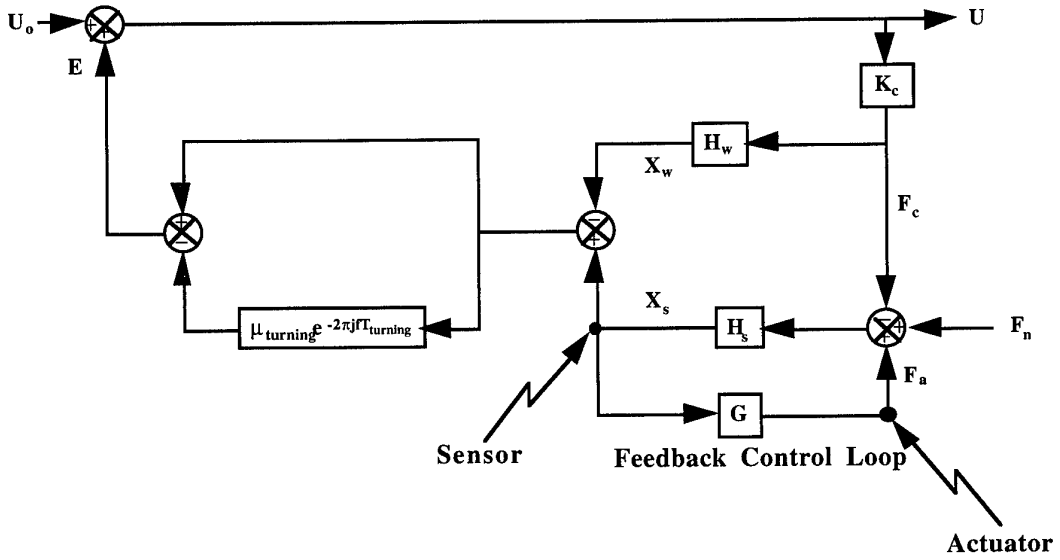

Figure 2. Controlled Cutting Process Signal Flow Diagram

The aim of our effort is to reduce the cutting depth error E. This error is proportional to (X_S - X_W), the relative displacement between the ram and the workpiece. Typically, workpiece connections to the foundation are very stiff for translational motion, compared to the ram stiffness. Hence, we neglected the workpiece motion and focused our attention on reducing only the ram displacement.

3. Results

The objective of this work was to demonstrate that ASC can reduce chatter on a production machine tool using a production quality component using inexpensive, commercially available equipment. We tested the system under typical machining conditions with the ASC system turned alternately off and on.

The ASC system was tested on a Giddings & Lewis VTL. The machined component was a production quality nickel alloy forging of 24 inch diameter. The ASC system hardware consisted of the following:

(1) Wilcoxon F8 shaker with amplifier and impedance matching device.
(2) Kistler accelerometers.
(3) Banshee II digital signal processor, hosted on a Gateway 2000 80486 PC.

A representative test had these machining parameters: (1) plunge cut, (2) turning rate of 10 rpm, and (3) feedrate of 11.1 milli-inches/rev. Without control, chatter developed within the first few seconds of cutting. The dominance of this chatter is quite apparent in the ram vibration spectrum. Figure 3 shows a very high vibration response at 1000 Hz.

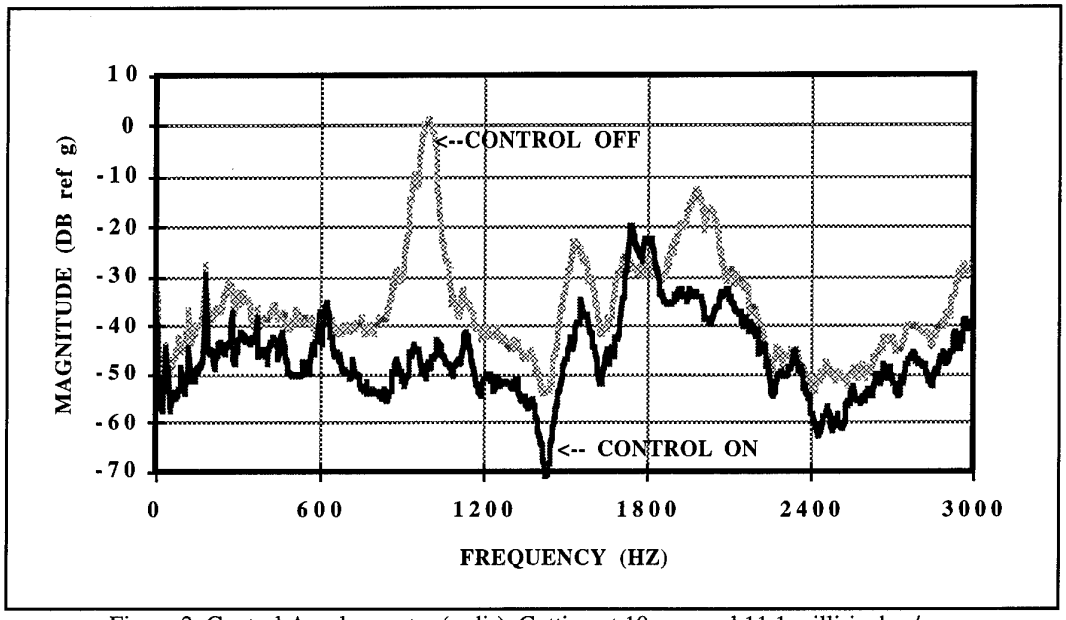

Figure 3. Control Accelerometer (x-dir); Cutting at 10 rpm and 11.1 milli-inches/rev

Figure 4 shows the surface variation on a section of the workpiece after cutting. The wavelength of the highly noticeable narrowband oscillation of the surface variation (0.0125 inch) equals the distance the workpiece turns through during one period at the chatter frequency. This clearly indicates that this surface variation is caused by the chatter.

When the test was repeated with the ASC system turned on, chatter did not develop. The narrowband dominance was eliminated in both the vibration power spectrum and the surface finish. The spectrum level

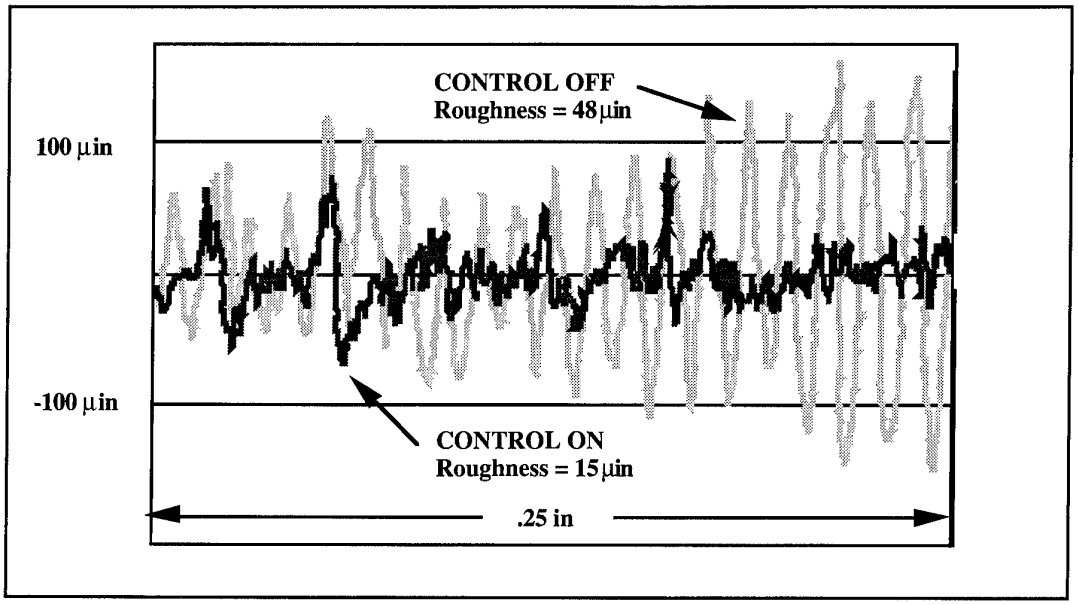

Figure 4. Surface Variation; Cutting at 10 rpm and 11.1 milli-inches/rev

at the chatter frequency was reduced 45 dB. This reduction translated to a two-thirds decrease in surface roughness[4] : from 48 to 16 microinches. The manufacturer's acceptance threshold is 32 microinches.

4. Evaluation

The correlation between the accelerometer data and surface variations was very high. The significant peaks on the accelerometer power spectra and the peak count derived from the surface measurements show that control based on dynamic measurements had the expected impact on the surface finish.

The ASC system reduced vibrations within the control band substantially. The control bandwidth was fairly small (300 Hz) because of large phase shifts associated with shaker internal resonances and time delay through the controller hardware. This poor phase characteristic caused vibration increases outside the control band.

The Wilcoxon F8 shaker was not adequate to control chatter for all the conditions tested. It only provided limited use for testing at 10 rpm. Its frequency band for peak efficiency was too high for chatter control and caused out-of-band vibration increases to become severe in some circumstances. It became clear that the commercially available actuator technology was the major limiting factor for achieving robust chatter control.

5. Conclusion

This effort proved that ASC can reduce chatter in a production machine tool with tough materials like nickel. In so doing, the ASC decreased the workpiece surface roughness by as much as two-thirds. By optimizing the ASC hardware and integrating it into the existing machine tool design, we believe that robust, chatter-free machining is possible and practical for a wide range of machining conditions. Recent developments in actuator technology should help the ASC system achieve better and more robust performance.

The future goal is to build on the current project to design and fabricate a factory floor prototype. This prototype will be integrated into the machine tool and will be compatible with its hardware and electronics.

[4] Roughness is the standard deviation of the surface variation and is measured using the TalySurf technique.

SESSION 8

Paper presented at the Second European Conf. on Smart Structures and Materials, Glasgow 1994, Session 8

Potentials and Problems in Space Applications of Smart Structures Technology

by
D.C.G. Eaton and D. P. Bashford
ESA/ ESTEC ERA Technology Ltd

INTRODUCTION

The well known addage "don't run before you can walk !" seems to apply to most emerging materials. It typically takes ten years before a material is sufficiently well characterised for commercial aerospace application. Much has to be learnt not only about the material properties and their susceptibility to the effects of their working environment but also about the manufacturing process and the most effective configuration related application. No project will accept a product which has no proven reliability and attractive cost effectiveness in its application

The writers firmly believe that smart structures and their related technologies must follow a similar development pattern. Indeed, faced with a range of interdisciplinary problems it seems likely that "partially smart" techniques may well be the first applications. These will place emphasis on the more readily realisable features for any structural application.Prior use may well have been achieved in other engineering sectors.

Because ground based applications are more readily accessible to check and maintain, these are generally the front runners of smart technology usage. Nevertheless, there is a strong potential for the use of smart techniques in space applications if their capabilities can be advantageously introduced when compared with traditional solutions..

This paper endeavours to give a critical appraisal of the possibilities and the accompanying problems. A sample overview of related developing space technology is included. The reader is also referred to chapters 90 to 94 in ESA's Structural Materials Handbook (ESA PSS 03 203 , issue 1.).It is envisaged that future space applications may include the realisation and maintainance of large deployable reflector profiles , the dimensional stability of optical payloads, active noise and vibration control and in orbit health monitoring and control for largely unmanned spacecraft. The possibility of monitoring the health of items such as large cryogenic fuel tanks is a typical longer term objective.

SENSORS AND ACTUATORS

These are likely to be critical constituent parts of a smart structure. In any space application they will have to be mean with their usage of the spacecraft mass ,volume and electrical power budget. They will have to work for a minimum of five years and probably much longer in some project applications. They will have to survive the launch environment and the longer term effects of the in orbit environment. Some typical sample problems that may have to be addressed are:

0-8194-1700-9/94/$6.00

What are the advantages of optical fibres/sensors over conventional strain gauges ,accelerometers,thermocouples? Do they accurately measure the measurand of interest?
Can the optical signal analyser be readily accommodated in a spacecraft system?
Is there sufficient redundancy to compensate for failed sensors?
Can the sensors(actuators) respond within the required time interval?
Can the actuators provide the required force and displacement?
Will actuators/sensors designed for in orbit operation be compatible with the structure manufacturing process and survive the launch environment?

Clearly the importance of some of these questions will be application dependent but some general feeling of confidence in the use of "off the shelf" items has to be established before introduction of optical fibres into composite space structures can be seriously entertained .Work of a similar nature is probably needed for actuators. Westland Aerospace are conducting practical investigations into the problems and solutions involved in realising embedded optical fibres.Some additional work has been conducted at Dornier for ESA.

ACTIVE CONTROL : THE IMPORTANCE OF ONBOARD DATA HANDLING-IN ORBIT HEALTH MONITORING

The Olympus telecommunications spacecraft carried a microacceleration measurement package called PAX which was designed to measure and transmit to ground stations the mechanical vibrations produced by on-board equipment. such as reaction wheels, stepper motors, relays,etc. The prime purpose was to detect the disturbances likely to be imposed on sensitive optical payloads as will fly on Artemis and other future spacecraft.A second achievement was the ability to monitor the health of these equipment items by reviewing their vibration signatures. Within this framework the work was extended to establish automatic signal recognition. Work is continuing at ISVR Southampton University inorder to establish the feasibility of introducing automated condition monitoring as a standard spacecraft service . This involves investigations into the efficient use of both the onboard data handling equipment and the power resources of the spacecraft.Whilst this application is one stage removed from actual control it is believed that important lessons will be learnt as to the ability to deal with the signals that will have to be synthesised in any control system, dealing with, for example, jitter avoidance for future optical payloads. A further PAX experiment is scheduled to fly on the Artemis spacecraft. Additional work, which is of relevance to smart systems, continues to examine the near and far field transmission characteristics of the host structure with respect to the excitation source . (See also the section on Microvibrations below.).

ANTENNA TECHNOLOGY

Current antenna reflectors in Europe rely almost entirely on the use of stiff polymer composite face sheets/honeycomb sandwich core constructions where the required surface profile has been realised during manudacturee 2). For most current applications this will suffice up to a diameter of about three meters. Where larger diameters are required the reflector must be stowed compactly during launch and subsequently unfurled when in orbit. This necessitates alternative forms of construction of which mesh antennas are a

typical example. American and Russian versions have flown and the technology has also been developed in Europe .One of the main problems that has to be resolved for unfurlable antennas is the assurance that the necessary surface profile can be realised after deploying the reflector in the zero gravity conditions of space. Clearly, if the shape can be "tuned" by the use of sensors and actuators in orbit this could reduce the complexity of ground testing and even the method of antenna construction. The challenge to the "smart" engineer is to demonstrate a reliable cost effective system whilst not placing additional pressures on the resources budget identified for the "passive"configuration. The shape could of course be realised from different thin shell or membrane concepts of which the mesh configuration is but one example. A study being undertaken by ERA and Dornier includes some initial assessments of "smart" technology for antennas and will examine the potential of the competing transducer systems for shape control. A breadboard configuration using collocated piezoelectric transducers for strain control is being developed. In practice it is difficult with most currently marketed transducers to realise efficient thermal strain control because of the high coefficient of thermal expansion of the transducer material.

MICROVIBRATIONS

Microvibrations can be of concern for experiments requiring zero gravity conditions or for telescopes where jitter can disturb the pictures.A typical example is the Silex Laser optics telecommunications payload which will fly on the top platform of Artemis. The platform vibrations must be kept to a very low level because the accuracy of the incident beam tracking must be better than 0.2 arcsec. This has led to a number of investigations into the size of disturbing source vibrations such as those examined during in orbit health monitoring . These may emanate from such sources as momentum and reaction wheels where dynamic forces and torques can be generated by rotor imbalances and bearing noise.Combinations of transients and more steady state excitation can be produced by stepper motors as used for solar array drives, attitude pointing mechanisms and mirrors. Transients can be expected from the operation of relays.

In other applications latching valves , vibratory fluid motion generated by turbines and compressors in mechanical coolers and the operation of the stability and control thrusters will give rise to transient and random excitations.

Thermally generated shocks can also create unwanted vibrations. The jitter experienced by the Hubble Space Telescope is a case in point. As the Telescope went from night to day the sharp thermal changes induced "stick-slip" vibratory phenomena in the bi-stem solar blanket deployment booms. This was resolved by introducing adequate thermal protection which deployed with the booms .In that example, the effective cure was achieved by passive means. However, it is evident that the use of the emerging smart technology could assist in resolving this type of problem.

Work has started on assessing the feasibility of smart applications in this microvibration field:
In a series of investigations related to both acoustic and microvibration applications elements of the old Marots structure have been the subject of both theoretical and experimental modal synthesis (eg see figure 1.).This

characterised structure is therefore a suitable vehicle for the assessment of both passive and active methods of vibration reduction . Both viscoelastic and electrical damping techniques will be examined in a study led by Matra .By and large, the importance of air damping is confined to frequencies greater than 200 Hz when considering any experimental requirements.

In many optical payloads the prevention of distortion due to quasi static loads is avoided by the introduction of isostatic mounts often in the form of flexures . In the absence of airborne acoustic excitation these provide the sole means of unwanted vibration transmission. An investigation has therefore been initiated to establish if there are ways and means of eliminating the transmitted vibrations at such locations . This could involve both passive or active damping systems

ACTIVE NOISE AND VIBRATION CONTROL

The increase in the size of launcher payload carrying capability means larger payload fairings and higher external noise levels.The current Ariane 5 fairing design solution represents a compromise in taking account of the launch loads into orbit fairing jettison requirements, etc. As a result the configuration is more susceptible to low frequency noise transmission. Corresponding supplementary passive means of noise reduction could lead to afairing mass penalty of around twenty percent .

Theoretical and experimental studies of the active control of sound transmission into an enclosed cylinder which approximates to a 1/6 scale model of the Ariane 5 payload fairing have been conducted by ISVR, Southampton University. The optimal effects of controlling the internal soundfield using a piezo ceramic transducer mounted on the cylinder have been assessed (eg see figure 2)

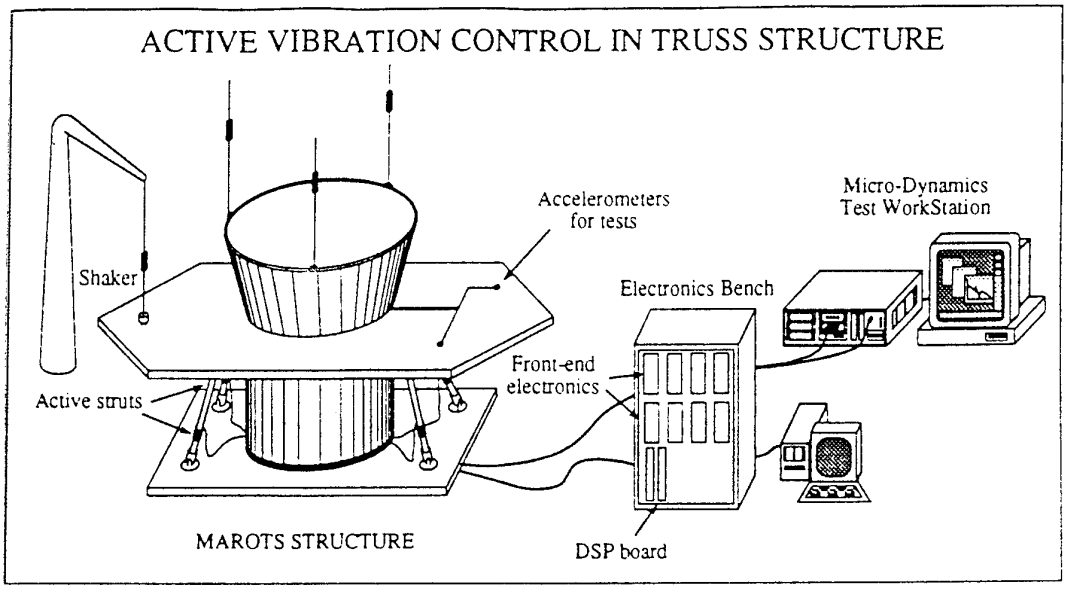

Figure 1. Use of Marots structural elements by MATRA for vibration control studies

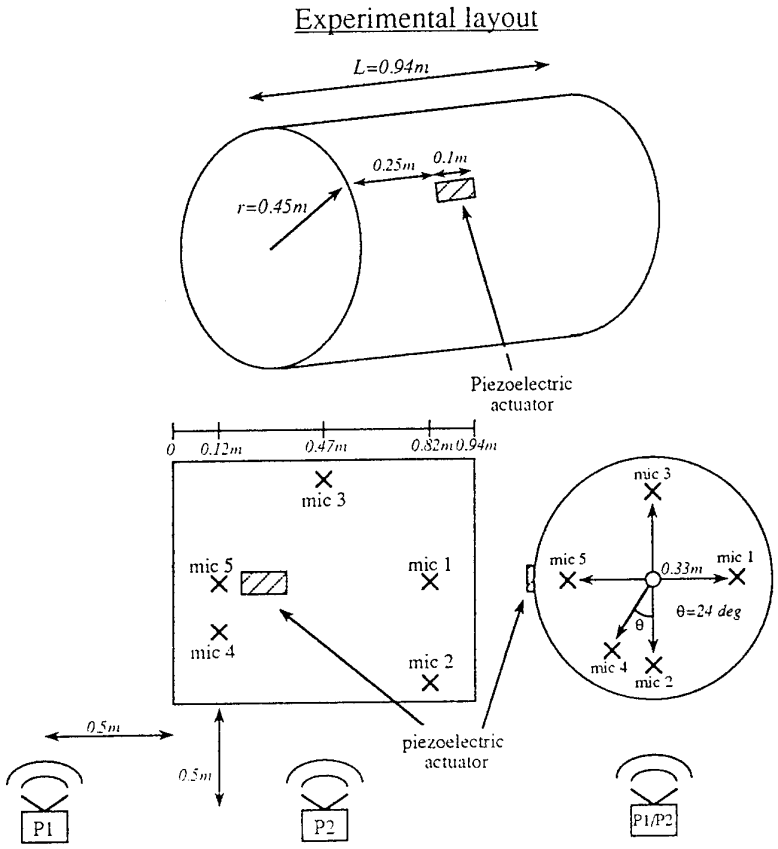

Figure 2 Internal noise reduction studies related to launcher payload fairings using active control techniques (ISVR, Southampton University)

DYNAMIC ANALYSIS ON SMART MATERIALS

W. Ben wu, Ph. D.

Chairman and Professor
Department of Mechanical Engineering
Chang Gung College of Medicine and Technology
Tao-Yuan, Taiwan

ABSTRACT

Active vibration control of smart structural materials has been achieved by using distributed piezoelectric actuators. Numerical simulation and experimental testing have been conducted to investigate vibration suppression of the advanced materials.

1. INTRODUCTION

The development of smart materials and adaptive structures is an emerging technology with significant commercial and engineering applications. In this paper, smart materials subjected to an impulsive loading are simulated numerically and tested experimentally. Comparisons of results are presented.

2. NUMERICAL SIMULATION

The flowchart used to perform the computer simulation of the active control system is presented in Figure 1. To solve the modal equation of motion, the linear acceleration step by step method with Wilson- θ modification was used. In this simulation program, some of the subroutines were called from IMSL computer library (International Mathematical & Statistical Library) which were very easy and convenient use. Since the rotational degree of freedom is involved, the control voltage to suppress the vibration of the system is equal to negative sing of the tip angular velocity times a constant. The control voltage can create the surface traction q(x,t) which will generate the geometric stiffness and the moments at each nodal points. The proper control voltage for a specific system can be determined just by changing the amplification gain.

In the research, the active damper was uniformly distributed. A steel beam with dimensions 17 x 2.7 x 0.1 cm and An aluminum plate with dimensions 12 x 7.5 x 0.04 cm were employed for investigation. Transient forces with magnitudes of 10 Newtons and 0.2 Newtons were applied to excite the beam and the plate, respectively.

0-8194-1700-9/94/$6.00

3. SIMULATION RESULTS OF A CANTILEVER BEAM

To investigate the effectiveness of the control method, the peak of each oscillating cycle for the tip modal point was connected to obtain the families of decay envelopes in the positive direction. Results show a dramatic improvement when the maximum control voltage is increased from 0 to 1000 volts.

When the maximum control voltage is increased from 100 to 1000 volts, the time to decay the envelope to 5% of the maximum amplitude are all about 50% , 35% , 22% , and 12.5% of uncontrolled decay time, respectively. The passive effect of bonding piezo film is quite obvious, the decay time can be shorten up to 20% .

4. SIMULATION RESULTS OF A CANTILEVER PLATE

A transient impact is applied on the point (a/3, 0) to excited the cantilever plate. When the twisting angular velocity Ω_x or bending angular velocity Ω_y are used as the control parameter, the control method is quite similar to using Lyapunov control law for smart beam systems. From results, one can see that when twisting angular velocity Ω_x is used, the control effectiveness of this feedback system is very limited. But when bending angular velocity Ω_y is chosen, a satisfactory effectiveness is obtained. This means bending angular velocity Ω_y is a good control parameter for this cantilever plate but twisting angular velocity Ω_x is not. The reason is that when a plate is excited by a transient impact, showing the bending mode as the dominant one, bending vibrations will decay much slower than twisting vibration. So, when using Ω_y as a control parameter, the feedback control voltage will maintain a greater magnitude, compared with the case of using Ω_x . For some cases, if the twisting mode is the dominant one, then the twisting angular velocity must be chosen as the control parameter to obtain control voltages with higher magnitudes.

5. EXPERIMENTAL ANALYSIS

In the research, piezo films named "Kynar" made by Pennwalt Corporation were employed as sensors and actuators. The thickness of the film is 28 μ m. A general purpose epoxy with low viscosity was used as the bonding agent. Due to the limitation of equipment in the laboratory, the maximum control voltage can only be set at 120 volts. From the results of numerical simulations, a cantilever beam and a cantilever plate are found as the cases which has obvious control effect for control voltage not greater than 120 volts. For this reason, the cantilever beam and plate are chosen to perform the vibration suppression in the experimental analysis.

Figure 2 is a schematic of the cantilever beam with PVDF(DT4-028K) bonded on both surfaces fixed on a stable fixture. An impact hammer was used to excite the structure. Either one of the piezo films was used to be the sensor or the actuator. For cantilever plate system, the setup is exactly the same, but the specimen is substituted by an aluminum plate with same dimensions of surface bonded actuator. The effectiveness of this feedback control system is monitored by the non contact Fotonic Sensor. According to Lyapunov control law, the effective control parameter is the tip angular velocity, so that if the sensing signal sensed

by this piezo film was differentiated by a differentiator, the tip angular velocity can be taken to be the control parameter. Applying this sensing voltage through the audio amplifier(Hafler 500) and charge amplifier (Kister 504E), the control voltage is achieved to suppress the vibration of the flexible structure.

6. TESTING RESULTS OF CANTILEVER BEAM

An impact force of 10 Newtons was applied to the 4th nodal point (40% length off the fixed end) of a cantilever beam. Since a constant impact force for each excitation was hard to be obtained, a computerscope package "WAVEPAK" was used to measure the magnitude of each impact. If the error is less then 2% of the standard one, then the test is acceptable.

Results indicate that the time to decay the tip displacement within a deadband with control voltage increased from 30 volts to 120 volts are about 75% , 60% , 50% , and 45% of uncontrolled system, respectively. Comparisons of numerical simulations and experimental testings are shown in Figure 3. It is in good agreement when V_{max} = 100 volts. The difference of decay envelopes between simulations and experimental results is due to the effect of air drag.

7. TESTING RESULTS OF A CANTILEVER PLATE

When no feedback voltage was applied, a plate oscillated with a very long decay time. For the same situation, except that a feedback control voltage with maximum value of 50 volts was applied to the system, vibrations of the plate were suddenly suppressed. By tracing the envelopes of various control voltages to form a family of decay envelopes, the control effectiveness of different control voltages could be evaluated. Tests with the bending angular velocity control showed that for V_{max} = 10, 30, 50 volts, decay times were shorten 30%, 45% , and 70% , respectively.

The comparison of simulated and experimental results is illustrated in Figure 4. In the experiment, air drag is included, but not in the numerical simulation. When the plate is uncontrolled, it decays sooner than that predicted numerically. On the other hand, due to imperfect bonding of the piezo film, control effectiveness for experiment is always poorer than that for simulation.

8. CONCLUDING REMARKS

Numerical simulations show a dramatic improvement of the intelligent system using the Lyapunov control law when control voltages are increased from 0 to 1000 volts. Based on the same control algorithm, experimental results are less effective but in agreement with those from numerical simulations. Some discrepancies for controlled and uncontrolled cases need further investigation.

For effective vibration control of cantilever beams and plates, the angular velocity at the tip of the free end is proven to be a suitable feedback control parameter. Damping analysis of smart materials through the modal testing provides essential material characteristics for active vibration control analysis.

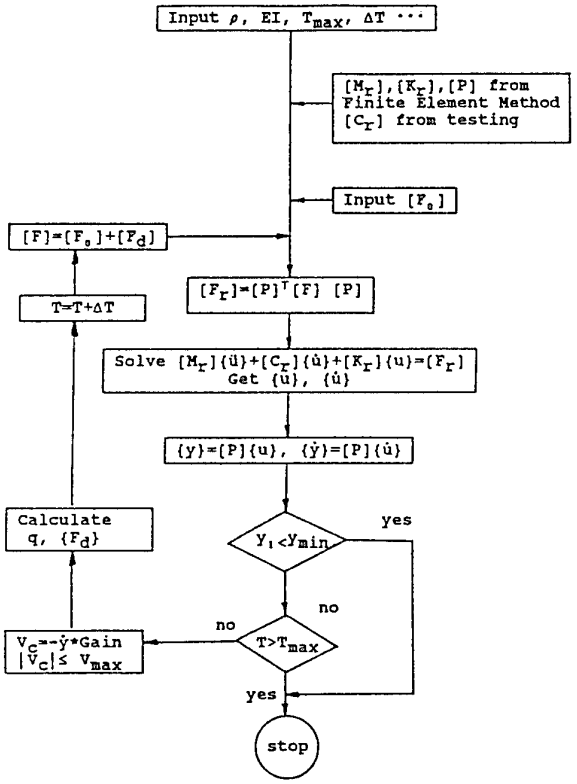

Figure 1 Flow Diagram for Computer Simulation

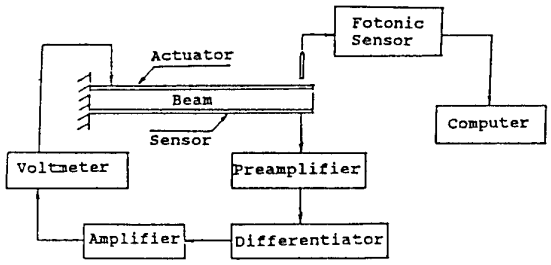

Figure 2 Schematic of the Experimental Setup

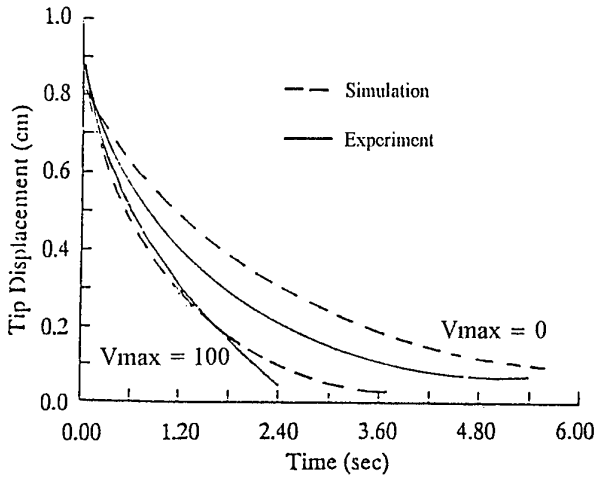

Figure 3 Comparison for a Cantilever Beam with Lyapunov Control

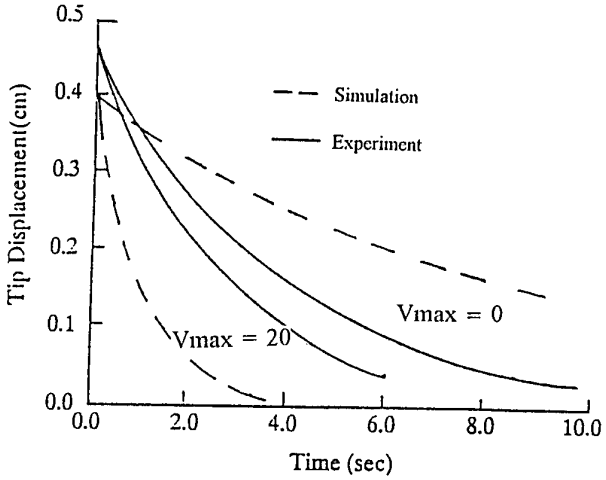

Figure 4 Comparison for a Cantilever Plate with Bending Angular Velocity Control

Efficient Use of Induced Strain Actuators in Aeroelastic Active Control

Victor Giurgiutiu*, Zaffir Chaudhry**, Craig A. Rogers***
Virginia Polytechnic Institute and State University,
Blacksburg, VA 24061-0261, USA

Efficient Static Design

Consider a stacked actuator of nominal (free-stroke) displacement u_{ISA}, and internal stiffness k_i. During static operation, the total induced energy, E_{ISA}, gets divided between the internal and external subsystems: part of it, E_e, is transmitted to the external application, while the rest, E_i, remains stored in the internal compressibility of the stack. The value of E_{ISA}, and its repartition between E_e and E_i, depends on the stiffness ratio $r = k_e/k_i$. It can be easily shown (Giurgiutiu, Chaudhry, and Rogers, 1993) that

$$E_{ISA}(r)=\frac{r}{1+r}E_{ref},\quad E_e(r)=\frac{r}{(1+r)^2}E_{ref},\quad E_i(r)=\frac{r^2}{(1+r)^2}E_{ref},\quad E_{ref}=\frac{1}{2}k_i\cdot u_{ISA}^2 \tag{1}$$

Dividing through by E_{ref} yields the non-dimensional energy coefficients $E'_{ISA}(r)$, $E_e'(r)$, $E_i'(r)$. Figure 1a (Giurgiutiu, Chaudhry, and Rogers, 1994a) shows their variation with the stiffness ratio, r. It can be seen that the externally delivered energy, E_e', reaches a maximum at $r = 1$. Figure 1b shows the variation of the energy transmission efficiency $\eta(r)$ with the stiffness ratio r. At the stiffness-match point, the energy transmission efficiency is only 50%. Figure 1b also illustrates another important concept, *viz.* that of *conjugate stiffness ratios*. Consider $r_1 = 1/4$ and $r_2 = 4$. The corresponding external energy delivery is, in both cases, the same: $E(r_1) = E(r_2) = 0.16E_{ref}$. But the energy transmission efficiency is widely different, *viz.* $\eta(r_1) = 80\%$ while $\eta(r_2) = 20\%$. The *soft* design ($r_1 = 1/4$) is 4 times more efficient than the *stiff* design ($r_2 = 4$). Under static conditions, the best use of an actuator is made when the internal and external stiffness are matched. The maximum attainable energy delivery is $(E_e)_{\max}=\frac{1}{4}E_{ref}$. If stiffness match cannot be ensured, a "soft" design ($r < 1$), will always be more efficient than a "stiff" design ($r > 1$).

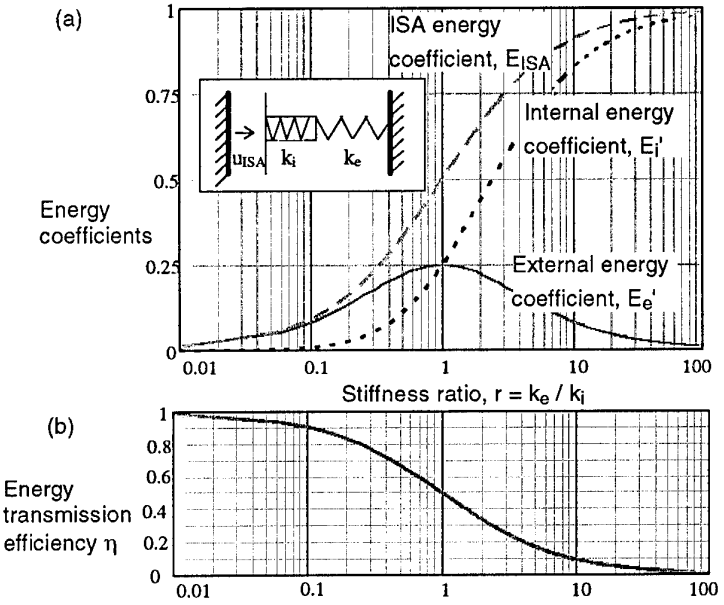

Figure 1 Variation of energy coefficients and energy transmission efficiency with stiffness ratio, r, under static operation.

Efficient Dynamic Design

Figure 2 presents an ISA stack coupled with a external dynamic system consisting of mass, spring and damper. In aero-servo-elastic control, the mass, spring and damper values vary with the operating frequency, and also with airspeed and length scale. For the present exploratory study, constant mass, spring and damper values are considered. Hence, the equivalent dynamic stiffness can be written as: $\bar{k}_e(\omega) = (-\omega^2 m_e + i\omega c_e + k_e)$ Assuming the natural frequency of the external system as ω_0, one expresses the complex dynamic stiffness as:

---

*Visiting Professor, *Engineering Science and Mechanics Department*, Member AIAA, AHS, RAeS
**Research Scientist, *Center for Intelligent Material Systems and Structures* Member AIAA, ASME
***Professor, *Director of the Center for Intelligent Material Systems and Structures* Member AIAA, ASME *

0-8194-1700-9/94/$6.00

$$\bar{k}_e(\omega) = [1-(\frac{\omega}{\omega_0})^2 + i\,2\zeta(\frac{\omega}{\omega_0})]\,k_e = [(1 - p^2) + i\,2\zeta p]\,k_e\,, \tag{2}$$

where $p = \omega/\omega_0$ is the frequency ratio, and ζ is the internal damping of the external system. The *real* and *imaginary* parts of the complex dynamic stiffness signify in-phase and out-of-phase force reactions. At low frequency ($p \rightarrow 0$), the inertial and damping terms in the dynamic stiffness expression vanish, and the static stiffness k_e is predominant. This is the *quasi-static dynamic* operation. At higher frequencies, but still below external resonance ($0 < p < 1$), the effective stiffness is reduced by $(1 - p^2)$, while the dissipative (out-of-phase) component grows as $2\zeta p$. As the mechanical resonance is approached ($p \rightarrow 1$), the reactive inertial forces balance the reactive elastic forces, and hence the real part of the dynamic stiffness vanishes. At resonance ($p = 1$), only the imaginary part of the dynamic stiffness is non-zero i.e., dissipative forces are predominant. Above resonance ($p > 1$), the inertial forces dominate, and stiffness magnitude increases parabolically. A phase shift of 90° is recorded at resonance, and an overall phase shift of 180° takes place as the operating point passes from sub-resonance into post-resonance. Using the complex dynamic stiffness, Giurgiutiu, Chaudhry, and Rogers, 1994b defined the *dynamic stiffness ratio*, $\bar{r}(\omega) = \bar{k}_e(\omega)/\bar{k}_i$, $\bar{k}_i = k_i(1+\eta)$. The dynamic stiffness ratio is a frequency dependent complex quantity.

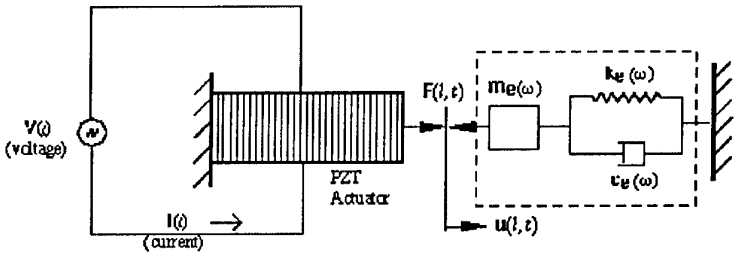

Figure 2 The dynamic ISA system (after Liang, Sun, and Rogers, 1993)

The ISA is driven by alternating voltage, $V(t)$, and current, $I(t)$, which induce an alternatively varying strain. The resulting dynamic displacement, $u(x, t; \omega)$ varies with time and position. Neglecting wave propagation effects inside the stack yields a linear variation of the displacement along the stack length. Displacement compatibility and force balance between the stack and the external mechanical impedance are imposed at $x = l$. The dynamic displacement expression takes the form (Giurgiutiu, Chaudhry, and Rogers, 1994b):

$$\hat{u}(x,t;\omega) = \frac{1}{1 + \bar{r}(\omega)}\frac{x}{l}\,\hat{u}_{ISA}\sin\omega t\,. \tag{3}$$

where $\hat{u}$ signifies motion amplitude, and $\hat{u}_{ISA}$ is the free-stroke amplitude. At the interface between the internal and external systems, we obtain the external displacement:

$$u_e(t;\omega) = \bar{u}_e\sin\omega t = \frac{1}{1 + \bar{r}(\omega)}\,\hat{u}_{ISA}\sin\omega t, \quad \bar{u}_e = \frac{1}{1 + \bar{r}(\omega)}\,\hat{u}_{ISA}\,. \tag{4}$$

where $\bar{u}$ signifies complex motion amplitude. Using the *dynamic stiffness* concept we extend the *stiffness match* concept from static analysis into dynamic analysis. The dynamic stiffness concept allows direct analytical continuation between the static and dynamic regimes. To get an incremental understanding of the salient points, three situations will be progressively considered: (a) the quasi-static dynamic operation; (b) the undamped dynamic operation; and (c) the damped dynamic operation.

Quasi-static Dynamic Operation

Under quasi-static dynamic operation, damping and inertial effects are neglected ($\bar{k}_e(\omega) = k_e$). Hence, no phase shift occurs, and all displacement and force amplitudes are real:

$$u_{ISA}(t) = \hat{u}_{ISA}\sin\omega t, \quad u_e(t) = \hat{u}_e\sin\omega t, \quad u_i(t) = \hat{u}_i\sin\omega t, \quad F(t) = k_e\hat{u}_e(t) \tag{3}$$

The energy principles developed for static operation are directly translated into power principles. Use instantaneous power expression $P(t) = F(t)\cdot\dot{u}(t) = \hat{P}\sin 2\omega t$, $\hat{P} = \frac{1}{2}\hat{F}\cdot\hat{\dot{u}}$, to get:

$$\hat{P}_{ISA}(r)=\frac{r}{1+r}P_{ref},\quad \hat{P}_e(r)=\frac{r}{(1+r)^2}P_{ref},$$
$$\hat{P}_i(r)=\frac{r^2}{(1+r)^2}\hat{P}_{ref},\quad P_{ref}=\omega E_{ref}=\omega\frac{1}{2}k_i u_{ISA}^2 \qquad (6)$$

A plot of these expressions *vs* stiffness ratio, *r*, is given in Figure 3. The plot closely resembles that of Figure 1, only that instead of energy coefficients we have power coefficients. For quasi-static dynamic operation, the maximum power delivery from an ISA device is achieved when the internal and external stiffness are matched. Under quasi-static dynamic operation, the *static stiffness match principle* still applies.

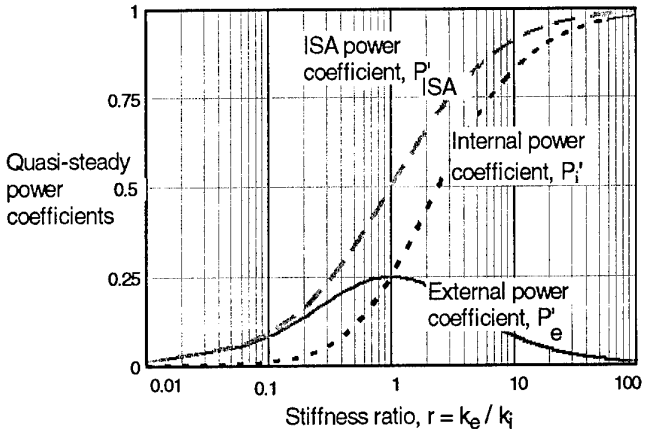

Figure 3 Quasi-steady power variation with static stiffness ratio

Undamped Dynamic Operation

Many dynamic utilizations of ISA technology do not take place under quasi-static conditions. For mechanical resonances in the 10 to 50 Hz frequency range, inertial forces cannot be neglected. As the mechanical resonance of the external system is approached, the reactive inertial forces are subtracted from the reactive elastic forces, and the effective stiffness ratio is modified. A system with statically matched stiffness will not retain its optimal condition under full dynamic operation. This is illustrated in Figure 4. For a statically matched system, the external power coefficient at p = 0 (quasi-static operation) is optimum, i.e. it has the maximum possible value, 0.25. As the frequency increases, its power coefficient decreases. At p = 1 (i.e. at external resonance), the power coefficient becomes zero. This behavior is expected, since the equivalent dynamic stiffness of the external system decreases with frequency and upsets the static stiffness match. At resonance, the equivalent dynamic stiffness is virtually zero, hence no force is transmitted, and thus no power. For a soft external system (r = 1/ 4), a similar behavior is observed. The starting point at $p = 0$ (quasi-static conditions) is lower, since the unmatched static stiffness gives less than optimal quasi-static behavior. For the conjugate stiff system (r = 4), the behavior is entirely different. Under quasi-static conditions, the power coefficient of the conjugate stiff and soft systems was the same. As frequency increases, the stiff system drastically departs from the soft system. Its power coefficient increases, while that of the soft system decreases. This behavior is explained by the *dynamic softening* of the stiff system. As frequency increases, its stiffness decreases towards that of the internal system. When the external dynamic stiffness equals the internal stiffness, *dynamic stiffness match* is attained. The frequency value at which dynamic stiffness match occurs is given by

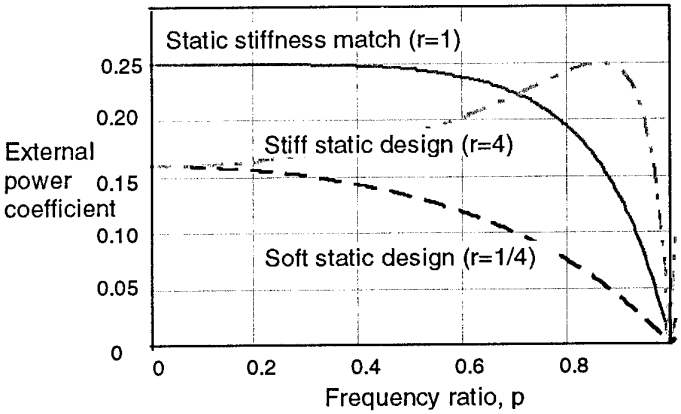

Figure 4 External power coefficient *vs* frequency ratio for an undamped dynamic system.

$$p_{match}(r)=\sqrt{1-(1/r)}\,. \qquad (7)$$

Figure 5 shows the variation of the dynamic stiffness match frequency with static stiffness ratio. For large static stiffness ratios, the dynamic stiffness match frequency approaches asymptotically the value 1. For moderate static stiffness ratios, values between 0 and 1 are obtained. For example, for a static stiffness ratio r = 4, the dynamic stiffness match takes place at $p_{match}(4) = \sqrt{3}/2 = 0.866$. This value corresponds to the local maximum of the power coefficient, as show in Figure 4.

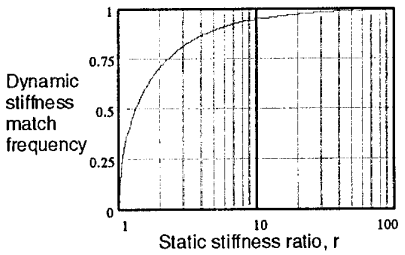

Figure 5 Dynamic stiffness match frequency *vs.* static stiffness ratio

The dynamic stiffness match principle is a powerful design tool. Depending on the type of design, either the static stiffness ratio, or the operating

frequency ratio can be modified to yield an operating point as close as possible to the optimum condition. Adequate use of the dynamic stiffness match principle in ISA systems design can yield significant weight savings and increased performance.

The Damped Dynamic System

For a system that presents internal and external losses, the dynamic stiffness is a complex quantity with real and imaginary components. The dynamic stiffness match principle has to take into account the additional aspects of complex power analysis. We define:

$$\overline{P}_e = \frac{1}{2}\overline{F}\cdot\overline{\dot{u}}_e, \quad \overline{F} = -\overline{k}_e\cdot\overline{u}_e, \quad \overline{\dot{u}}_e = i\omega\cdot\overline{u}_e,$$

$$P_{rating} = \left|\overline{P}_e\right|, \quad \cos\varphi = \arg(\overline{P}_e), \quad P_{av} = \left|\overline{P}_e\right|\cdot\cos\varphi \qquad (8)$$

The complex power $\overline{P}$ varies with the frequency parameter p, and the static stiffness ratio, r, as:

$$\overline{P}(r,p) = -i\frac{\overline{r}(r,p)}{\left[1+\overline{r}(r,p)\right]^2}P_{ref} \qquad (9)$$

Figure 6 presents the variation of power rating with frequency. It can be seen that, as expected, the statically matched system, and the soft system, display a decrease in power rating with frequency. The power rating of the stiff system increases until the dynamic stiffness match is attained; then it starts to decrease. These trends are consistent with the behavior displayed by the undamped system (Figure 5). An aspect specific to the damped system is the power dissipation factor, cosϕ (Figure 7). For a statically matched system, the power dissipation factor is positive (cosϕ > 0) and increases with frequency, as expected. Similar behavior is displayed by the soft system. The stiff system presents an unexpected behavior: below dynamic stiffness match, its power dissipation factor is negative (cosϕ < 0). Further aspects of this remarkable phenomenon are presented in Figure 8. As the external damping is increased from ζ = 5% to ζ = 10%, the amplitude of the negative power dissipation factor increases as well. Increasing the internal damping from η = 0 to η = 3% has an opposite effect, and decreases the negative power dissipation factor. Further investigation into this possible feed-back instability phenomenon, accompanied by experimental tests, are required.

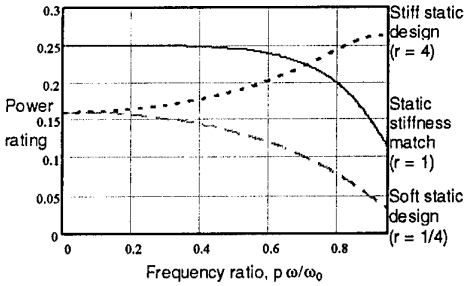

Figure 6 Variation of power rating with frequency ratio (ζ = 5%, η = 0).

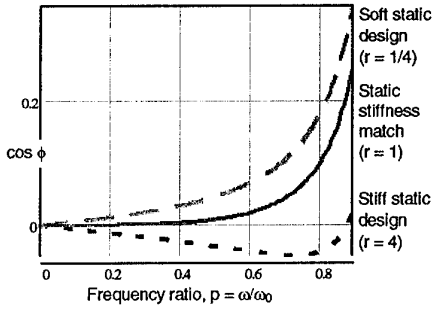

Figure 7 Cosϕ variation with frequency ratio for three stiffness ratios (ζ = 5%, η = 0)

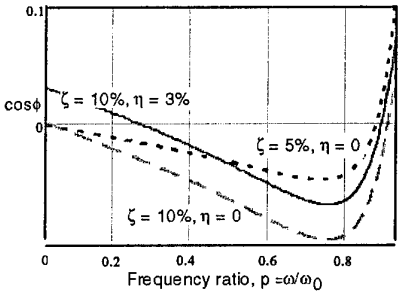

Figure 8 Variation of cosϕ with frequency for a stiff static design (*r* =4)

Acknowledgments

Army Research Office University Research Initiative Program, Grant No. DAAL03-92-G-0181, Dr. Gary Anderson, Program Manager.

Bibliography

Giurgiutiu, V., Z. Chaudhry, and C. A. Rogers, 1993, "The Use of Induced Strain Actuators for Rotor Blade Active Vibration Control", CIMSS Report #93-AVC-002, Center for Intelligent Material Systems and Structures, Virginia Polytechnic Institute and State University, Blacksburg VA 24061-0261, Dec. 1993.

Giurgiutiu, V., Z. Chaudhry, and C.A. Rogers, 1994a, "Engineering Feasibility of Induced-Strain Actuators for Rotor Blade Active Vibration Control", *1994 North American Conference on Smart Structures and Materials*, Orlando, FL, 13-18 February 1994 (in press).

Giurgiutiu, V., Z. Chaudhry, and C.A. Rogers, 1994b, "The Analysis of Power Delivery Capability of Induced Strain Actuators for Dynamic Applications", *ICIM'94, 2nd International Conference on Intelligent Materials*, Technomic Pub. Co., 1994, pp. 565-576.

Liang, C., F. P. Sun, and C.A. Rogers, 1993, "An Impedance Method for Dynamic Analysis of Active Material Systems", *34th AIAA/ASME/ASCE/AHS/ASC Structures, Structural Dynamics, and Materials Conference,* Hyatt Regency, LaJolla, CA, April 19-22, 1993, pp. 3587-3599.

SMART STRUCTURE APPLICATION FOR THE CHALLENGER AIRCRAFT

Capt. L. Grenier, National Defence Headquarters, Ottawa, Canada
F.A. Blaha, Canadian Marconi Company, Montreal, Canada

ABSTRACT

The Challenger aircraft fleet of the Canadian Forces will fly demanding missions, requiring the implementation of a fatigue management program based on the monitoring of in-flight aircraft load conditions. Conventional sensing techniques experience problems arising from severe electromagnetic interference (EMI). This paper describes the development of an EMI-insensitive smart-structure sensing concept for loads monitoring. Fiber-optic strain sensors, incorporated at critical structural locations, are used to monitor the fatigue life of the aircraft wing, fuselage, and empennage. A fiber-optic accelerometer is also incorporated in the system. A long-term plan is presented for the development of an advanced smart-structure concept which can support the continuous monitoring of fatigue-prone components, and provide the aircraft with near real-time damage location and assessment.

1. INTRODUCTION

The Canadian Forces operate a fleet of 15 Challenger CL-600 aircraft, of which ten fly in an environment exceeding the original mission profile. Fatigue inspection intervals for all structurally significant items have therefore been reduced in order to ensure continued airworthiness. To compensate for uncertainties in the analytical models, conservative assumptions are made in deriving these inspection intervals; this has a heavy impact on life-cycle costs.

As a partial solution to this problem, operational load conditions of individual aircraft are tracked[1]. The Aircraft Structural Integrity Program (ASIP), which is based on this concept, currently faces two main challenges. Its electronic sensors have limited performance and reliability, are difficult to install, and require lengthy and costly EMI/EMC qualification tests. In addition, many months typically elapse between the acquisition of in-flight data and subsequent data processing/interpretation.

Fiber-optic sensing and real-time on-board health monitoring techniques employing smart- structure technology[2] are expected to eliminate these problems, and will therefore be adopted for the CL-600 loads monitoring system. While full-scale implementation is the long-term goal, partial implementation is being performed as an interim solution. For this program to succeed, development and implementation costs must be offset by significant life-cycle cost reductions.[3]

2. BACKGROUND

The CL-600 Challenger is designed for an economic life of 30,000 hours. Fatigue monitoring is performed through measurement of airspeed, pressure altitude, roll rate, and vertical acceleration; strain measurement at six control points (two each on wing, empennage and fuselage) on the Challenger's primary structure; and measurement of discrete parameters including flap settings and main landing gear retractions. In view of the limited number of representative control points, extensive fatigue computations must be performed in order to derive fatigue indices for all structurally significant elements.

3. LONG-TERM SMART STRUCTURE APPROACH

3.1 System and Smart Structure Requirement

In the new maintenance concept, structural maintenance and repair is performed only as required, not as dictated by life-expectancy models based on individual aircraft tracking and scheduled non-destructive tests. The system must incorporate on-board signal processing to provide a near-real-time assessment of the airworthiness of the aircraft structure, and if necessary to warn the pilot and recommend restrictions of the flight regime;

0-8194-1700-9/94/$6.00

recommendations for required repairs, with an indication of accumulated damage at all critical locations, should be immediately available to ground and maintenance personnel.

For the realization of the proposed structural health monitoring concept, critical strain-sensor locations are classified on the basis of damage tolerance analysis[4] (DTA) and natural crack growth observed during full-scale fatigue testing[5]. For the full-scale implementation, 243 such locations have been selected: 211 on the basis of DTA, and 32 based on natural crack growth. To facilitate data management and interpretation, the airframe's structural components are grouped in a hierarchical fashion in which the top level comprises the six primary structures of the complete airframe: fuselage, wing, empennage, control surfaces, landing gear, and engine structure (Table 1). Table 2 lists the guidelines adopted for selecting fiber-optic strain and acceleration sensors and systems.

Table 1. Test Point Requirements

Description	No. of Groups	No. of Zones	No. of Analysis Points	Full-Scale Test Points	No. of Test Points, Full-Scale System	No. of Test Points, Near-Term Approach
Fuselage	4	21	58	14	72	14
Wing	6	31	77	18	95	20
Empennage	2	7	21	0	21	2
Control Surfaces	9	8	18	0	8	0
Landing Gear	2	5	3	0	13	0
Engine Structure	3	12	34	0	34	0
Complete Airframe	26	84	211	32	243	36

Table 2. Sensor and System Target Specifications

Strain Sensors	Acceleration Sensor	Sensor System
Local and uniaxial strain measurement Temperature-compensated to host Maximum strain level ±10,000 με Sensitivity 25 με Bandwidth 15 Hz MTBF 30,000 hours (economic life) Operating temperature -50 to +125°C	Range -1.5 to 3 g Accuracy 0.1 g Bandwidth 5 Hz	- Standard multi- or single-mode connectors and fibres - Performance undegraded by fibers up to 100 m long - Costs comparable to conventional sensors and systems

The complexity of the sensor array poses a challenge for data processing and interpretation. Expert systems and artificial neural network technologies are being considered for on-board and in-flight data processing.

For unanticipated structural damage assessment, continuous acoustic emission monitoring will be implemented[6].

All 243 strain signals are monitored at once when triggered by limit signals of vertical acceleration and airspeed. Unlike current operational loads monitoring systems, in-flight stress and vertical acceleration exceedances are computed, crack growth curves are generated and compared against baseline curves, and damage indices (or inspection interval factors) are stored on the aircraft for each component.

3.2 Smart Structure Development Plan

In order to reduce technological risk, satisfy immediate needs, and meet the long-term objective of on-line structural health monitoring, an incremental development plan has been adopted which incorporates the following critical steps and milestones:

- assessment of the analytical model limitations, using at least one year of loads monitoring data
- qualification of the fiber-optic strain sensing technology (an extensive test program has been started)
- implementation of the near-term loads monitoring concept, as a developmental milestone
- verification of costs/benefits, taking into account factors such as fewer inspections, timely repairs, acquisition cost and reliability.

4. NEAR-TERM SMART STRUCTURE IMPLEMENTATION

In the near term, a more extensive fiber-optic sensor network will replace its conventional counterpart in the operational loads monitoring system. This network is compared to a conventional system in Table 3. For purposes of redundancy, each sensor location has duplicate FO sensors installed.

Significant benefits of the smart structures approach are anticipated, even at the interim stage of development. These include improved reliability of the loads monitoring system and a more realistic prediction of required inspection intervals, with associated reductions in aircraft downtime and life-cycle costs.

Table 3. Comparison of Fiber-Optic and Conventional Sensor Systems

		NUMBER OF SENSOR LOCATIONS	
Sensor Type	Location	FO Sensor System	Conventional System
Strain Sensors	Left wing	2	0
	Right wing	18	2
	Forward fuselage	10	1
	Center fuselage	2	0
	Rear fuselage	2	1
	Empennage	2	2
	Subtotal	36	6
Vertical Acceleration		1	1
Rate of Roll		0	1
Airspeed		1	1
Barometric Altitude		1	1

5. FIBER-OPTIC STRAIN SENSORS AND SYSTEMS

5.1 Fiber-Optic Strain Sensor

An external-cavity fiber-optic sensor (EFOS) has been selected for this application as the candidate capable of meeting the requirements of Table 2. The EFOS's intensity-modulated concept is illustrated in Figure 2. The single-mode fiber of the sensor has a bandpass filter deposited at its end surface to form one side of the sensing cavity. The other side is formed by a mirror on a short auxiliary fiber. The return light of the sensor is thus divided into two parts: I_r is the light reflected by the bandpass filter, and I_t the light transmitted through the filter and reflected by the end mirror. I_t is a near-linear function of cavity length, D, and I_r provides self-referencing. Length, L_T, and the temperature coefficient of the mirrored end fiber can be selected to match the temperature coefficient of the host material. Key features of this EFOS include relatively modest system requirements, coupled with the ability to provide temperature compensation and polarization-independence.

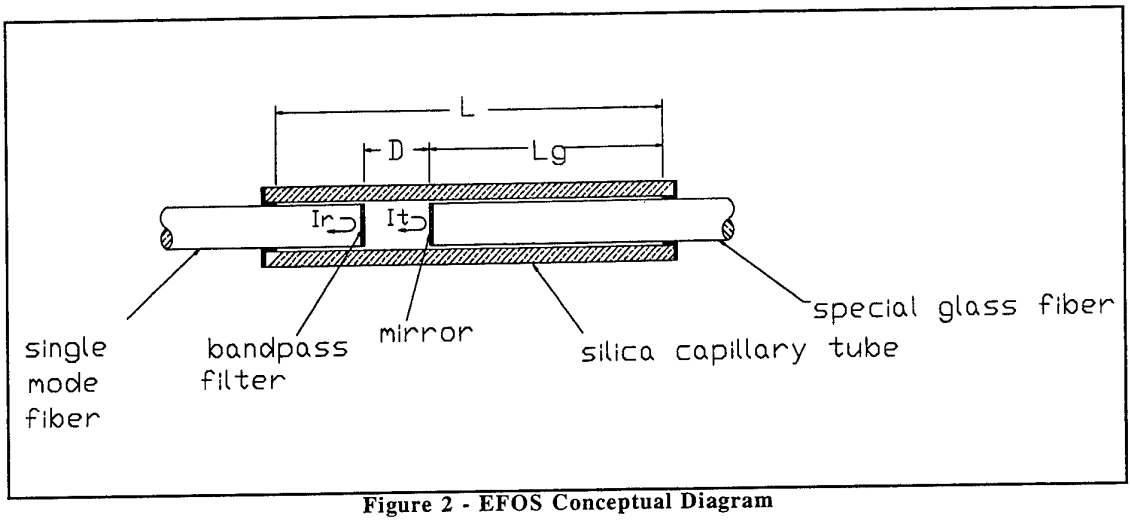

Figure 2 - EFOS Conceptual Diagram

5.2 Integrated-Optic Acceleration Sensor

A glass integrated-optic (IO) acceleration sensor employing a Mach-Zehnder interferometer as the sensing element (Figure 3) is being evaluated for this application.

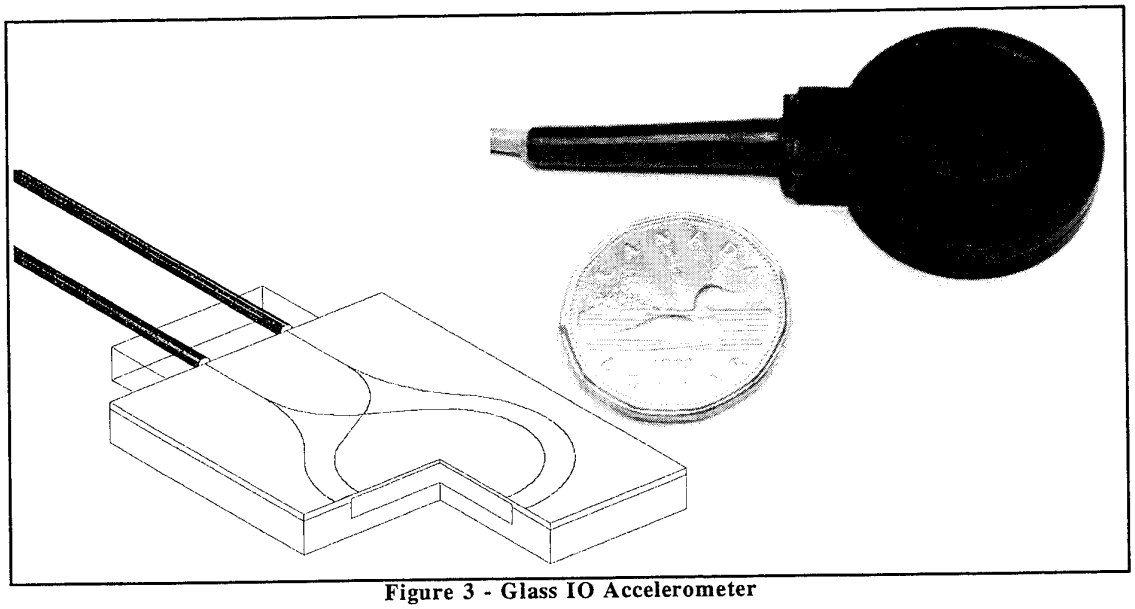

Figure 3 - Glass IO Accelerometer

5.3 Fiber-Optic Strain Sensor System

The light source employed in the system is an LED with a relatively broad emission spectrum (typically 50 nm, centered at 1300 nm). The return signal from the sensor is split to meet two detectors, one of them via a bandpass filter identical to the one in the sensor. The optical power ratio of the two detectors is a function of the sensor airgap length, D, and is independent of losses in the transmission line, splices or connectors.

A four-channel system is currently available on a single printed circuit board (Figure 4); a board which can accommodate eight channels is under development. Five of these cards will be housed in the system unit, providing 40 channels for the interim configuration of 36 sensors. A time division multiplexing concept will be implemented in the full-scale system.

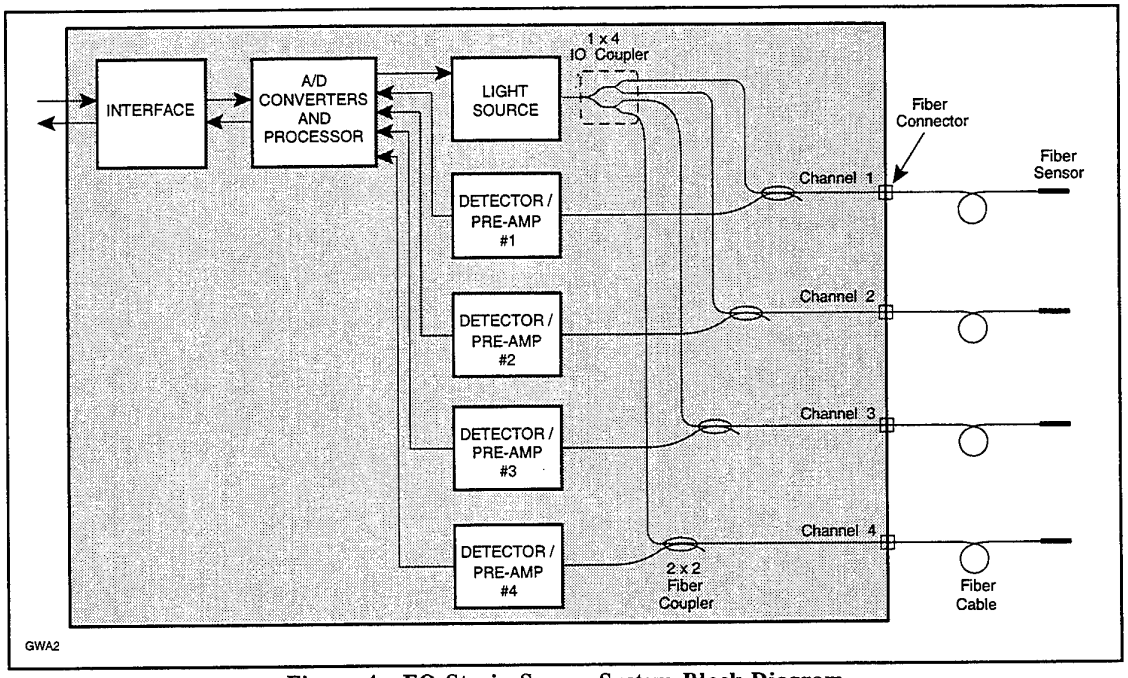

Figure 4 - FO Strain Sensor System Block Diagram

6. CONCLUSIONS

Fatigue management currently relies on extensive post-data analysis; this will change radically with the introduction of smart structures. Structural maintenance and repair will be performed on an as-required basis, and not as dictated by life expectancy models. The timeframe for the implementation of these new fatigue management concepts will depend on the availability of proven, cost-effective, large-scale sensor networks and associated data processing systems.

7. ACKNOWLEDGEMENTS

The authors wish to express their appreciation to the Department of Defence for permission to present this paper. The editorial assistance of Andrew Solkin of Canadian Marconi Company is also gratefully acknowledged.

8. REFERENCES

1. Agnes, G.S. and Silva, K., "Aircraft Smart Structures Research in the USAF Wright Laboratory", *75th Meeting of the AGARD Structures and Materials Panel*, Lindau, Germany, October, 1992.
2. Blaha, F.A. and McBride, S.L, "Fiber-Optic Sensor Systems for Measuring Strain and the Detection of Acoustic Emissions in Smart Structures", *75th Meeting of the AGARD Structures and Materials Panel*, Lindau, Germany, October, 1992.
3. Schmidt, W. and Boller, C., "Smart Structures - a Technology for Next Generation Aircraft", *75th Meeting of the AGARD Structures and Materials Panel*, Lindau, Germany, October, 1992.
4. *CC-144 Strength Summary - CL-600 Model*, Canadair Report RAS-600-802,, October 1990.
5. *CC-144 Force Structural Maintenance Plan*, Canadair Report RAS-601-910, March 1993.
6. McBride, S.L. et al, "Acoustic Emission Monitoring of Aging Aircraft Structures", *Review of Progress in Quantitative Non-Destructive Evaluation*, Vol. 11, pp. 2275-82, 1992.

Remotely interrogated sensor electronics (RISE) for smart structures applications

W.B. Spillman Jr.
S. Durkee
W.W. Kuhns
BFGoodrich Aerospace
Simmonds Precision Aircraft Systems
Vergennes, Vermont 05491

ABSTRACT

Smart structures research has focussed upon the many different subsystems making up the smart structure with the exception of the power/communication interface. In the case of embedded fiber optic sensors, an acceptable solution has yet to be found. A preferred solution would not involve physical interconnection between the power/interrogation subsystem and any embedded electronics. One method which offers promise to provide this solution is based upon inductive coupling between a surface mounted interrogation coil and an embedded coil connected to some local system. In this paper, a description of such a system is provided detailing its basic operating principles, the design/performance of a pc based demonstration system, results from sensors embedded in composite coupons and a discussion of how the system may properly be called a smart subsystem.

The field of smart structures has rapidly expanded over the past few years [1-7]. In this expansion, it has incorporated segments of the fields of robotics, artificial intelligence, adaptive control, engineered/adaptive materials, and others in a form of synthesis. Because it contains so many different aspects, it has been difficult to agree on a precise definition of a smart structure. Most workers in the field would agree, however, that a smart structure would contain some kind of structural element, some method of receiving information that is important for the structure to meet its design requirements, some method of processing that information and some method of reacting internally and/or externally in an adaptive fashion to that information. In this paper, as a working definition, we will utilize the definition of a smart structure that we have previously put forward [8], i.e. a smart structure is a non-biological physical system having (1) a definite purpose, (2) means and imperative to achieve that purpose, and (3) the pattern of functioning of a Turing machine (universal computer).

In the development of smart structures technology, one of the recognized needs is some method of interrogating/powering electronic or opto-electronic systems embedded within structures without having a physical interconnection. Such a system has recently been developed that relies upon inductive coupling [9] to non-invasively interrogate embedded off-the-shelf electrical sensors such as resistive strain gauges, capacitive fluid level sensors or inductive displacement sensors. A modified system has also been used to remotely power and interrogate a fiber optic sensor [10]. In this paper, the performance of this remotely interrogated sensor electronics (RISE) system with embedded semi-conductor strain gauges in glass epoxy and Kevlar composite coupons is presented along with details of the system.

The non-contact sensor interrogation concept, as shown in Figure 1, involves the use of inductive coupling to transfer both electrical power and information. An interrogation coil on the surface of the structure generates an ac magnetic field that couples to an embedded circuit consisting of a matching inductive coil, a capacitor and a resistor connected in series in a simple LRC configuration. The sensor may be any one of these electrical elements. Information from the sensor is obtained by monitoring the loading of the interrogation circuit. This particular configuration is that of a transformer and can be modeled using standard electrical engineering techniques, with the result that the voltage measured across the load resistor in the interrogation circuit is given by

$$V(\omega) = \frac{V_0(\omega)\, R_L}{R_L + j\omega L_p + \dfrac{\omega^2 K^2 L_p L_s [R - j(\omega L_s - \frac{1}{\omega C})]}{R^2 + (\omega L_s - \frac{1}{\omega C})^2}} \qquad (1)$$

0-8194-1700-9/94/$6.00

There are two unknowns in Equation (1) when the measurement to be made is the determination of strain gauge resistance, i.e. the inductive coupling parameter, K, and the strain gauge resistance, R. All other parameters are known. A load resistance, R_L, is connected in series with the interrogation coil having inductance, L_p. The embedded circuit has a coil with inductance, L_s, a capacitance, C, and the unknown strain gauge resistance, R, connected in series. The inductive coupling parameter, K, maps in a one-to-one fashion to the axial coil separation, x. In principal, since there are two unknowns, measurement of the voltage across the load resistor in the interrogation circuit at two different frequencies should allow K (or x) and R to be determined. The non-linear nature of Equation (1), however, makes unambiguous determination of these parameters difficult. This is primarily true if resistance is the unknown. If the sensor is inductive or capacitive, measurement of the resonance frequency of the circuit is sufficient to determine the value of the unknown parameter, as can be seen from an examination of Equation (1).

The basic interrogation technique was incorporated into a proof-of-concept demonstration system to interrogate strain gauge resistance. In the system, an initial measurement of voltage at low frequency was made. This measurement was used as the input for a neural processing algorithm that determined relative coil separation. The output from the first net was used as input for a second net that determined the frequency of a second voltage measurement and an amplifier gain. The output from this net was used to control a custom electronics module that actually made the measurement at the specified frequency with the given gain. The frequency of the second voltage measurement along with its magnitude were then used as inputs to a final neural net that determined the unknown strain gauge resistance. The custom electronics module was designed to operate under software control from a standard laptop PC computer and to be able to make measurements of the voltage on the load resistance of the interrogation circuit at any frequency and gain. The software architecture was implemented in the C programming language on a VAX/VMS system, then ported to the laptop DOS computer. The software consists of data structures, neural net processing functions, hardware control functions, and an executive that supplies the logic to accomplish the desired objectives. A menu and real-time bar graph allow the user to control the system and provide visual display of measured parameters. This implementation provides continuous display of strain gauge resistance as long as coil separation is consistent and within range. If the user moves the external coil, the software enters a loop where it continues to measure coil separation until it becomes stable again.

The basic system was used to interrogate resonant circuits having semiconductor strain gauges as the sensor embedded within glass epoxy and Kevlar epoxy test coupons. A number of coupons were fabricated and all embedded circuits survived the embedding and cure process. The coupons all had dimensions 30.5x5.3x0.4 cm with 16 plies each. The circuits were embedded between the 8th and 9th plies in each case, with the semiconductor strain gauges aligned parallel to the long axes of the coupons. The glass epoxy composite coupons were made using Cycom 59-20 1583 woven glass while the Kevlar epoxy coupons used alternating 0^o- 90^o fabric plies. Both types of coupons were cured in a hot press at 125 C while being compressed by a force of ~$5x10^4$ newtons. Access to each strain gauge was also provided by a pair of wires allowing direct comparison of inferred resistance (strain) vs actual resistance (strain). Following cure, the coupons were subjected to tension in a Dillon tensile tester with the tension applied along the long axes of the coupons in every case. Figure 2 shows a comparison of the voltage measured by the RISE system at the optimal frequency for a glass epoxy coupon vs the actual resistance values for an excursion up and down in tensile stress. A small hysteresis is observed that is due to strain relaxation during the time period between the measurement of voltage and the direct measurement of resistance. Figure 3 shows inferred and actual strains as a function of stress for a glass epoxy coupon while Figure 4 presents a plot of inferred strain vs actual strain for the same coupon. The inferred values for strain in each case were generated by the best fit to the data in Figure 2 so that the errors are due to the relaxation effect already mentioned. Even with those errors, however, average error in inferred strain was found to be ±1.7% of range while the maximum error was found to be ±2.8% of range, which is comparable to the strain gauge accuracy quoted by the manufacturer. Finally, a stress-strain curve for increasing tensile stress is shown for a Kevlar epoxy coupon in Figure 5. The interesting thing to note here is the large value of residual strain at zero stress due to the fabrication process.

In summary, the details of the design of a non-contact sensor interrogation system have been presented. The system is able to interrogate embedded electrical sensors, and in particular embedded resistive strain gauges. A prototype demonstration system that implemented a hierarchical processing architecture involving 3 neural networks and adaptive measurement was designed and fabricated. The system was then used to interrogate sensor circuits embedded in composite structures. The embedded sensor circuits were shown to be able to survive typical composite processing conditions and provide useful data concerning residual strains in structures. In terms of the smart structure definition presented, this particular system fits very well in that the system senses the environment via a

voltage measurement at low frequency, determines whether or not a sensing circuit is present, adaptively interrogates the circuit if it is present, and then repeats the process. The RISE system represents one technique that offers promise for incorporation into larger smart structures as part of subsystems for structural health monitoring and maintenance.

References:

1. SPIE Vol. 986, Proceedings of the Fiber Optic Smart Structures and Skins Conference, 1988.
2. SPIE Vol. 1170, Proceedings of the Fiber Optic Smart Structures and Skins Conference II, 1989.
3. SPIE Vol. 1370, Proceedings of the Fiber Optic Smart Structures and Skins Conference III, 1990.
4. SPIE Vol. 1588, Proceedings of the Fiber Optic Smart Structures and Skins Conference IV, 1991.
5. SPIE Vol. 1798, Proceedings of the Fiber Optic Smart Structures and Skins Conference V, 1992.
6. Proceedings of the 1st European Conference on Smart Structures and Materials, Glasgow, 1992.
7. Proceedings of the SPIE Smart Structures and Materials Conference '93, Albuquerque, 1993.
8. W.B. Spillman, Jr., "Instrumentation architecture development for smart structures", SPIE Vol. 1918, Proceedings of the Smart Sensing, Processing, and Instrumentation Session of the 1993 North American Conference on Smart Structures and Materials, pp. 165-171, 1993.
9. W.B. Spillman, Jr., et al, "Non-contact power/interrogation system for smart structures", to be published in SPIE Vol. 2191, Proceedings of the Smart Sensing, Processing, and Instrumentation Session of 1994 North American Conference on Smart Structures and Materials, Orlando, 1994.
10. M. de Vries et al, "Completely embedded fiber optic sensor", to be published in SPIE Vol. 2191, Proceedings of the Smart Sensing, Processing, and Instrumentation Session of 1994 North American Conference on Smart Structures and Materials, Orlando, 1994.

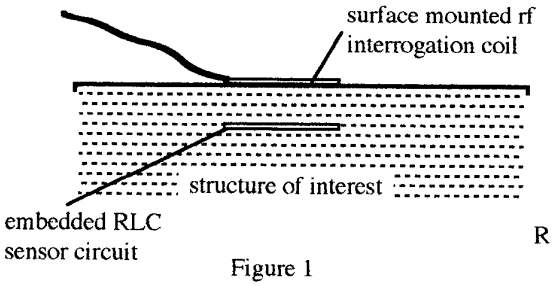

Figure 1

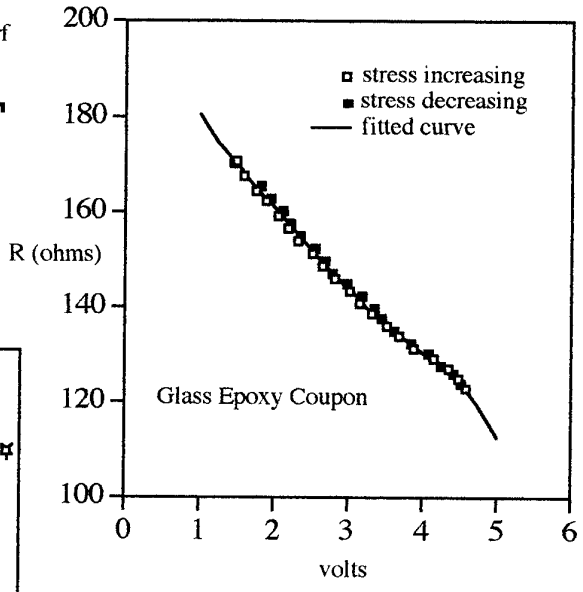

Figure 2

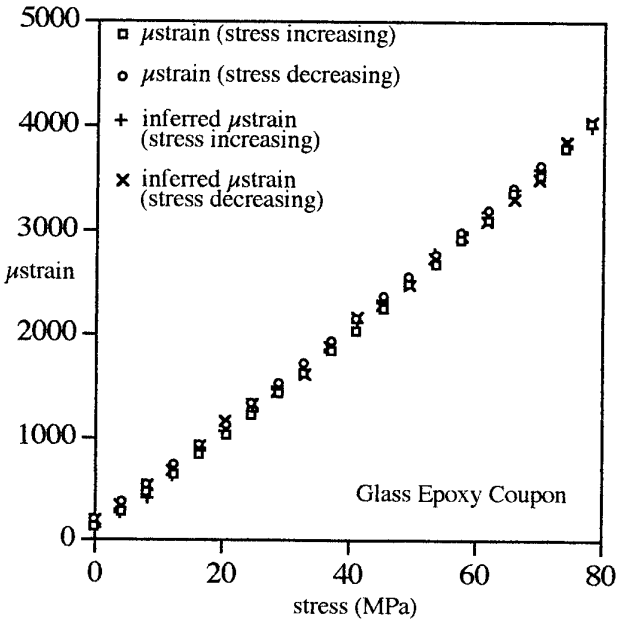

Figure 3

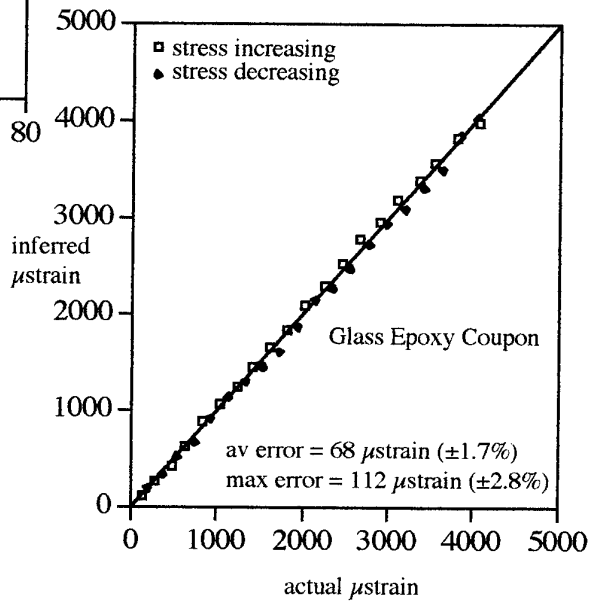

Figure 4

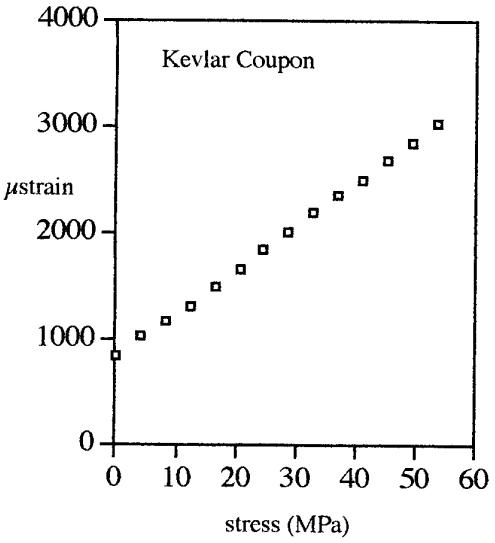

Figure 5

Paper presented at the Second European Conf. on Smart Structures and Materials, Glasgow 1994, Session 8

DYNAMIC LOAD MONITORING OF COMPOSITE STRUCTURES USING FIBER-OPTIC INTERFEROMETRIC STRAIN GAUGES

N. Fürstenau, W. Schmidt, D. Janzen, R. Schütze*, H. C. Goetting*

German Aerospace Research Establishment, Inst. f. Flight Guidance, *Inst. f. Structural Mechanics
Lilienthalplatz 7, D-38108 Braunschweig

Abstract

The performance of passive quadrature demodulated fiber-optic interferometric strain gauges is investigated, which are used for monitoring the strain on the surface of rods and plates made from Carbon fiber composites under dynamic load variations and in the presence of strong vibrations during flight tests.

Summary

A large number of fiber optic interferometric strain gauge concepts have been investigated during recent years (e.g. /1//2//3/), however very little experience exists up to now with respect to their practical applicability. In this paper we report the results of strain measurements using passive quadrature demodulated fiber-optic Michelson - interferometers surface adhered to CFRP plates and rods. Strain monitoring during quasistatic compression of a CFRP-rod in a load frame as well as in-flight optical strain measurements on a CFRP-plate, fixed to the main wing spar of a test aircraft serve for characterizing the sensor performance. The incremental fringe counting readout of the optical strain sensor (OSG) is compared to the strain indicated by a conventional resistive strain gauge (ESG).

Fig. 1 shows a schematic of a new version of the passive quadrature demodulated Michelson type interferometric sensor /3/ with light source and demodulation unit (RE).The linearly polarized light from a 1 mW HeNe laser is coupled into the polarization maintaining input fiber (PM) by means of a GRIN lens fiber coupler (G). Two equal length arms of a 3-dB directional coupler ($\Delta L=0$) with silvered end faces serve as reference (R) and sensing (S) arms of the interferometer. They are adhered to the surface of the CFRP structure near to a conventional resistive strain gauge (Hottinger Baldwin Meßtechnik, type 6/120LY61), as sketched in fig.2. The fiber jacket is removed from the sensitive sections of both the R and S arms of the interferometer. The sensing length L_S of the interferometer is defined by the surface adhered section of the S-arm. Measurements are performed using a single component acrylate type adhesive (HBM Z70) and a two component glue (HBM X60).

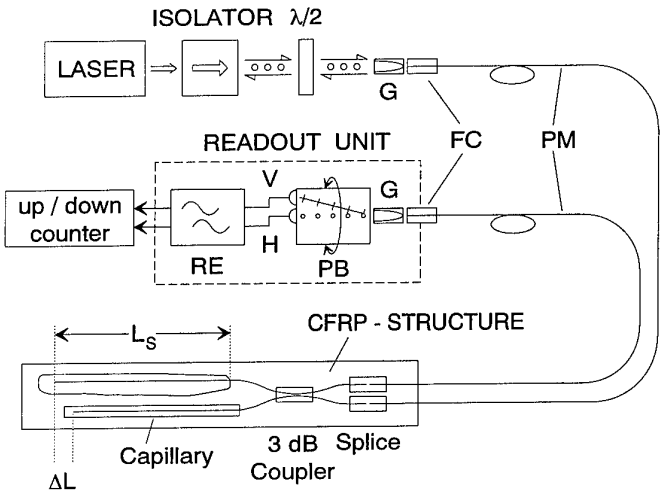

Figure 1: Schematic of interferometric strain gauge, surface adhered to CFRP structure, with optoelectronic readout unit for passive quadrature demodulation. For details see text.

For the sake of isolating the reference arm from the strain of the CFRP structure, the R arm is fed through a capillary fiber of 150 mm inner diameter, which, in turn, is glued to the structure beside the S-arm. The interference signal is guided to the demodulation unit via a PM-output fiber. The collimated output beam is split into two orthogonally polarized and phase shifted components (H, V) using a beam displacing prism (PB), with the polarizer axes aligned parallel to the birefringent axes of the PM-fiber. The required initial adjustment of the offset phase difference $\Phi_{HV} = \Phi_H - \Phi_V$ is achieved by utilizing the residual birefringence of the adhered S-

0-8194-1700-9/94/$6.00

fiber together with a suitable alignment of the input polarization via a corresponding rotation of the PM-input fiber in the first splice /4/. The H and V signals are fed into an up-down counter after passing through the readout unit (RE) which serves also for symmetrizing and automatic intensity-offset control. Counting pulses are produced at the zero crossings of both the V and H signals after offset subtraction.

A CFRP rod with foam core (length $l_R = 29.6 \pm 1$ mm, diameter d = 25 mm), as shown in Fig.2a was chosen for the quasistatic compression experiments with axial load up to 15 kN. An additional Fabry-Perot sensor, which is not used in these experiments, is embedded in the outer epoxy layer of this sample. OSG and ESG strain gauge data are related to the load F measured by means of a load cell. The electrical reference strain gauge is connected to a bridge amplifier (Hottinger Baldwin Messtechnik, model M50) with 500 Hz bandwidth.

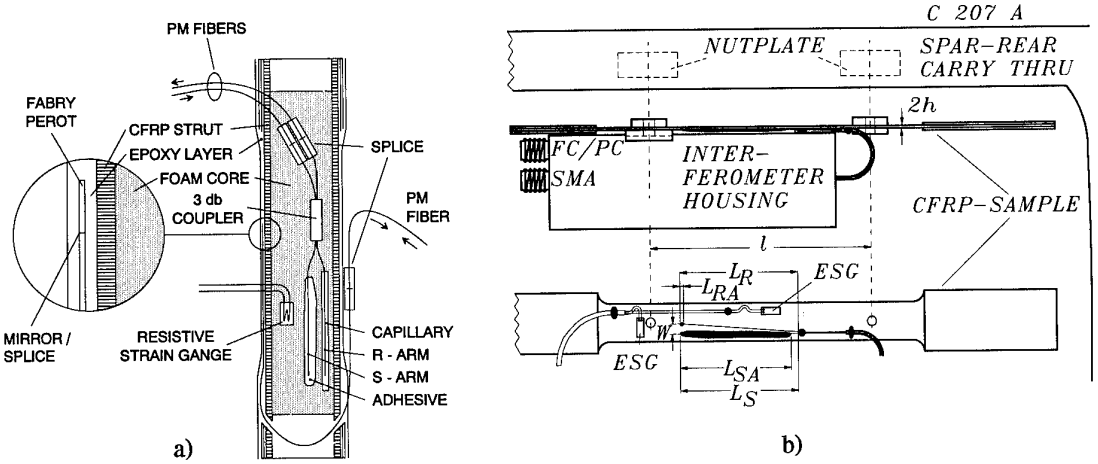

Figure 2: CFRP rod (a) and plate (b) used for load monitoring with surface adhered fiber optic Michelson interferometers and resistive strain gauge. Additional Fabry-Perot interferometer embedded in the epoxy layer on the rod surface.

Flight tests were performed using a CFRP plate of rectangular cross section (thickness 2h = 1 mm, width = 10 mm, length of strained section $l_P = 94.5$ mm) fixed at the main wing spar of the test aircraft and an earlier version of the sensor shown in fig.1 /6/. OSG and ESG strain gauge data are related to aircraft speed and vertical acceleration measured by means of a differential pressure sensor and a servo accelerometer respectively. Data is acquired using a single board unit containing a Z80 processor controlling a 16 channel A/D-converter with 8 ms conversion time and 3 10 MHz up-down counters. The data acquisition board is controlled by a 286 Laptop which is also used for storing the data for off line evaluation. The OSG readout electronics with He-Ne laser, the strain gauge bridge amplifier, and the data acquisition unit are mounted in a flight test rack which is fixed to the aircraft seat rails via shock mounts.

The theory of the passive quadrature demodulated double-polarisation interferometer has been described in detail in previous papers /3//4//5/. The two orthogonally polarized interference signals (H, V) with different phase offset Φ_H, Φ_V are described by

$$P_{H,V} = \frac{P_0 T_{H,V}}{4(1+\mu_{H,V})} \left(1 + \mu_{H,V} \cos(\Delta\Phi + \Phi_{H,V}) \right) \qquad (1)$$

with P_0 = input power, T = interferometer transmissivity, μ=fringe contrast. The offset phase difference Φ_{HV} can be adjusted such that the H and V signals are in quadrature by utilizing the residual and externally induced birefringence of the interferometer arms. The gauge factor relating the measurand induced phase difference, $\Delta\Phi$, to the fiber strain is given by $G = \Delta\Phi / \Delta L = \Delta\Phi/\varepsilon/L$ (ε = relative strain $\Delta L/L$, L = length of sensitive fiber section). G is obtained as /3//6/ G = 1.318 deg/$\mu\varepsilon$ /mm = 3.66 2πrad/μm = 14.6 $\pm$ 0.1 counts/μm. Counting half fringes of both quadrature signals ($\pi/2$ - phase shift increments) this corresponds to a strain resolution of G^{-1} = 0.0683 μm/count ($\pm$0.0001).

The quasistatic compression measurements of the CFRP rod are performed by gradually increasing the load F up

to between F_{max} = 10 and 15 KN with speed values between 0.75 and 7.5 mm/s, and decreasing F to 0 kN . The results of a typical run using the surface adhered Michelson interferometer (using HBM Z70 adhesive) are shown in fig. 3 and 4. In fig. 3 the incremental readout of the OSG is plotted versus the strain measured by the ESG. The latter indicates a maximum strain value of 1400 με. The deviation from the generally linear OSG vs. ESG characteristic at low strain values is due to slightly oblique mounting of the rod in the load frame and different locations of OSG and ESG on the circumference of the cylindrical rod. A constant variation of strain under increasing load starts at different times on different circumference locations. Fitting the strain interval 170 ≥ ε ≥ 1000 με for increasing or decreasing load separately yields a linear OSG vs. ESG characteristic with a sensitivity of 0.9892 ± 0.0004 counts/με and a gauge factor G = 0.1252 counts/με/cm = 12.52 counts/μm with L_S = 79.0 ± 0.5 mm.

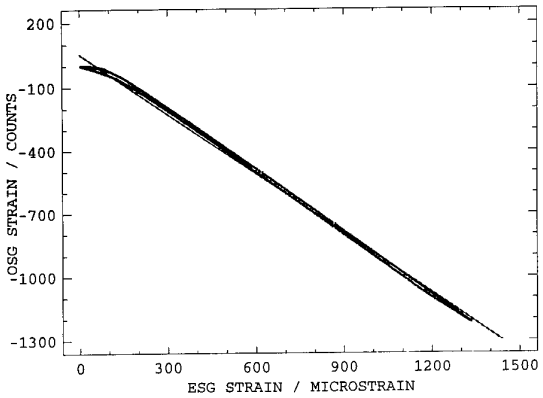

Figure 3: OSG vs. ESG obtained with CFRP-rod under compressive load up to 10 kN. Sampling rate 30 Hz.

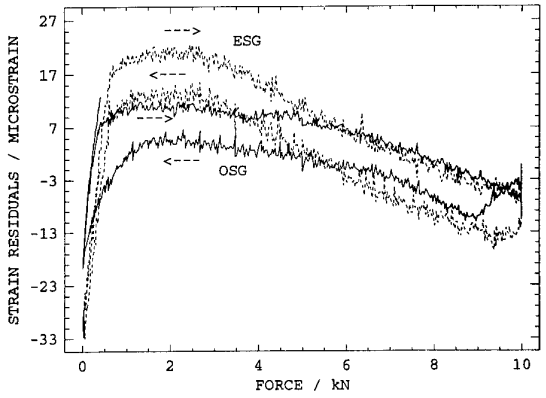

Figure 4: Residuals from linear regression of OSG (solid line) and ESG (dotted line) vs. load .

The OSG sensitivity is reduced by 15 % with respect to ESG as well as the theoretically expected value. The latter was veryfied in earlier experiments using the two component HBM-X60 adhesive /3/. Fig. 4 shows the residuals of the linear regression lines through the OSG and ESG vs. F data, exhibiting the magnitude of the hysteresis and noise of the two sensors besides the above mentionend nonlinearity. OSG and ESG can also be compared by evaluating the OSG vs. F and ESG vs. F data, verifying the OSG sensitivity 14 % smaller than the ESG sensitivity.

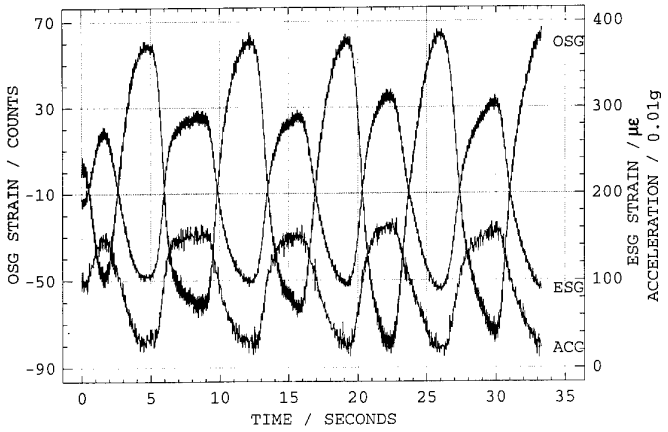

Figure 5: OSG (left ordinate), ESG, and accelerometer data (both right ordinate) from alternating acceleration flight. Sampling rate 30 Hz.

As an example of the flight test data, fig. 5 shows the responses of ESG, OSG and accelerometer to a series of 5 acceleration cycles between roughly 0 g and +1.7 g (normal to the wing) during parabolic flight maneuvers over a period of 35 seconds. Here, the S-arm of the OSG is fixed at its end points using HBM X60. The correlations between OSG, ESG and accellerometer are obvious. The slope of the fit through the OSG vs. ESG data indicates

a strain sensitivity of 1.26 ± 0.01 με/mm which differs by 1.5% from ground test result, and by 4.5% from the theoretically predicted value. During loading of the sample, variations in the birefringence of the interferometer arms cause the relative phase Φ_{HV} between the two polarization components to vary from quadrature. If the variation approaches 90 degrees, unambiguous fringe counting becomes impossible and the counter loses track. Significant birefringence variation is observed when large sections of the sensing arm are covered by the hard X60 glue, producing anisotropic transverse stress under external load /3/.

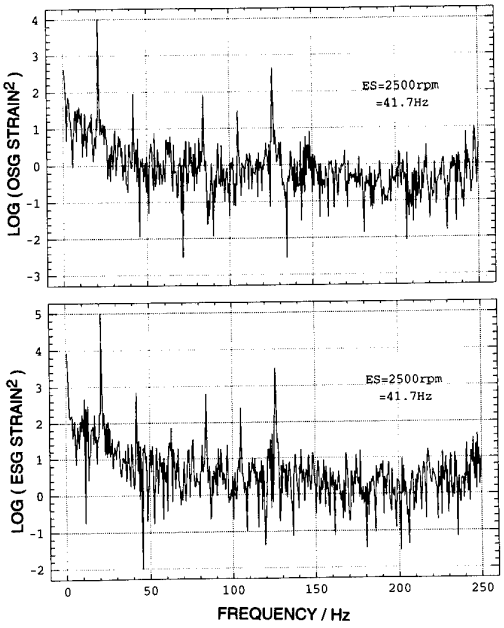

Figure 6: Power spectra of 2s 500 Hz acquisition during steady normal flight (engine speed =2500 rpm = 41.7 Hz). Upper graph: OSG output, vertical axis, $\log_{10}(\text{counts}^2)$; lower graph: ESG output; vertical axis, $\log_{10}(\text{ADC digits}^2)$, 2 digits = 1 με.

After recovery of tracking, the incremental strain sensitivity is not changed, but an arbitrary offset is introduced. Several short term lock-losses occurred during the acquisition of the data shown in figure 5. The insufficient stability of the input polarization under large temperature variations is an additional reason for lock losses. This partly accounts for the difference of this slope from that produced in the ground test.

Figure 6 shows the spectra produced by fast Fourier transforms of the OSG and ESG data from a 2 second 500 Hz acquisition during normal steady flight. The peak-to-peak amplitude of the vibrational noise on the time series plots is approximately 6 με at 20.8 Hz (=half the engine speed). The majority of the prominent spectral peaks corresponds to subharmonics and harmonics of the engine rotation rate. The two spectra agree very well with respect to the prominent peaks, indicating that, at least for small amplitude vibrations, the dynamic response of the OSG extends to at least the 250 Hz upper frequency limit for this spectrum.

Load measurements on CFRP structures under realistic environmental conditions using passive quadrature demodulated fiber optic interferometric strain gauges have been performed. Reasonable agreement between the optically and electrically measured strain values is observed. Under flight conditions, the stability of the present optical setup proves sufficient for continuous readout over time periods of the order of minutes. The performance of the double polarization interferometer depends significantly on the adhesive used to adhere the sensing fiber to the surface. An improvement with respect to signal stability is expected by using small temperature stabilized laser diode packages, with Peltier cooler, optical isolator and fiber pigtail in a common housing, instead of the HeNe - laser systems with bulk optical components.

/1/ Valis, T., Hogg,D., Measures,R.M.: Fiber-optic Fabry-Perot strain rosettes. Smart Mater. Struc. 1 (92) 227 - 32
/2/ Waite,S.R., Tatam,R.P. Jackson,A.: Use of optical fibre for damage and strain detection in composite materials. Composites 19 (1988) pp 435-442
/3/ Fürstenau, N., Schmidt, W., Goetting, H.-C.: Simultaneous interferometric and polarimetric strain measurements on composites using a fiber-optic strain gauge. Applied Optics 31 (1992) pp 2987-2993
/4/ Fürstenau, N.: Performance of the double-polarization method in interferometric digital force sensing by fiber- tension bending. SPIE-Proc. vol.891, (1988) pp 209-214
/5/ Fürstenau, N., Janzen, D.D., Schmidt, W.: In-flight strain measurements on structurally integrated composite plates using fiber-optic interferometric strain gauges. Smart Materials and Sructures 2 (1993) pp 2987-2993
/6/ Butter, C.D., Hocker, G.B.: Fiber Optics Strain Gauge, Appl. Optics. 17 (1978) 2867-2869

Paper presented at the Second European Conf. on Smart Structures and Materials, Glasgow 1994, Session 8

FIBRE BRAGG GRATING STRAIN SENSORS FOR AEROSPACE SMART STRUCTURES.

P.D.Foote

British Aerospace Operations Ltd.
Sowerby Research Centre, Filton, Bristol, U.K.

Abstract

Fibre Bragg grating strain sensors have been embedded in carbon fibre composite beams at BAe. A programme of work to develop sensory structures is addressing issues of fibre sensor embedding, multiplexing, optical connection and temperature compensation.

Introduction

A medium to long term requirement is recognised for smart 'sensory' structures in aircraft [1]. Sensory structures are generally passive, containing networks of sensors capable of monitoring, for example, strain and temperature. A nervous system provides a convenient analogy. The principle motivation for developing sensory structures for aircraft is their application in structural health monitoring which encompasses damage detection and assessment, strain history, and envelope 'exceedure'. Embedded forms of sensor, usually in composite materials, are favoured in that they are integral to the material which is being monitored and are protected from accidental damage. Potentially they offer 'cradle to grave' vigilance over their host structures.

Approach

Intrinsic optical fibre sensors seem ideally suited to the realisation of sensory structures. Studies in the UK [2] and elsewhere have shown that they can be embedded in modern aircraft composites without showing degradion or significantly compromising the strength of the host material. The non-intrusive nature of these devices is supplemented by the usual advantages, when compared with electrical sensors, such as immunity to electro-magnetic interference and the capacity for multiplexing many devices in a single fibre lead allowing distributed measurement.

Of the many types of intrinsic fibre sensors the fibre Bragg grating (FBG) is an outstanding recent development. A FBG sensor's attributes include: its amenability to automatic mass production using single laser pulses, the delivery

0-8194-1700-9/94/$6.00

of absolute measurements allowing static and dynamic sensing, its wavelength multiplexed nature providing immunity to light level fluctuations and its down-lead insensitivity. The only disadvantages with FBGs are that they are single mode fibre devices and they require high resolution spectral analysis to extract measurement data. At British Aerospace FBGs made using a frequency doubled, argon laser source have been successfully embedded in small test beams made of carbon fibre reinforced plastic (CFRP). Once embedded the devices have demonstrated sensitivity to strain in three-point bend tests.

The work is currently being conducted within a UK collaborative programme led by BNR Europe Ltd. in which Aston University, Exitech Ltd. and Hull University are producing a range of fibre grating devices. The techniques of interferometric side writing are being used for both type I and type II grating production. Additionally, phase mask diffraction and mask image projection techniques are being evaluated. Fixed period and chirped gratings are being produced.

This work has focussed attention on a number of key issues which British Aerospace is currently addressing in a sensory structures programme:

1. The sensing capability of FBGs.
2. Their resilience to the process of embedding in carbon fibre composite material.
3. The choice of multiplexing/de-multiplexing techniques.
4. Connectors for the embedded fibres.
5. Temperature compensation.

Autoclave or hot press preparation of thermoset CFRPs entail temperatures up to 200° C and pressures up to 100 psi. These are harsh conditions for delicate fibres but provided they are protected by, for example, teflon sleeving, at their points of ingress to the host material they remain intact and functional at the end of the process. The FBGs themselves do not suffer any significant degradation at these temperatures, even those of the 'type 1' photorefractive form. Figure 1 shows the reflection spectrum of a single run of fibre containing two FBG sensors embedded in a composite beam. The sensors are located at the mid-point either side of and equidistant from the strain neutral axis of the beam. The dotted spectrum results when the beam is bent in a three point bend rig. The inner and outer gratings experience simultaneous compressive and tensile strain respectively. Wavelength calibrated strain measurements with these embedded sensors have been made which agree with predicted values to within 10% while displaying good linearity.

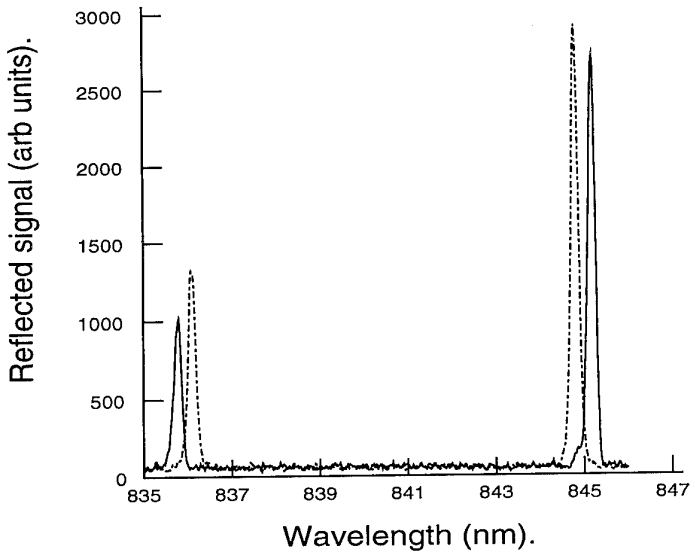

Figure 1: Reflection spectrum of two embedded FBG sensors. The sensors are embedded either side of the strain neutral axis in a carbon fibre beam. The dotted curve shows the effect on the spectrum of bending the beam.

The multiplexing technique currently being investigated at British Aerospace is based on a broad-band SLED source with tunable narrow band detection using a grating spectrometer. Tunable filter devices including fibre Fabry-Perot and bulk acousto-optic devices are also being evaluated as spectral demodulation components. This approach does, however, present problems of signal to noise due to the low spectral power densities characteristic of broad-band sources especially when coupled with single-mode fibre. Alternative approaches based on tunable fibre lasers using intra-cavity Fabry-Perot wavelength filters may overcome this problem. Self-contained fibre lasers could even be fully fibre-intrinsic by using FBGs as pump separators and as output couplers (using broad-band chirped gratings). The gains in sensitivity promised by such lasers would make their further development worthwhile despite their relative complexity when compared with proven LED technology.

For the eventual realisation of practical sensory structures using embedded optical fibre the development of suitable single mode fibre connectors is essential. The manufacturing, operational, and maintenance environments all require rugged, reliable connectors. Current connector technology has been developed to suit mainly the telecomms end user whose requirements are not generally compatible with those associated with aerospace sensory structure applications. Connectors must be developed which can tolerate the harsh embedding conditions required for composite sensory structures and maintain integrity for many make/remake operations.

Cross sensitivity between strain and temperature exists for nearly all strain sensors and is frequently overlooked. An aircraft skin may endure temperature

excursions of -60^{0}C to 200^{0}C under normal operation. For a FBG sensor this could mean an apparent strain offset of between 2000 and 4000 $\mu\epsilon$ (assuming a wavelength sensitivity of 5-10 parts/million/^{0}C).

Temperature compensation must be sought either by devising suitable sensor deployment configurations or by independent temperature measurement. Bending strain measurements may be thermally compensated by arranging sensors either side of the strain neutral axis. Differential tensile and compressive strain measurements are, by common mode rejection, temperature insensitive (the composite beam results of figure 1 were achieved in this fashion). Linear strain must, however be combined with an independent temperature measurement. One approach may be to form FBG sensors within a fibre Raman scatter-based distributed temperature sensor. This would supply independent temperature and strain measurements. Alternativly, dual gratings operating at widely spaced wavelengths and exploiting dispersion in the fibre's thermo-optic effects could be used.

Conclusions

Embedded fibre optical sensing using fibre Bragg gratings in sensory structures are being developed at British Aerospace for future aircraft applications. This development necessitates investigation of the key issues of resilience to embedding, sensor multiplexing, optical connection and temperature compensation.

Acknowledgements

The author acknowledges the assistance of partners in the LINK project 'GIFTS' IED2/430/30/57 and the support of the DTI and SERC.

References

1. P.A.Tutton and F.M.Underwood *'Structural health monitoring using embedded fibre optic sensors'* AGARD Conf. Proc. Smart structures for aircraft and spacecraft, **531** 1993.

2. S.S.J.Roberts, R.Davidson *'Mechanical properties of composite materials containing embedded fiber optic sensors.'* SPIE **1588** Fiber optic smart structures and skins IV, Boston, 1991

3. K.Byron, H.Rourke, P.D.Foote, M.Goodwin, C.Ragdale, M.Gower, S.Mihailov, I.Bennion, P.Dyer, R.Farley and F.Payne *'Fabrication of fibre grating structures and applications in systems'.* 1994 UK IT Forum Conference Digest, Heriot-Watt University, 1994.

SESSION 9

ENABLING ARCHITECTURE

CEDRIC PRICE - Principal - Cedric Price Architects
MA (Cantab) - Co-Founder Lightweight Enclosures Unit
RIBA - First AA Senior Research Fellow 92-93
AA Diploma

The application of SS&M to architecture must occur at the concept stage of design.

Unless this happens, these dynamic technologies will be used merely to refine methods, systems, structures and components already existing.

Understanding and appreciating their future importance by architects at this stage is essential. The prime reasons for this urgency are, firstly, that the socio/economic gestation period for architecture is lengthy in comparison with other artifactual endeavours in "the enclosure business". Secondly, such an introduction enables the whole assumed academic definitions of dimensions, tolerances and component compatibility in relation to assembly, to be questioned. This is because SS&M introduce TIME as an essential fourth dimension in the very definition of their usefulness. Key relevance is that the Time element is measurable in an appropriate and comparable dimension.

Because of this similarity in the measurable scale of both systems and component, their eventual assembly, maintenance and demolition (or re-assembly) can be realised in a superior socio-economic constructive matrix.

Due to previously assumed incompatibility of the measurement of Time with that of the normal architectural dimensions of length, breadth, height and weight, Time has remained idle or vague on such questions as 'ageing' or redundancy.

Thus products with 'SELL BY' dates clear to all are produced in 'antique' shelters. Similarly, University graduates are produced in medieval ruins. More serious is the housing of people in products that in every technological respect are far inferior to a pair of Hush Puppies.

Thus is occasioned an opportunity to correlate appropriate process and desired product without the adverse effect of an intermediate container insensitive to the speeds of the former.

The range and depth of beneficial responses and actions during the process of ageing of any building can alter the design form of the building itself.

This, however, is achieved only as a result of a new and continuously updated 'alphabet' of possibilities being offered to designers before they start on assembling the 'words to construct the 'sentences' that form the built environment.

The current draft European Building Codes include amongst their proposals making the architect jointly responsible for their 'product' throughout its life - construction, use, alteration, re-use and demolition. This adds a valuable sense of urgency to architects' awareness of their future responsibilities.

It should alert a notoriously lazy profession as to the value of and hopefully, to a new attitude as to how to keep in touch - continuously rather than intermittently - with others' technologies. In addition, and in the medium term, I would wish my Profession to generate fields of beneficial social exploitation enabled by SS&M.

Primarily these would be preventative of social ills rather than curative. They would utilise the minimal human role as intermediary in the process of continuous quality control and maintenance, seasonal change in friendly barriers, and relocation and redundancy.

c Cedric Price
26.6.94

0-8194-1700-9/94/$6.00

DESIGNING ADAPTIVE SYSTEMS FOR BUILDINGS

ADE ADEKOLA

BA(Hons) Arch., AA Dipl.

MANIT RASTOGI

B-Arch, AA Grad. Dipl., A.I.I.A., M.C.A.

Abstract:

Of importance in buildings designed to posses adaptive and responsive relationships with their environment is the design of their control mechanisms, whose dynamics should be structurally congruent with the prevailing environment around the building element.

(1). INTRODUCTION

Dynamic systems define the integrity of a co-existing whole with active and passive parts. They can be defined as systems capable of self change whilst remaining self monitoring. There can be considered to be three classes (see diagram) which all embody a structure to give the system integrity and stability, an actuator to enact changes, a sensor to monitor the environment and the system and any changes in both, and a controller to process data from the sensors, provide the judgement criteria for change and predict the implications of any changes. The sensors, actuators and the controller can be seen as three interacting, mutually supporting systems, through which the intelligence of the whole system (structure) is diffused.

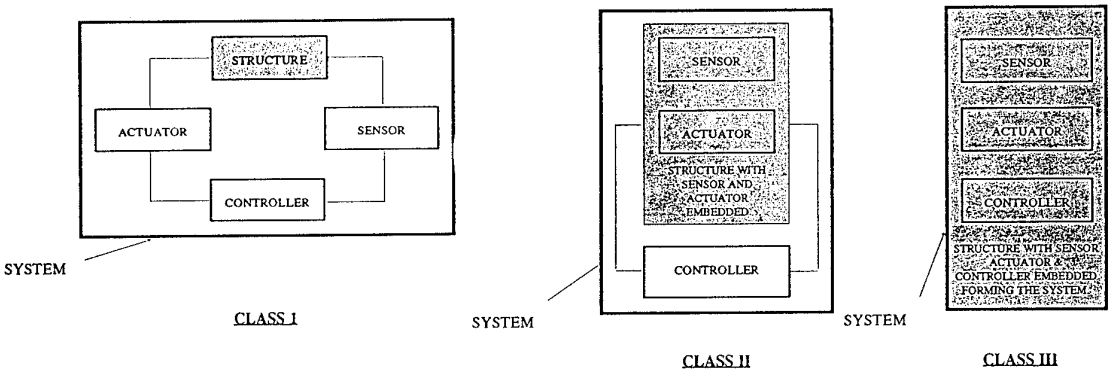

The unique capabilities of computing imply many possible roles in the control and design of buildings as adaptive systems. Adjustment mechanisms consisting of user manipulation of the system can be designed so as to require no specialist training on the part of the user, while still leaving scope for decisions based on subjective phenomena, or unpredictable patterns of use. This type of user control takes advantage of the human minds complexity, allowing for sensitive interaction that is at present not possible with the awkward interfaces required for user/computer interaction. The central function of structure, both digital and physical, is then to provide a framework in which the user can make appropriate decisions.

We consider there is a strong link between dynamic systems and living systems. Dynamics systems being based on a close analogy of the artificial representation of living systems.

(2). LIVING SYSTEMS AS GENERATORS FOR ADAPTIVE BUILDINGS.

Living systems/organisms have a diverse behavioural repertoire; they must co-ordinate their many possible actions into coherent behaviour directed towards their long term goal, survival. Living organisms exhibit a certain organisation in their behaviour, some behaviour normally takes precedence over others, some actions are mutually exclusive (any action that utilises the same motor apparatus for incompatible actions). The switches between different behaviour patterns depends both upon environmental conditions and the internal state of the system, they must continually compare current and predicted values to adjust to their relevant model parameters. The information to accomplish this task is provided by their senses.

0-8194-1700-9/94/$6.00

(3). SENSORS FOR INTELLIGENT BUILDINGS

A sensor can be considered as that which detects aspects of an environment and conveys information of that given environment to the internal mechanism of a system, thus allowing the system to restructure or readjust its position (adapt) in that given environment towards the appropriate goal directives of that particular system.

Sensory systems in intelligent buildings should serve the purposes of:
(1). Providing information of the current state and position of the building.
(2). Providing information of the current state of the environment (internal and external)
(3). Monitor the effects of any environmental changes on the building.
(4). Provide the internal mechanism with all the relevant parameters before it enacts a change in the building.

If the above characteristics were embodied in a building then condition (1). can be considered to provide the building with the quality of self awareness. Condition (2). can be said to provide the building with the quality of awareness. Conditions (3 & 4). can be said to provide the building with the capacity to model itself in the environment, hence giving it the means of evaluating the effect of any changes it might make prior to the act.

With these qualities the building can be considered to begin to embody the basic characteristics of consciousness.

(4). ARTIFICIAL CONSCIOUSNESS IN BUILDINGS.

The basic aspects that classify consciousness can be considered to be:
(1). Awareness: That is the capacity to know, store and remember. Memory is an integral part of awareness.

(2). Self awareness: That is the capacity to know one's position in relation to one's environment. It is a manifestation of the objective notion of the subject. It is the beginning of a control mechanism.

(3). Intentionality: These are the generators of much of what living organisms do. It is in essence a protective mechanism. The basic feature of intentional states are propositional content, direction of fit and condition of satisfaction.

(4). Ability to construct mental models: This is about communication and understanding. In order to understand one's fellow man, it is important to be able to abstract and construct a model of their mental model and embed that model into that of another and so on.

(5). Capacity for prediction, judgement and change: This is about competition and survival in a changing domain. As suggested by Nicholas Humphrey, the capacity for conscious thought allows an individual to rehearse in its mind the possible reactions that would be elicited from another by a particular action.

If a building were to embody these characteristics or artificially represent consciousness in a human environment, they should be dynamic systems capable of self input, self change and be environmental monitoring/adaptive.

(5). SELF INDUCING DEVICE

This is a study of designing and manufacturing a first class of dynamic systems, capable of self input and self change whilst also being able to monitor its environment (represented as interactors).

The concept was that of a design of a flexible mast structure (based on Frei Otto's design) where the sensory and actuative elements were separate from the structure itself. The structure is made up of 12 tensioning arms (connected to the mast with tension cables), a base board on which the arms are mounted and a central articulated mast. (see diagram).

The actuators are 12 solenoids with returning springs connected to the arms.
Tilt switches are mounted on each arm as sensors, providing the controller with the current state and position of the structure hence giving the device self awareness. There are 12 keyboard (interactive) switches (can be replaced by any other environmental sensor) which send signals to the controller from the interactors (people) in the environment hence giving the device awareness.

The controller is a computer reading signals from the sensors and sending signal to the solenoids. The controller runs a program to facilitate judgement criteria for the device.
The program was developed so that at any time the device has:
(1). A store of factual information; this is the intentional state of the device under its different modes.

(2). A repertoire of skills; SID is capable of 4096 individual movements and exhibits modal behaviour in terms of sequential movements.
(3). A hierarchy of criteria of evaluation or priorities.

The primary purpose of the device is to interact with people, so it's primary goal directive is the intentional state interact. In order to facilitate this state the device tries to lure people to interact by exhibiting seductive behaviour. It's first mode of behaviour is its luring mode, it regresses in behaviour if it is not interacted with (Luring - Distress - Sulking - Arrogant - Obsessive) and ends up with an obsessive character where it's behaviour is self generated by the sensors on each arm and it totally ignores signals from it's interactors. It's behaviour can be pacified before it reaches it's obsessive mode if it is interacted with, in which case it progresses in behaviour (Arrogant - Sulking - Distress - Luring - Playful) and ends up in a playful mode where it's behaviour is totally generated by it's interactors. It's playful mode is designed so SID exhibits just reflex action, thus leading it's interactors to believe it exercises no judgement hence they get bored stop interacting and it's behaviour regresses again.

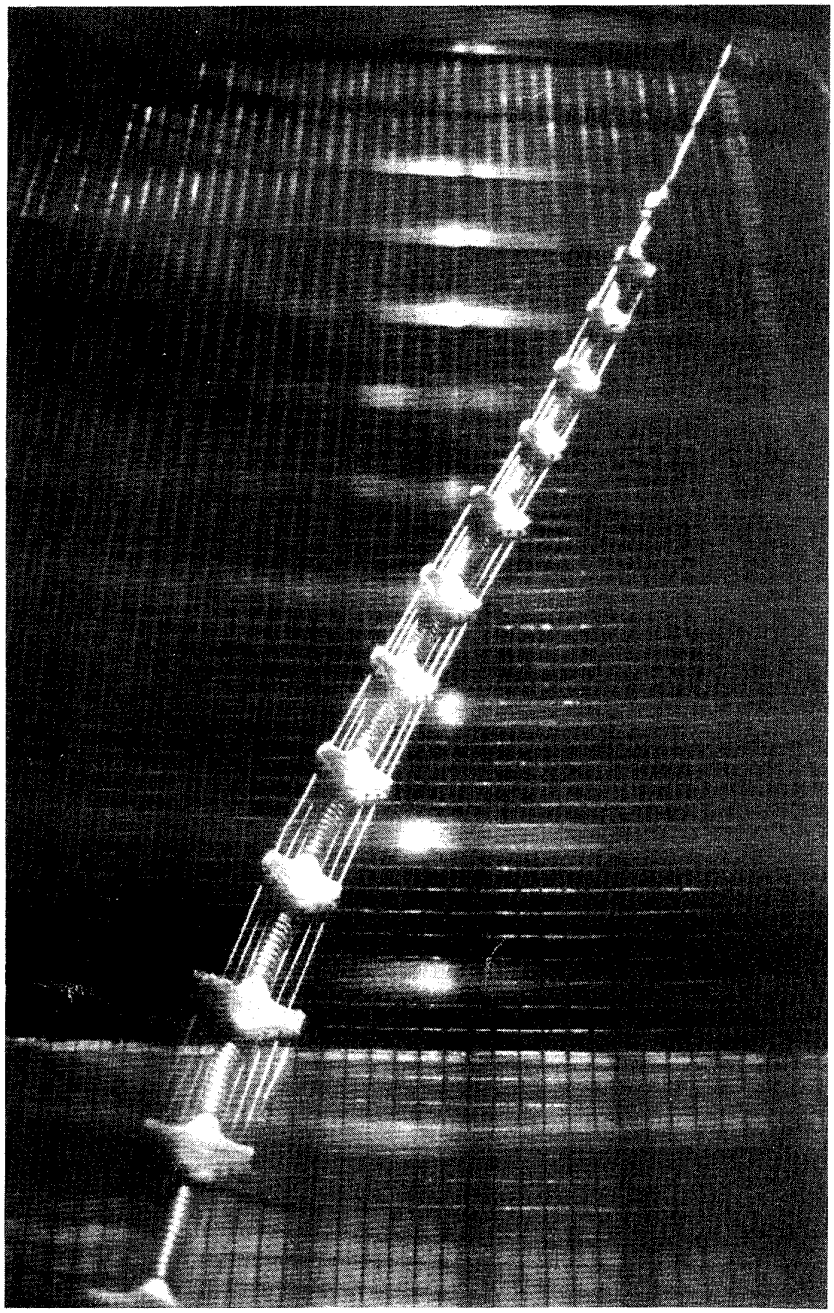

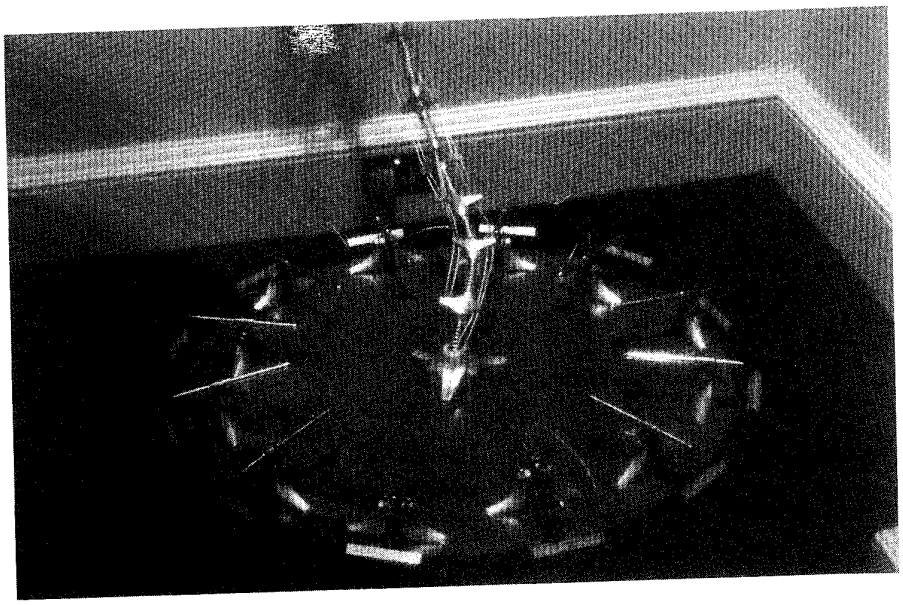

(6). CONCLUSION.

Embodying the basic characteristics of living systems to respond to their environment, SID has the capacity to store (through the controller) or react to the information coming from it's interactors. The device can exhibit reflex reaction or it can evaluate the signals - to a programming parameter- to exhibit or inhibit a mode of behaviour thus exercising judgement.
It is believed this sort of evaluation of criteria can be embodied in buildings to enact various changes leading to a dynamic internal and external environment.

(7). REFERENCES.

(1). Miller J.G. **Living Systems.** McGraw-Hill 1978
(2). Beer R.D. **Intelligence as an Adaptive Behaviour.** Academic Press 1990
(3). Haugeland J. **Mind Design.** MIT Press 1987
(4). Fischler M.A. Firschein O. **Intelligence The Eye, the Brain, and the Computer** Addison-Wesley 1987
(5). Young D. **Nerve Cells and Animal Behaviour.** Cambridge University Press 1989
(6). Blakemore C. Greenfield S. **Mindwaves.** Blackwell 1989

A NEW APPROACH TO INEXPENSIVE, PRINTED ELECTROCHROMIC DISPLAYS.

JAMES P. COLEMAN

MONSANTO CHEMICAL GROUP,800 N.LINDBERGH, ST LOUIS, MO.63167,USA

1.BACKGROUND

In developing some initial ideas on inexpensive "smart structures" which could sense, indicate, record and respond, it became apparent to us that a cheap, lightweight, flexible and versatile display mechanism would be of considerable commercial utility for this and many other applications. We therefore initiated a probe to look at what might be possible, focussing mainly on electrochromic systems.

Electrochromic displays[1] are charge-controlled devices, essentially rechargeable batteries whose electrodes change colour on charging or discharging. Figure (1) shows a typical, conventional electrochromic device in display mode. Use of two transparent electrodes would give a "smart window".

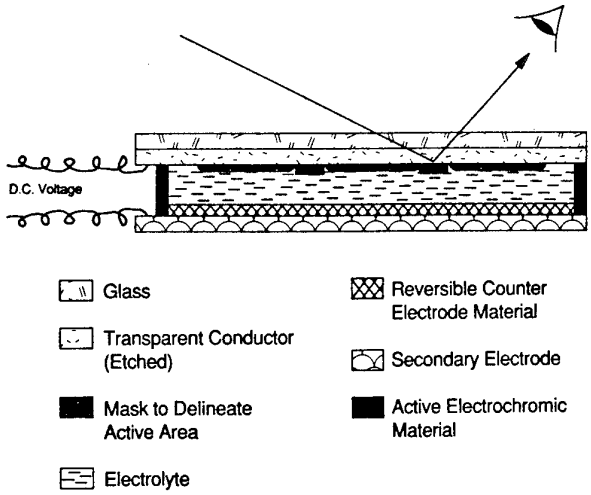

Figure (1)

Conventional Electrochromic Display

Some of the most commonly used electrochromic materials include tungsten oxide, conductive polymers, such as polyaniline or polypyrrole, and various viologen compounds. We have not thus far attempted to prepare new electrochromic materials, but have tried instead to construct a more practical system in which these materials might be used.

Conventional electrochromic displays have a number of drawbacks: the "sandwich" structure, in addition to requiring alignment, necessitates the use of a transparent electrode such as indium-tin oxide (ITO) or thin films of precious metals such as gold. These materials are not only expensive but also render scaleup to large devices difficult because of their low sheet conductivity.

0-8194-1700-9/94/$6.00

In many cases, vacuum deposition techniques are required, either for the transparent electrodes or the electrochromic materials.

2. OUR APPROACH

To overcome these drawbacks we set out to develop a system[2] which may be produced in existing high speed printing equipment, use virtually any conductor - particularly commercial conductive inks - and have all the active components formulated into inks. Accomplishing this required two modifications of the conventional system: (1) the use of interdigitated electrodes printed face up on the substrate and (2) the invention of a protective coating system which could simultaneously support the electrochromic reaction, prevent corrosion of the underlying metal electrodes and visually mask the electrode structure until switched. This particular approach has not been described before[3]. Figure (2) shows our first, simple circuit design for a 7-segment display.

Figure (2)
Early 7-Segment Design

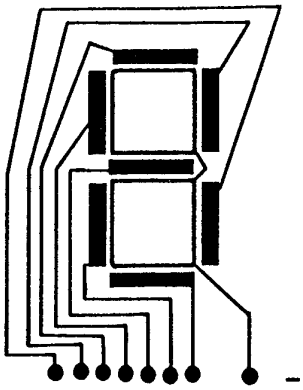

Figure (3)
Our Approach

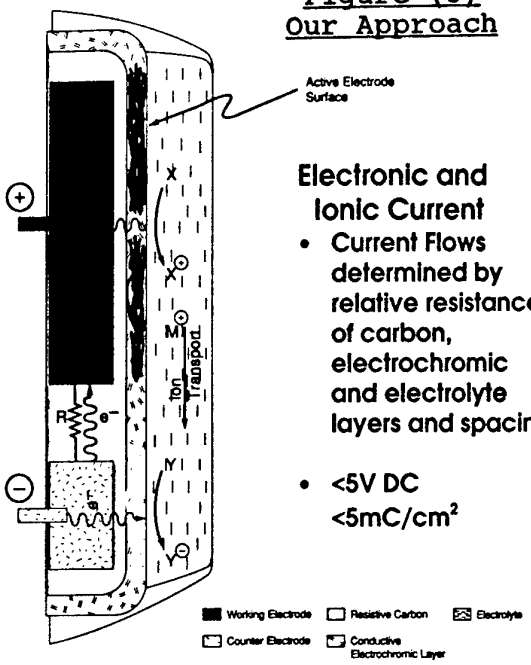

Electronic and Ionic Current

- Current Flows determined by relative resistances of carbon, electrochromic and electrolyte layers and spacings.
- <5V DC <5mC/cm²

In developing a protective coating system we needed electrical conductivity, electrochemical stability (operating potential range) and acceptable optical properties, i.e. a light colour, so that electrochromic changes might be easily observed. Our initial approach was to prepare a dispersion of ITO powder in a solution of SBS rubber in toluene. When coated over an electrode of copper on polyester film, it was possible to electrochemically deposit polyaniline from an aniline-sulphuric acid solution and to redox cycle the polyaniline between its three different states - blue, green and yellow. The copper is thus isolated from electrochemical activity and functions only as a shaped

conductor. Whilst ITO powder proved the concept of a "protected electrode" we found another material which had some practical advantages: this was titanium dioxide coated with electrically conductive antimony-tin oxide, available from Mitsubishi Materials Company as an off-white powder. We were able to prepare smoother dispersions from this material with similar results.

Polyaniline is a robust electrochromic material which we decided to study a little further: however, we wanted to avoid having to deposit it electrochemically each time we made a device. We therefore chemically polymerised aniline onto the antimony-tin oxide/TiO_2 to give a light green powder, versus the almost black of pure polyaniline. This material, when dispersed into SBS rubber-toluene and coated onto either copper or silver electrodes and dried, switched rapidly and reversibly in dilute aqueous acid electrolytes with application of very low (1-3V) DC voltages. We had thus demonstrated the basis for an electrochromic ink or paint. Other electrochromic inks using polypyrrole or poly(xylylviologen) were similarly prepared.

One further innovation should be mentioned: our test electrodes at this time were simply parallel strips of either electroless copper or silver ink on polyester film, separated by a gap of about a millimeter. We found that the protective, electrochromic coatings could be applied completely across both electrodes and the intervening gap without significantly affecting electrochromic performance. This would provide a significant benefit when printing very fine electrode patterns, thus avoiding the need for very tight registration tolerances.

As a result, our new device functions as shown in cross section in figure (3).

3. DEVICE FABRICATION.

The circuit shown in figure (2) was screen-printed in silver ink on polyester film: after masking the connecting lines with insulating paint, a layer of polyaniline ink was applied, followed by a layer of 10% aqueous poly-AMPS (poly{acrylamido, methylpropanesulphonate}). The electrolyte was allowed to dry partially before laminating with adhesive polyester film. Applying as little as 1V DC caused the anode segments show up dark blue against the uniform green background and the cathode to lighten slightly in colour. On removing the applied voltage, the colour rapidly disappeared via self-neutralisation of charge.

4. FURTHER DEVELOPMENTS.

More sophisticated circuits have now been printed in conductive inks, as shown in figure (4), and we continue to make further improvements.

Small 7-Segment
(<0.5 inches)

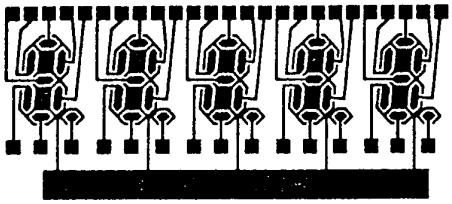

Large 7-Segment
(2-4 inches)

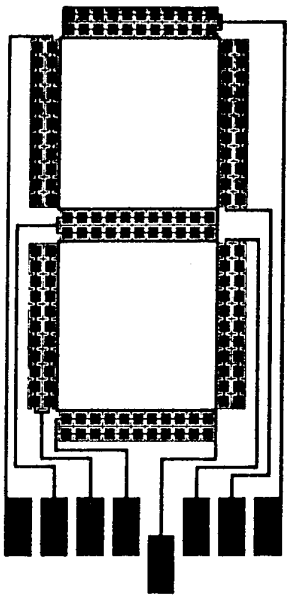

Switchable Lettering

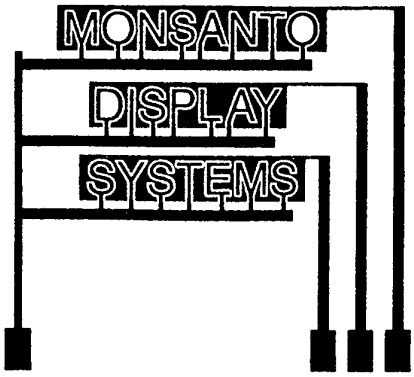

Figure (4)

In addition to polyaniline, we have looked at other electrochromic systems including tungsten and molybdenum oxides, viologens and bismuth deposition, as reported by B. Warszawski[4]. Simple electrolytes to date include aqueous solutions of hygroscopic salts gelled with polymers such as polyvinyl alcohol or cellulose derivatives.

Qualitatively, switching speeds look very good (< 1 second) and we have produced devices still active after several months.

5. CONCLUSIONS.

Whilst there remains a considerable amount of commercial development work to done, this probe has encouraged us that there is indeed a real possibility of producing low cost, active display systems in commercial printing operations. We are continuing to pursue the commercial development of this technology.

6. REFERENCES.

1.Electrochromic Materials.ECS Symposium Proceedings,90-2,(1990)
2.J.P.Coleman, US Patent pending, (1994)
3.M.Brandon & B.Piggin,IBM Tech.Discl.Bull.,21,5,p.2047,(1978)
N.Leventis & M.Wrighton, US 5,189,549, (1993)
4.B.Warszawski,ECS Ext.Abs.,92-2,785,(1992,Toronto Meeting)

Paper presented at the Second European Conf. on Smart Structures and Materials, Glasgow 1994, Session 9

THE POTENTIAL OF INCORPORATED ACCELEROMETERS FOR THE IN VIVO ASSESSMENT OF HIP STEM LOOSENING.

G. Lowet, G. Van der Perre

Division of Biomechanics and Engineering Design, K.U.Leuven, Belgium

Abstract

The feasibility of vibration analysis for the detection of loose hip prostheses was studied. Based on the non-linear vibrational behaviour, the fixation quality of the implant can be assessed.

1. INTRODUCTION

The detection of prosthesis loosening in total hip replacement remains a problematic issue. Common techniques such as radiography and arthrography have not been shown to be very effective. Although originally developed for the assessment of fracture healing, vibration analysis was proposed as a method for the detection of loose prostheses [1,2]. In this paper, we will discuss the principles used in the vibration analysis in relation with the detection of loose prosthesis and discuss the potential and limitations.

2. VIBRATION ANALYSIS

For the assessment of a healing fracture, the resonant frequency of the healing leg can be compared to the frequency of the intact contralateral leg. Immediately after fracture, the resonant frequency of the fractured leg will be much lower, but as the bone regains its stiffness, the resonant frequency will increase [2]. Determining the resonant frequencies of a femur with fixed implant and with loose implant showed a lower resonant frequency in the case of the loose implant [2]. However, for clinical practice, this would imply that for every patient with a hip replacement, a control measurement must be made at the time that the implant is securely fixed. Measurements made at later times could be compared to that 'normal' value in order to detect loosening. This however, seems to be a quite unpractical approach, and, furthermore, the resonant frequency of the femur can also alter in time due to other causes (e.g. remodelling, osteoporosis).

A totally different approach is to focus on the non-linear vibrational behaviour of the bone when the prosthesis gets loose. When a linear structure (which is the case for a femur with entirely fixed implant) is subjected to a harmonic force at given frequency, the structure will start vibrating at that given frequency. For a non-linear structure (femur with loose implant), several harmonic signals will be added to the fundamental response. This approach has successfully be applied in a pilot study on 10 cadaver specimens and 7 patients. A clear distortion of the response signal (indicating the presence of higher harmonics) was seen for the cases with loose implants [3]. This however, provided only a qualitative description of the signals observed.

Another way to study the non-linear behaviour of the structure is to excite the structure with force inputs of different magnitude. For a linear structure, the magnitude of the response signal would be linearly related to the magnitude of the force input, for a non-linear structure, this relationship disappears.

The key issue is to find a quantitative parameter that would contain information on the fixation quality of the prosthesis. If such parameter would not only allow to decide on whether the prosthesis is loose or fixed, but would also relate to the amount of relative displacement of the prosthesis in the femur, that parameter would be of major clinical importance.

3. CHOICE OF EXCITATION FREQUENCY

When the excitation frequency equals the resonant frequency, inertial and elastic forces in the structure are in balance and the applied force only needs to neutralize the damping of the structure. Although in the pilot study mentioned earlier, distortion on the signal was seen over a broad range of frequencies (when the prosthesis was loose), it is likely that in order to gain optimal sensitivity, excitation at the resonant frequency would be advantageous.

0-8194-1700-9/94/$6.00

4. TECHNICAL LIMITATIONS

In vivo, the force must be transferred through the skin and muscles surrounding the femur. As this soft tissue acts as a low pass filter, the frequency of the input signal is limited to 1000 Hz, even when the force is applied to places with minimal soft tissue covering, such as the femoral condyle. The same limitation applies to the accelerometer which is used to measure the bone response and was pressed against the greater trochanter in the pilot study [3]. When one wants to determine the content of the higher harmonics in the response signal, this still reduces the frequency range for the force input. If for instance the second harmonic has to be measured, the force input is limited to about 300 Hz (second harmonic at 900 Hz, near the 1000 Hz limit). We will further propose solutions to this problem.

5. STATE OF THE ART

Both from literature and own experiments, it is clear that the looseness of a prosthesis can clearly be observed by studying the non-linear response. Possible quantitative parameters are the ratio between power in the higher harmonics and power at the fundamental frequency of the response signal. A valuable alternative is to excite the structure with two different force amplitudes (F1 and F2) and to monitor the magnitude of the acceleration response (a1 and a2) at that frequency. For a fixed prosthesis, the ratio (a1.F2)/(a2.F1) should equal 1. If the ratio is clearly different from unity, this indicates loosening of the prosthesis.
Own in vitro experiments revealed that a higher sensitivity was reached when the accelerometer was fixed directly to the implant, instead of fixing it to the greater trochanter. The measurement axis of the accelerometer should be placed parallel to the direction of force input.
From experiments on three fresh femurs with implanted Müller prostheses, it was concluded that the ratio (a1.F2)/(a2.F1) was also indicative for the relative movement between prosthesis and femoral shaft under physiological loading.

6. PERSPECTIVES FOR FUTURE IMPLANT DESIGN

From our experiments, it was concluded that an accelerometer mounted into the prosthesis would significantly increase the feasibility of the vibration technique. It increases the quality of the signal obtained and extends the frequency range that can be applied. The actual sizes of commercially available accelerometers allow for such mounting. The problem is then situated at the level of the signal transfer from the accelerometer to a spectrum analyser. A telemetry system should be developed that is able to transfer signals with frequency components of up to 2000 Hz.
Such fully implantable system could provide an easy way to check the fixation quality of the prosthesis when doubt is cast on the integrity. Using the non-linear approach and with the parameters proposed, there is no need for a reference or 'control' value. From one measurement, the trained operator should be able to conclude on the fixation of the implant.

[1] Chung, J.K., Pratt, G.W., Babyn, P.S. and Pross, R. A new diagnostic technique for the evaluation of prosthetic fixation. In: Proceedings of the first annual conference of the IEEE Engineering in Medicine and Biological Society, New York, 1979, pp. 158-160

[2] Van der Perre, G. Dynamic analysis of human bones. In: Functional Behaviour of Orthopaedic Biomaterials (Eds. P. Ducheyne and G.W. Hastings) 1984, pp. 99-159 (CRC Press, Baca Raton, Florida)

[3] Rosenstein, A.D., McCoy, G.F., Bulstrode, C.J., McLardy-Smith, P.D., Cunningham, J.L. and Turner-Smith, A.R. The differentiation of loose and secure femoral implants in total hip replacement using a vibrational technique: an anatomical and pilot clinical study. Proc. Instn. Mech. Engrs, Part H: Journal of Engineering in Medicine, Vol. 203, pp. 77-81, 1989

Paper presented at the Second European Conf. on Smart Structures and Materials, Glasgow 1994, Session 9

'SMART' CONSUMER PRODUCTS WITH A 'PATHFINDER' PRODUCT DEVELOPMENT STRATEGY.

Alec Robertson *MA(RCA) MCSD FRSA*

School of Design & Manufacture
De Montfort University, Leicester, England.

It is generally acknowledged that technologies diffuse through industry and that the rate of diffusion varies both within different industries and according to the circumstances. Innovation is a process involving risk, especially during the adoption and adaptation of a powerful new technology. Central to a consumer products success using new technology is the quality of their designs and the nature of their forms. Form is of prime importance in influencing the purchasing decisions of consumers and it is also influential in determining the relationships between people in its use environment.

The acceptance of a new product into the world is often unduly *ad hoc*. Many failures are created for each success and there are few guidelines to assist the formulation of a strategy for creating an appropriate form. It is suggested below that success of consumer products incorporating 'smart structures' may be determined not only by the function of products and systems , but also by the form they take.

The definition of a desirable product form depends entirely on the point of view taken: technological, commercial, ecological, cultural and social. However any design using new will incorporate the old and the new. The probability of acceptance of a new product is enhanced by maintaining a fine balance between imaginative and creative form and that with which people are familiar and prefer: a new design may be rejected if it is too novel and unfamiliar, or too traditional. The acceptance of a new product and its subsequent development depends on the success designers and engineers have when dealing with the initial forms, particularly using new technology such as 'smart structures'.

Classifications of Designs.

The classification of products into types is usually done by function eg. washing machine, and by specific model features eg.. BMW 325 i. However, many products have similar models with similar features competing in the marketplace. How can the acceptability of a product be designed from the perspective of form?

Four archetypes of products are suggested as being helpful in guiding the design of product form with the introduction of 'smart' technology:

a. "horseless carriage" products (HCD's) - designs embodying new technologies using on traditional design concepts and forms by default.

b. "radical products" - designs with completely new forms introduced without user testing.

c. "pioneer" products - innovative designs incorporating an educational function.

d. "pathfinder" products - planned "horseless carriages" aimed to assist the assimilation of new technology.

The 'Horseless Carriage"Design or HCD.

The form of early automobiles resembled that of horse drawn carriages except for an engine, which was "bolted on" as an extra. The term is however used in this context with a broader

0-8194-1700-9/94/$6.00

meaning. It refers to any product that has yet to evolve into a stable and "mature" form after the application of new technology.

For example, the first use of plastics copied the forms of traditional materials; the form of products made in metal was used for plastic products of the same type. It has taken many years for the use of plastics to become "mature" i.e. regarded as materials in their own right, with their own qualities and form-giving properties. Likewise replacing the electromechanical switches in a washing machine by tiny microprocessors did not affect the initial form of washing machines incorporating them. Was a successful HCD of the past was the Ekco Model A22 Radio, designed by Wells Coates in 1945 and made by E. K. Cole and Company? It uses plastics technology, which was revolutionary at the time, and electronics but it resembles the form of familiar wooden mantelpiece clocks of the era.

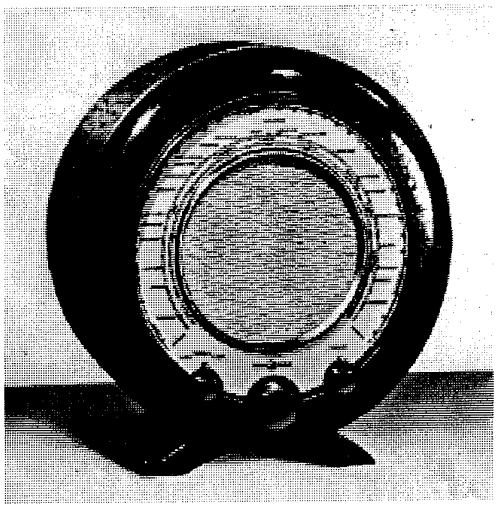

Why were such 'horseless carriages' designed? Clearly if form follows functions then there was not perceived to be a need for radical innovation in form. However, this might have been because the possibilities opened up were not envisioned. With hindsight many early models of products can be defined as HCDs. A contemporary HCD is more difficult to define as it is necessary to envisage future possibilities and ramifications for form. Creative engineers and designers are amongst those people with this ability. For example, folklore has it that when a company introduced their first wrist watch designed with a liquid crystal display that mimicked mechanical hands of a traditional watch face and presented to an audience of creative designers to the shock of the company representative they found it amusing. The designers intuitively recognised the design to be an HCD because they saw the potential for digital display of time using liquid crystal technology. This does not mean however that the company designers and engineers of this watch did not give it an appropriate form for the evolutionary phase of the introduction of liquid crystal technology in their product range and its acceptance in general.

Change in form as a result of new technology is not always desirable.The early models of new products have to pass many hidden tests to survive when both objective and subjective judgments are made on them during the initial phase of introduction. This is when the concept of an HCD is important.

The Radical Design.

A new technology or design idea often gives rise to radical innovation in form. In many cases people introduced to new products say, "What is it, what does it do, how does it work?" These products mystify people as in their research, design and development process no user testing or simulation was done to ensure their design and form was acceptable or marketable.

The Pioneer Product.

In a pioneer product there are radically new functions, technologies and forms however care is taken over their introduction through user-testing and simulations. As a result signs, instructions and explanations are incorporated into these innovative products to assist people. They incorporate an overt educational function aimed at assisting the creation of a bona fide place for themselves in the world.. An example of a past "pioneer" product is an early model of an NCR cash register . It had a sign on top of the pop up cash display saying, *"This Registers the Amount of your Purchase"*, something people have no difficult in understanding today. Information design is crucial to the success of 'pioneer' products.

The Pathfinder Product.

The anticipation of an appropriate form for a product to ensure it satisfies the needs of economic, ecological, cultural and social points of view is a central part of planning for any new product. The need to introduce a new technology in a product design can however overwhelm other needs, and this can result in a form which has been determined by the technology. New materials are often introduced and as a result a form is diminished as its qualities are displaced with the materials.

Central to the concept of an HCD is the fact that new technology does not dominate the form of a product. The notion may act therefore as a mediator between conflicting factors influencing product form where innovation has to be implemented carefully. A positive term is proposed for a "planned HCD" - a "pathfinder" product. The form of a "pathfinder" product is made to follow a generally acceptable evolutionary development. It may adopt metaphors, shapes, functions and organisational structures of the past while also incorporating new ideas and technologies within a strategic design plan. This plan will take the product from the present to a desirable future form in a considered, controlled and responsible way.

'Pathfinder' Product Planning with CYB-ERG

Radical innovation is taking place today with 'smart' structures. Instead of the bolt-on engines of yesteryear today's HCDs and "pioneer" products have bolt-on 'intelligence' within smart structures. There are likely to be many casualties of innovation as there were with the adoption and adaptation of motive power technologies to craft processes and tools in the First Industrial Revolution. It seems appropriate therefore that organisations look at the concept of a "pathfinder" product closely and use it to help ensure short term acceptability for new products.

One aspect of product innovation has significant influence on the direction taken in their metamorphosis. This is the decision to enhance or displace human involvement. The

relationship between the control, use of motive power, and power to process information in products is depicted in the CYB-ERG framework shown below.. It shows the underlying evolution of human-tool relationships in terms of the capability to replace or enhance the physical and mental tasks of a person.

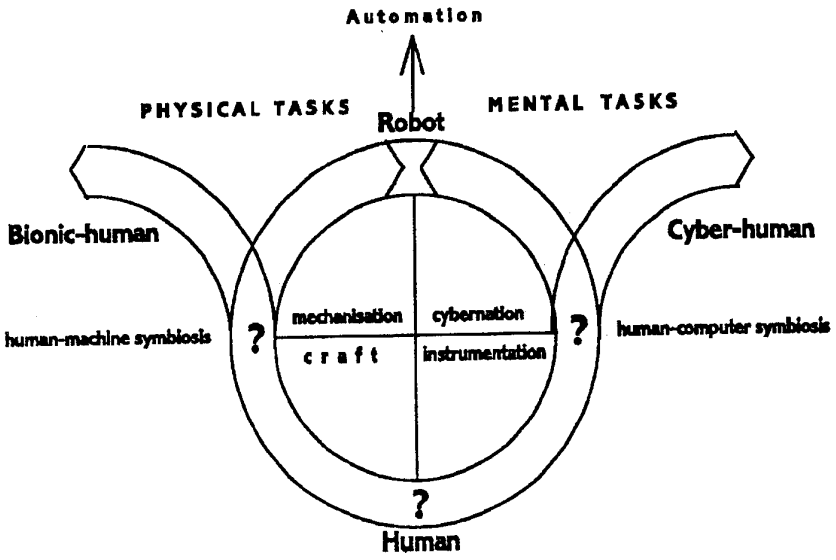

What policy for the evolution of form - pathfinder, pioneer or horseless carriage?

CYB-ERG -The evolution of human-tool relationships.

An HCD phase can take place at two main parts of CYB-ERG - at the beginning when a type of tool is invented, and when additional power is added to the tool, whether motive power or information processing power. It is at these two parts where a "pathfinder" strategy could be taken. The design and engineer envisages future evolution of forms of product along the CYB-ERG curves to help the development of an acceptable 'smart' product.

Conclusion

Forecasting the need for future products is a necessary one undertaken by many organisations. Predicting the possible and, more importantly, the desirable forms of tomorrow is difficult and creating a "pathfinder" product with a fine balance between the old and the new together within a strategic plan for its metamorphosis will not be an easy task. Knowledge from cognitive psychology, human computer interface design, human factors and marketing can contribute to this. However product planning can be assisted by harnessing the skills, insights and creativity of designers and engineers capable of envisioning the evolution of product form .

Speculation on the evolution of artifacts incorporating 'smart structures' is needed. For example, with mechatronics, speech recognition and voice synthesis software artifacts may take on the characteristics of people and more explicitly represent human characteristics; the rude / funny /arrogant / left-wing/right-wing consumer product may well appear.

As sophisticated "time control" of artifacts is possible with 'smart structures' they will become more animated. For example, architectural form may become less frozen in space and more like visual music with smart environmental control systems as responsive as botanic ones. Will buildings take on the forms of plants and flowers? As products will become more adaptable with 'smart structures', people will 'tune' products to suit themselves and thus become designers. A paradigm shift from static 3D design to dynamic 4-dimensional design will appear for future industries.

Also as more artifacts incorporate efficient 'smart structures' one result of this could be that ecological pressure groups will unwittingly see many of their materials resource goals achieved, but movement uses energy so there will be challenges for design and engineering ethics and professional responsibility.

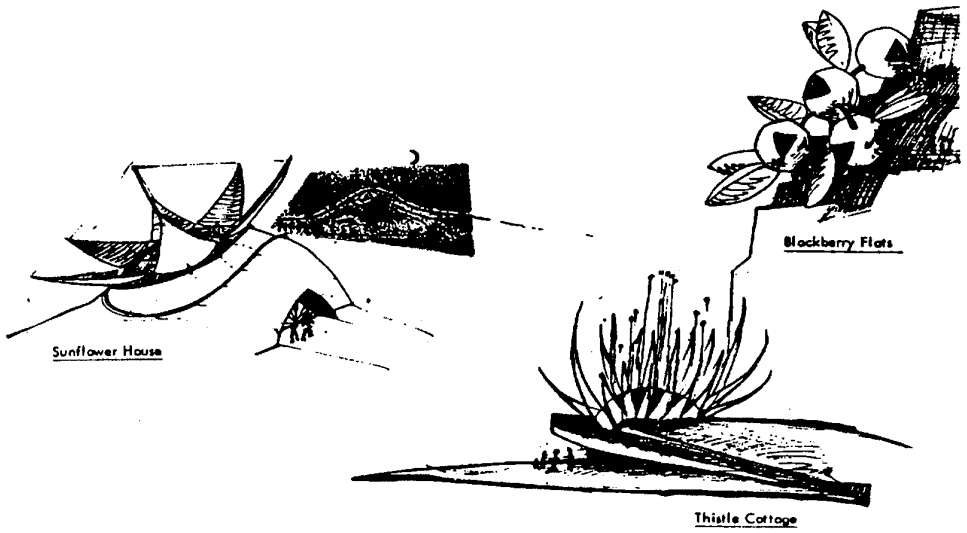

Botanic Architecture with smart structures?

The value of using the concepts of HCD, radical, pioneer and pathfinder products with CYB-ERG is that innovation may be made less *ad hoc,* more explicit, and therefore more controllable with less risk. The concepts might also be used to help control the pace of innovation where its consequences need to be taken into account. It might also help explain why past designs had their particular forms. The subject of "form" may, as a result of the concepts become more important and give 'design' more influence in determining the nature of artifacts.

Designers and engineers might be able to contribute more to the mitigation of the negative consequences of innovation with new technology as well as to the creation of new products and wealth generating industries of the 21st Century using 'smart' structures and technology.

References

Robertson, A., "CYB-ERG: A proposed model for assisting innovation in products, and their design". Paper in Creativity and Innovation Network Journal.Vol. 9, No. 3, July-Sept., 1983. Manchester Business School.

Robertson, Alec."Technolust versus creative design: some implications of intelligent products for design". Intelligent Consumer Products Symposium. Institute of Electrical Engineers / Chartered Society of Designers. London ,1992. IEE Digest No. 1992/013.

Robertson, Alec. "Speculation on the future of engineering the environment and communications design". Proc.. First International Conference on Environmental Engineering. De Montfort Univ. Leicester. 21 Sept. 1993.

Robertson, Alec. "Pathfinder products: reducing risk is design innovation" Proc.. The International Forum on Design Management Research in Education. 1-3 June 1994. Design Management Institute/ ESCP Senior. Paris.

Copyright © Alec Robertson 1994. /DMU.

Paper presented at the Second European Conf. on Smart Structures and Materials, Glasgow 1994, Session 9

SINGLE-CRYSTAL INDICATORS OF FATIGUE AND PLASTIC DEFORMATION DAMAGE

Yu.G.Gordienko and E.E.Zasimchuk

Institute of Physics for Metals of the Ukrainian Academy of Sciences, 36 Vernadsky St, Kiev, 252142, Ukraine,

ABSTRACT

Specially prepared thin single-crystal plates rigidly fastened to the sample surface area are shown to be effective as sensor elements (indicators and detectors) of the deformation damage of multi-phase commertial alloys under fatigue and static loading. It is proposed to estimate the lifetime and the strain of basic material by monitoring the geometric characteristics of band patterns on the detector surface. It is shown that density, direction of deformation bands and fractal dimension of band patterns on surfaces of indicators correlate with the number of cycles, maximum applied stress (fatigue loading) and plastic strain, temperature (static loading).

1.INTRODUCTION

The complex-alloyed multy-phase alloys (MPA) have the very inhomogeneous structure, and their behavior in the mechanical field is determined by a number of simultaneous processes. The plastic shape change promoting the deformation damage of the alloy structure is just one of such processes and is hardly controllable by conventional techniques, such as direct measuring or the analysis of deformation damage of the structure (spreading of X-ray diffraction reflections, hardening and substructure analisis, etc.). As a rule the plastic deformation of MPA is localized within separate microvolumes under any chosen loading conditions. Since it is difficult to predetermine such volumes, the analysis of shape change is complicated.

On the definite stage of loading the plastic deformation of single-crystals is localized in elements of band structure; localization of deformation and structural transformations define band stability after loading action is removed (Persistent Slip Bands, Shear Bands, etc.). Localization of deformation in band causes also a forming of surface relief, which is stable to following heating, agressive environments action, etc. This fact can become a basis of designing single-crystal sensors (in the form of thin plates) of deformation damage. Sensors can be stiffly attached to the analyzed construction in the points of possible localization of deformation. The series of results, which confirm the effectiveness of single-crystal sensors (detectors) used for the analysis of deformation damage under fatigue or static loading of sample made of technical alloy, were obtained in our laboratory.

2.EXPERIMENTAL

We used the single-crystal foil[1] as a detector to analyze the deformation damage and the lifetime of the aircraft alloy samples at the static uniaxial and fatigue loading. The composition of alloy is as follows: Cu - 4% wt, Mg - 1.3% wt, Mn - 0.6% wt, Al - 94.1% wt. The 30 mm long fatigue indicator was made of single-crystal aluminium foil (99.99% wt Al). The aluminium plates were cut of the melt grown single crystal by the Bridgeman technique. The high purity of the material and the relatively low growth rate ensured the absence of the cell composition microinhomogeneity and the low angle ($< 15^{o}$) boundaries. The indicator was stuck on a flat specimen 1.2 mm thick[2]. The preliminary experiments shown that the presence of detectors in the working part of the sample did not change mechanical properties at any used testing procedures.

The TEM study of the alloy structure after the mechanical treatment did not enable to reveal classic symptoms of the deformation damage (an increase of the dislocation density, the appearance of dislocation clews, boundaries, etc.). Only 0.7 - 2.5 μm size inclusions statistically distributed over the area under investigation are seen at the micrographs. Neither direct methods of structure and deformation surface relief study nor indirect ones (i.e., the analysis of hardening and X-ray scattering peculiarities) did not allow to reveal any evident signs of damage (i.e., manifestation of forming the sites of destruction) in the final state of material under the loading. The analysis of various parameters of structure regularly changing during deformation of single phase materials is impeded, because of their complex dependence on the phase transformations during loading.

The information about the deformation damage of the sample material near detector was derived from the analysis of the detector surface relief. For this purpose the surface of single crystal

0-8194-1700-9/94/$6.00

plate was grinded and electrolitically polished. To analyze the relief of detector surface the light microscope was used. The direction of bands observed on the surface (with regard to the tension axis) and the striation density k ($k=l/n$, where n is the number of bands crossing the l length segment of line perpendicular to the striation direction) were determined. The fractal dimension of the band patterns was calculated by "yardstick" method [3].

3.RESULTS

The following features of the surface relief were observed for fatigue loading:

1)the striation density, k, rapidly increases with number of loading cycles, N, by:

$$k = CN^c,$$

where c = 0.248 for maximum applied stress σ = 140 MPa and c = 0.577 for σ = 180 MPa, C is the constant [2].

2)the angle between the striation inclination and the loading axis is about 80° and does not change with the N and increase of σ;

3)the striation direction does not correspond to traces of crystal slip;

4)the sites of destruction (microcracks) are parallel to the striation direction;

5)the fractal dimension of the band patterns (Fig.1), which was equal to 0.99 (σ = 140 MPa) at the outset of the loading, slowly decreased in the wide range of loading cycles and underwent sharp decrease before destruction.

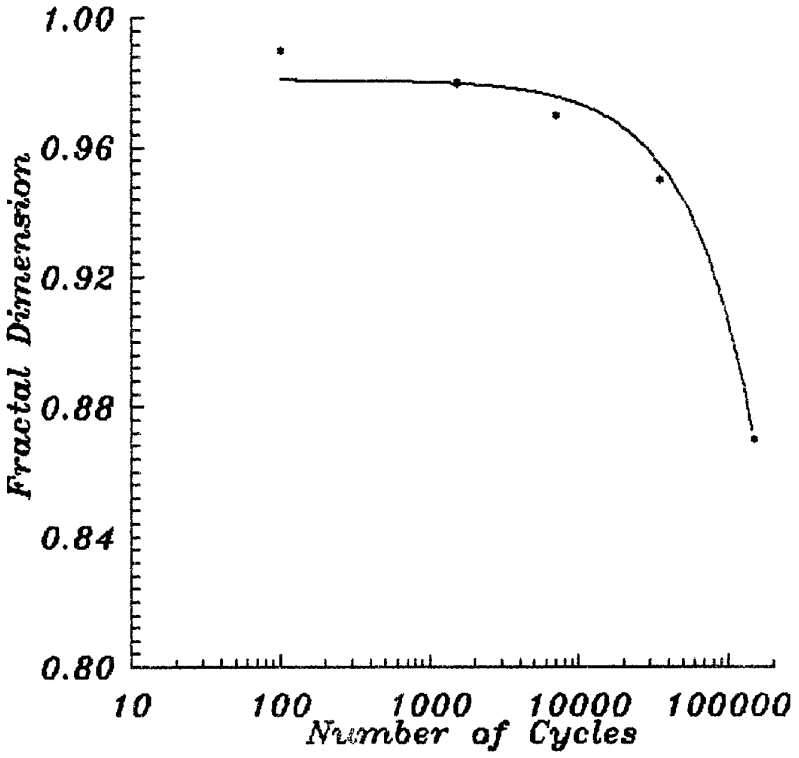

Fig.1.

The singly-applied static loads of indicators installed on above mentioned samples brought to light the same features of relief. On the whole the deformation bands had the same properties mentioned in 2)-4). The striation density, k, rapidly increases with the applied strain, ε, by:

$$k = B\varepsilon^b,$$

where b = 0.861, B is the constant[2]. The main differences are existence of pattern of the secondary bands and non-monotonous dependence of its fractal dimension as a function of the applied strain. The direction of bands was 57° relative to the tensile axis. As to the fractal dimension, been initially equal to 0.99, it falled to 0.33 (up to ε = 3 %) and then slowly increased along with the strain increasing. Moreover, the dependence of fractal dimension as a function of temperature can be observed. This dependence was also observed by other investigators and is known for different materials [3-5]. However, the very careful calibration of the indicators is necessary for their usage.

4.DISCUSSION

Formation of band structures (Persistent Slip Bands - PSBs, Shear Bands - SBs and others) in crystals under loading is well known to be related with defect localization [6-8]. The proposed models [9] are often based on the assumptions about cooperative behavior of defects (dislocations, vacancies and others) and, in general, are described by the set of non-linear partial equations of reaction-diffusion type. It is known that appearance of instability with regard to spatial inhomogeneous disturbances is possible in the systems. Development of instability leads to spatial structures ("dissipative contrast structures") [10,11], which consist of alternating regions with very different values of defect concentration. This process can be the basis of structure formation of spatial band patterns as persistent slip bands (PSBs) in crystals under fatigue loading and as shear bands (SB) in crystals under static loading. However, the well-known models [9] cannot fully explane the defect patterns observed in single crystals under fatigue loading [2] and single-applied static loading [3-5].

The fractal dimension D (calculated by "yardstick" method [4]) of equidistant and randomly distributed bands is equal to 1. It allows to suppose that at the beginning of the loading the surface relief was mainly caused by outlets of single dislocations, which form patterns of randomly distributed bands (D = 0.99). However, further, ordering in the defect system attributed to self-organization effects in ensemble of dislocations and point-type defects [12], could lead to the very high localization of defects in small region of crystal. The temporal evolution of the spatial inhomogeneties in crystal lead to localization of deformation and significant change of the crystal behavior, which is followed by appearence of the complicated band patterns. The change of their fractal dimension can be evidence of structure evolution and forthcoming changes of behavior of the material. The changes can lead to significant macroscopic consequences (i.e., destruction of fatigued samples, high plasticity and destruction of uniaxial tensioned samples). Thus, calculation of the fractal dimension of patterns on the surface of indicator can allow to predict the drastic changes in its behavior. Using pairs indicators - basic sample with the similar lifetime characteristics, it is possible to predict lifetime of industrial constructions by fractal geometry analysis of surface patterns.

5.CONCLUSIONS

The method proposed allows to obtain the quantitative information about the accomodation of deformation damage in the material during the fatigue and static loading:
- the extent of plastic strain during uniaxial loading;
- the direction of applied load during fatigue and uniaxial loading;
- the number of applied cycles with high accuracy;
- the maximum applied stress in fatigue;
- the extent of reliability and safety of materials in fatigue.

The method is a very cheap and can be applied in the hardly accessible and aggressive mediums, where special devices cannot be used.

ACKNOWLEDGMENTS

This work was supported, in part, by the Ukrainian State Committee for Science and Technology and Soros Foundation Grant awarded by American Physical Society.

REFERENCES

1.E.E.Zasimchuk, A.I.Radchenko and M.V.Karuskevich, Otkrytiya Izobreteniya (USSR), 27, 171 (1990).
2.E.E.Zasimchuk, A.I.Radchenko and M.V.Karuskevich, Fatigue Fract. Engng. Mater. Struct. 15, No.12, 1281 (1992).
3.B.Sprusil and F.Hnilica, Czech.J.Phys. B 35, 897 (1985).
4.T.Kleiser and M.Bocek, Z.Metallkde, 77, 582 (1986).
5.I.R.Gobel, Z.Metallkde, 82, 853 (1991).
6.U.Essmann, Phys.Stat.Sol.(a), 12, 723 (1965).
7.A.S.Malin and M.Hatherly, Met.Sci., 13, No.8, 463 (1979).
8.E.E.Zasimchuk and L.I.Markashova,Mater.Sci.Engng.,A127, 33 (1990)
9.L.P.Kubin (editor), G.Martin (editor), Proceedings of the International C.N.R.S. Meeting. Dif. and Def. Data. B3,B4 (1988).
10.V.A.Vasiliev, Yu.M.Romanovsky and V.G.Yahno, Autowave processes, (Nauka, Moscow, 1987).
11.B.S.Kerner and V.V.Osypov, Autosolitons (Nauka,Moscow,1991).
12. Yu.G.Gordienko, E.E.Zasimchuk, Phil.Mag. (in print).

Paper presented at the Second European Conf. on Smart Structures and Materials, Glasgow 1994, Session 9

Stress-Fail Indicator for Agricultural Packaging Materials

Alaster McDonach
Smart Structures Research Institute, University of Strathclyde, Glasgow

Jeff Nichols
Agripac Ltd, Dundee

Abstract: *This paper describes the design and development of a low cost indicator mechanism that is triggered by overloading. The method is applied to Flexible Bulk Containers (FIBCs) and detects overloading during handling.*

BACKGROUND

Increasingly, packaging materials are being designed to satisfy complex multifunctional demands. this is in parallel with demands for cost reductions. In the area of agricultural materials, the response to this has been to develop Flexible Intermediate Bulk Containers (FIBCs). The industry standard some years past involved stacking low weight (50-100kg) bags on wooden pallets and transporting these pallets from manufacturer to end-user site. With the advent of FIBCs these labour intensive methods of handling 0.5 tonne, 1 tonne and 2 tonne loads have been superseded. In their place, single point lift and multiple point lift bags have reduced the cost of handling and storing bulk materials. These bags are simple to manufacture and yet provide a convenient medium to contain bulk materials. They are easily stacked and finally, do not require sophisticated lifting equipment during transportation.

Their low cost of manufacture stems from the simplicity of the weaving and sewing methods used in construction. Polypropylene tape is drawn and then woven into either a sheet or tub which can be cut and sewn to form a container and either lifting handles may be attached separately or alternately fashioned out of the body material.

PRODUCT SAFETY

With such a low cost product, performance and cost effectiveness is significantly influenced by its overall design. Safety issues are dealt with by standardisation on performance requirements. Once a design can be shown to meet certain standards it is then qualified for commercial use. However, with such standards, safety is ultimately dependent on proper handling and proper lifting. Mishandling which may compromise the carrying capacity of the bag could go unnoticed and future operator safety could easily be comprised. To add to overall confidence in the product and improve operator safety it was suggested that this product would benefit from a stress-fail material that would be incorporated into each product. This is especially the case since high loads are can be produced in the lifting and stacking of these products. Test results on fully loaded containers have shown that even moderate drop heights of 20-30cm will produce a peak decelerationof between 5g and 6g.

INDICATOR FAIL MECHANISM

Successful implementation of any stress-fail indicator not only requires a faithful and repeatable trigger point but its incorporation into the product should not significantly add to the cost of manufacture. Further, the trigger mechanism should be independent of influences from the environment. It should, if possible, follow any product degradation such as chemical or UV attack on the base material properties.

0-8194-1700-9/94/$6.00

Studies on bag failure mechanisms revealed that the bags fail at seams found either in the handle area or at the bottom closure of the container. In very large bags, circumferential failure is possible, however, the majority of bag failures are in the vertical direction across transversely loaded seams.

A variety of potential mechanisms were considered as possible stress fail indicators including effects such as stress whitening (ref 1) and "tele-tale" threads at seams. Each of these suffered from various disadvantages in terms of visibility, cost of implementation or repeatability. While observing tape failure, it was noticed that there was significant fibrillation of the tape material, by a release of residual strain, following tape breakage. This suggested the possibility of creating the structure shown in figure 1 as a stress-fail indicator. The front tape is self-coloured to match the normal material. However, the tape has been engineered to fail at a much lower strain level. The backing tapes are in a contrast colour with a breaking strain level similar to the normal bag tapes. With this structure where the bright coloured and contrasting background tapes are revealed indicating overstressing of the bag This has the added feature that the "piggy-back" tapes are easily incorporated into the manufacturing process. Success of the method is however dependent on obtaining a suitably low breaking strain material, appropriate strain transfer between front and back tapes, and a correlation between seam damage prior to failure and the imposed strain levels within the invisible sections of the bag.

STRESS-FAIL MATERIALS

Some of the necessary elastic properties of possible stress-fail materials are shown in Figure 2. The polypropylene tape with a higher draw ratio is an excellent candidate since it is the same as the base material and it comes in a tape format which is easily incorporated into the current manufacturing process. With increasing draw ratio, the tape stiffness is increased and the ultimate breaking strain decreases. (ref 2). In terms of product design, the required breaking strain can be measured from tests on completed bags.

STRAIN MEASUREMENTS

Figure 3 details how the bags were loaded and the areas where the strain measurements were made. Graph 1 shows the typical strain values measured in testing a 0.5 tonne bag. From this graph, we can deduce the trigger level needed for a "Stress-Fail" indicator tape to be approximately 2.9 tonnes (5.5% strain), for a "Smart Stripe" located near the filling slit of the bag. This would give a trigger level of 6 times the design load.

RESULTS

Special tapes with these properties were prepared and woven into 0.5 Tonne bags. During static load trials, they did indeed fail at 2.9 tonnes and provided a visible indicator of overloading of the bag prior to failure.

CONCLUSIONS

A simple and low cost method of providing an overload indicator has been devised for use with Flexible Intermediate Bulk Containers (FIBCs). It is simple to incorporate into the current manufacturing processes and provides a significant improvement in safety during the transport and storing of bulk agricultural materials. Further tests are required to ensure that the dynamic loading of the stripe is similar to that in the static load case and also to investigate the fatigue behaviour of the new Product. This will be reported at the conference.

REFERENCES

1 Ossman, H., and de Haas, H.,"Progress in Fibre Extrusion of Polypropylene"1977, 20th year in Textiles conference, USA, Paper IV.

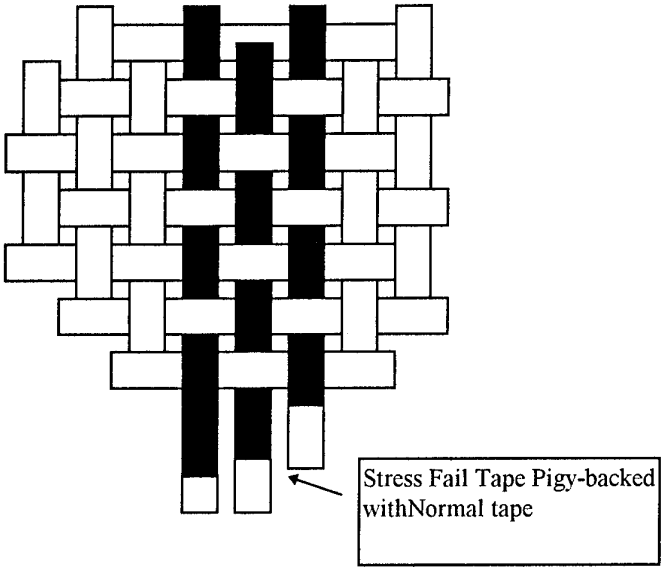

FIGURE 1

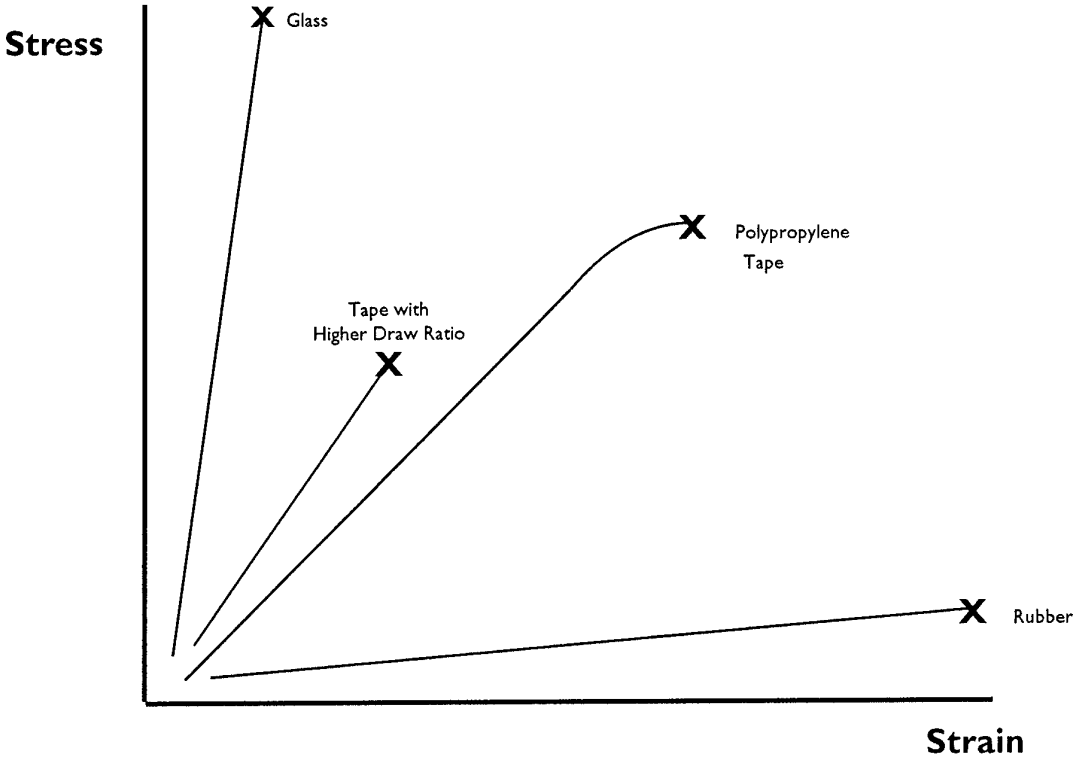

Figure 2

Stress-Strain Behaviour of Possible Stress-Fail Materials

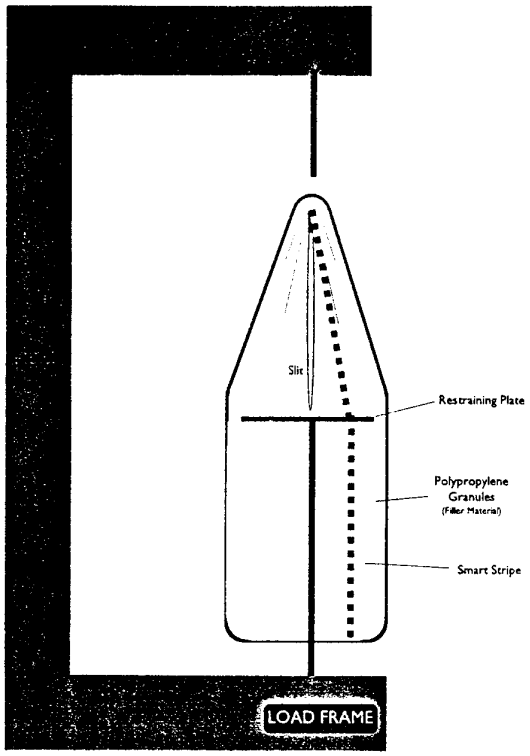

Figure 3
Static Loading Arrangement for FIBC

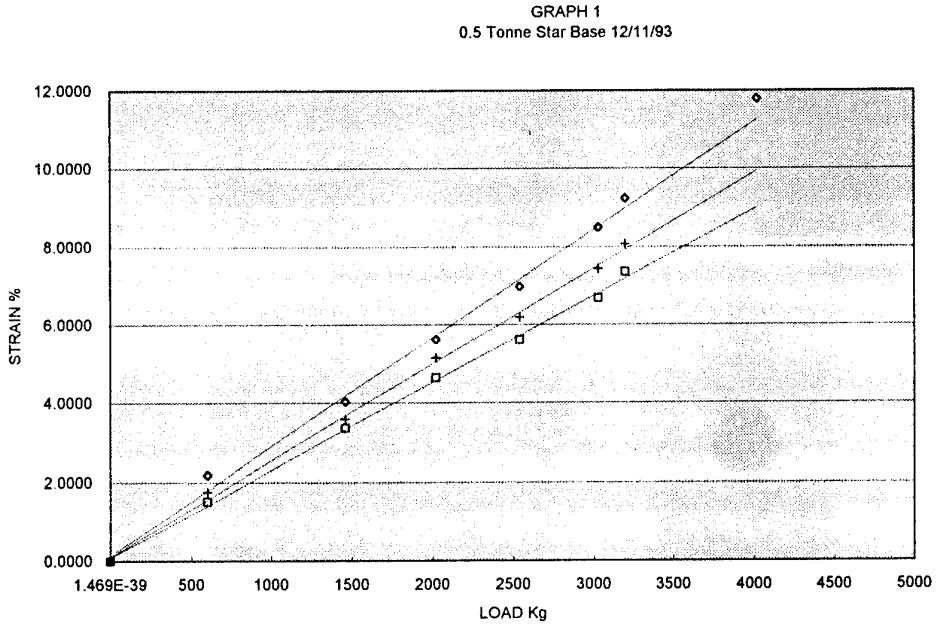

GRAPH 1 Strain Load Curve for 0.5 tonne bag Showing Warp Strain Levels at Three Different Points Around the Bag Circumference.

DESIGNING BUILDING SKINS AS ENERGY EFFICIENT MODULATORS.

ADE ADEKOLA

BA(Hons) Arch, AA Dipl.

MANIT RASTOGI

B-Arch, AA Grad. Dipl., A.I.I.A., M.C.A.

ABSTRACT.

Homeostasis refers to the process by which living organisms maintain internal bodily balance and equilibrium. For buildings, to embody the principles of homeostasis gives them a potential of becoming truly energy efficient and thus effective.

(1). INTRODUCTION:

It is becoming more apparent that buildings contribute significantly to the serious environmental problems of the planet. On the eve of the oil embargo, it was cheaper to burn lights continuously in glass buildings, day and night, than to install light switches. Pre-oil crisis modernity lacked environmental consciousness as a design parameter. Industrialisation and abundance of energy led to reliance on mechanical HVAC and lighting systems and the consequent degeneration of the building envelope as an environmental moderator. The building envelope had become oblivious of the climate and indoor conditions were mechanically controlled by the user.

The resultant energy crisis, global warming and damage to the ozone layer has resulted in a paradigm shift over the last 25 years.

The objective now is that of redefining the parameters involved in the design of buildings and their constituent elements and components.

In general terms, the materials that are of interest in this field are those that can 'alter state' in response to external stimuli (either directly or through some medium of control), or those that can in any way provide a new solution to a particular design criteria, or project the development of new design criteria.

We will show in this paper designs for building envelopes, as passive skins and active and thus adaptive skins.

(2). ENVIRONMENTALLY RESPONSIVE MODELS

Conventional building design with its profligate use of energy and materials embody static materials and by that virtue, generally display environmental inadequacies, they are unable to optimise their physical properties to variations in the environment. Fundamental omissionsof the potential of energy and environment concerns and their integral role in the evolution of architecturaldesign results in buildings that are then often reinvested with visually exaggerated use of so called 'Hi - technology'to achieve comfort conditions. Making an architecture which is conscious of it's energy balance would not only make a considerable impact on global energy consumption, but could also heighten public awareness of this vital issue therebygenerating a physiological and psychological relationship between society, environment and architecture.

To make such abuilding is to create a system linked to its surrounding environment and subject to a range of interactions affected by seasonal and daily changes in climate and by the requirements of the users varying intime and space. Designing low energy buildings involves the requirement of a frame of reference againstwhich the building process may be evaluated taking into account the inherent as well as infusedenergy of the materials from their production to their assembly. The scope of the 'comfort zone' could be furtherbroadened to encompass factors other than thermal comfort. The response factor today mostly deals with seasonabr diurnal variations whereas the need is for optimisation of all of these toresult in a dynamic response both to external and internal conditions.

0-8194-1700-9/94/$6.00

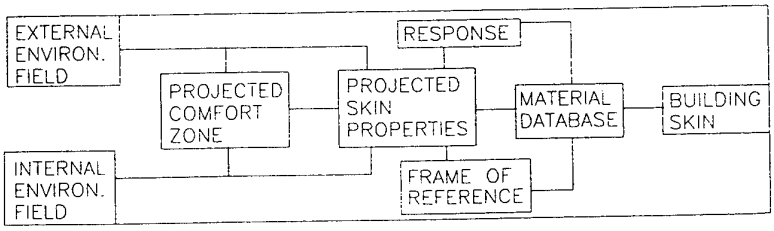

(3). ADAPTIVE SKINS.

A building skin may be defined as a single system of interrelated compatible components: a combination of Opaque (walls and roof), translucent (window), transparent (windows) and Void (opening) components and a summation of external elements such as blinds, louvers, shading devices, overhangs etc.; of which each component serves and impacts particular environmental criteria.

The influences and the requirements of the enclosure of a building are cumulative both in it's generation and it's consequence. The development of the enclosure as a form of shelter to the contemporary requirements of a 'user defined' space have led to complex and varied inter-relationships (spatial, environmental, structural and psychological) of the functions of the building skin on man, the environment and the building itself.

In what follows we will outline the type of building components/systems that should be investigated if the environmental issue is to be taken as a serious part of the design process.

(4). PASSIVE COOLING CLADDING SYSTEM. (P.C.C.S)

Passive systems differ from active systems in that they are primarily driven by sources of energy that nature provides, whereas active systems need natural energy to be converted into other forms to be driven.

Cladding systems are protective coverings systems. The PCCS is a system designed to provide the general protective covering to buildings, as conventional cladding systems do, whilst also being capable of providing a means of air cooling for the building interior.

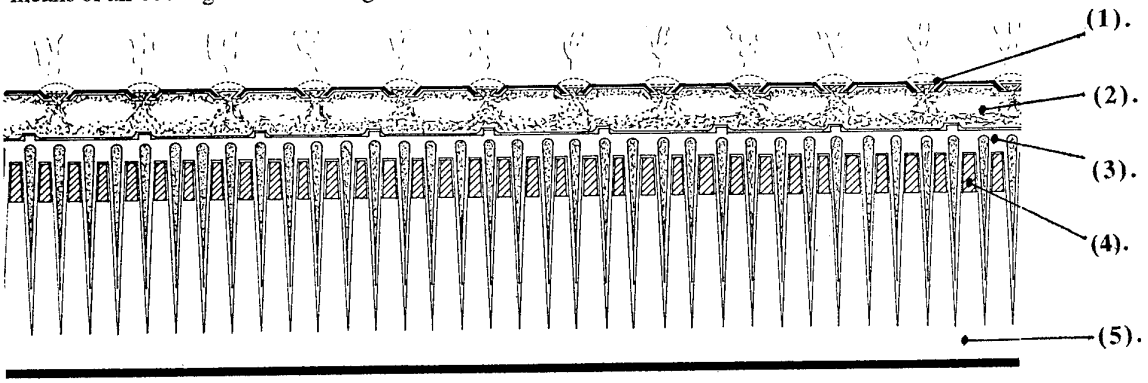

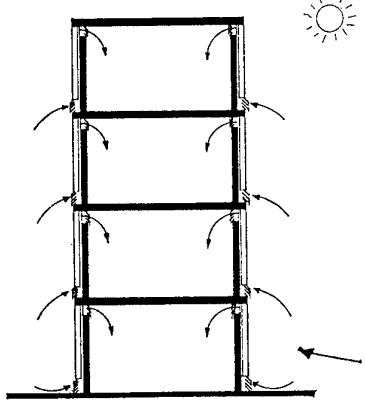

Each panel is made up of an outer surface which is perforated in a way and manner as to allow a fluid to evaporate through it (1). The next layer to the outer surface is that of a thick fluid absorbent material, which when dry has good insulation properties (2). Making very good contact to this absorbent material is a good heat conductor, which has attached to it a series of cooling foils (3). Protecting the main body of the conductor is an insulation barrier, out of which the cooling foils protrude (4). The cooling foils are housed in a chamber of which's construction is of a nature as to allow air to circulate over the foils freely and to channel the air into a building onto which the panels act as cladding (5).

Diagram of system assembled onto a building, arrows represent natural convection currents causing warm air to flow over cooling fins. The resultant effect is cooling to the building interior.

(5). SURFACE KINETIC INTEGRAL MEMBRANE. (S.K.I.M.)

SKIM is an explorative design of a composite material towards the realisation of a dynamic system where the actuative and the sensory layer are embodied within the structure of the material. The design exploits the use of electro-rheological fluid and current carrying coils - inducing a magnetic field - as the actuative material within a flexible latex membrane.

The composite design had three effective layers; the first being a flexible latex layer with peizo electric sensors embedded within it - this layer acts as a feed forward control interface. The second layer, the most complex, has three components, ER fluids, localised contact electrodes, and current carrying coils arranged in concentric circles to induce magnetic fields. The third layer is in effect a mirror of the first and acts as a feed back control interface. With this basic composite structure various profiles can be induced in the material.

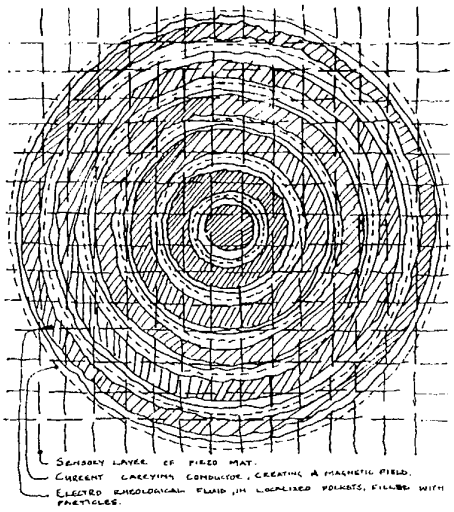

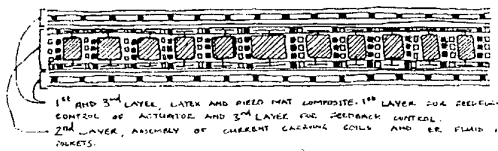

S.K.I.M. (SURFACE KINETIC INTEGRATING MEMBRANE)

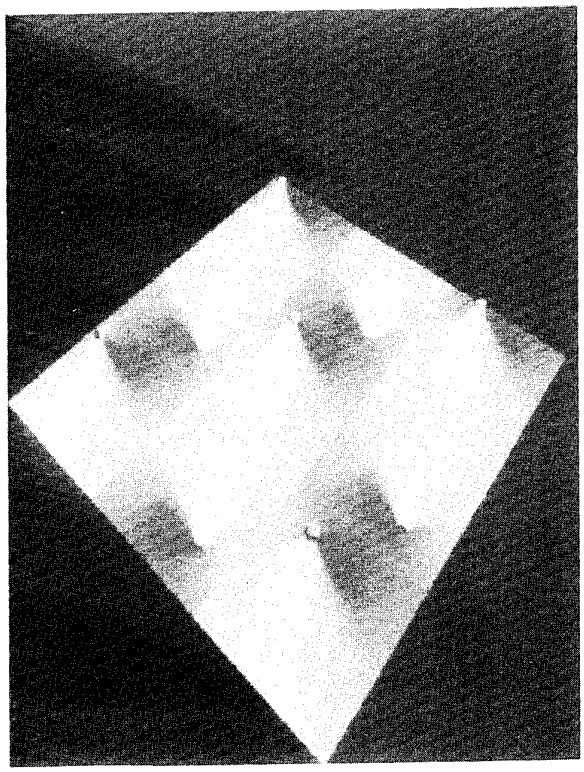

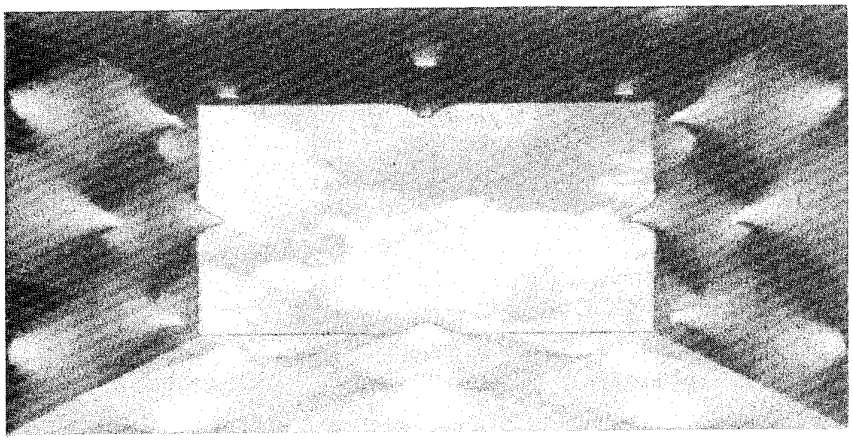

(6). A RESPONSIVE ROOFING MODEL.

This is a design and study of a roofing system that can change its physical properties to optimise towards various functional requirements of a building. It is shown here as a breathing roof, that enhances ventilation within a building. The design is that of a composite which utilises SMA's.

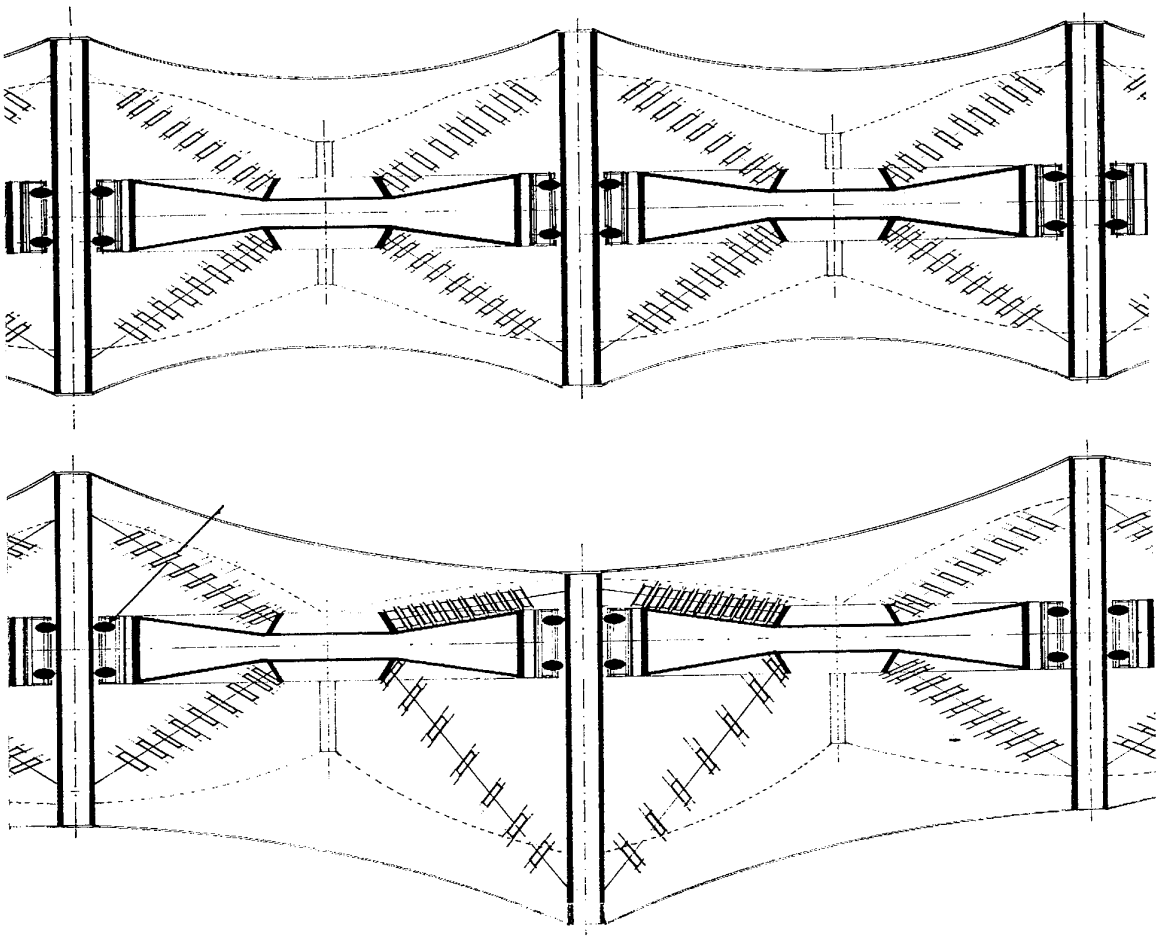

(7). CONCLUSION.

We as architects share part of the responsibility to humanity to propose and design environmentally sensitive building options, and the onus is as much ours as it is for engineers and material scientists to work out the operating dynamics of these designs, so that collectively we build truly energy efficient environments. In the words of Konosuke Matsushita " *collective wisdom, combined with concerted effort, is the true basis of human strength. Individuals may be powerless, but if we join forces we can move history or change our destinies*".

(8). REFERENCES.

(1). **Energy in Architecture.** The European Passive Solar Handbook. 1992 Batsford for Commission of the European Communities.
(2). Sandori P. **The Dynamic Wall.** (1990, Jan) Canadian Architect.
(3). Wilson F. **The Changing Nature of Building Skins.** (1989, March) Architecture, The AIA Journal.

Paper presented at the Second European Conf. on Smart Structures and Materials, Glasgow 1994, Session 9

CURRENT RESEARCH IN TIMED RELEASE OF REPAIR CHEMICALS FROM FIBERS INTO MATRICES

Professor Carolyn M. Dry
Associate Professor
School of Architecture
University of Illinois, Urbana-Champaign

ABSTRACT

The subject of this research is the enhancement of properties beyond that available in an original hardened material by the release of "healing" chemicals such as adhesives from hollow fibers into cementitious matrices in response to loading. Thus, the sensing of a crack by the fibers or the breaking of coating starts the activation of a remedial process (i.e., the release of a sealing or adhering chemical). This capacity for self-healing occurs whenever and wherever cracks are generated.

In terms of fracture mechanics, this research concerns the repair of cracks and rebonding of fibers by chemicals released from hollow fibers at the fiber wall and into the adjacent cracks. The overall property change is an increased flexural toughening. The mechanisms for that appears to be an adhesive rebonding of the fibers and a crack-filling with adhesives which causes the material to become stronger when it is bonded inside cracks or pores.

SELF-REPAIR MECHANISMS

Designs capable of passive, smart self-repair consist of several parts: 1) an agent of deterioration such as dynamic loading which induces matrix cracking, 2) a stimulus to release the repairing chemical such as fiber breakage, 3) a fiber, 4) a coating or fiber wall which can be removed or changed, broken in response to the stimulus, 5) a chemical carried inside the fiber, and 6) a method of hardening the chemical in the matrix such as drying the polymer adhesive.

Several time release designs to repair microcracks and rebond fibers have been investigated. They are:

1. Tensile or flexural loading breaks the hollow fiber releasing its chemical.
2. Loading causes debonding of the (hollow porous) fiber from the matrix. Stripping away of the coating causes the release of its chemical through the pores of the fiber wall.
3. Tensile loading stretches the fiber, causing lateral contraction due to Poisson's effect, thus releasing the chemicals from the pores of the fiber wall membrane.

OPTIMIZATION

To optimize the materials data is to be generated on: 1) the adhesive action of various glues, 2) the wetting of pores and cracks by adhesives in matrices, 3) the porosity of the matrix, 4) cracking behavior of the matrix with various fibers, 5) the time if set of adhesive and strength of set, 6) the mechanism of strength and ductility increase, 7) the variation of the above variables in bending, compression strength and fatigue.

TESTING

The testing being done to generate this data are 1) X-ray of cements, 2) visual assessment of dyed adhesive chemical release in cement, 3) recording of auditory sounds, or acoustic emissions, and 4) cross comparison of X-ray and strength data of release in various matrices. In this paper we describe the use of X-rays to inspect samples.

0-8194-1700-9/94/$6.00

The use of X-rays to "see" the bending of fibers release of adhesives was an unexpected success due to the hard work of my research assistant William McMillan. The test set-up consists of simple X-ray beam passing through the samples pulled in front of the beam (as seen in photo 1). The results of the X-ray tests are relatively readable (see photo 2). The dark line indicates a crack, the white lines the wire reinforcing, and the grey areas are cracks containing adhesives and most likely the released glues are the grey blotches. X-ray diffraction analysis will be used to confirm these findings.

The results of bending test samples containing glass fibers versus samples with no glass fibers were clearly different. The occurrence of cracking of the glass fibers versus influence of metal wires can be seen in Figure 1. The results of bending tests on some other samples reveal an increase in strength in bending and ductility (see Figure 2). A comparison of the records of the first loading (before release of the chemical) and the second bend test loading (after release of the adhesive into the matrix) reveals several important facts. The tops of the diagrams of the adhesive-filled samples are rounded, which reveals an elastic yielding as opposed to the sharper points in the diagram shape in the controls. Also, the adhesive-loaded samples carried more of the load on the second bend than on the first bend, while in general that was not the case for the controls.

The inference made from this is that the crack opening displacement curve for the controls follows the normal reduction in load resistance, while the adhesive-filled samples reverse it, in that crack-opening displacement is reduced with the next loading and the samples carry more load in the second test.

CONCLUSIONS

Tests on cement mortar samples with a smaller number of metal reinforcing fibers and glass fiber which released adhesive upon bending revealed that 1) in these tests bending flexural strength was increased for the second loading event as compared to controls without adhesive, 2) most of the controls showed a decrease in flexural bending strength at the second test, 3) flexural bending strength enhancement was obtained without major amounts of reinforcing fibers.

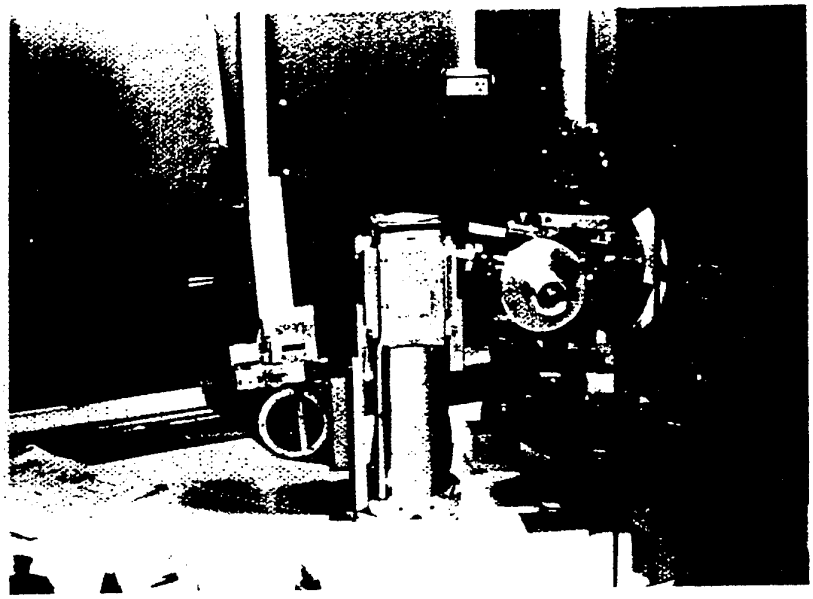

PHOTO 1

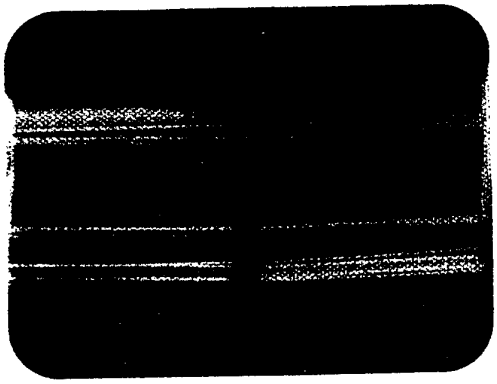

PHOTO 2

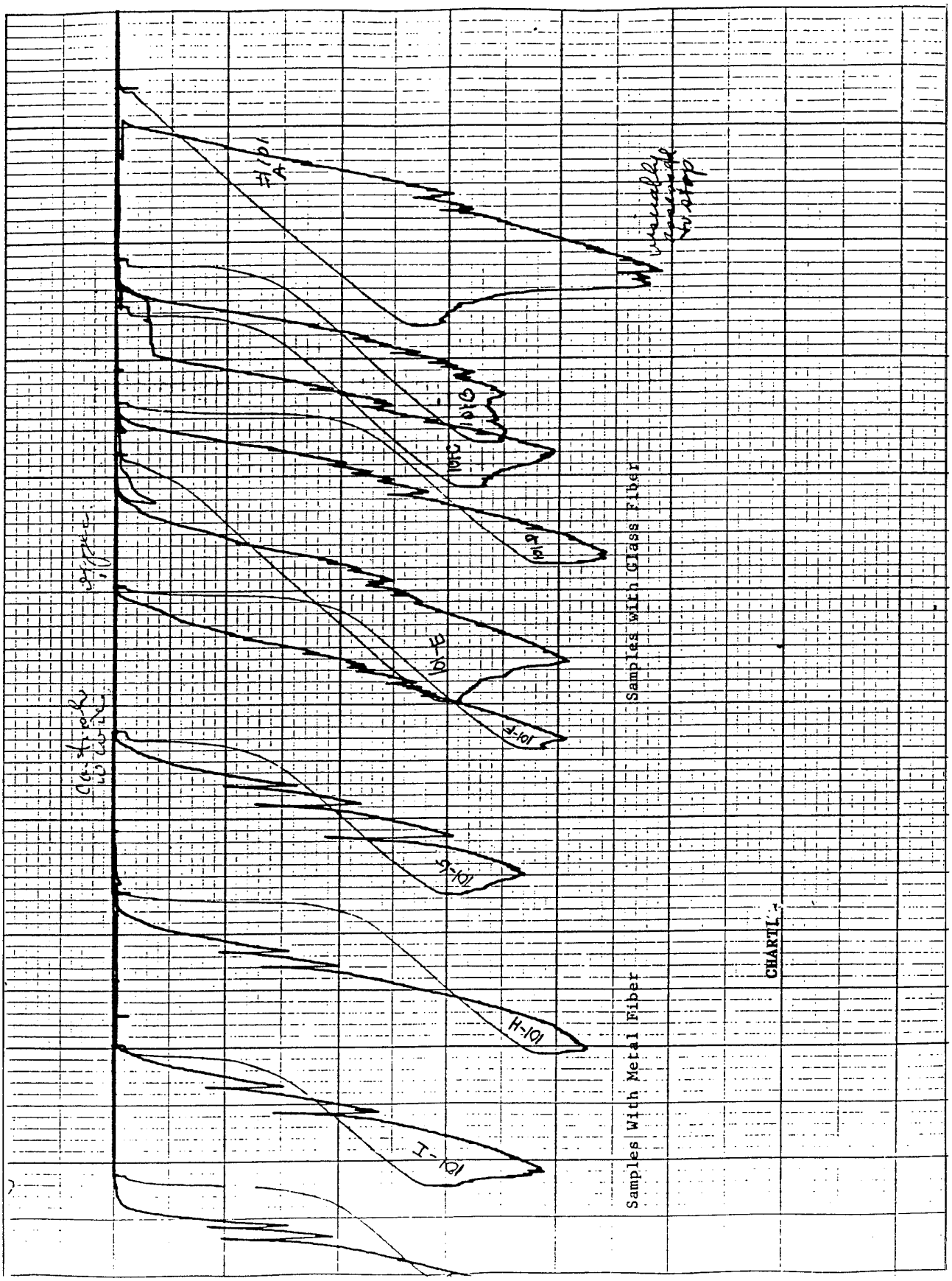
Samples with Glass Fiber
Samples With Metal Fiber
CHART

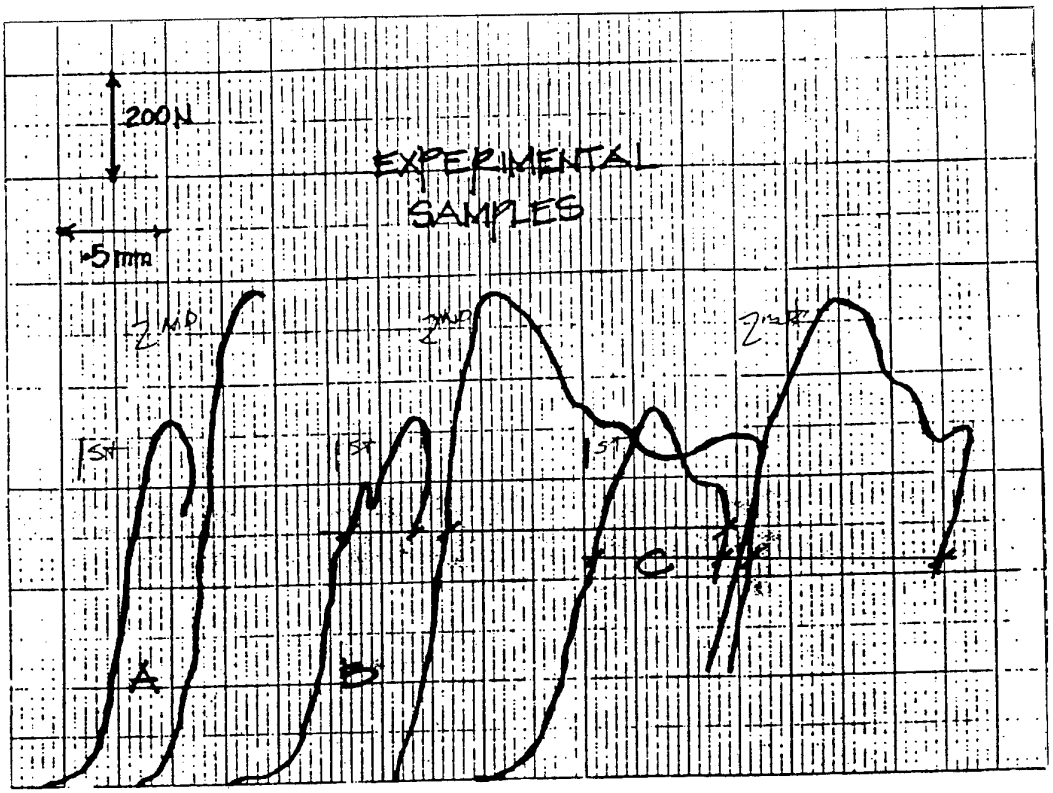

LOAD DISPLACEMENT DIAGRAM FOR EACH SAMPLE FOR FIRST AND SECOND 3-POINT BEND TEST

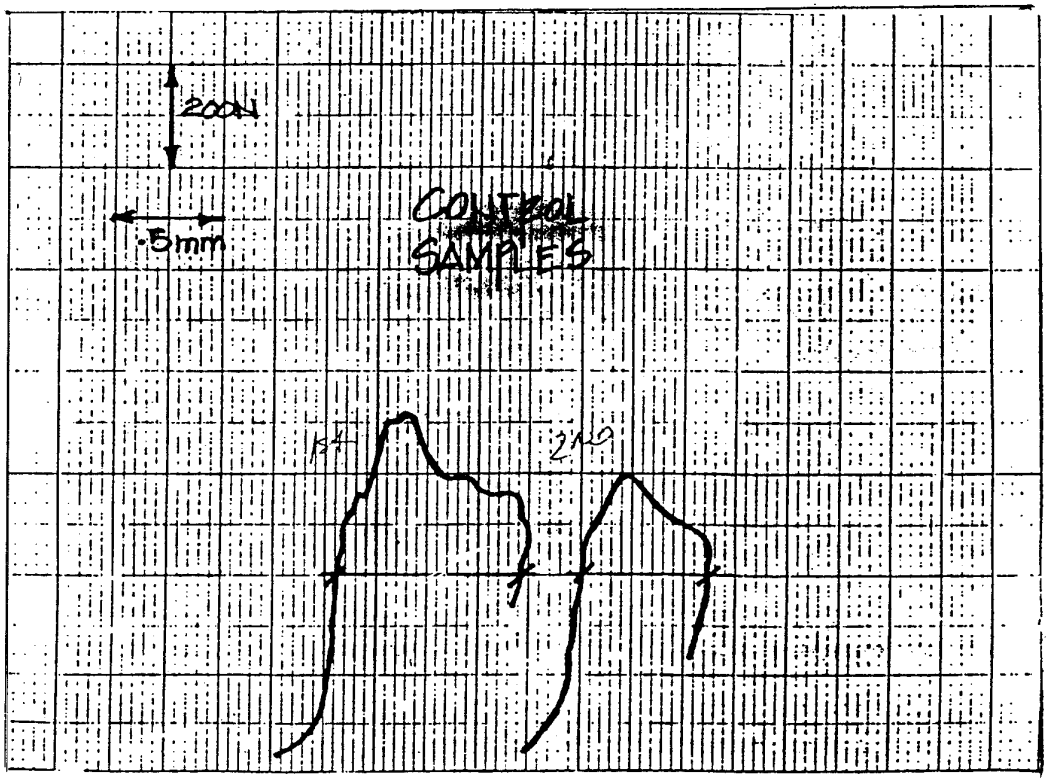

CHART II

LOAD DISPLACEMENT DIAGRAM FOR EACH SAMPLE FOR FIRST AND SECOND 3-POINT BEND TEST

SESSION 10

Paper presented at the Second European Conf. on Smart Structures and Materials, Glasgow 1994, Session 10

Electro-opto-mechanical Design of Fiber Optic Smart Structures

James S. Sirkis
University of Maryland
Department of Mechanical Engineering
College Park, Maryland 20742
301-405-5265 (Ph.) 301-314-9477 (FAX)

1 Introduction

The field of *fiber optic smart structures* has recently been an active area of research with many important advances in sensors, manufacturing and structural reliability. These areas of fiber optic smart structures have progressed independently to the level that separate design criteria are beginning to be formulated. As has been emphasized time and again, fiber optic smart structures is a multidisciplinary field that requires an integrated approach to system design and testing. This paper describes one such integrated design approach for composite material-based fiber optic smart structures. Both design for sensor performance and structural reliability are considered. The design for sensor performance presents a rational design philosophy for choosing the appropriate combination of sensors and demodulators to faithfully record the target strain in a *smart structure.* The design for structural reliability provides a rational approach for ensuring that the structure will support its design loads.

2 Design for Sensor Performance

The optical fiber sensor system designer is generally confronted with a series of design objectives. These design objectives will be specified in terms of minimum measurable strain (resolution), maximum measurable strain (range), frequency response, linearity, repeatability, and other more specialized criteria. The maximum and minimum detectable phase define the dynamic range of the sensor system. Frequently, the maximum detectable strain and frequency response are the primary design criteria since optical fiber sensor systems are noted for their high sensitivity, linearity, and repeatability. The sensor system will most likely be specified in terms of strain, but the true optical fiber sensor system measurand is phase. Different optical configurations produce different proportionalities between phase and strain thereby yielding the designer the flexibility in choosing the optical sensitivity. This flexibility is required because all electrical systems, including optical fiber sensor demodulators, have limits on maximum detectable phase and frequency response. In many cases these limits can best be classified as a *range-bandwidth* constant of the demodulator. The product of the maximum detectable phase and the frequency of most demodulator systems is fixed by the electronic design. A larger phase signal can only be detected if it has low frequency content, and conversely, a high frequency phase signal can only be detected to if it has a small magnitude. This behavior is demonstrated in Fig. 1 by the frequency response of the maximum detectable phase for several configurations of the phase-generated carrier differential cross multiplier (DCM) demodulator [2]. The different curves in this graph correspond mainly to different carrier frequencies.

The optical and electrical sensor system design starts by identifying the target strain dynamic range and frequency response. It is important to understand that most structural systems will possess natural frequencies within the bandwidth of interest as shown in Fig. 2. Since the optical fiber sensor must be capable of measuring all potential structural strains

0-8194-1700-9/94/$6.00

within the design bandwidth, the strain at the most energetic harmonic forms the starting point of the design. For simplicity, assume the structural response can be represented as an envelope function that is inversely proportional to frequency and that this envelope function encompasses all harmonics with in the target bandwidth. This response can be approximated mathematically as

$$\varepsilon f = constant = \varepsilon^{max} f_{max}; \tag{1}$$

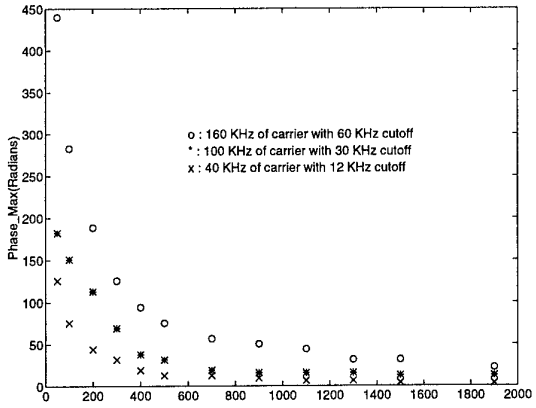

Figure 1: Demodulator Design Envelope.

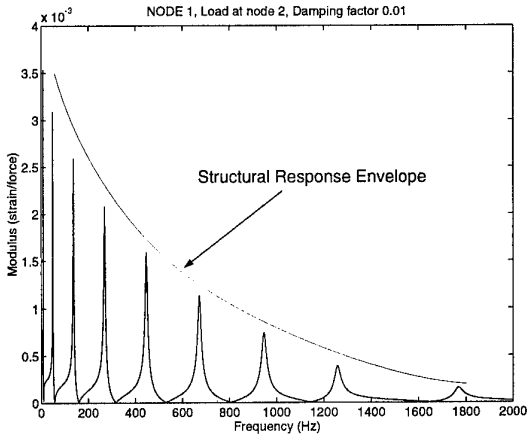

Figure 2: Structural Design Envelope.

where ε is the normal strain, f is the frequency, and ε^{max} is the maximum normal strain component at the most energetic natural frequency, f_{max}, of the structure. This expression assumes that the sensor has sufficient sensitivity to meet the minimum detectable strain requirements as is usually the case with interferometric optical fiber sensors. Eq. (1) can be rearranged to approximate the frequency response of the maximum strain state that the sensor system must be capable of measuring faithfully

$$\varepsilon = \varepsilon^{max} f_{max}/f. \tag{2}$$

The target response of the structure provided in Eq. (2) is used to determine the frequency response of the maximum phase that the demodulation electronics must be capable of measuring. The strain state is related to the phase response of optical fiber sensor by the phase-strain constitutive relations. These relations are generally sensor specific, but in their simplest form can be written as

$$\Delta\phi = \frac{KL}{\lambda}\varepsilon; \tag{3}$$

where λ is the optical source wavelength, L is the sensor gage length, and K is a constant that describes the intrinsic strain sensitivity of the sensor. A more detailed discussion of the many forms in which Eq. (1) can be found is provided in Ref. [1]. The optical sensitivity, K, is determined by the choice of optical configuration of the sensor. Table 1 gives the typical values for K for the popular sensor types. In the table, IFP stands for intrinsic Fabry-Perot and EFP stands for Extrinsic Fabry-Perot. Notice that the values in Table 1 span three orders of magnitude. Wavelengths of typical solid state optical sources used in sensor fabrication range form $670nm$ to $1550nm$. Tailoring the wavelength enables roughly a factor of

Table 1: Intrinsic Sensitivity of Optical Fiber Sensors.

	Michelson, IFP,	Polarimetric	Dual Mode	EFP	Mach-Zehnder
$K(Rads./\mu\varepsilon)$	14.50	7.25	$1.02x10^{-1}$	$3.98x10^{-2}$	12.57

two design flexibility in choosing the phase sensitivity.

The final design equation is found by combining Eqs. (2) and (3) to predict the required frequency response of the maximum detectable phase for the demodulator in terms of the optical design variables K, L, and λ

$$\Delta\phi = \frac{KL}{\lambda}\frac{f_{max}}{f}\varepsilon^{max}. \tag{4}$$

This equation constitutes an estimate of the target response for the sensor and demodulator.

At this point the design process can take several paths. The frequency response of the strain-induced maximum phase (Eq. (4)) must fall within the frequency response of the maximum detectable phase of the demodulator. One can 1) start with a fully characterized demodulator system and then adjust the optical design variables, (K, λ and L) to force the load induced maximum phase into the demodulator maximum detectable phase envelope, 2) start with a specific sensor configuration and design the performance of a modulator to meet the desire design requirements, or 3) use some combination of the the first two options. The first option is most attractive since sensor fabrication is generally easier and more flexible than demodulator development. Furthermore the phase sensitivity of a given sensor can be tuned over a large range by tailoring the gage length. The intrinsic sensitivity and operating wavelength offer more discrete control over the design process since they are set by choosing a type of sensor or the type of laser source. The design example in Sect. 4 will show how to implement this philosophy

3 Design for Structural Reliability

In many aspects design for structural reliability is easier than the sensor system design because the design for structural reliability need only consider the structural response of the embedded sensors and the host material. *Easier,* however, does not mean *easy* since much is still unknown about the mechanics of optical fibers embedded in composite materials. Fortunately the research in the macro- and micromechanics of embedded optical fibers has matured to the level that one can develop a design philosophy. This section provides the thermomechanical properties of many of the constituents used in designing fiber optic smart structures and then discusses important failure modes and failure models. The thermomechanical properties provided in this section constitute the inputs in the fiber optical smart structural design process while the failure modes used constitute the design criteria.

Optical fiber and coating properties are used to determine local interaction between the optical fiber and the surrounding host medium, which is used in estimating optical fiber and host structural failure, and in designing the sensor system requirements. Standard optical fibers are generally fabricated from chemically doped amorphous silica, and are considered homogeneous and isotropic. The dopant concentrations are usually less than five percent and do not greatly influence thermomechanical properties. Bow-tie and PANDA high-birefringent optical fibers can be treated as homogeneous and isotropic with effective properties calculated based on volumetric averages. The mechanical properties of amorphous silica are provided in

Table 2: Amorphous Silica Thermomechanical Properties.

Material	Young's Modulus (E_f)	Poisson's Ratio (ν_f)	CTE α	UTS	Fracture Toughness (K_{IC})
Silica	$69GPa$	.19	$5x10^{-7}(1/C_o)$	$3.5GPa$	$.8MPa - m^2$
Polyimide	$4.5GPa$	.35	$36.0x10^{-7}(1/C_o)$	$172.0MPa$	$2.0MPa - m^2$

Table. 2 where CTE is the coefficient of thermal expansion and UTS is the ultimate tensile strength. The UTS quoted in this table is for a coated optical fiber that has never had its original coating removed. Once the coating material is removed the UTS drops by roughly a factor of 3. Polyimide is fast becoming the off-the-shelf coating of choice for fiber optical smart structure applications due to its small thickness (typically less that $20\mu m$), thermal stability at composite cure temperatures and because it bonds well to epoxy matrix materials. Table 2 also provides the thermomechanical properties of polyimide. While not a thermomechanical property, it is appropriate to comment about optical fiber diameter in this section. Since this paper is restricted to fiber optic smart structures utilizing interferometric sensors, only single mode fibers warrant comment. These types of fiber come in standard diameters of $80\mu m$ and $125\mu m$ depending on the manufacturer and operating wavelength.

Composite laminates with embedded optical fibers are treated as composite laminates with effective properties that may or may not be altered by the presence of the optical fibers. The discussion shall distinguish between optical fibers embedded parallel and not parallel to adjacent reinforcing fibers. It is by now well understood that optical fibers embedded at relative angles other than parallel to the reinforcing fibers creates lenticular resin rich region that perturbs the local microarchitecture of the composite. Experimental, numerical and analytical results available form the open literature are used to estimate the thermomechanical properties of the composite laminates with embedded optical fibers. Whenever the evidence is not clear, the guidelines shall err on the conservative side. Finally, the discussion is limited to graphite/epoxy host systems since these systems have seen the greatest level of investigation.

To start with, there is no evidence available in the open literature that suggests that the stiffness constants, CTEs or Poison's ratios are measurably altered by the presence of embedded optical fibers. This is not the case with strength properties, which are dependent on the optical fiber diameter, coating, and composite material system. However, several heuristic rules for graphite/epoxy systems have emerged from the results cited in the open literature. When the optical fiber is embedded parallel to the reinforcing fibers, the longitudinal tensile and compressive, and interlaminar shear strength of the laminate remain unaltered [4-6]. The experimental data provided by Roberts and Davidson [5], on the other hand, suggests that reduction in transverse tensile strength occurs, and it depends quite heavily on the adhesion characteristics and diameter of the optical fiber and coating material. Based on their data, upper bound strength reduction guidelines of 50% for transverse tensile strength and 60% for transverse compressive strength are suggested when the optical fiber is embedded parallel to the reinforcing fibers.

The situation changes somewhat when the optical fiber is not parallel to the reinforcing fibers. In this case the transverse strength properties appear to remain unaltered, as does the longitudinal tensile strength [5-7]. However, the longitudinal compressive strength can be reduced by upwards to 80% depending on the optical fiber diameter and the orientation of the optical fiber relative to the reinforcing fibers. Longitudinal compressive strength is reduced via microbuckling caused by the resin pocket initial waviness as well as macrobuckling caused by asymmetries caused when optical fibers are not embedded at the mid-plane of symmetric

laminates. Case and Carman [8] present analytical design curves for longitudinal compressive strength reductions in terms of the optical fiber diameter and orientation relative to the reinforcing fibers since these parameters determine the wavelength of the resin pocket. Based on their results, a conservative estimate for the longitudinal compressive strength reduction for most orientations and $125\mu m$ fiber diameters (or less) is 80%.

The primary structural level failure modes in fiber optic smart structures are quasi-static over stress and possibly fatigue. Impact resistance of graphite/epoxy laminates is not altered by embedding optical fibers so long as the optical fibers are less than $250\mu m$ in diameter [9]. The quasi-static overstress in the constituents of a fiber optic smart structure is predicted with standard failure models using the strength data provided in the previous paragraphs. The maximum principal stress failure criterion is typically used for the optical fiber and Tsai-Hill or Tsai-Wu failure criteria are commonly used for the composite system. The data regarding fatigue failure of composites with embedded optical fibers is still very limited. While the data suggest that the fatigue life of composite laminates loaded in the longitudinal tension are not altered by embedded optical fibers [10,11], this data is far from conclusive. Roberts and Davidson [12] suggest that embedded optical fibers can alter the initiation of fatigue cracks in the plies local to the embedded optical fiber. This suggests using the following conservative technique of determining first-ply fatigue failure. This can be estimated by first using numerical or analytical stress analysis to determine local static stress concentration factors caused by embedded optical fibers. The stress concentration factor is then multiplied by the mean and alternating fatigue stresses, and the fatigue life is estimated using the modified mean and alternating stresses with fatigue life data for the same laminate without embedded optical fibers. Note that this approach is conservative and is suggested in the absence of explicit experimental evidence. More complete fatigue data for composites with embedded optical fibers is clearly needed.

The mechanical design of fiber optic smart structures follows the design procedures for traditional composite materials by treating the system as a composite structure whose mechanical properties have in some cases been altered by the presence of the embedded optical fibers. The effective strengths of AS4/3501 graphite/epoxy laminates are $X_T = 3040MPa, X_C = 680.MPa, Y_T = 41.MPa$, and $Y_C = 70MPa$; where X_T and X_C are the longitudinal tensile and compressive strengths and Y_T and Y_C are the transverse tensile and compressive strengths, respectively. Strength reductions due to optical fibers can be calculated using these values and the percentages provided in the previous paragraphs. These composite material properties are used with the failure models to choose the laminate stacking sequence and thickness to meet the mechanical design criteria on stiffness, strength, and fatigue life. Failure of embedded optical fibers is rarely a limiting consideration in the mechanical design of the system (except at entrance/egress points), so optical fiber failure is generaly not incorporated into the design objectives. Once the composite structure design is complete, it is sufficient to confirm that optical fiber failure will not occur.

4 Design Example

Consider the example where three uncoated optical fiber sensors are embedded parallel to the reinforcing fibers at the mid-plane of a $[0_3/90_3/0_3]$ graphite/epoxy (AS4/3501) plate (See Fig. 3). The normal operating conditions of the plate will be such that it experiences only in-plane normal forces. The purpose of the embedded optical fiber sensors are to identify any anomalous transverse low velocity impact events. The mechanical design will be developed under the simplifying assumptions that the manufacturing induced residual stresses can be neglected and that the optical fibers are spaced at greater that ten optical fiber radii so that sensor-sensor mechanical interaction can be neglected. The engineering constants and the

Table 3: AS4/350 Graphite/Epoxy Laminate Properties.

E_{11}	E_{12}	μ_{23}	ν_{23}	ν_{12}	ν_{21}	h	α_1	α_2
$242.5GPa$	$7.15GPa$	$2.27Gpa$	.242	.389	.015	$125\mu m$	$-.68x10^{-6}c^o$	$31,85x10^{-6}c^o$

laminate thickness for AS4/3501 are provided in Table 3.

The design starts by determining the laminate stresses in terms of the normal loads per unit length. This can be done using classical laminated plate theory [13]. The calculated stress states are average in the sense that the local stress raisers caused by the optical fibers are not calculated explicitly. Instead the stress raisers are taken into account by the reduced effective strength properties of the composite.

The stresses in the optical fiber are calculated in terms of the far-field average stress using closed form generalized plane strain assumptions much like those used in Ref. [1]. While these local stresses are not used to determine host failure, they are used to confirm that embedded optical fiber failure is not a critical design criteria. The Tsai-Hill failure model using the modified effective properties of the host is used to predict failure in the host material and the maximum principal stress failure criterion using the one-third rule for optical fiber strength is used for the optical fiber.

Fig. 4 shows the individual failure surfaces for the optical fiber, and zero and ninety degree laminates calculated using the data and procedures outlined above. These surfaces define the combinations of external forces (N_x and N_y) that will cause failure in the respective components of the systems. Load combinations contained within each surface define the region where failure will *not* occur. The intersection of the regions contained within all three failure surfaces define the safe loading conditions for the entire smart structure. Notice that the safe region is completely define by the composite laminates and not by the optical fiber.

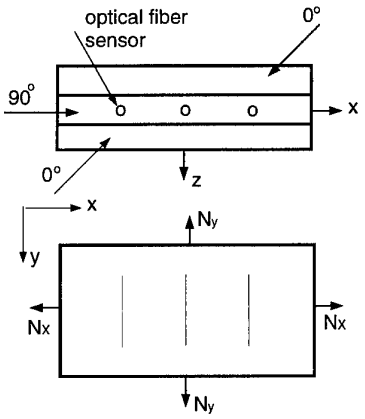

Figure 3: Design Example.

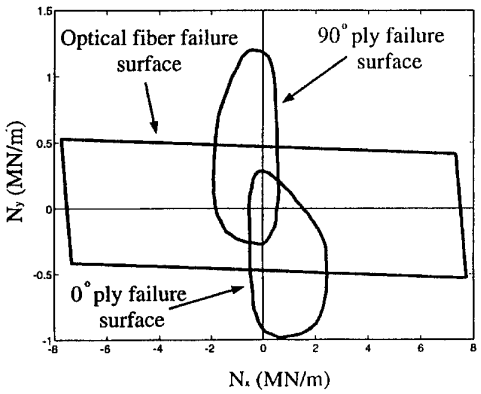

Figure 4: Design Example Failure Surfaces.

The sensor design of this fiber optical smart structure follows the process outlined in Sect. 2. The sensor is designed for a typical transverse low velocity impact loading scenario using the optimized DCM demodulator maximum detectable phase data in Fig. 1. Instead of performing a numerical analysis of the composite system to determine the maximum strain (ε_{max}) and its associate frequency (f_{max}), a simple test of a typical impact event is used. This

test is conducted by bonding a resistance strain gage to the surface of a clamped plate subjected to transverse impact of typical low velocity energy. Fig. 5a shows the resulting strain trace and Fig. 5b shows its Fourier transform, which clearly indicates that the critical design frequency is roughly $50Hz$. Fig. 5a shows the the critical design strain is $6000\mu\varepsilon$. A 1.67 factor of safety is added into the design process by arbitrarily raising the peak strain to $10,000\mu\varepsilon$.

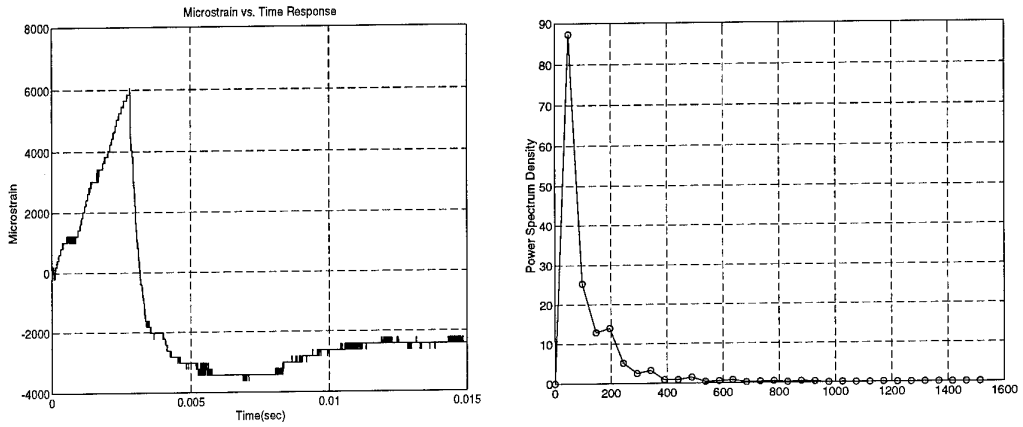

Figure 5: (a) Strain Trace of a Typical Low Velocity Impact Event. (b) Fourier Transform of Data in (a).

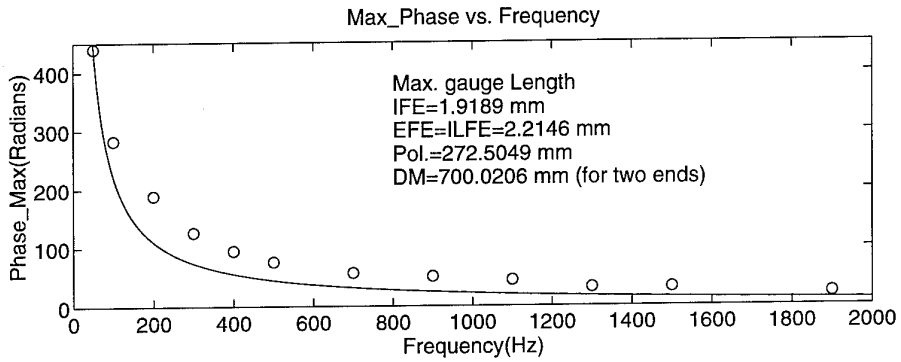

Figure 6: Sensor/Demodulator Design Curves.

Fig. 1 shows that the maximum detectable phase at $50Hz$ is roughly 440 *radians* using the $160KHz$ carrier data. Using this data with the intrinsic sensitivities in Table 1, Eq. (4) can be used to calculate the maximum acceptable gage lengths for the majority of the popular sensor configurations. The design curves for the sensors, all of which fall on top of each other, are shown in Fig. 6 plotted with the demodulator response envleope for a $160KHz$ carrier. The gage lengths used to generate the sensor response curves are also provided in Fig. 6. The combinations of sensors and gage lengths provided in Fig. 6 constitute the choices from

which the final sensor design will be selected. The final down-selection of the sensor will be based on additional constraints on the gage length, transverse sensitivity, thermal sensitivity or other mission specific information.

5 Conclusions

This paper has outline a method of designing fiber optic smart structures. The design approach considers electrical, optical and mechanical performance and attempts to formulate a rational approach to meeting all design criteria. It is clear that no single design philosophy will hold for all possible combinations of structures, sensor and demodulators, but the approach presented in this paper can be a model for other design scenarios.

6 Acknowledgements

The partial financial support of the Army Research Office (Contract No. DAAL-03-72-G-0121, Dr. Gary Anderson, contract monitor) is gratefully acknowledged.

7 References

1. Sirkis, J. S., Opt. Eng., 32 (4), pp. 763-773, 1933.
2. Dandridge et al, Appl. Optics, 20 (14), pp. 2337-2339, 1981.
3. Waite et al,, Composites, 19 (4), pp. 228-294, 1988.
4. Lu et al, Proc. ASME WAM Vol. AD-35, pp. 419-426, 1993.
5. Roberts et al, Proc. Fiber Optic Smart Structs. and Skins IV, SPIE Vol. 1588, pp. 326-341, 1991.
6. Carman, et al Proc. Smart Materials and Intelligent Systems, SPIE Vol. 1917, pp. 307 - 316, 1993.
7. Jensen et al, Jou. of Smart Mats. and Structs., 1 (2), pp. 24-35, 1992.
8. Case et al, "Compressive Strength of Composites Containing Embedded Sensors and Actuators," to appear in the Jou. of Int. Mat. Sys. and Structs.
9. Sirkis et al, Low Velocity Impact of Laminated Graphite/epoxy Panels: Part I - Macroscale," to appear in the Jou. of Comp. Mats.
10. Jensen et al, Proc. 1991 SEM Spring Conf., Milwaukee, pp. 233-238, 1991
11. Melvin et al. Proc. of Active Mats. and Adapt. Structs., IOP, pp. 801-804, 1991.
12. Davidson, et al, Proc. 1st European Conf. on Smart Structs. and Mats., IOP, Bristol, pp. 115-122, 1992.
13. Agarwal et al, ANALYSIS AND PERFORMANCE OF FIBER COMPOSITES, Wiley-Interscience, New York, 1980.

Paper presented at the Second European Conf. on Smart Structures and Materials, Glasgow 1994, Session 10

DISTRIBUTED STRAIN SENSING WITH FIBER BRAGG GRATING ARRAYS EMBEDDED IN CRTM™ COMPOSITES

E.J. Friebele, C.G. Askins, and M.A. Putnam
Naval Research Laboratory
Washington, DC 20375 USA

J. Florio, Jr., A.A. Fosha, Jr., R.P. Donti, and C.D. Mosley
BP Chemicals, Inc.
Auburn, WA 98002 USA

ABSTRACT

Fiber Bragg grating sensor arrays fabricated during optical fiber drawing have been embedded in fiber-resin composite panels made by the Continuous Resin Transfer Molding™ (CRTM™) process. The sensors accurately measure strain induced during both curing and bending tests.

1. INTRODUCTION

There has been significant progress in the fabrication of fiber Bragg gratings (FBG's) since the first demonstration of side-written FBG's by Meltz et al.[1] using multiple pulses of interfering beams of an ultraviolet laser. Most significantly, FBG's have been formed with a single 20 ns excimer laser pulse, obviating the need for holographic stability during the exposure, and FBG's have been written both at a single reflective Bragg wavelength λ_B[2] and at preselected wavelengths[3] during the drawing of a preform into an optical fiber. By eliminating the time-consuming and labor-intensive handling of the fiber necessitated by off-line techniques, in-line fabrication enables low-cost fabrication of large numbers of FBG's configured in contiguous arrays. Using an interferometer in which the intersection angle of the interfering beams, the intersection point, and the focus are all under computer control, we have demonstrated the fabrication of multielement FBG arrays where the λ_B of each grating can be precisely and reproducibly controlled. Since the wavelength shift in λ_B is linearly proportional to strain on the grating, several techniques have been devised for determining λ_B of the individual elements multiplexed in a single fiber FBG array, including the use of a tunable fiber Fabry Perot filter[4] or an unbalanced Mach-Zehnder interferometer.[5] The FBG arrays and the associated instrumentation for interrogating their Bragg wavelengths form the basis of an unobtrusive distributed strain sensing system for smart structures applications.

Fiber-resin composites are finding increasing numbers of military and civilian applications because of their high stiffness-to-weight ratio, high strength, and immunity to degradation from chemical exposure. These include airplane wing panels and fuselages, submersible hulls, bridge decks, trusses for civil structures, and spacecraft. Traditional manufacturing of graphite-epoxy composites involves laying up prepreg cloth or tape and then curing the structure at elevated temperature and hydrostatic pressure in an autoclave.

Recently, the Continuous Resin Transfer Molding (CRTM™) process has been developed as a cost-effective alternative for fabricating linear composite structures such as "C" channels, panels or beams. As shown in Figure 1, in the CRTM™ process, fiber cloth tape is drawn from spools on a creel rack into a die where it is injected with resin. The impregnated preform is then pulled through a region of the die at elevated temperature for resin curing, and finished product emerges from the output end of the die. A fly-away cutoff saw sections the product into the desired length. Various fiber-resin systems have been used, and a number of different product configurations have been fabricated. In general, the properties of the CRTM™ composites compare favorably with those made by conventional autoclave techniques.

For many smart structures applications it is desirable to measure the strain distributed throughout a structure both to monitor in-service strain levels and to determine the onset of failure. In practice, distributed strain measurements are difficult to make with conventional resistance strain gages or piezoelectric sensors

0-8194-1700-9/94/$6.00

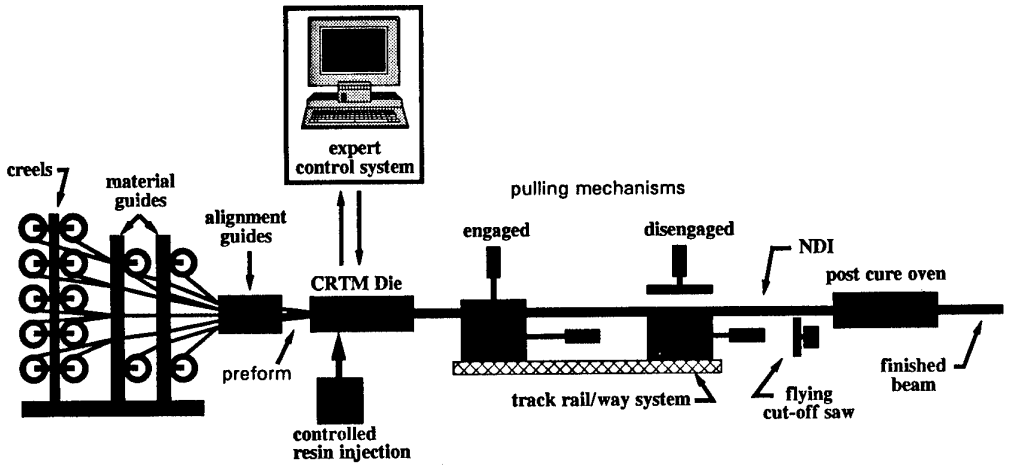

Figure 1. Schematic diagram of the Continuous Resin Transfer Molding™ process which is controlled by an expert system with non-destructive inspection of the final product.

because each sensor must be individually wired to a bridge amplifier or high impedance amplifier, and baseline offsets are encountered. By contrast, FBG arrays provide the capability of multiplexing a number of sensors along a single optical fiber, and the measured λ_B is linearly related to strain at the site of the grating with no baseline offset. Furthermore, the geometry of optical fibers is inherently compatible with fiber-resin composite systems, provided the diameter of the optical fiber is limited to <100 μm.

This paper reports the fabrication of multielement FBG arrays and the first reported embedding of these arrays in glass/vinyl-ester composite products during the CRTM™ process. Distributed strain measurements of the products during bending tests using the embedded FBG strain sensors are compared with calculated strains and measurements made using conventional electrical gages.

2. EXPERIMENTAL

The FBG arrays were fabricated in single mode Ge-doped silica core optical fibers during fiber draw using the computer-controlled interferometer and line-narrowed KrF excimer laser, as previously described.[3] The cut-off wavelength of the fiber was 780 nm; the fiber OD was 77 μm, and the NA was 0.23. Each array consisted of a 10 m lead-in fiber, a single reference grating written at 808 nm (which would remain outside the composite), 7 gratings separated in wavelength by 2 nm and in length by 0.4 m, followed by another 10 m lead-out fiber. Although the array could be addressed from a single end, both lead-in and lead-out fibers were used for redundancy. Immediately following writing, a uv-cured epoxy acrylate polymer coating was applied and cured. An ink marker was added to aid in locating the FBG's. The spectra of the gratings were measured in the laboratory with a 1 m grating spectrometer and an OMA; 1 pixel corresponded to 0.4 Å.

A 10 ply glass-vinyl ester composite panel ~15 cm wide was used for the initial demonstration of FBG embedding during CRTM™. The optical fiber sensors were inserted between the 9th and 10th ply to distance them as far as possible from the neutral axis. Access to the optical fiber was attempted by transitioning through the surface layer, then coiling a length of fiber inside layers of high temperature tape adhered to the surface of the layup. However, the tape caught on the die, causing the fiber to stretch and break, leaving a short pigtail exiting the composite surface. Much better success was had by leaving the coiled pigtail inside the composite in a tape-sealed delamination packet at the ends of each sensor section. Five complete sections were fabricated in all during a continuous pultrusion, and four had at least one surviving lead-out fiber.

3. RESULTS AND DISCUSSION

A spectrum of one FBG array measured prior to embedding is shown in Fig. 2. In this case, two

reference gratings (A and B) were included at 808 nm, and they are clearly evident, as are the 7 gratings for embedding between 810 and 822 nm (C-I). (The weak spectral feature on the high wavelength side of some reflection peaks may be an artifact of the spectrometer or a birefringence effect. High resolution measurements using a narrow-line, tunable titanium-sapphire laser are currently in progress to elucidate the spectral nature of these reflectance peaks.) The spectrum of the array after embedding is shown at the top of Fig. 2. For clarity, external strain was applied to grating B to move it away from grating A, which is used as the reference grating. The reflection from the 7 embedded gratings is clearly measurable, but all Bragg wavelengths have increased. Because the thermal expansion coefficient of the composite is much greater than that of the optical fiber, we expected that the FBG sensors would be placed under compression as the composite shrank during cooling; this would have caused a decrease in λ_B in the embedded gratings. We attribute the tensile state in the FBG's (>1% for gratings G and H) to a higher pull force on the optical fiber than on the fabric as they enter the die, and this differential stress was locked in by the resin cure during CRTM™ processing. This locked-in tensile stress is greater than any compressive forces acting on the FBG's due to differential shrinkage on cool-down. Note that this stress is not uniform along the length of the composite--the wavelength shift of grating C is much less than that of gratings D-I, and the shifts among the latter group are not equal. In particular, there is sufficient additional tension on grating H to cause its Bragg wavelength to cross that of grating I. In addition, there is evidence of non-uniform stress across the gage length of some sensors, e.g., gratings F-I, which causes their reflection peaks to broaden and decrease in amplitude. The tensile stress on the optical fiber can be relieved by accurately matching the tensile stress on the fiber and composite cloth at the die entrance.

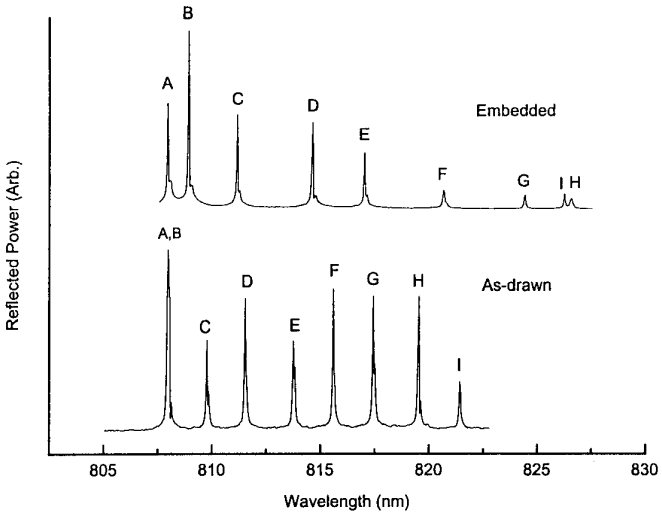

Figure 2. Reflectance spectra of as-drawn and embedded FBG sensor arrays.

The composite panel was placed in 3-point bending with the gratings located on the concave side of the board, and the spectra of the embedded FBG array in both flat and loaded panels are shown in Fig. 3. Once again, grating B has been arbitrarily strained away from reference grating A. The panel was supported on pivots located approximately under gratings C and I, and as expected, their Bragg wavelengths have not shifted significantly, indicating minimal additional stress. By contrast, each of the sensors between the pivots shows a decrease in Bragg wavelength due to the compressive stress induced in the gratings. Note that for grating H, this is sufficient to bring its reflection peak in coincidence with that of grating I.

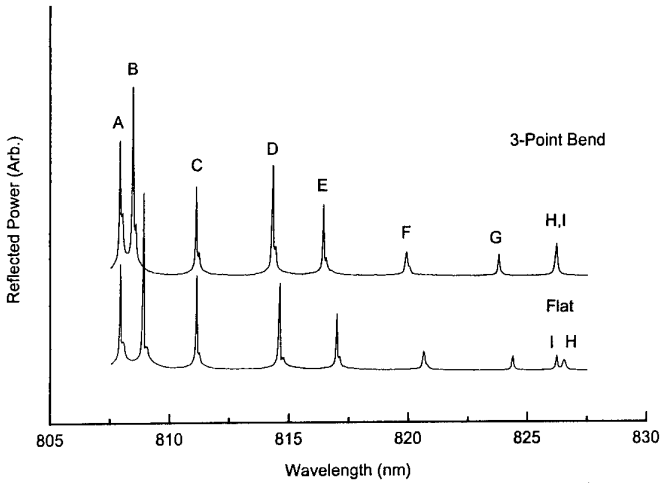

Figure 3. Reflectance spectra of FBG arrays embedded in a CRTM™ composite panel measured flat and under 3-point bending with a 1.35 kg load at its mid-point.

The strains have been derived from the wavelength shifts of each of the FBG's (assuming $1/\lambda_B d\lambda/d\varepsilon = 0.74$) and are plotted in Fig. 4 for the cases where the panel was uniformly supported on a table, hanging under its own weight, and additionally loaded with 0.45, 1.21, and 1.35 kg masses at the center.

To accurately determine the wavelength shift of each grating, its individual reflectance spectrum in the "flat," supported case was first fitted by the sum of 2-4 Gaussians. This calculated spectrum was then translated in wavelength for best correlation with the measured spectrum of that grating in each of the strained cases. This correlation method gives a resultant error of <1/4 pixel = 0.1Å = 17 με. Note that the measurement accuracy is degraded for gratings H and I, which have weak reflectance spectra that are overlapped in some of the loaded cases (Fig. 3).

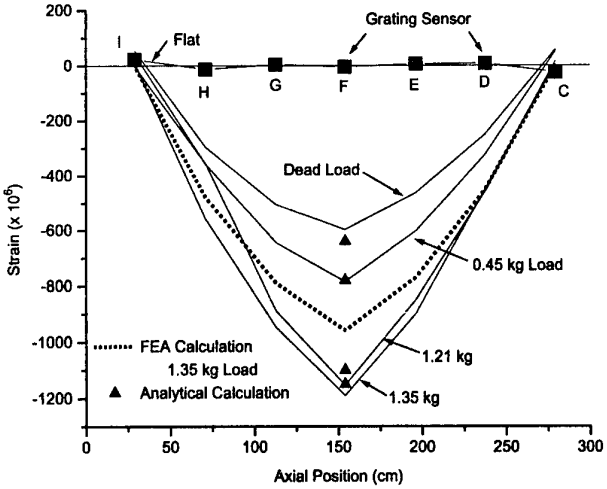

Figure 4. Comparison of strain in the CRTM™ beam measured with the FBG sensors with the results of finite element and analytical calculations.

The experimental results are compared with the results of two calculations. First, the beam midpoint strains were calculated analytically based on the measured deflected shape of the beam for each of the 4 load cases. Vectors of the end reactions were derived from the measurements of the slope at the ends of the beam. The beam moments were then calculated using the sum of the perpendicular distance from these vectors to the beam center times the vector magnitude, and the opposing moment of the weight of half of the beam. These moments were then used to calculate the strains using standard methods. It is apparent that there is excellent agreement between the calculated and experimental maximum strains--the average deviation is only 14 με, which is on the order of the error in strain measurement. Second, a preliminary nonlinear finite element calculation of the 1.35 kg load case was performed using COSMOS. As shown in Fig. 4, the agreement with experiment is not as good, and the variance at the center of the beam is 230 με. This preliminary finite element numerical analysis is being reviewed to insure that the nonlinear model is representative of the actual experiment. At this time, the authors feel that the analytical solution based on the deflected shape is the more accurate of the two predictive techniques. These calculations are being refined and the strains are being measured with electrical gages at the sites of the grating sensors. Comparisons of these results are in progress.

4. SUMMARY AND ACKNOWLEDGEMENTS

In summary, the present paper reports initial results of embedding FBG sensor arrays produced on-line during optical fiber drawing in a fiber-resin composite using the CRTM™ process. The gratings survived the embedding process, and subsequent measurements have shown that they were embedded under considerable tensile load (>1%). The strain distribution of the beam under 3 point bending has been determined from shifts in λ_B of each of the gratings with a precision of <17 με, and the midpoint strains compare favorably with the result of analytical calculation. These results establish the potential of fabricating low-cost fiber-reinforced composite smart structural elements with embedded optical fiber sensors. In the near future, FBG sensor arrays will be embedded in graphite-epoxy composite elements for airframes using the CRTM™ process.

The authors wish to acknowledge the financial support of ARPA under the Affordable Polymeric Composite Material Synthesis and Processing program in accordance with ARPA Technology Agreement No. MDA972-93-2-0004.

5. REFERENCES

1. G. Meltz, W.W. Morey and W.H. Glenn, Opt. Lett. **14**, 823-825 (1989).
2. L. Dong, J.-L. Archambault, L. Reekie, P.St.J. Russell and D.N. Payne, Elect. Lett. **29**, 1577-1578 (1993).
3. C.G. Askins, M.A. Putnam, G.M. Williams and E.J. Friebele, Opt. Lett. **19**, 147-149 (1994).
4. A.D. Kersey, T.A. Berkoff and W.W. Morey, Opt. Lett. **18**, 1370-1372 (1993).
5. A.D. Kersey, T.A. Berkoff and W.W. Morey, Electron. Lett. **28**, 236-238 (1992).

Paper presented at the Second European Conf. on Smart Structures and Materials, Glasgow 1994, Session 10

Structural Strain Mapping using a Wavelength/Time Division Addressed Fiber Bragg Grating Array

M. A. Davis, D. G. Bellemore[§] and A. D. Kersey
Code 5674
Optical Sciences Division
Naval Research Laboratory
Washington, D.C. 20375

Abstract
We describe a multiplexed nine element Bragg grating array used for strain mapping over a plate which is subjected to deflection forces. The system comprises two sub arrays of gratings which are sequentially addressed, and read via a single interrogation system into a PC. Real time strain distributions of the plate are determined and displayed.

Introduction
Recent advances in the area of fiber Bragg grating (FBG) technology indicate that these devices possess the potential for cheap, reliable, and easily multiplexed strain sensing elements. Several interrogation techniques have been developed to derive the strain information from the reflected wavelengths of the gratings, including edge filters [1], tunable filters [2] and interferometric demodulation [3], and research in this general area of instrumentation continues at a rapid pace. The inherent wavelength-encoded strain information obtained from FBG sensor elements provides a number of system advantages including, a fixed strain-wavelength responsivity, the ability to address several gratings at different wavelengths along a single fiber, and the ability to derive unambiguous strain measurements without the need for continuous monitoring and tracking of the returned signal. In addition to the inherent wavelength division addressing capability of FBG sensors, the devices can also be addressed using frequency and time division based multiplexing techniques. When surface attached to or embedded within a structural material, an array of FBGs can provide detailed strain mapping without significantly modifying the structural properties. A conceptual design is shown in Figure 1, where many FBG strain sensors are surface attached to, or embedded in a plate, and interrogated using wavelength and time division multiplexing. This approach provides a powerful sensing tool for the analysis of structural loading and deformation, shape analysis [4], characterization of vibrational modes, monitoring of residual stress, and damage detection. In this paper we describe our initial experimental demonstration of this concept, using a FBG array comprising nine elements which are 'read' using a single scanning fiber Fabry-Perot optical filter.

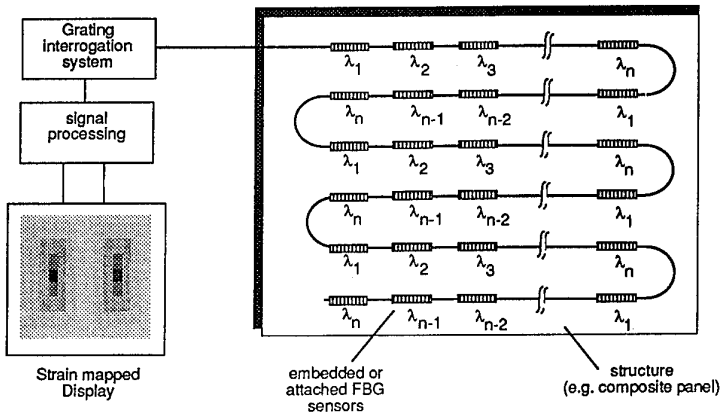

Figure 1. Conceptual representation of the strain mapping approach based on FBG arrays

0-8194-1700-9/94/$6.00

Principle & Experimental System

The FBG strain mapping system is shown in Figure 2. Two edge-emitting LED sources (E-LEDs) are used to illuminate two series (or sub arrays) of FBG elements. The first four gratings in each sub array (FBG_1 - FBG_4 and FBG_5 - FBG_8) reflect approximately equal wavelengths of 1275 nm , 1280 nm ,1285 nm, and 1290 nm and the additional grating in the sub array of five elements (FBG_9) reflects at nominally 1295 nm. The gratings have a consistent peak reflectivity of > 85 %, and bandwidths of ~ 0.3 nm. The two sub arrays of FBG elements are illuminated by separate ELEDs, and the reflected optical components from each array are combined using a 3 dB coupler and fed to a single detection system. This detection system is based on a single wavelength-scanning fiber Fabry Perot (FFP) filter. This filter is scanned over the wavelength range occupied by the gratings (i.e. over the range 1273 to 1297 nm) by the application of a voltage ramp applied to piezoelectric elements in the filter. The free spectral range of the filter is ~ 27 nm, large enough to ensure that only one FP passband overlaps this wavelength range during the scan. A photodetector is used to monitor the optical power passed by the FFP. The instrumentation system was designed to allow sequential time-multiplexed addressing of the two FBG sub arrays. In order to accomplish this, the two ELED sources are driven on/off synchronously with the ramp applied to the FFP filter, but in anti-phase with each other, such that ELED1 is powered during the up-scan in wavelength and ELED2 is powered during the down-scan. In this way, both sub-arrays are interrogated by the electro-optics system during a single ramp period of the FFP filter scan. In order to determine the Bragg wavelengths of the gratings in each series, a dithered-filter approach is used [3]. With this approach, the photodetector signal is mixed electronically with the dither frequency and low pass filtered (accomplished using the lock-in-amplifer). This technique allows a series of waveforms to be generated which correspond to the derivative of the grating reflection profiles. These signals exhibit zero-crossing at the Bragg wavelengths, and thus are easily read into a desk-top computer (PC) for processing using a ADC. We have previously demonstrated that this approach is capable of resolving strains at the few μstrain level.

For the purpose of demonstrating the strain mapping concept, the gratings were surface attached to a 66 cm by 35.5 cm, 0.15 cm thick aluminum plate, which was firmly clamped on all edges. This plate was divided into 9 cells (i.e. a 3 by 3 matrix form), and a FBG element was surface attached in approximately the center of each cell. As depicted in Figure 2, the gratings were arranged with each individual grating oriented perpendicularly to the closest boundary of the plate.

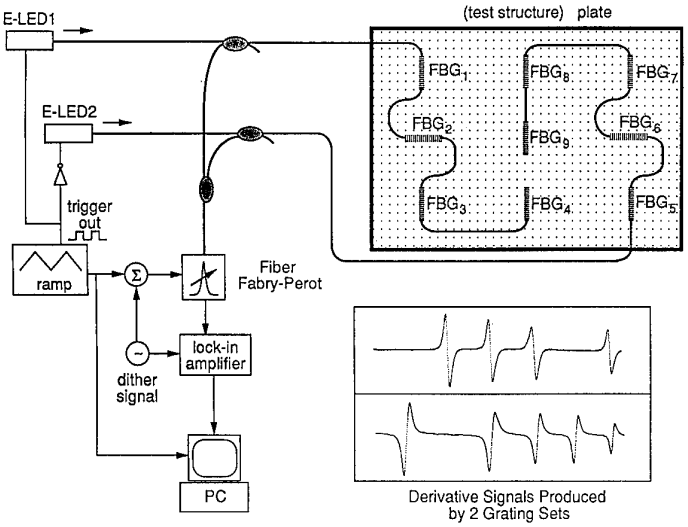

Figure 2. Experimental 9 FBG system used to monitor & map strain in a rigidly supported plate.

Results

The insets in Figure 2 show the form of the derivate signals produced by the two FBG sub arrays. The variation in the overall amplitude of the signals is due to the profile of the ELED sources used, and do not affect the zero-crossing detection scheme used to monitor the strains. In order to test the operation of the strain mapping scheme, the wavelength shifts monitored by the system were displayed on the PC using bar-graph indicators to show the strain at each sensor location.

Figure 3 shows examples of the response of the system to deflecting forces applied to the plate. These plots are essentially screen down-loads of the real-time display . The center line through each bar indicates the zero-strain point, and as seen, the gratings respond to both tensile and compressive strains. The indicator in the figure gives a marker for a strain level of 500 μstrain. This was calibrated from the known voltage-to-wavelength response of the FFP filter, and the FBG strain-to-wavelength responsivity of the gratings at ~ 1.3 μm. The location of the force is indicated by the open circle. As seen, the strain distribution indicates highest strain reading at a FBG when the force is close to that element, as would be intuitively expected. The response, however, was found to be highly localized, indicating that the stress concentrations are close to the point of the applied force. We are currently working on software processing of the strain data to generate plate deflection contour plots in real time which will allow us to determine the plate deformation, and location of the applied force.

Summary

We have reported the operation and performance of a multiplexed nine element Bragg grating array for mapping the strain levels in a plate which is subjected to deflection forces. Strain levels detected by the gratings are read via a single electro-optic interrogation system into a PC. Real time strain distributions of the plate are determined and displayed.

Acknowledgements

This work is supported by the Naval Research Laboratory program on Metamorphic Materials.

References

1. S. M. Melle, K Liu and R. M. Measures, "A passive wavelength demodulation system for guided-wave Bragg grating sensors", Photonics Technol. Lett., 4, p. 516, 1992.
2. A. D. Kersey, T. A. Berkoff and W. W. Morey, " Multiplexed fiber Bragg grating strain sensor system with a fiber Fabry-Perot wavelength filter", Optics Letters, 18, p. 1370, 1993.
3. A. D. Kersey, T. A. Berkoff and W. W. Morey, " High resolution fiber grating based strain sensor with interferometric wavelength shift detection", Electronics Letters, 28, p. 236, 1992.
4. M. A. Davis et al., "Fiber optic Bragg grating array for shape and vibration mode sensing", Proc. North American Conf, on Smart Materials & Structures, SPIE vol. 2191 paper #10, Orlando, Feb., 1994.

[§]SFA, Inc. 1401 McCormick Dr. Landover, MD

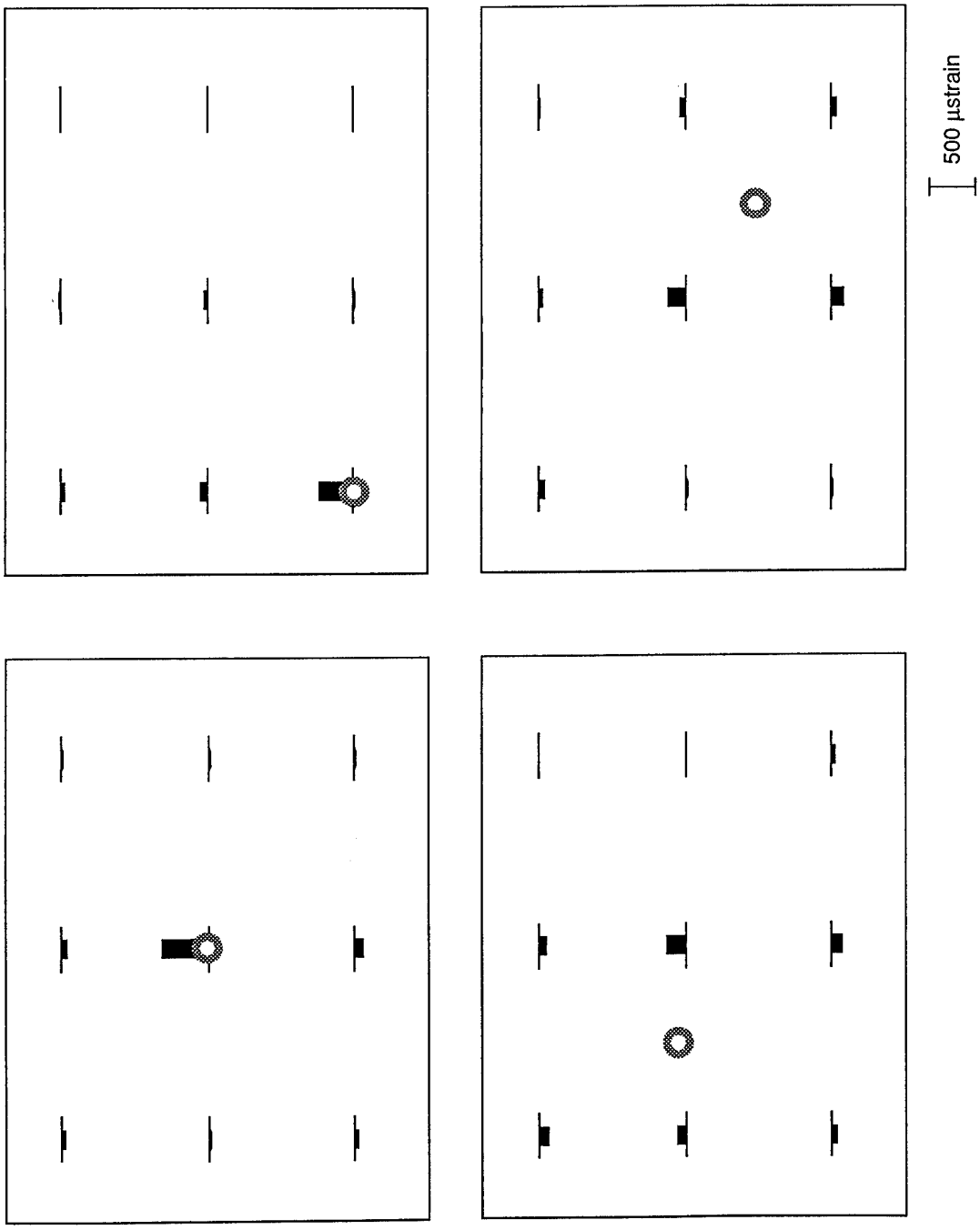

Figure 3. Screen plots of the mapped strain information from the multiplexed 9 element FBG array for 4 different plate deflecting forces (indicated by the open circle). The marker indicates the amplitude corresponding to a 500 µstrain level.

Paper presented at the Second European Conf. on Smart Structures and Materials, Glasgow 1994, Session 10

FINITE ELEMENT MODELING OF THREE-DIMENSIONAL INTEGRAL SENSORS FOR THE CONTROL OF AEROELASTIC STRUCTURES

M. N. Abdul-Wahed

Professor, Faculty of Mechanical Engineering, Aleppo University
Aleppo. Syria

T. A. Weisshaar

Professor, School of Aeronautics and Astronautics, Purdue University
West Lafayette, Indiana, USA 47907-1282

ABSTRACT

For control of structures with aeroelastic loads, torsion and bending must be sensed and controlled independently. Tailored piezoelectrics with skewed sensing axes can provide decoupled sensing of both bending and twist using the same set of sensors. This paper discusses the use of a finite element model to evaluate the effectiveness of anisotropic piezoelectric sensors for shape control sensing. Using a finite element representation for a plate-like structure covered by PVDF laminates, it is shown that integral sensors can accurately capture system independent bending and torsion displacement by measuring the induced electric charges without any additional signal processing efforts. The contribution of this work is to suggest an expression that relates sensed output from anisotropic sensors to plate or lifting surface bending and twist. An expression for the bending and torsion is tested with the finite element model. It is found that bending slope is accurately measured, but that twist is less likely to be accurately approximated by the sensor output.

1.0 INTRODUCTION

The attribute which has made piezoelectric sensors attractive for structural control is their ability to be integrated into a structure. This is in contrast to point sensors where the use of distributed-parameter control theory requires the use of an extensive number of point sensors to collect enough information to characterize the system response. As a result, the real time computation and signal processing with multi-point sensors becomes a serious problem.

The unique property of electromechanical anisotropy in special kinds of PVDF piezopolymers was used for the first time by Lee and Moon [1] to design micro actuators and sensors, where bending and/or twist was actuated and/or sensed. This is particularly important for aeroelastic control of wings and other lifting surfaces. Lee and Moon used a laminated beam model derived from the classical lamination theory. Abdul-Wahed and Weisshaar [2,3], have developed a finite element model that considers the electromechanical anisotropy. This model was used to study direct actuation control of adaptive wings to create decoupled bending or twist with skewed PVDF actuators.

Because of the interest in effective sensor combinations and realistic structures, the same finite element technique was extended in Reference 4. This paper shows how tailoring of PVDF sensors can be used to measure decoupled bending and/or twist deflections of controlled structures and then used to explore the distributed sensing mechanism. The theory is restricted to linear piezoelectrics but, takes into account orthotropic mechanical and electromechanical properties of the sensor.

The basic building block finite element model used in this study is a solid brick element whose degrees of freedom include translational displacements and electrical displacements at each node. The electrical displacements correspond to the electrical potential ϕ. There are three displacement and one electrical degrees of freedom per node and there are 8 nodes per element. The displacement field includes DOFs for incompatible modes using a "bubble function" given in Reference 5. These incompatible displacements and modes were added to avoid element locking under parasitic shear and to soften the extra thin brick element in the transverse direction.

These shape functions were used to generate elemental mass, stiffness and external load matrices which were then assembled to obtain a structural equilibrium equation for the discretized structure. This equation has the following form:

0-8194-1700-9/94/$6.00

$$\begin{bmatrix} [M_{uu}] & [0] \\ [0] & [0] \end{bmatrix} \begin{Bmatrix} \ddot{u} \\ \ddot{\phi} \end{Bmatrix} + \begin{bmatrix} K_{uu} & K_{u\phi} \\ K_{\phi u} & K_{\phi\phi} \end{bmatrix} \begin{Bmatrix} \{u\} \\ \{\phi\} \end{Bmatrix} = \begin{Bmatrix} \{F_m\} \\ \{0\} \end{Bmatrix} \tag{1}$$

where u represents mechanical nodal displacements, ϕ represents electrical nodal displacements (nodal voltages) related to sensor output from the piezoelectric elements and F_m the nodal loading vector. The notations $\ddot{\mathbf{u}}$ and $\ddot{\phi}$ represent differentiation with respect to time. The M_{ij} elements are inertia elements, while the K_{ij} elements are stiffness matrix elements.

Equation 1 shows electro-mechanical coupling in the structure, but no electrical inertia or damping is included in this model. The only electrical boundary condition is that one of the two electrodes belonging to the sensing layer must be grounded. In this way the number of unknown nodal potentials is equal to $NNS/2$ where NNS is the total number of the sensing nodes. This is equivalent to having one virtual "independent" electrode per active node.

Once Equation 1 is solved to obtain the sensed nodal voltages, the open-circuit voltages can be used to obtain the corresponding sensor closed-circuit charge q_i. Each discrete piezoelectric sensing finite element is equivalent to a condenser connected in parallel to the adjacent element. The closed-circuit charge for each finite element can be expressed by

$$q_{je} = \iint_{S_e} \phi(x,y) dc_\alpha = \frac{\varepsilon}{t} \iint_{S_e} \phi(x,y) dx dy \tag{2}$$

where $c_\alpha = \dfrac{\varepsilon S_e}{\mathbf{t}}$ is the element capacity, ε is the dielectric constant, s_e and t are the element surface and thickness respectively. The elemental sensed charges q_{ip} are then summed up for all elements of the sensing layer to obtain the overall sensed charge q_i:

$$q_i = \sum_{j=1}^{N_s} q_{je} \tag{3}$$

where N_s the number of elements of the sensing layer. The examples considered in the following section will demonstrate some essential features of anisotropic integral sensors using simple plate and beam models.

2.0 BENDING SENSORS/TWIST SENSORS FOR BEAMS AND PLATES

By combining several tailored layers of PVDF sensors together into one "host" structure, different "sensing missions" can be given to them, depending on layer's placement, orientation and wiring method. Suppose we have, as shown in Figure 1, two similar sensing layers of the same dimensions and poling direction, one bonded on each side of a cantilevered host place and suppose the lower layer with opposite skew angle i.e., $\alpha_i = \alpha_j$ where i and j denote the sensing layer number. Hence, the two sensors exhibit mirror symmetry with respect to the mid-plane of the plate.

These sensors can be used to sense either pure bending or twist. The bending slope is sensed by the difference between the charge quantities on the upper and lower surface, while the sum of the charge outputs is proportional to the twist. For this sensing, it is imperative that the sensor be anisotropic if it is to sense twist. These expressions are developed and described for simple beams and rods in Reference 4 and are independent of the finite element analysis. These are approximations and we wish to test their validity with the finite element model.

The accuracy of expressions developed for bending slope and twist in terms of sensor output and anisotropic piezoelectric constants was tested using the finite element model. Consider a configuration with a 1 mm. thick aluminum plate partially sandwiched between two thin (25 μm thick) piezo films. The plate, which is 80 mm long and 40 mm wide, is subjected to a pure bending moment of 0.2 N-m., uniformly distributed at the free edge of the plate.

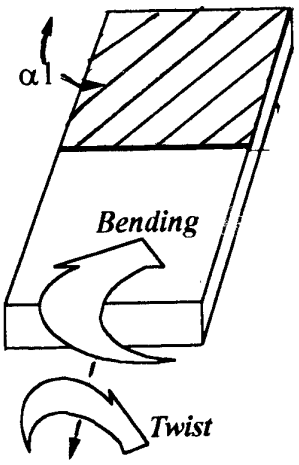

Figure 1 - Cantilevered host plate with asymmetrical PVDF layers

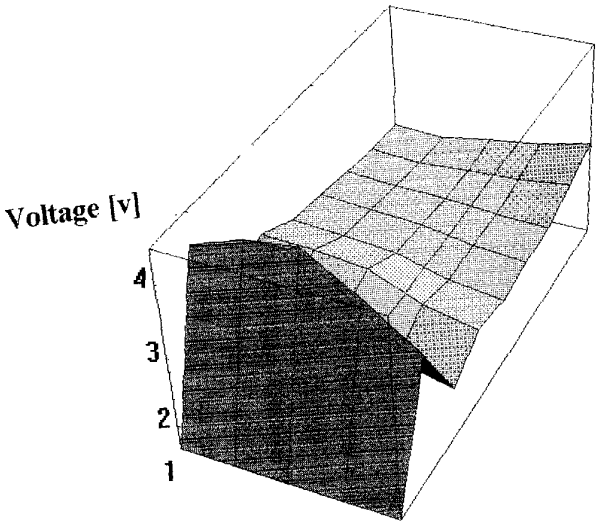

Figure 2 - Theoretical sensed voltage distribution over the upper sensor layer - pure bending.

As a result of this loading, the quantity of charge $(q_1 - q_2)$ sensed by both sensors provides the bending slope at the sensor end point. Figure 2 shows a surface plot of the nodal voltage distributions $\phi(x,y)$ sensed by the upper and lower layers; the sensors cover the entire plate. The voltage field is axisymmetric. The sensed charge q_1 (upper layer) and q_2 (lower layer) are shown in Figure 3. The sensed quantity $\theta = \frac{dw}{dy} = \frac{(q_1 - q_2)}{2tb\left(e_{31}\sin^2\alpha + e_{32}\cos^2\alpha\right)}$ represents the slope deflection. Figure 4 shows values of sensed θ_h. versus y_s, together with the theoretically predicted bending slope obtained from the nodal displacement field. The sensed charges $(q_1 - q_2)$ represent, with great fidelity, the bending slope.

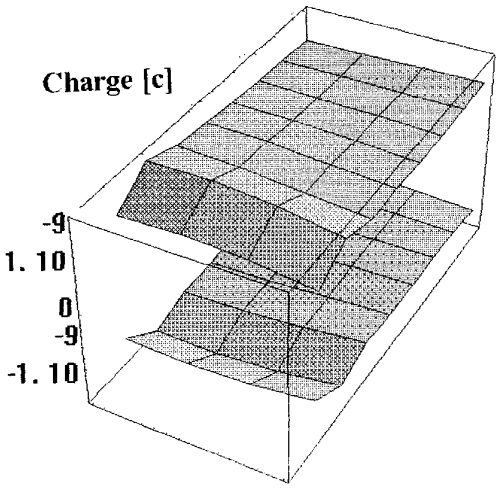

Figure 3 - Charge distribution on upper and lower sensor layers - pure bending

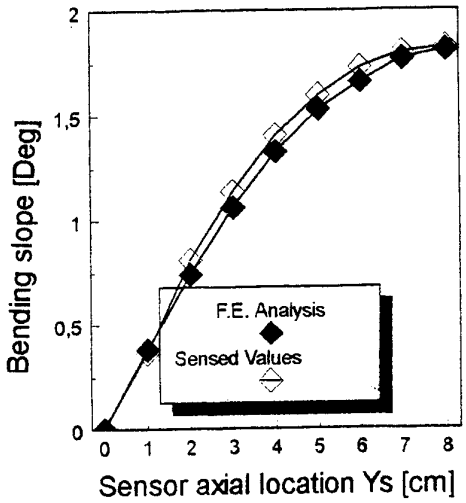

Figure 4 - Comparison between sensed bending slope and actual beam bending slope - pure bending

The same plate is subjected to a twisting moment of 0.04 N-m. applied at the tip. The twist angles and sensed charge are related by the expression $twist = \frac{(q_1 + q_2)}{2tb(e_{31} - e_{32})\sin\alpha\cos\alpha}$ shown respectively in Figures 5 and 6. The agreement between the calculated and the sensed angles in Figure 5 is not as good as those in the case of bending. This is due to the warping effects which are not taken into account by the beam model. This warping effect is clearly revealed by the finite element analysis, influencing the displacement field as well as the sensed charge distribution. Due to the fact that the shear strain field assumed by the beam theory is constant over the axial direction, the sensed charge distribution had to be uniform over all the elements. Indeed, the charge distribution given by Figures 5 and 6 shows the distortion due to warping.

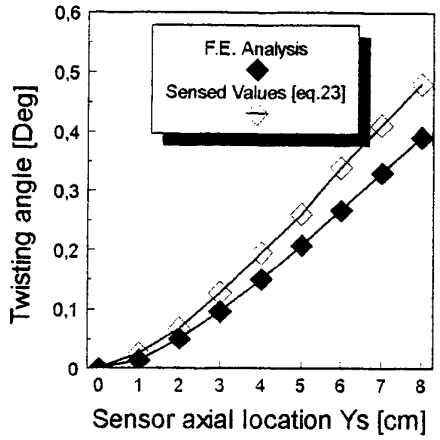

Figure 5 - Twist angle distribution and approimate sensed values

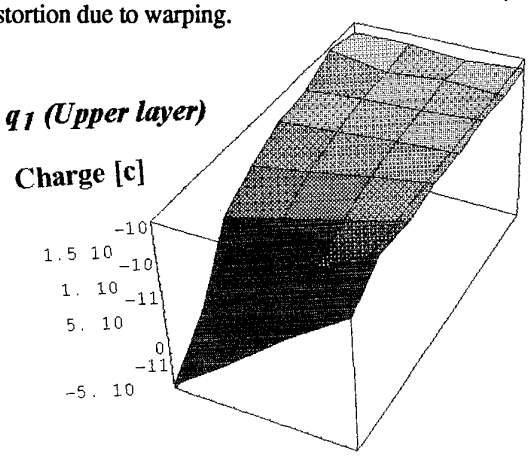

Figure 6 - Calculated charge distribution due to twisting moment applied to tip of plate.

3.0 CONCLUSIONS

An effective and versatile method of finite element analysis to investigate the relationship between bending and torsional displacement and the output of integral sensors, having in-plane electromechanical orthotropicity, has been outlined. A correlation between finite element and plate/beam models has been also carried out. Among the conclusions of this study are:

- Electromechanical anisotropy is useful for tailoring sensors for the shape control of adaptive structures.
- Straightforward sensing equations, relating beam and/or plate displacements in bending and/or torsion to sensed charges can be used, with a good approximation, for the prediction of the bending and/or twisting "content" in plate-like structures.
- 'PVDF sensors can measure the system dynamics with very little signal processing. Potential applications of these sensors are dynamic model control and aeroelastic control of lifting surfaces.

4.0 REFERENCES

1. Lee, C. K. and Moon, F. C., "Laminated Piezopolymeric Plates for Torsion and Bending Sensors and Actuators," *Journal of the Acoustical Society of America*, **85** (6), June 1989.

2. Abdul-Wahed, M. N., "Finite Element Modeling for Piezoelectric Structures," AAE Aeroelasticity Report 92-5, School of Aeronautics and Astronautics, Purdue University, West Lafayette, Indiana, August 1982.

3. Abdul-Wahed, M. N. and Weisshaar, T. A., "Active Tailoring of Adaptive Lifting Surfaces for Aeroelastic Applications," Presented at the 1993 North American Conference on Smart Structures and Materials '93, New Mexico, February 1993.

4. Abdul-Wahed, M. N., "Integrated Piezoelectric Sensors as Elements of Smart Structures," Presented at ASST Meeting on *Sensors: Principles, Technologies & Applications*, November 8-14, 1993, Damascus, Syria.

5. Cook, R. D., Concepts and Applications of Finite Element Analysis; Third Edition, John Wiley & Sons, New York, 1989.

Paper presented at the Second European Conf. on Smart Structures and Materials, Glasgow 1994, Session 10

EIGHT ELEMENT TIME-DIVISION MULTIPLEXED FIBER GRATING SENSOR ARRAY WITH INTEGRATED-OPTIC WAVELENGTH DISCRIMINATOR

T. A. Berkoff* and A.D. Kersey
Optical Sciences Division, Code 5676
Naval Research Laboratory
Washington, D.C. 20375

ABSTRACT

An eight element time-division multiplexed fiber Bragg grating sensor array is demonstrated using an unbalanced integrated-optic discriminator to facilitate demodulation of Bragg wavelength shifts in the return signals. The system exhibits a wide sensing range with a detection capability of < 1 μ-strain/√Hz rms at low frequencies.

INTRODUCTION

Recently, considerable research has focused on the use of fiber Bragg gratings (FBG) for sensing elements [1,2]. These devices have the potential to impact sensing trends in many engineering-based applications, including strain and structural health monitoring in civil structures. For these applications, there is a need for the development of multiplexed sensor configurations that can provide quasi-static strain information from the sensors. Due to the inherent wavelength division encoded nature of the outputs from FBG sensors, wavelength division multiplexing can be used to address a series of sensors. The number of sensor elements that can be accommodated under a single source spectrum profile, however, is limited. Alternative techniques to multiplexing include time and frequency based approaches. To further increase the multiplexing capability, it may be possible to augment wavelength-division addressing with time or frequency addressing. Recently, a four-element time division multiplexed system was described which used a fiber Mach-Zehnder interferometer for high resolution dynamic strain measurements [3-5]. In this system, the interferometer arms were subject to low frequency drift, which limited the ability of the system to monitor low frequency, quasi-static strain perturbations. In this paper we demonstrate an eight element time-division multiplexed FBG sensor system utilizing an integrated optic interferometric discriminator which provides the capability of quasi-static strain measurements.

PRINCIPLE

The principle of the interferometric detection technique has been described in detail elsewhere [4]. Briefly, the strain-induced wavelength shift of a FBG sensing element is transposed into a shift in the phase of the interference signal at the output of an unbalanced interferometer by passing the light reflected from the FBG through the interferometer. The technique provides very high sensitivity to weak dynamic strain perturbations of the FBG element when a large optical path imbalance is used in the interferometer. A sensitivity of ~ 0.6 nano-strain/√Hz has been demonstrated using this approach. The sensitivity is limited by the largest magnitude of the optical path difference (OPD) which can be utilized, which is dependent on the effective coherence length of the FBG return signal (typically ~ 1 cm). One drawback of this approach is that the system cannot determine quasi-static strain changes without the use of a fringe-counting device. This necessitates continual tracking of the system output, thereby eliminating an important advantage normally associated with FBG sensors. The use of a short OPD in the interferometer provides a reduced sensitivity, but can allow a wide strain range to be accommodated within a single fringe, or 2π phase shift range. The system scale-factor (i.e. interferometer phase shift change for a given strain perturbation at the grating) is given by

0-8194-1700-9/94/$6.00

$$\frac{\delta\phi}{\delta\varepsilon} = \frac{2\pi D}{\lambda}\,\xi \qquad (1)$$

where ξ is the normalized dependence of the Bragg wavelength on fiber strain, i.e., $\xi = (1/\lambda)(\delta\lambda/\delta\varepsilon)$, D is the interferometer path imbalance, and λ is the nominal Bragg wavelength. As an example, for an interferometer with an OPD of 100 μm, a wavelength shift of ~ 17 nm (free spectral range) is required to produce a 2π interferometer phase shift at a wavelength of ~ 1.3 μm. For 1.3 μm gratings, this corresponds to a strain range of ~17,000 μ-strain, or ~ ± 8,500 μ-strain. Interferometric phase detection approaches such as synthetic heterodyne demodulation allow the phase of the interferometer to be read in a linearized form, thus producing a wide sensing range.

With this configuration for detection of wavelength shifts, a series of FBG sensing elements can be interrogated using time-division multiplexing with a pulsed broad-band source as depicted in Figure 1. By careful selection of the fiber lengths in the system, an appropriate round-trip time delay for each FBG element is obtained. Consequently, a single optical pulse launched into this array will produce a series of return pulses, each pulse corresponding to a FBG sensor element. By passing the pulse train through an interferometric wavelength discriminator, the wavelength encoded pulse information is converted to phase information and is subsequently detected using a high bandwidth photodetection circuit. Individual sensor pulses can be demultiplexed using a an electronic circuit capable of gating out a single pulse within the pulse train signal allowing passive phase detection methods to be employed to recover sensor strain information from each sensor channel. The maximum pulse repetition rate (duty cycle) for the system is determined by the delay time between channels τ, and is given by $1/(\tau N)$ where N is the number of sensor channels.

EXPERIMENTAL DEMONSTRATION

In the system presented here, an unbalanced integrated optic Mach-Zehnder (IOMZ) interferometer manufactured by Integrated Optics Limited, was used as the wavelength discriminator. Figure 2 shows the measured wavelength dependence of this device when illuminated with the broad-band source (FWHM ~ 40 nm). As can be seen, the free spectral range (FSR) for this device is ~8.4 nm, which corresponds to an optical path difference of 201 μm. From this measurement and Eqn. 1, a strain-to-phase shift calibration factor for this system was thus determined to be 744 μrad/μ-strain.

To initially demonstrate the operation of the IOMZ discriminator, a single FBG element was illuminated in continuous wave (non-pulsed) mode using a 1.3 μm wavelength, ~350 μW broad-band edge emitting LED source via a single mode coupler and fiber. The FBG return signal was passed through the IOMZ discriminator and then to a photodetector. Synthetic heterodyne demodulation of sensor strain information was accomplished by applying serrodyne (ramp) modulation at ~2 kHz to the phase modulator of the IOMZ discriminator. Much higher ramp modulation frequencies are possible with the IOMZ device used. The carrier signal contained the FBG sensor strain information of interest encoded as a phase shift and was converted to an analog voltage using a lock-in amplifier configured as a phase detector. Figures 3a & 3b show the lock-in output during two different 10.5 minute time intervals obtained from a FBG sensor element attached to the root of a cantilever beam subjected to strain perturbations from 50 μ-strain up to 2000 μ-strain by displacement of the beam. Utilizing the full 2π radian range of the lock-in amplifier available, maximum strain range of ~ 8500 μ-strain pk-pk can be achieved within a single 2π phase span. From the smaller strain perturbations in Figure 3a, a strain resolution of ~ 2 μ-strain rms was determined. The output drift was also measured during a sixty minute time interval from which a random drift (1 σ) of 3.4 μ-strain/hr was obtained.

To demonstrate time-division multiplexing with the IOMZ discriminator, an eight element fiber-grating sensor system was configured with two sets of 4 FBG elements coupled to either port of a 2x2 coupler to form two 'branches' of the array. TheE-LED source and the IOMZ were then coupled to the other two ports. The gratings in each branch were spaced by 5 meters of fiber, and the FBG set in one branch were delayed with respect to the other by an additional 20 meters of fiber by the addition of a delay coil. By applying a 40 nsec width pulse at 1/9 duty cycle to the broad-band source supply current, a series of eight return pulses were produced at the photodetector output for each pulse launched into the system by the source. Figure 4 shows the pulse applied to the broad-band source (top trace) and the resultant photodetector output pulse train obtained with the carrier modulation applied to the IOMZ discriminator (bottom trace). This pulse train contains the multiple sensor strain information, a single channel of information was then discriminated from the other channels using a high speed sample-and-hold circuit. As before, carrier modulation applied to the IOMZ discriminator provides a signal suitable for passive demodulation using a lock-in amplifier. Figure 5 shows a measurement of the low frequency noise performance of the multiplexed system. In this case, a single pulse was gated out from the detector output, and processed using the synthetic heterodyne demodulation scheme. A low-frequency (6 Hz) strain perturbation of 33 μ-strain rms was applied to the appropriate grating element via a piezo-electric transducer. The low-frequency noise floor in Figure 5 corresponds to a noise equivalent strain of 0.6 μ-strain/$\sqrt{Hz}$ rms. The performance of the multiplexed system was limited primarily by the low light levels. In future implementations of this system, higher power fiber based sources can be utilized, which should significantly improve performance.

SUMMARY

An eight element fiber grating sensor system was demonstrated using time division based multiplexing and a integrated-optic chip wavelength discriminator. The wide range and sensitivity for low frequency, quasi-static type measurements obtained demonstrate the potential of this approach for multi-point structural strain sensing applications.

ACKNOWLEDGEMENTS

The authors wish to acknowledge M.A. Davis, D.G. Belmore, M.J. Marrone, and R.S. Weis for their assistance. This work was sponsored in part by the Office of Naval Research.

REFERENCES

1. K.O. Hill, Y. Fujii, D.C. Johnson, and B.S. Kawasaki, "Photosensitivity in optical fiber waveguides: Application to reflection filter fabrication," Applied Physics Letters, Vol. 32, p. 647, May 1978.
2. Meltz, G., Morey, W.W., and Glenn, W.H.: "Formation of Bragg gratings in optical fiber by a transverse holographic method", Optics Lett., 14, p.823, 1989.
3. Kersey, A.D., Berkoff, T.A. and Morey, W.W.: "High resolution fiber grating based strain sensor with interferometric wavelength shift detection", Electronic Lett., 28, p. 236, 1992.
4. Kersey, A.D., Berkoff, T.A., and Morey, W.W.: "Fiber optic Bragg grating strain sensor with drift-compensated high-resolution interferometric wavelength shift detection", Optics Letters, Vol. 18, No. 1, p. 72, 1993.
5. R.S. Weis, A.D. Kersey, and T.A. Berkoff, "A four element fiber grating sensor array with phase sensitive detection," Proceedings, North American Conference on Smart Structures and Materials, Smart Sensing, Processing, and Instrumentation, Vol. 2191, p. 150, 1994.

*SFA, Inc., 1401 McCormick Drive, Landover, Maryland

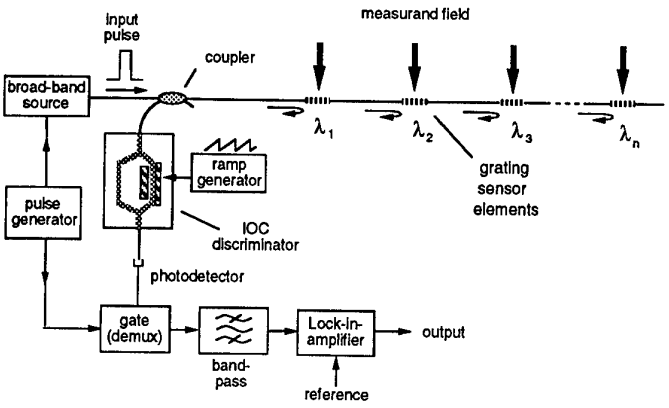

Figure 1. Time division mulitplexed fiber grating sensor system utilizing an integrated optic Mach-Zehnder interferometer.

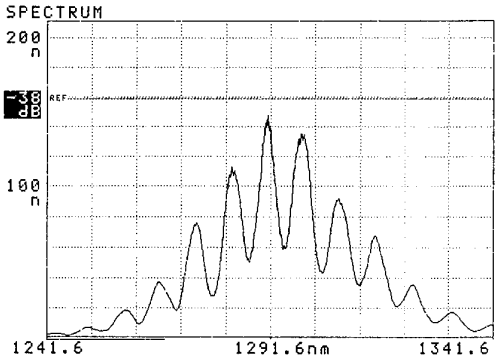

Figure 2. Output wavelength dependence of the integrated optic discriminator when illuminated with the broad-band source.

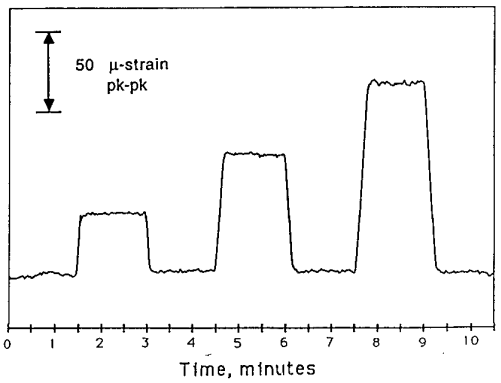

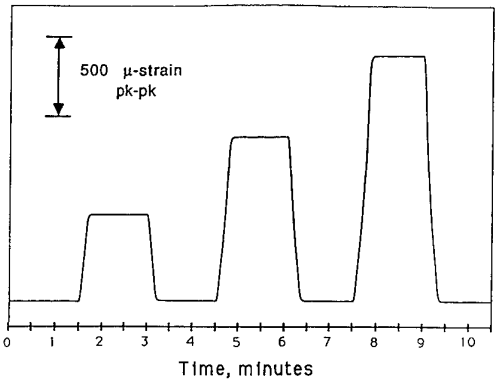

Figures 3a&b. Lock-in-amplifier output voltage obtained for a single FBG sensor system during a 10.5 minute time span. Multiple step changes in strain starting from 50 μ-strain (left trace) to 2000 μ-strain (right trace) pk-pk were obtained by attaching the FBG sensor to the root of a cantilever beam and deflecting the end of the beam.

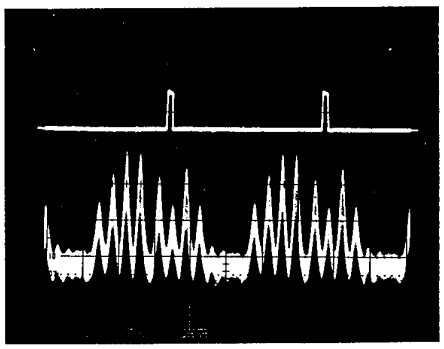

Figure 4. Top trace is the pulse applied to the broad-band source, bottom is the resultant pulse train at the photodetector output from the eight element FBG system.

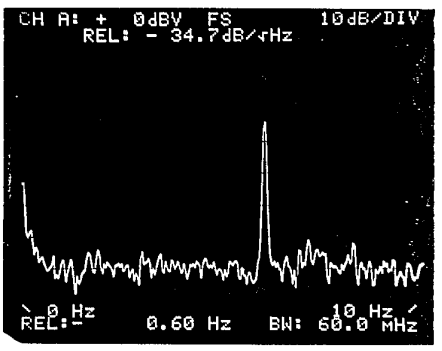

Figure 5. Power spectrum obtained from from a single sensor from the FBG array using Synthetic heterodyne demodulation when a 6 Hz, 33 μ-strain rms signal is applied. The noise floor corresponds to ~ 0.6 μ-strain/√Hz rms.

Paper presented at the Second European Conf. on Smart Structures and Materials, Glasgow 1994, Session 10

A Novel Fibre Optic Stress/Strain Sensor, Using the Near-Infrared SPATE Effect (FONI-SPATE)

J.P. Dakin, J.L. Cruz*
(Optical Fibre Group)

P.A.S. Reed, I. Sinclair
(Engineering Materials Group)

University of Southampton
Highfield, Southampton
SO17 1BJ, UK

*On leave from Dept. Appl Physics, University of Valencia

Abstract

A new fibre optic stress/strain sensor, utilising near-infrared SPATE, is reported which is suitable for monitoring hot materials. The fibre is merely arranged to collect the grey body emission from a heated metal sample. When the sample is subject to transient stresses, the radiation is modulated because of the adiabatic changes in the temperature of the material surface. The modulation of the light is monitored, via a silica optical fibre, using a near- infrared GaInAs photo-detector. This is also believed to be the first demonstration of SPATE in the near infrared region of the spectrum.

Introduction

The technique called SPATE (Stress Pattern Analysis by Thermal Emission)[1,2] has found considerable success for the monitoring of vibration in mechanical structures, engines etc. The method relies on the adiabatic heating and cooling that occurs in a cyclically stressed sample, which results, in turn, in a transient variation of the infrared emission from the surface. The temperature change, ΔT, that results from the stress is given[2] by:-

$$\Delta T = -T \cdot \frac{\alpha}{C\rho} \Delta(\sigma_1 + \sigma_2)$$

where T is the absolute temperature, α is the thermal expansion coefficient, C is the specific heat at constant stress, ρ is the density and $\Delta(\sigma_1 + \sigma_2)$ is the sum of the transient changes in the principal stresses in the surface region. Clearly, the strain is related to the stress via the elastic constants of the material. Like an ideal gas, the temperature of the specimen reduces during expansion and increases during compression.

For conventional SPATE systems, the thermal changes are observed using an infrared thermal-imaging camera and the video signal is processed to observe changes in the infrared emission. These changes occur synchronously with the vibrational frequency of the specimen. However, if the material is heated above 200°C, there is a significant emission tail in the near infrared region 2.0 → 2.5 μm, where short lengths ($\sim$1 metre) of silica fibre are still reasonably transparent. In addition, high performance "extended" GaInAs detectors can be used to detect low levels of radiation in this region. With our new method, surface strain sensing becomes possible, using a probe which is remoted via a silica fibre cable. In addition, the probe may potentially be embedded in a material (or pushed into a narrow-bore hole in a specimen) in order to measure strain at internal surfaces. Thus, although not readily capable of providing a 2-dimensional display, as possible with conventional SPATE, we have formed a new flexible probe, which is capable of measuring in less accessible places.

0-8194-1700-9/94/$6.00

Theory

The spectral radiance, R, of a grey body, at a temperature, T, is given by[3]:-

$$R = \frac{2c^2h}{\lambda^5} \frac{d\lambda}{e^{\frac{hc}{\lambda KT}}-1} \cdot \epsilon$$

where C = velocity of light, h = Plank's constant, λ = wavelength, $d\lambda$ is the wavelength interval, K is the gas constant and ϵ is the surface emissivity. If an optical fibre, of area A, is placed in a position such that a strained specimen totally fills its acceptance cone, a power P_r is collected, where:-

$$P_r = \int\int\int R \,.\, \cos\theta \,.\, dA \,.\, d\Omega \,.\, d\lambda$$

For small collection angles, it can be simply shown that:-

$$P_r \simeq \pi^2.a^2.(N.A)^2 \int_{\lambda_1}^{\lambda_2} R\,d\lambda$$

where N.A is the numerical aperture of the fibre and a is the fibre radius. This power, P_r, is the same as that which would be collected if the fibre were to be butted against the specimen (i.e. the spacing from the sample is not critical when calculating the collected power).

Provided $T \leq 800°K$ and $\lambda \leq 2.5\mu m$, then $e^{\frac{hc}{\lambda KT}} \gg 1$, and the equation for the collected light can be more simply evaluated to give the power, P_r, as a function of the temperature, T, and the change in power ΔP_r as a function of change in temperature, ΔT. From equation (1), the optical intensity modulation index $\Delta P_r / P_r$ can then be related to the stress. The constant of proportionality depends both on the material properties and the temperature of the sample. However, the former are normally known for common materials and the temperature can be inferred from the total optical power received, as this is a highly sensitive function of temperature[4]. Strain can, of course, be deduced from the stress if the elastic properties of the material are known.

From the above formulae, the ratio of the optical intensity modulation index, $\Delta P_r / P_r$, to the stress, $\Delta(\sigma_1 + \sigma_2)$, has been calculated, as a function of absolute temperature, T. This linear relationship is shown graphically in Fig. 1 for two temperatures. For these curves, we have assumed that the fibre/detector light-receiving combination has a uniform response up to a long wavelength cut-off at 2·5 μm. (A vertical band-edge has been assumed at this wavelength).

Experiment

In order to test our new method, we mounted a stainless steel (type 304) test coupon in an Instron 8501, servo-hydraulic, testing machine and arranged for it also to be electrically heated using a low-voltage, high-current source. The coupon was subjected to a mean longitudinal stress of 3·5 KN, plus a cyclical (sinusoidal, F = 20 Hz) longitudinal stress component of up to 5·0 KN p-p. A fibre-bundle cable, with 16 silica-cored fibres (Heraeus Fluosil, type SWU 1.1 ; core ϕ = 200 μm, N.A. = 0·23) was used to guide light to an Epitaxx GaInAs photodetector (long-λ cut-off at 2.6 μm). The bundle was larger than the detector, and, because of this, tests showed it coupled only 5 times as much optical power to the detector as did a single fibre of the same type. The apparatus is shown in Fig 2(a). Fig. 2(b) shows the response from the sensor (upper curve) when the coupon was subjected to a cyclic stress of 5·0 KN p-p. The lower curve shows the stress, as indicated by the Instron load cell output. The middle curve is a pre-filtered version of the optical signal, which was passed through a filter having a 10 Hz → 50 Hz bandpass characteristic. The upper middle curves were subjected to multiple averaging (4096 averages) on a Philips PM3392 digital oscilloscope, in order to improve the signal/noise ratio.

Our measurements show that the detected signal (top curve) followed the sinusoidal stress signal (bottom curve) in terms of waveform, phase and polarity. The response was also found to be linear with applied stress, as shown by the two curves in Fig. 3, taken at temperatures of 676 K and 710 K. The observed optical modulation index was 0·52%, corresponding to a scale factor of $4{\cdot}3.10^{-6}$% KN^{-1} m^2, with the sample heated to 710°K. This corresponds to the theoretically expected value of $3{\cdot}9.10^{-6}$% $KN^{-1}m^2$, using values of $\alpha = 18.10^{-6}$ K^{-1}, $C = 5.10^2$ $J.Kg^{-1}K^{-1}$, $\rho = 8.10^3$ $Kg.m^{-3}$ in equation 1.

In order to use the method for stress/strain sensing at these temperatures, it is necessary to take a least 128 averages of the signal, in synchronism with the applied stress signal. However, the optical signal strength, and hence the signal/noise ratio, is expected to increase dramatically if the temperature of the test coupon were to be increased, or if fibres and detectors having a longer-wavelength IR response were to be used. For example, if the stressed sample were at 1000°K, the radiated signal would be 10^3 times greater, even when using the same silica fibre.

Conclusions

We have, for the first time, demonstrated the feasibility of constructing a simple fibre-remoted stress/strain sensor, using infrared emission from hot samples. In addition, we believe this is the first demonstration of the use of the SPATE method in the near infrared region of the spectrum. The method could have a number of practical applications for monitoring strain in naturally-hot structures (e.g. engine components, turbine blades, etc), where the use of conventional sensors may prove difficult, and it may be particularly advantageous for measurement in relatively-inaccessible areas.

References

1. Mountain D.S., Webber J.M.B., "Stress pattern analysis by thermal emission (SPATE)" Proc. SPIE vol 164 (1978) pp 189-196.

2. Stanley P., "Thermoelastic stress analysis: progress and prospects", 9th International Conference on Experimental Mechanics, August 1990, Copenhagen, Denmark.

3. Kingslake R., "Applied Optics and Optical Engineering", vol IV, chapter 8, Academic Press (1967), ISBN 0-2-406604-7.

4. Dakin J.P., Kahn D.A., "A novel fibre optic temperature probe" Optical & Quantum Electronics 9 (1977) pp 540-544.

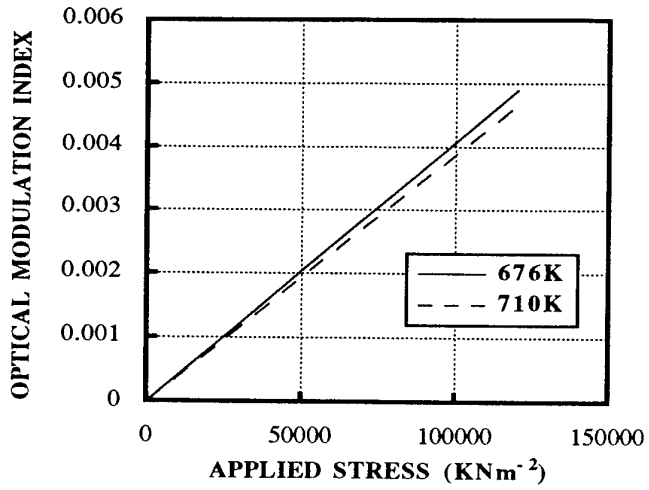

1. Relationship (theoretical) between the optical intensity modulation index, $\Delta P_r/Pr_r$, and the material stress, $\Delta(\sigma_1+\sigma_2)$ at two temperatures (Our calculation assumes a fibre/detector response cut-off at 2.5μm).

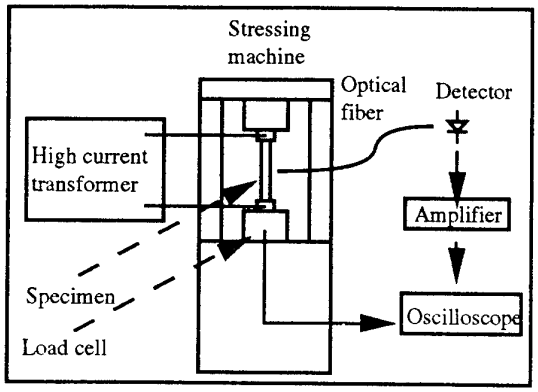

2(a). Apparatus for testing the FONI-SPATE system, using INSTRON servo-hydraulic, testing machine.

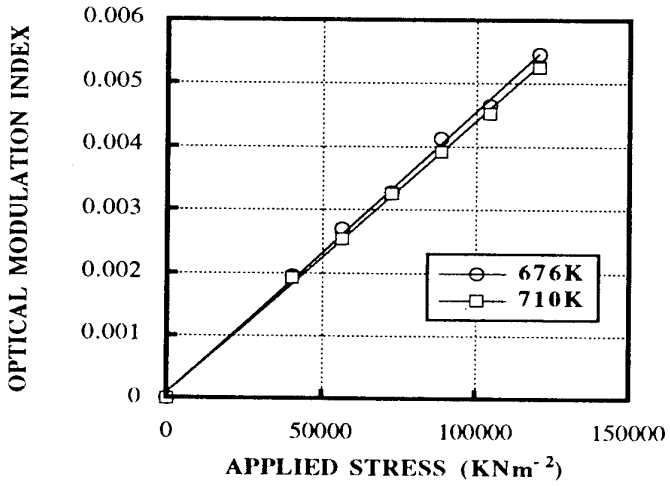

3. Experimental variation of optical modulation index $\Delta P_r/P_r$ with applied unidirectional stress $\Delta(\sigma_1)$ at two temperatures.

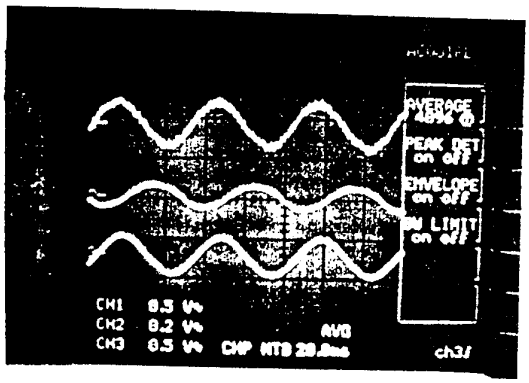

2(b). Signals on Philips PM3392 oscilloscope. Upper track is detected A.C optical signal component (averaged 4096 times) and lower trace is signal from load cell. The middle trace was the detected signal passed through a 10 Hz → 50 Hz filter. prior to averaging.

Paper presented at the Second European Conf. on Smart Structures and Materials, Glasgow 1994, Session 10

Ferroelectric Ceramic and Epoxy Composite Films as Pyroelectric Detectors

M.P. Wenger, P. Blanas†, R.J. Shuford† and D.K. Das-Gupta

School of Electronic Engineering Science, University of Wales, Dean Street, Bangor, Gwynedd, LL57 1UT, UK

†U.S. Army Research Laboratory, Materials Directorate, Arsenal Street, Watertown, MA. 02172-0001, USA

Abstract

Thin films of ferroelectric ceramic and epoxy composites with 0-3 connectivity have been produced by dispersing a ceramic powder in a thermosetting epoxy resin. Calcium Modified Lead Titanate [PTCa] powder with grain size of less than 10μm was mixed with an epoxy resin and curing agent and then formed into thin films of approximately 100μm. The pyroelectric behaviour of these composites with 50% and 60% volume loading of ceramic is reported in this present work.

Introduction

The use of the piezoelectric and pyroelectric properties of ferroelectric ceramic and polymer composites as sensors in transducers has gained much interest in the past years. Ferroelectric ceramics have a tendency to possess high pyroelectric coefficients and a correspondingly high permittivity. Polymers can be either ferroelectric or not, but tend to have low values of permittivity. The suitability of a pyroelectric material as a detector is usually determined by its Figure of Merit (FOM_p) and is defined for a thin film composite as

$$FOM_p = \frac{p}{\varepsilon} \qquad \ldots(1)$$

where p is the pyroelectric coefficient and ε the permittivity of the composite. The FOM_p for a composite material can thus be determined by the properties of the constituent materials and reflects the responsivity of the material. The permittivity, due to the ceramic alone will be lowered by the inclusion of the ceramic into a low permittivity polymer matrix. The corresponding pyroelectric coefficient will also be lowered but the value of the FOM_p may be greater than that of the constituent materials alone.

Other determining factors in the choice of materials for certain applications can be the size of the sensing material. Composite materials possess an advantage over ceramics alone in their ability to be formed into large area targets. The use of a thermosetting epoxy as a polymer matrix provides ease of composite manufacture as well as providing low manufacturing cost.

0-8194-1700-9/94/$6.00

Fabrication of Composite Films

In a 0-3 connectivity ceramic/polymer composite, ceramic powder is dispersed randomly in a polymer matrix. The quantity of the ceramic can be calculated using the following equation

$$M_c = \left(\frac{\phi}{1-\phi}\right)\rho_c V_p \qquad ...(2)$$

to obtain the mass M, of the ceramic for a given ceramic volume fraction ϕ, where ρ_c is the density of the ceramic and V_p the volume of the epoxy resin used. The subscripts c and p refer to the ceramic and the polymer respectively. The composite density is then given by

$$\rho = \phi\rho_c + (1-\phi)\rho_p \qquad ...(3)$$

where ρ_p is the density of the polymer.

Epikote 828 (Shell) and curing agent K61B (Anchor Chemicals) were used to produce a matrix of a thermosetting polymer. A few drops of the curing agent were added to 1 cc of the epoxy resin in a small container. The measured amount of the ceramic powder was gradually added to the epoxy whilst stirring continuously to ensure an even distribution of ceramic throughout the polymer.

The composite mixture was placed in a vacuum chamber and outgassed at room temperature for two hours. At this stage it was removed from the container and placed on a clean, smooth piece of aluminium foil and replaced into the vacuum chamber. The composite was outgassed for a further two hours at 60°C.

The composite was then removed from the vacuum chamber, together with the foil, and another piece of foil was placed on top of the composite. These were located between two milled steel plates and the assembly was placed in a temperature controlled mechanical press at 60°C. A maximum pressure of 250 kg cm^{-2} was gradually applied. The composite was left to cure for another 2 - 4 hours at 60°C.

The cured material was removed from the assembly and the foil gently peeled away to expose a smooth thin film, (80 - 300μm). Aluminium electrodes were evaporated onto the surface of the films which were poled by applying a DC electric field in the range of 15 - 30 MVm^{-1} between the electrodes. The poling process was performed with the sample immersed in a bath of insulating silicon oil at 100°C. The magnitude of the poling field was limited by the electrical breakdown strength of the composite.

Pyroelectricity: Results and Discussion

Composite films of PTCa/P(VDF-TrFE) and PTCa/Epoxy of varying ceramic volume fraction have been studied extensively so far to determine their piezoelectric and pyroelectric properties. The piezoelectric properties of these composites have been reported [1] and their suitability as sensing materials in transducers has been considered.

The pyroelectric properties of these composites were measured using a direct method [2]. The phenomenon of pyroelectricity arises from the temperature dependency of the spontaneous polarisation present in ferroelectric materials. Thus a change in temperature produces a change in spontaneous polarisation which manifests itself as surface charge on the electrodes of the sample. If the electrodes are short circuited a current will flow from one electrode to the other via the external circuit. The pyroelectric coefficient, p in this configuration is defined as

$$p = \left(\frac{dP_s}{dT}\right)_{E,X} = \left(\frac{dQ/A}{dT}\right)_{E,X} \cong \frac{1}{A}\left(\frac{dQ}{dT}\right)_{E,X} \qquad \ldots(4)$$

where P_s is the polarisation of the sample, Q the surface charge produced, A the area (assumed not to vary significantly) and T the temperature. The subscripts E and X refer to the electric and stress fields respectively which are kept constant. By suitable manipulation of equation (4) the pyroelectric coefficient becomes

$$p = \frac{1}{A}\left[\left(\frac{dQ}{dt}\right)\left(\frac{dt}{dT}\right)\right]_{E,X} = \frac{I}{A}\left(\frac{dt}{dT}\right)_{E,X} \qquad \ldots(5)$$

where t is the time. Therefore while knowing the rate of change of temperature and measuring the current, the pyroelectric coefficient can be determined.

The samples were placed in a cryostat and heated/cooled at a constant rate of 1.5 ^{o}C/min between 10 - 70 ^{o}C. The electrodes of the samples were shorted circuited via a Keithley 616 Digital Electrometer to monitor the current. The output of the electrometer was read directly by a computer via an analogue to digital converter at temperature intervals of 0.5 ^{o}C. The temperature ramp was controlled by an Eurotherm 818P Model.

This procedure is the same for the Thermally Stimulated Discharge Current measurements and therefore it was necessary to ensure that the contribution due to space charge was kept to a minimum. The sample was therefore annealed, for an extended period of time by keeping the electrodes short circuited whilst the temperature was held above the measuring temperature (@ 80 ^{o}C). A number of temperature cycles were performed to ensure the value of the pyroelectric coefficient was reversible on the heating and cooling part of the cycle (figure 1).

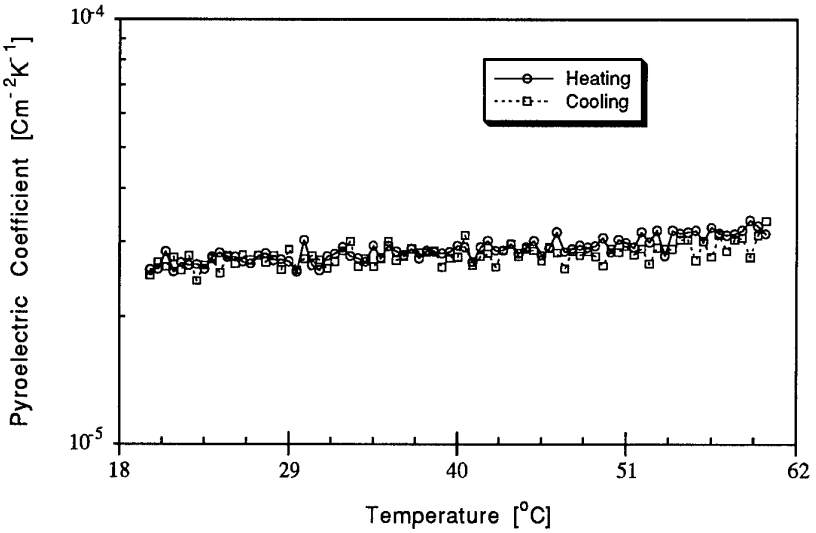

Figure 1 - Plot of the pyroelectric coefficient against temperature on a heating cycle and cooling cycle for PTCa/Epikote 60/40vol%. True reversibility can be seen from the graph.

As stated earlier the pyroelectric figure of merit, FOM_p can be used to characterise the suitability of a material for use as a sensor. The permittivity of the samples were obtained from measurements of their capacitance and conductance by using a conventional capacitance bridge (General Radio, Model 1621) at 1 kHz at a variety of isothermal temperatures. Values of the pyroelectric coefficient, permittivity and FOM_p for composites of PTCa/Epoxy and their individual constituent materials can be seen in table 1.

Material	p @ 30°C (x10^{-3})	ε_r @ 1 kHz	FOM_p
PTCa	380.0	220.0	1.73
Epikote 828	-	4.1	-
PTCa/Epikote 50/50vol%	20.4	24.0	0.85
PTCa/Epikote 60/40vol%	29.7	30.1	0.99

Table 1 - Pyroelectric properties of PTCa, Epikote 828 and composites of the constituent materials at 50/50vol% and 60/40vol%.

Acknowledgements

This work is financially supported by the US. Army Research Laboratory (Watertown - US) and we are grateful to Siemens (Munich - Germany) and GEC - Marconi Materials Research (Caswell - UK) for supplying the ceramic used in the research.

References

1. C. Dias, M.P. Wenger, P. Blanas, R.J. Shuford, Y. Hinton , D.K. Das-Gupta, *Intelligent Piezoelectric Composite Materials for Sensors.* To be presented at the 1994 International Conference on Intelligent Materials, Williamsburg, Virginia, USA.

2. Byer, R.L. and C.B. Roundy, *Pyroelectric coefficient direct measurement technique and application to a nsec response time detector.* Ferroelectrics, 1972. **3**: p. 333-38.

Paper presented at the Second European Conf. on Smart Structures and Materials, Glasgow 1994, Session 10

FIBRE OPTIC SENSOR OF ELECTROSTATIC FIELD WITH MECHANICAL RESONATOR.

A.V. Churenkov, M.A. Skorobogatyi, A.D. Loiko

Moscow Institute of Physics and Technology,
Department of General Physics,
141700, Dolgoprudny, Moscow Region, Russian Federation.

ABSTRACT

New type of fibre optic sensor of electrostatic field is considered. Using the interferometric detection technique the sensitivity of about 0.2 $(V/m)/\sqrt{Hz}$ was achieved. Theoretical evaluation yields the thermal fluctuation limit of sensitivity of about $2.5 \cdot 10^{-4}$ $(V/m)/\sqrt{Hz}$.

1. INTRODUCTION

The interferometric optical systems have found a wide application in research and industry as providing the displacement sensitivity of parts of angstrom. With the creation of fibre optic interferometers, the new opportunities for the development of resonator-based devices have appeared. The fibre optic Fabry-Perot interferometer has a number of advantages as compared with interferometers of other types (Mihelson and Mach-Zahnder), such as simplicity and insensitivity to phase fluctuations of light in fibre and couplers [1-3]. At present, the development of fibre optic sensors of electric field follows generally the way of optical signal modulation by means of piezoelectric action on the fibre [4-6]. In spite of simplicity of the scheme, the sensitivity of these sensors is rather low and equals about 10 V/m.

In this paper a new fibre optic sensor of electrostatic field is considered. Using the interferometric detection technique the sensitivity of about 0.2 $(V/m)/\sqrt{Hz}$ was achieved. In many cases the physical limitation for the sensitivity of interferometer-based sensors originates from thermally generated vibrations [7,8]. It is shown in this paper that the thermal fluctuation limit of sensitivity is about $2.5 \cdot 10^{-4}$ $(V/m)/\sqrt{Hz}$.

2. PRINCIPLE OF OPERATION

The scheme of the sensor is shown in Fig.1. The resonator in the form of a cantilever beam made of metallic glass is placed between the isolated capacitor plates. The alternating voltage $U_\omega \cos \omega t$ is applied to the capacitor, so that the alternating electric field emerges between the edges of the capacitor plates. When the measured electric field E_0 is applied to the resonator, the electric charges are induced on it. The alternating field of the capacitor acts on these charges giving rise to excitation of resonator flexural vibration. The amplitude of oscillation is proportional the induced charge and, hence, to E_0. The partially reflecting surface of the cantilever and the output end of the fibre form the low contrast Fabry-Perot cavity. Oscillation of the resonator modulates the path length of the interfering rays, so that an intensity-modulated light is propagating back along the fibre and the directional coupler to the photodetector, when the cavity is illuminated with CW radiation of laser diode. As a result, the amplitude of phase modulation of output signal is proportional to E_0. To increase the signal-to-noise ratio the oscillation was excited at the resonator natural frequency ω and detected with the aid of lock-in amplifier.

0-8194-1700-9/94/$6.00

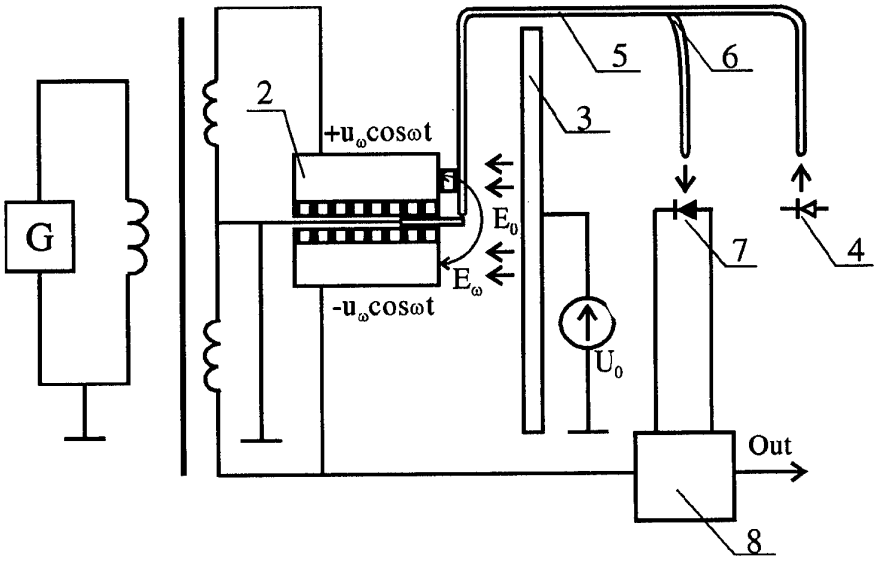

Fig.1 The scheme of fiber optic electric field sensor.
1-resonator, 2-cubic capacitor, 3-test plate, 4-CW laser diode, 5-optical fiber, 6-directional coupler, 7-photodiode, 8-lock-in amplifier.

3. EXPERIMENTAL RESULTS

The sensitive element used in the experiment consists of the cubic capacitor with length a=2 cm and the isolated cantilever beam which is placed between the capacitor plates. The resonator of length l=5 mm, width b=2 mm and thickness h=35 μ m was made of metallic glass. Met-glass was chosen as a material of the resonator because of its excellent mechanical properties and high reflectivity. Partially reflecting surface of the resonator and the end of single-mode fibre form the cavity of Fabry-Perot resonator, which is illuminated by CW semiconductor laser source of wavelength $\lambda = 0.85\,\mu$ m. We adjusted the fibre to equalize the amplitudes of the waves reflected from the fibre tip and from the resonator surface. The perpendicularity of the fibre and the cantilever beam was controlled by of microscope over the mirror image of the fibre on the plate of resonator. When the alternating voltage of amplitude U_ω=170 V was applied to the capacitor, the oscillation at the resonator natural frequency f=672 Hz was excited. The oscillator quality factor was measured to be Q=167. The coefficient of conversion S of the electric field E_0 into the amplitude of phase modulation was measured by applying the constant voltage U_0=17 V on a test plate, which generated an uniform electric field near the sensitive element. The plate was placed at the distance 8 cm from the capacitor. The intensity of modulated light $I(t)$ was proportional to $\sin\varphi(t)$,where $\varphi(t) = \varphi_0 + \Delta\varphi \sin\varphi t$. The value $\Delta\varphi$ was proportional to the applied voltage U_0, and the measured conversion coefficient was $S = \Delta\varphi/E_0 = 7.4 \cdot 10^{-4}$ rad/(m/V). The value φ_0 was adjusted by applying the magnetic field perpendicular to the resonator plate to maintain $\varphi_0 = 2\pi k$ (where k is an integer constant).

Small permanent signal was also observed after removing the constant voltage U_0 from the test plate. The reason was probably in an electric charge accumulated at the tip surface of the fibre used in interferometer.

4. THEORETICAL MODELLING

A stationary uniform electric field with the intensity E_0 induces the charge distribution on the metal surface of cubic capacitor. Therefore, the cantilever beam will be acted upon by resultant electric field, the intensity of which exceeds E_0. To calculate the stationary charge distribution on the sensitive element we replace the cube with the edge $2a$ by an imaginary cylinder of length $2a$ and radius a. Since the characteristic resonator size is much smaller than that of capacitor, we may suggest that such a

replacement has a small effect on the electric field near the resonator. In such a formulation the problem allows analytical solution by solving two-dimensional Laplas equation, which is invariant with respect to conform mappings [13]. We find finally the following expression for the linear density of charge distribution:

$$\sigma(x) = 12\,\varepsilon_0 E_0\left\{\sin\left[\pi\left(1-\frac{x}{l}\right)\right] + \frac{2x}{a}\left[1+\exp\left(\frac{a}{l}\left(\frac{2x}{l}-1\right)\right)\right]\right\} \tag{1}$$

where ε_0 is the dielectric constant.

When an alternating voltage is applied to the capacitor, the electric field E_ω is induced near the capacitor ends. The field has the form of concentric circles with centers on the line joining two capacitor plates [9]:

$$E_\omega = \frac{u_\omega}{\pi r}\cos\omega t \tag{2}$$

where r is the radius of circle. Under the action of E_ω the charged resonator is acted upon by harmonic force $F(x,t) = F_\omega(x)\cos\omega t = \sigma(x)E_\omega$, which excites mechanical transverse oscillations.

The Fourier projection Φ of the exciting force F_ω on the fundamental flexural mode of oscillation $\psi(x)$ is given by the following expression [10]:

$$\Phi = \frac{\int_0^l F_\omega(x)\,\psi(x)\,dx}{\int_0^l \psi^2(x)\,dx} \tag{3}$$

Thus, the resonance displacement of the cantilever is described by the expression [11]:

$$Y(x,t) = \frac{Q\,\Phi}{\mu\,\omega^2}\psi(x)\cos\omega t \tag{4}$$

where $\mu = m/l$, and m is the mass of the resonator. From the equations (1)-(4) we can find the expression for the amplitude of resonator tip vibrations $Y(l)$.

The oscillation of the resonator modulates the phase of interferometer output signal. The coefficient of conversion of applied electrostatic field into the interferometer phase modulation is

$$S = (4\pi/\lambda)\,(Y(l)/E_0) \tag{5}$$

Substituting the parameters of the sensor in (4) and (5) we have found the theoretical prediction for conversion coefficient $S_t = 9.5\cdot 10^{-4}$ rad/(V/m), which appeared to be in a good correspondence with the coefficient $S_e = 7.4\cdot 10^{-4}$ rad/(V/m) observed experimentally.

Finally, the minimum detectable electric field limited by thermal vibrations of the resonator was evaluated from fluctuation-dissipation theorem [12]. Taking the signal-to-noise ratio equal to 1, we find the minimum detectable intensity of field $E_{min} = 2.5\cdot 10^{-4}$ (V/m)/$\sqrt{\text{Hz}}$.

5. REFERENCES.

1. Tudor M.J., Andres M.V., Foulds K.W.H., Naden J.M., "Silicon resonator sensors: interrogation techniques and characteristics", IEE Proc., v.135, Pt.D, pp.364-368, 1988

2. Andres M.V., Tudor M.J., Foulds K.W.H., "Analysis of an interferometric optical fibre detection technique applied to silicon vibrating sensors", Electron. Lett., v.23, pp.774-775, 1987

3. Churenkov A.V., Listvin V.N., "Microresonator fiber optic sensors" (overview), Advances in Optical Fibre Sensors, SPIE, pp.125-134, 1992, Selected Papers from the International Conf.on Optical Fibre Sensors, 9-11 October 1991, Wuhan, China.

4. Vohra S.T., Bucholtz F., Kersey A.D., "Fiber-optic dc and low-frequency electric-field sensor", Opt.Lett., v.16, pp.1445-1447, 1991

5. Imai M., Shimizu T., Ohtsuka Y., Odajima A., "An Electric-field sensitive fiber with coaxial electrodes for optical phase modulation", J.of Lightwave Technology, v.5, pp.926-931, 1987

6. Faseroptische Sensoren, Teil 3. "Faseroptische Spannungsmessung", Bohnert Klaus. Bull. Schweiz. Electrotechn. Ver.,1991, v. 82, No.5, pp. 27-32 (in German)

7. Mermelstein M.D., "Fundamental limit to the performance of fiber optic metallic glass DC magnetometers", Electron. Lett., v.21, pp. 1178-1179, 1985

8. Listvin V.N., Alexandrov A.Ju., Kozel S.M., Churenkov A.V., "Fiber optic sensor of magnetic field with micromechanical ferromagnetic resonator", Letters in the Journal of Technical Physics, v.16, pp.36-39, 1990.

9. Neiman L.P., Dimirgjan K.S., "Theoretical basis of electrotechniques", St.Peterburg: Energoizdat, 1981, p.231-232 (in Russian).

10. Timoshenko S., Young D.H., Weaver W., "Vibration problems in engineering", John Wiley&Sons, Inc., 1974

11. Babakov I.M., "The theory of oscillation", Moscow: Nauka, 1965 (in Russian)

12. Landau L.L., Lifshitz E.M., "Electrodynamics of continuous media", Pergamon Press, Oxford, Chap.VII, 1981

13. Sidorov Yu.V., "Lectures on the theory of the function of complex variable", Moscow: Nauka, 1982. (in Russian)

Multiplexed Fibre-Optic System for Both Local and Spatially-Averaged Strain Monitoring

H Geiger [a], M G Xu [a], M A Longstaff-Tyrell [a], J P Dakin [a], N C Eaton [b], P J Chivers [c]

[a] Optical Fibre Group, Department of Electronics & Computer Science, University of Southampton, Southampton SO17 1BJ, UK; Email: hg@orc.soton.ac.uk

[b] Consultant to Westland Aerospace, 16 Kings Road, East Cowes PO32 6SE, UK

[c] Westland Aerospace, East Cowes PO32 6RH, UK

Abstract

An optical fibre sensor system to interrogate point sensors (Bragg gratings) and optical path length between point sensors is discussed. The paper describes interrogation schemes capable of measurement resolutions better than 100 microstrain based on simple optics, telecommunications electronics and sophisticated signal processing.

1 Introduction

Sensor systems are an essential component of smart structures in order to provide information to the control system.[1] To control smart structures effectively, the sensor provides information (strain, temperature etc) in both a localised and a spatially-averaged manner. The ideal optical fibre sensor would be a *distributed* sensor,[2] but this is still difficult to achieve with a realistic level of hardware. We present an approach combining both point sensors and long gauge-length sensors in a *multiplexed* sensor system, providing information almost as valuable as a distributed sensor system.

Our sensing system (Fig 1) combines Bragg gratings[3] to interrogate points with an *Optical Time Domain Reflectometry* (OTDR) system to interrogate the distance between the gratings. The mechanical and thermal environment **around** the gratings changes the reflected wavelength, and the environment **between** the gratings changes the time delay between the reflected signals. The fibre-optic probe is mechanically small (≈ 150 μm outer diameter) and of continuously cylindrical shape. It can be embedded in both civil structures and composites and does not degrade the mechanical properties of the structure.[4]

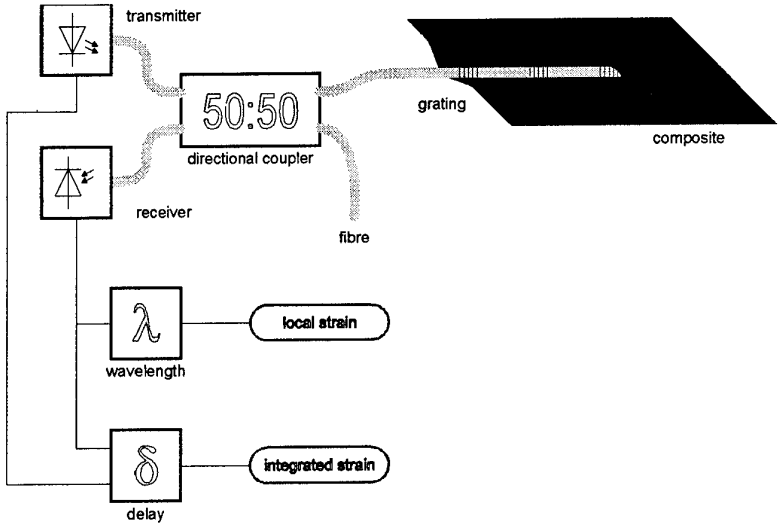

Fig 1: Multiplexed sensor system to resolve local and spatially-averaged strain

0-8194-1700-9/94/$6.00

Development of this system has concentrated on two aspects: a system to monitor the wavelength of multiple gratings (short gauge-length sensor) and a precision OTDR to monitor the optical path length between these sensors (long gauge-length sensor).

2 SHORT GAUGE-LENGTH SENSOR

Various schemes to detect small wavelength shifts of Bragg gratings have been developed. These include the filter-edge demodulation method where the edge of a filter or a wavelength-division coupler is used to convert wavelength changes to amplitude variations,[5,6] interferometric approaches,[7,8] the use of frequency-locked grating pairs,[9] and laser-sensor concepts where the grating sensor determines the lasing frequency.[10]

However, all above methods have limitations when it is desired to interrogate the wavelength of many gratings in a frequency-agile manner. In this paper we present advances on our method of constructing an interrogating system for fibre Bragg grating sensors using an *acousto-optic tunable filter* (AOTF).[11]

2.1 Grating Interrogation Scheme

Operation of our dedicated interrogation system (Fig 2) is similar to the system we proposed earlier[11]: A grating is illuminated with a broadband source, thereby filtering the light at the Bragg wavelength λ_p. This band-filtered light is then coupled through the acousto-optic tunable filter onto a suitable photodiode.

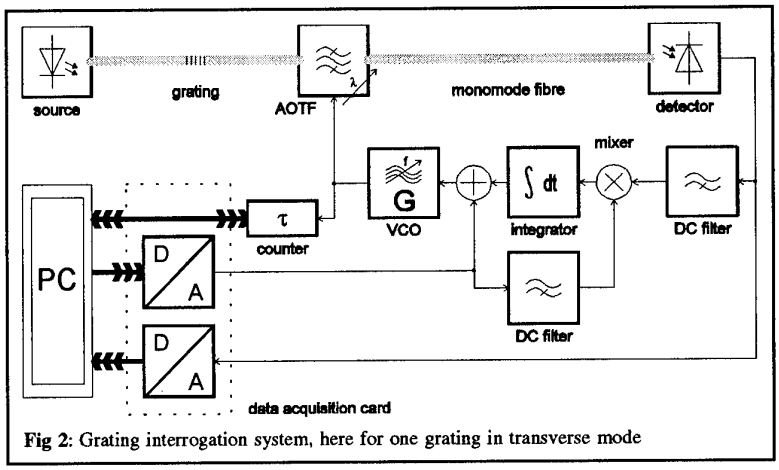

Fig 2: Grating interrogation system, here for one grating in transverse mode

An AOTF is a narrow-band optical bandpass filter whose centre wavelength λ_{AOTF} depends on an applied RF frequency.[12] By sweeping the RF frequency, the detector records the spectrum of the source filtered at λ_p. This is similar to the function of an optical spectrum analyser.

The PC generates a square wave with DC offset, toggling a *voltage-controlled oscillator* (VCO) between two RF frequencies. The VCO then toggles the AOTF between two optical wavelengths.[13] When the modulating square wave is mixed with the resulting AC signal from the detector, an error signal occurs if the mean AOTF wavelength does not correspond to λ_p. The sign of the error signal indicates whether the mean wavelength is above or below λ_p. If the error signal is integrated and added to the square wave, the mean AOTF wavelength is locked to λ_p. The mean RF frequency measured by the counter hence indicates the Bragg wavelength.

2.2 Modes of Operation

The circuit can operate in two different modes:

1) *scan mode*: Here the feedback circuitry is not connected and hence the PC can scan the AOTF. From the detector signal the PC can identify the VCO voltage corresponding to the grating wavelength λ_p.
2) *lock-in mode*: In this mode the PC sets the DC offset of the VCO voltage so that the AOTF wavelength is within the grating bandwidth. Then the feedback is closed and the circuit locks onto the Bragg wavelength and tracks it.

The system has scope for interrogating multiple gratings at different wavelengths either (i) simultaneously using the scan mode or (ii) in time-division multiplexing using the lock-in mode. The AOTF can also be driven by the VCOs of multiple feedback circuits in lock-in mode to track multiple gratings simultaneously.

The VCO and the frequency counter have been built and tested in scan mode with a quartz filter simulating the optical system. The software interface for the scan mode has also been developed. Computed results based on earlier measurements[11] predict a scale factor of -98 Hz/$\mu\varepsilon$[†].

3 Long Gauge-Length Sensor

Our precision *Optical Time Domain Reflectometry (OTDR)* system uses hardware already developed for telecommunications. Such an OTDR should form a suitable basis for practical sensing systems. It allows monitoring the range of reflective markers on optical fibres,[14,15] which can then be related to strain or temperature of the fibre.[16]

To enhance the range resolution of conventional OTDR, our system design uses a modified **electrically** coherent receiver[‡] (*correlator*) to detect the reflections from the fibre. Conventional OTDR uses a delay in the correlator that can only be switched in discrete steps, usually in multiples of the pulse duration. We report a method to improve range resolution by sweeping the delay continuously. We use the triangular shape of the autocorrelation function of a pulse to measure the time delay (ie optical range) of reflected signals more accurately.

3.1 Theoretical Background

An OTDR measures the reflections from an optical fibre[17] to characterise attenuation and reflective points along the fibre. Optical pulses of length τ and periodicity T (Fig 3, top left) are sent into the fibre and the returned power is monitored by an electrically coherent receiver. The output of the coherent receiver is the crosscorrelation between transmitted pulse and received signal.

If there is only one reflective point on the fibre, the output of the coherent receiver is approximately proportional to the autocorrelation of the transmitted signal (Fig 3, bottom left). If two or more pulses are received (eg from multiple reflections) the OTDR response has the form of a crosscorrelation (Fig 3, bottom right) between the two upper traces in Fig 3.

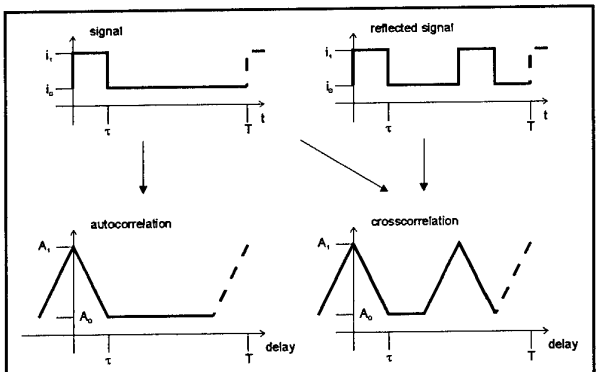

Fig 3: Correlation of a pulse of length τ with itself (*autocorrelation*) and with two similar pulses (*crosscorrelation*)

For many sensor systems a typical OTDR spatial resolution of 1-10 m is sufficient, but there is a need to monitor each reflective point with a range accuracy below 1 mm. Our current technique overcomes this problem by interrogating the slopes of the correlation peak.[††] These slopes (bottom of Fig 3) are normally not used because receivers of OTDRs do not allow a continuous sweep of the output.

[†] microstrain

[‡] *matched filter* or *correlation detector*; to be distinguished from **optically** coherent (ie interferometric) receivers, as used eg in *coherent OTDR*

[††] UK patent application 9407077.8

3.2 OTDR Interrogation Scheme

In the system in Fig 4, a digital signal intensity-modulates a 780 nm CD-type laser and is received by a fast silicon photodiode. Integrated circuits for fast telecommunication links support the electro-optic design.[18]

A PC controls the high-resolution delay system and acquires the output from the coherent receiver. Hence any receiver output can be converted to the corresponding delay, and only data from the regions of interest (ie the slopes of the peaks) need to be acquired.

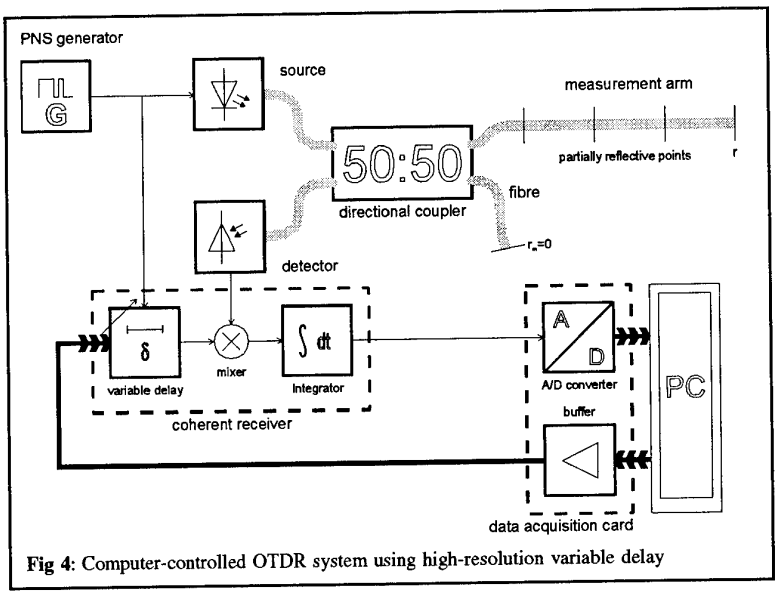

Fig 4: Computer-controlled OTDR system using high-resolution variable delay

The PC varies the delay over the region of interest whilst acquiring the receiver output. Then it detects the peaks in the receiver output and curve-fits a line to either slope of every received peak. The delay corresponding to the intercept of each peak's slopes is the time delay from that particular reflection.

Use of a *pseudo-random binary sequence (PRBS)* improves the duty cycle and hence the signal-to-noise ratio.[19] Because the technique relies solely on delay information, it is insensitive to both amplitude and polarisation changes. In other approaches, amplitude changes may either limit the performance[20] or force the use of more complex coding schemes.[21,22] Radial strain in the optical fibre could cause problems in polarisation-based systems.

This system shows, as an example, a reflection from 12.183685 m range with a standard deviation of 440 μm (≈ 36 ppm) within a measurement time of 1 sec.

4 Conclusions

We have presented a general concept combining point sensors with long-gauge length sensors to produce a versatile monitoring system for short and long gauge lengths.

As a short gauge-length sensor we discussed a Bragg grating interrogation scheme capable of addressing multiple gratings. The long gauge-length sensor described is a precision OTDR system monitoring the difference between multiple reflective points.

Both schemes have demonstrated high accuracy and should be suitable for monitoring both static and dynamic signals. Each approach uses a simple optical setup and sophisticated signal processing to achieve a robust sensor system.

5 Acknowledgements

Initial work on this contract was funded by the Optoelectronics Research Centre (ORC) at Southampton University and the European Space Agency (ESA). The ORC is a UK government funded interdisciplinary research centre. The authors would also like to thank Mr R. Heath-White of Laser Service, Ltd. for the loan of the AOTF manufactured by Crystal Technology Inc.

The authors gratefully acknowledge funding during the last two years under a programme sponsored by Westland Aerospace, the UK Department of Trade and Industry (DTI), and the Engineering and Physical Science Research Council (EPSRC).

References

1. Measures R M, "Smart composite structures with embedded sensors", *Composites Engineering*, 1992, vol 2, no 5-7, pp 597-618

2. Dakin J P, "Multiplexed and distributed optical fibre sensor systems", *Journal of Physics, E: Scientific Instrumentation*, 1987, vol 20, pp 954-967

3. Meltz G, Morey W W, Glenn W H, "Formation of Bragg gratings in optical fibers by a transverse holographic method", *Optics Letters*, 1989, vol 14, no 15, pp 823-825

4. Eaton N C, "Studies of mechanical effects of optical fibre sensors in composite material", *European Space Agency Symposium on Advanced Materials*, 1994, Nordwijk, Netherlands

5. Melle S M, Liu K, Measures R M, "A passive wavelength demodulation system for guided-wave Bragg grating sensors", *IEEE Photonics Technology Letters*, 1992, vol 4, no 5, pp 516-518

6. Davis M A, Kersey A D, "All-fiber Bragg grating strain-sensor demodulation technique using a wavelength-division coupler", *Electronics Letters*, 1994, vol 30, no 1, pp 75-77

7. Kersey A D, Berkoff T A, Morey W W, "High-resolution fibre-grating based strain sensor with interferometric wavelength-shift detection", *Electronics Letters*, 1992, vol 28, no 3, pp 236-238

8. Kersey A D, Berkoff T A, Morey W W, "Fibre Fabry-Perot demodulation for Bragg grating strain-sensors", *Proceedings OFS (9)*, 1993, Florence, pp 39-42

9. Jackson D A, Ribeiro A B L, Reekie L, Archambault J L, Russell P St J, "Simultaneous interrogation of fibre optic grating sensors", *Proceedings OFS(9)*, 1993, Florence, pp 43-46

10. Melle S M, Alavie A T, Karr S, Coroy T, Liu K, Measures R M, "A Bragg grating-tuned fibre laser strain sensor system", *IEEE Photonics Technology Letters*, 1993, vol 5, no 2, pp 263-266

11. Xu M G, Geiger H, Archambault J L, Reekie L, Dakin J P, "Novel interrogation system for fibre Bragg grating sensors using an acousto-optic tunable filter", *Electronics Letters*, vol 29, no 17, p 1510f

12. Chang I C, "Acousto-optic tunable filter", *Optical Engineering*, 1981, vol 20, no 6, pp. 824-829

13. Xu M G, Geiger H, Archambault J L, Reekie L, Dakin J P, "Novel frequency-agile interrogating system for fibre Bragg grating sensors", *Proceedings SPIE*, 1993, vol 2071, pp 59-65

14. Hartog A H, Conduit A J, Payne D N, "Variation of pulse delay with stress and temperature in jacketed and unjacketed optical fibres", *Optical & Quantum Electronics*, 1979, vol 11, pp 265-273

15. Zimmermann B D, Claus R O, Kapp A A, Murphy K A, "Fiber-optic sensors using high-resolution optical time domain instrumentation systems", *Journal of Lightwave Technology*, 1990, vol 8, pp 1273-1277

16. Butter C D, Hocker G B, "Fiber optics strain gauge", *Applied Optics*, 1978, vol 17, no 18, pp 2867-2869

17. Healey P, "Instrumentation principles for optical time domain reflectometry", *Journal of Physics E: Scientific Instrumentation*, 1986, vol 19, pp 334-341

18. McDonald M D, Millicker D J, Nordblom S W, "A silicon-bipolar chip set for fiber-optic applications to 2.5 Gbit/s", *IEEE Journal on selected areas in communications*, 1991, vol 9, no 5, pp 664-672

19. Okado K, Hashimoto K, "Optical cable fault location using correlation technique", *Electronics Letters*, 1980, vol 16, no 16

20. Rao Y J , Uttamchandani D, Culshaw B, Steer P, Briancon J, "Spread-spectrum technique for passive multiplexing of reflective frequency-out fibre optic sensors exhibiting identical characteristics", *Optics Communications*, 1993, vol 96, pp 214-217

21. Newton S A, "A new technique in optical time domain reflectometry", *Optoelektronik Magazin*, 1988, vol 4, no 1, pp 21-33

22. Kersey A D, Dandridge A, Davis M A, "Low-crosstalk code-division multiplexed interferometric array", *Electronics Letters*, 1992, vol 28, no 4, p 351f

Finite Element Analysis of Embedded Optical Fibre Sensors

NC Eaton[1], RC Drew[2], H Geiger[3], P Chivers[4], JP Dakin[3].

[1] Consultant to Westland Aerospace, 16 Kings Road, East Cowes, PO32 6SE, UK

[2] Duetto Ltd, PO Box 396, Southampton, SO16 3ZA, UK

[3] ORC, University of Southampton, Southampton, SO9 5NH, UK

[4] Westland Aerospace, East Cowes, PO32 6RH, UK

Abstract

Micromechanical Finite Element (FE) analysis was used to model stress and strain fields in and around embedded optical fibres (EOF's) in flexural test coupons of carbon fibre composite. The coupons were used in studies of EOF effects on macroscopic laminate properties[1]. The FE method allows complex material inhomogeneities, laminate boundaries and load conditions to be modelled.

Finite Element Analysis

Other researchers have modelled EOF's using FE analysis[2]. The work presented here goes further since: i) much higher element densities are used, allowing detailed resolution of the stress and strain fields in the OF core, ii) realistic representation of boundaries, plies and loads are used, iii) component stresses and strains (σ_x, σ_y,τ_{xy}, ε_x,ε_y) allow OFS response to be predicted, iv) all general types of local laminate disruption are considered.

The models are based on measurements from real microstructures. The laminate consists of 8 woven carbon plies (5-harness textile type). Each ply is approximated by two layers of orthogonal carbon fibres. Three microstructure types arise from details of laminate construction and EOF orientation. Fig 1 type shows the OF embedded between adjacent plies consisting of carbon fibres aligned orthogonally at 0° and 90° to the OF axis. If carbon fibres in adjacent plies are parallel, Fig 2 type results when carbon fibres are at 90°, and Fig 3 type when carbon fibres are at 0° to the OF axis. In the Fig 2 type microstructure a resin pocket exists either side of the EOF.

3-point bend tests were simulated where the model contained representative laminate boundary conditions and laminate dimensions, values and positions of applied loads, and position of the EOF. In the models presented here the EOF is in the mid-plane; models with the EOF in other positions will also be analysed. Tension, compression and shear test models are planned. Model accuracy is being checked by EOF Bragg grating measurements.

The OF and coating was modelled using triangular elements, with a mesh density which decreased with radial distance from the OF centre. The laminate was modelled using quadrilateral elements. An OF core region (diameter 10 μm) was defined. FE models (no loads applied) representing type 2 & 3 microstructures are shown in Figs 4-5 where shades are used to distinguish regions. Laminate properties are based on a mixture of uni-directional and woven fibre composite properties (both with AS4 carbon fibre in 3501 epoxy resin). The EOF modelled was a 125 μm o.d. silica OF with a 155 μm o.d. polyimide coating.

Shear stress is plotted in Fig 6 and corresponding shear strain is plotted in Fig 7. In both figures shades indicate relative values. A full set of results will be presented, but are not reproduced due to space limitations. Shear stress distribution in the laminate and the OF is modified by the EOF. Higher stresses exist in the OF and at localised points in the laminate.

1. Eaton, N. *Studies of Mechanical Effects of Optical Fibre Sensors Embedded in Composite Materials.* European Space Agency Symposium on Advanced Materials, Noordwijk, 1994.

2. Davidson, R, Roberts, S. *Finite Element Analysis of Composite Laminates Containing Transversely Embedded Optical Fiber Sensors* First European Conference on Smart Structures and Materials, Glasgow, 1992.

0-8194-1700-9/94/$6.00

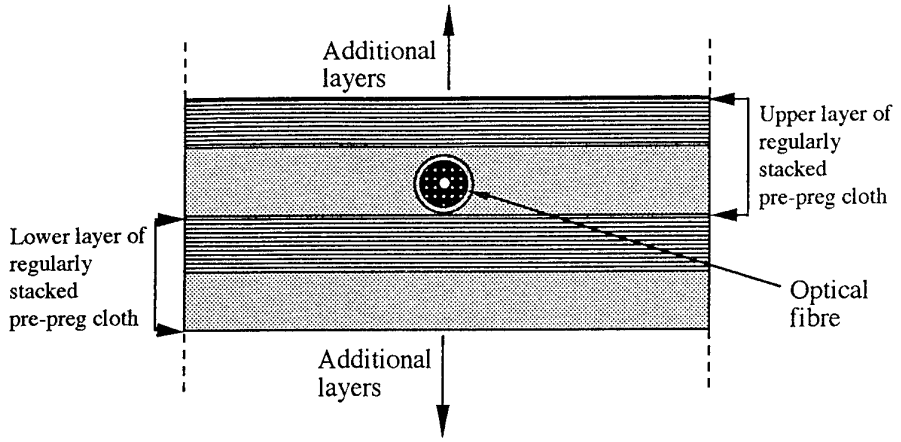

FIGURE 1

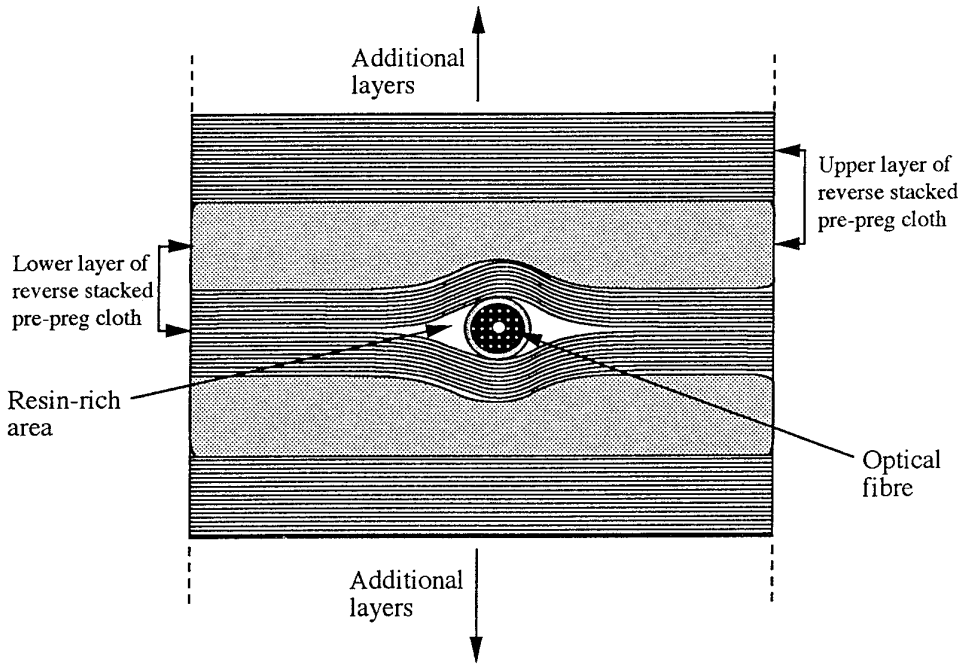

FIGURE 2

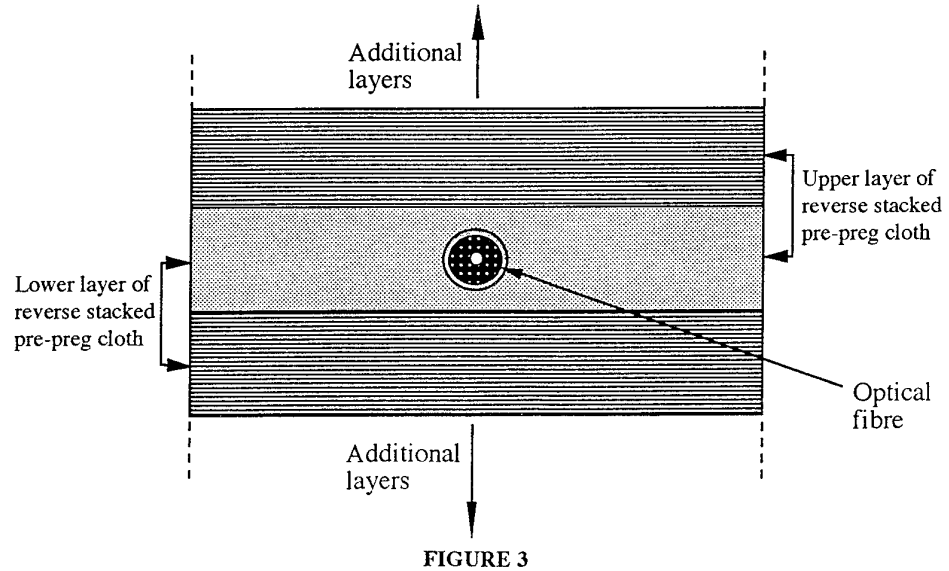

FIGURE 3

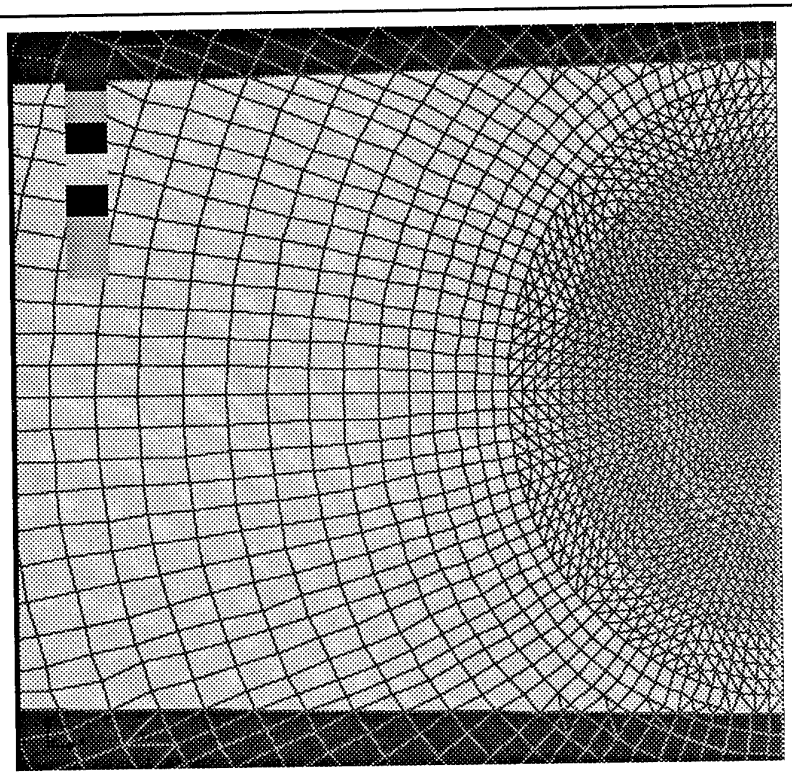

Fig. 4: FE model of type 2 microstructure

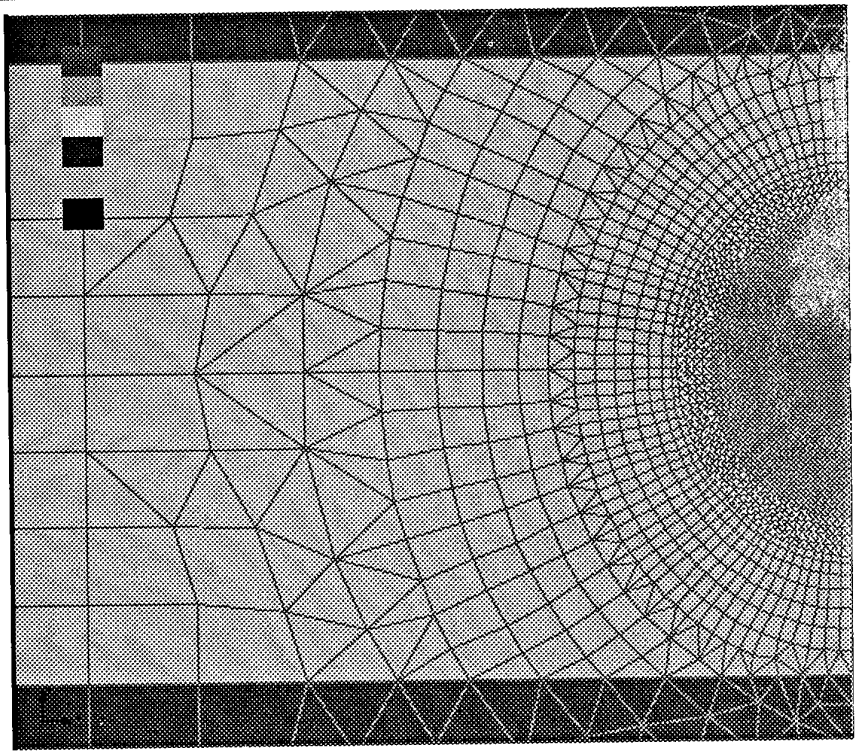

Fig. 5: FE model of type 2 microstructure

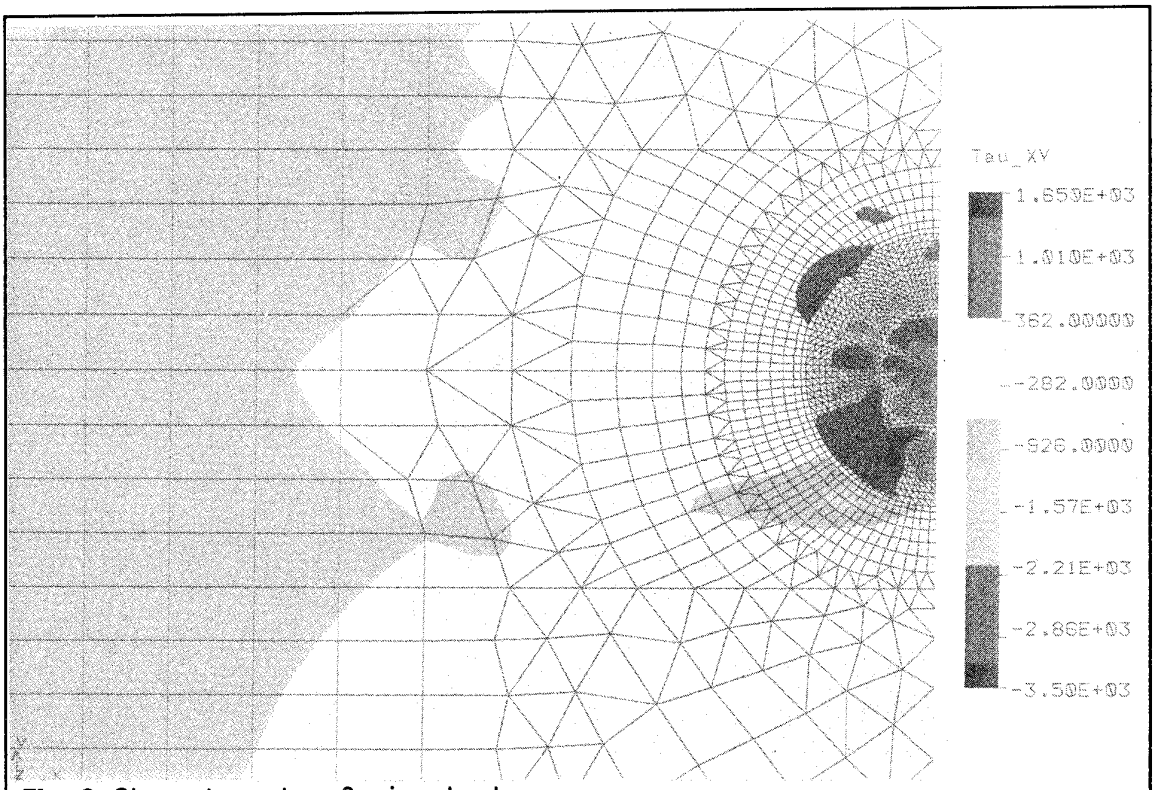

Fig. 6: Shear stress, type 3 microstructure

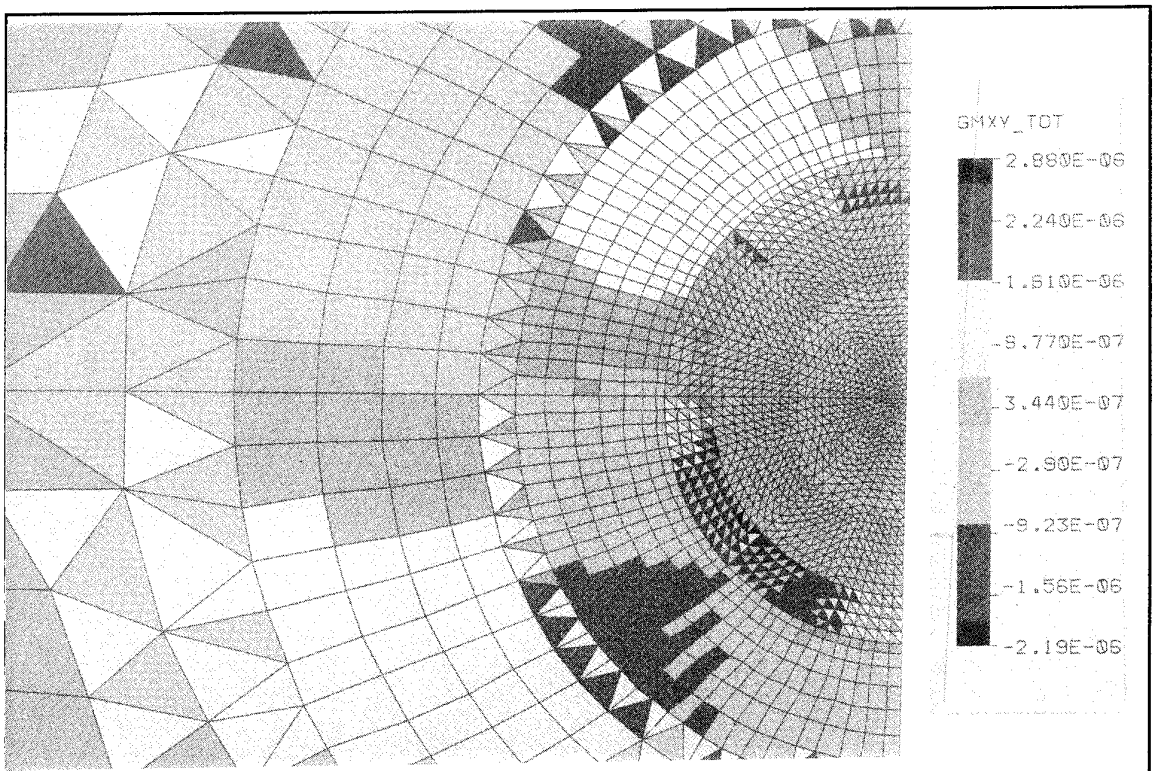

Fig. 7: Shear strain, type 3 microstructure

SMART INTEGRATED TRANSDUCER FOR AN OPTOELECTRONIC (BIO-) CHEMICAL SENSOR

Anatolij A. Beloglazov, Petr I. Nikitin

General Physics Institute of Russian Academy of Sciences
38, Vavilov st., Moscow 117942, Russia
Fax: (095) 135-0270 E-mail: bel@sens.gpi.msk.su

The problem of chemical and biological sensing, i.e., identification of components of various media and measuring their concentrations, is of extreme importance in science, technology, medicine, environmental monitoring, etc.

Principally, the problem could be solved by means of purely optical methods, particularly, tunable diode laser spectroscopy [1]. Due to the spectral resolution by an order or two of magnitude higher than Doppler width of spectral lines, it provides ideal selectivity and suitable sensitivity in gas sensing. However, such techniques require bulk, expensive laboratory equipment and qualified personnel. This results in a very high cost of analysis and makes the method unsuitable from the commercial standpoint.

A known alternative approach to the problem of media analysis is sensing by microelectronic tools, mainly, through change of resistance or capacitance of semiconducting bulk or thin film samples [2]. Such sensors are rather sensitive, cheap, batch-fabricated, relatively simple in operating and, hence, are most advantageous from a practical point of view. But the problems of selectivity, stability and reproducibility of the microelectronic sensors seem to be hardly solved in the near future.

In this connection, the development of new principles of sensors is an urgent need. One of the most powerful tools for both chemical and biological sensing is surface plasmon resonance (SPR) technique. Surface plasmon (SP) is a TM polarized electromagnetic wave which exists at a conductor - dielectric interface and can be optically excited in a resonant manner by means of either a prism in the total internal reflection (TIR) configuration or a grating on the conductor surface [3]. The wave decays exponentially to both sides from the interface and the conditions of SP excitation (angle of incidence of exciting radiation or its wavelength) are extremely sensitive to the properties of a medium near the interface.

During the last decade, the Kretschmann technique [4] of SP excitation in the TIR arrangement has been widely used as a base of various sensors. In the work by Liedberg et. al. [5], gas sensors and biosensors based on SPR were proposed. In this method, the position of the intensity minimum of radiation reflected by a metal film covering a prism and contacting with a tested medium is measured. The capability of monitoring media changes corresponding to its refraction index shift Δn as small as 10^{-5} was reported. In a case of a sucrose solution testing, the resolution as high as 24 - 65 ppm (Δn at the level of 10^{-6}) was achieved [6].

However, a sensor relied on the TIR technique of SPs exciting is, substantially, a purely optical one with all intrinsic drawbacks of its practical applications. In particular, one of disadvantages is the necessity of a reflecting beam registration. Such a sensor has to include either a mechanical angular scanning system with a reflected light spot displacement compensation or a photodetector matrix registering the divergent reflected beam passed through a special optics. It makes an overall device rather complicated and expensive, and, in a number of cases, restricts the device's capabilities and the area of possible applications.

In Ref. [7] another conception of SPR (bio-) chemical sensors was proposed for the first time, namely: information is obtained in the form of an electric signal coming directly from a SP coupler, the latter being simultaneously a sensing element. A corresponding sensor's design is shown in Fig.1. A thin noble metal film (Ag, Au) is deposited onto a semiconducor (GaAs, Si) grating surface to form a Schottky barrier interface. A resonant enhancement of the photo-e.m.f. generated in the Schottky barrier structure takes place when SPs are resonantly excited on the metal film grating surface of the structure. The SPs are scattered into the

0-8194-1700-9/94/$6.00

semiconductor due to the evanescent wave at the metal/semiconductor interface, giving rise to electron-hole pairs generation. Thus, for a definite angle Θ of a laser diode radiation incidence there is a narrow-shaped resonant maximum of a photosignal from the Schottky barrier connected with a measuring circuit as a photoelement or a photodiode.

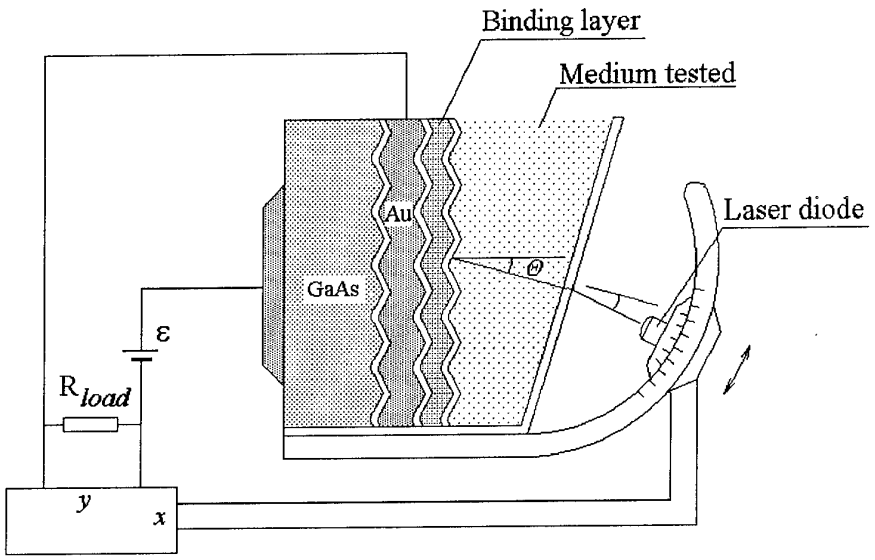

Fig.1

The sensing effect, as in a conventional SPR-based transducer, results from a change of the refraction index n of the medium to be tested and/or the binding layer. But, by contrast, the SPR position is affected not only by the value of the SP wave vector but by the incident light wave vector component parallel to the metal surface as well. Hence, they both contribute to the sensor sensitivity. For a simple refractometer (without binding layer), these two contributions to the voltage sensitivity correspond to the second and first terms of the following formula:

$$\frac{dV}{dn} \approx -\frac{1}{n}\cdot[\cos\Theta\cdot\sin\Theta+\cos\Theta\cdot(\frac{|\varepsilon'_m|}{|\varepsilon'_m|-n^2})^{3/2}]$$

where ε'_m is a real part of a metal permittivity at the light frequency ($\varepsilon'_m < 0$, $|\varepsilon'_m| > n^2$). For real Schottky photodiodes with a signal maximum 1 V, optimization of a grating period gives a response $\Delta V = 2.8$ mV for $\Delta n = 10^{-5}$.

The proposed integrated transducer enables us to combine advantages of all the approaches mentioned above, namely:

a) As conventional types of SPR sensors, the proposed one is applicable for testing gas and liquid media containing both chemical and biological components. It has no destructive action on a medium. Proper selectivity of the sensor can be achieved by using an adequate binding layer. Such a layer provides volume or surface reactions with analyte particles, binding them in a selective manner. Typical examples are reactions of phthalocyanines with nitrogen oxides [8] and antigen-antibody coupling [9], respectively.

b) The transducer proposed is simply an optoelectronic pair consisting of a diode laser radiation source and a Schottky photodetector. It is compatible with conventional microelectronics technologies and, hence, it could be cheap and batch-fabricated.

c) As in conventional laser spectroscopy, our transducer's design provides interaction of laser radiation with tested medium component molecules in the volume or adsorbed on a surface of a binding layer. This

enables to excite them in a highly selective manner, particularly, to produce free atoms and radicals. Such a selective excitation of the tested medium component, as well as photo-induced modification of the surface of a special binding layer, can initiate a reaction of coupling of analyte molecules on the layer surface. It is known, that sensing of excited molecules, free atoms and radicals (instead of particles in a ground state) increases the sensitivity of measurements by several orders of magnitude [10].

The transducer proposed is, in fact, a smart structure which converts directly refraction index or desired component concentration of a medium to the electric signal.

In our experiments, Ag/GaAs Schottky structure with the grating period of 460 nm, laser diode and He-Ne laser at the wavelengths 670 and 630 nm, respectively, were used. The SPR maximum photosignal to the background ratio was 7:1 and FWHM was 0.3°. The refraction index resolution at the level of 10^{-5} - 10^{-6} has been achieved in cases of air, ethyl alcohol and sucrose solutions in water. Corresponding resolution of a sucrose water solution concentration was 0.01%. Regimes of sucrose concentration to the photodiode signal conversion are illustrated in Fig.2; (a) shows a regime with fixed concentrations and scanned incidence angle while (b) corresponds to a fixed angular position and variable concentrations. In the last case, there is a linear range at small concentrations with a sensitivity 40 mV/percent. The linear range was moved along the concentration axes by angular adjustment.

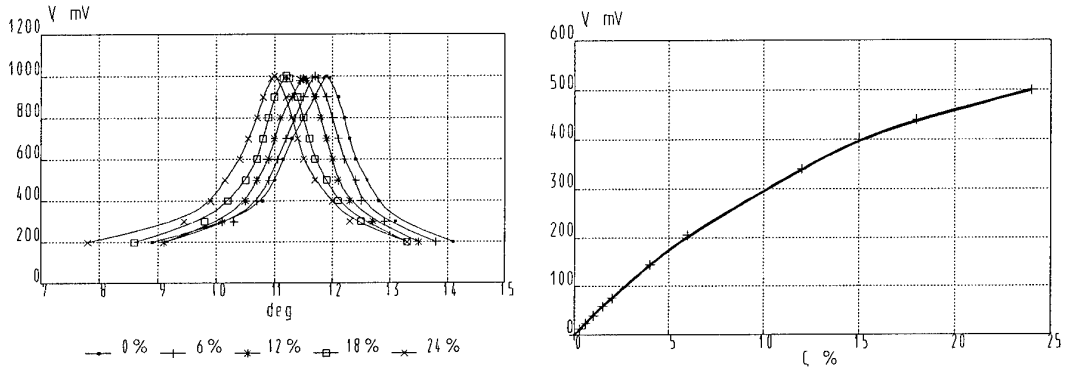

a) b)

Fig.2

The work on binding layer development and improving SPR properties of Schottky structures is under way now. In our opinion, the transducer proposed could be widely used for high sensitivity and broad dynamic range concentration measurements in organic and inorganic media as a smart sensing structure.

ACKNOWLEDGEMENT

The work was supported by the Russian Foundation of Fundamental Research under Grant No.93-02-15720.

REFERENCES

1. A.I.Nadezhdinski, Modern trends in diode laser spectroscopy, *SPIE,* vol. 1724 Tunable Diode Laser Applications (1992) 2-17 and references therein.

2. P.T.Moseley, Materials selection for semiconducting gas sensors, *Sensors and Actuators B*, 6 (1992) 149-156.

3. G.N.Zhizhin, M.A.Moskaleva, E.V.Shomina and V.A.Yakovlev, in V.M.Agranovich and D.L.Mills (eds.), *Surface Polaritons*, North-Holland, Amsterdam, New York, Oxford, 1982, Ch.3, p.93.

4. E.Kretschmann, Die Bestimmung optischer Konstanten von Metallen durch Anregung von Oberflachenplasmaschwingungen, *Zeitschrift fur Physik*, 241 (1971) 313-324.

5. B.Liedberg, C.Nylander and I.Lundstrom, Surface plasmon resonanse for gas detection and biosensing,

Sensors and Actuators, 4 (1983) 299-304.

6. F.Villuendas and J.Pelayo, Optical fibre devices for chemical sensing based on surface plasmon excitation, *Sensors and Actuators*, A21-A23 (1990) 1142-1145.

7. P.I.Nikitin and A.A.Beloglazov, A multi-purpose sensor based on surface plasmon polariton resonance in a Schottky structure, *Sensors and Actuators A*, 42 (1994) 547-552.

8. J.P.Lloyd, C.Pearson and M.C.Petty, Surface plasmon resonance studies of gas effects in phthalocyanine Langmuir-Blodgett films, *Thin Solid Films*, 160 (1988) 431-443.

9. S.Lofas, M.Malmqvist, I.Ronnberg, E.Stenberg, B.Liedberg and I.Lundstrom, Bioanalysis with surface plasmon resonance, *Sensors and Actuators B*, 5 (1991) 79-84.

10. E.E.Gutman, Space and aircraft sensors, *Book of Abstracts "Eurosensors VII", Budapest* 1993, 15-17.

ANALYSIS OF THE LOCAL STRESS FIELD IN A COMPOSITE MATERIAL WITH AN EMBEDDED EFPI-SENSOR

Klas Levin & Sören Nilsson

FFA, The Aeronautical Research Institute of Sweden, Box 11021, S-161 11 Bromma, Sweden

ABSTRACT: Finite element analysis has been performed to determine the local stress field in a tensile loaded composite specimen with an embedded EFPI-sensor. The sensor/coating and the coating/composite interfaces have been distinguished as the sites where failure is initiated due to stress concentrations caused by the cavity in the EFPI-sensor. An increase in the strength of the interfaces is an important task to improve the reliability of embedded sensors.

1. INTRODUCTION

One of the most important tasks in achieving an optimal and reliable performance of embedded optical fibre sensors in aircraft health monitoring systems is to clarify the influence of the mismatch of geometrical and mechanical properties on the sensor-host interaction. A sensor which is a strong candidate for use in such a system is the extrinsic Fabry-Perot interferometer, EFPI, sensor. However, experimental and analytical investigations of traditional EFPI-sensors have demonstrated that stress concentrations at different positions in the sensor can cause premature damage followed by a loss of function of the sensor under realistic loading conditions. A new sensor has therefore been developed [1] which is tailored to reduce the effect of the geometrical mismatch between the sensor and the composite materials.

This paper concerns the new improved design of the EFPI-sensor. To determine the critical regions for damage initiation, finite element analyses have been performed of the improved EFPI-sensor embedded in a tensile loaded composite specimen. In order quantitatively to determine the fracture mechanisms and locations, different failure criteria have been applied to the complex three-dimensional stress field evaluated. It is essential to determine the effect of the curing process on the material-sensor system. A local microstructure occurs in the composite as a result, changing the stresses in the sensor-coating and coating-composite interphases. The local fibre volume content was determined and used in the computational modelling of the composite material. Applying this approach to obtain the microstructure elasticity characteristics is thought to improve the accuracy of the calculation of the host material-sensor interaction.

2. FINITE ELEMENT MODEL

The configuration analysed was a specimen with a length of 120 mm and a width of 24 mm cut from a cross-ply laminate which consisted of 20 plies $(0_2/90_2/0_2/90_2/0_2)_s$, with the optical sensor embedded in the central layer parallel to the fibre direction. The material used in the specimen was Fiberdux 6376/HTA with typical elastic properties for carbon-fibre-reinforced epoxy materials. The geometry of the sensor is shown in Fig 1 including a 3 μm thick polyimide coating. The design and manufacture of the EFPI-sensor studied is further presented in [1].

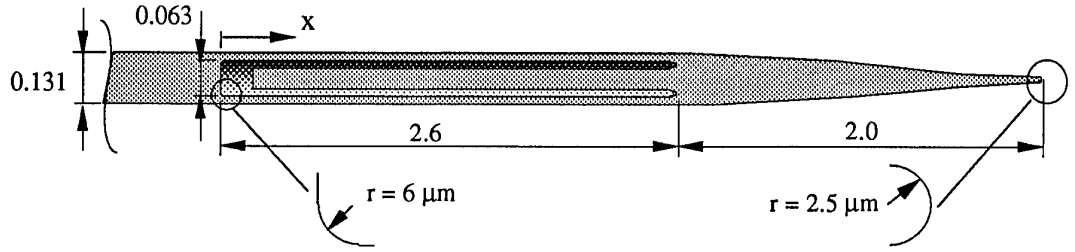

Fig. 1 Geometry of the sensor. Dimensions in mm.

A FE-mesh of the specimen was created to permit the stresses in the sensor and the surrounding material to be analysed. For reasons of symmetry, only a quarter of the specimen was modelled. Perfect bonding between the sensor, the coating and the composite material was assumed. Material data used in the analyses were: for the sensor and polyimide coating; E_{glass} = 70 GPa and ν_{glass} = 0.16, $E_{polyimide}$ = 3 GPa and $\nu_{polyimide}$= 0.3 and for the composite material; E_{11} = 145 GPa, $E_{22} = E_{33}$= 10.5 GPa, $G_{12} = G_{13}$ = 5.25 GPa, G_{23} = 3.3 GPa, $\nu_{12} = \nu_{13}$ = 0.3 and ν_{32} = 0.60. The FE-mesh consisted of a total of 466 20-noded elements and 171 15-noded elements. The load was applied as a uniform displacement in the length direction generating a uniform tensile strain of 0.25%. Initial experiments indicated by a discrepancy in the output signal from the sensor at this strain level that failure had been initiated in the interface between the sensor and the coating.

The compacting process during the curing can be described as that the plies are compacted in subsequent steps from the top to the bottom, in which resin flow occurs both parallel and normal to the plies [2]. Such a process is expected prevail in autoclaving. The waviness of the carbon fibres significantly contributes to their decreased movability around the optical fibre during curing. As a consequence, the formation of a matrix-rich region along the

0-8194-1700-9/94/$6.00

obstructive optical fibre is promoted by the resin flow parallel to the carbon fibres, whereas at the top of the optical fibre the carbon fibres are not obstructed to the same extent. Consequently, the variation in fibre volume content around the optical fibre can be expected not to be uniform. To evaluate the detailed distribution of the fibre volume content around the polyimide-coated optical fibre in terms of local averages, multiple samples were taken from laminates at equivalent distances along the length of the optical fibre. In an image analysis software, the magnification was chosen so that one pixel corresponded to approximately 0.5 x 0.5 μm. The image windows consisted of 16 by 16 pixels. In the digitized image the carbon fibre and matrix phase are identified on the basis of their different grey levels. A further description of the experimental procedure is given in [3]. The location of each symbol in Fig 2 corresponds to the coordinate in the centre of the image window. There is clearly a region adjacent to the optical fibre where fibre volume content is lower than the nominal value indicated in the figure by the continuous line. The extent of the region with low fibre volume content is dependent on the direction. An approximately elliptical circumferential distribution of the fibre volume content around the embedded optical fibre was found. The region does not extend as far in the vertical direction as in the horizontal direction. The region was estimated to extend about 20 μm and 8 μm in the horizontal and vertical directions respectively.

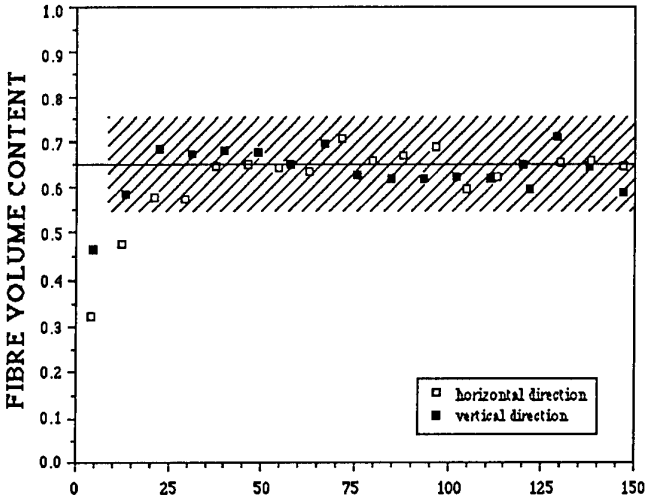

Fig 2 Distribution of the fibre volume content

From the spatial variation of the fibre volume average together with the elastic properties of the constituents, an estimate of the distribution of elastic properties in terms of local averages was obtained. The prediction of the effective stiffnesses follows a scheme based on self-consistent micromechanical theory [4]. A simple approach was taken in the finite element model, where the gradient in the elastic properties around the optical sensor was assumed to change stepwise. In each step, the elastic constants were set equal to the elastic properties corresponding to the fibre volume content in the centre of the element. To take into account the circumferential variation in fibre volume, the size of the elements was gradually changed around the sensor to fit the fibre volume distribution determined

3. FAILURE CRITERIA

The stress/strength ratios in the glass and polyimide coating were determined using the failure strengths for silica glass σ_{glass}= 6000 MPa and polyimide $\sigma_{polyimide}$ = 131 MPa [5,6]. From the consideration that the load direction corresponded to the fibre direction in the ply with the embedded sensor, the tensile fibre failure criterion due to Hashin [7] was applied: $R^2 = \left(\sigma_{xx}^2 / X^2\right) + (\sigma_{xy}^2 + \sigma_{xz}^2)/S^2$ where R, X and S denote the stress/strength ratio, tensile strength and shear strength respectively. The stress/strength ratio indicates the margin to failure for the predicted failure mode. Failure occurs when R = 1. In this analysis, the strength values were X = 2090 MPa and S = 131 MPa [8].

The average values of the continuous stresses across the interface were calculated in the sensor and the coating at points close to the interface. These average values were used in the failure criterion:

$R_{int}^2 = \left(\sigma_{rr} / Y_{int}\right)^2 + \left(\sigma_{r\theta}^2 + \sigma_{xr}^2\right) / S_{int}^2$ where R_{int}, Y_{int} and S_{int} are the stress/strength ratio in the interface, the interface tensile strength and shear strength respectively. The interface shear strength S_{int} was determined to be approximately 18 MPa for the sensor/polyimide coating interface, whereas the interface tensile strength was determined to be 13.3 MPa from the initial experiment, using the result from this FE-analysis and applying the given failure criterion. The same interface strengths as for the glass/polyimide interface were arbitrarily assumed for the coating/composite interface due to lack of definitive data.

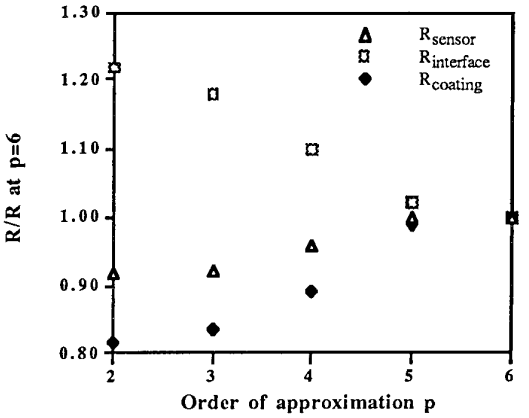

Fig 3. Convergence of the solution

4. RESULTS AND DISCUSSION

The analyses were performed using the self adaptive FE-code STRIPE [9]. During the analysis, the order of approximation *p* in each element was increased up to a given maximum value. By studying the stresses at each *p*-level, it was possible to evaluate the convergence of the solution. Although the

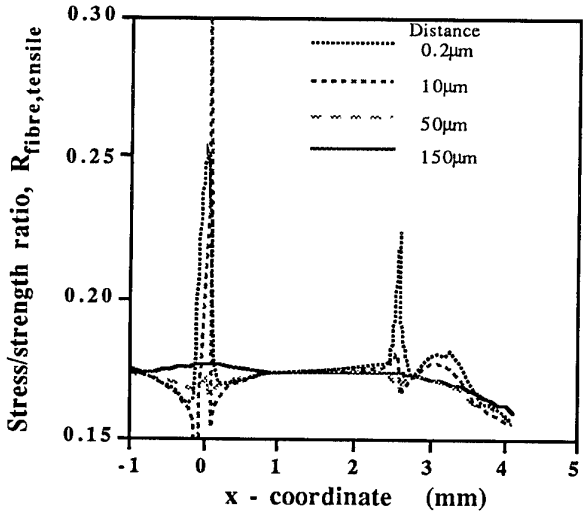

Fig. 4 Stress/strength ratio in the composite. Coordinate system is defined in Fig.1

FE-mesh was rather coarse where some of the elements had a high geometrical aspect ratio a good convergence of the solution was obtained when the analysis was performed with p=6. This is illustrated in Fig. 3, where the convergence is shown at the location where the largest stress/strength ratios occurred in the sensor, in the sensor/coating interface and in the polyimide coating. The difference in the numbers between the iterations p=5 and p=6 was less than 3 %. The number of degrees of freedom was 78 770 at the highest order of approximation.

In Fig. 4, the variation of the stress/strength ratio for tensile fibre failure in the composite material along the sensor is shown at four different distances from the coating/composite interface in the mid-plane of the specimen. Close to the sensor there are two distinct stress concentrations extending only a few tens of microns. These coincide with the locations of the ends of the cavity in the sensor as a result of the abrupt change in local stiffness in the sensor. The longitudinal stress in the sensor has to be transferred from the solid glass fibre to the part of the sensor with a cavity. At 10 μm from the composite/coating interface, the stress/strength ratio is at its maximum. Further from the sensor it is observed that the peaks vanish and have almost completely disappeared as close as 150 μm from the interface. The largest stress/strength ratio is 0.30 which is 1.7 times greater than the stress/strength ratio far from the sensor. There is a good margin for fibre failure in the composite. Therefore, this failure mode is not particularly significant for the performance of the sensor system.

In Figs 5 & 6, the stress/strength ratios are given close to the interface along lines in the mid plane of the specimen within the sensor and the coating. Two stress concentrations can be observed in the same region as for the composite. A significant reduction in the maximum stress/strength ratio in the polyimide is observed when stiffness variation is included in the FE-model, whereas the influence on the stress/strength ratio in glass can be ignored. Despite the complex sensor geometry, the margin to failure is of the order of 6-8, although it should be noted that the failure strength in the sensor is locally reduced due to the heat-induced stresses in the fused zones. However, the tensile strength of the sensor was determined to be substantially larger than the strain level in this analysis [1].

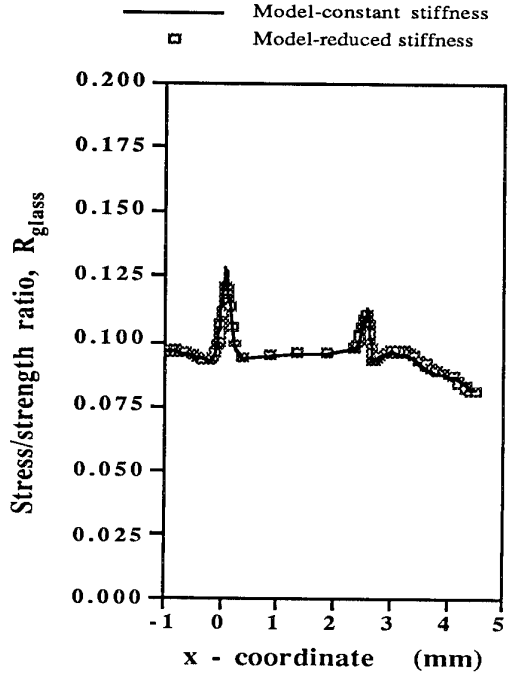

Fig. 5 Stress/strength ratio in the sensor close to the sensor/coating interface

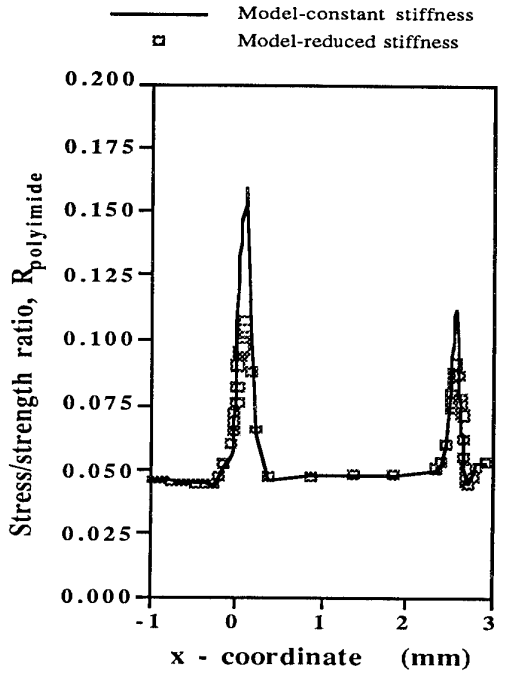

Fig. 6 Stress/strength ratio in the polyimide coating close to the sensor/coating interface

The results for the sensor/coating interface are presented in Fig 7 as a stress/strength ratio plot along a line parallel to the sensor in the mid-plane of the specimen. Two stress concentrations are present in the regions corresponding to the ends of the cavity in the sensor. The highest stress/strength ratio decreased by approximately 9 % when the stiffness was stepwise reduced in the analysis. The stress distribution due to the variation in fibre volume content around the optical fibre was only slightly affected. The stress/strength ratio for the polyimide/composite interface showed similar behaviour, although the peaks were slightly lower. However, this result is an estimation because the same strength data has been applied as for the sensor/polyimide interface. An important observation was that, in tensile loading, the radial stress across the interface is tensile. A sign reversal as occurs in compressive loading can be helpful in avoiding interfacial debonding.

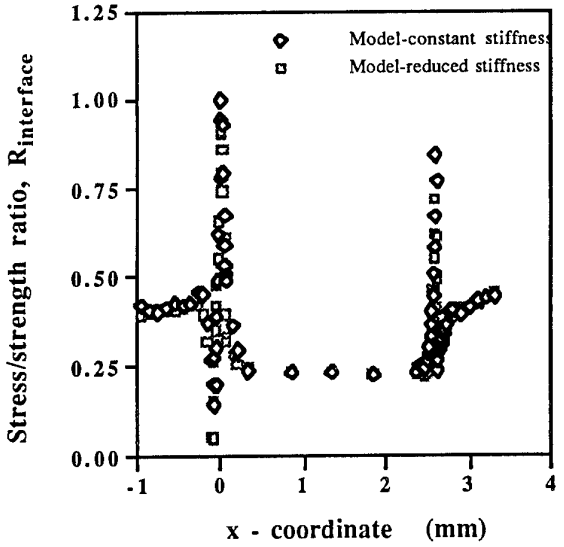

Fig. 7 Stress/strength ratio for the sensor/polyimide interface.

The stress analyses have identified that the cavity in an EFPI-sensor creates large stress concentrations. Within the sensor and the composite material they are rather small and they decay at a short distance, i.e. 150 μm, from the sensor. As a result an embedded sensor affects only a small area around its location and cannot significantly alter the global stress distribution. The narrowly extended stress peaks are a source of failure in the interface between the sensor and the polyimide coating. When the interface has failed, the accuracy of the measured signal declines, resulting in a loss of function of the sensor. To further improve the mechanical performance of embedded EFPI-sensors in a composite material it is necessary to increase the strength of the interfaces. However, the levels of the stress concentrations in the interface are uncertain due to the assumption of linear elasticity in the analysis. If a viscoelastic material model for polyimide had been used in the analysis, the stress concentration would have been decreased. The assumption of perfect bonding is also an idealization. Due to relaxation and micro-debonding, the stress transfer across the interfaces is not perfect. Moreover the results indicate that the stress concentrations are reduced if the radii of the cavity inside the sensor are increased and the diameter of the cavity is decreased. The possibility of achieving a smoother transition of stresses in the sensor is however limited due to a number of factors such as requirements with regard to manufacturing and sensor function.

ACKNOWLEDGMENT

The reported work is part of a joint project on Smart Composite Structures sponsored by the FMV- Defence Materiel Administration, Sweden. The joint group consists of; FFA-The Aeronautical Research Institute of Sweden, ONERC-Optical Network Research Center of Ericsson Business Network, Sweden, Electr.Eng., Virginia Tech, USA, IOF-Institute of Optical Research, Sweden. The project is technically directed and coordinated by Dr. P.Sindelar, FFA.

REFERENCES

[1] Henriksson, A & Brandt, F., "Design and manufacturing of an EFPI-sensor for embedding in carbon/epoxy composites," submitted to 10th Optical Fibre Sensors Conference, Oct 1994, Glasgow

[2] Tang, J-M., Lee,W.I., and Springer,G.S.,"Effects of Cure Pressure on Resin Flow, Voids, and Mechanical Properties, "Journal of Composite Materials, Vol. 21, May 1987

[3] Levin, K.& P. Sindelar, "Assessment of the fibre volume distribution around optical fibres," FFA TN 1993-12, 1993

[4] Siboni, G., "Prediction of the effective elastic properties of multiphase composite media with orthotropic constituents," Composites Science and Technology, Vol 50, pp 293-298, 1994

[5] Handbook of composites, vol 1, Strong fibers, Editor. W.Watt&B.V.Perov Elsevier Science Publishers B.V. 1985

[6] DuPont material data sheet.

[7] Hashin, Z., "Failure criteria for unidirectional fiber composites," Journal of Applied Mechanics, Vol 47, p239, June 1980

[8] Finn, S.R.&Springer, G., "Delaminations in composite plates under transverse static or impact loads -a model," Çomposite Structures, Vol 23, p177, 1993

[9] Andersson, B.&Falk, U.,."Self-adaptive analysis of three-dimensional structures using a p-version of finite element method," FFA TN 1987-31

Author Index

Abdul-Wahed, M. N., 346
Abdunur, Charles, 154
Adekola, Ade, 297, 320
Aiken, R., 258
Akerley, Steve, 258
Alavie, A. T., 162
Allaei, Daryoush, 152, 198
Ambrose, Timothy P., 148
Askins, Charles G., 338
Baier, H., 254
Barberis, Angelo, 220
Barboni, Renato, 71
Basedau, Frank, 168
Bashford, D. P., 264
Bellemore, D. G., 342
Beloglazov, Anatoli A., 375
Berkoff, Timothy A., 350
Blaha, Franz A., 277
Blanas, P., 358
Bonniau, Philippe, 236
Breitbach, Elmar J., 11
Burford, Mary K., 113
Burrows, A. P., 36
Butler, Raymond J., 109, 117
Carman, Gregory P., 113
Casciati, F., 206
Caussignac, Jean-Marie, 232
Chaudhry, Zaffir A., 273
Chauvel, D., 224
Chazelas, Jean, 236
Chivers, P. J., 366, 371
Churenkov, Alexander V., 362
Cioranescu, Doina, 75
Clark, D. T., 2
Claus, Richard O., 113
Coleman, James P., 301
Cruz, J. L., 354
Culshaw, Brian, 186, 236
Curtis, Iain L., 202
Dakin, John P., 354, 366, 371
Das-Gupta, D. K., 358
Davidson, Roger, 117
Davis, Michael A., 342
De Rossi, Danilo, 19
Dean, Peter D., 59
Dill, M. J., 202
Done, G. T. S., 242
Donti, R. P., 338
Doran, Conrad J., 98, 109
Drew, R. C., 371
Dry, Carolyn M., 324
Durkee, S., 282
Eaton, D. C. G., 264
Eaton, Nicholas C., 366, 371
Elamari, Adil, 216
Elspass, Wilfried J., 121
Escobar, Priscila, 220
Faravelli, L., 206
Flockton, Stuart J., 55
Florio, J., Jr., 338
Foote, P. D., 290
Fosha, A. A., Jr., 338
Friebele, E. Joseph, 338
Friend, Clifford M., 94
Fürstenau, Norbert, 286
Fuhr, Peter L., 148
Gardiner, Peter T., 186
Gattulli, Vincenzo, 67
Gaudenzi, Paolo, 71
Geiger, Harald, 366, 371
Giurgiutiu, Victor, 273
Glass, G. K., 172
Goetting, H. C., 286
Gordienko, Y. G., 312
Graham, Neil B., 31
Greene, Jonathan A., 113
Grenier, L., 277
Guerin, J. J., 224
Gusmeroli, Valeria, 220
Habel, Wolfgang R., 168, 176, 180
Hanahara, Kazuyuki, 51
Harrison, D. K., 63
Healey, R., 63
Höpcke, Monika, 168
Hofmann, Detlef, 176, 180
Huang, Shangyuan H., 162
Huston, Dryver R., 148
Inaudi, Daniele, 216
Inou, Norio, 47
Inoue, Yutaka, 190
Irgens, Fridtjov, 140
Irving, P. E., 128
Jänker, P., 80
Janzen, Douglas D., 286
Jensen, Alf E., 140
Jurczyszyn, M., 232
Kasai, T., 246
Kemp, Martin, 136
Kersey, Alan D., 342, 350
Komatsu, K., 246
Kuhns, W. W., 282
Kulagina, V., 102
Lammering, Rolf, 11, 90
LeBlanc, Michel, 162
Legrain, Isabelle, 250
Leonov, Yury, 102
Lequime, Michael, 224
Levin, Klas, 379

Leygonie, M., 224
Link, D., 63
Loiko, A. D., 362
Løkberg, Ole J., 140
Longstaff-Tyrell, M. A., 366
Lowet, G., 305
Lutinskaya, Marina, 102
Maaskant, Robert, 162
Martin, W., 80
Martinelli, Mario, 220
McDonach, Alaster, 316
McGown, A., 186
McKenzie, I., 186
Measures, Raymond M., 162
Melcher, Jörg, 11
Michie, W. Craig, 186, 236
Miesner, J., 258
Morabito, Paolo, 220
Morgan, Neil B., 94
Mosley, C. D., 338
Mukai, Yoichi, 190
Murphy, Kent A., 113
Muto, Norio, 27
Narkiewicz, J. P., 242
Nichols, Jeff, 316
Nikitin, Petr I., 375
Nilsson, Sören, 379
Nitzsche, Fred, 11
Noharet, B., 236
O'Regan, S., 258
Packman, A., 258
Page, C. L., 172
Paradies, R., 121
Petitjean, Benoît, 250
Pietsch, C. R., 254
Polster, Helmut, 168
Price, Cedric, 296
Putnam, Martin A., 338
Rastogi, Manit, 297, 320
Reed, P. A. S., 354
Reznichenko, Vladimir V., 102
Roberts, Scott S. J., 117
Robertson, Alec, 307
Rogers, Craig A., 273
Saint Jean Paulin, Jeannine, 75
Sano, M., 246
Schindler, K., 121
Schmidt, Walter, 286
Schütze, R., 286
Shimotai, Naoko, 47
Short, N. R., 172
Shuford, R. J., 358
Simonsen, Henrik D., 228
Sinclair, I., 354
Sirkis, James S., 330
Skorobogatyi, M. A., 362
Spies, Ruben D., 86
Spillman, William B., Jr., 282
Storøy, Helge, 140
Strambi, Giulio, 71
Sturland, Ian M., 128
Sugita, Minoru, 27
Sugiyama, Yoshihiko, 51
Sun, David, 113
Tachibana, Eizaburo, 190
Tardy, A., 232
Téral, Stephane, 232
Thiagarajan, C., 128
Thomas, M. D., 55
Thompson, Larry D., 132
Tomlinson, Geoffrey R., 36
Toppani, E., 224
Tran, Tuan A., 113
Tunnicliffe, D., 128
Turpin, Marc, 236
Udd, Eric, 210
Uesugi, Takefumi, 47
Unver, Erdal A., 258
Van der Perre, G., 305
Varadan, Vasundara V., 194
Varadan, Vijay K., 194
Voss, Karl F., 144
Vurpillot, Samuel, 216
Walsh, Douglas, 236
Wang, Gunnar, 140
Wanser, Keith H., 144
Weisshaar, Terrence A., 346
Wenger, M. P., 358
Westermo, Bruce D., 132
Worden, K., 36
Wu, W. Ben, 269
Xu, Ming-Gang, 366
Yanagida, Hiroaki, 27
Yao, T., 206
Zasimchuk, E. E., 312
Zhou, Erping, 63